Universitatea "Politehnica" din Bucureşti
DEPARTAMENTUL DE ELECTROTEHNICĂ

ASOCIAŢIA INGINERILOR ELECTRICIENI ŞI ELECTRONIŞTI DIN ROMÂNIA

Simpozionul Naţional de Electrotehnică Teoretică

National Symposium of Theoretical Electrical Engineering

SNET'12

VOLUMUL CONFERINŢEI

14 decembrie 2012

Facultatea de Inginerie Electrică

Universitatea "Politehnica" din Bucureşti

HTTP://SNET.ELTH.PUB.RO

ISSN 2067-4147 (online)

Copyright ©

Universitatea “Politehnica” din Bucureşti, DEPARTAMENTUL DE ELECTROTEHNICĂ

ASOCIAȚIA INGINERILOR ELECTRICIENI ŞI ELECTRONIŞTI DIN ROMÂNIA

COLECTIV AUTORI,

Revista LUCRĂRILE SIMPOZIONULUI NAŢIONAL DE ELECTROTEHNICĂ TEORETICĂ

Vol. 3, No. 1, <<Volumul conferinţei: Simpozionul Naţional de Electrotehnică Teoretică, 14 decembrie 2012, Universitatea “Politehnica” din Bucureşti>>

Bucureşti, Decembrie 2012

ISSN 2067-4147

EDITOR: MIHAI MARICARU

© Copyright

Toate drepturile asupra prezentului volum sunt rezervate organizatorilor conferinţei SNET 2012 şi autorilor. Nici o parte din acest volum nu poate fi reprodusă, stocată sau transmisă, indiferent prin ce formă, fără acordul prealabil, scris, al autorilor.

Universitatea "Politehnica" din Bucureşti
DEPARTAMENTUL DE ELECTROTEHNICĂ

ASOCIAŢIA INGINERILOR ELECTRICIENI ŞI ELECTRONIŞTI DIN ROMÂNIA

Simpozionul Naţional de Electrotehnică Teoretică

14 Decembrie 2012,

Facultatea de Inginerie Electrică

Universitatea *"Politehnica"* din Bucureşti

COORDONAREA CONFERINŢEI SNET'12

Preşedinte
Prof.dr.ing. Florea Ioan HĂNŢILĂ

Preşedinţe de onoare
Prof.dr.ing. Andrei ŢUGULEA, *membru titular al Academiei Române*

Comitetul ştiinţific
Prof. dr. ing. Valentin IONIŢĂ, *U.P.B., Preşedinte*
Prof. dr. ing. Petru ANDEA, *U.P.Timişoara*
Prof. dr. ing. Horia ANDREI, *U. Târgovişte*
Prof. dr. ing. Oszkár BÍRÓ, *T.U. Graz*
Prof. dr. ing. Gabriel BAZACLIU, *U.P.B.*
Prof. dr. ing. Ion BĂNICĂ, *U.P.B.*
Prof. dr. ing. Ioan CIRIC, *U. Manitoba, FIEEE, membru al Academiei de Electromagnetism, MIT*
Prof. dr. ing. Radu V. CIUPA, *U.T.Cluj-Napoca*
Prof. dr. ing. Florin CONSTANTINESCU, *U.P.B.*

Prof. dr. ing. Paul CRISTEA, *membru titular al Academiei Române*
Prof. dr. ing. Toma DORDEA, *membru titular al Academiei Române*
Prof. dr. ing. Radu ENACHE, *H.P.-România*
Prof. dr. ing. Alexandru FRANSUA, *U.P.B.*
Prof. dr. ing. Horia GAVRILĂ, *U.P.B.*
Prof. dr. ing. Sorin GRIGORESCU, *U.P.B.*
Prof. dr. ing. Mihai IORDACHE, *U.P.B.*
Prof. dr. ing. Dumitru-Marcel ISTRATE*, U.T.Iaşi*
Prof. dr. ing. Teodor LEUCA, *U. Oradea*
Prof. dr. ing. Marlene MARINESCU, *U.Wiesbaden*
Prof. dr. ing. Dan MICU, *U.T.Cluj-Napoca*
Dr. ing. Paul MINCIUNESCU, *I.C.P.E.-S.A.*
Prof. dr. ing. Alexandru MOREGA, *U.P.B.*
Prof. dr. ing. Călin MUNTEANU, *U.T.Cluj-Napoca*
Prof. dr. ing. Valentin NĂVRĂPESCU, *U.P.B.*
Prof. dr. ing. Petre-Marian NICOLAE, *U. Craiova*
Prof. dr. ing. Andrei NICOLAIDE, *U. Transilvania Braşov*
Dr. ing. Paul PENCIOIU, *I.C.P.E.-S.A.*
Prof. dr. ing. Claudia POPESCU, *U.P.B.*
Dr. ing. Vergil RACICOVSCHI, *I.C.P.E.-S.A.*
Prof. dr. ing. Costel RĂDOI, *U.P.B.*
Prof. dr. ing. Alecsandru SIMION*, U.T.Iaşi*
Prof. dr. ing. Emil SIMION, *U.T.Cluj-Napoca*
Prof. dr. ing. Dumitru TOADER, *U.P.Timişoara*
Prof. dr. ing. Vasile ŢOPA, *U.T.Cluj-Napoca*
Prof. dr. ing. Nicolae VASILE, *I.C.P.E.-S.A.*
Prof. dr. ing. Mihai VASILIU, *U.P.B.*

Comitetul de organizare

Ş.l.dr.ing. Mihai MARICARU, *mihai.maricaru@upb.ro*, *Preşedinte*
As.ing. Adelina BORDIANU
Ş.*l.*dr.ing. Oana Mihaela DROSU
Dr.ing. Mihaela MATEESCU
Ş.l.dr.ing. Iosif Vasile NEMOIANU
Ş.*l.*dr.ing. Dragoş NICULAE
Ş.l.dr.ing. Veronica PĂLTÂNEA
Ş.*l.*dr.ing. Lucian PETRESCU
Ş.*l.*dr.ing. Mihai REBICAN
Ş.*l.*dr.ing. Marilena STĂNCULESCU
As.dr.ing. Marian VASILESCU
Ing. Cătălin MOICEANU, *webmaster*

Universitatea "Politehnica" din Bucureşti
DEPARTAMENTUL DE ELECTROTEHNICĂ

ASOCIAŢIA INGINERILOR ELECTRICIENI ŞI ELECTRONIŞTI DIN ROMÂNIA

Simpozionul Naţional de Electrotehnică Teoretică

14 Decembrie 2012,

Facultatea de Inginerie Electrică

Universitatea *"Politehnica"* din Bucureşti

CUPRINS

1.	Analiza unor regimuri de avarie de la un generator sincron de putere utilizând programe software dedicate	Petre-Marian NICOLAE, Dinuţ-Lucian POPA, Ileana-Diana NICOLAE	pp. 9-14
2.	Regularizarea condițiilor inițiale inconsistente din circuitele patologice	Daniel IOAN	pp. 15-20
3.	High efficiency LLC resonant converter	Sergiu OPREA, Mihai-Constantin TĂNASE, Adriana FLORESCU	pp. 21-26
4.	Convergence problems in transient analysis of circuits containing MEMS	Florin CONSTANTINESCU, Alexandru G. GHEORGHE, Miruna NIŢESCU	pp. 27-31
5.	Analiza stabilitatii unui motor sincron alimentat de la invertor sursa de curent	Vasile MANOLIU	pp. 32-37

6.	Analysis of three-phase induction machine operating under transient dynamic braking by using the mathematical model in total fluxes	Alecsandru SIMION, Leonard LIVADARU, Radu-Voinea COCIU, Adrian MUNTEANU	pp. 38-43
7.	Modeling of the 3D electrode growth in electroplating	Marius PURCAR, Călin MUNTEANU, Alexandru AVRAM, Vasile ŢOPA	pp. 44-49
8.	Influence of temperature on the potentiality of low power integrated systems used for producing AC electricity and adjusting its parameters	Ion VONCILĂ, Nicolae BADEA, Ion PARASCHIV	pp. 50-55
9.	A numerical study of the magnetic field source in magnetic drug targeted transport and fixation	Cristina SAVASTRU, Alexandru M. MOREGA	pp. 56-61
10.	Nucleotide sequence complex representation	Paul Dan CRISTEA, Aurora Rodica TUDUCE	pp. 62-67
11.	Dual tasking: gait and tremor in Parkinson's disease – acquisition, processing and clustering	Sorin POHOAŢĂ, Oana GEMAN, Adrian GRAUR	pp. 68-73
12.	Control of a single phase SRM of special topology using two power supplies	Nicolae-Daniel IRIMIA, Alecsandru SIMION, Leonard LIVADARU, Ovidiu DABIJA, Sorin VLĂSCEANU	pp. 74-79
13.	Sinusoidal control of a single phase special topology SRM, without rotor position sensor	Nicolae-Daniel IRIMIA, Alecsandru SIMION, Ovidiu DABIJA, Sorin VLĂSCEANU, Adrian MUNTEANU	pp. 80-85
14.	Soluţionarea regimului periodic al circuitelor cu elemente rezistive având caracteristici liniarizate pe porţiuni	Lilica CORLAN	pp. 86-89
15.	A numerical study of the heat transfer management provided by a thermoelectric sink-and-fan system	Jean B. DUMITRU, Alexandru M. MOREGA, Mihaela MOREGA	pp. 90-95

16.	Estimation of Van der Pol oscillator parameters based on transfer functions	Mihai IORDACHE, Lucia DUMITRIU, Lucian MANDACHE, Dragoş NICULAE	pp. 96-99
17.	Package capacitors' impact on system supply impedance	Alin-Constantin FLOREA	pp. 100-105
18.	"Behind scene" for one of the keys to portability: the battery	Viorel Constantin PETRE	pp. 106-109
19.	Digital mixer with current steering DAC	Cătălin BRÎNZEI, Florin CONSTANTINESCU, Iulian URSAC	pp. 110-115
20.	THD analysis in multi-level converters	Cristina CHIOREAN, Teodor VAIDA, Horia BĂLAN	pp. 116-121
21.	Algoritmi de optimizare evolutivi utilizaţi în proiectarea dispozitivelor de încălzire prin inducţie	Mihaela NOVAC, Ecaterina VLADU, Ovidiu NOVAC, Adriana GRAVA	pp. 122-127
22.	Proiectarea optimală a unui dispozitiv de încălzire prin inducţie	Teodor LEUCA, Ecaterina VLADU, Mihaela NOVAC, Ștefan NAGHI, Bogdan-Ciprian STANCIU	pp. 128-133
23.	Identificarea parametrilor circuitelor rezonante utilizate în transferul wireless al puterii electromagnetice	Daniel DAN, Dragoş NICULAE, Mihai IORDACHE	pp. 134-139
24.	Energy efficiency elements in homes electric heating	Nicolae VASILE, Alexandru-Gabriel GURGU	pp. 140-145
25.	Dual loop PLL for a radio frequency transceiver	Iulian URSAC, Cătălin Adrian BRÎNZEI	pp. 146-151
26.	Frequency mixer based on a resistor string digital-to-analog converter	Cătălin BRÎNZEI, Iulian URSAC	pp. 152-157
27.	Characterisation of circulant networks using eigenvalues, singular values and condition number	Dan Micu, Gilbert De Mey	pp. 158-161

28.	Aplicaţie MathCAD şi simulare MATLAB-Simulink pentru circuite electrice trifazate cu sarcini dezechilibrate particulare	Adrian PANĂ, Alexandru BĂLOI, Florin MOLNAR-MATEI	pp. 162-167
29.	Low power, temperature and process compensated CMOS ring oscillator	Mihai Eugen MARIN, Răzvan Cristian MARIN	pp. 168-171
30.	Non-symmetry power in three-phase systems	Liliana Marilena MATICA	pp. 172-176
31.	The influence of elementary cell properties on losses for soft magnetic composite materials	Adelina Rodica BORDIANU	pp. 177-182
32.	Experimental results versus FEM based analysis of a squirrel cage induction motor	Sorin VLĂSCEANU, Alecsandru SIMION, Nicolae_Daniel IRIMIA, Adrian MUNTEANU, Ovidiu DABIJA	pp. 183-188
33.	Evaluarea caracteristicilor magnetice ale pieselor feromagnetice	Marilena STĂNCULESCU, Paul ANDREI, Mihai MARICARU, Marian VASILESCU, Ioan Florea HĂNŢILĂ	pp. 189-193
34.	Încălzirea carcaselor prin curenţi turbionari	Ştefan Valeriu MINCULETE, Mihai MARICARU, Stelian MARINESCU, Marius Aurel COSTEA, Florea Ioan HĂNŢILĂ	pp. 194-199
35.	Study on the magnetic field produced by coils of certain shapes	Ioana-Gabriela SÎRBU, Lucian MANDACHE, Mihai IORDACHE	pp. 200-205
36.	The possibility to produce asynchronous motors with high energetically parameters	Maria Daniela STOCHIŢOIU, Dragoş PĂSCULESCU, Alin Cristian GRUBER	pp. 206-209
37.	New implementation of Preisach model	Octavian TABĂRĂ	pp. 210-215
38.	Parametrii S în aplicaţii de înaltă frecvenţă	Gabriela CIUPRINA, Aurel-Sorin LUP, Alina TOMESCU	pp. 216-221

39.	Eroarea de metodă în determinarea experimental analitică a câmpului unui electromagnet pentru acceleratoarele de particule	Daniel DAN, Daniel IOAN	pp. 222-227
40.	Transient and steady state analysis through simulations of an axial-field single-pole single-phase switched reluctance motor prototype	Ovidiu DABIJA, Alecsandru SIMION, Leonard LIVADARU, Adrian MUNTEANU, Nicolae-Daniel IRIMIA	pp. 228-233
41.	Aspects regarding the numerical analysis of the induction hardening process for spherical parts using a multilayer inductor	Mircea Nicolae ARION, Gabriel Remus CHEREGI, Vasile Darie SOPRONI, Carmen Otilia MOLNAR	pp. 234-239
42.	Modelarea câmpului electromagnetic cuplat cu cel termic într-un aplicator de microunde și utilizarea unui algoritm de optimizare	Simina (VICAŞ) COMAN, Teodor LEUCA, Ovidiu COMAN	pp. 240-245
43.	Procesarea unor semifabricate din lemn în câmp de radiofrecvenţă	Marcela Ioana LAZA (BULC), Dragoş SPOIALĂ, Gabriel CHEREGI	pp. 246-251
44.	Analiza comparativă privind utilizarea unor programe de specialitate pentru validarea proiectării unor transformatoare de mare putere	Dorinel CONSTANTIN, Petre-Marian NICOLAE	pp. 252-257
45.	Wireless energy transfer in a medium-range charging area	Corneliu URSACHI, Elena HELEREA	pp. 258-263
46.	FEM modeling of the induction motor with rotor faults	Anca CIOBANU, Elena HELEREA	pp. 264-269
47.	Efficiency of 2D homogenization formulas for magnetic nanocomposite materials	Lucian PETRESCU, Adelina BORDIANU, Valentin IONIŢĂ	pp. 270-275
48.	Aspecte privind teste de emisii şi imunitate la perturbaţii electromagnetice în celule GTEM	Petre-Marian NICOLAE, Dan-Gabriel STĂNESCU, Marian-Ştefan NICOLAE	pp. 276-281
49.	Analiza temperaturii şi umidităţii la dezhidratarea ciupercilor în câmp de microunde	Mircea PANTEA, Adriana GRAVA, Marcela LAZA (BULC)	pp. 282-287

50.	Influenţa frecvenţelor înalte asupra uscării perelor întregi şi feliate glasate cu pudră de zahăr	Mircea PANTEA, Adriana GRAVA, Marcela LAZA (BULC), Marius SILAGHI	pp. 288-293
51.	Dielectric properties and electromagnetic interference shielding behavior of multi-walled carbon nanotubes MWCNT's/polymer composites	Ştefan URSACHE, Romeo Cristian CIOBANU, Vlad SCARLATACHE, Alina NEAMŢU	pp. 294-299
52.	Dielectric and magnetic measurements for nanocomposite materials	Vasilica Alina NEAMŢU, Cristina BRĂTESCU, Ramona BURLACU, Ştefan URSACHE	pp. 300-305
53.	Considerations concerning the losses separation in amorphous cobalt based ribbons	Veronica PĂLTÂNEA, Gheorghe PĂLTÂNEA, Horia GAVRILĂ	pp. 306-309
54.	Peştera - generator eolian	Tudor ISOC	pp. 310-315
55.	Optimization conditions of stator winding insulation of hydrogenerator	Mihaela RĂDUCA, Cornel HAŢIEGAN, Ana-Maria BUDAI, Eugen RĂDUCA, Nicolina POP	pp. 316-321
56.	Analiza comportamentului la descărcarea pentru o baterie $LiFePO_4$ utilizată la un ATV electric	Emilian LEFTER, Bogdan-Adrian ENACHE, Ştefan OPREA	pp. 322-327
57.	PV charger system using a synchronus buck converter	Adriana FLORESCU , Sergiu OPREA	pp. 328-333
58.	Investigations on the use of multilevel converters in wind energy generation	Lucian PÂRVULESCU, Dan FLORICĂU	pp. 334-337

ANALIZA UNOR REGIMURI DE AVARIE DE LA UN GENERATOR SINCRON DE PUTERE UTILIZÂND PROGRAME SOFTWARE DEDICATE

Petre-Marian NICOLAE, Dinuț-Lucian POPA, Ileana-Diana NICOLAE
Universitatea din Craiova, B-dul Decebal 107, 200440, Craiova; pnicolae@elth.ucv.ro

Abstract. În acest articol sunt studiate fenomenele tranzitorii la apariția unui regim de avarie prin scurtcircuit trifazat la un generator de 315 MW, cu ajutorul software-ului dedicat de simulare EMTP-RV. Sunt efectuate două teste diferențiate prin locația punctului de scurtcircuit, unul la mașina sincronă iar celălalt după transformatorul coborâtor, acest fapt permițându-ne observarea comportamentului sarcinii şi in special a generatorului, în ambele cazuri. Acest studiu poate deveni o bază de plecare în alegerea temporizării protecțiilor şi reglarea parametrilor de acordare a regulatorului de excitație.

1 Introducere

Maşina sincronă este o maşină de c. a. a cărei turație rămâne constantă în regim stabilizat, independent de sarcină cu condiția de a nu depăşi sarcina maximă admisibilă, calculată la proiectare.

În exploatarea sistemelor electroenergetice pot apărea regimuri de funcționare tranzitorii, de avarie sau de funcționare anormală care conduc la încălziri suplimentare a echipamentelor, deteriorări sau chiar distrugerea lor şi pot duce la întreruperi ale furnizării energiei electrice prin scoaterea din funcțiune a grupului, ceea ce constituie pierderi materiale însemnate.

Pentru mărirea siguranței în exploatare şi asigurarea continuității în alimentarea cu energie electrică, se prevăd dispozitive automate de protecție care sesizează regimurile de avarie, producând deconectarea elementelor supuse deranjamentelor sau dând semnale de avertizare, înainte ca defecțiunea apărută să devină periculoasă. La configurarea acestor elemente de protecție este necesară cunoaşterea parametrilor regimurilor de avarie.

Studierea proceselor tranzitorii din sistemele electroenergetice, reglarea parametrilor de funcționare a generatoarelor sincrone pentru aceste regimuri de funcționare reprezintă o problemă actuală iar rezolvarea acesteia, cu considerarea tuturor factorilor, este complicată şi este realizabilă practic numai folosind programele de simulare dedicate [1].

2 Chestiuni teoretice

Folosirea unui reglaj automat de tensiune al generatoarelor, sensibil şi rapid, contribuie la ipoteza că modificarea condițiilor exterioare generatorului nu influențează sensibil asupra funcționării surselor echivalente [2].

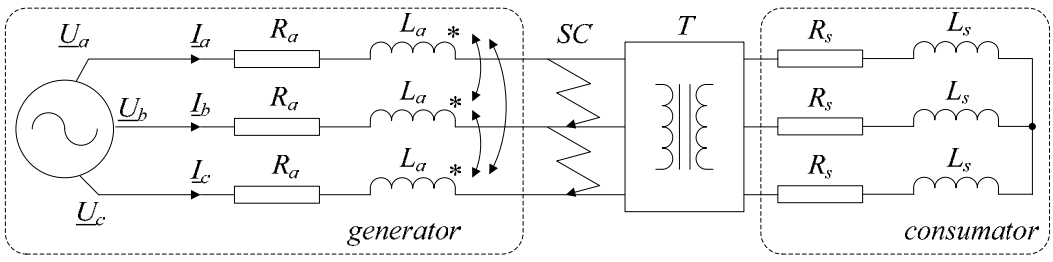

Fig 1: Configurația sistemului analizat.

Presupunem configurația din Fig. 1, cu apariția unui scurtcircuit trifazat metalic în punctul K. Mărimile ce caracterizează regimul premergător avariei în acest circuit sunt $\underline{U}_a$, $\underline{U}_b$, $\underline{U}_c$, $\underline{I}_a$, $\underline{I}_b$, $\underline{I}_c$. După apariția scurtcircuitului, schema se descompune în două circuite independente, din care unul rămâne conectat cu sursa, iar al doilea formează un circuit închis, în care curentul se menține până când energia fluxului magnetic înmagazinată se transformă în căldură absorbită de rezistența acestui circuit. Deoarece impedanța circuitului rămas conectat la sursă s-a micşorat, curentul în circuit creşte şi în general se modifică şi defazajul acestuia.

Presupunem curenții ce corespund noului regim stabilizat din acest circuit $\underline{I}_a'$, $\underline{I}_b'$, $\underline{I}_c'$. În orice moment, pentru faza *A* se poate scrie ecuația [2]:

$$u_a = r_a\, i_a + L_a \frac{di_a}{dt} + M \frac{di_b}{dt} + M \frac{di_c}{dt} \qquad (1)$$

care, având în vedere relația $i_b + i_c = -i_a$, se poate scrie astfel:

$$u = r_a\, i + L_k \frac{di}{dt} \qquad (2)$$

unde : $L_k = (L_a - M)$ este inductanța rezultantă a fazei. Introducerea acestor inductanțe permite scrierea ecuației diferențiale de echilibru în aceeaşi formă ca şi pentru un circuit monofazat. Soluția ecuației are forma [2]:

$$i = \frac{U_m}{Z_k}\sin(\omega t + \alpha - \varphi_k) + Ce^{-\frac{r_a}{L_k}t} \qquad (3)$$

unde: Z_k este impedanța de scurtcircuit; φ_k - argumentul impedanței de scurtcircuit în formă complexă sau unghiul de defazaj al curentului în acest circuit; α - unghiul care determină valoarea tensiunii fazei *A* la $t = 0$ (faza inițială); *C* - o constantă determinată din condițiile inițiale.

Primul termen al părții drepte a expresiei (3) reprezintă componenta periodică a curentului şi este curentul permanent al noului regim. In condițiile considerate acesta este constant ca amplitudine ($I_{perm} = U_m / Z_k$). Al doilea termen reprezintă componenta liberă, aperiodică, a curentului. Aceasta se amortizează după o exponențială, având ca exponent constanta de timp a circuitului, determinată de raportul parametrilor rețelei $T_a = L_k / r_a$. Valoarea maximă posibilă a componentei aperiodice a curentului este determinată nu numai de faza de conectare, ci şi de regimul anterior. Dacă curentul e defazat înainte, valoarea maxima a curentului aperiodic poate fi şi mai mare.

Maximele curentului apar pentru $\alpha = 0$, adică în regimul anterior scurtcircuitului curentul a fost zero în circuitul dat. Valoarea maximă a curentului aperiodic poate atinge amplitudinea componentei periodice, dacă în momentul scurtcircuitului această componentă trece prin maximumul său pozitiv sau negativ.

Curentul de şoc de scurtcircuit se determină de obicei pentru valoarea maximă a componentei aperiodice, considerând că această valoare apare aproximativ după o semiperioadă, ceea ce la frecvența de 50 Hz reprezintă aproximativ 0,01 s de la apariția scurtcircuitului.

3 Simularea regimului de scurtcircuit trifazat la un generator sincron

A fost realizată o simulare la scurtcircuit a unui generator sincron ce aparține unui grup energetic, în software-ul de simulare EMTP-RV (Electro Magnetic Transient Processes) program specializat de analiza tranzitorie în domeniul electromagnetic [3], [4].

Datele generatorului sunt prezentate în Tabelul 1.

Tabel 1: Parametrii generatorului sincron analizat.

Putere nominală	315 MW
Tensiune nominală	24 ± 5% kV
Curent nominal	9.740 A
Rezistență : - stator - rotor	 2,23 mΩ 125 mΩ
Constante de timp tranzitorii: - la scurtcircuit trifazat - a curentului aperiodic	 T'_{d3} = 1 s T_a = 0,28 s
Constante de timp subtranzitorii: - la scurtcircuit trifazat	 T''_{d3} = 0,07 s
Masă rotor	57 t

Generatorul sincron de 315MW furnizează energie electrică sistemului energetic prin intermediul a 3 transformatoare: a) unul ridicător 24-120 kV; b) unul coborâtor de 120-24 kV; c) unul coborâtor de 24/6 kV. Avem un consumator echivalent de 300 MW/ 185 MVAr pe barele de 24 kV si un motor asincron de 8.200 kW pe barele trafo de 6 kV în stare stabilă de funcționare (regim staționar).

Pentru a observa comportarea în funcție de locul în care se produce scurtcircuitul, au fost simulate doua regimuri de avarie, unul la maşina sincronă (Fig. 2) iar celălalt după transformatorul coborâtor de 24/6 kV ce alimentează motorul asincron.

3.1 Scurtcircuit pe barele generatorului

Schema echivalentă în programul de simulare EMTP-RV este prezentată în Fig. 2.

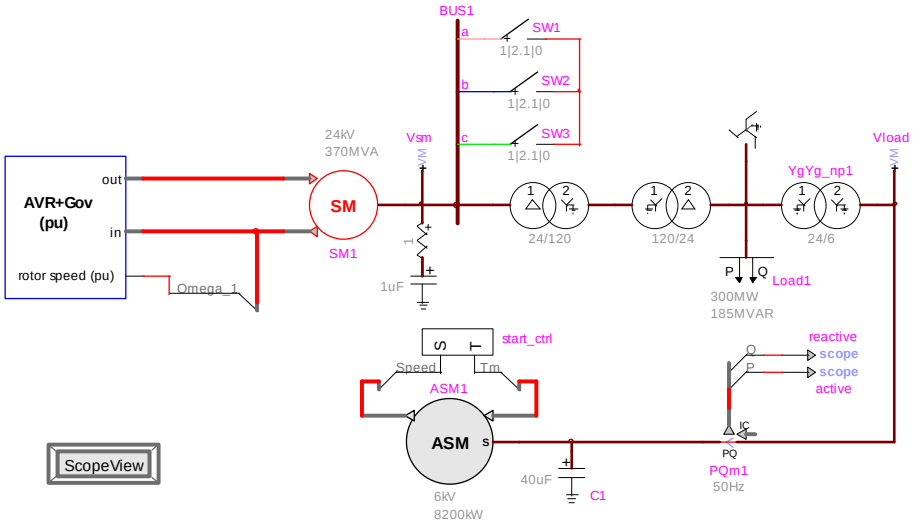

Fig. 2: Schema echivalentă a circuitului.

Se poate observa generatorul *SM1* cu regulatoarele aferente, contactoarele programabile pentru scurtcircuit *SW1*, *SW2*, *SW3*, transformatoarele şi sarcina echivalentă *Load1* şi motorul asincron *ASM1*. În acest caz curenții ajung la valori foarte mari, fiind limitați doar de rezistența şi reactanța statorului. Componenta aperiodică este prezentă timp de 1,5 s (Fig. 3 (a)).

Foarte importantă este funcționarea înfăşurării scurtcircuitate de amortizare deoarece are scopul de amortizare a pendulațiilor rotorului la variații de sarcină prin reducerea curenților

pulsatorii induşi de stator în înfăşurarea de excitație. Sistemul homopolar al curenților din stator determină o solenație pulsatorie ce duce la un cuplu pulsator. Aceasta solenație este observabilă şi în curentul din înfăşurarea de excitație (Fig. 3 (b)) până la dispariția componentei aperiodice a curentului de scurtcircuit [5], [6].

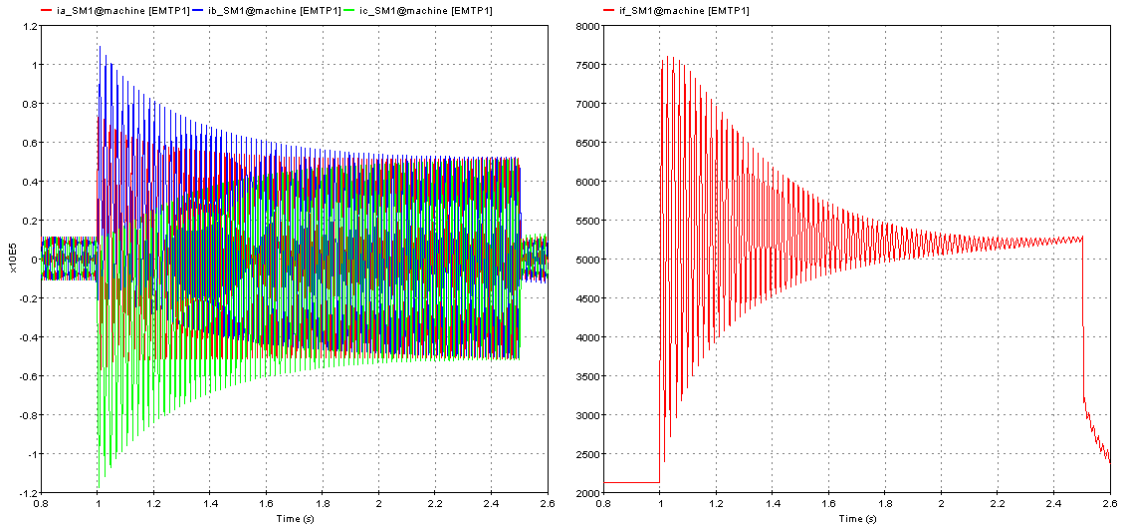

(a) (b)

Fig. 3: Curenții prin stator (a) şi înfăşurarea de excitație (b).

Dacă protecțiile la frecvență şi tensiune nu ar acționa, ar avea loc situația din Fig. 4. Se observă o scădere a frecvenței în primul moment, datorită comportării ca o frână a regimului de scurtcircuit, urmată de o creştere până la 1,22 u.r. în momentul deconectării scurtcircuitului. Ulterior generatorul este restabilizat de regulatorul de turație în 7,5 s.

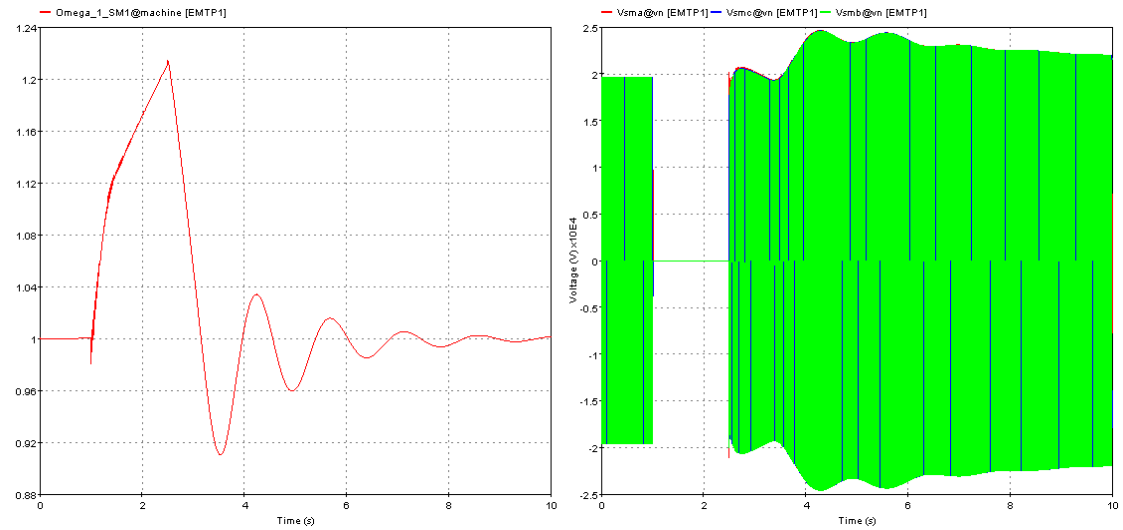

(a) (b)

Fig. 4: Variația frecvenței (a) şi a tensiunii la bornele generatorului (b).

A fost studiată şi influența avariei asupra sarcinii de 6 kV, care constă dintr-un motor asincron.

Deoarece evoluția mărimilor de stare ale motorului au dependențe reciproce neliniare, rezolvarea acestei probleme ridică greutăți deosebite in mod obişnuit, eliminate prin utilizarea programului de simulare.

Imediat după scurtcircuit se constată pentru scurt timp curenți statorici de valoare aproape dublă față de curenții de pornire ai motorului, maşina trece în regim de generator cedând energia reactivă înmagazinată. După restabilirea sistemului, supratensiunile de la generatorul sincron determină supratensiuni pe statorul motorului asincron, care produc şi oscilații mecanice rotorice.

3.2 Scurtcircuit pe barele de 6 kV

Acest scurtcircuit este produs într-un punct îndepărtat de generator (Fig. 5)

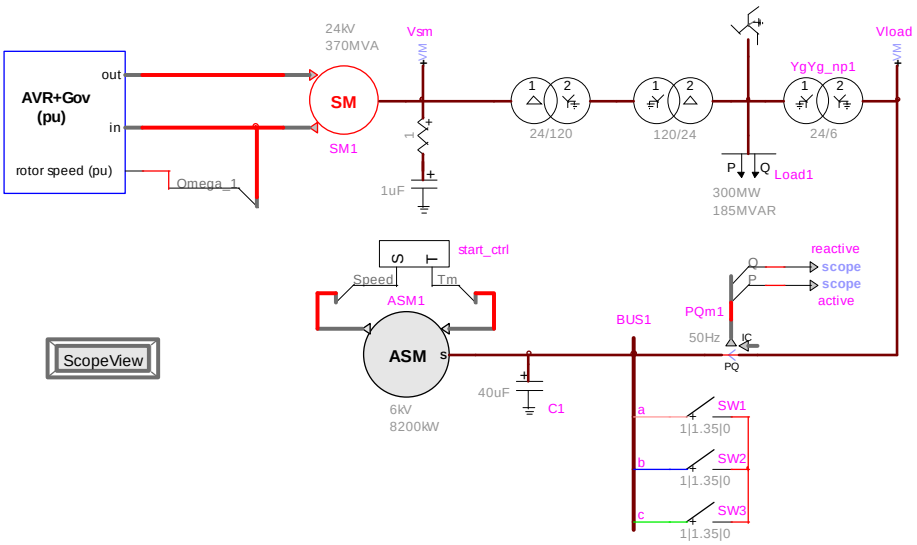

Fig 5: Schema echivalentă a circuitului în cazul apariției scurtcircuitului pe barele de 6 kV.

După cum se observă din curbele de variație, are o influență mult mai mică asupra acestuia, curenții închizându-se şi prin impedanțele transformatoarelor deci fiind limitați față de primul caz (Fig. 6).

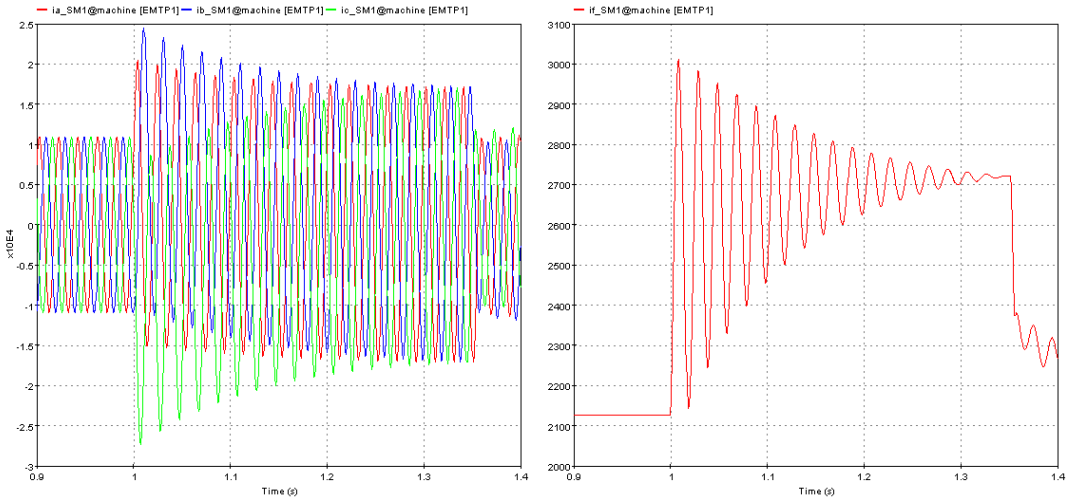

(a) (b)

Fig. 6: Curenții prin stator (a) şi prin înfăşurarea de excitație (b).

La scăderea tensiunii generatorului, provocată de scurtcircuit, intra in funcțiune instalația RAT, tinzând sa ridice tensiunea pana la nivelul normal (Fig. 7 (a)). De asemenea intră în funcțiune şi regulatorul de frecvență, ce măreşte viteza de antrenare a generatorului pentru a compensa comportarea de frână pe care o are scurtcircuitul, şi restabileşte sistemul în scurt timp la valoarea nominală, după dispariția defectului (Fig. 7 (b)).

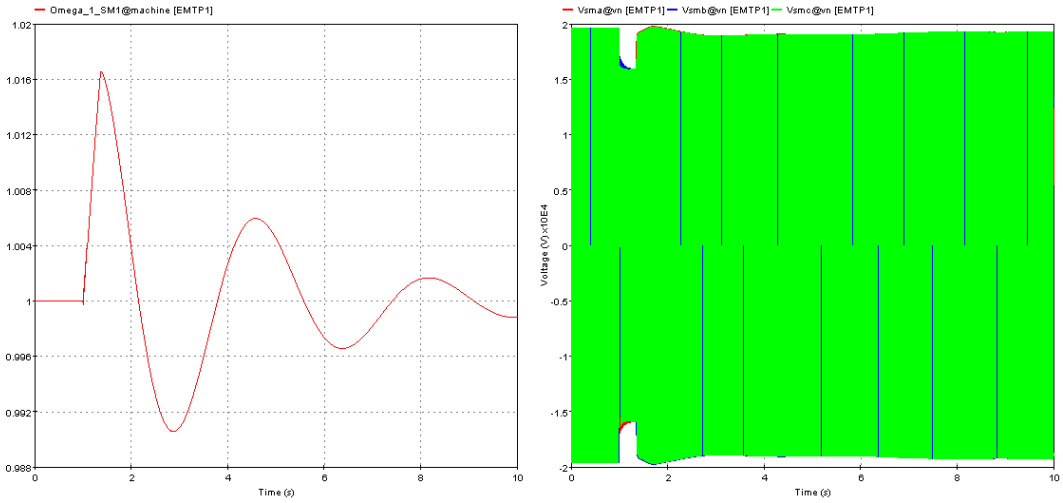

(a) (b)

Fig. 7: Frecvența (a) şi tensiunea la bornele generatorului (b).

De această dată, tot pentru scurt timp, la motorul asincron curenții statorici devin puțin mai mari față de cazul anterior, maşina consumă energie reactivă înmagazinată, apoi după restabilizarea sistemului nu mai există acele supratensiuni pe stator, deci nici oscilații mecanice rotorice.

4 Concluzii

- Prin simulările efectuate în software-ul EMTP-RV, studierea desfăşurării procesului de scurtcircuit la generatorul sincron de 315 MW ne permite determinarea facilă a diverşi parametri şi are un interes practic, în special în alegerea temporizării protecțiilor şi reglarea parametrilor de acordare a regulatorului de excitație [7].
- Au fost simulate doua cazuri de scurtcircuit diferențiate prin amplasarea locului in care se produce acesta şi observat că, in primul caz , scurtcircuitul fiind la bornele generatorului are o influență mult mai mare asupra acestuia decât in al doilea caz, in care scurtcircuitul se produce intr-un punct mai depărtat, şi anume în secundarul transformatorului de 6 kV. A fost observată şi influența regimului de avarie asupra motorului în ambele cazuri.

Referințe

[1] P. M. Nicolae. *Calitatea energiei electrice în sisteme electroenergetice de putere limitată*, Ed. Tehnică, 1998.
[2] S. A. Ulianov. *Regimuri tranzitorii ale sistemelor electrice*, Ed. Tehnica, 1967.
[3] EMTP-RV, EMTPWorks 2.1.0 GUI. *Help Docs and Tutorials*, Hydro Quebec.
[4] H. Dommel. *EMTP Theory Book*, Microtran Power System Analysis Corporation, 1996.
[5] K.R. Padiyar. *Power System Dynamics : Stability and Control, 2nd edition*, BS Publications, 2002.
[6] P.M. Anderson and A. A. Fouad. *Power System Control and Stability, 2nd edition*, IEEE Press Power Engineering Series, Wiley-Interscience, 2003.
[7] *IEEE guide for synchronous generator modeling practices in stability analyses*, IEEE Standard P1110, Chapter 6, 2002.

REGULARIZAREA CONDIȚIILOR INIȚIALE INCONSISTENTE DIN CIRCUITELE PATOLOGICE

Daniel IOAN
Universitatea "Politehnica" din Bucureşti, Spl. Independenţei 313, 060042, Bucureşti; lmn@lmn.pub.ro

Abstract. În lucrare se prezintă o procedură generală de regularizare a condițiilor inițiale inconsistente, pentru circuitele electrice patologice, care conțin bucle formate din surse de tensiune și condensatoare sau secțiuni formate din surse de curent și inductoare. Se discută importanța problemei rezolvate, pentru analiza simbolică sau numerică a circuitelor, dar și relația dintre abordarea propusă și altele.

1 Introducere

Lucrarea abordează una dintre dificultățile circuitelor electrice patologice, care conțin bucle de surse de tensiune și condensatoare sau secțiuni formate din surse de curent și inductoare. Aceste circuite pot avea condiții inițiale inconsistente, care nu respectă constrângerile algebrice impuse de structura circuitului, de pe durata regimului tranzitoriu, deoarece la momentul inițial pot avea loc comutații, care modifică topologia circuitului. Astfel de circuite pot fi analizate corect în domeniul timpului, doar după aplicarea unei proceduri de regularizare, prin care condițiile inițiale inconsistente se transformă în unele consistente. Această procedură este de fapt analiza regimului tranzitoriu, care are loc în intervalul infinit mic (-0,+0), din jurul originii. În circuitele nepatologice, acest regim tranzitoriu nu există, deoarece variabilele de stare sunt continue în timp, dar în cazul circuitelor patologice, variabilele de stare pot avea la momentul inițial $t = 0$ salturi, ce trebuie determinate.

În lucrarea clasică [1] regularizarea se bazează pe conservarea sarcinii din secțiunile de condensatoare și a fluxului prin buclele de bobine. Această abordare restrictivă este încă recomandată în multe cursuri universitare, chiar recent apărute. Pentru rezolvarea acestei probleme s-au propus în literatură mai multe metode și abordări diferite, bazate pe: transformata Laplace; ecuații diferențial-algebrice DAE; integrări numerice sau minimizări de energie [2-6]. Într-o lucrare recentă [7] se face o trecere în revistă a istoricului acestor abordări. Metoda pe care o descriem în prezenta lucrare are avantajul că este una generală, și nu folosește cunoștințe de matematici avansate, funcții generalizate (exceptând impulsuri Dirac, definite formal ca derivata funcției treaptă, a lui Heaviside) sau analiza algebrică a sistemului de ecuații DAE. Rezultatele se extind la circuitele electrice neliniare, cu ecuații quasi-liniare, descrise în [5].

În secțiunea 2 a lucrării se deduc ecuațiile diferențial-algebrice ale circuitelor patologice și felul în care acestea se reduc la ecuații de stare. În secțiunea 3 se prezintă și se fundamentează procedura de regularizare a condițiilor inițiale, iar secțiunea 4 este dedicată concluziilor studiului.

2 Ecuațiile circuitelor cu elemente reactive în exces

In continuare va fi prezentată o metoda sistematică de formulare a ecuațiilor de stare la circuite liniare cu elemente în exces, care generează sisteme DAE de index superior. În acest scop vom presupune că circuitul este alcătuit din: rezistoare dipolare sau multipolare, inclusiv surse comandate liniar; bobine cuplate sau nu; condensatoare, toate elemente ideale lineare și surse independente, ideale de curent și tensiune. Vom mai presupune că exista un *arbore numit regulat,* care conține toate elementele sursele ideale de tensiune, nici o sursă ideal de curent, cât

mai multe condensatoare (eventual toate) și cat mai puține bobine. În consecință, nu există bucle formate din surse idealele de tensiune și nici secțiuni formate din surse ideale de curent, în schimb pot exista bucle formate exclusiv din condensatoare sau condensatoare și surse ideale de tensiune, cât și secțiuni formate din bobine și eventual surse ideale de curent. Spunem că circuitul conține *elemente reactive - acumulatoare de energie în exces (condensatoarele din coarbore și bobinele din arborele regulat).* Dacă sunt îndeplinite aceste condiții, vom înlocui condensatoarele care nu sunt în exces cu surse ideale de tensiune (cu t.e.m. $\mathbf{u}_{Ca}$) și condensatoarele în exces cu surse ideale de curent (cu c.e.m. $\mathbf{i}_{Cc}$), iar bobinele care nu sunt în exces cu surse ideale de curent (cu c.e.m. $\mathbf{i}_{Lc}$) și bobinele în exces cu surse ideale de tensiune (cu t.e.m. $\mathbf{u}_{La}$). Circuitul rezistiv astfel format are un arbore normal și îndeplinește deci condiția necesară de bună formulare, neavând bucle formate din surse ideale de tensiune și secțiuni formate din surse ideale de curent.

Cu notațiile din http://www.lmn.pub.ro/~daniel/BazeELTH-6-Teoremele%20circuitelor.pdf, conform teoremei superpoziției-liniarității, soluția acestui circuit excitat hibrid are expresia:

$$\begin{bmatrix}\mathbf{u}_{Lc}\\ \mathbf{u}_{Cc}\\ \mathbf{i}_{Ca}\\ \mathbf{i}_{La}\end{bmatrix}=\begin{bmatrix}\mathbf{R}_{LcLc} & \mathbf{R}_{LcCc} & \mathbf{A}_{LcCa} & \mathbf{A}_{LcLa}\\ \mathbf{R}_{CcLc} & \mathbf{R}_{CcCc} & \mathbf{A}_{CcCa} & \mathbf{A}_{CcLa}\\ \mathbf{B}_{CaLc} & \mathbf{B}_{CaCc} & \mathbf{G}_{CaCa} & \mathbf{G}_{CaLa}\\ \mathbf{B}_{LaLc} & \mathbf{B}_{LaCc} & \mathbf{G}_{LaCa} & \mathbf{G}_{LaLa}\end{bmatrix}\begin{bmatrix}\mathbf{i}_{Lc}\\ \mathbf{i}_{Cc}\\ \mathbf{u}_{Ca}\\ \mathbf{u}_{La}\end{bmatrix}+\begin{bmatrix}\mathbf{R}_{Lcj} & \mathbf{A}_{Lcj}\\ \mathbf{R}_{Ccj} & \mathbf{A}_{Ccj}\\ \mathbf{B}_{Caj} & \mathbf{G}_{Cae}\\ \mathbf{B}_{Laj} & \mathbf{G}_{Lae}\end{bmatrix}\begin{bmatrix}\mathbf{j}\\ \mathbf{e}\end{bmatrix};$$

$$\begin{bmatrix}\mathbf{u}_{j}\\ \mathbf{i}_{e}\end{bmatrix}=\begin{bmatrix}\mathbf{R}_{jLc} & \mathbf{R}_{jCc} & \mathbf{A}_{jCa} & \mathbf{A}_{jLa}\\ \mathbf{B}_{eLc} & \mathbf{B}_{eCc} & \mathbf{G}_{eCa} & \mathbf{G}_{eLa}\end{bmatrix}\begin{bmatrix}\mathbf{i}_{Lc}\\ \mathbf{i}_{Cc}\\ \mathbf{u}_{Ca}\\ \mathbf{u}_{La}\end{bmatrix}+\begin{bmatrix}\mathbf{R}_{jj} & \mathbf{A}_{je}\\ \mathbf{B}_{ej} & \mathbf{G}_{ee}\end{bmatrix}\begin{bmatrix}\mathbf{j}\\ \mathbf{e}\end{bmatrix}. \qquad (1)$$

Primele n_L+n_C ecuații reprezintă partea algebrică a unui sistem DAE cu $2(n_L+n_C)$ variabile. La acestea adăugăm ecuațiile constitutive ale elementelor acumulatoare de energie (scrise în regula de la generatoare, pentru a asigura egalitatea curenților și tensiunilor, deoarece pentru partea rezistivă s-a folosit regula de la receptoare):

$$\begin{bmatrix}\mathbf{u}_{Lc}\\ \mathbf{i}_{Ca}\end{bmatrix}=\begin{bmatrix}-\mathbf{L}_{c} & \mathbf{0}\\ \mathbf{0} & -\mathbf{C}'_{a}\end{bmatrix}\frac{d}{dt}\begin{bmatrix}\mathbf{i}_{Lc}\\ \mathbf{u}_{Ca}\end{bmatrix};$$

$$\begin{bmatrix}\mathbf{u}_{La}\\ \mathbf{i}_{Cc}\end{bmatrix}=\begin{bmatrix}-\mathbf{L}_{a} & \mathbf{0}\\ \mathbf{0} & -\mathbf{C}'_{c}\end{bmatrix}\frac{d}{dt}\begin{bmatrix}\mathbf{i}_{La}\\ \mathbf{u}_{Cc}\end{bmatrix}. \qquad (2)$$

Aici s-a notat cu $\mathbf{L}_c$ matricea inductanțelor propriii și mutuale din coarbore iar cu $\mathbf{L}_a$ matricea inductanțelor în exces (din arbore). Cu $\mathbf{C}'_a$ s-a notat matricea diagonală a capacităților din arbore iar cu $\mathbf{C}'_c$ matricea diagonală a capacitaților în exces. În continuare, vom presupune că aceste patru matrice sunt pozitiv definite. Aceste n_L+n_C ecuații reprezintă partea diferențială a sistemului DAE. Având rangul n_L+n_C, matricea $\mathbf{E}$ a acestui sistem este singulara, deci sistemul are index mai mare că zero.

Variabilele de semi-stare în exces $\mathbf{u}_{Cc}$ si $\mathbf{i}_{la}$ nu pot avea valori inițiale arbitrare, deoarece ele se exprimă în funcție de $\mathbf{u}_{Ca}$ și respective $\mathbf{i}_{Lc}$ folosind teoremele lui Kirchhoff pe buclele și secțiunile generate de elementele în exces:

$$\begin{aligned}&\mathbf{u}_{Cc}=-\mathbf{D}_C\mathbf{u}_{\mathbf{C}a}-\mathbf{D}_e\mathbf{e};\\&\mathbf{i}_{La}=\mathbf{D}_L^T\mathbf{i}_{\mathbf{L}c}+\mathbf{D}_j^T\mathbf{j}.\end{aligned}\tag{3}$$

Acestea sunt "*constrângerile ascunse*" ale sistemului DAE. Înlocuind relațiile algebrice care exprimă $\mathbf{u}_{Cc}$ și $\mathbf{i}_{La}$, cu aceste constrângeri, pot fi eliminate din (1) variabilele în exces și rezultă un sistem cu $n_{Lc}+n_{Ca}$ ecuații de stare, și tot atâtea variabile de stare (grade de libertate):

$$\begin{aligned}&\begin{bmatrix}\mathbf{u}_{\mathbf{j}}\\ \mathbf{i}_{\mathbf{e}}\end{bmatrix}=\begin{bmatrix}\mathbf{R}_{\mathbf{j}\mathbf{L}c} & \mathbf{A}_{\mathbf{j}\mathbf{C}a}\\ \mathbf{B}_{\mathbf{e}\mathbf{L}c} & \mathbf{G}_{\mathbf{e}\mathbf{C}a}\end{bmatrix}\begin{bmatrix}\mathbf{i}_{\mathbf{L}c}\\ \mathbf{u}_{\mathbf{C}a}\end{bmatrix}+\begin{bmatrix}\mathbf{R}_{\mathbf{jj}} & \mathbf{A}_{\mathbf{j}e}\\ \mathbf{B}_{\mathbf{ej}} & \mathbf{G}_{\mathbf{ee}}\end{bmatrix}\begin{bmatrix}\mathbf{j}\\ \mathbf{e}\end{bmatrix}+\\&\begin{bmatrix}\mathbf{R}_{jCc} & \mathbf{A}_{\mathbf{j}LA}\\ \mathbf{B}_{\mathbf{e}Cc} & \mathbf{G}_{\mathbf{e}La}\end{bmatrix}\begin{bmatrix}\mathbf{0} & -\mathbf{L}_a\mathbf{D}_{\mathbf{c}}\\ \mathbf{C}_c'\mathbf{D}_L^T & \mathbf{0}\end{bmatrix}\frac{d}{dt}\begin{bmatrix}\mathbf{i}_{\mathbf{L}c}\\ \mathbf{u}_{\mathbf{C}a}\end{bmatrix}+\begin{bmatrix}\mathbf{R}_{jCc} & \mathbf{A}_{\mathbf{j}LA}\\ \mathbf{B}_{\mathbf{e}Cc} & \mathbf{G}_{\mathbf{e}La}\end{bmatrix}\begin{bmatrix}\mathbf{0} & -\mathbf{L}_a\mathbf{D}_e\\ \mathbf{C}_c'\mathbf{D}_j^T & \mathbf{0}\end{bmatrix}\frac{d}{dt}\begin{bmatrix}\mathbf{j}\\ \mathbf{e}\end{bmatrix}.\end{aligned}\tag{4}$$

Trebuie să remarcăm faptul că această operație a reformulat problema inițială, înlocuind-o cu una mai mult sau mai puțin "echivalentă". Ea poate fi făcută, doar atunci când condițiile inițiale satisfac constrângerile ascunse, lucru care nu se întâmplă întotdeauna. Dacă nu satisfac constrângerile (3), ele se numesc *condițiile inițiale inconsistente*, iar folosirea acestei metode in cazul lor poate genera grave erori de modelare și implicit soluții greșite. Ecuațiile (4) au forma:

$$\begin{aligned}&\mathbf{E}\frac{d\mathbf{x}}{dt}=\mathbf{A}\mathbf{x}+\mathbf{B}\mathbf{y}+\mathbf{F}\frac{d\mathbf{y}}{dt};\\&\mathbf{v}=\mathbf{C}\mathbf{x}+\mathbf{D}\mathbf{y}+\mathbf{G}\frac{d\mathbf{x}}{dt}+\mathbf{K}\frac{d\mathbf{y}}{dt},\end{aligned}\tag{5}$$

unde

- $\mathbf{x}=\begin{bmatrix}\mathbf{i}_{\mathbf{L}c}\\ \mathbf{u}_{\mathbf{C}a}\end{bmatrix}$ sunt variabilele de stare: curenții prin bobinele din coarbore și tensiunile condensatoarelor din arbore;
- $\mathbf{y}=\begin{bmatrix}\mathbf{j}\\ \mathbf{e}\end{bmatrix}$ sunt excitațiile: c.e.m și respective t.e.m. ale surselor independente;
- $\mathbf{v}=\begin{bmatrix}\mathbf{u}_{\mathbf{j}}\\ \mathbf{i}_{\mathbf{e}}\end{bmatrix}$ sunt răspunsurile circuitului: tensiunile surselor ideale de curent și curenții surselor de ideale de tensiune.

Chiar dacă circuitul conține n_L+n_C elemente acumulatoare de energie, prin eliminarea semistărilor în exces, s-a obținut un spațiul al stărilor cu o dimensiune mai mică, doar de $n_{Lc}+n_{Ca}$. Matricele care intervin în (5) au expresiile :

$$\begin{aligned}&\mathbf{E}=\begin{bmatrix}-\mathbf{L}_c & \mathbf{0}\\ \mathbf{0} & -\mathbf{C}_a'\end{bmatrix}+\begin{bmatrix}\mathbf{A}_{\mathbf{L}c\mathbf{L}a} & \mathbf{R}_{\mathbf{L}c\mathbf{C}c}\\ \mathbf{G}_{\mathbf{C}a\mathbf{L}a} & \mathbf{B}_{\mathbf{C}a\mathbf{C}c}\end{bmatrix}\begin{bmatrix}\mathbf{L}_a\mathbf{D}_L^T & \mathbf{0}\\ \mathbf{0} & -\mathbf{C}_c'\mathbf{D}_C\end{bmatrix},\mathbf{A}=\begin{bmatrix}\mathbf{R}_{\mathbf{L}c\mathbf{L}c} & \mathbf{A}_{\mathbf{L}c\mathbf{C}a}\\ \mathbf{B}_{\mathbf{C}a\mathbf{L}c} & \mathbf{G}_{\mathbf{C}a\mathbf{C}a}\end{bmatrix},\\&\mathbf{B}=\begin{bmatrix}\mathbf{R}_{\mathbf{L}c\mathbf{j}} & \mathbf{A}_{\mathbf{L}c\mathbf{j}}\\ \mathbf{B}_{\mathbf{C}a\mathbf{j}} & \mathbf{G}_{\mathbf{C}a\mathbf{e}}\end{bmatrix},\mathbf{F}=-\begin{bmatrix}\mathbf{A}_{\mathbf{L}c\mathbf{L}a} & \mathbf{R}_{\mathbf{L}c\mathbf{C}c}\\ \mathbf{G}_{\mathbf{C}a\mathbf{L}a} & \mathbf{B}_{\mathbf{C}a\mathbf{C}c}\end{bmatrix}\begin{bmatrix}\mathbf{L}_a\mathbf{D}_j^T & \mathbf{0}\\ \mathbf{0} & -\mathbf{C}_c'\mathbf{D}_e\end{bmatrix},\\&\mathbf{C}=\begin{bmatrix}\mathbf{R}_{\mathbf{j}\mathbf{L}c} & \mathbf{A}_{\mathbf{j}\mathbf{C}a}\\ \mathbf{B}_{\mathbf{e}\mathbf{L}c} & \mathbf{G}_{\mathbf{e}\mathbf{C}a}\end{bmatrix},\mathbf{D}=\begin{bmatrix}\mathbf{R}_{\mathbf{jj}} & \mathbf{A}_{\mathbf{j}e}\\ \mathbf{B}_{\mathbf{ej}} & \mathbf{G}_{\mathbf{ee}}\end{bmatrix}\begin{bmatrix}\mathbf{j}\\ \mathbf{e}\end{bmatrix},\mathbf{G}=\begin{bmatrix}\mathbf{R}_{jCc} & \mathbf{A}_{\mathbf{j}LA}\\ \mathbf{B}_{\mathbf{e}Cc} & \mathbf{G}_{\mathbf{e}La}\end{bmatrix}\begin{bmatrix}\mathbf{0} & -\mathbf{L}_a\mathbf{D}_{\mathbf{c}}\\ \mathbf{C}_c'\mathbf{D}_L^T & \mathbf{0}\end{bmatrix},\\&\mathbf{K}=\begin{bmatrix}\mathbf{R}_{jCc} & \mathbf{A}_{\mathbf{j}LA}\\ \mathbf{B}_{\mathbf{e}Cc} & \mathbf{G}_{\mathbf{e}La}\end{bmatrix}\begin{bmatrix}\mathbf{0} & -\mathbf{L}_a\mathbf{D}_e\\ \mathbf{C}_c'\mathbf{D}_j^T & \mathbf{0}\end{bmatrix}.\end{aligned}\tag{6}$$

Dacă **E** este inversabila, atunci ecuațiile de stare se pot scrie sub forma:

$$\begin{aligned}&\frac{d\mathbf{x}}{dt}=\mathbf{E}^{-1}\mathbf{A}\mathbf{x}+\mathbf{E}^{-1}\mathbf{B}\mathbf{y}+\mathbf{E}^{-1}\mathbf{F}\frac{d\mathbf{y}}{dt};\\&\mathbf{v}=[\mathbf{C}+\mathbf{G}\mathbf{E}^{-1}\mathbf{A}]\mathbf{x}+[\mathbf{D}+\mathbf{G}\mathbf{E}^{-1}\mathbf{B}\mathbf{y}]\mathbf{y}+[\mathbf{G}\mathbf{E}^{-1}-\mathbf{F}]\mathbf{K}\frac{d\mathbf{y}}{dt},\end{aligned}\tag{7}$$

care se deosebește de forma canonică a ecuațiilor de stare, prin faptul că atât în ecuația de stare cat și în cea de ieșire intervin termenii dependenți de derivatele fată de timp ale semnalelor de intrare, mai exact ale parametrilor surselor din buclele generate de condensatoarele în exces și respectiv din secțiunile generate de bobinele în exces. Dacă în aceste bucle/secțiuni nu există surse (adică în circuit nu există bucle de condensatoare, care să conțină și surse de tensiune și nici secțiuni formate din bobine și surse de curent), atunci matricele **F** și **K** sunt nule, iar ecuațiile de stare capătă forma DAE standard:

$$\begin{aligned}&\mathbf{E}\frac{d\mathbf{x}}{dt}=\mathbf{A}\mathbf{x}+\mathbf{B}\mathbf{y};\\&\mathbf{v}=\mathbf{C}\mathbf{x}+\mathbf{D}\mathbf{y},\end{aligned}\tag{8}$$

în care răspunsul nu conține derivate ale semnalelor de intrare. Matricea **E** este inversabilă, dacă circuitul rezistiv generat prin înlocuirea condensatoarelor din arbore cu surse ideale de tensiune, cele din arbore cu izolatoare perfecte, a bobinelor din coarbore cu surse ideale de curent și a celor din arbore cu conductoare perfecte este corect formulat. Ecuațiile hibride ale acestui circuit duc chiar la ecuațiile de stare, în forma canonică:

$$\begin{aligned}&\begin{bmatrix}\mathbf{u}_{\mathrm{L}c}\\ \mathbf{i}_{\mathrm{C}a}\end{bmatrix}=\mathbf{A}\begin{bmatrix}\mathbf{i}_{\mathrm{L}c}\\ \mathbf{u}_{\mathrm{C}a}\end{bmatrix}+\mathbf{B}\begin{bmatrix}\mathbf{j}\\ \mathbf{e}\end{bmatrix}\Leftrightarrow\begin{bmatrix}-\mathbf{L}_c & \mathbf{0}\\ \mathbf{0} & -\mathbf{C}'_a\end{bmatrix}\frac{d\mathbf{x}}{dt}=\mathbf{A}\mathbf{x}+\mathbf{B}\mathbf{y};\\&\mathbf{v}=\mathbf{C}\mathbf{x}+\mathbf{D}\mathbf{y}.\end{aligned}\tag{9}$$

După rezolvarea acestor ecuații, se pot determina variabile în exces folosind relațiile:

$$\begin{aligned}&\mathbf{u}_{Cc}=-\mathbf{D}_C\mathbf{u}_{\mathrm{C}a}-\mathbf{D}_e\mathbf{e}\\&\mathbf{i}_{La}=\mathbf{D}_L^T\mathbf{i}_{\mathrm{L}c}+\mathbf{D}_j^T\mathbf{j}\end{aligned}\quad\text{si apoi}\quad\begin{bmatrix}\mathbf{u}_{\mathrm{L}a}\\ \mathbf{i}_{\mathrm{C}c}\end{bmatrix}=\begin{bmatrix}-\mathbf{L}_a & \mathbf{0}\\ \mathbf{0} & -\mathbf{C}'_c\end{bmatrix}\frac{d}{dt}\begin{bmatrix}\mathbf{i}_{\mathrm{L}a}\\ \mathbf{u}_{\mathrm{C}c}\end{bmatrix}.\tag{10}$$

Soluția finală a problemei se obține prin superpoziția soluției determinată anterior cu soluția circuitului obținut prin pasivizarea tuturor surselor, cu excepția celor care reprezintă elementele în exces (deci cu sursele independente pasivizate, cu condensatoarele din arbore substituite cu conductoare perfecte și bobinele din coarbore substituite cu izolatoare perfecte, dar cu condensatoarele în exces înlocuite cu surse ideale de curent de valoare $\mathbf{i}_{\mathrm{C}c}$ și bobinele în exces înlocuite cu surse ideale de tensiune de valoare $\mathbf{u}_{\mathrm{L}a}$). Semnalele de ieșire au deci expresia hibridă inițiala, în care intervin atât variabilele de stare, cat și variabilele în exces, dar și semnalele de intrare.

3 Regularizarea condițiilor inițiale inconsistente

Trebuie sa remarcăm un aspect foarte important, care pune sub semnul întrebării corectitudinea aplicării metodei variabilelor de stare în cazul elementelor în exces. Eliminarea variabilelor de semistare în exces, pe baza constrângerilor ascunse poate genera grave greșeli de modelare a realității, atunci când condițiile inițiale nu satisfac aceste constrângeri. In acest caz, pentru a obține soluția corectă. trebuie aplicată o procedură de *regularizare a condițiilor inițiale inconsistente,* prin care acestea sunt transformate în unele consistente, și apoi se poate aplica eliminarea variabilelor de semistare în exces. Dificultatea este sporită deoarece în astfel de situații, nu poate fi aplicată nici verificarea bazată pe bilanțul energetic. Aceasta este explicația faptului că circuitele cu elemente în exces se mai numesc și *circuite patologice.*

Revenim la procedura de regularizare a condițiilor inițiale inconsistente pentru un circuit patologic, pe care o să o fundamentăm, folosind transformarea operațională a relațiilor (2):

$$\begin{bmatrix}\mathbf{u}_{\mathrm{L}c}\\ \mathbf{i}_{\mathrm{C}a}\end{bmatrix}=\begin{bmatrix}-\mathbf{L}_c & \mathbf{0}\\ \mathbf{0} & -\mathbf{C}'_a\end{bmatrix}\frac{d}{dt}\begin{bmatrix}\mathbf{i}_{\mathrm{L}c}\\ \mathbf{u}_{\mathrm{C}a}\end{bmatrix}\Rightarrow\begin{bmatrix}-\mathbf{L}_c & \mathbf{0}\\ \mathbf{0} & -\mathbf{C}'_a\end{bmatrix}^{-1}\begin{bmatrix}\mathbf{u}_{\mathrm{L}c}(s)\\ \mathbf{i}_{\mathrm{C}a}(s)\end{bmatrix}=s\begin{bmatrix}\mathbf{i}_{\mathrm{L}c}(s)\\ \mathbf{u}_{\mathrm{C}a}(s)\end{bmatrix}-\begin{bmatrix}\mathbf{i}_{\mathrm{L}c}(-0)\\ \mathbf{u}_{\mathrm{C}a}(-0)\end{bmatrix};\Rightarrow$$
$$\begin{bmatrix}\mathbf{u}_{\mathrm{L}a}\\ \mathbf{i}_{\mathrm{C}c}\end{bmatrix}=\begin{bmatrix}-\mathbf{L}_a & \mathbf{0}\\ \mathbf{0} & -\mathbf{C}'_c\end{bmatrix}\frac{d}{dt}\begin{bmatrix}\mathbf{i}_{\mathrm{L}a}\\ \mathbf{u}_{\mathrm{C}c}\end{bmatrix}\Rightarrow\begin{bmatrix}-\mathbf{L}_a & \mathbf{0}\\ \mathbf{0} & -\mathbf{C}'_c\end{bmatrix}^{-1}\begin{bmatrix}\mathbf{u}_{\mathrm{L}a}(s)\\ \mathbf{i}_{\mathrm{C}c}(s)\end{bmatrix}=s\begin{bmatrix}\mathbf{i}_{\mathrm{L}a}(s)\\ \mathbf{u}_{\mathrm{C}c}(s)\end{bmatrix}-\begin{bmatrix}\mathbf{i}_{\mathrm{L}a}(-0)\\ \mathbf{u}_{\mathrm{C}c}(-0)\end{bmatrix}. \quad (11)$$

Prin completare cu ecuațiile părții rezistive, se obține in sistem de ecuații liniare, care are ca soluție toți curenții si tensiunile operaționale din elementele reactive. După transformata Laplace inversă rezultă valorile regularizate ale variabilelor de semistare, ca limita (la dreapta) pentru *t* tinde către zero. Pentru *s* tinde către infinit, relațiile operaționale capătă forma:

$$\begin{bmatrix}-\mathbf{L}_c & \mathbf{0}\\ \mathbf{0} & -\mathbf{C}'_a\end{bmatrix}^{-1}\begin{bmatrix}\underline{\mathbf{u}}_{\mathrm{L}c}\\ \underline{\mathbf{i}}_{\mathrm{C}a}\end{bmatrix}=\begin{bmatrix}\mathbf{i}_{\mathrm{L}c}(+0)\\ \mathbf{u}_{\mathrm{C}a}(+0)\end{bmatrix}-\begin{bmatrix}\mathbf{i}_{\mathrm{L}c}(-0)\\ \mathbf{u}_{\mathrm{C}a}(-0)\end{bmatrix}\Rightarrow\begin{bmatrix}\underline{\mathbf{u}}_{\mathrm{L}c}\\ \underline{\mathbf{i}}_{\mathrm{C}a}\end{bmatrix}=\begin{bmatrix}-\mathbf{L}_c & \mathbf{0}\\ \mathbf{0} & -\mathbf{C}'_a\end{bmatrix}\begin{bmatrix}\Delta\mathbf{i}_{\mathrm{L}c}\\ \Delta\mathbf{u}_{\mathrm{C}a}\end{bmatrix},$$
$$\begin{bmatrix}-\mathbf{L}_a & \mathbf{0}\\ \mathbf{0} & -\mathbf{C}'_c\end{bmatrix}^{-1}\begin{bmatrix}\underline{\mathbf{u}}_{\mathrm{L}a}\\ \underline{\mathbf{i}}_{\mathrm{C}c}\end{bmatrix}=\begin{bmatrix}\mathbf{i}_{\mathrm{L}a}(+0)\\ \mathbf{u}_{\mathrm{C}c}(+0)\end{bmatrix}-\begin{bmatrix}\mathbf{i}_{\mathrm{L}a}(-0)\\ \mathbf{u}_{\mathrm{C}c}(-0)\end{bmatrix}\Rightarrow\begin{bmatrix}\underline{\mathbf{u}}_{\mathrm{L}a}\\ \underline{\mathbf{i}}_{\mathrm{C}c}\end{bmatrix}=\begin{bmatrix}-\mathbf{L}_a & \mathbf{0}\\ \mathbf{0} & -\mathbf{C}'_c\end{bmatrix}\begin{bmatrix}\Delta\mathbf{i}_{\mathrm{L}a}\\ \Delta\mathbf{u}_{\mathrm{C}c}\end{bmatrix}, \quad (12)$$

care pune in evidență discontinuitatea $\Delta\mathbf{x}=\mathbf{x}(+0)-\mathbf{x}(-0)$, definită ca diferența intre limita la dreapta si limita la stânga în origine), adică saltul pe care variabilele de stare îl au în vecinătatea momentului inițial. Relația finală este obținută și prin integrarea pe această vecinătate a ecuației diferențiale originale. Aici s-a notat:

$$\underline{\mathbf{x}}=\int_{-0}^{+0}\mathbf{x}(t)dt=\lim_{s\to\infty}s\left[\frac{1}{s}\mathbf{X}(s)\right],\qquad \mathbf{X}(s)=\mathcal{L}(\mathbf{x}(t)), \quad (13)$$

mărime cu valoare nula, în cazul variabilelor de stare continue in origine și nenulă, în cazul variabilelor cu condiții inițiale inconsistente. In acest ultim caz, mărimea integralei reprezintă factorul ce multiplică impulsul Dirac unitar al mărimii duale variabilei respective de stare (tensiunea la bornele bobinelor in exces si curentul prin condensatoarele in exces). Folosind ecuațiile părții rezistive, rezultă

$$-\begin{bmatrix}\mathbf{L}_c & \mathbf{0}\\ \mathbf{0} & \mathbf{C}'_a\end{bmatrix}\begin{bmatrix}\Delta\mathbf{i}_{\mathrm{L}c}\\ \Delta\mathbf{u}_{\mathrm{C}a}\end{bmatrix}+\begin{bmatrix}\mathbf{A}_{\mathrm{L}c\mathrm{L}a}\mathbf{L}_a & \mathbf{R}_{\mathrm{L}c\mathrm{C}c}\mathbf{C}'_c\\ \mathbf{G}_{\mathrm{C}a\mathrm{L}a}\mathbf{L}_a & \mathbf{B}_{\mathrm{C}a\mathrm{C}c}\mathbf{C}'_c\end{bmatrix}\begin{bmatrix}\Delta\mathbf{i}_{\mathrm{L}a}\\ \Delta\mathbf{u}_{\mathrm{C}c}\end{bmatrix}=\begin{bmatrix}\mathbf{R}_{\mathrm{L}c\mathrm{L}c} & \mathbf{A}_{\mathrm{L}c\mathrm{C}a}\\ \mathbf{B}_{\mathrm{C}a\mathrm{L}c} & \mathbf{G}_{\mathrm{C}a\mathrm{C}a}\end{bmatrix}\begin{bmatrix}\underline{\mathbf{i}}_{\mathrm{L}c}\\ \underline{\mathbf{u}}_{\mathrm{C}a}\end{bmatrix}+\begin{bmatrix}\mathbf{R}_{\mathrm{L}c\mathrm{j}} & \mathbf{A}_{\mathrm{L}c\mathrm{j}}\\ \mathbf{B}_{\mathrm{C}a\mathrm{j}} & \mathbf{G}_{\mathrm{C}a\mathrm{e}}\end{bmatrix}\begin{bmatrix}\underline{\mathbf{j}}\\ \underline{\mathbf{e}}\end{bmatrix}\Rightarrow$$
$$-\begin{bmatrix}\mathbf{L}_c & \mathbf{0}\\ \mathbf{0} & \mathbf{C}'_a\end{bmatrix}\begin{bmatrix}\mathbf{i}_{\mathrm{L}c+}\\ \mathbf{u}_{\mathrm{C}a+}\end{bmatrix}+\begin{bmatrix}\mathbf{A}_{\mathrm{L}c\mathrm{L}a}\mathbf{L}_a & \mathbf{R}_{\mathrm{L}c\mathrm{C}c}\mathbf{C}'_c\\ \mathbf{G}_{\mathrm{C}a\mathrm{L}a}\mathbf{L}_a & \mathbf{B}_{\mathrm{C}a\mathrm{C}c}\mathbf{C}'_c\end{bmatrix}\begin{bmatrix}\mathbf{i}_{\mathrm{L}a+}\\ \mathbf{u}_{\mathrm{C}c+}\end{bmatrix}=$$
$$-\begin{bmatrix}\mathbf{L}_c & \mathbf{0}\\ \mathbf{0} & \mathbf{C}'_a\end{bmatrix}\begin{bmatrix}\mathbf{i}_{\mathrm{L}c-}\\ \mathbf{u}_{\mathrm{C}a-}\end{bmatrix}+\begin{bmatrix}\mathbf{A}_{\mathrm{L}c\mathrm{L}a}\mathbf{L}_a & \mathbf{R}_{\mathrm{L}c\mathrm{C}c}\mathbf{C}'_c\\ \mathbf{G}_{\mathrm{C}a\mathrm{L}a}\mathbf{L}_a & \mathbf{B}_{\mathrm{C}a\mathrm{C}c}\mathbf{C}'_c\end{bmatrix}\begin{bmatrix}\mathbf{i}_{\mathrm{L}a-}\\ \mathbf{u}_{\mathrm{C}c-}\end{bmatrix}+\begin{bmatrix}\mathbf{R}_{\mathrm{L}c\mathrm{j}} & \mathbf{A}_{\mathrm{L}c\mathrm{j}}\\ \mathbf{B}_{\mathrm{C}a\mathrm{j}} & \mathbf{G}_{\mathrm{C}a\mathrm{e}}\end{bmatrix}\begin{bmatrix}\underline{\mathbf{j}}\\ \underline{\mathbf{e}}\end{bmatrix}, \quad (14)$$

în care s-a notat $\mathbf{x}_-=\mathbf{x}(-0),\mathbf{x}_+=\mathbf{x}(+0)$, și s-a ținut cont de faptul că variabilele de stare (curenții din bobinele coarborelui si tensiunile condensatoarelor din arbore) sunt funcții clasice (nu au in componența lor impulsuri Dirac) și în consecință, au integrale nule pe intervale de măsură nulă. Folosind constrângerile ascunse (3), evaluate la momentul +0, rezultă

$$\mathbf{u}_{\mathrm{C}c+}=-\mathbf{D}_C\mathbf{u}_{\mathrm{C}a+}-\mathbf{D}_e\mathbf{e}(+0);$$
$$\mathbf{i}_{\mathrm{L}a+}=\mathbf{D}_L^T\mathbf{i}_{\mathrm{L}c+}+\mathbf{D}_j^T\mathbf{j}(+0),\Rightarrow \quad (15)$$

$$\left(\begin{bmatrix}\mathbf{A}_{\mathbf{L}cLa}\mathbf{L}_a & \mathbf{R}_{\mathbf{L}cCc}\mathbf{C}'_c\\ \mathbf{G}_{CaLa}\mathbf{L}_a & \mathbf{B}_{\mathbf{C}aCc}\mathbf{C}'_c\end{bmatrix}\begin{bmatrix}\mathbf{D}_L^T & 0\\ 0 & -\mathbf{D}_C\end{bmatrix}-\begin{bmatrix}\mathbf{L}_c & \mathbf{0}\\ \mathbf{0} & \mathbf{C}'_a\end{bmatrix}\right)\begin{bmatrix}\mathbf{i}_{\mathbf{L}c+}\\ \mathbf{u}_{\mathbf{C}a+}\end{bmatrix}=-\begin{bmatrix}\mathbf{L}_c & \mathbf{0}\\ \mathbf{0} & \mathbf{C}'_a\end{bmatrix}\begin{bmatrix}\mathbf{i}_{\mathbf{L}c-}\\ \mathbf{u}_{\mathbf{C}a-}\end{bmatrix}+$$
$$\begin{bmatrix}\mathbf{A}_{\mathbf{L}cLa}\mathbf{L}_a & \mathbf{R}_{\mathbf{L}cCc}\mathbf{C}'_c\\ \mathbf{G}_{CaLa}\mathbf{L}_a & \mathbf{B}_{\mathbf{C}aCc}\mathbf{C}'_c\end{bmatrix}\begin{bmatrix}\mathbf{i}_{\mathbf{L}a-}\\ \mathbf{u}_{\mathbf{C}c-}\end{bmatrix}+\begin{bmatrix}\mathbf{R}_{\mathbf{L}c\mathbf{j}} & \mathbf{A}_{\mathbf{L}c\mathbf{j}}\\ \mathbf{B}_{C\mathbf{aj}} & \mathbf{G}_{C\mathbf{ae}}\end{bmatrix}\begin{bmatrix}\underline{\mathbf{j}}\\ \underline{\mathbf{e}}\end{bmatrix}-\begin{bmatrix}\mathbf{A}_{\mathbf{L}cLa}\mathbf{L}_a & \mathbf{R}_{\mathbf{L}cCc}\mathbf{C}'_c\\ \mathbf{G}_{CaLa}\mathbf{L}_a & \mathbf{B}_{\mathbf{C}aCc}\mathbf{C}'_c\end{bmatrix}\begin{bmatrix}\mathbf{D}_j^T\mathbf{j}(+0)\\ -\mathbf{D}_e\mathbf{e}(+0)\end{bmatrix}. \quad (16)$$

Rezolvând sistemul (16) de ecuații algebrice liniare, reale, rezultă valorile inițiale regularizate (limita la dreapta, pentru +0) ale variabilelor de stare (curenții din bobinele coarborelui si tensiunile condensatoarelor din arbore). Folosind constrângerile ascunse (3) se determină valorile regularizare și ale variabilelor de stare în exces. Iar apoi, folosind integralele ecuațiilor constitutive (2), se obțin curenții din condensatoare și tensiunile la bornele bobinelor. Coeficienții impulsurilor Dirac ce descriu aceste semnale sunt proporționali cu saltul pe care variabila de semistare o are in origine. Procedura se poate aplica atât numeric, cât și simbolic.

4 Concluzii

Din analiza prezentată observăm că metoda cea mai simplă de analiză a circuitelor cu elemente în exces, dar și cea mai robustă este cea bazată pe reprezentarea operațională, care are avantajul că transformă operatorii de derivare în relații algebrice și reprezintă condițiile inițiale ca termeni în ecuațiile rezolvate, tratându-le implicit ca surse independente echivalente. Deoarece prin metoda operațională, se analizează circuitul nu numai în regimul tranzitoriu din intervalul $(0,\infty)$ ci și cel din vecinătatea originii (-0,+0), ținând cont de singularitățile care apar, și regularizând automat condițiile inițiale inconsistente, cu această metodă este eliminat și riscul impunerii greșite a condițiilor inițiale, risc relatat anterior. Reprezentarea operațională a ecuațiilor circuitelor electrice permite fără dificultăți analiza lor simbolică, dar și cea numerică, în domeniul frecvenței. Deoarece nu putem face deosebirea, din punct de vedere fizic între variabile de stare si cele de semistare în exces, ci dimpotrivă, deoarece soluția este determinată de valorile inițiale ale tuturor acestor variabile (de semistare, în exces sau nu), în consecință, curenții tuturor bobinelor și tensiunile tuturor condensatoarelor din circuit sunt „*variabile de stare - în sens fizic*”. Acesta, în baza definiției variabilelor de stare, ca fiind acele mărimi fizice, ale căror valori inițiale determină, alături de excitații, evoluția ulterioară a sistemului.

În concluzie, notăm că utilizarea variabilelor de stare nu este cea mai eficientă metodă de analiză numerică sau simbolică a circuitelor electrice, în schimb, ea este de neînlocuit pentru analiza calitativă a acestor circuite. În plus, mai notăm că abordarea DAE este mai riguroasă și mai generală, decât cea bazată pe eliminarea variatelor de semistare în exces, care nu poate rezolva corect probleme, cărora nu li s-a aplicat procedura de regularizare a condițiilor inițiale.

Referinţe

[1] S. Seshu and N. Balabanian, *Linear Network Analysis*. Wiley, New York, 1964.

[2] A. Opal and J. Vlach. Consistent initial conditions of linear switched networks. *Circuits and Systems, IEEE Transactions on* **37** (1990) 364-372.

[3] J. Tolsa, M. Salichs. Analysis of linear networks with inconsistent initial conditions, *Circuits and Systems I, IEEE Transactions on,* **40** (1993) 885 – 894.

[4] J. Vlach, J.M. Wojciechowski, and A. Opal. Analysis of nonlinear networks with inconsistent initial conditions. *Circuits and Systems I, IEEE Transactions on* **42**, (1995) 195-200.

[5] D. Estevez Schwarz, Consistent initial values for DAE systems in circuit simulation, Citeseer, 1999

[6] H.G. Brachtendorf. "On consistent initial conditions for circuit's DAEs with higher index." *Circuits and Systems I, IEEE Transactions on* **48** (2001) 606-612.

[7] R. Frasca, et al. Linear passive networks with ideal switches: Consistent initial conditions and state discontinuities. *Circuits and Systems I, IEEE Transactions on* **57** (2010) 3138-3151.

HIGH EFFICIENCY LLC RESONANT CONVERTER

Sergiu OPREA*, Mihai-Constantin TANASE*
MICROCHIP, Bucharest, Romania, sergiu.oprea@microchip.com, mihai.tanase@microchip.com

Adriana FLORESCU
"Politehnica" University of Bucharest, Splaiul Independenței 313 Bd., 060042, Bucharest, adriana.florescu@upb.ro

Abstract. The mathematical analysis, design, modeling, simulation and experimental implementation of a LLC resonant converter used in a conversion system that transforms the 230Vac of the energy distribution network into 12 Vdc are presented in this paper. System's conversion efficiency is over 90% for all the power range between 0W and 100W. Only the power blocks are detailed. The digital control with a dsPIC from the Microchip company of the entire conversion system will be the subject of another more detailed paper.

1 Introduction

Among many topologies of dc-dc converters, the designer must select the suitable one according to the specified application and taking account of many constrains such as: high efficiency, high operating frequency, large ranges of the input or output voltages etc. The resonant converters represent a good option because of their specific high efficiency together with low power commutation losses, unlike the traditional PWM-based control implementations [1].

During the period 1970-1980, traditional PWM converters were limited to operating frequencies around 20-50KHz because during transitions between on and off states both the voltages and currents of the switches are high, thus resulting power losses. As a primary solution, snubber circuits used to protect the switches proved to be power consumers and reducing converter's efficiency. At the begining of 1980's resonant converters were developped. The basic ideea of a resonant converter is their command, either when their voltage is zero (ZVS) or their current is zero (ZCS). Thus, the waveform through the power devices is close to the sinusoidal one, which represent a major benefit conparing with the rectangular waveform of the classical converters that causes electromagnetic inferences (EMI) during the commutation process. The commutation moment must be chosen close to the zero transition of the sinusoidal voltage or current in order to obtain lower power losses, higher operating frequencies and higher density powers through the power semiconductor devices implemented as switches [2].

As the name indicates, the LLC resonant converter includes two inductances (LL) and a capacity (C) that generate a sinusoidal voltage or current on the switches. Any classical topology of dc-dc converter can be transformed into a resonant one using such an additional resonant circuit, but such a topology with more electrical components may not be in all cases justified compared with the complex scheme of the obtained resonant converter [3].

The LLC resonant converter with high dc-dc convertion ratio and high efficiency presented in this article is included in a ac-dc conversion system supplyied by the ac national grid. Other specific applications of the LLC resonant converters are: flat panel monitors/TVs, 85+ ATX PCs or small form factor PCs, wherever the requirements on efficiency and power density are getting tougher. The maximul power ranges for LLC resonant converters are between 100W and 1500W and their maximum efficiency is generaly over 85%. [4]

2 Mathematical analysis, modeling and design of the proposed LLC resonant converter

The operating principle of the proposed half-bridge LLC converter is presented in the circuit topology (fig.1). The *230Vac* grid voltage is converted into V_{in}*=324Vdc* using a bridge rectifier (it doesn't appear in fig.1) that supplies the commutation net represented by switches Q_1 and Q_2 (which are MOSFET tranzistors) which transform the continuous voltage waveform into a rectangular one. The resonannt half-bridge LLC tank includes the capacitor C_r, the inductance L_r and the magnetizing inductance L_m of transformer (with a turn ratio of n:1) considered ideal. The circuit continues with another bridge rectifier with diodes D_1 and D_2, the output filter with the capacitor C_{out} and the resistive load R_0 where from the output voltage V_{out} is collected.
All above mentioned reprezent power blocks in fig.1, while the digital control with dsPIC44F from the Microchip Company [5] and the auxiliary blocks that insure the right operation according to the control algortihm will be detailed in another paper.

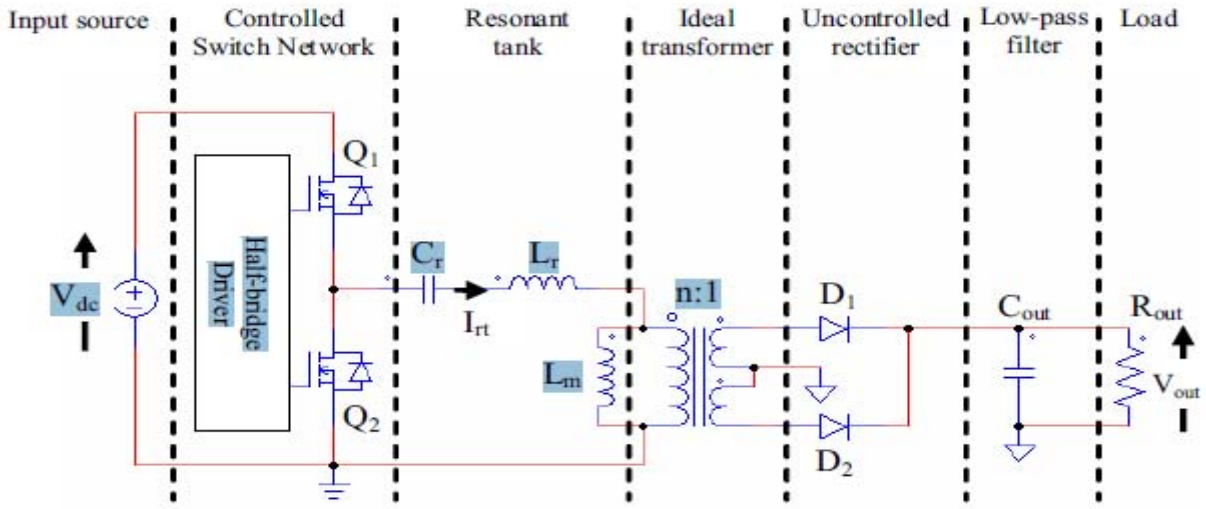

Fig.1: LLC resonant half-bridge converter

After mathematical analysis with Laplace operator of the entire circuit in fig.1 was achieved (the resonant tank and the trasformer were treated as a two-port model having a transfer function H(s)), it was demonstrated that the module of the transfer function (simply called voltage gain) at the switching frequency f_{sw} is:

$$M(f_{sw}) = n \cdot |H(s)| = 1 / \sqrt{\left(+1 - \frac{}{f_n^2} \right)^2 + Q^2 \cdot \left(f_n - \frac{1}{f_n} \right)^2}, \qquad (1)$$

where $\lambda = L_r/L_m$ is the inductance ratio, $f_n = f_{sw}/f_r$ is the normalized frecquency, $f_r = 1/2\sqrt{L_r C_r}$ is the resonance frequency, $Z_0 = \sqrt{L_r / C_r}$ is the characteristic impedance and $Q = {}^2 Z_0 P_{out} / 8n^2 V_{out}^2$ is the quality factor.

***

The numerical design specifications in this paper are:

- Input voltage range: $V_{dc} \in [V_{dc,min} = 280V, V_{dc,max} = 360V]$;
- Nominal imput voltage: $V_{dc,nom}$*=324V;*
- Regulated output voltage: V_{out}=12V;
- Maximum output power: P_{out}*=120W*;
- Resonant frequency: f_r*=200KHz;*

- Maximum operating frequency: f_{max}=270KHz;
- Parasitical capacitance at node N: C_{zvs}=4.3nF;
- Deadtime for Q_1 and Q_2 switching net: T_D=200ns.

General criteria for design:

- The converter will be designed to work at resonance at nominal imput voltage;
- The converter must be able to regulate down to zero load at maximum input voltage;
- The converter will always work in ZVS in the whole operating range.

The design includes ten-step procedure:

Step 1: To fulfill the first criterion, impose that the required gain at nominal input voltage equals unity and calculate the transformer turn ratio:

$$M_{nom} = 2n \cdot \frac{V_{out}}{V_{dc.nom}} = 1 \quad \Rightarrow \quad n = \frac{V_{dc}}{2V_{out}} = 13.5 \tag{2}$$

Step 2: Calculate the maximum and minimum required gain at the extreme values of the input voltage range:

$$M_{max} = 2n \cdot \frac{V_{out}}{V_{dc,min}} = 1.157 \tag{3}$$

$$M_{min} = 2n \cdot \frac{V_{out}}{V_{dc.max}} = 0.9 \tag{4}$$

Step 3: Calculate the maximum normalized operating frequency (according to its definition):

$$f_{n,max} = \frac{f_{max}}{f_r} = 1.35 \tag{5}$$

Step 4: Calculate the effective load resistance reflected at transformer primary side:

$$R_e = \frac{8n^2 V_{out}^2}{^2 P_{out}} = 177.27\,\Omega \tag{6}$$

Step 5: Impose that the converter operates at maximum frequency at zero load and maximum input voltage:

$$= \frac{(1 - M_{min}) \cdot f_{n,max}^2}{M_{min} \cdot \left(f_{n,max}^2 - 1\right)} = 0.246 \tag{7}$$

Step 6: Calculate the maximum Q value to work in the ZVS operating region at minimum input voltage and full load condition:

$$Q_{zvs1} = \frac{95}{100 M_{max}} \sqrt{\frac{1}{} + \frac{M_{max}^2}{M_{max}^2 - 1}} = 0.572 \tag{8}$$

Step 7: Calculate the maximum Q value to work in the ZVS operating region at no-load condition and maximum input voltage:

$$Q_{zvs2} = \frac{2}{} \cdot \frac{f_{n,max}}{(\ -1) f_{n,max}^2 -} \cdot \frac{T_D}{R_e C_{zvs}} = 0.342 \tag{9}$$

Step 8: Choose the maximum quality factor for ZVS in the whole operating range:

$$Q_{zvs} = 0.3384 < min\left(Q_{zvs,1}, Q_{zvs,2}\right) = 0.342 \tag{10}$$

Step 9: Calculate the minimum operating frequency at full load and minimum input voltage, according to the following approximate formula:

$$f_{min} = f_r \cdot \sqrt{\frac{1}{1+\frac{1}{\cdot}\left(1-\frac{1}{M_{max}^{1+(Q_{zvs}/Q_{max})^4}}\right)}} = 157.953KHz \quad (11)$$

Step 10: Calculate the characteristic impedance of the resonant tank and all component values:

$$Z_0 = Q_{zvs} R_e = 60\Omega \quad (12)$$

$$C_r = \frac{1}{2\ f_r Z_0} = 13.2nF \quad (13)$$

$$L_r = \frac{Z_0}{2\ f_r} = 48\ \ F \quad (14)$$

$$L_m = \frac{L_r}{} = 194\ \ H \quad (15)$$

For the above calculated data, the voltage gain M for different switching frequencies in the range 1KHz-1MHz are shown in fig.2, where the maximum value is obtained for 199.99Hz. The gain waveform proves an accurate digital control with dsPIC33F from Microchip company for a large scale of the input voltages.

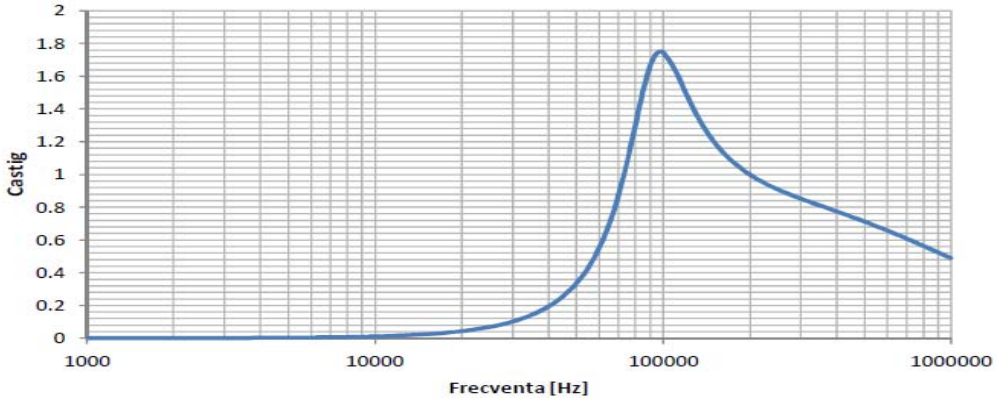

Fig.2: Conversion ratio for LLC resonant converter

3 Power LLC resonant converter simulated with SIMetrix

Convergence is often a problem with many simulators especially in power electronics because the wide range of currents, voltages and conductances present in power circuits stretches the precision of the underlying algorithms. SIMetrix is a mixed-mode circuit simulation package designed for professional electronics engineers that comprises a substantially enhanced SPICE simulator, schematic editor and waveform viewer all seamlessly integrated into one program.
The simulated values in fig.3 are: V_{in}=330VDC, V_{out}=12VDC, I_{out}=10A, f_{sw}=199kHz. There is a difference between the simulated and the real circuit: simulation in fig.3 used a bridge diode rectifier, while the experimental circuit used two MOSFETs transistors that offer low voltages on their connecting terminals, thus increasing converter's efficiency. MOSFTEs transistors Q_1 and Q_2 were driven on and off symmetrically with a rectangular waveform with a 50% duty cycle at a frequency near to the resonance one and no overlapping. To the on switching state the dead time T_D was added in order to avoid shortcircuits because of the delay times during the turn-on and turn-off states of Q_1 and Q_2.

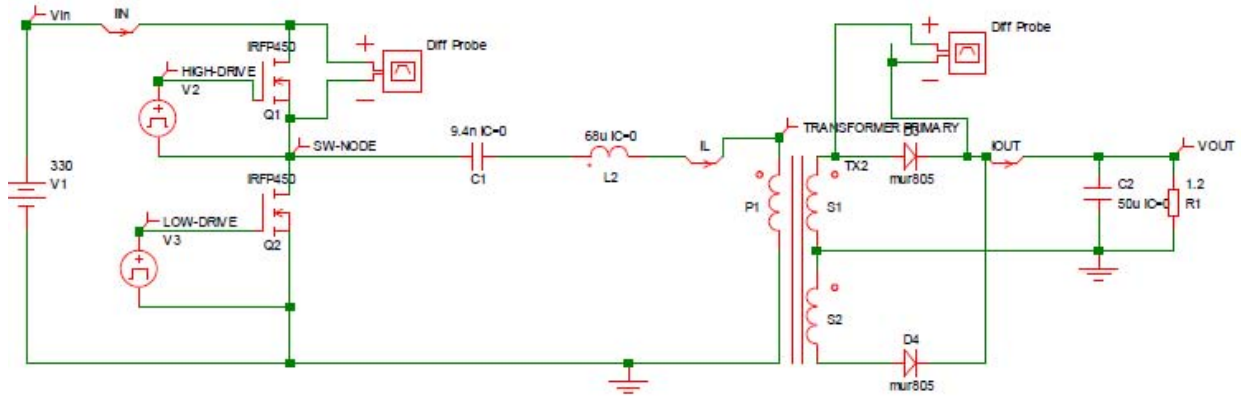

Fig.3: LLC resonant converter simulated with SIMetrix program

Fig.4 is a loop of the voltage and current represented in time that shows the advantage of the resonant topologies compared with the classical ones, namely to reduce power switching losses. It can be observed that, because of the deadtime T_D, the voltage on MOSFETs transistors are able to touch a near zero voltage, this moment being the begining of ZVS switching mode with no losses.

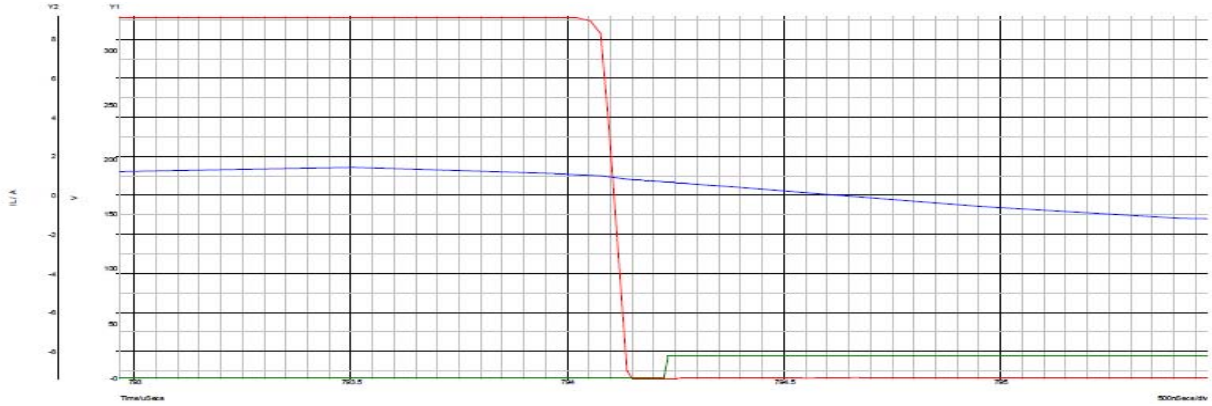

Fig.4: ZVS transition voltage and current waveforms

Fig.5 illustrates the output voltage $V_{out}(t)$ for the chosen switching frequency $f_{sw}=199Hz$, that was also chosen in fig.2. Converter's stability is demonstrated by the ripple of 30mV, that is only 0.25% of the output voltage, but V_{out}=12Vdc is diminished to the approximate value of 11.25Vdc because of suplimentary voltage drops on the transformer and rectifying bridge.

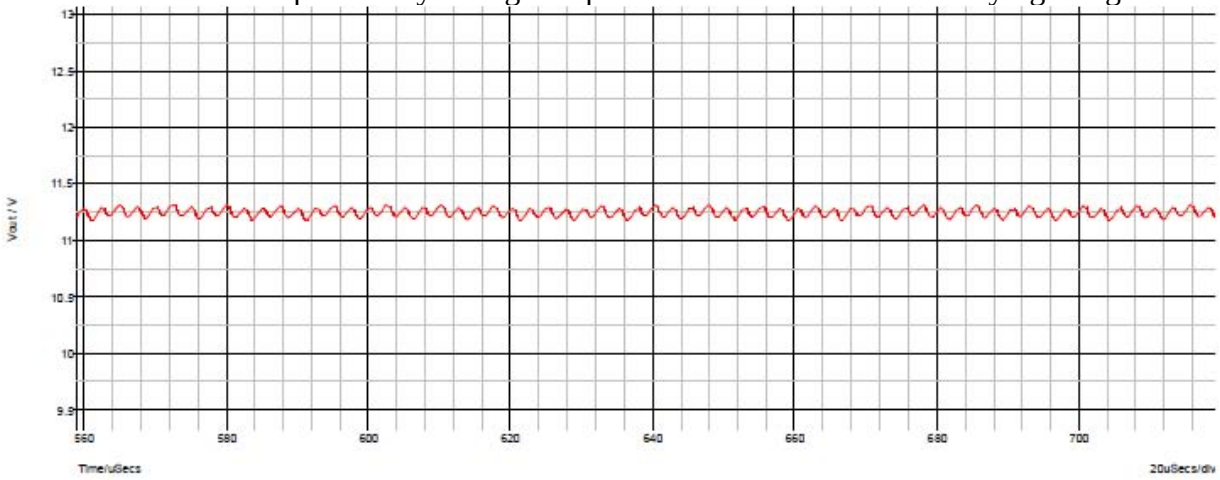

Fig.5: Output voltge $V_{out}(t)$ waveform

5 Experimental results

The practical implementation is presented in fig.6 and includes both the power blocks described in this articole and the control block represented by the Microchip dsPIC33F and two MOSFETs drives. In addition, there are a current sensor and an auxiliary flyback power source. The difficulties appeared because of the high frequency transformer that affect converter's performances. Also, the control becomes difficult for maximum load and minimum input voltage because the gain curve in fig.2 must be high to keep the stability of the output voltage.

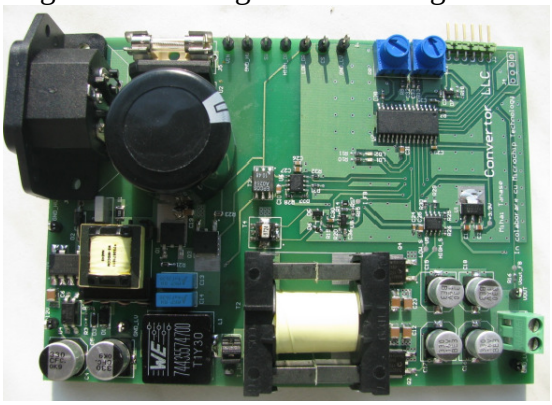

Fig.6. Practical implementation of the LLC resonant converter controlled by sdPIC33F

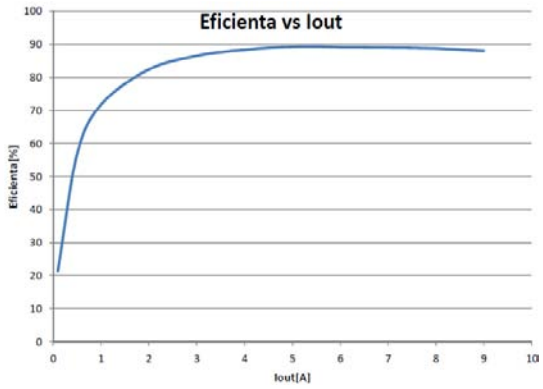

Fig.7: Converter's efficiency evolution vs. load current

Fig.7 illustrates that the efficiency grows with the load value so that the power losses on dsPIC and MOSFTEs transistors are negligible within the range 4A-8A, when LLC resonant converter reaches over 90% efficiency.

6 Conclusions

Though the topology and its design are more complicated, compared with classical converters, the high efficiency obtained by LLL resonant converters allows higher power density and smaller dimensions, which are this topology's main advantages. Other advantages are: soft-switching of all semiconductor devices (in this paper ZVS was chosen, resulting from a correct design of the resonant tank), ability to accommodate an extremely broad load range with an acceptable frequency variation (also this property results from a correct design of the resonant tank), magnetic integration (which allows the combination of different magnetic devices into a single physical device), smooth waveforms with low dv/dt edges, low EMI emissions, small filtering requirements and high switching frequency capability.

The paper presents a LLC-ZVS resonant converter with over 90% applied in high conversion ratio practical implementations, such as ac-dc grid converters. This paper focused only on the power circuit. Another paper will be focused on the digital control using a Microchip dsPIC controller.

References

[1] F.Luo, H.Ye, M.Rashid, *Digital Power Electronics and Applications*, Elsevier Academic Press, 2005
[2] S. Buso, P. Mattaveli, *Digital Control in Power Electronics*, Morgan and Claypool Pblishers, 2006
[3] J.-W. Huang, S.-C. Wang, Y.-H. Liu, *Design of a digitally-controlled LLC resonant converter*, International Conference on Information and Electronics Engineering, Bangkok, Thailand, 2011
[4] M.Z. Youssef, P.K. Jain, *A front End Self-Sustained LLC resonant converter*, Annual IEEE Power Electronics Specialists Conference, Aachen, Germany, 2004
[5] dsPIC33FJ16GSX02/X04, High-Performance, 16-bit Digital Signal Controllers, Datasheet, Microchip Inc. 2009

Convergence Problems in Transient Analysis of Circuits Containing MEMS

Florin CONSTANTINESCU, Alexandru Gabriel GHEORGHE, Miruna NITESCU
"Politehnica" University, Bucharest, Romania; florin.constantinescu@upb.ro

Abstract. An accelerometer using femtofarad time-variable capacitive sensors is studied. A new circuit model for a linear time-variable capacitor, on which these sensors are based, is proposed. A scaling factor is introduced in this model in order to avoid the transient analysis failure. Some open problems related to the transient analysis convergence are discussed.

1 Introduction

In the last years the microelectromechanical systems (MEMS) like actuators, pressure sensors, accelerometers, gyroscopes and others know an unprecedented development. These devices are parts of some complex electrical/electronic systems working at relatively high frequencies. In order to design these complex systems the MEMS circuit models are incorporated in intricate circuits whose transient analysis must be performed. Due to unusual parameter values as femtofarad capacities this transient analysis made by commercial simulators as SPICE or SPECTRE fails to converge.

A schematic for the acceleration measurement using a commercial capacitive accelerometer [1, 2] is studied in this paper from the viewpoint of the transient analysis convergence. The sensor structure and its operation together with the electronic circuit used for the acceleration measurement are presented in Section 2. A new equivalent circuit for a linear time-variable capacitor is described in Section 3. In order to avoid the transient analysis failure a scaling factor is introduced in this equivalent circuit. The results obtained with the circuit simulators SPICEP, PSPICE and SPECTRE for various values of this scaling factor are given in Section 4. Some open problems related to the transient analysis failure for this acceleration measurement schematic are discussed in Section 5.

2 Capacitive accelerometer

The acceleration sensor structure is given in Fig. 1. A movable microstructure is attached by means of two springs to the substrate, which remains fixed. This microstructure can move only up and down. All fixed plates are connected together as well as the mobile plates. A lot of capacitors connected in parallel are created by this way between the movable and the fixed plates. For a pair of plates two capacities can be identified:

$$C_1 = \frac{\varepsilon A}{d+x} = C_0 - \Delta C \text{ and } C_2 = \frac{\varepsilon A}{d-x} = C_0 + \Delta C \quad (1)$$

where A is the capacitor area, d is the distance between the plates corresponding to a null acceleration of the movable microstructure, ε is the dielectric permittivity, and x is the displacement between the fixed and the movable plates. It follows that:

$$C_2 - C_1 = 2\Delta C = 2\varepsilon A \frac{x}{d^2 - x^2} \text{ or } \Delta C x^2 + \varepsilon A x - \Delta C d^2 = 0 \quad (2)$$

For $x << 1$ it results $x \approx d\frac{\Delta C}{C_0}$ (3)

The equilibrium equation between the elastic and inertial forces gives $a = kx/m$, which leads finally to $a = K\Delta C$. (4)

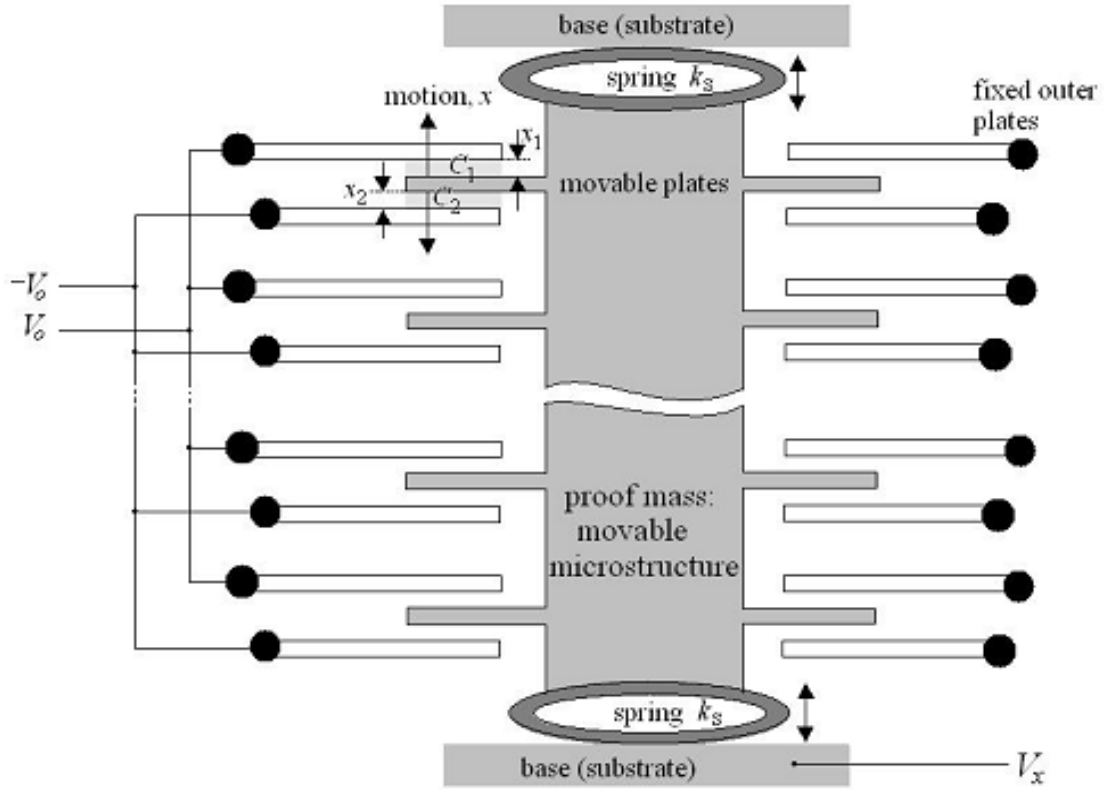

Figure 1: Capacitive accelerometer sensor.

It follows that a signal proportional to ΔC is a measure of the instantaneous acceleration. The current through a linear time-variable capacitor with a capacity C(t) is

$$i = \frac{dq}{dt} = \frac{d}{dt}(C(t)\cdot u(t)) = \frac{dC(t)}{dt}\cdot u(t) + C(t)\cdot\frac{du(t)}{dt} \qquad (5)$$

where u(t) is the capacitor voltage. In order to obtain a signal proportional with C(t) the first term in (5) must be negligible with respect to the second one. The schematic for the acceleration measurement is given in Fig. 2.

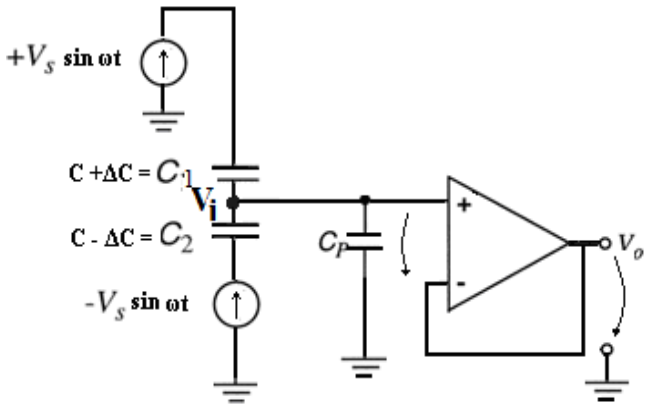

Figure 2: Acceleration measurement

The output potential V_o can be computed as: $V_0 = \frac{\Delta C}{C} V_S \sin \omega t = \frac{a}{KC} V_S \sin \omega t$ (6)

For the transient analysis we consider a sinusoidal acceleration with f_a=1KHz and a sinusoidal supply V_s=1V with f=1MHz, so that the capacity is:

$C + \Delta C = 100 + 2 \cdot \sin(2\pi f_a t)\,[fF]$ (7)

3 Equivalent circuit of a linear time-variable capacitor

A time-variable capacitor model has two-ports: the main one at which it behaves as the desired device, and the control port at which the function representing the time variation of the capacity is applied. A model of this kind is given in [3]. Because this model doesn't allow *C(t)* to take a zero value, we developed a new one starting from the equation (5). This model, shown in Fig. 3, exhibits a linear time-variable capacitor behavior between the terminals 1 and 2. The control voltage is applied between the node *CTRL* and ground.

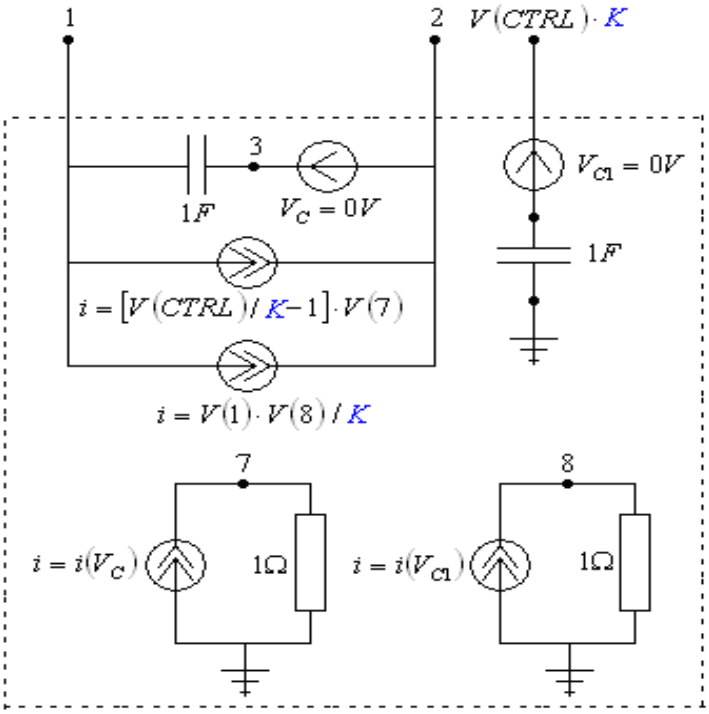

Figure 3: Linear time-variable capacitor model

For the schematic in Fig. 2, according to (7), the control voltage *V(CTRL)* has the order of magnitude of 10^{-13} V. In order to improve the transient analysis convergence *V(CTRL)* may be multiplied by a factor *K*. To obtain the same behavior at the port (1, 2) the same K must be introduced in the expressions of two control factors as it is shown in Fig. 3.

4 Transient analysis results

Some tests have been performed on the schematic in Fig. 2 with the time-variable capacities given by (7). To this end three commercial time domain simulators have been used: PSPICE, SPICEP, and SPECTRE. If *K=1* all simulators have convergence problems and the transient analysis is stopped, the error "time step too small" being pointed out. Some tests with *K=10, 10^2, 10^3,…* have been performed. The voltage V_0 is shown in Fig. 4-Fig.6 for two values of K.

PSPICE:
reltol=1e-3 abstol=1e-29 vntol=1e-23
K=1e+3 K=1e+4

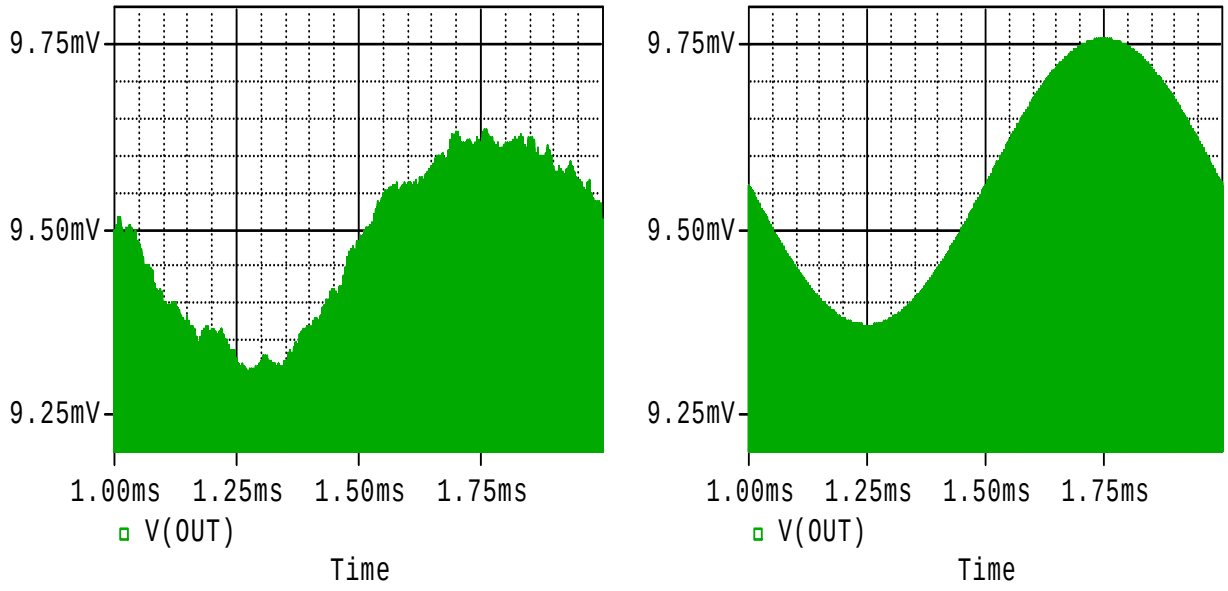

Figure 4: Transient analysis results for PSPICE

SPICEP:
reltol=1e-3 ABSTOL=1e-29 VNTOL=1e-23
K=1E+3 K=1E+4

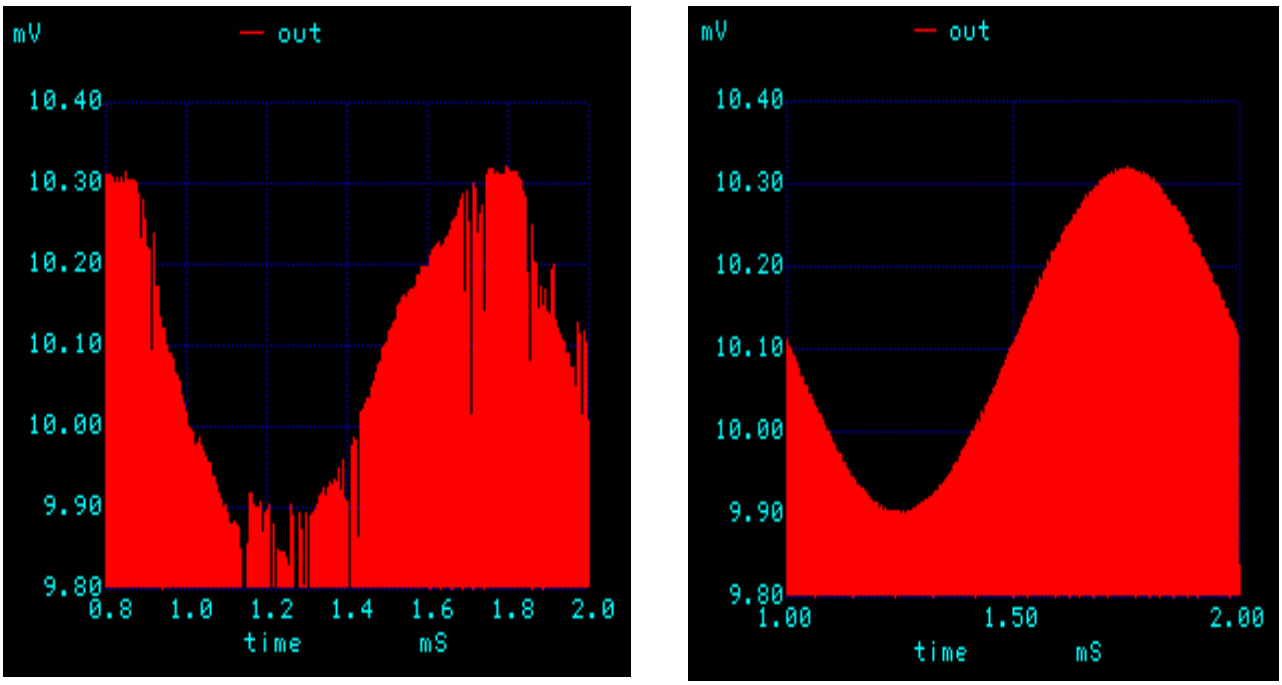

Figure 5: Transient analysis results for SPICEP

SPECTRE:
reltol=1e-3, iabstol=1e-29, vabstol=1e-23

K=1E+3

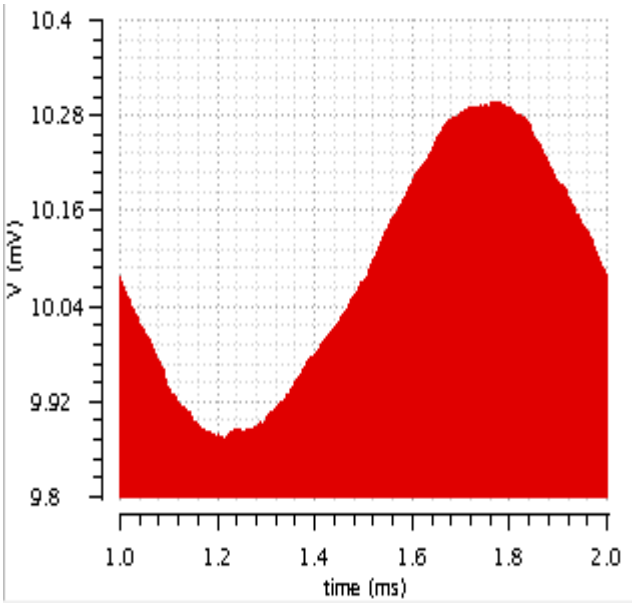

K=1E+4

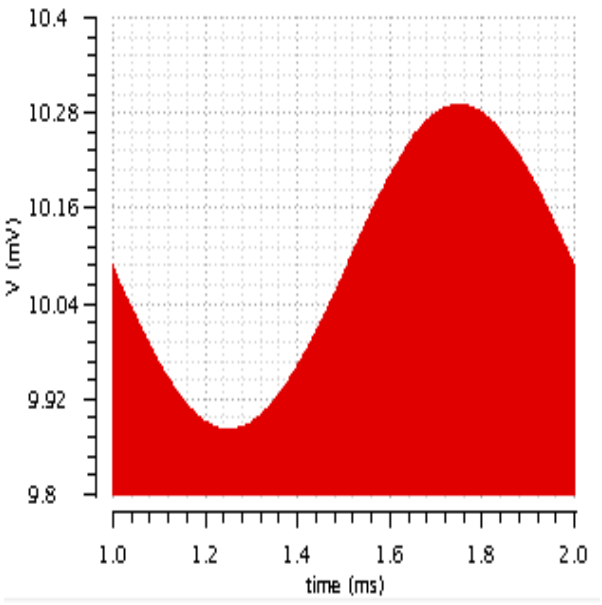

Figure 6: Transient analysis results for SPECTRE

The relative error *reltol* as well as the absolute errors for currents and voltages are the same for all simulators. For all simulators, whose transient analysis algorithms are similar, the waveform corresponding to $K=10^3$ is computed with visible errors, while the waveform corresponding to $K=10^4$ seem to be computed correctly as well as for $10^4<K<10^7$.

5 Discussion

Computation of the condition number of the Jacobian for various SPICEP solutions show that it increases as the time step decreases. This suggests that the time step is reduced due to the erroneous solutions obtained in solving the companion model circuit. For example, if the trapezoidal rule is used, the companion model of a linear 1F capacitor contains a resistor having a *h/2* resistance where h is the time step; if the signal period of 10^{-6}s is divided in 10^3 intervals this resistance will be 0.5 10^{-9} Ω which can be too small to lead to an acceptable value for the condition number. At the same time a 1pF capacitor is associated to a resistance of 0.5 KΩ which may be seen as an acceptable value.

Some open problems can be formulated starting from this case study:

- How to design MEMS circuit models in order to avoid this kind of behavior?
- Is it suitable to define different absolute errors *vabstol* and *iabstol* on subcircuits rather than use the same absolute errors for the whole circuit?
- Is it suitable to define different time steps on subcircuits [4] rather than use the same value of *h* for the whole circuit?

References

[1] S. Senturia, *Microsystem Design*, Boston, Kluwer Academic Publishers, 2002.

[2] M. Nitescu, *Microelectromechanical Systems*, course draft (in Romanian), http://ferrari.lce.pub.ro/studenti, 2009-2012.

[3] C. Basso, SPICE analog behavioral modelling of variable passives, *Power Electronics Technology*, April 2005, pp. 58, www.powerelectronics.com.

[4] A. Verhoeven et al, A general compound multirate method for circuit simulation problems, Eindhoven University of Technology, 2004.

ANALIZA STABILITĂŢII UNUI MOTOR SINCRON ALIMENTAT DE LA INVERTOR SURSĂ DE CURENT

Vasile MANOLIU
Facultatea de Inginerie Electrică, Universitatea „Politehnica” din Bucureşti, Spl. Independenţei 313, 060042, Bucureşti; vmanoliu@gmail.com

Abstract Stabilitatea în funcţionare a sistemelor de acţionare cu motoare sincrone poate fi investigată utilizând modele ale micilor perturbaţii. Lucrarea prezintă o analiză a stabilităţii în funcţionare pentru un motor sincron alimentat de la un convertor static de frecvenţă cu invertor sursă de curent. Pe baza ecuaţiilor funcţionale scrise în sistemul *d-q*, stabilitatea este studiată utilizând criteriul Routh-Hurwitz, pentru modelul cu mici variaţii. Pentru un unghi dat de autopilotare (de comandă a poziţiei), motorul sincron este evaluat în diferite situaţii – cu şi fără sarcină, cu şi fără înfăşurări de amortizare. Atunci când se apreciază variaţia unghiului de autopilotare în raport cu variaţia cuplului de sarcină sau când motorul sincron funcţionează fără înfăşurări de amortizare, se constată instabilitate în funcţionare.

1 Introducere

Motoarele sincrone cu excitaţie electromagnetică alimentate de la invertoare sursă de curent sunt utilizate în aplicaţii specifice, cum ar fi: antrenarea compresoarelor şi a pompelor centrifugale, trenuri de mare viteză, etc. În general, analiza stabilităţii în funcţionare este realizată utilizând modele matematice ale micilor perturbaţii, iar unul dintre criteriile cele mai utilizate este criteriul Routh-Hurwitz.

În [1] este prezentată o analiză de regim staţionar a stabilităţii pentru un motor sincron alimentat de la invertor sursă de curent. Prin intermediul unei funcţii de transfer exprimând dependenţa de mici variaţii a unghiului de câmp β de variaţia de mic semnal a cuplului, a fost posibilă analiza stabilităţii pe baza criteriului Routh-Hurwitz.

În [2] stabilitatea statică în cazul funcţionării în regim staţionar pentru un motor sincron convenţional este analizată prin intermediul relaţiei dintre variaţiile de mic semnal ale cuplului electromagnetic şi ale unghiului intern.

Pentru un sistem de acţionare cu motor sincron fără comutaţie, prevăzut cu controlul unghiului limită constant, în [3] este investigată stabilitatea utilizând criteriul Routh-Hurwitz; studiul este concentrat asupra punctelor de funcţionare în planul curent – viteză.

Fig. 1 prezintă circuitul echivalent invertor de curent – motor sincron cu excitaţie electromagnetică; înfăşurările de amortizare scurtcircuitate sunt notate cu *D* şi *Q*.

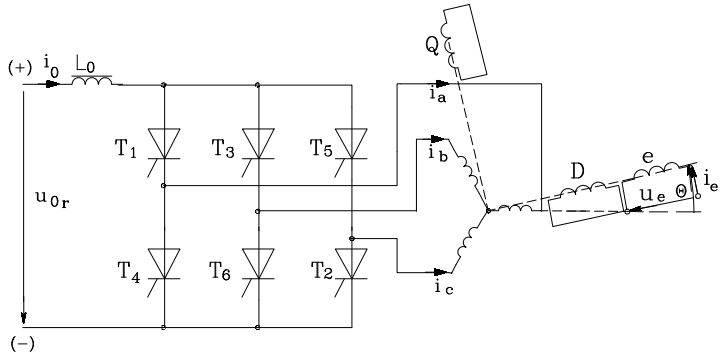

Fig. 1 - Circuitul echivalent invertor de curent – motor sincron.

Cuplul electromagnetic, produs prin interacţiunea dintre câmpurile magnetice generate de către înfăşurările de excitaţie şi cele statorice, este condiţionat de o poziţionare adecvată (relativă) a celor două câmpuri, exprimată în funcţie de unghiul de comandă a poziţiei (de autopilotare) *x*.

Prin obţinerea funcţiilor de transfer în care se utilizează variaţii de mici semnal ale diverselor mărimi, obiectivul lucrării de faţă este verificarea posibilităţii ca maşina sincronă, echipată cu înfăşurări de amortizare, alimentată de la un invertor, să poată suporta mici perturbaţii în sarcină. De asemenea, se consideră evaluarea stabilităţii sistemului de acţionare în absenţa înfăşurărilor de amortizare.

2 Metode

2.1. Ecuaţii şi funcţii de transfer

În această analiză, motorul sincron considerat are poli aparenţi şi este prevăzut cu înfăşurări de amortizare (câte o înfăşurare pe fiecare axă). Folosind transformarea Park, armonica fundamentală a curentului statoric pentru un unghi de comandă a poziţiei *x*, poate fi reprezentată prin componentele directă şi în cuadratură (fig. 2):

$$I_d = -I_s^{(1)} \cdot \sin x \tag{1}$$

$$I_q = I_s^{(1)} \cdot \cos x \tag{2}$$

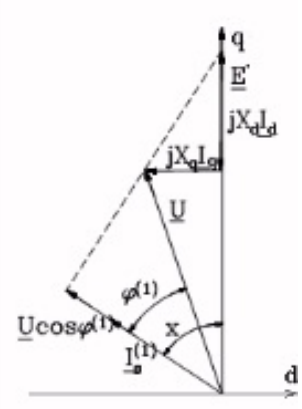

Fig. 2 - Diagrama de fazori simplificată a motorului sincron supraexcitat.

Un motor sincron poate să fie supus unei diversităţi de perturbaţii electrice sau mecanice, conducand la un (scurt) proces tranzitoriu care poate să se finalizeze într-o stare de funcţionare anormală, caracterizată prin absenţa unei corespondenţe riguroase între viteza rotorului şi frecvenţa convertorului. Daca perturbaţia este de valoare foarte mică, ecuaţiile diferenţiale neliniare care descriu procesul tranzitoriu, pot fi linearizate. În acest context, se va presupune că toate variabilele operaţionale prezintă mici deviaţii în jurul valorilor corespunzătoare funcţionării într-un punct dat, de regim staţionar.

Utilizând indexul "*0*" pentru valori de regim staţionar, şi exprimând micile perturbaţii prin "Δ", expresiile operaţionale ale variaţiilor curenţilor după axele directă şi în cuadratură, I_d şi I_q, sunt:

$$\Delta I_d(s) = (-I_s^{(1)} \cdot \cos x_0) \cdot \Delta x(s) \tag{3}$$

$$\Delta I_q(s) = (-I_s^{(1)} \cdot \sin x_0) \cdot \Delta x(s) \tag{4}$$

Expresia cuplului electromagnetic în variaţii de mic semnal şi în valori relative este, după o serie de calcule [1]:

$$\Delta M_e(s) = [(l_d - l_q)\cdot i_{q0} - l_{mq}\cdot i_{Q0}]\cdot \Delta i_d(s) + [(l_d - l_q)\cdot i_{d0} + l_{md}\cdot i_{D0} + l_{md}\cdot i_{e0}]\cdot \Delta i_q(s) + l_{md}\cdot i_{q0}\cdot \Delta i_e(s) + l_{md}\cdot i_{q0}\cdot \Delta i_D(s) - l_{mq}\cdot i_{d0}\cdot \Delta i_Q(s) \quad (5)$$

Ecuaţiile în mici perturbaţii ale tensiunilor de excitaţie şi corespunzând înfăşurărilor de amortizare, *D* şi *Q*, sunt exprimate astfel:

$$0 = \Delta U_e(s) = (R_e + s\cdot L_e)\cdot \Delta I_e(s) + s\cdot L_{md}\cdot(\Delta I_d(s) + \Delta I_D(s)) \quad (6)$$

$$0 = \Delta U_D(s) = (R_D + s\cdot L_D)\cdot \Delta I_D(s) + s\cdot L_{md}\cdot(\Delta I_d(s) + \Delta I_e(s)) \quad (7)$$

$$0 = \Delta U_Q(s) = (R_Q + s\cdot L_Q)\cdot \Delta I_Q(s) + s\cdot L_{mq}\cdot \Delta I_q(s) \quad (8)$$

Din ecuaţiile de mai sus, se pot exprima variaţiile curenţilor de excitaţie şi prin înfăşurările de amortizare, ΔI_e, ΔI_D si ΔI_Q, în funcţie de variaţiile componentelor curenţilor indusului după cele două axe, ΔI_d si ΔI_q. După o serie de calcule şi exprimând (6)-(8) în valori relative, înlocuind expresiile variaţiilor de curent în (5), rezultă:

$$\Delta M_e(s) = \frac{(g_1 s^3 + g_2 s^2 + g_3 s + g_4)\cdot \Delta i_d(s) + (h_1 s^3 + h_2 s^2 + h_3 s + h_4)\cdot \Delta i_q(s)}{l_1\cdot s^3 + l_2\cdot s^2 + l_3\cdot s + l_4} \quad (9)$$

în care coeficienţii polinomiali de la numărător şi de la numitor se exprimă în funcţie de parametrii maşinii.

Substituind expresiile variaţiilor de curent Δi_d şi Δi_q în relaţia variaţiei cuplului, exprimând curenţii în unităţi relative, o primă formă a funcţiei de transfer poate fi exprimată astfel::

$$H_1(s) = \frac{\Delta M_e(s)}{\Delta x(s)} = \frac{p_1\cdot s^3 + p_s\cdot s^2 + p_s\cdot s + p_4}{l_1\cdot s^3 + l_2\cdot s^2 + l_3\cdot s + l_4} \quad (10)$$

Relaţiile dintre unghiul de poziţie şi unghiul de autopilotare (de comandă a poziţiei) au fost obţinute din analiza variaţiei cuplului static, utilizând FLUX 2D [4]. Corespondenţa între secvenţele de conducţie şi unghiul de poziţie θ este prezentată în Tabelul 1.

Tabel 1

Tiristoare în conducţie	Unghi de poziţie
T_1 şi T_2	$-\pi/2 - x_0$
T_2 şi T_3	$-\pi/6 - x_0$
T_3 şi T_4	$\pi/6 - x_0$
T_4 şi T_5	$\pi/2 - x_0$
T_5 şi T_6	$5\pi/6 - x_0$
T_6 şi T_1	$7\pi/6 - x_0$

Pornind de la ecuaţia de mişcare, ca rezultat al unei mici variaţii bruşte a cuplului de sarcină, ΔM_s, rotorul va întârzia în raport cu câmpul (nemodificat) rezultant statoric cu unghiul geometric $\Delta\theta$ [2]. În consecinţă, micile variaţii ale unghiului intern al motorului (aşa cum este descris în [2]) şi ale unghiului de autopilotare au acelaşi semn şi aceeaşi valoare.

Prin urmare, o mică modificare a vitezei unghiulare Ω poate fi asociată cu o variaţie invers proporţională a unghiului de autopilotare. Astfel, se poate scrie:

$$\frac{d\Omega}{dt} = -\frac{1}{p}\cdot\frac{d^2(\Delta\theta)}{dt^2} = -\frac{1}{p}\cdot\frac{d^2(\Delta x)}{dt^2} \quad (11)$$

Prin aplicarea modelului cu mici perturbaţii şi a transformatei Laplace, după unele calcule, funcţia de transfer exprimând dependenţa unghiului de autopilotare de variaţia cuplului de sarcină, devine:

$$H_2(s) = \frac{\Delta x(s)}{\Delta M_s(s)} = \frac{l_1 \cdot s^3 + l_2 \cdot s^2 + l_3 \cdot s + l_4}{k_1 \cdot s^5 + k_2 \cdot s^4 + k_3 \cdot s^3 + k_4 \cdot s^2 + k_5 \cdot s + k_6} \quad (12)$$

Analiza stabilităţii în regim staţionar pentru funcţia de transfer (relaţia (12)) este realizată calculând rădăcinile ecuaţiei caracteristice (numitorul funcţiei de transfer egalat cu 0) şi aplicând criteriul Routh-Hurwitz.

2. 2. Criteriul Routh – Hurwitz

Criteriul Routh-Hurwitz este o metodă pentru determinarea stabilităţii unui sistem liniar, prin examinarea locaţiilor rădăcinilor ecuaţiei caracteristice a sistemului.

Fie ecuaţia caracteristică asociată unei funcţii de transfer (numitorul funcţiei de transfer egalat cu 0):

$$a_n \cdot s^n + a_{n-1} \cdot s^{n-1} + ... + a_1 \cdot s + a_0 = 0 \quad (13)$$

Dacă toate rădăcinile ecuaţiei caracteristice au partea reală negativă, sistemul este stabil. Dacă este îndeplinită condiţia de mai sus, se calculează (şi se completează) tabloul Routh-Hurwitz, după cum urmează:

s^n	a_n	a_{n-2}	a_{n-4} ….
s^{n-1}	a_{n-1}	a_{n-3}	a_{n-5} ….
s^{n-2}	b_1	b_2	b_3 ….
s^{n-3}	c_1	c_2	c_3 ….
.			
s^1			
s^0			

în care:

$$b_1 = -\frac{1}{a_{n-1}} \cdot \begin{vmatrix} a_n & a_{n-2} \\ a_{n-1} & a_{n-3} \end{vmatrix}; \quad b_2 = -\frac{1}{a_{n-1}} \cdot \begin{vmatrix} a_n & a_{n-4} \\ a_{n-1} & a_{n-5} \end{vmatrix}; \quad ...$$
$$c_1 = -\frac{1}{b_1} \cdot \begin{vmatrix} a_{n-1} & a_{n-3} \\ b_1 & b_2 \end{vmatrix}; \quad c_2 = -\frac{1}{b_1} \cdot \begin{vmatrix} a_{n-1} & a_{n-5} \\ b_1 & b_3 \end{vmatrix}; \quad ... \quad (14)$$

Condiţia necesară pentru ca părţile reale ale tuturor rădăcinilor să fie negative, este ca valorile din prima coloană a tabloului să aibă acelaşi semn. Numărul rădăcinilor polinomiale care sunt în semiplanul drept este egal cu numărul modificărilor de semn din prima coloană.
Dacă ecuaţiile sistemului sunt scrise în forma matriceală "spaţiul stărilor":

$$\begin{cases} \dot{X} = A \cdot X + B \cdot U \\ Y = C \cdot X + D \cdot U \end{cases} \quad (15)$$

atunci polii funcţiei de transfer *Y(s)/U(s)* se obţin rezolvând ecuaţia: *det(s·I-A)* = 0, în care *I* este matricea unitate, iar *s* este variabila operaţională.

2.3. Studiul secvenţei de comutaţie

Secvenţa de comutaţie este influenţată de următorii parametri: Φ_D, Φ_Q, Φ_e, i_k, i_o, i_e. Pe baza parametrilor maşinii si a valorii constante a curentului circuitului intermediar, se poate calcula variaţia temporală a curentului de comutaţie, i_k [4]. Ecuaţia curentului de comutaţie i_k este:

$$\frac{di_k}{dt} = \omega_n \cdot \left(-\frac{r_k}{l_k} \cdot i_k + \frac{u_k}{l_k} \right) \quad (16)$$

Pentru ecuaţiile în forma matriceală, fluxurile înfăşurărilor de amortizare şi curenţii de excitaţie şi din circuitul intermediar, se pot considera ca variabile de stare.
Pentru cazul descris mai sus, deoarece elementele matricii de stare *A* conţin funcţii trigonometrice ale unghiului de poziţie θ, sistemul este variabil în timp. Utilizând mediul de programare Matlab-Simulink, se poate obţine o precizie rezonabilă prin împărţirea domeniului intervalului de comutaţie în mici intervale incrementale, pentru care sistemul variabil în timp poate fi tratat ca unul invariabil în timp, pentru fiecare increment [5].
În acest caz, se poate aproxima: $\sin\theta \cong \theta$; $\cos\theta \cong 1$.

Considerând, în sistemul de mai sus, constanţa fluxurilor asociate înfăşurărilor de excitaţie si de amortizare, dar şi a curentului din circuitul intermediar, considerând ca mărime de comandă tensiunea circuitului de excitaţie, u_e, se poate rescrie o ecuaţie de stare simplificată, conţinând ca mărimi de stare curenţii i_k, i_0 si i_e, Ecuaţia (16) se poate rescrie sub forma:

$$\dot{X} = A \cdot X + B \cdot U \tag{17}$$

în care $X = [i_k \;\; i_0 \;\; i_e]^T$.
Comutaţia se încheie când i_k atinge valoarea curentului circuitului intermediar.

3 Rezultate

3.1. Stabilitatea maşinii sincrone cu înfăşurări de amortizare

Maşina sincronă (din instalaţia experimentală [4]) are următorii parametri (valori în unităţi relative): r_s = 0.07; l_e = 1.397; l_d = 1.102; l_q = 0.758; l_{md} = 1.005; l_{mq} = 0.661; l_D = 1.096; l_Q = 0.812; l'_d = 0.379; l''_d = 0.166; l''_q = 0.22; $l_{\sigma D}$ = 0.091; $l_{\sigma Q}$ = 0.151; r_D = 0.022; r_Q = 0.087; r_e = 0.02; $l_{\sigma e}$ = 0.39.

Stabilitatea statică a fost investigată pentru un unghi de autopilotare $x_0 \approx 60^\circ$.

Tabloul Routh pentru funcţia de transfer $H_1(s)$ indică, pe prima coloană, valorile: 0,422; 0,0879; 0,0047; 0,000038, fiind asigurată stabilitatea. Atunci când se modifică unghiul de autopilotare, rezultatele îşi păstrează convergenţa.

Stabilitatea statică în funcţionarea în regim staţionar exprimată în [2] prin relaţia $(dM_e/d\theta)_{\theta=\theta 0} > 0$ justifică ideea verificării stabilităţii prin rezolvarea ecuaţiei caracteristice rezultate din numitorul funcţiei de transfer $H_1(s)$. De remarcat faptul că termenul "unghi intern" [2] corespunde, într-o analiză de mici variaţii, termenului "unghi de autopilotare" exprimat în prezenta lucrare.

Pentru funcţia de transfer $H_2(s)$ valorile din prima coloană a tabloului Routh prezintă o modificare de semn, ceea ce indică instabilitate.

3.2. Stabilitatea maşinii sincrone fără înfăşurări de amortizare, la mersul în gol

La mersul în gol, $x_0 \approx 90^\circ$, funcţia de transfer a sistemului de acţionare electrică, pentru motorul fără înfăşurări de amortizare se modifică astfel [1]:

$$H'_2(s) = \frac{\Delta x(s)}{\Delta M_s(s)} = \frac{1}{J \cdot s^2 + l_{md} \cdot i_{f0} \cdot i_s + (l_{md} - l_{mq}) \cdot i_s^2} \tag{18}$$

Rădăcinile ecuaţiei caracteristice sunt pur imaginare şi complex conjugate. Conform criteriului Routh-Hurwitz, sistemul este marginal stabil (sau neamortizat) la mersul în gol al motorului fără înfăşurări de amortizare.
În cazul în care înfăşurarea de amortizare este considerată la mersul în gol, $(x = 90^\circ)$, valorile de pe prima coloană a tabloului Routh nu îşi modifică semnul; de aceea, situaţia privind stabilitatea rămâne nemodificată.

În general se observă că un motor sincron fără înfăşurări de amortizare nu satisface criteriul de stabilitate în regim staţionar.

3.3. Stabilitatea pentru intervalul de comutaţie

Pentru o viteză rotorică (în unităţi relative) $\nu = 1$ şi un unghi de autopilotare $x_0 = \pi/4$, se obţin următorii coeficienţi ai matricii variabilelor de stare:

$a_{11} = -97.1$; $a_{12} = 632.6$; $a_{13} = 1014.8$; $a_{21} = a_{22} = a_{23} = a_{31} = a_{32} = 0$; $a_{33} = -4.5$.

astfel încât determinantul matricii $(s \cdot I - A)$ are expresia:

$s^3 + 101.6 \cdot s^2 + 436.95 \cdot s = 0$.

Deoarece termenul liber este zero, completând tabloul Routh, se obţine comportarea unui sistem marginal stabil, atunci când se consideră comutaţia curentului, în ipotezele simplificatoare specificate.

Şi în acest caz, în absenţa înfăşurărilor de amortizare, se obţine comportarea unui sistem marginal stabil (neamortizat).

4 Concluzii

Stabilitatea statică, aşa cum a fost definită în [4] consideră perturbaţii de valoare foarte mică, fiind caracterizată de condiţia: $(dM_e/d\theta)_{\theta=\theta 0} > 0$. Aşadar, indiferent de tipul de alimentare, variaţia cuplului electromagnetic în raport cu unghiul intern trebuie să fie pozitivă.

Atunci când se foloseşte principiul autopilotării, este mai firească exprimarea stabilităţii în regim staţionar în raport cu unghiul de autopilotare. Deşi, practic, stabilitatea este asigurată pentru orice valoare a lui x_0 cuprinsă între 10° si 80°, atunci când se investighează comportarea variaţiei unghiului de autopilotare în raport cu variaţia cuplului de sarcină, stabilitatea evaluată prin criteriul Routh-Hurwitz nu se confirmă. Cu toate acestea, există cel putin două argumente care justifică, totuşi manifestarea stabilităţii în funcţionare în cazul sistemului de acţionare cu motor sincron autopilotat: valoarea curentului circuitului intermediar nu este (riguros) constantă, iar în structura schemei de comandă se regăsesc, pe lângă regulatorul curentului i_0, şi două generatoare de funcţii, dintre care unul implementează relaţia dintre curentul statoric şi unghiul de autopilotare.

În [3] se stabileşte, de asemenea, că schema de control la unghi limită constant prezintă o instabilitate intrinsecă, în special la sarcini mari şi funcţionare la viteze ridicate.

De obicei, instabilitatea în funcţionare în cazul unui motor sincron alimentat de la invertor sursă de curent poate fi asociată cu situaţia în care unghiul de autopilotare devine mai mic decât unghiul de cuplu. Absenţa înfăşurărilor de amortizare conduce, pe lângă niveluri inacceptabile ale unghiului de suprapunere în comutaţie, la condiţii de instabilitate funcţională.

Referinţe

[1] A. B. Chattopadhyay, S. Thomas, R. Chatterjee. *Analysis of steady state stability of a CSI fed synchronous motor drive system with damper winding included*, Trends in Applied Sciences Research 6 (9), pp. 992-1005, 2011

[2] A. Fransua, R. Magureanu. *Electrical Machines and Drive Systems*, The Technical Press Oxford, 1984.

[3] S. Fukuda, S. Sasaka. *Constant margin-angle control of commutatorless motor using microcomputer*, IEEE Trans. on Industry Applications, vol. IA-23, no. 5, pp. 855-861, 1987.

[4] V. Manoliu. *Motorul sincron autopilotat*, Ed. ICPE, Bucuresti, 1999.

[5] Y. He, Y. Wang. *The state-space analysis of excitation regulation of self-controlled synchronous motor with constant margin-angle control*, IEEE Trans. on Power Electronics, vol.5, no.3, pp. 269-275, 1990.

Analysis of Three-Phase Induction Machine Operating under Transient Dynamic Braking by Using the Mathematical Model in Total Fluxes

Alecsandru SIMION, Leonard LIVADARU, Radu-Voinea COCIU, Adrian MUNTEANU
Technical University "Gh. Asachi" Iasi, Bd. D. Mangeron 51-53, 700050, Iasi, Romania
asimion@ee.tuiasi.ro

Abstract. The three-phase induction machine that operates under the specific conditions of dynamic braking can be translated as an induction machine under variable state, transient and unbalanced. This duty can be analysed by using first order differential equations that contains nothing but the total fluxes of the phase windings and the rotation angle of the rotor. Consequently, the currents are excluded and there is a reduced number of variables.

1 Introduction

The increasingly utilization of induction motors is facilitated, among other things, by the possibilities of an efficient braking with reduced investments [1]-[3].

It is a fact that the three-phase induction machines have some remarkable qualities as regards braking, which eventually leads to the stop of the driven mechanism at a precise spot when it comes to positioning systems.

One of the methods used for the induction machine braking is the so-called dynamic braking, or d.c. braking. The next comments refer to this braking procedure, Fig. 1. If the machine has cage rotor (Fig. 1a) then the dynamic braking involves disconnection of the stator winding from the mains (K1 is opening the main circuit) and almost instant connection of the K2 and K3 contactors. The stator winding is now connected to a d.c. source and the induction machine becomes a synchronous generator with reversed structure. The d.c. excitation is placed on stator, and the mechanical energy from the shaft is transformed in electric energy, which subsequently produces thermal effects upon cage winding.

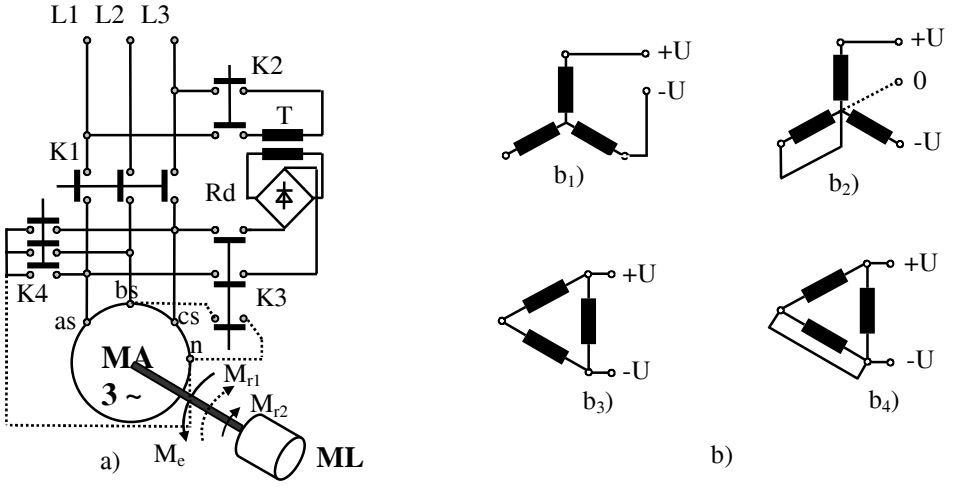

Figure 1: Dynamic braking of three-phase induction machine: a) Schematic diagram, b) Connection types of the stator winding to d.c. source.

The torque developed now inside the machine has an opposite direction to the rotation of the rotor and consequently there is a deceleration or, in other words, a braking. Fig. 1b shows different connection types of the stator winding corresponding to the initial connection: Y (b1, b2) and Δ

(b3, b4). The study presented in this paper uses the b2 connection: two stator phases are series connected and supplied from the d.c. source and the third phase is short-circuited.

2 The mathematical model in total fluxes of the three-phase induction machine

The study by simulation of the three-phase induction machine under transient dynamic braking can be performed by using together the 6 equations of the electric circuits [3,4,5] and the 2 movement equations (eq. 6.224 from [3]), where the particular values of the stator voltages corresponding to the d.c. supply are:

$$\bar{u}_{as}=+U;\quad \bar{u}_{cs}=-U;\quad \bar{u}_{bs}=0;\quad \bar{u}_{ar}=\bar{u}_{br}=\bar{u}_{cr}=0 \tag{1}$$

Under symbolic method, one obtains a first order equation system containing 8 equations:

$$\bar{\psi}_{as}\left(\bar{s}+\nu_{st}\right)=+U-\nu_{sr}\left(\bar{\psi}_{bs}+\bar{\psi}_{cs}\right)+\frac{1}{3}\nu_{\sigma s}\left[\left(2\bar{\psi}_{ar}-\bar{\psi}_{br}-\bar{\psi}_{cr}\right)\cos\theta_R+\sqrt{3}\left(\bar{\psi}_{cr}-\bar{\psi}_{br}\right)\sin\theta_R\right] \tag{2-1}$$

$$\bar{\psi}_{bs}\left(\bar{s}+\nu_{st}\right)=0-\nu_{sr}\left(\bar{\psi}_{cs}+\bar{\psi}_{as}\right)+\frac{1}{3}\nu_{\sigma s}\left[\left(-\bar{\psi}_{ar}+2\bar{\psi}_{br}-\bar{\psi}_{cr}\right)\cos\theta_R+\sqrt{3}\left(\bar{\psi}_{ar}-\bar{\psi}_{cr}\right)\sin\theta_R\right] \tag{2-2}$$

$$\bar{\psi}_{cs}\left(\bar{s}+\nu_{st}\right)=-U-\nu_{sr}\left(\bar{\psi}_{as}+\bar{\psi}_{bs}\right)+\frac{1}{3}\nu_{\sigma s}\left[\left(-\bar{\psi}_{ar}-\bar{\psi}_{br}+2\bar{\psi}_{cr}\right)\cos\theta_R+\sqrt{3}\left(\bar{\psi}_{br}-\bar{\psi}_{ar}\right)\sin\theta_R\right] \tag{2-3}$$

$$\bar{\psi}_{ar}\left(\bar{s}+\nu_{rt}\right)=0-\nu_{rs}\left(\bar{\psi}_{br}+\bar{\psi}_{cr}\right)+\frac{1}{3}\nu_{\sigma r}\left[\left(2\bar{\psi}_{as}-\bar{\psi}_{bs}-\bar{\psi}_{cs}\right)\cos\theta_R+\sqrt{3}\left(\bar{\psi}_{bs}-\bar{\psi}_{cs}\right)\sin\theta_R\right] \tag{2-4}$$

$$\bar{\psi}_{br}\left(\bar{s}+\nu_{rt}\right)=0-\nu_{rs}\left(\bar{\psi}_{cr}+\bar{\psi}_{ar}\right)+\frac{1}{3}\nu_{\sigma r}\left[\left(-\bar{\psi}_{as}+2\bar{\psi}_{bs}-\bar{\psi}_{cs}\right)\cos\theta_R+\sqrt{3}\left(\bar{\psi}_{cs}-\bar{\psi}_{as}\right)\sin\theta_R\right] \tag{2-5}$$

$$\bar{\psi}_{cr}\left(\bar{s}+\nu_{rt}\right)=0-\nu_{rs}\left(\bar{\psi}_{ar}+\bar{\psi}_{br}\right)+\frac{1}{3}\nu_{\sigma r}\left[\left(-\bar{\psi}_{as}-\bar{\psi}_{bs}+2\bar{\psi}_{cs}\right)\cos\theta_R+\sqrt{3}\left(\bar{\psi}_{as}-\bar{\psi}_{bs}\right)\sin\theta_R\right] \tag{2-6}$$

$$\begin{aligned}\dot{\theta}_R\left(\bar{s}+\frac{k_z}{J}\right)=\left(\frac{p}{J}\right)\Big\langle-\left(\frac{p}{2}\right)\Lambda_3\Big\{&\sin\theta_R\left[\bar{\psi}_{as}\left(2\bar{\psi}_{ar}-\bar{\psi}_{br}-\bar{\psi}_{cr}\right)+\bar{\psi}_{bs}\left(2\bar{\psi}_{br}-\bar{\psi}_{cr}-\bar{\psi}_{ar}\right)+\bar{\psi}_{cs}\times\right.\\&\left.\left(2\bar{\psi}_{cr}-\bar{\psi}_{ar}-\bar{\psi}_{br}\right)\right]+\sqrt{3}\cos\theta_R\left[\bar{\psi}_{as}\left(\bar{\psi}_{br}-\bar{\psi}_{cr}\right)+\bar{\psi}_{bs}\left(\bar{\psi}_{cr}-\bar{\psi}_{ar}\right)+\bar{\psi}_{cs}\left(\bar{\psi}_{ar}-\bar{\psi}_{br}\right)\right]\Big\}-M_{st}\Big\rangle\end{aligned} \tag{2-7}$$

$$\frac{d\theta_R}{dt}=\dot{\theta}_R=\omega_R \tag{2-8}$$

where, we have used the well-known notations for the hybrid parameters (eq. 6.309-1 to 6.309-5 from [3]). Both the permenace of a three-phase machine, Λ_3, and the hybrid parameters, ν_{ij}, can be expressed in corelation with the measurable parameters of the machine: stator and rotor phase resitances, leakage and linkage inductances.

Unlike the cage rotor machines where the rotor voltages are equal to zero for the rated duty, the wound rotor machines allow the connection of an external impedance, a three-phase resistance for example, capable to modify the torque and consequently the speed and the braking time. Hereinafter we deduce the equations that are necesary to draw up the schematic diagram of a three phase induction machine with imposed parameters (SI units); R_s=2; R_r=2; L_{hs}=0,09; $L_{\sigma s}$=$L_{\sigma r}$=0,01; J=0,05; p=2; k_z=0,02; ω_1=314,1. With the expressions (6.309-1,2,3,4,5) from [3], the hybrid parameters have the following values: ν_{st}=135,5=ν_{rt}; ν_{sr}=32,26=ν_{rs}; ν_s=103,24=ν_r; $\nu_{\sigma s}$=96,43=$\nu_{\sigma r}$; Λ_3=32,26. These values are then used in (1-1,2,...,8), which allow the achievement of the block-diagram, Fig. 2.

Then, the applied voltages and the values of the load torque coresponding to a certain sequence of operating duties are filled in. The upper-left part of the block diagram (Fig. 2), where usually lay the voltage sources, is now occupied by specific calculus blocks made of adders, multipliers and/or step signal generators, which mainly allow the simulation of

replacement of the a.c. sources from the *as* and *cs* phases with d.c. sources necesary for the start of the braking duty. The moment time of the braking corresponds to an overload operation of the machine (the load torque has a value of 1,5 M_{eN}, M_{eN}-rated torque). The third phase, *bs*, is short-circuitd in order to intensify the braking process.

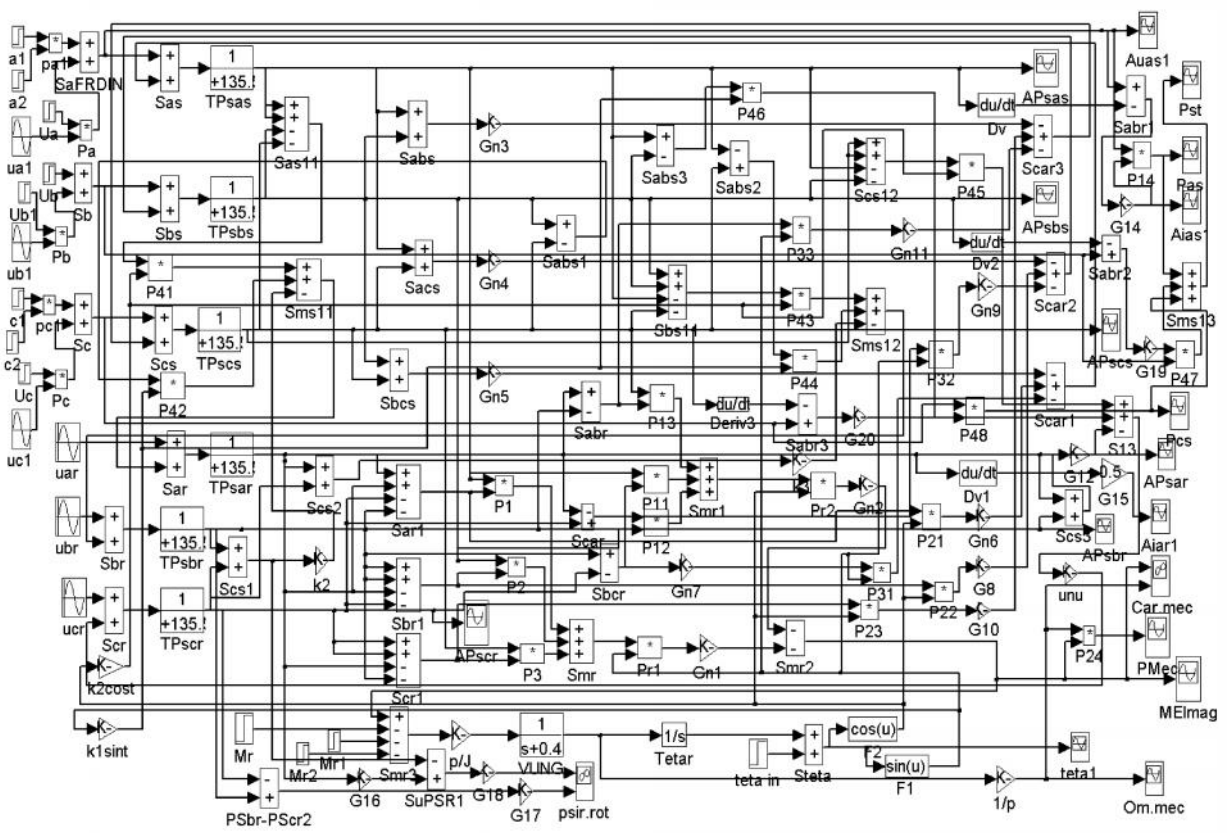

Figure 2: Block diagram. Three-phase induction machine with the following duty sequence: **RV1**= P-SS-FD-D – no-load start-up(0-0,25s) – overload operation (0,25s-t_{fd})($t_{fd} \approx 0,4$s) –dynamic braking, as-cs connected to d.c. source ($\approx 0,4$- $\approx 0,53$s), disconnection of the d.c. source ($\approx 0,53$s-0,75s) *a3afd100*

3 Simulation results of dynamic braking

A) In this section we present the results obtained for the variable regime **RV1**, denoted with the acronym P-SS-FD-D, performed in Matlab environment. It contains the following duties:

- (P) no-load start-up of the cage motor under symmetrical condition, t=0. The load torque is represented by the viscous friction torque, which depends proportionally to rotor speed. Its value arises to approx. 3Nm, which corresponds to rated speed. This torque acts up to t=0.25s.

– (SS) torque enforcement with a value of 100 Nm ($\approx 1,5M_{eN}$). It is about an overload duty within the range (0,25s – t_{fd}) where $t_{fd} \approx 0,4$s corresponds to the moment of braking.

- (FD) dynamic braking (within t_{fd} and t_d, where t_d corresponds to the disconnection of the d.c. source). The d.c. voltage applied to *as* and *cs* phases has the values U_{as}=+60V and U_{cs}=-60V while the *bs* phase is short-circuited. Simultaneously, the load torque is diminished 20 times and its value attains 5Nm (which is a reasonable value for the practical situations when there is a mechanical step-down gear). The braking process ends when the speed becomes null ($t_d \approx 0,53$s) but this moment time is not clearly determined since it depends, among others, on the position of rotor corresponding to the moment of the d.c. source connection.

- (D) disconnection of the d.c. source and short-circuit of the *as* and *cs* phases (opening of K2 and K3 and closing of K4) at the moment time $t_d \approx 0,53$s when the rotor speed is null and the windings

dissipate the remanent magnetic energy. The magnetic fluxes decrease in time and become null at t=0,75s.

Fig. 3 presents the time variation of the applied voltage on *as* phase. One can see the presence of the harmonic voltage (pulsation of 314.1 rad/s) up to the moment of braking. At t_{fd} =0,4s the d.c. voltages are applied to *as* and *cs* phases (U_{as}=+60V, U_{cs}=-60V). The rotor decelerates to zero value ($t_d \approx 0{,}53$s) and afterwards the machine is disconnected from the d.c. source and the stator phases are short-circuited. Within the range $t_d \approx 0{,}53$s to t_f = 0,75s the machine is „energy-depleted" and the magnetic energy is thermally dissipated.

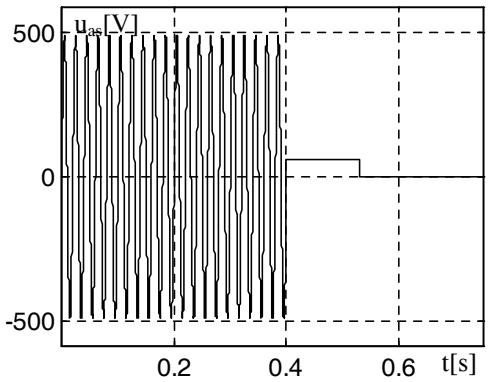

Figure 3: Stator phase voltage, u_{as}=f(t)

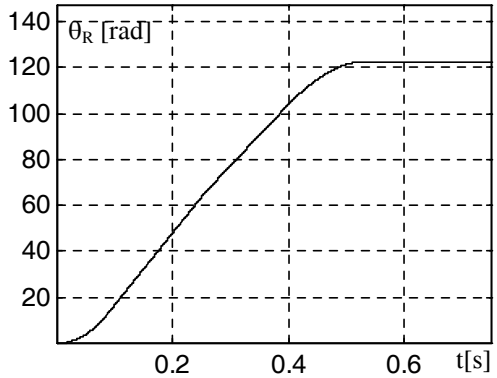

Figure 4: Rotation angle, θ_R=f(t)

If the machine drives a positioning system then the variation of the rotor angle θ_R over the full cycle is necessary, Fig. 4. Over the initial area, the value increases cuasi parabolic. Then there is a linear increase corresponding to no-load operation. The slope rising becomes smaller for overload operation and then there is a quick decrease of its value during braking. Finally, the rotor stop corresponds to the prescribed position.

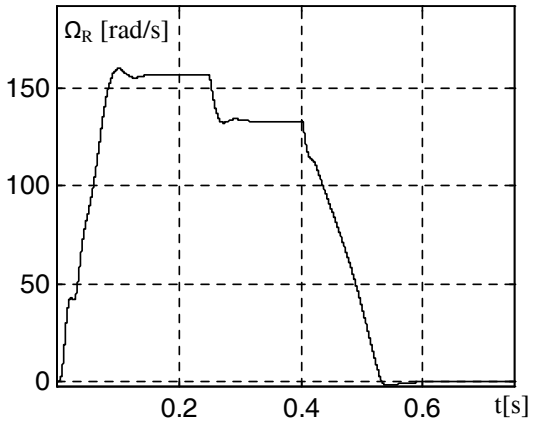

Figure 5: Rotor angular speed, Ω_R=f(t)

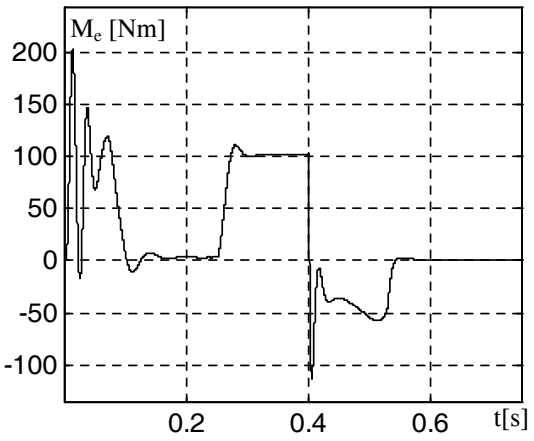

Figure 6: Electromagnetic torque, M_e=f(t)

Fig. 5 shows the variation of angular speed over the full cycle, P-SS-FD-D. One can notice that the time of dynamic braking is of t_{fd}=0,13s and is similar in value to no-load start-up time. This length depends obviously on d.c. supply voltage. The variation of the electromagnetic torque, Fig. 6, put in view a significant torque value (approx. -100Nm) that arises when the d.c. source is connected and determine the rapid deceleration.

The total stator fluxes coresponding to *as* and *cs* phase are presented in Fig.7 and Fig. 8. When the machine is connected to the mains (t=0), a magnetic transient process starts as well. Its length depends on time constant of the machine. This process ends with the syncronism. The

flux values reach maximum 2Wb. Their values decrease somehow for under load operation and create a three-phase symmetric system with an amplitude of about 1.3Wb. The connection to the d.c. source modifies the harmonic shape into a cuasi continuous one but the amplitude remains constant. After the disconnection of the d.c. source, the flux values slowly decrease to zero value.

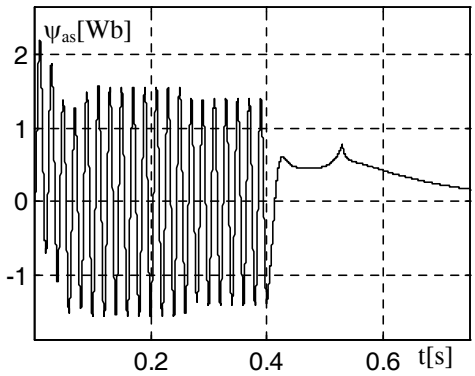

Figure 7: Total stator flux of *as* phase, $\psi_{as}=f(t)$

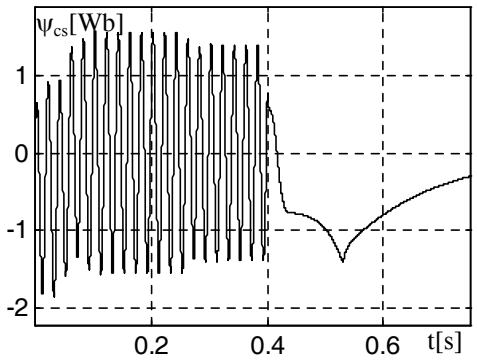

Figure 8: Total stator flux of *cs* phase, $\psi_{cs}=f(t)$

The transient process can be also analysed by means of dynamic mechanical characteristic, $\Omega_R=f(Me)$, Fig. 9. The point operation starts from O point (origin) and tracks succesively OMSNFQO (according to rows). It has to be noticed that the connection of the d.c. sources moves the point operation from N to F where the torque has a high negative value that facilitate the braking process. Interesting information concerning the phenomena that take place inside the machine are offered by the hodograph of the resultant rotor flux, Fig. 10. The time evolution involves track of different cycles, denoted from 1 to 13: O-S, no-load start-up; S-F, overload operation; F-D, dynamic braking till d.c. source decoupling; D-O, free stop and energy dissipation.

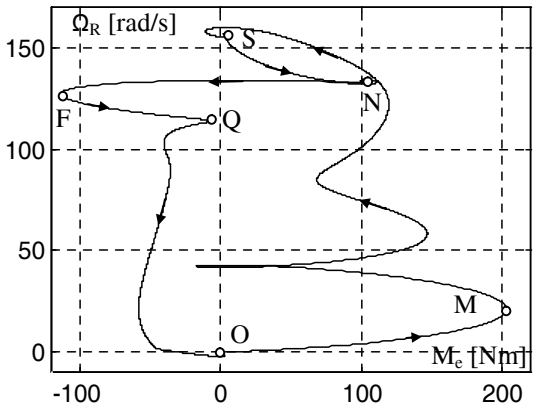

Figure 9: Dynamic mechanical characteristic, $\Omega_R=f(t)$

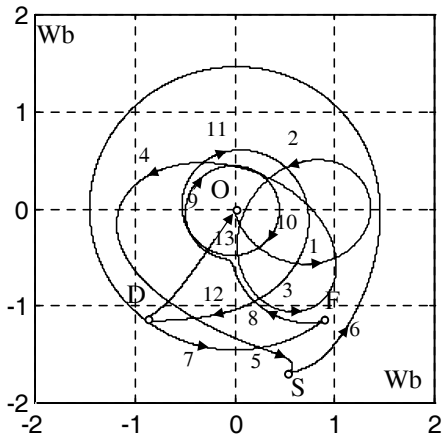

Figure 10: Hodograph of resultant rotor flux

B) The next results correspond to a second variable duty - **RV2**, denoted with the acronym P-SS-FD*-D, which is rather similar with the above presented one. The difference consists in the inverse polarity of the d.c. source, that is U_{as}=-60V and U_{cs}=+60V.

A first consequence is the significant increase of the braking torque and consequently the decrease of the braking time. The rotation angle of the rotor is also diminished from 122 [rad] to 112 [rad]. This phenomenon is visible on the time variation characteristic of the rotor speed. Now the braking process stops at t_d = 0,475s, which means a length of approx. t'_{df} = 0,075s. The new behaviour is presented in Fig. 11 and Fig. 12.

The dynamic characteristic corresponding to **RV2** regime shows a much higher initial braking torque of -200Nm, point F, Fig. 11. The decrease of this torque has also a different shape in comparison to **RV1**. As regards the hodograph of the resultant rotor flux, it has to be pointed out that that the evolution of the rotor flux during braking process is essentially influenced by its initial position and by the flux created as a consequence of d.c. supply.

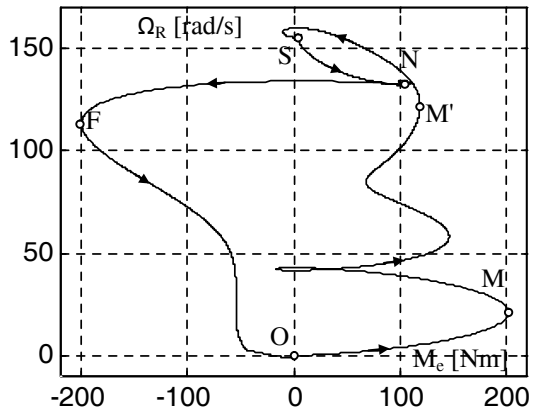

Figure 11: Dynamic characteristic - **RV2**

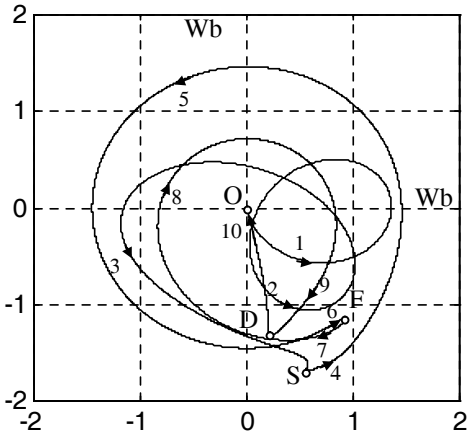

Figure 12: Rotor flux hodograph - **RV2**

4 Conclusion

- The study of the three-phase induction machine under dynamic braking duty, which is an unbalanced transient duty, can be performed with high accuracy according to the proposed approach. It is used a system of first order differential equations that contains as quantities nothing but the total fluxes of the windings and the rotation angle of the rotor. The phase currents are excluded and consequently the number of variables is reduced.
- This new and original approach allows the obtaining of accurate information concerning the instantaneous phenomena that take place inside the electric machine. On the basis of this information one can adopt proper strategies concerning the most favorable moment time of connecting the d.c. source in order to get a controllable braking time, usually the minimum time, which is important mainly for tracking and positioning systems.
- As evaluation tool, the hodograph of the resultant rotor flux is used since it has real didactic advantages in the right interpretation of the physical phenomena that define the behaviour of the machine under the mentioned duty and the time tracking of the operation point on the dynamic mechanical characteristic.

References

[1] H. Rentzsch. *Handbuch fur Elektromotoren, 3., uberarb. Auflage*, Brown Boveri and Cie Aktiengesellschaft, Mannheim, W. Girardet Verlag, Essen, 1980.

[2] I. Boldea and L. Tutelea. *Electric machines-Steady state, Transients and Design with MATLAB,* CRC Press, 2010.

[3] Al. Simion. *Masini electrice, v. III, Masina asincrona* , Ed. PIM Iasi, 2012.

[4] Al. Simion. Study of the Induction Machine Unsymmetrical Condition Using In Total Fluxes Equations. *Advances in Electrical and Computer Engineering*, **1** (Febr 2010) 34-41.

[5] Al. Simion, L. Livadaru and A. Munteanu. Mathematical Model of the Three-Phase Induction Machine for the Study of Steady-State and Transient Balanced and Unbalanced Regimes. In: *Induction Motors – Modelling and Control*, InTech, Rijeka, 2012, pp. 3-44.

Modeling of the 3D Electrode Growth in Electroplating

Marius PURCAR, Calin MUNTEANU, Alexandru AVRAM, Vasile TOPA
Technical University of Cluj-Napoca, Baritiu Street 26-28, 400027 Cluj-Napoca, Romania;
marius.purcar@ethm.utcluj.ro

Abstract. A general applicable numerical technique for the simulation of three-dimensional (3D) electrode growth in electroplating is presented. The electrode is found displacing each node of the mesh proportional with, and in the direction of the local current density according to Faraday's law. Applying the potential model, local current density is computed using the Boundary Element Method (BEM). A 3D electroplating simulation example is presented.

1. Introduction

Dilute solution theory [1] provides the general equations describing the electrochemical processes. For example, when the electrode reactions take place at low rates, such that the concentration gradients are neglected, the potential distribution may be found only using Laplace's equation. Hence, the resulting model describes the ohmic effects in the electrolyte and is known as the Potential Model (PM) [2]. Several authors applied the PM to compute the current density distribution and hence the electrode growth rate for electroplating applications. Alkire *et. al.* applied in [3] the finite element method (FEM) to solve the resulting Laplace equation, with nonlinear boundary conditions that account for electrode charge transfer reactions. Deconinck *et. al.* [2] discretized the equations of the PM using the BEM in order to compute the changing electrode profile for nonlinear boundary conditions. They also presented a complete study of the electrode evolution function of the electrode reactor dimension for different angles between the electrode and an adjacent insulator. Using the finite difference method (FDM), Bozzini and Cavallotti [4] presented numerical simulations for the Cr-plating process on corner-shaped cathodes.

Most of the works presented above applied an Euler scheme for the integration of Faraday's law with respect to the time, combined with the displacement of the discretization nodes of the electrode surface. This method, referred as the string theory in [5], derives from the Lagrangian approach of changing boundary problems that implies the grid boundary to be attached to the moving front.

A limited number of publications deal with three dimensional (3D) current density distribution simulations in electrochemical reactors, but in the field of 3D electroplating they are very scarce. Applications that consider current density distributions for more complex 3D geometries can be found in the field of cathodic protection and wafer plating [9, 10]. Purcar and Bortels [11-13] applied the principles of advanced CAD integrated approach for 3D electrochemical machining simulations.

In this purpose, the present paper presents a general simulation approach of the 3D electroplating applications with strong non-linear boundary conditions including reaction efficiency. In the following section, the basics principles of the 3D electrode shape change algorithm are illustrated.

2. Mathematical model and numerical solution method

The electrochemical process (e.g. electroplating, electroforming, electro erosion, etc.) develops continuously in time. In order to simulate the evolution of the electrode profile, the

continuous process time must be divided into a sequence of discreet time steps. For each time step two problems should be usually solved:

i. The electrochemical model (a steady state problem that eventually provides the local electrode growth rate) and
ii. The electrode growth problem (a time dependent problem which calculates the shape of the electrode surface at each time step).

The electrode growth rate, provided by Faraday's law, ensures the coupling of the two problems.

2.1. Electrochemical model

In most practical cases (e.g. 3D simulations), the dilute solution theory which describes the migration, convection, diffusion and electrode reactions in electrolytes [1] is subjected to important simplifications. Hence, considering the electrolyte solution very well stirred (situation often met in the practical situations) concentration gradients can be neglected (except for a very thin layer near the electrodes where the electrochemical reactions occurs). Assuming charge conservation in the bulk and the conductivity of the electrolyte constant, potential model yields.

The potential model is described by the Laplace equation for the electrolyte potential U, whereas the phenomena occurring in the diffusion layer and at the electrode interface [1] (e.g. the electrochemical reactions) are included in the boundary conditions.

$$\nabla^2 U = 0 \quad \bar{J} = -\sigma \cdot \bar{\nabla} U \,, \tag{1}$$

where σ represents the conductivity of the electrolyte in [$\Omega^{-1}m^{-1}$], U the electrolyte potential in [V] and $\boldsymbol{J}$ the current density in [A/m^2].

2.2. Boundary conditions

The boundary conditions in equation (1) are divided into insulators and electrodes [2, 7, 8]. As no current can flow through the gaseous medium in contact with the electrolyte and electrochemical cells walls, the normal current density is zero.

At the interface between the electrode and the electrolyte, known as double layer [1], electrochemical reactions occur. The electrochemical reaction driving force is expressed at each point of the electrode by a potential difference and is called the charge transfer overpotential or polarization η [1, 2, 7, 8].

Function of the overpotential sign, oxidation (positive η) or reduction (negative η) occurs at the electrodes. The electrochemical reaction is incorporated in the PM as a non-linear boundary condition and in the most general situation is written as:

$$J_n = f(\eta), \tag{2}$$

Such function is usually obtained measuring the physicochemical parameters of the electrolyte and approached with a spline function as in [2, 7, 8].

For a more general definition of the electrochemical reactions (2) (e.g. incorporating the side effects like gas evolution), it is necessary to provide additional information (such the efficiency θ for gas evolving side reactions - in particular hydrogen evolution). In that case the efficiency θ is below 100 %.

2.3. Electrode growth rate

The amount of material reduced at the cathode is directly proportional to the amount of the electrical charge flowing between the electrodes. This can be expressed using Faraday's law:

$$m = \frac{M \cdot I \cdot T}{z \cdot F}, \tag{3}$$

with: m the dissolved or deposited mass [kg], I the total current that flows between the electrodes [A/m2], T the total process time [s], M the atomic weight of the metal [kg/mol], F the Faraday's constant [96485 C/mol] and z the electric charge [C].

The deposited mass $m=\rho \cdot dV$, where ρ is metal density [kg/m^3] defined on an infinitesimal $dV=dh \cdot dS$ volume. Hence, the local electrode growth dh can be simply computed from (3) as:

$$dh = \theta \cdot \frac{M \cdot T \cdot J_n}{\rho \cdot z \cdot F} \tag{4}$$

where $J_n = I/ds$ is the normal current density through an infinitesimal surface ds at the electrode surface. The efficiency θ incorporates in the local electrode growth dh the contribution of the side effects, e.g. hydrogen evolution.

3. Numerical solution method

The equations (1-2) generally describe geometries with arbitrary boundary conditions which cannot be solved analytically. The solutions can be obtained using different discretization techniques (e.g. BEM, FEM, FDM, etc.), which assume the approximation of the continuous solution as a set of quantities at discrete locations, often on an irregularly spaced mesh.

A flexible grid generator creates an unstructured triangular mesh separately for each face of the computational domain [14]. The mesh is optimally refined towards the zones where a steep variation of field variables is expected but generates coarse elements at any other position, see figure 2 right.

3.1. BEM for electrolyte and electrode reactions

In order to solve the simplified charge conservation equation (1), BEM is more suitable over other discretization methods (FEM and FDM) because the conductivity of the electrolyte is considered constant. One of the BEM advantages is that only the boundaries of the computational domain must be discretised.

The boundary S_Γ of the computational domain is meshed with N_e non-overlapping elements defined by nodes $\boldsymbol{\chi}_i = (x_i, y_i, z_i)$ in $\boldsymbol{R^3}$ (i=1…N_p). The characteristic BEM equation for the contribution to a point i is [15]:

$$c^i U^i + \sum_{e=1}^{N_e} \int_{S_e} U \frac{\partial w^*}{\partial n} dS_\Gamma = \sum_{e=1}^{N_e} \int_{S_e} w^* Q \, dS_\Gamma \tag{5}$$

with $w^*=1/(4\pi r)$ the 3D Green function (r being the position relative to point i), $Q=\partial U/\partial n$ the inward flux on the boundary nodes and c^i is an integration constant for each point i. The index e ranges over all elements of the domain and integration is performed over the surface S_e of each element. Triangular elements with linear shape functions for the unknown potential U and flux field Q are used, hence, restricting the unknowns to the nodal values i.

BEM equation (5) results into the system of equations:

$$[\boldsymbol{H}] \cdot [\boldsymbol{U}] = [\boldsymbol{G}] \cdot [\boldsymbol{Q}] \tag{6}$$

where $\{\boldsymbol{Q}\}$ is a vector of size N_p containing the values of the electric field normal to the boundary S_Γ in each point, $\{\boldsymbol{U}\}$ is a vector of size N_p containing the value of the potential in each node and $[\boldsymbol{H}]$ and $[\boldsymbol{G}]$ are square matrices of size N_pxN_p.

Including in (6) the boundary conditions on the electrodes (overpotentials) and insulators the system (6) is reordered such that all unknowns are put to the left hand side:

$$\begin{bmatrix} [\boldsymbol{H}] & -[\boldsymbol{G}] \\ [\boldsymbol{0}] & [\boldsymbol{1}] \end{bmatrix} \cdot \begin{Bmatrix} \boldsymbol{U} \\ \boldsymbol{Q} \end{Bmatrix} = \begin{Bmatrix} \{\boldsymbol{0}\} \\ \boldsymbol{f}(\boldsymbol{\eta}) \end{Bmatrix} \tag{7}$$

As for most of the electrochemical process the overpotential η is non-linear, a Newton-Raphson iterative algorithm is applied to solve the system (7).

Numerical validation of the BEM model has been performed in [6]. Results showed a very good agreement with the analytical values, with a relative error below 2% in direct relation to the surface mesh refinement.

3.2. Electrode shape change computation

In order to compute the electrode profile, the continuous process time T is divided into a discreet sequence of time points t_m (m=0, 1, ... N_t). Given the fact that at any nodal point of the boundary the current density is known, equation (4) reduces to N_p equations, one for each nodal point i and the electrode growth rate becomes:

$$\frac{d\bar{h}(\boldsymbol{\chi}_i,t)}{dt} = -\left[\theta \cdot \frac{M}{\rho \cdot z \cdot F}\right] \cdot \sigma \cdot J_n(\boldsymbol{\chi}_i,t) \cdot \boldsymbol{1}_n, \tag{8}$$

where the unit normal is oriented outwards from the computational domain. The new boundary is easily found displacing each node on the electrode proportional with and in the direction of the local growth rate (figure 1).

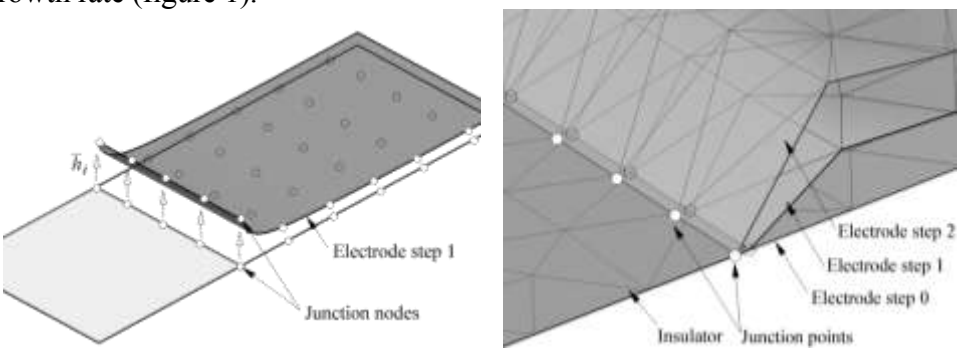

Figure 1: Displacement of the boundary nodes.

4. Electroplating simulation near a singularity

This example presents the 3D copper electroplating simulation on a square plate electrode embeded in an insulating plane (incident angle between the electrode and insulator surface = 180°). These applications are specific to electronics, e.g. PCB industry.

The reactor configuration is given in figure 2. The cathode that needs to be plated is a square plate of 12.9x12.9 cm^2, embedded by an insulating basis of 30.9x30.9 cm^2. The anode has the same dimensions as the insulating basis and is at 6 cm from the cathode.

The same physico-chemical input parameters as in [2] and [7] are used. The applied voltage between the anode and cathode is 0.505 V. The total process time T_F = 60 hours is divided in 20 constant time steps, Δt_F =3 hours.

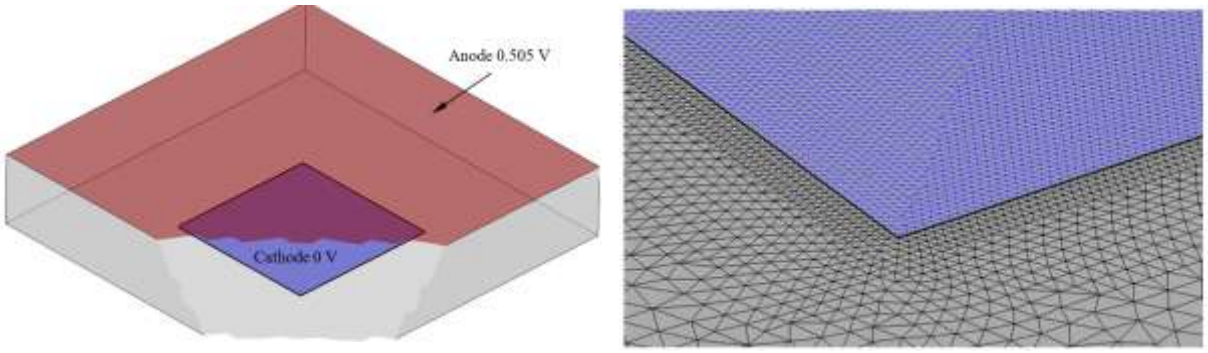

Figure 2: Geometry of the electrochemical cell and the triangular surface mesh in the vicinity of the singularity (insulating plane).

The governing Laplace equation is solved using the 3D BEM, which yields the normal current density distribution at the electrode surface. In a second step using the equation (8), the nodal points are displaced proportional with the normal current density. The process is repeated until the total process time is achieved.

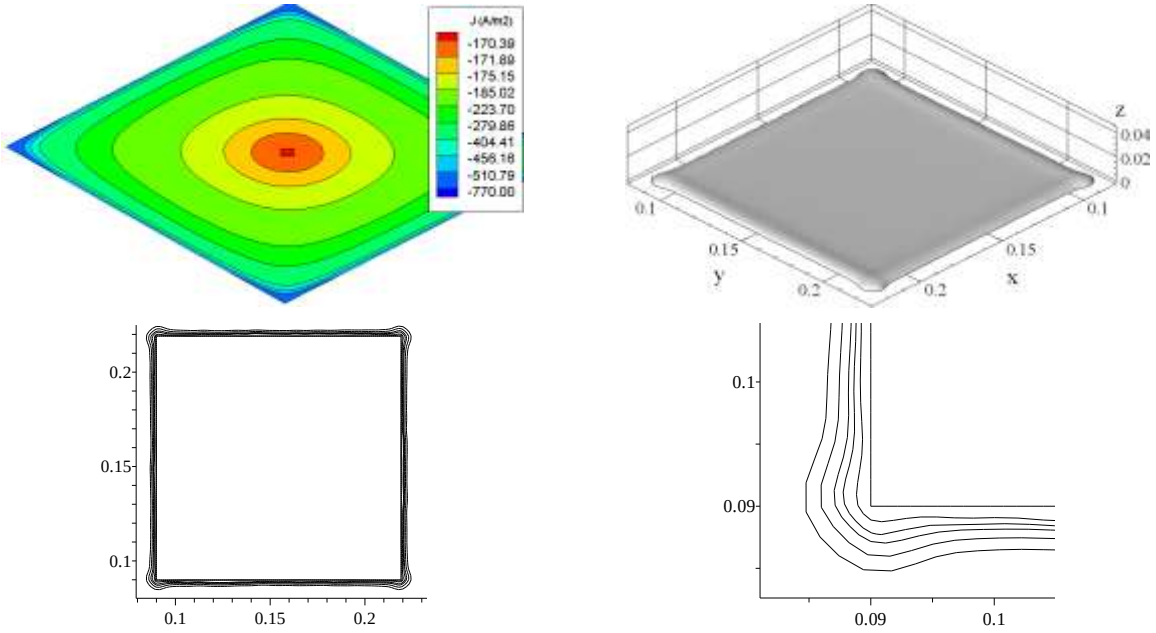

Figure 3: Current density distribution at the first time step (top left); Final 3D deposition profile (top right); history of the deposition profile in the insulating plane (bottom left); detail of the deposition profile at the corner of the cathode every 12 hours (bottom right).

The resulted average current density on the cathode's surface is c.a. -327 A/m2 for the first time step and the peak current density at the corners of the cathode -770 A/m2 (figure 3 top left).

The final shape of the cathode is illustrated in figure 3 top right. The history of the simulated profile in the insulating plane is shown in figure 3 bottom. The results in figure 3 demonstrate that due to the edge effects between the cathode and the insulator plane, a non-uniform shape change will manifest in time.

5. Conclusion

The principles of 3D electrode shape change simulations in the computational electroplating have been presented. The simulation tool is based on the potential model solved with a standard 3D BEM approach for calculation the current density distribution at the electrode and nodal

displacement method to find the electrode growth profile. In order to reveal the method, an example dealing with the 3D simulation of electroplating near an insulator (singularity) is presented. This example clearly demonstrated that the 3D computational method can easily predict non-uniform shape change evolutions in time due to the edge effects between the cathode and the insulating plane. The methodology developed in this paper proved robustness when dealing with and combining distinctive stages in the electrode growth simulations process, such as the current density computation and nodal displacement.

Acknowledgments

This work was supported within the research program POSDRU/89/1.5/S/ 57083.

References

[1] J J. Newman, *Electrochemical Systems 2'nd edition Englewood*, New Jersey: Prentince-Hall, 1991, pp. 378.
[2] J. Deconick, *Current distribution and electrode shape change in electrochemical systems- A boundary element approach*, Lecture Notes in Engineering Springer-Verlag, 1992, pp. 86.
[3] R. Alkire, T. Bergh, TL. Sani, *Predicting Electrode Shape Change with Use of Finite Element Methods*, J. Electrochem. Soc. 125, pp. 1981, (1978).
[4] B. Bozzini, PL. Cavallotti, *Numerical modelling of the growth of electrodeposited chromium on corner-shaped cathodes*, Int. J. Mater. Prod. Tec., 15(1-2), pp. 34, (2000).
[5] JA. Sethian, *Level Set Methods and Fast Marching Methods: Evolving Interfaces in Computational Geometry*, Cambridge, Cambridge University Press, 1999, pp. 10.
[6] J. Lee, JB. Talbot, *Simulation of Particle Incorporation during Electrodeposition Process*, J. Electrochem. Soc., 152(10), pp. C706-C715, (2005).
[7] M. Purcar, J. Deconinck, B. Van den Bossche, L. Bortels, *Electroforming simulations based on the level set method*, EPJAP. 2 (39), pp. 85 (2007).
[8] M. Purcar, V. Topa, C. Munteanu, R. Chereches, A. Avram, L. Grindei, *Optimisation of the layer thickness distribution in electrochemical processes using the level set method*, IET Science, Measurement & Technology, Volume 6, issue 5 , p. 376 - 385, (2012).
[9] M. Purcar, B. Van den Bossche, L. Bortels, J. Deconinck, P.Wesselius, *Numerical 3D Simulation of a CP system for a Buried Pipe Segment Surrounded by a Load Releiving U-shaped Vault*, Corrosion 59, pp. 1019-1028, (2003).
[10] M. Purcar, B. Van den Bossche, L. Bortels, J. Deconinck, *Three-Dimensional Current Density Distribution Simulations for a Resistive Patterned Wafer*, J. Electrochem. Soc., 151 (9), pp. D78-D86, (2004).
[11] M. Purcar, L. Bortels, B. Van den Bossche, J. Deconinck, *3D electrochemical machining computer simulations*, J. Mater. Process. Technol. 149 (1–3), pp. 472–478, (2004).
[12] L. Bortels, M. Purcar, B. Van den Bossche, J. Deconinck, A user-friendly simulation software tool for 3D ECM. J. Mater. Process Technol. 149 (1–3), 486–492, (2004).
[13] M. Purcar, A. Dorochenko, L. Bortels, J. Deconinck, B. Van den Bossche, *Advanced CAD integrated approach for 3D electrochemical machining simulations*, J. Mater. Process. Technol. 203, pp. 58–71, (2008).
[14] A. Dorochenko, A. Athanasiadis, L. Bortels, H. Deconinck, *Integration of grid generation and electrochemical engineering simulation software in a CAD environment*, EUA4X 2005, Annual Conference at TCN CAE 05, Lecce, Italy, October (2005).
[15] C.A. Brebbia, *Boundary Element Techniques – Theory and Applications in Engineering*, Springer-Verlag Berlin, Heidelberg, 1983.

Influence of temperature on the potentiality of low power integrated systems used for producing AC electricity and adjusting its parameters

Ion VONCILĂ, Nicolae BADEA, Ion PARASCHIV
„Dunărea de Jos" University, Galați, Romania, Ion.Voncila@ugal.ro

Abstract. The paper deals with a comparative analysis of an integrated system suggested for production and adjustment of AC power parameters, used for power supplying in isolated places operating at environmental temperatures, varying in a large range (winter-summer). PDE software from Macsyma was used for this analysis. The results obtained show that the temperature variation influences the potentiality of these electromagnetic systems, but the structural particularities of the integrated system diminishes these consequences.

1. Introduction

Due to the diversity of applications, a large number of electrical machines work in hostile environments in terms of the range of variation of ambient temperature. Even in temperate continental climate, there are large differences between ambient temperatures encountered in winter season (-30°C) and the same ambient temperature encountered in hot summers (+40°C). As a result, besides the electromagnetic requierments, electrical machines also have to bear- as structures - the tensions caused by temperature gradients in the environment. The issues caused by these additional tensions are even more serious in the integrated structures encountered in the case of wind to electricity energy conversion systems which, running at medium and high power, are placed not only in enclosures located practically at ambient temperature but also at a certain altitude (sometimes this can be an aggravating factor). Nacelles in which these structures are placed (particularly, electrical generator) can offer, in many cases, a certain level of protection against the tension of the environment. The situation is worse for structures used for small power systems wind to electricity energy conversion, where permanent magnet synchronous generators are generally used. Both properties of conductor materials and properties of ferromagnetic materials (either temporary magnetism or permanent magnetism) varies with temperature, and in the case of variations - in a wide range of ambient temperature - the balance between the two areas (internal electric machine and external represented by environment) is always different. Therefore the local area where the system is situated provides conditions for the manifestation of other properties of constituent materials [1], [3], [5].

In the work [2] has been proposed a new structure for an electrical machine (an integrated system consisting of a permanent magnet synchronous generator and a transformer). The new system has been subjected to a comparative analysis in relation to a simple structure (an axial permanent magnet synchronous generator, double air gap without ferromagnetic stator core [4]) in terms of magnetic field distribution and specific forces developed. The proposed integrated system has proved viable and able to meet the requirements of users in isolated sites that can be used successfully so as to convert wind energy into electricity. This paper attempts to visualize the behavior of the proposed conversion integrated in a strenuous environment (ambient temperature variations in a wide range) specific to particular isolated sites. In order to resolve the proposed problem the PDE-ase software was used, which allows solving - by finite element - problems of both, electromagnetic or thermal field. The primary goal of the new analysis is to indicate how changes in ambient temperature in a wide range affects the potentiality of the proposed integrated system, and its functional characteristics (dependent on the characteristics of constituent materials), respectively.

2. Mathematical modeling of the integrated system in terms of environmental temperature variation

The mathematical model requires the connection of two problems that have the same cause: the electric current passes through coils placed on ferromagnetic stator core (Figure 1).

The system of equations (1) [6], [7], [8] groups the equations that model the two processes: the first equation models the magnetic field developed within the structure while the second equation models the thermal field developed in it. For each of these two problems boundary domain conditions have been imposed as shown in Figure 1- due to symmetry, the design takes half of the proposed structure.

$$\begin{cases} rot\left[\frac{1}{\mu}\cdot\left(rot\,\bar{A}-\bar{I}\right)\right]=\bar{J} \\ div(-k\cdot grad(T))=p_d \end{cases} \tag{1}$$

$$\begin{cases} \bar{A}(P)=0 & P\in Fr_1(D) \\ \frac{\partial\bar{A}(P)}{\partial\bar{n}}=0 & P\in Fr_2(D) \end{cases} \tag{2}$$

where:

$\bar{A}$ - the magnetic potential vector;

$\bar{I}$ - the magnetic polarization vector;

$\bar{J}$ - the current density vector;

μ - the magnetic permeability;

k - the thermal transmissivity (thermal conductivity) of the various materials structure;

T - the developed temperature;

p_d - power developed per unit volume of the structure;

$Fr_1(D)$ - the boundary on which the Dirichlet condition is applied;

$Fr_2(D)$ - the boundary on which the Neumann condition is applied.

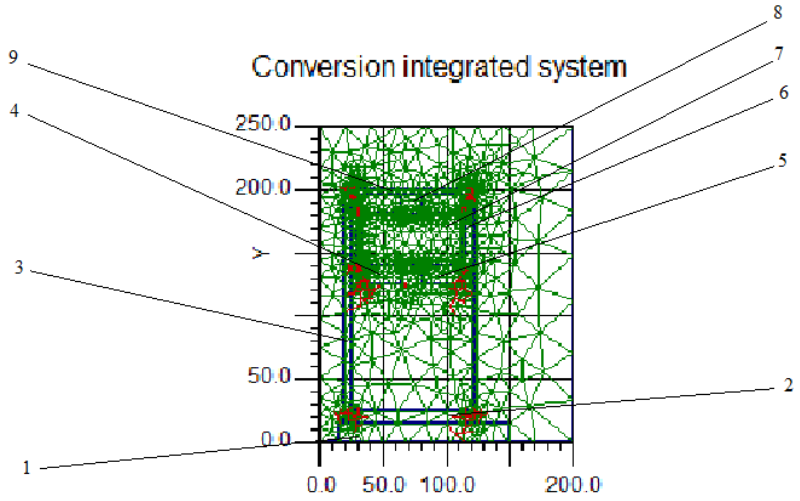

Figure 1. Domain of integration for the proposed integrated system

The following notations were used in Figure 1: 1 - rotor shaft; 2 - inner iron core; 3 – flange; 4 - reaction winding of the generator (respectively, the primary winding of the transformer); 5 - transformer secondary winding; 6 - permanent magnet of NdFeB (synchronous generator

excitation); 7 - iron core (stator synchronous machine + transformer); 8 - piece aluminum fixing stator core; 9 - box (with an active role).

It is worth noting that (simplifying assumptions used in the mathematical model):

- Although the coils are isolated from the core, the insulation was not noted in Figure 1 and was not accounted for by its properties in the model;
- In order to maintain the core coils, but also so as to exclude the end cap effect (swelling of magnetic field lines crossing the middle of the air gap) polar pieces were used (a change in the ferromagnetic core section from the air gap). They are not listed in Figure 1, but different section (enlarged) of air gap around the ferromagnetic core were taken into account, in the model;
- The use permanent magnets used were considered anisotropic, their magnetization being axial;
- The size of the air gap (also unlisted in Fig. 1) was considered constant in the entire pole piece and acceptable value of mechanical point of view (g=1[mm]).

3. Results. Discussion

The simulations carried out - based on the mathematical model - for the two extremes of ambient temperature (-30°C - in winter season respectively +40°C in summer season) are presented below. Figure 2 shows the spatial variation of magnetic vector potential - for the system examined - when the operation occurs in the winter (Fig. 2, a) and in the summer (Fig. 2, b), respectively. Potential variations are very small for this wide range of variation in ambient temperature, and this is because variations with temperature of the characteristics of permanent magnets and the resistance of both coils placed on ferromagnetic core (outer stator) have been neglected.

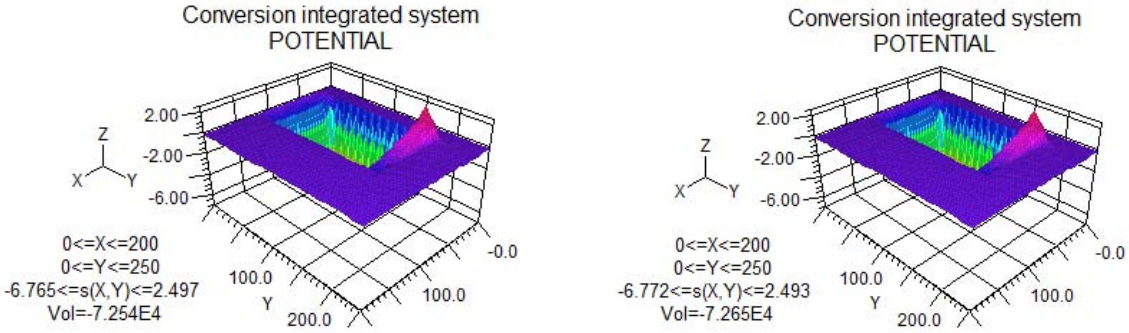

Figure 2. Spatial variation of the magnetic vector potential - in the proposed integrated system - for extreme values of ambient temperature considered: a) -300C (winter); b) +400 C (summer)

The disregard for the above mentioned issues may be accepted in the first instance, and practice, taking into account the fact that the electric machine has a special construction (there is plenty of air and thermal equilibrium is achieved rather easily, not endangering the integrity of the proposed integrated system). Nevertheless, a rigorous analysis must take into account the variation with temperature of the intrinsic properties of the constituent materials of the structure.

Figure 3, with the multiple simplifying assumptions taken, presents the distribution of the magnetic induction vector in the proposed integrated structure at ambient temperature of -30°C (winter), while Figure 4 presents the same temperature distribution ambient to +40°C (summer). The main goal of this comparative analysis is to demonstrate that the proposed structure - with its constructive particularities - has a low sensitivity to thermal influences of the environment

and major parts of the this structure - responsible for the development of forces - are little perturbed by variations thermal environment. Duet o the fact temperature can create chaos within a structure, it was considered that the best analysis of this influence can be achieved by visualizing vector fields (in particular, the magnetic flux density).

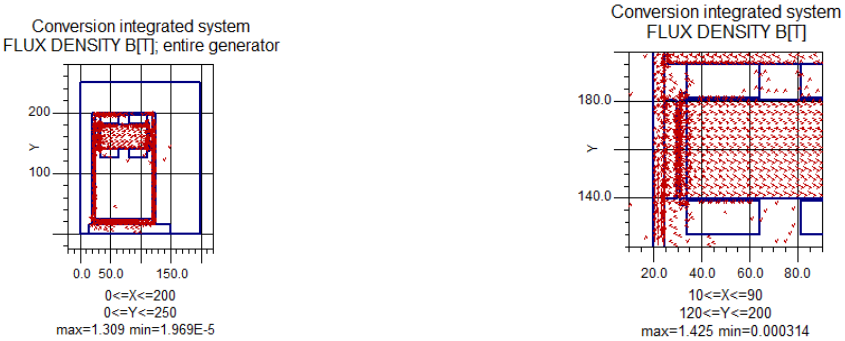

Figure 3. Distribution of magnetic induction vector of integrated system proposed for ambient temperature -30°C (winter): a) the entire generator; b) detail the permanent magnets - embedded transformer

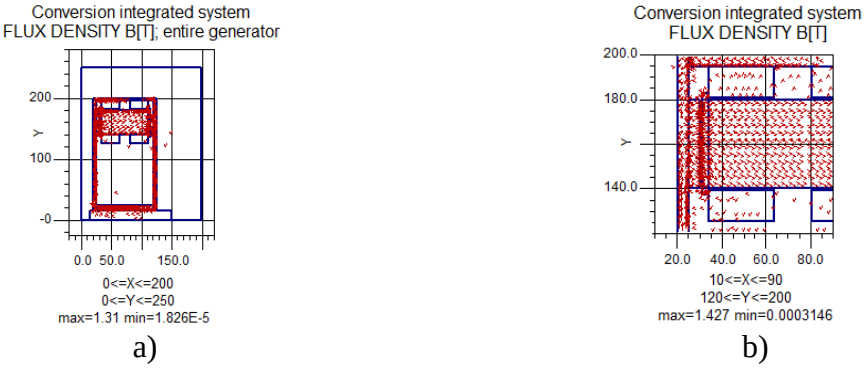

Figure 4. Distribution of magnetic induction vector of integrated system proposed for ambient temperature +40°C (summer): a) the entire generator; b) detail the permanent magnets - embedded transformer

Figures 5 and 6 present the distributions of magnetic field lines in the structure, the magnetic flux density and magnetic field intensity for the two extremes of ambient temperature: -30^0 C (winter) – fig. 5; $+40^0$ C (summer) – fig. 6.

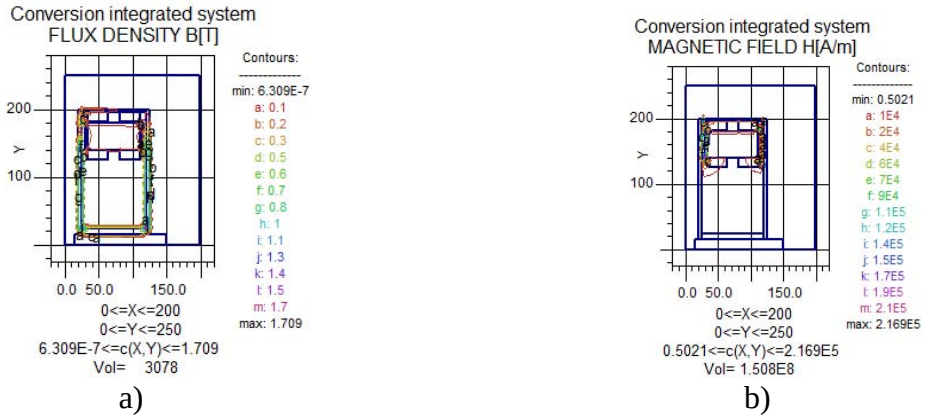

Figure 5. Distribution of magnetic induction field lines, respectively, magnetic field intensity of the integrated system proposed for ambient temperature -30°C (winter): a) magnetic flux density; b) magnetic field intensity

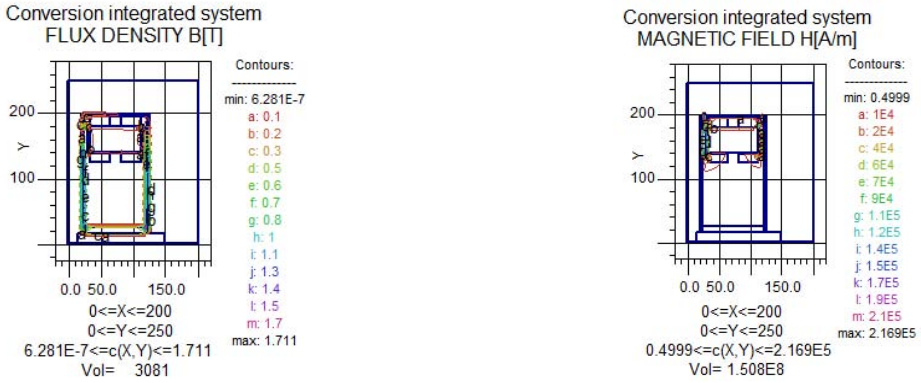

a) b)

Figure 6. Distribution of magnetic induction field lines, respectively, magnetic field intensity of the integrated system proposed for ambient temperature +40°C (summer): a) magnetic flux density; b) magnetic field intensity

Figures 7 and 8 show the spatial variation of specific energy and the distribution of temperature (in the analyzed structure) , respectively- and especially the manner in which the internal heat balance between the heat source and external source (represented by environment) is created - in both emblematic cases studied: the ambient temperature of -30°C (winter) - fig. 7, and the ambient temperature of +40°C (summer) - fig. 8, respectively.

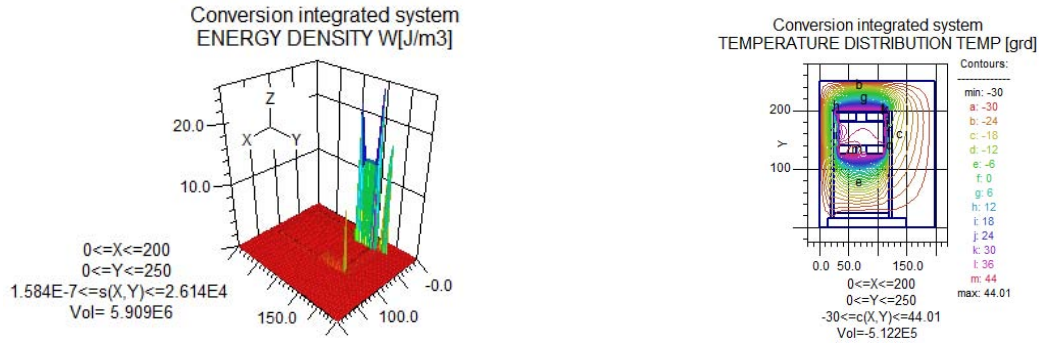

a) b)

Figure 7. Spatial variation of specific energy, respectively, the temperature distribution of the integrated system proposed for an ambient temperature of -30°C (winter): a) spatial variation of specific energy; b) temperature distribution

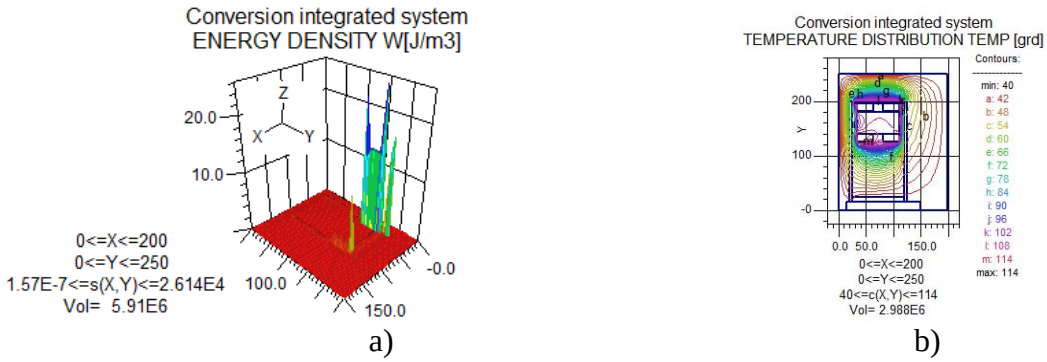

a) b)

Figure 8. Spatial variation of specific energy, respectively, the temperature distribution of the integrated system proposed for an ambient temperature of +40°C (summer): a) spatial variation of specific energy; b) temperature distribution

For usual current densities in existing windings (as in conventional electric machines), the specific energy is higher in the reaction winding synchronous generator area (which is also, the integrated electrical transformer primary winding), and lower in the transformer secondary area. This behavior is duet o the fact that the permanent magnets are anisotropic. This irregularity of specific energy, in the structure will be reflected in the amplitude of specific forces developed, for which the structure being analyzed (reduced reaction on the transformer) is a variant of reference for an efficient system for practice.

4. Conclusions

The simplified analysis performed in this paper has highlighted the following aspects of the particular proposed structure:

- the structure has a great potential, potentiality that is less affected by temperature changes in the environment;
- due to structural features, seasonal changes in a wide range of ambient temperature the effects - neglecting temperature variation parameters - of the magnetic flux density (and magnetic field), respectively, the specific energy (implicitly, specific forces developed) are very little;
- the temperature distribution in the structure (for both extremes of ambient temperature analysis) - and in the immediate proximity of electromagnetic conversion system - shows the occurrence of thermal peaks, which justifies as a first approximation, the the aspects neglected in modeling. A maximum temperature (in a hot summer) of 114°C is acceptable for NdFeB magnets, which is lower than the class index of insulating materials used at present (F, H and C).

Nevertheless, for the practical implementation of the proposed generator an improvement onthe geometry of the structure and a rigorous analysis that takes into account the variation with temperature, such as winding parameters and reference sizes (magnetic characteristics) of permanent magnets is necessary. It is also mentioning that the analysis will have visualize the double interaction: electrical machine - environment (the source of disturbance being electrical machine) and environment - electrical machine (environment being the source of disturbance), respectively.

5. References

[1**] –** D. Joo, J.H. Cho, K. Woo, B.T. Kim, D.K. Kim. Electromagnetic Field and Thermal Linked Analysis of Interior Permanent-Magnet Synchronous Motor for Agricultural Electric Vehicle, *IEEE Transactions on Magnetics*, **10** (2011) 4242- 4245.

[2] – I. Voncilă, M. Costin. Integrated system of production and adjustment of AC electric energy parameters for low power isolated sites that use wind energy as primary energy, *Annals of the University of Craiova, Electrical Engineering series*, **35** (2011) 134-139.

[3] – I. Voncilă, N. Badea. Comparative analysis of the environmental interaction for various configurations of power machines, *Journal of Electrical Engineering*, **4** (2008) 287-292.

[4] – I. Voncilă, N. Badea, I. Dobrotă. The distribution of magnetic field and the development of forces in synchronous machines with double air gap, *Acta Electrotehnica*, **3** (2004) 29 – 32.

[5] - I. Voncilă, N. Badea, I. Dobrotă. The behaviour of asymmetric frontal couplings with permanent magnets in magnetic powder and high temperature environments, *Proceedings of CNAE 2002*, (2002) 251 - 255.

[6] - ***PDE-ase., *Reference manual tutorial handbook of demonstration*, SPDE, Inc., 1995.

[7] - C.I. Mocanu - *Teoria câmpului electromagnetic*, Editura Didactică şi Pedagogică, Bucureşti, 1981.

[8] - Gh. Hortopan – *Aparate electrice*, Editura Didactică şi Pedagogică, Bucureşti, 1980.

A Numerical Study of the Magnetic Field Source in Magnetic Drug Targeted Transport and Fixation

Cristina SAVASTRU[1], Alexandru M. MOREGA[1,2]

University POLITEHNICA of Bucharest, Romania
Gheorghe Mihoc-Caius Iacob" Institute of Statistical Mathematics and Applied Mathematics, Romanian Academy, amm@iem.pub.ro

Abstract. The magnetic field source is a key part of the process of targeting the medication in regions of therapeutic concern in the Magnetic Drug Targeting (MDT) and its optimization deserves due attention. This paper presents a mathematical model and numerical simulation results on MDT where the magnetic field source is an electrical current carrying planar spiral coil, aimed at producing a higher gradient magnetic field. A simple yet consistent mathematical model for the hemodynamic flow that conveys the biocompatible drug and the external magnetic field is formulated and solved for numerically. Another concern is the heating that accompanies the electrical current, hence its minimization, and the heat transfer problem is then considered. The results suggest that the current carrying coil may successfully replace the permanent magnet in MDT.

1. Introduction

Recently, magnetic nanoparticles are being used to help improving the treatment for malignant cells while proving to be less invasive than traditional procedures (*e.g*. chemotherapy). One such promising therapy is *Magnetic Drug Targeting* (MDT), where superparamagnetic nanoparticles (SNP) are used to carry the medication in regions of interest (ROIs) such as tumoral entities. MDT seems to have less unwanted side effects, being able to remove tumors cells without affecting the healthy tissue.

MDT implies complex interactions between the drug, which coats magnetic nanoparticles, the blood flow, which transports the medication, and the tissue where the drug fixation is provided by an external magnetic field. The active (magnetic) substance is injected into the blood stream to be transported to the ROI, where magnetization body forces produced by the external magnetic field act into fixing it [1-6].

The external magnetic field source is then a key element in the proper fixation of SNP transported drugs. Since the magnetic body forces are more important in regions of high magnetic field gradients, an important issue is its optimization [7-9].

While previous studies [8,9] were concerned with optimizing a permanent magnet for high gradient field, in this work we propose an electrical current carrying coil as field source [7]. One side effect of using intense currents is the heating that comes with them. In this study we evaluate the overheating produced by Joule effect with the aim of reducing it.

2. The Mathematical Model

In this work we study the magnetic field – flow – heat transfer interactions when the MDT field source is an electrical current carrying coil therefore other issues such as the vessel morphology, while important [9], are discarded. The blood vessel in this case is considered a straight cylinder, with rigid walls. All materials (blood, tissue, *etc*.) are assumed continuum media.

The mathematical model is describes the magnetic field, the blood flow and the heat transfer in a muscular mass, containing a large artery, of “resistance type” [10], in a region where an external magnetic field acts.

The magnetic field model

The Physical model of MDT problem in stationary magnetic field produced either by a permanent magnet or an electric current conduction (a coil) is described by the fallowing equations [9]

Ampère's law

$$\nabla \times \mathbf{H} = \mathbf{J}, \tag{1}$$

the magnetic flux law

$$\nabla \cdot \mathbf{B} = 0, \tag{2}$$

the constitutive law

$$\mathbf{B} = \mu_0 \mathbf{H}, \text{ (air and tissue)} \tag{3}$$

$$\mathbf{B} = \mu_0 \mu_{r,mag} \mathbf{H} + \mathbf{B}_{rem}, \text{ (permanent magnet)} \tag{4}$$

$$\mathbf{B} = \mu_0 [\mathbf{H} + \mathbf{M}_{ff}(\mathbf{H})], \text{ (ferrofluid)} \tag{5}$$

where **H** [A/m] is the magnetic field strength, **B** [T] is the magnetic flux density, $\mu_0 = 4 \cdot \pi \cdot 10^{-7}$ H/m is the magnetic permeability of air, $\mu_{r,mag}$ is the relative magnetic permeability of the permanent magnet, $\mathbf{B}_{rem}$ [T] is the remanent magnetic flux density, $\mathbf{M}_{ff}(\mathbf{H})$ [A/m] is the magnetization of the blood and magnetic nanoparticles aggregate fluid.

Using the magnetic vector potential **A** [Wb/m] and the divergence free gauge condition

$$\mathbf{B} = \nabla \times \mathbf{A}, \quad \nabla \cdot \mathbf{A} = 0, \tag{6}$$

the model (1)-(6) is leads to the second order PDE

$$\nabla \times \left(\mu_0^{-1} \nabla \times \mathbf{A} - \mathbf{M} \right) = \mathbf{J}. \tag{7}$$

The associated boundary condition is magnetic insulation ($\mathbf{n} \times \mathbf{A} = 0$), overall.

The Hemodynamic Model

In this study we are concerned with large, "resistive" type of arteries [9,10], where the fluid (blood) may be assumed viscous, Newtonian. Its flow is unsteady (pulsatile), incompressible, laminar, described by

momentum balance (*Navier-Stokes*)

$$\rho \left[\frac{\partial \mathbf{u}}{\partial t} + (\mathbf{u} \cdot \nabla)\mathbf{u} \right] = -\nabla \left[-p\mathbf{I} + \eta \left(\nabla \cdot \mathbf{u} + (\nabla \cdot \mathbf{u})^T \right) \right] + \mathbf{f}_{mg}, \tag{8}$$

and *mass conservation law*

$$\nabla \cdot \mathbf{u} = 0. \tag{9}$$

Here **u** is the velocity field, *p* [Pa] is pressure, ρ [kg/m^3] is the mass density, η [Pa·s] is the dynamic viscosity, and **I** is the unity matrix [9].

The magnetic field problem and the hemodynamic problem are coupled (in a single direction) through magnetization forces. The magnetic body forces, due to the fluid aggregate magnetization in an external magnetic field are given by [7-9]

$$\mathbf{f}_{mg} = \mu_0 (\mathbf{M} \cdot \nabla)\mathbf{H}. \tag{10}$$

The boundary conditions are zero velocity (no-slip) at the vessel walls and – to model a

pulsatile flow – the pressure conditions [9]

$$P_{in}(t) = P_0\left[1 + a\sin\left(\pi\left(t + 3/2\right)\right)\right], \quad (11)$$

$$P_{out}(t) = P_1\left[1 + a\sin\left(\pi\left(t + 3/2\right)\right)\right], \quad (12)$$

were P_{in} and P_{out} are the inlet and outlet pressures. In equations (11), (12) t [s] is the time, P_0 = 13,300 Pa, P_1 = 13,100 Pa, and a = 0.2 is a nondimensional parameter.

The Heat Transfer Model

When the magnetic field is an electric current, the heat produced by Joule effect may be a menace to the adjacent tissue. The heat transfer problem is then described by and analyzed with *the energy equation*

$$\rho c_P\left[\frac{\partial T}{\partial t} + (\mathbf{u}\cdot\nabla)T\right] = \nabla(k\nabla T) + Q. \quad (13)$$

Here c_P [J/kg·K] is the specific heat at constant pressure, k [W/m·K] is the heat conductivity, and Q [W/m^3] is the heat source (inside the coil, by Joule effect). The boundary conditions for the heat transfer problem, the flow and magnetic field problem are represented in Figure 1. A moderate convection heat transfer coefficient (h = 2 W/m·K) is assumed.

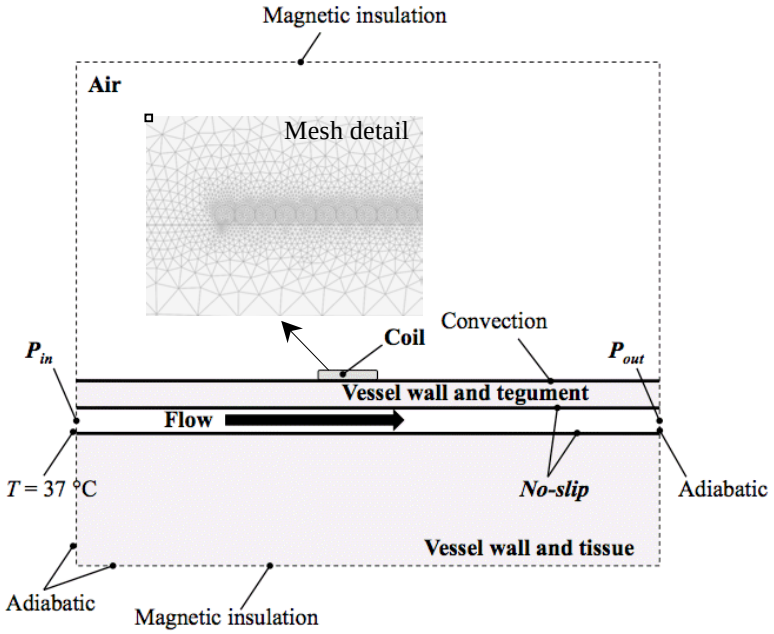

Figure 1: Computational domain and boundary conditions for magnetic field, flow field, heat transfer.

The mathematical model was solved numerical by the Galerkin finite element method (FEM), as implemented by [11].

3. Numerical Simulation Results

First, the magnetic field is solved for two powering scenarios: (i) continuous and (ii) intermittent powering. We assume that in the intermittent regime the on-off switching occurs at a very slow commutation rate such that the magnetic field produced by the current is stationary.

This problem is solved only once, in the beginning, and the magnetic body forces are

computed. Next the hemodynamic problem is solved for the pulsating flow conditions (11) and (12), for the two powering strategies. There magnetic field – flow interaction is one way, in the sense that the flow is influenced by the magnetic field while the magnetic field is not perturbed by the flow.

Finally, the transient heat transfer problem is solved for the two powering schemes.

The 2D Model

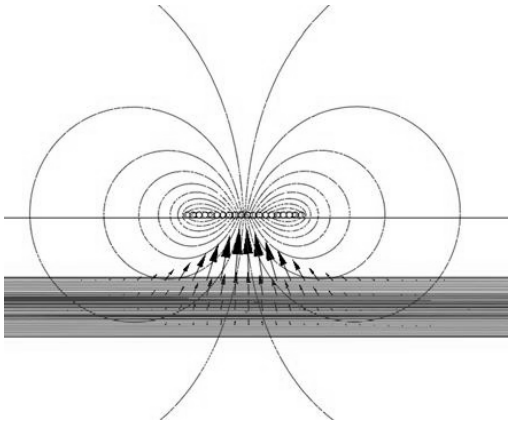

Figure 2: The flow field (streamlines), the magnetic flux density, and magnetization forces.

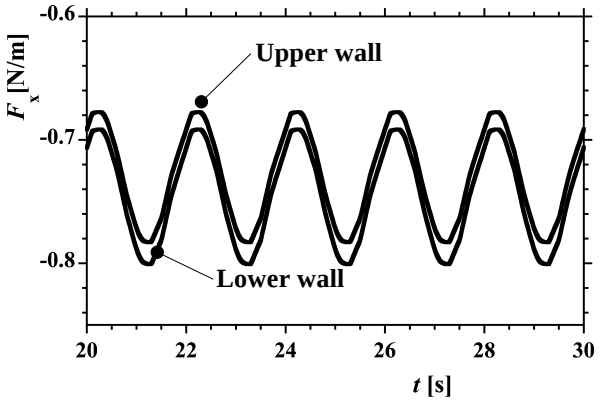

Figure 3: Per unit total friction force at the walls, in flow direction.

Figure 2 shows the magnetic field, the magnetic body forces and the flow, for the maximum flow rate. The area below the coil center is the region of highest magnetic body forces.

Figure 3 presents the total fiction force in the interval 20…30 s, opposite to the natural flow. The values recorded at the upper wall are larger and the effect of the magnetic forces explains the discrepancy: the viscous force at the upper wall is larger as the effect of the magnetization forces is more important here (figure 2).

It is worth mentioning that the first four periods of the flow (~8 s) were discarded since they bear the influence of the initial flow conditions.

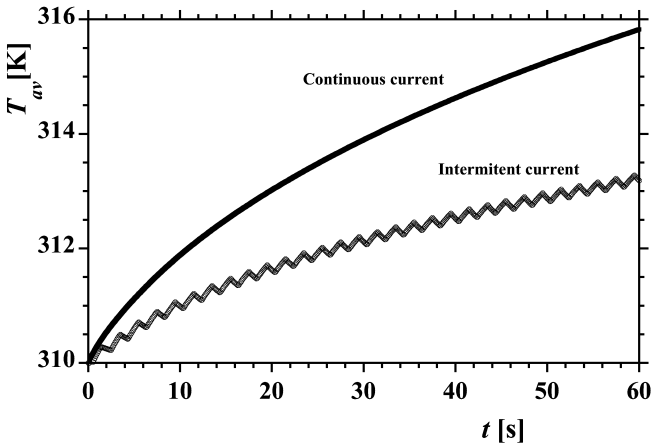

Figure 4: The average temperature on the skin, under the coil, for continuous and intermittent powering.

Figure 4 shows heat transfer results through average temperature profiles for the two powering schemes, continuous and intermittent considered adjusting the coil for maximum and minimum flow. An important conclusion may be drawn: the intermittent powering leads to a much slower heating thus allowing for a longer application of the procedure without

diminishing the fixation effects of the magnetic field. On the contrary, the heating effect that accompanies the continuous powering scheme may require shorter MDT protocols – the 42 ºC threshold is attained in approx. 1 min., and a continuing the procedure may damage the tissue.

The 3D Model

The 2D computational model may represent a less realistic image of the fully 3D problem. For instance, the effect of the curvature of the turns and that of the vessel do not concur in to an axial symmetric model. It is then important to see if the results for the magnetic field – flow, and heat transfer interactions obtained by the more convenient 2D modeling are still valid when a 3D model, better approaching the real case, is used.

To reduce the complexity of the problem, we assume that assuming that the coil is made of concentric turns (instead of the spiral). Therefore the computational domain may be reduced to half, in view of the symmetry with respect to the *x0y* plane (figure 5).

The electrical currents in the coil are obtained as the solution of a set of electrokinetic problems, one for each turn. The boundary conditions for each turn are: insulated outer surface, imposed current density (10 A/mm^2) at one cross section end and ground for the other end. The boundary conditions for the magnetic field, flow, and heat transfer problems are essentially those assumed in the 2D model (figure 1).

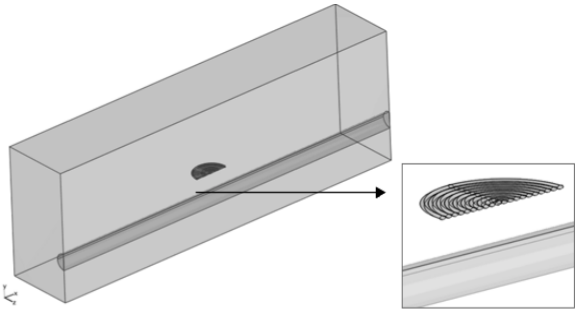

Figure 5: The computational domain.

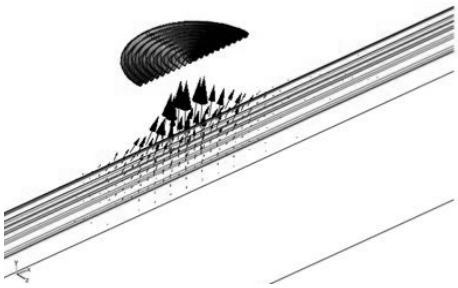

Figure 6: Electric potential, magnetization body forces and velocity field.

Figure 6 shows the electrical potential on the coil, the magnetic body forces and the flow for maximum flow rate.

Figure 7: The magnetization body forces – cross-sectional view.

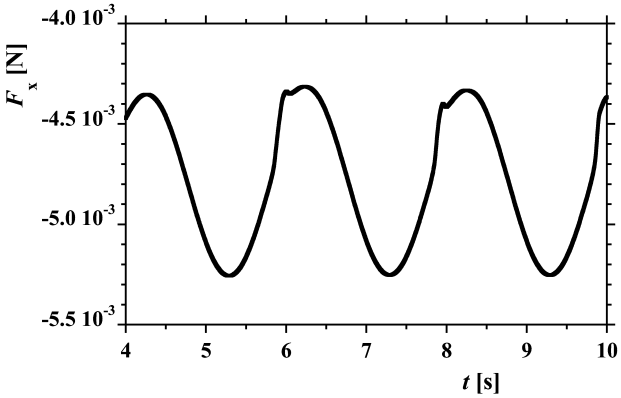

Figure 8: The total friction force at the vessel wall, in flow direction.

In figure 7, a cross sectional view shows off the profile of the magnetic forces on the vessel

wall that are focused towards the planar coil center. Although there are no “upper” and “lower” parts of the vessel wall (as in figures 1,2) it is clear that wall friction enhancement by magnetic targeting is significant at the side of the wall placed bellow the coil. This result suggests that the coil is to be positioned such that the ROI is located between the coil and the vessel.

Figure 8 presents the total friction force in flow direction. This result is consistent with the 2D result in an order of magnitude sense.

The heat transfer part in the 3D problem makes the object of a future research.

4. Conclusions

Magnetic drug targeting therapy poses design concerns such as the optimization of the magnetic field sources, able to efficiently fixing medication in the regions of therapeutic interest. Most notably, high magnetic field gradient configurations are at a prime since they provide for larger magnetic body forces.

Permanent magnets can be successfully replaced with coils. In this study we propose a spiral, planar coil that may be powered either continuously or intermittently.

However when electric currents to produce the magnetic field unwanted side effects may occur, for example an excessive heating of the adjacent tissue. It was shown that this effect can be significantly reduced by intermittently powering the coil. Replacing the 2D model with 3D is necessary for a better approach to reality.

Acknowledgement – The work was conducted in the Laboratory for Electrical Engineering in Medicine, affiliated with BIONGTEH platform at UPB.

References

[1] W. Schütt, C. Grüttner, U. Häfeli, M. Zborowski, J. Teller, H. Putzar, C. Schümichen. Applications of magnetic targeting in diagnosis and therapy – possibilities and limitations: a mini-review, *Hybridoma*, **6**, 1 (1997).

[2] C.C Berry, A.S.G Curtis, Functionalisation of magnetic nanoparticles for applications in biomedicine. *J. Phys. D: Appl. Phys*. **36**, 2003, R198 doi: 10.1088/0022-3727/36/13/203

[3] B. Shapiro. Towards dynamic control of magnetic fields to focus magnetic carriers to targets deep inside the body, *J. of Magnetism and Magnetic Materials*, **321** (2009) pp. 1594–1599.

[4] M. Arruebo, R. Fernández-Pacheco, M.R. Ibarra, J. Santamaría. Magnetic nanoparticles for drug delivery, *Nanotoday*, **2**, 3 (2007) pp. 22-32.

[5] C. Alexiou, R. Jurgons, R.J. Schmid, C. Bergemann, J. Henke, W. Erhardt, E. Huenges, F. Parak. Magnetic drug targeting-biodistribution of the magnetic carrier and the chemotherapeutic agent mitoxantrone after locoregional cancer treatment, J. *Drug Target*. **11**, 3 (2003) pp. 139-149.

[6] P.A. Voltairas, D.I. Fotiadis, L.K. Michalis. Hydrodynamics of magnetic drug targeting, *J. Biomech*., **35** (2002) pp. 813–821.

[7] A.M. Morega, M. Morega. A FEM analysis of Magnetically induced biomagnetic fluid mixing, *Rev. Roumaine Sci. Techn. Electrotech. et Energ*., **50**, 2 (2005) pp. 239-248.

[8] A.M. Morega, A.A. Dobre, M. Morega, D. Mocanu. Computational modeling of arterial blood flow, Proc. Second MediTech Conference, 23-26 September 2009, Cluj-Napoca, Romania, 2009.

[9] A.M. Morega, A.A. Dobre, M. Morega. Numerical simulation of magnetic drug targeting with flow – structural interaction in an arterial branching region of interest, 17-19 Nov. 2010 Comsol Conference, Versailles, France, 2010.

[10] R.A. Feijóo, *Computational methods in biology*, 2nd Summer School LNCC/MCT, Petrópolis, January, 2000.

[11] Comsol Multiphysics, v. 3.5a (2010), COMSOL A.B., Sweden.

Nucleotide Sequence Complex Representation

Paul Dan CRISTEA, Aurora Rodica TUDUCE
University "Politehnica" of Bucharest, Spl. Independentei 313, Romania, pcristea@dsp.pub.ro

Abstract. The paper present recent developments in the nucleotide genomic signal (NuGS) methodology. NuGS approach is based on the conversion of symbolic nucleotide sequences into numeric genomic signals. NuGS method proved adequate for both large scale analysis of genomic sequences, by revealing hidden regularities and symmetries, and for local analysis, important for the study of gene dynamics.

1 Introduction

Nucleotides are the monomers of nucleic acids, DNA and RNA. The nucleobases are the key components that provide the identity of nucleotides, thus their function as letters in the genetic alphabet. The primary nucleobases are adenine (A), cytosine (C), guanine (G) – shared by DNA and RNA, thymine (T) – only in DNA, and uracil (U) – which replaces T it in RNA. The order of nucleotides along a strand stores the genetic information.

A triplet of successive nucleotides forms a codon, which encodes amino acids according to the so called standard Genetic Code [1], which is valid for the coding segments (exons) of most nuclear genomes. There are 43 = 64 codons, which encode the 20 amino acids building the proteins, and the 'stop' or 'terminator' marking the end of a gene and of protein synthesis. A gene can comprise several exons. The total of the protein encoding part of the genome is only 2-3% in homo sapiens, but reaches over 95% in archaea and bacteria. The intergenic part of the human genome contains repetitive, quasi-random sequences and a large amount of transposable elements that bear a close resemblance to the DNA of some independent entities like viruses and bacteria. A significant part of the inter-gene chromosomal DNA plays an important role in the control of protein synthesis, conjointly with other gene regulatory systems.

There is a sharp contrast between the deceivingly simple structure of DNA nucleotide chains – an unbranched linear code written in a four letters alphabet, and the overwhelming complexity of the protein tri-dimensional structure. Correspondingly, the complexity of the proteome ─ the set of proteins existing in a cell, tissue, organ or the whole body, exceeds by far the complexity of the genome. The total number of genes in the human genome is only about 32,000, while the proteome comprises more than one million proteins, many of them transitory. The key to organism complexity is not in the number of genes, but in the way parts of the genes are expressed and combined to build different proteins by using alternative splicing. The regulatory mechanisms that control these processes in every cell are sensitive to signals from the environment and from the other cells, tissues and organs in the organism. Nevertheless, the nucleotide chains in DNA molecules and the amino acid chains in various proteins are the bearers of the same genetic information, despite of the many changes that can be introduced by pre- and post-translational processes and the essential role of the way proteins are 3D packed.

2 Representation of Genomic Information

The representation genomic information can be either symbolic or numerical.

The symbolic representation uses directly the four symbols of the nucleotides, A, C, G and T (or U). The analysis and computational methods are applied directly to the symbolic nucleotide sequences, as they are obtained at the output of the sequencing machines, or as they are retrieved from the genomic databases. The symbolic approach has the advantage of simplicity, important for storage, retrieval and transmission of genomic data, but it also has significant disadvantages in

what concerns the processing of data, as it restricts the methodology to pattern matching and statistical analysis [2].

The numerical representation uses an additional conversion step to map each individual nucleotide symbol of a sequence into a corresponding numerical value [3, 4]. The numerical representation allows the effective use of powerful digital signal processing techniques, initially developed in the domains of communications and networking, but which can be applied successfully to genomic research as well. The numeric approach is able to reveal many features of genome structure, symmetries and regularities, which are sometimes hidden and would be difficult to identify by symbolic representation and processing techniques [5, 6].

We have developed and used a specific approach, the nucleotide genomic signal (NuGS) methodology, which can be applied at various scales, going from the global to the local analysis of nucleotide sequences. The large scale analysis of genomic sequences reveals not only ostensive features of extant DNA sequences, at the scale of entire chromosomes, or even entire genomes, but also ancestral features, which existed in DNA sequences but disappeared during subsequent evolution, under the pressure of species separation [4, 5].

3 Binary Indicator Sequences and their Fourier Transforms

A straightforward method to numerically characterize symbolic DNA nucleotide sequences is to use binary indicator sequences. The method attaches four binary indicator sequences $u_A[k]$, $u_C[k]$, $u_G[k]$, and $u_T[k]$, $k \in \{0, 1,\ldots, N\text{-}1\}$, to a symbolic DNA string $Nu[k]$ of N nucleotides, seen as characters in the alphabet {A, C, G, T}. Each indicator sequence $u_X[k]$ keeps track of the occurrence of a symbol X in the sequence:

$$u_X[k]=\begin{cases} 1, & \text{when } Nu[k]=\text{X}, \\ 0, & \text{otherwise,} \end{cases} \qquad \text{X} \in \{\text{A, C, G, T}\},\ k \in \{0, 1, \ldots, N\text{-}1\}. \tag{1}$$

The Discrete Fourier Transforms (DFTs) of the binary sequences $u_A[k]$, $u_C[k]$, $u_G[k]$ and $u_T[k]$, $k = 0,\ldots, N\text{-}1$, can be defined as for any other digital sequence of N entries. The corresponding DFT sequences, $U_A[h]$, $U_C[h]$, $U_G[h]$, and $U_T[h]$, $h = 0,\ldots, N\text{-}1$, respectively, have also N entries each, given by the equations:

$$U_X[h]=\sum_{k=0}^{N-1} u_X[k]\, e^{-j2\pi hk/N}, \quad \text{X}\in\{\text{A, C, G, T}\}, \quad h\in\{0,1,\ldots,N-1\}, \tag{2}$$

which provide together the four-dimensional frequency spectrum of a nucleotide sequence. The cumulated power spectrum of the four binary sequences DFTs,

$$S[h]=\sum_{X}\left|U_X[h]\right|^2=\left|U_A[h]\right|^2+\left|U_C[h]\right|^2+\left|U_G[h]\right|^2+\left|U_T[h]\right|^2,\ h\in\{0,1,\ldots,N-1\}, \tag{3}$$

has the interesting property that, for most coding regions (exons), there is a period three peak in $S[.]$ (see [7]). Unfortunately, there are many exceptions, and the resolution is not good enough to allow exact exon location.

The distribution of symbols along a sequence can also be described by cumulative occurrence sequences defined in function of the binary indicator sequences. For a symbolic DNA string $x[k]$ of N nucleotides, one can define the four *cumulative occurrence sequences*:

$$c_X[k]=\sum_{h=0}^{k} u_X[h],\ \text{X} \in \{\text{A, C, G, T}\},\ k \in \{0, 1, \ldots, N\text{-}1\}. \tag{4}$$

In several representations of genomic sequences, bipolar binary imbalance sequences are used to describe the nucleotide distribution. An imbalance sequence $u_{X\text{-}Y}[.]$ gives the difference in the number of occurrences between the symbols X and Y in the symbolic sequence $Nu[.]$:

$$u_{X\text{-}Y}[k]=u_X[k]-u_Y[k]\in\{-1, 1\},\ X, Y \in \{A, C, G, T\}, k \in \{0, 1, \dots, N\text{-}1\}. \quad (5)$$

Binary indicator sequences can also be used to describe nucleotide sequences in terms of classes comprising more then one nucleotide (poly-nucleotides). For instance, it can be convenient to use binary indicator sequences for di-nucleotide classes, which form three dichotomic pairs $\binom{4}{2}=6$:

- weak $(u_W[.] = u_A[.] + u_T[.]$, and strong bonds $(u_S[.] = u_C[.] + u_G[.])$, (6)
- purines $(u_R[.] = u_A[.] + u_G[.])$, and pyrimidines $(u_Y[.] = u_C[.] + u_T[.])$, (7)
- amino $(u_M[.] = u_A[.] + u_C[.])$, and keto $(u_K[.] = u_G[.] + u_T[.])$. (8)

Definitions (2, 4, 5) can be easily extended to the di-nucleotide indicator sequences (6 - 8).

4 Nucleotide Complex Representation

We define the *nucleotide complex representation* [4, 5, 6] by the mapping $Nu \to \mathbb{C}\{Nu\}$, which establishes a one-to-one correspondence between the nucleotides $Nu \in \{A, C, G, T\}$ and their complex representations $\mathbb{C}\{Nu\}$ belonging to the set of complex numbers $\{a, c, g, t\}$:

$$a=\mathbb{C}\{A\}=1+j,\quad c=\mathbb{C}\{C\}=-1-j,\quad g=\mathbb{C}\{G\}=-1+j,\quad t=\mathbb{C}\{T\}=1-j, \quad (9)$$

represented in figure 1.

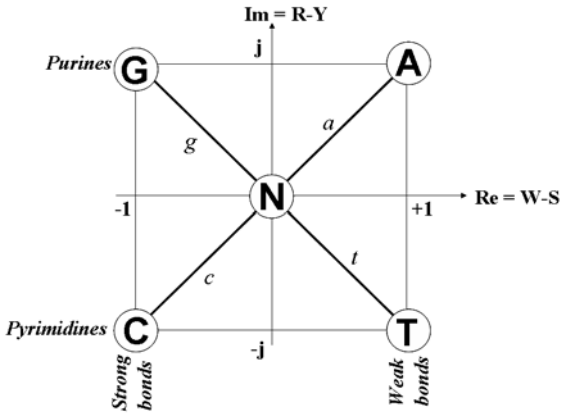

Figure 1: Complex representation of single-nucleotide classes.

The representations in (9) and Figure 1 are complex numbers having all the same absolute value $\sqrt{2}$, but different canonic arguments:

$$\arg(a)=+\frac{\pi}{4},\ \arg(c)=-\frac{3\pi}{4},\ \arg(g)=+\frac{3\pi}{4},\ \arg(t)=-\frac{\pi}{4} \quad (10)$$

The phase of a complex number is a periodical magnitude, as a complex number does not change when its phase varies with an arbitrary integer multiple of 2π – the phase period. The arguments given in (10) are the phases of the nucleotide representations $\{a, c, g, t\}$ belonging to the canonic domain $(-\pi, +\pi]$.

The edges of the square in Figure 1 correspond to the di-nucleotide classes:

$$\begin{aligned} &\text{Re} = +1 \leftrightarrow \text{weak bonds, Re} = -1 \leftrightarrow \text{strong bonds,} \\ &\text{Im} = +1 \leftrightarrow \text{purines,} \qquad \text{Im} = -1 \leftrightarrow \text{pyrimidines.} \end{aligned} \tag{11}$$

Thus, the real and imaginary parts of the nucleotide complex representation describe the membership of nucleotides to the {W, S, R, Y} di-nucleotide classes.

The mapping (9) can be applied to a symbolic sequence of nucleotides, $Nu[k]$, $k \in \{0, 1, \dots, N\text{-}1\}$, which is transformed into a complex digital signal $\boldsymbol{C}\{Nu[k]\}$, $k \in \{0, 1, \dots, N\text{-}1\}$.

The real and imaginary parts of the signal samples are given by:

$$\boldsymbol{C}\{Nu[k]\} = u_{\text{W-S}}[k] + j\, u_{\text{R-Y}}[k] \;,\; k \in \{0, 1, .., N\text{-}1\}, \tag{12}$$

where $u_{\text{W-S}}[k]$ and $u_{\text{R-Y}}[k]$ are the imbalance sequences between the weak - strong, and purine - pyrimidine di-nucleotide classes, respectively.

5 Phase Nucleotide Genomic Signals

The *argument sequence* resulting from (10) is the simplest phase signal. Using the binary nucleotide indicator sequences $u_{\text{A}}[k]$, $u_{\text{C}}[k]$, $u_{\text{G}}[k]$, and $u_{\text{T}}[k]$, $k \in \{0, 1, \dots, N\text{-}1\}$, defined in (1), and the arguments of the nucleotide representation given in (10), the argument sequence results:

$$\arg\{\boldsymbol{C}\{Nu[k]\}\} = \frac{\pi}{4}\left(u_{\text{A}}[k] - 3u_{\text{C}}[k] + 3u_{\text{G}}[k] - u_{\text{T}}[k]\right) \quad k \in \{0,1,\cdots,N-1\}. \tag{13}$$

This is a one-dimensional one-to-one representation of nucleotide sequences as complex number sequences, useful for the local analyses of nucleotide sequences. For the global study of the distribution of nucleotides and of di-nucleotides along a sequence, there are other phase signals which can be adapted from Signal Theory for the analysis of any sequences having complex entries. Two phase signals are particularly useful for this purpose, the *cumulative* and the *unwrapped* phases.

The *cumulative phase* is defined as the sum of the arguments of the complex representations of the sequence as a signal, from the first (0) to the current, k^{th}, sample:

$$\theta_c[k] = \sum_{h=1}^{k} \arg(\boldsymbol{C}\{Nu[h]\}), \quad k = 0,1,\dots,N-1, \tag{14}$$

where $Nu[h]$ is the h^{th} nucleotide, $h = 1,\dots,k$, in the sequence of N nucleotides, and $\boldsymbol{C}\{Nu[h]\}$ is its complex representation, with the arguments belonging to the canonic domain $(-\pi, +\pi]$.

Using the cumulative occurrence sequences $c_{\text{A}}[k]$, $c_{\text{C}}[k]$, $c_{\text{G}}[k]$, $c_{\text{T}}[k]$, $k \in \{0, 1, \dots, N\text{-}1\}$, defined in (4), the cumulative phase (14) can be written as:

$$\theta_c[k] = \frac{\pi}{4}\left(3\left(c_{\text{G}}[k] - c_{\text{C}}[k]\right) + c_{\text{A}}[k] - c_{\text{T}}[k]\right) = \frac{\pi}{4} N[k], \quad k \in \{0,1,\cdots,N-1\}, \tag{15}$$

where $N[k]$ is the *nucleotide imbalance*,

$$N[k] = 3\left(c_{\text{G}}[k] - c_{\text{C}}[k]\right) + c_{\text{A}}[k] - c_{\text{T}}[k]), \quad k = 0, 1, \dots, N-1, \tag{16}$$

a signature of the distribution of nucleotides in the sequence. The values $c_{\text{A}}[k]$, $c_{\text{C}}[k]$, $c_{\text{G}}[k]$, and $c_{\text{T}}[k]$ give the number of occurrences of the A, C, G, and T nucleotides, respectively, in the first k entries of the sequence. If the distribution of nucleotides in each pair of the single-nucleotide classes *week* (A-T) and *strong* (G-T) were balanced, the *nucleotide imbalance* would be close to zero along the sequence, which is not the case for prokaryotes [5].

The *unwrapped phase* is defined as the phase of the elements in the sequence, corrected by adding or subtracting a multiple of 2π (*i.e.*, $2m\pi$, $m \in \boldsymbol{Z}$, $\boldsymbol{Z}$ – the set of integers), in such a way

that the absolute value of the difference of phase between any two successive entries of the sequence becomes smaller or equal to π:

$$\theta_u[0] = \arg(\mathcal{C}\{Nu[0]\}),$$
$$\theta_u[k] = \arg(\mathcal{C}\{Nu[k]\}) + 2m\pi,\ m \in Z,\ k = 1,..., N-1, \text{ so that } \left|\theta_u[k] - \theta_u[k-1]\right| \le \pi. \quad (17)$$

The inequality $|\theta_u[k]- \theta_u[k-1]| \le \pi$ gives two solutions whenever $\arg(\mathcal{C}\{Nu[k]\})$ and $\arg(\mathcal{C}\{Nu[k-1]\})$ differ in absolute value exactly with π. For the complex representation in figure 1 and the arguments (10), this happens for AC, CA, GT, and TG. The standard MATLAB® *unwrap* function returns $\theta_u[k]= \theta_u[k-1]+\pi$, if $\arg(\mathcal{C}\{Nu[k]\}) > \arg(\mathcal{C}\{Nu[k-1]\})$, and $\theta_u[k]= \theta_u[k-1]-\pi$, in the opposite case. This is not convenient for the analysis of nucleotide sequences, where diametrically opposed pairs of nucleotides (such as AC and CA) should be equivalent in what concerns the phase difference between the complex representations of their components. The two solutions must be considered together and equally valid, so that unwrapped phase should vary equiprobably with π and $-\pi$, and the net results should be zero.

As a consequence, we classified the 16 di-nucleotides in only three classes:
- *neutral*, comprise both the di-nucleotides that have the complex representations of their components superposed (AA, CC, GG, TT), and those with the components diametrically opposed with respect to the origin (AC, CA, CG, GC), as shown in figure 2a;
- *positive*, for which the complex representations of the components are rotated in the trigonometric direction with respect to each other (AG, GC, CT, TA), figure 2b;
- *negative*, for which the complex representations of the components are rotated clock-wise with respect to each other (AT, TC, CG, GA), figure 2c.

For neutral di-nucleotides the unwrapped phase remains the same ($\Delta\theta_u[k] = 0$), for positive di-nucleotides it increases with $\Delta\theta_u[k] = +\pi/2$, and for the negative di-nucleotides it decreases with $\Delta\theta_u[k] = -\pi/2$.

Using (10) and (17), the unwrapped phase results:

$$\theta_u[k]= \theta_u[0]+\sum_{h=1}^{k}\Delta\theta_u[h]=\theta_u[0]+\frac{\pi}{2}(n_+[k]-n_-[k])=\theta_u[0]+\frac{\pi}{2}P[k],\quad k\in\{1,..,N-1\}, \quad (18)$$

where $n_+[k]$ is the number of positive di-nucleotides (AG, GC, CT, TA), $n_-[k]$ is the number of negative di-nucleotides (AT, TC, CG, GA) occurring among the first k entries of the sequence.

$P[k]$ is the *di-nucleotide imbalance*, a signature of the distribution of di-nucleotides (pairs of nucleotides) in the sequence, given by:

$$P[k]=n_+[k]-n_-[k],\quad k\in\{1,..,N-1\}. \quad (19)$$

In all practical cases, $\theta_u[0]$ is negligible.

As they have a direct statistical significance and are expressed by integer numbers, it is convenient to use the *nucleotide imbalance* (N) and the *di-nucleotide imbalance* (P) in the genomic signal analysis, instead of the *cumulated phase* (θ_c) and the *unwrapped phase* (θ_u), respectively.

6 Conclusion

The *Nucleotide Genomic Signal* (NuGS) methodology that we have developed and used [4, 5, 6] is based on the conversion of symbolic nucleotide sequences into numeric genomic signals. The representation we adopted is *unbiased*, *i.e.*, it is adequate for a large variety of problems

related to DNA analysis. To achieve such a versatility, the representation is not using the *cardinality* of numbers – their capacity to express and handle quantities, using instead their *ordinality* – the capacity to orderly label and classify objects, to handle the order of objects.

The large scale analysis of genomic sequences reveals not only ostensive features of extant DNA sequences, at the scale of entire chromosomes or genomes, but also ancestral features, which existed in DNA sequences and disappeared during evolution, under the pressure of species separation.

The local analysis of nucleotide sequences is important for the study of gene dynamics [8], especially for tracking the development of pathogen resistance to treatment. Such results can help fast diagnosis and early assessment of drug efficiency, allowing a systematic use of the advances in molecular medicine in support clinical decisions [6, 9, 10].

Genome regularities also allow to *predict* the nucleotides in a DNA sequence, using a methodology similar to time series prediction, and to estimate the cell self repair potential in processes such as replication, transcription or crossover.

The striking regularities revealed with the NuGS approach correspond to surprising symmetries in the distribution of nucleotides and pairs of nucleotides along DNA sequences in archaea, bacteria and eukarya. As a consequence, a genome appears to be – from the structural point of view – more than a *plain text,* as it also satisfies regularities evoking *rhythm* and *rhyme* in poems.

References

[1] http://www.ncbi.nlm.nih.gov/Taxonomy/Utils/wprintgc.cgi

[2] R. Durbin, S. Eddy, A. Krogh, and G.Mitchison, *Biological Sequence Analysis. ProbabilisticModels of Proteins and Nucleic Acids*, University Press, Cambridge, UK, 1998.

[3] I. Cosic, Macromolecular bioactivity: Is it Resonant Interaction between Molecules? - Theory and Applications, *IEEE Trans. on BME,* 41, pp. 1101-1114, 1994.

[4] P. D. Cristea. Conversion of Nitrogenous Base Sequences into Genomic Signals. *Journal of Cellular and Molecular Medicine* **6**(2) 279–303, 2002.

[5] P. D. Cristea. Representation and analysis of DNA sequences. In: E. Daugherty, I. Shmulevich, J. Chen, and Z. J. Wang (eds.), *Genomic Signal Processing and Statistics*, Eurasip Book Series on Signal Processing and Communications, Hindawi Publ. Corp., 2005, pp. 15–65.

[6] P. D. Cristea, Rodica Tuduce, J. Cornelis, R. Deklerck, I. Nastac, M. Andrei, Signal Representation and Processing of Nucleotide Sequences, *Proc. of the 7th IEEE Intl. Conf. on Bioinformatics and Bioengineering*, Harvard Medical School, Boston, USA (2007) 1214-1219.

[7] J. A. Berger, S. K. Mitra, and J. Astola, Power spectrum analysis for DNA sequences, *Proc. of the 7th Intl. Symp. on Signal Processing and its Applications*, 2, pp. 29-32, 2003.

[8] P. D. Cristea, Building Phylogenetic Trees by Using Gene nucleotide Genomic Signals, *34th Annual International IEEE EMBS Conference*, August 28 - September 1, 2012, Hilton, San Diego, California, USA.

[9] S. T. Cole, R. Brosch, J. Parkhill, et al. Deciphering the biology of Mycobacterium tuberculosis from the complete genome sequence. *Nature,* **393**(6685), pp. 537-544, 1998.

[10] A. Telenti *et al.*, Detection of rifampin-resistance mutations in Micobacterium tuberculosis, *Lancet*, **341**, pp. 647-650, 1993.

Dual tasking: gait and tremor in Parkinson's disease – acquisition, processing and clustering

Sorin POHOAȚĂ, Oana GEMAN, Adrian GRAUR
Ştefan cel Mare University of Suceava, Universității 13, RO-720229, Suceava, Romania
sorinp@eed.usv.ro, geman@eed.usv.ro, adrian.graur@usv.ro

Abstract. A major area of bioinformatics involves analysis and processing of large databases, in order to extract new information useful in the medical field, where making a medical diagnosis is laborious and very important. The Parkinson's disease (PD) is the most frequent neurologic illnesses, and is associated with tremor symptoms, and postural instability. The time series specific to tremor and gait signals in PD were firstly acquired using Xbox™ and Wii™ tools and analyzed later using tools derived from linear and chaotic analysis. The obtained data were classified using K-means clustering and other Data Mining algorithms. This paper emphasizes the importance of non-linear dynamics specific parameters in Parkinson gait and tremor analysis. By analyzing gait and tremor for patients with PD, this paper brings an insight over the most important information used for PD Screening Expert Systems.

1 Introduction

Bioinformatics is a field of science that involves biology, computer science and information technology. The ultimate goal of this science is to enable the discovery of new knowledge in medicine, including the development of new algorithms and statistics which allow the extraction from a large number of data of those elements that have common features and development and implementation of tools that enable of an efficient access and manipulation of different types of biomedical information.

Any success in knowledge discovery data depends on the ability to analyze various classes of specific data and to apply the appropriate methods for extraction of the main features. In this context, the analysis of data dynamics (nonlinear dynamics) raises problems in using specific methodology, hence resulting in the need for finding new work methodologies. There is insufficient data in the literature, that describes the methodology of obtaining new meta-knowledge specific to nonlinear dynamic processes, such as biomedical signals (tremor, speech and gait).

Parkinson's disease is a complex neurologic disorder, second in line after Alzheimer, characterized by symptoms including tremor, rigidity and bradykinesia. In Europe there were reported about 1.2 million Parkinson patients, estimated range between 4 and 6.5 million people worldwide and about 1% of older adults [1]. In Romania there are over 72.000 PD patients and the Romanian government spends over 1 billion Euros every year on medication [1]. The lack of a good clinical test (inexistence of biomarkers for PD diagnosis), combined with the patient's reticence to attend a physician determines late correct diagnosis. "Tremor is the first symptom that people with Parkinson's disease notice. The typical Parkinson's gait develops over time as a result of the features of Parkinson's disease such as *bradykinesia* (slowness of movement and difficulty with walking or gait disturbance), *postural instability* (balance), and *rigidity* (increased tone). The distinctive gait of a person with Parkinson's disease comprises of features such as stooped posture, slowness to start walking, short shuffling steps and a tendency to run with reduced arm swing" [2]. The aim of this paper is to find an instrument for PD screening, using gait and tremor signals.

Currently, there are insufficient evidences in the literature about the application of dynamical time series analysis for tremor evaluation on one hand and evaluation of the changes in brain rhythms in connection with the body movement impairment on the other hand. This vital information may be combined with the meta-knowledge system designed for archiving clinical and physiological inductions and other information about tremor and the prescribed trajectory of hand (or leg) movement to be used for Parkinson's disease screening. Our contribution, therefore, has major impact as currently there is no clinically approved automatic system for monitoring Parkinson's disease patients.

2 Gait and tremor – database structure

The Parkinson's disease manifests itself very differently from one individual to another, sometimes taking several years to notice a significant deterioration of daily activities. Currently, there is no screening test for early detection of Parkinson's disease. Symptoms become increasingly visible as the disease progresses. An early sign that may indicate (without binding) Parkinson's disease is invisible hand tremor. Developing new methods in order to extract new features that can help obtaining an early diagnostic of Parkinson tremor or other neurological disease (Essential tremor, Cerebellar tremor, Psychogenic tremor, Wilson's disease) is a challenge [3].

In a recent research conducted by the authors of this paper, the physiological information and the time series parameters measured from tremor and gait have been combined in developing an automatic diagnostic system for Parkinson's monitoring. We demonstrate that nonlinear dynamics parameters of PD gait signals can be used on knowledge discovery domain. A disturbed gait is a common debilitating symptom; patients with severe gait disturbances are prone to fall and may lose their functional independence [4]-[6].

Our database contains gait measures from 20 patients with PD and 40 health controls. The database includes the vertical ground reaction force records of subjects as they walked at their usual pace. We use a Xbox™ 360 250Gb with KINECT™ Sensor, system which includes a advanced video camera to analyse the position and movement of the body with 30 frames per second and transfers the motions of the subject from the process of examinating the patient. Also, we studied the stride-to-stride dynamics, the variability of these time series and nonlinear dynamic parameters, using the methodologies described in [7], [8]. Grasp, move, and release trajectory is another gait signal to be processed. The dynamics of the gait movement will be estimated using the trends in chaos measurement and included for further analysis and data fusion.

The data used in this paper are recorded using a box including accelerometers (such as those in a Wii™), pressure sensors, and inevitably a microcontroller which runs the data acquisition, analogue to digital conversion, and transmitting the data through a Bluetooth wireless communication system.

In this study, 20 PD (Parkinson's disease tremor), and 40 NT (Normal tremor) subjects were analyzed. All patients are suffering moderate to severe postural tremor. This postural tremor cannot be differentiated on clinical features (frequency, amplitude).

The Wii™ Remoteknown as the Wiimote™, is the primary controller for Nintendo's Wii™ console [9]. A main feature of the Wii™ Remote is its motion sensing capability, which allows the user to interact with and manipulate items on screen via gesture recognition and pointing through the use of accelerometer and optical sensor technology [10], [11]. We chose to use a computer game device, the Nintendo, as a simple wireless accelerometer. We consider that Wii™ Remote Nintendo may be an attractive tool to be used as an accelerometer for tremor

monitoring by physicians and laboratory technicians. The Wii™ Remote contains an accelerometer that has a range of ±3 G, which is sufficient for tremor recording [12], [13].

Nintendo has three-axes: *x* - lateral, *y* - anteroposterior, and *z* - vertical. The device records both acceleration induced by hand movement and by the gravitational force. If the controller is rotated, the gravity accelerometer affects the values on the *x*, *y*, and *z* axes [9].

Using a Wii™ Remote this system is capable to analyze frequency and to estimate the amplitude of tremor between 3-15 Hz (NT tremor is between 5-12 Hz, and PD tremor is between 4-6 Hz). The Wii™ Remote and PC are connected by Bluetooth - Human Interface Device Profile. The tremor analysis program was developed using Visual C 2010 Professional. The acceleration sampling period was set at 10 ms in the Nintendo [13].

In Fig. 1 are presented the two time series for normal tremor and PD tremor, for the case *x* (lateral) = 0, *y* (anteroposterior) = 0, and *z* (vertical) =1 (equilibrium state).

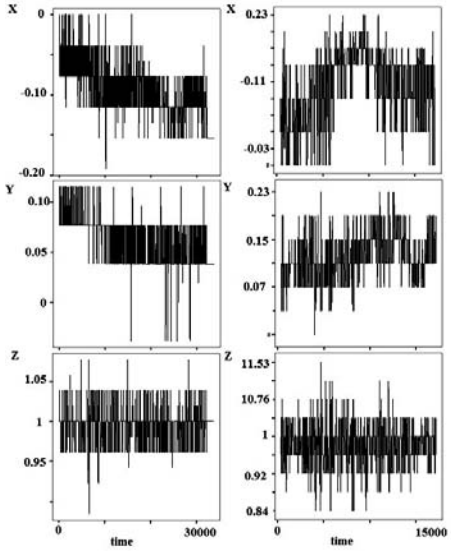

Figure 1: Time series for NT (first column) and PD tremor (second column), for the equilibrium state.

The accelerometer built into Wii™ Remote (Nintendo) measures gravitational and non-gravitational acceleration and the results of this paper suggest that Nintendo will be useful for measurement and analysis of tremor using the methodologies described in [10], [11].

3 Data processing

For the linear and nonlinear analysis of tremor signals, we used several software packages such as CDA (Chaos Data Analyzer Programs) [14], NLyzer (Nonlinear Analysis in Real Time) [15], TISEAN (Nonlinear Time Series Analysis) [16].

The linear signal analysis is performed using mostly Fourier analysis. For each time series (3500 samples) we picked up the analysis parameters as follows (see Fig. 2): the auto-correlation function – ACF; the power spectrum – FFT; statistical moments (skewness, average value, standard deviation); Fast Mutual Information; spectral density; "embedding" (the constant delay time, the embedding dimension 2); conditional entropy.

We used CDA (Chaos Data Analyzer Programs) for nonlinear signal analysis. With this software solution the phase diagram, the probability distribution, the tremor signal power spectrum, the dominant frequencies, the maximal Lyapunov exponent, the correlation

dimension, the capacity dimension, the correlation function and the Poincaré sections can be analyzed [17]-[120]. The main nonlinear dynamic determinant is the Lyapunov exponent that must be positive for a chaotic process. Using the CDA software solution on the gait signals of our database, we found that the Lyapunov exponent value varies between 0.05 and 0.92, depending on the analyzed signal. We used NLyzer, Nonlinear Analysis in Real Time software solution as well, for identifying the nonlinear specific elements [21]-[23]. Various values for the fractal dimension and various shapes for the auto-correlation function or attractors were obtained. The Lyapunov exponent values vary between 0.05 and 0.92 ("normal" gait) and for the Parkinson patients the variation is between 0.01 and 0.04.

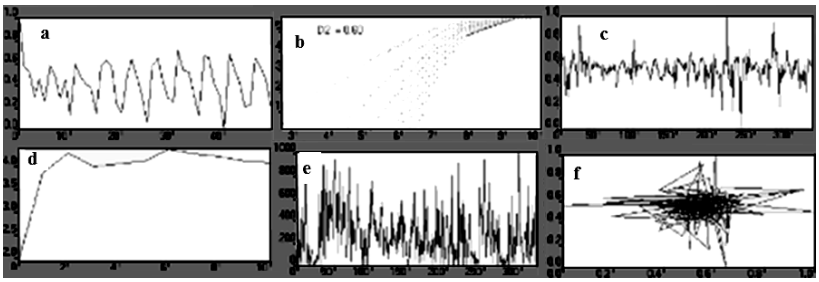

Figure 2: The nonlinear analysis for a PD gait time series - fast mutual information (a), the correlation dimension (b), the normalized gait time series (c), the capacity dimension (d), the gait time series (e) and the time series “strange" attractor (f).

In order to reduce the representation parameter numbers and keeping the essential information, we used numerical parameters for analysis.

4 Data Mining Tools

For this phase of the work we used Weka, a free collection of learning algorithms for Data Mining. We used tools for preprocessing, using data classification, regression, association rules, and visualization [24]. Weka is an open source under the GNU General Public License. The best results were obtained using a SVM (Support Vector Machine) classifier and an Artificial Neural Network ANN. For example we have chosen only the data from Parkinsonian tremor signal analysis.

Figure 3 illustrates Parkinsonian tremor - A class, and normal tremor - B class. The points x in the feature space are mapped into the hyperplan defined by the relation: $\sum_i \alpha_i K(x_i, x) = const$.

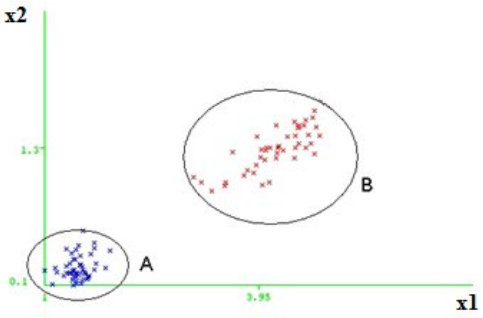

Figure 3: Weka Classification for A – Parkinsonian tremor and for B – normal tremor using SVM (Support Vector Machine) (figure capture).

5 Conclusion

We argue that nonlinear dynamic parameters of Parkinsonian gait and tremor have certain peculiarities and can be used in knowledge-discovery [21]-[23]. These data and new knowledge will be integrated in a Knowledge-based System aimed to screening Parkinson's disease.
Finally, the dynamics of the gait movement or tremor will be estimated using the trends in chaos measurement and included for further analysis and data fusion.

The data used in this task are recorded using a box including accelerometers (such as those in a Wii™), pressure sensors, and inevitably a microcontroller which runs the data acquisition, analog to digital conversion, and transmitting the data through a Bluetooth wireless communication system. Nonlinear parameters can provide essential information in the differential diagnosis, in comparison with classical linear parameters. They often distinguish between cyclic (also called "ordered") and chaotic systems or time series [24], [25].

Advanced signal processing methods involved in data fusion and constrained optimization may be used in combining physiological information within the algorithms and mathematical expressions. Patient examination can be done using advanced video systems, observing patient through surprised movements in the stored images.

In analysis of Parkinson's disease there have been advances in clinical examinations and description of the disease symptoms. To enable handling these so called verbal information the clinical observations, impressions, and diagnosis of the disease have to be archived, analyzed, and mathematically described. Knowledge-based systems plus a fuzzy decision maker is a good example for such systems. Using a rule-based system, the verbal inductions are mapped to numerical data by exploiting a set of rules. The achieved data will then be used as constraints to our fusion learning algorithms.

Acknowledgments - This paper was supported by the project "Progress and development through post-doctoral research and innovation in engineering and applied sciences – PRiDE – Contract no. POSDRU/89/1.5/S/57083", project co-funded from European Social Fund through Sectorial Operational Program Human Resources 2007-2013.

We extend our sincere gratitude to Ph.D Horia-Nicolai TEODORESCU (Gheorghe Asachi Technical University of Iaşi) and Dr. Radu VATAVU (Ştefan cel Mare University of Suceava, Romania) for their technological support to this paper. We are also very grateful to Dr. Radu VASILCU and the subjects with PD who took part in this research.

References

[1] National Parkinson Foundation, http://www.parkinson.org (15.11.2012).
[2] http://www.physionet.org/physiobank/database/gaitpdb/ (15.11.2012).
[3] S. Frenkel-Toledo, N. Giladi, C. Peretz, T. Herman, L. Gruendlinger, J.M. Hausdorff. Treadmill walking as a pacemaker to improve gait rhythm and stability in Parkinson's disease, *Movement Disorders*, 20(9) (2005), 1109-1114.
[4] J.M. Hausdorff, J. Lowenthal, T. Herman, L. Gruendlinger, C. Peretz, N. Giladi. Rhythmic auditory stimulation modulates gait variability in Parkinson's disease, *Eur. J Neuroscience*; 26 (2007), 2369-2375.
[5] G. Yogev, N. Giladi, C. Peretz, S. Springer, E.S. Simon, J.M. Hausdorff. Dual tasking, gait rhythmicity, and Parkinson's disease: Which aspects of gait are attention demanding?, *Eur J Neuroscience*, 22 (2007), 1248-1256.
[6] S.A. Makhortykh, R.A. Semechkin. Study of magnetic field of the brain in Parkinson's disease, *Bulletin of Experimental Biology and Medicine*, vol. 147, no. 3 (2009), 375-377.

[7] Hăgan, M., Teodorescu, H-N., Sîrbu, A., Data Processing for Posturography and Gait Analysis, *The 3rd International Symposium on Electrical and Electronics Engineering*, (2010), pp. 267-272.
[8] http://www.physionet.org/physiobank/database/gaitndd/ (15.11.2012).
[9] http://www.nintendo.co.uk/NOE/en_GB/systems/technical_details_1072.html, (15.11.2012).
[10] N. Mamorita, T. Iizuka, A. Takeuchi, M. Shirataka, N. Ikeda. Development a System for Measurement and Analysis of Tremor Using a Three-axis Accelerometer, *Methods Inf. Med*., No. 48, (2009) pp. 589-594.
[11] R.A. Clark, A.L. Bryant, Y. Pua, P. McCrory, K. Bennell, M. Hunt. Validity and reliability of Nintendo Wii Balance Board for assessment of standing balance, *Gait & Posture*, No. 31, (2010) pp. 307-310.
[12] O. Geman, Data Processing for Parkinson's Disease Tremor, Speech and Gait Signal Analysis, *Proceedings IEEE International Conference E-Health and Bioengineering Conference*, (2011), ISBN 978-606-544-078-4.
[13] O. Geman. Data Processing for Parkinson's Disease Tremor, Speech and Gait Signal Analysis, *IEEE International Conference - 2011 E-Health and Bioengineering Conference*, EHB, ISBN 978-606-544-078-4, Iasi, Romania, 24-26 November, (2011).
[14] Chaos Data Analyzer, http://sprott.physics.wisc.edu/cda.htm (15.11.2012).
[15] NLyzer (Nonlinear Analysis in Real Time), http://www.iap.tu-darmstadt.de/NLyzer/ (15.11.2012).
[16] TISEAN (Nonlinear Time Series Analysis), http://www.mpipks-dresden.mpg.de/~tisean/ (15.11.2012)
[17] H.N. Teodorescu, A. Kandel. Nonlinear Analysis of Tremor and Applications, *JJME Japanese Journal of Medical Electronics and Biological Engineering*, vol. 13 (5) (1999), 11-19.
[18] O. Geman, C. Zamfir. Nonlinear Dynamics Parameters and K-means Clustering Algorithm Used in DBS Treatments Analysis Results, Advances in Intelligent Systems and Technologies, *Proceedings ECIT2010 - 6th European Conference on Intelligent Systems and Technologies*, (2010).
[19] H.N.L. Teodorescu, M. Chelaru, A. Kandel A., et al. Fuzzy methods in tremor assessment, prediction, and rehabilitation, *Artificial Intelligence in Medicine*, vol. 21 issue: 1-3, (2001) pp. 107-130, DOI: 10.1016/S0933-3657(00)00076-2.
[20] M. Titcombe, L. Glass, D. Guehl, A. Beuter. Dynamics of Parkinsonian tremor during deep brain stimulation, *Chaos*, vol. 11, no. 4, (2001).
[21] C. Zamfir, O. Geman (Voroneanu). An Adaptive System to Simulate the Parkinson Tremor, *Proceedings AMSE 2004 International Conference on Modelling and Simulation*, University of Lyon, France, 5-7 July, (2004).
[22] O. Geman (Voroneanu), H.N. Teodorescu, C. Zamfir. Nonlinear Analysis and Selection of Relevant Parameters in Assessing the Treatment Results of Reducing Tremor, using DBS Procedure, *Proceedings International Joint Conferences on Neural Networks IJCNN'2004*, Budapest, Hungary, 25-29 July, (2004).
[23] O. Geman, C. Zamfir. Nonlinear Dynamics Parameters and K-Means Clustering Algorithm Used in DBS Treatments Analysis Results, *6th European Conference on Intelligent Systems and Technologies*, Iasi, Romania, 7-9 October, (2010).
[24] http://www.cs.waikato.ac.nz/ml/weka/ (15.11.2012).
[25] S. Sanei, T. Lee, and V. Abolghasemi. A new adaptive line enhancer based on singular spectrum analysis, *IEEE Trans. on Biomedical Engineering*, vol. 59, no. 2, (2012) pp. 428-434.
[26] S. Sanei. *Adaptive Processing of Brain Signals*, John Wiley & Sons, (to be published in 2012).

Control of a Single Phase SRM of Special Topology using Two Power Supplies

Nicolae-Daniel IRIMIA, Alecsandru SIMION, Leonard LIVADARU, Ovidiu DABIJA, Sorin VLĂSCEANU

"Gheorghe Asachi" Technical University of Iasi, Faculty of Electrical Engineering, 700050, Iaşi, Romania; sckummi@yahoo.com

Abstract. This paper presents the control of a single phase special topology SRM (Switched Reluctance Machine). The Soft Switching control strategy was applied during each energizing cycle of the stator phase. The control scheme also includes a phase current control loop and a rotor angular velocity control loop, both of them using a Hysteresis type regulator. For supplying the stator phase, two DC power sources of different voltage amplitudes were utilized. The first voltage source is about 230 V, while the second one is about 1150 V. In order to connect both power sources into the circuit, a static power converter of special structure was developed. The simulation results using Matlab/Simulink software package are presented at the end of the paper.

1 Introduction

This paper presents the control of a single-phase special topology SRM using two power sources for energizing the stator coil of the machine. A special control structure and a special topology static power converter were designed for the interconnection of that two power sources to the terminals of the stator phase winding and thus energizing the phase by the predetermined control logic. The simulation results were obtained by using the Matlab/Simulink software package, for different working regimes of the SRM.

2 The Parameters of the Single Phase Switched Reluctance Motor

Figure 1 presents the schematic view of the single-phase, single-pole, axial magnetic field SRM.

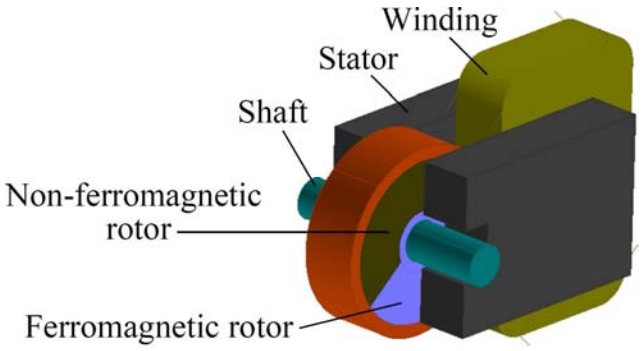

Figure 1: The schematic view of the single-phase switched reluctance machine.

When the voltage is applied to the stator phase, the motor creates torque in the direction of increasing inductance [1]. The motor is driven by a sequence of current pulses applied in the stator phase [1]. The current pulses must be applied to the respective phase in an exact rotor position to the energized phase [1]. The torque changes direction at the aligned position [2].

The switched reluctance machine used in this paper is a single phase special topology motor, being provided with only one stator pole and axial magnetic flux.

The parameters of the special topology switched reluctance machine are presented in Table 1.

Table 1: Single-phase switched reluctance motor parameters.

Stator resistance	0.6 Ω
Inertia	0.003 kg·m^2
Friction	0.0005 N·m·s
Unaligned inductance at 1A	0.0414 H
Aligned inductance at 1A	0.0892 H
Unaligned inductance at 20A	0.0369 H
Aligned inductance at 20A	0.0531 H
Maximum current	20 A
Maximum flux linkage	1.062 V·s
Nominal voltage supply	230 V

3 Simulink Schematic Diagram for the Control of the Single-Phase Switched Reluctance Machine

The principle scheme from Simulink comprises:

- Two DC voltage sources of different amplitudes.
- A static converter provided with controllable power semiconductor components of IGBT type (Insulated Gate Bipolar Transistor) and one ultrafast discharging diode;
- A stator phase current control loop;
- A rotor angular velocity control loop;
- A rotor position sensor;
- The single-phase switched reluctance machine of special topology.

In the classical method, the winding voltage is reduced from positive DC bus voltage to zero by letting the current freewheel in the machine winding [3]. After half a resonant cycle, the voltage across the winding is changed from zero to the negative DC source voltage and maintained at that until the current is reduced to zero [3]. To apply this method, the SRM converter must be capable of applying positive, zero, and negative voltage across the machine phases [3].

In case of the control method presented in this paper, the time corresponding to the decreasing slope of the stator phase current (at the end of each energizing cycle) is further reduced (of about 5 times lower), compared to the classical situation.

The two power sources are represented by ideal DC voltage sources of different voltage amplitudes. The first power source voltage amplitude is 230 V, while the second one voltage amplitude is about 1150 V (a value which is 5 times greater than the nominal value). This voltage amplitude of 1150 V was chosen according to the limit of stator winding insulation breakdown.

At the beginning of each energizing cycle corresponding to the machine's stator phase, according to the implemented control logic, the DC voltage source with the amplitude of 230 V is connected to the terminals of the stator phase winding (through the static power converter of special topology). Once the stator phase current reaches the imposed upper limit (in this case 20.5A), the stator phase winding energizing process is interrupted until the current decreases to the minimum accepted limit (in this case 19.5 A) at which value the process restarts. During this process, the stator phase winding is short-circuited through the static power converter. Thus, the energy accumulated in the magnetic field of the stator phase is dissipated on its own electrical resistance through the discharging diode and the lower right IGBT (both from the converter structure) which is maintained in the conduction state. Thus the current ripple is significantly reduced. At the end of each of these energizing cycles, the DC voltage source with the amplitude of 1150 V is connected with reverse polarity to the terminals of the stator phase winding, forcing the current through the stator coil to decrease in a very short time.

Due to the high voltage amplitude corresponding to the second power source, whose value is 5 times greater than the output rated voltage of the first power supply, namely 1150 V compared to 230 V, the downward slope of stator phase current changes accordingly. This provides a time period for decreasing of the stator phase current of about 5 times lower, compared to the classical situation. Thus, the transfer of the energy accumulated in the magnetic field of the stator phase, at the end of each energizing cycle, back to the power supply, is about 5 times faster, also compared to the classical situation. A first advantage of this command method of the SRM is the possibility of changing the turn-off angle of the machine stator phase, as close to the corresponding position of maximum phase inductance, currently without a negative torque on the motor shaft. This negative torque generally appears due to currents in stator phase winding on the portion of the decreasing phase inductance [4].

The Simulink block diagram corresponding to the control circuit of the switched reluctance machine is presented in figure 2.

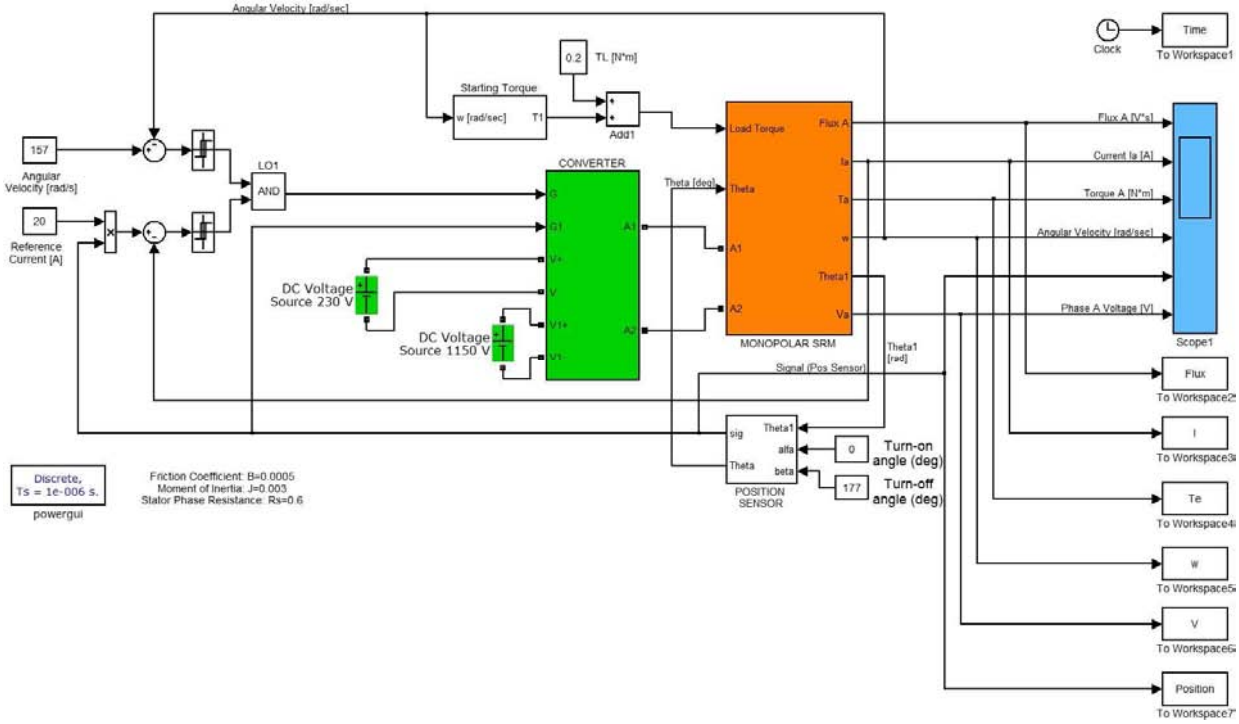

Figure 2: Simulink block diagram corresponding to the control of the single-phase switched reluctance machine.

The control circuit also includes a stator phase current regulator and a rotor angular velocity regulator, both of Hysteresis type. The reference value for the stator phase current is 20 A, being allowed a maximum variation of 0.5 A from it. Also, the reference value for the angular velocity of the rotor was established to 157 rad/s, being allowed a maximum variation of 1 rad/s to it. Thus, it was obtained a simultaneous control of both parameters. The Turn-on and Turn-off angles for energizing and respectively discharging the energy accumulated in the stator phase magnetic field are: 0 deg (unaligned position – minimum inductance value) and 180 deg (aligned position – maximum inductance value).

4 The Structure of the Static Power Converter

The static power converter has a special structure being provided with four controllable semiconductor components of IGBT type and also one ultrafast discharging diode. For improving

the current ripple during the energizing interval of the stator phase, the Soft Switching technique was also implemented. Figure 3 shows the Simulink diagram corresponding to the static power converter and also some of the related logic blocks. The stator phase winding is connected to: A1 and respectively A2 terminals shown on the graphic.

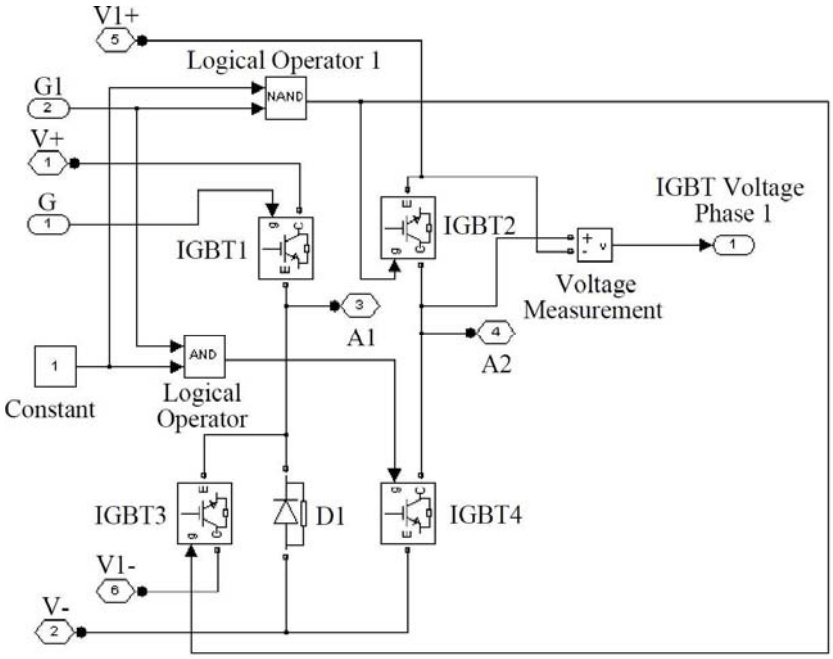

Figure 3: The static power converter topology.

The Soft Switching control technique implies that one transistor (usually the upper-left transistor of the converter) is controlled by PWM pulses, while another transistor (the lower-right transistor) is left turned-on during the entire commutation period for the respective phase. This control strategy determine a lower current ripple, compared to the case when both transistors are simultaneously controlled by PWM pulses (appropriate method corresponding to the Hard Switching control technique). Thus, the torque ripple is also reduced accordingly.

5 Simulation Results

Modelling and simulation of the control scheme corresponding to the single-phase switched reluctance machine was done using the Matlab - Simulink software package. The results of these simulations are presented as follows. Figure 4 shows the waveforms corresponding to the start-up of the single-pole SRM, in case of zero load torque. However, a torque of about 0.05 N·m is still being present due to the friction resistance. The rated phase current is about 20 A. The reference value of the rotor angular velocity is established to 157 rad/s.

Figure 5 presents a zoom-in of the waveforms corresponding to the single-phase SRM shown in figure 4. It can be observed that the waveform of the stator phase current is almost rectangular due to the control method applied. Also, the electromagnetic torque developed by the switched reluctance machine is always positive. The Soft Switching technique implemented during each energizing cycle of the stator phase can be easily visualized. As supposed, at the end of each energizing cycle, the 1150 V reverse polarity voltage was applied to the terminals of the stator phase winding, determining the rapidly decreasing of the phase current from 20 A back to zero.

Figure 6 shows the waveforms corresponding to the SRM for a load torque of 0.2 N·m.

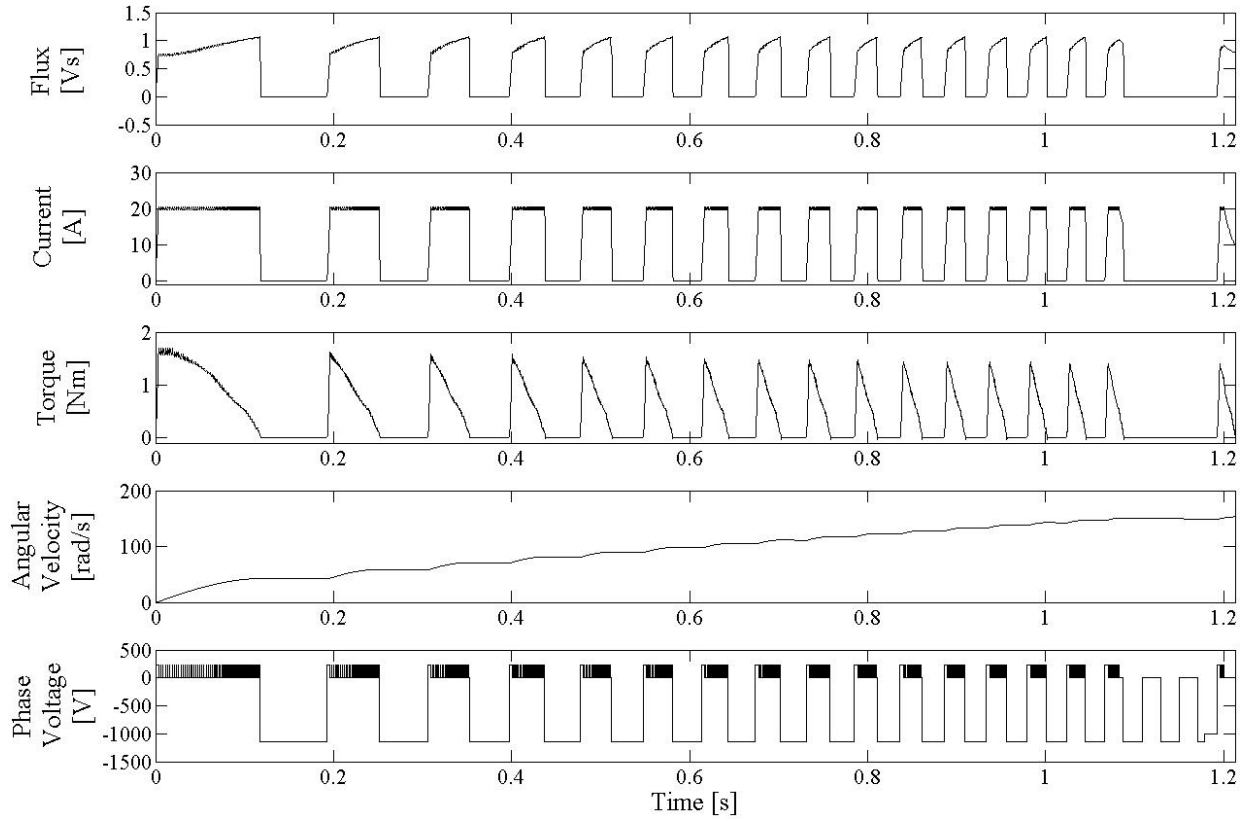

Figure 4: The waveforms corresponding to the start-up of the single-phase SRM, for zero load torque.

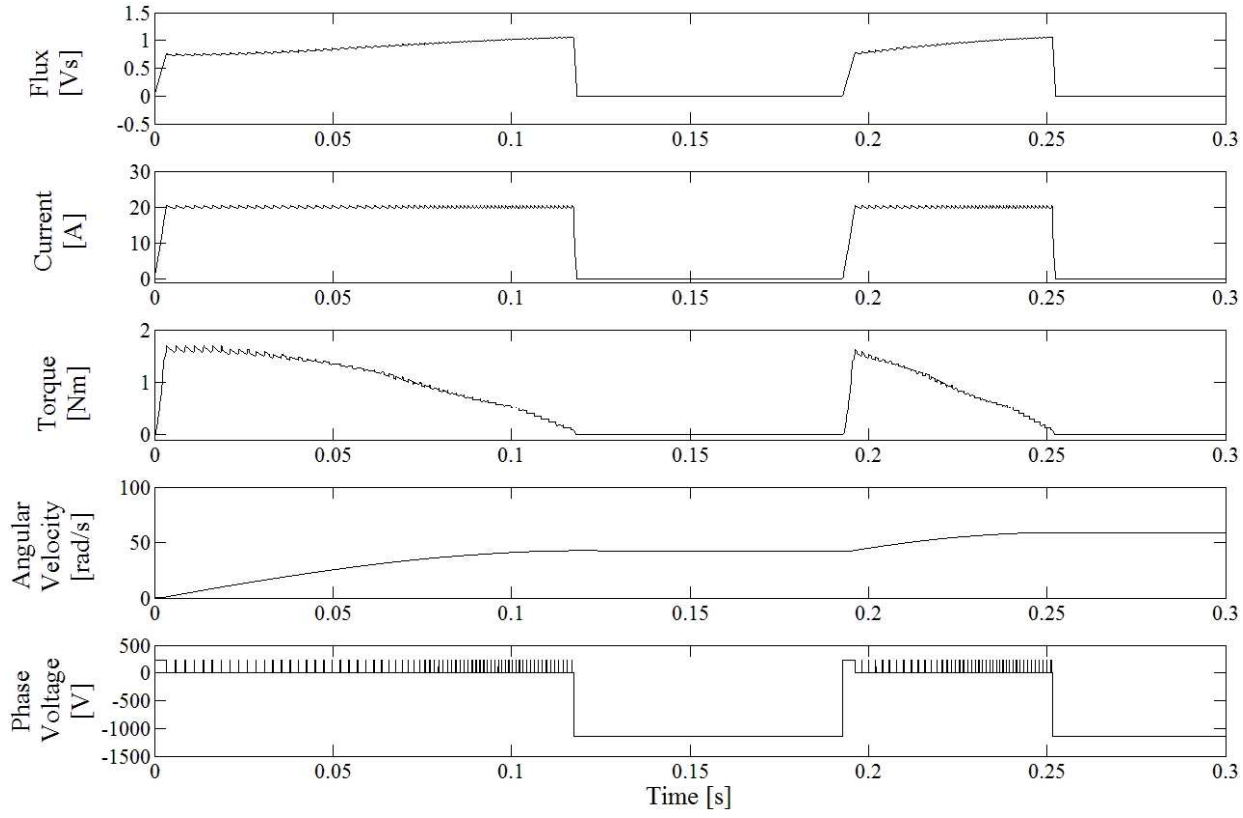

Figure 5: The zoom-in of the waveforms shown in figure 4.

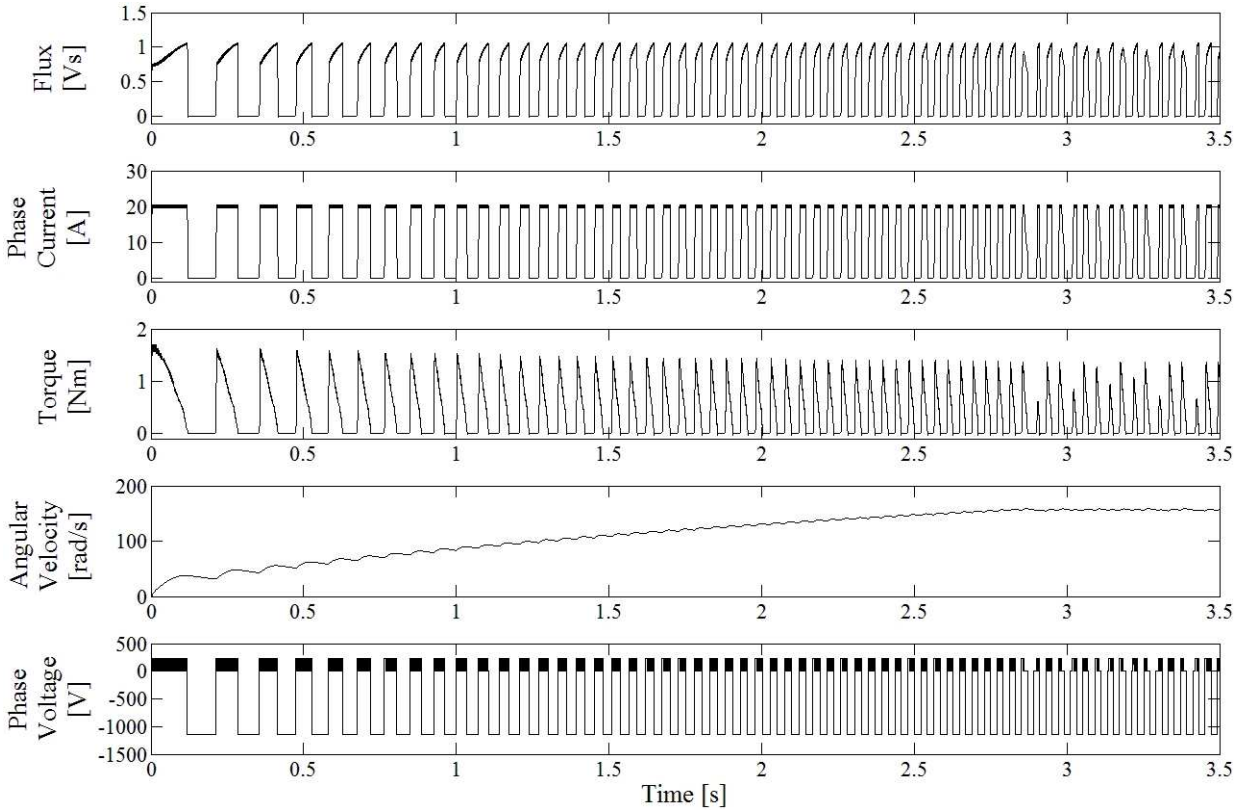

Figure 6: The waveforms at the start-up of the single-phase SRM, for a load torque of 0.2 N · m.

6 Conclusions

The control method presented in this paper involves the use of two power sources of different voltage amplitudes for energizing and also discharging the energy accumulated in the SRM stator phase, during each commutation cycle. A first advantage of this method is that the time corresponding to the decreasing slope of the stator phase current is about 5 times lower, compared to the classical situation. A second advantage is the possibility of changing the turn-off angle to a value as close to the aligned position. This will determine the increase of the positive electromagnetic torque period, for the same operating conditions of the machine. Another advantage is the cancellation of the negative torque produced by the SRM.

Acknowledgment - This paper was realised with the support of POSDRU CUANTUMDOC "DOCTORAL STUDIES FOR EUROPEAN PERFORMANCES IN RESEARCH AND INOVATION" ID79407 project funded by the European Social Found and Romanian Government.

References

[1] Freescale Semiconductor Application Note, *3-phase Switched Reluctance Motor Control with Hall Sensors using a 56f80x, 56f8100 or 56f8300 device*, AN1912 Rev. 2, 9/2005.

[2] O. Dabija et al., *Modeling and Simulation of an axial field single-pole single-phase switched reluctance motor*, OPTIM 2012, Braşov, Romania, 2012.

[3] R. Krishnan, *Switched reluctance motor drives: modeling, simulation, analysis, design, and applications*, The Bradley Department of Electrical and Computer Engineering Fellow, 2001.

[4] Irimia Nicolae-Daniel, Simion Alecsandru, Livadaru Leonard, Dabija Ovidiu, Vlăsceanu Sorin, *The Control of a 6/4 Switched Reluctance Motor by means of a DC Voltage Supply with DC High Voltage Intermediary Circuit*, EPE 2012, Iaşi, Romania, 2012.

Sinusoidal Control of a Single Phase Special Topology SRM, Without Rotor Position Sensor

Nicolae-Daniel IRIMIA, Alecsandru SIMION, Ovidiu DABIJA, Sorin VLĂSCEANU, Adrian MUNTEANU

"Gheorghe Asachi" Technical University of Iasi, Faculty of Electrical Engineering, 700050, Iaşi, Romania; sckummi@yahoo.com

Abstract. This paper presents the sinusoidal control of a single phase variable reluctance motor of special topology, without any rotor position sensor. A sinusoidal AC current source was used for the energizing of the stator phase winding, considering the cases when only positive alternations or both alternations of the supply current waveform were utilized. A specialized electrical circuit was designed in order to connect the power supply to the terminals of the stator phase winding. Simulations were performed using Matlab / Simulink software package.

1 Introduction

This paper presents the sinusoidal control of a single-phase special topology variable reluctance machine (VRM), considering the cases when only positive alternations or respectively both alternations of the supply current waveform were used to energize the stator phase of the motor. In this work are also presented: the parameters of the single-phase special construction VRM, Simulink block diagrams corresponding to the sinusoidal control of the single-pole variable reluctance machine, the results of the simulation obtained with Matlab/Simulink software package and also some conclusions.

2 The Sinusoidal Control Principle of the VRM

Figure 1(a) presents the sinusoidal control principle of a single-phase variable reluctance machine, in case of the positive currents alternations used to energize the stator coil of the motor. At the top of the figure is presented the ideal waveform of the stator phase inductance of the machine, where can be observed the two limits corresponding to the unaligned and respectively aligned positions of the rotor compare to the stator pole. In the middle of the figure are presented the waveforms of the alternating currents for zero electromagnetic torque. At the bottom of the figure are presented positive alternations of the currents corresponding to a non-zero electromagnetic torque developed by the machine. It can be seen that by using only the positive alternations of the current for energizing the stator phase of the machine, the developed torque can reach the maximum value, without any negative torque production. This is achieved due to the presence of the positive current alternation only on the portion of the positive slope of the motor inductance, for a corresponding load torque. The angular velocity of the variable reluctance machine is about 314rad/s for this situation.

In the figure 1(b) is presented the sinusoidal control principle of a single-phase VRM, in case of both alternations of the current waveform. At the top of the figure is presented the ideal inductance waveform of a single-pole VRM, while in the middle of the figure is the phase current waveform for zero electromagnetic torque and at the bottom of the figure is shown the movement of the stator current waveform to the position where the torque developed by the machine corresponds to the shaft load torque if any (and also the friction torque). The higher the value of the load torque, the more obvious is the movement of the current waveform to the position of the positive slope inductance. The reason is that the necessary electromagnetic torque developed by

the machine increases proportional with the value of the load torque which is applied to the rotor shaft. For increasing the value of the electromagnetic torque, the average of the stator phase current corresponding to the portion of positive slope inductance must increase accordingly; at the same time, the average of the phase current on the portion of the decreasing inductance must decrease so that the negative torque production to decrease accordingly.

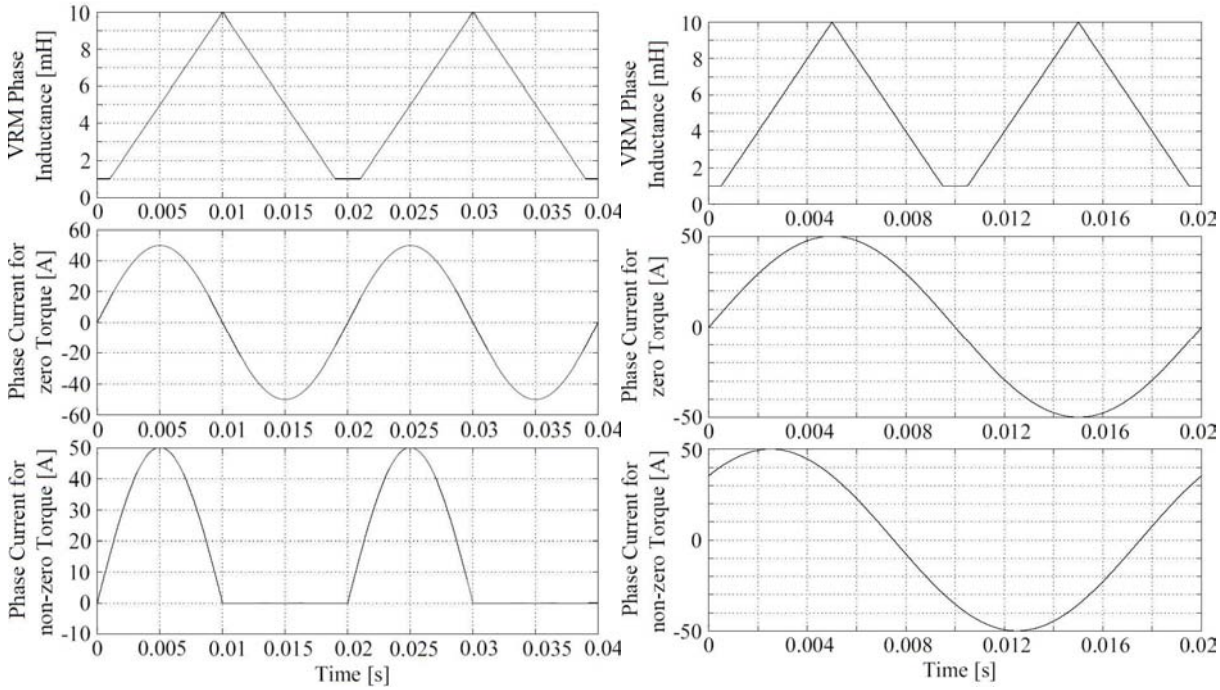

Figure 1: Sinusoidal control principle of a single-phase VRM for: (a) positive current alternations and (b) both stator current alternations.

3 The Parameters of the Single-Phase Special Construction Variable Reluctance Machine (VRM)

The variable reluctance machine used in this paper is a single phase, single pole, axial type magnetic flux, special topology motor. The parameters of this machine are presented in Table 1.

Table 1: Single-phase switched reluctance motor parameters.

Stator resistance (Ω)	0.6
Inertia (kg·m^2)	0.003
Friction (N·m·s)	0.0005
Initial speed Ω_0 (rad/s)	0.0
Initial position θ_0 (rad)	0.0
Unaligned inductance at 1A (H)	0.0414
Aligned inductance at 1A (H)	0.0892
Unaligned inductance at 20A (H)	0.0369
Aligned inductance at 20A (H)	0.0531
Maximum current (A)	20
Maximum flux linkage (V·s)	1.062
Nominal voltage supply (V)	230

4 Simulink Block Diagrams Corresponding to the Sinusoidal Control of the Single Phase VRM

Figure 2 presents the Simulink principle scheme for the sinusoidal control of the single phase VRM in case of positive alternations of the stator phase current. It is well known that a current source (the ideal AC Current Source 1 in this case) should never be let without a load connected to its terminals, because of the very high induced voltage amplitude that could appear. Thus, for the negative current waveform alternations (when the current through the stator phase winding is zero), a special circuit was developed for reducing the power losses to a minimum. This circuit is represented by the R1 and R2 resistors and also the D1 diode. In case of the positive waveform alternations, the current flows only throw the stator phase winding, by the D2 diode, thus energizing the coil.

While the voltage across the terminals of the AC current source is positive, the IGBT1 is maintained in the conduction state, short-circuiting the R3 resistor. The main role of the R3 resistor is to dissipate any remained energy accumulated in the magnetic field of the machine's stator phase, after the current through the power source changes its flow direction.

This control technique has the main advantage that is relatively simple to implement, has no need of any sensor position or many controllable power semiconductor devices. The main disadvantage is the need to initially drive the rotor to a certain speed for synchronising with the frequency of the stator phase current imposed by the power source.

The signal provided by the position sensor from the figure is used only for the scope visualization.

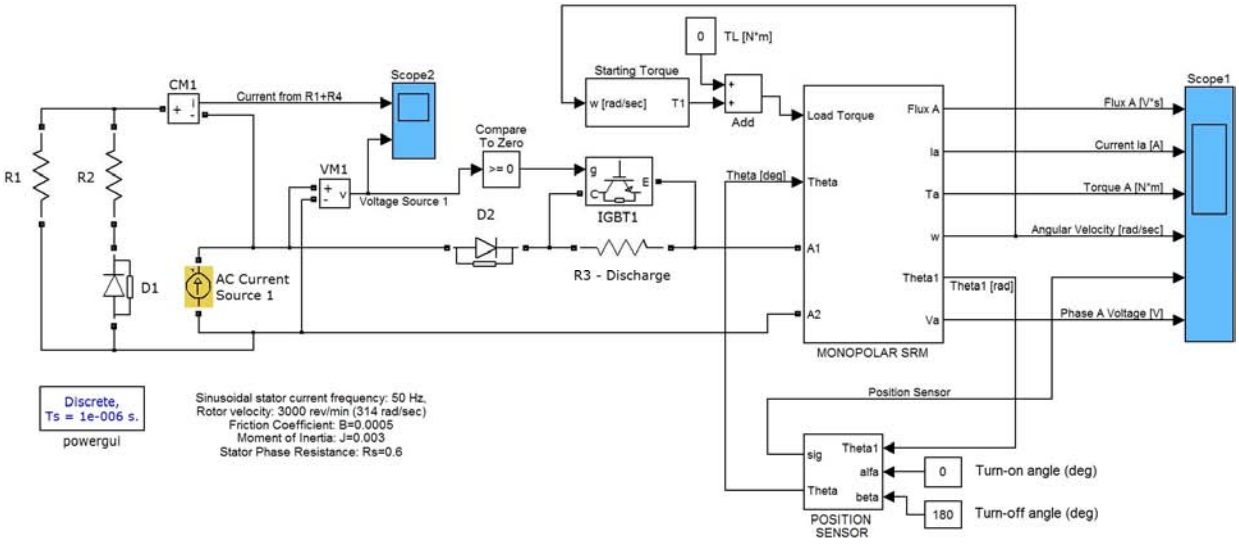

Figure 2: Simulink block diagram for the sinusoidal control of the VRM, positive current alternations.

Figure 3 presents the Simulink block diagram corresponding to the sinusoidal control of a single-pole VRM, in case of both alternations of the stator phase current. For permitting the changing of the current direction through the stator phase, a special circuit provided with four IGBTs was designed.

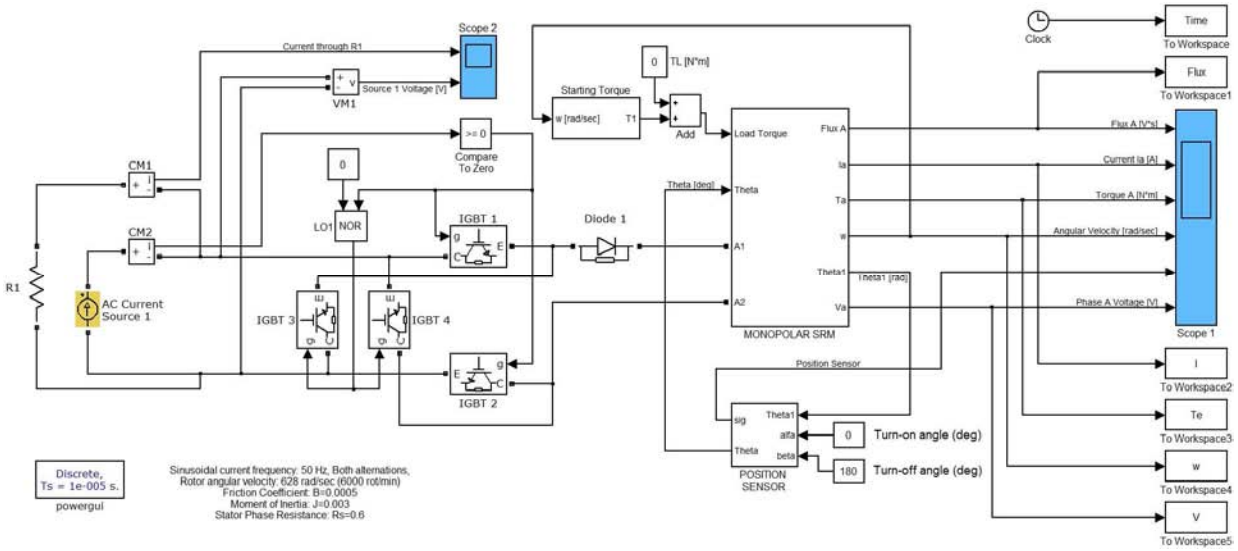

Figure 3: Simulink principle scheme for the sinusoidal control of the VRM, both current alternations.

5 Simulation Results

The results of the simulation were obtained using the Matlab/Simulink software package. Some of these results are presented as follows.

Figure 4 presents the waveforms corresponding to the start-up regime of the single-phase VRM in case of the sinusoidal control method using only positive current alternations. The value of the load torque is zero for this situation. The frequency of the stator phase current is 50 Hz and its amplitude is about 20 A. It can be observed that the angular velocity of the rotor is self-maintaining around the value of 314 rad/s (with a maximum variation of about 6 rad/s from it), corresponding to the frequency of the phase current. Also, it can be seen that only the positive alternations of the stator phase current were utilized in this situation. The average of the electromagnetic torque developed by the single-phase VRM varies around 0.157 Nm, which also represents the value of the friction torque (the load torque being zero in this case).

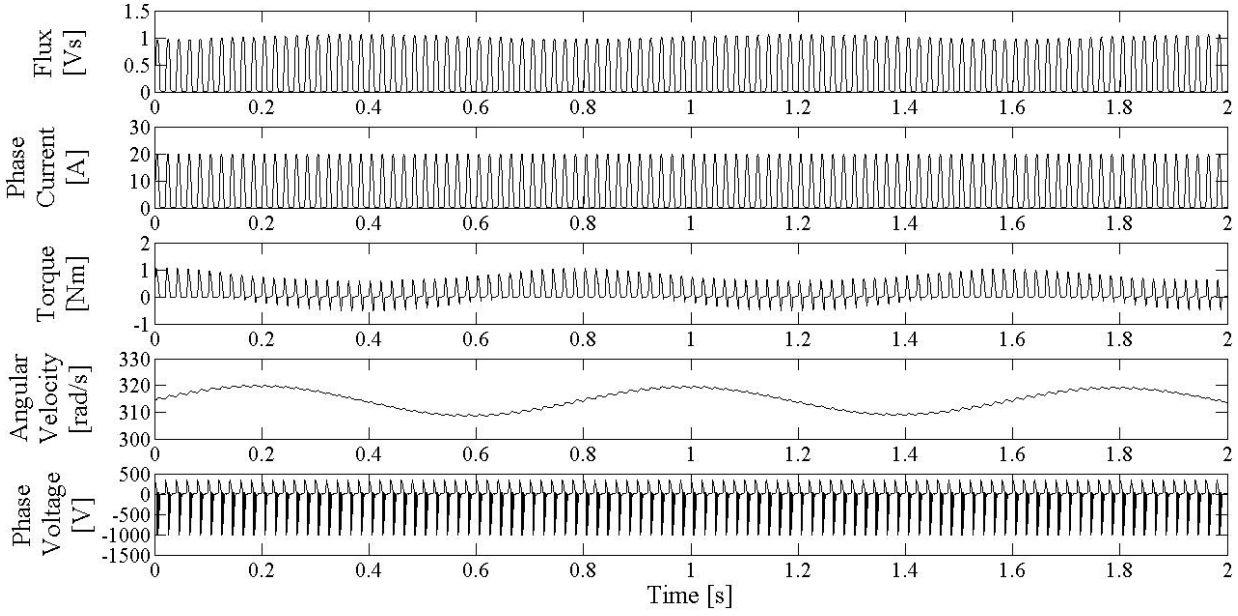

Figure 4: Waveforms of the VRM start-up process, for positive current alternations and no-load torque.

Figure 5 shows a zoom-in of the same waveforms and the same conditions presented in figure 4. It can be observed that only the positive alternations of the stator phase current waveform are used in this situation for energizing the stator coil of the machine. The negative phase voltage value appears because of the inductive character of the stator phase of the VRM.

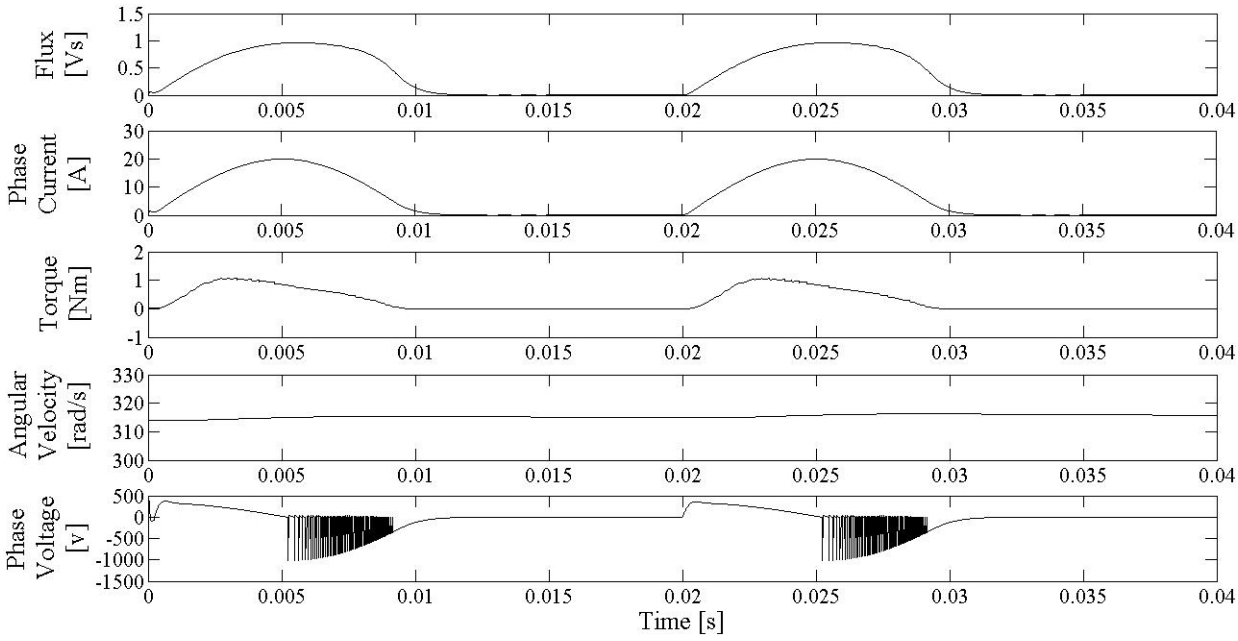

Figure 5: The zoom-in of the waveforms presented in figure 4.

In figure 6 are presented the waveforms corresponding to the start-up regime of the VRM, in case of the sinusoidal control, using only the positive alternations of the stator phase current. The load torque is 0.16 N·m. It can be seen that the angular velocity of the rotor is self-maintained around the value of 314 rad/s, with a maximum variation of about 2 rad/s to it. The average value of the electromagnetic torque developed by the VRM is about 0.317 N·m (compensating the friction torque and also the load torque).

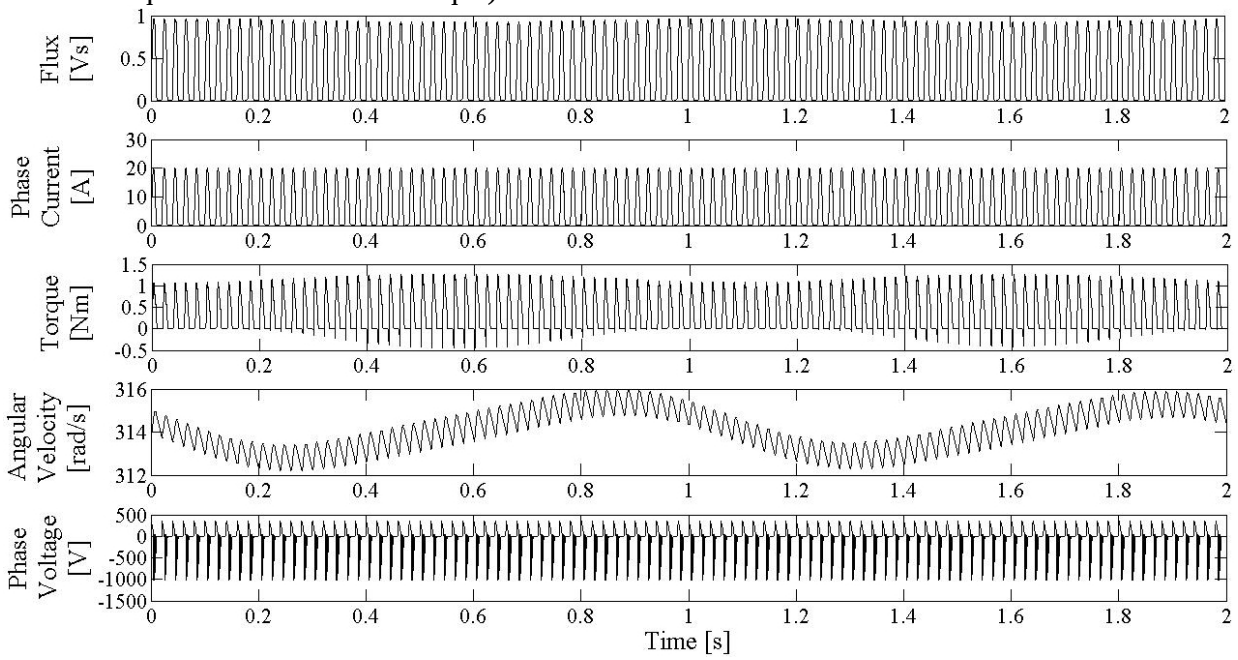

Figure 6: Waveforms of the VRM start-up process, positive current alternations, load torque: 0.16 Nm.

Figure 7 shows the waveforms corresponding to the start-up regime of the single-phase VRM in case of the sinusoidal control method using both positive and negative stator current alternations. The value of the load torque is zero for this situation. The frequency of the stator phase current is 50 Hz and its amplitude is about 20 A. The angular velocity of the rotor is self-maintaining around the value of 628 rad/s, with a maximum variation of about 2 rad/s from it.

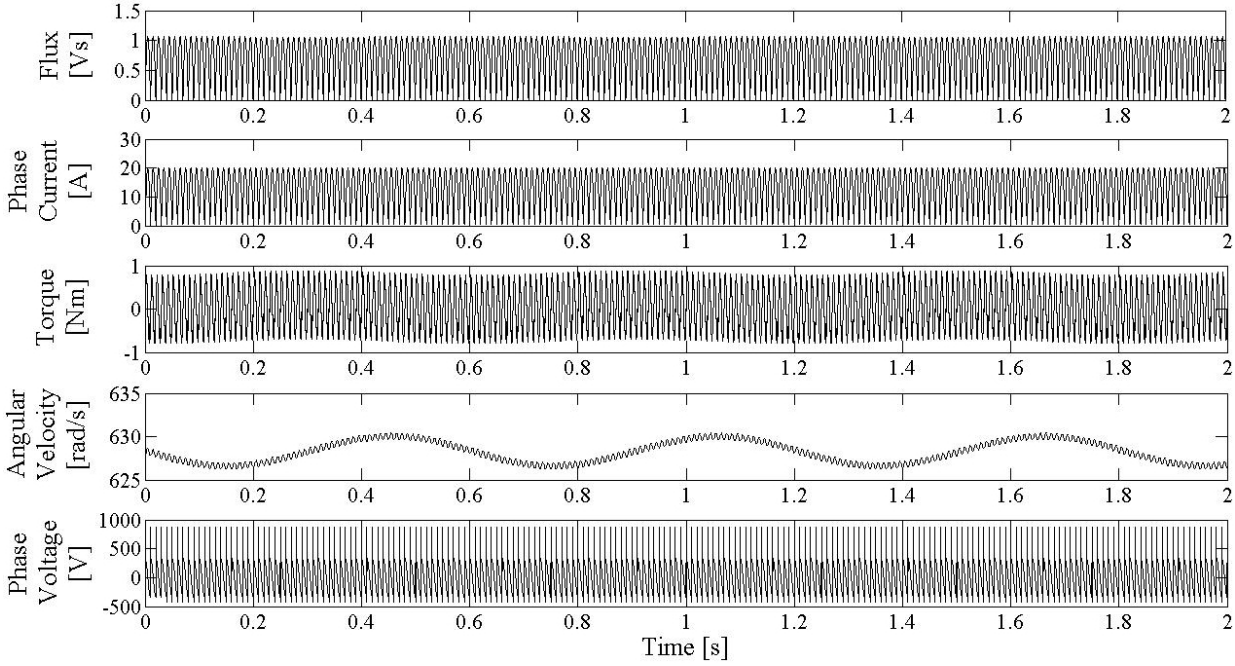

Figure 7: Waveforms of the VRM start-up regime, for both current alternations and no-load torque.

6 Conclusions

The sinusoidal control of a single-phase special topology variable reluctance machine presented in this paper, in case of positive and respectively both stator currents alternations, has the main advantage that is relatively simple to implement, has no need of any sensor position or even many controllable power semiconductor devices. The main disadvantage is represented by the need to initially drive the rotor to a certain speed for synchronising with the frequency of the stator phase current imposed by the power source.

Acknowledgment - This paper was realised with the support of POSDRU CUANTUMDOC "DOCTORAL STUDIES FOR EUROPEAN PERFORMANCES IN RESEARCH AND INOVATION" ID79407 project funded by the European Social Found and Romanian Government.

References

[1] R. Krishnan, *Switched reluctance motor drives: modeling, simulation, analysis, design, and applications*, The Bradley Department of Electrical and Computer Engineering Fellow, 2001.

[2] O. Dabija et al., *Modeling and Simulation of an axial field single-pole single-phase switched reluctance motor*, OPTIM 2012, Braşov, Romania, 2012.

[3] Freescale Semiconductor Application Note, *3-phase Switched Reluctance Motor Control with Hall Sensors using a 56f80x, 56f8100 or 56f8300 device*, AN1912 Rev. 2, 9/2005.

[4] T. J. E. Miller, *Electronic control of switched reluctance machines*, Power engineering series, 2001.

[5] Irimia Nicolae-Daniel, Simion Alecsandru, Livadaru Leonard, Dabija Ovidiu, Vlăsceanu Sorin, *Sinusoidal Control of a 6/4 Variable Reluctance Machine without Rotor Position Sensor*, OPTIM 2012, Braşov, Romania, 2012.

SOLUȚIONAREA REGIMULUI PERIODIC AL CIRCUITELOR CU ELEMENTE REZISTIVE AVÂND CARACTERISTICI LINIARIZATE PE PORȚIUNI

Lilica CORLAN
Universitatea "Politehnica" din Bucureşti, Spl. Independenţei 313, 060042, Bucureşti;
lilicamaria2004@yahoo.com

Abstract. Demodulatoarele MA sunt realizate cu diode care pot fi modelate cu rezistoare neliniare cu caracteristici liniarizate pe porțiuni. Efectuând analiza tranzitorie cu ajutorul modelelor companion, la fiecare pas de timp se rezolvă un circuit rezistiv neliniar prin metoda Katzenelson.

1 Introducere

Lucrarea are ca obiectiv circuitele care au câteva elemente rezistive cu caracteristici liniarizate pe porțiuni și în special diode.

Caracteristicile *u-i* ale diodelor pot fi bine aproximate cu două semidrepte care pleacă din 0.

Pentru evaluarea circuitelor liniare cele mai cunoscute metode de analiză în domeniul timp sunt: discretizarea în domeniul timp cu metoda Katzenelson şi, cea mai agreată, procedura Newton-Raphson, la orice pas de timp..

2 Analiza în domeniul timp

Pentru analiza în domeniul timp se înlocuiesc elementele de circuit cu memorie (bobine, condensatoare) cu elemente de circuit care nu sunt dinamice, cum sunt rezistoarele sau sursele ideale de tensiune sau de curent.

La orice pas de timp t_{k+1} se vor afla valorile pentru curenții care strabat circuitul și tensiunile la bornele elementelor de circuit la momentul respectiv de timp. Valorile curenților și tensiunilor depind de cele de la pasul de timp t_{k+1} la care se realizează calculele și de cele de la pasul anterior de timp t_k. Se consideră cunoscute valorile la pasul 0 ale tensiunilor la bornele condensatoarelor şi curenţilor prin bobine.

Iniţial se consideră relația curent-tensiune pentru un condensator:

$$i_C(t) = C\frac{du_C(t)}{dt} \tag{1}$$

unde:

- $i_C(t)$ este curentul instantaneu prin condensator,
- C reprezintă capacitatea condensatorului [F],
- $\frac{du_C(t)}{dt}$ este variația instantanee a tensiunii la bornele condensatorului [V/sec] [1].

Dacă pasul de timp este constant $\Delta t = t_{k+1} - t_k$, atunci:

$$\left[i_C(t_{k+1}) + i_C(t_k)\right] \cdot \frac{t_{k+1} - t_k}{2} = C\left(u_C(t_{k+1}) - u_C(t_k)\right) \Leftrightarrow$$

$$\Leftrightarrow u_C(t_{k+1}) = i_C(t_{k+1}) \cdot \frac{\Delta t}{2C} + \left[u_C(t_k) + i_C(t_k) \cdot \frac{\Delta t}{2C} \right] \tag{2}$$

Între relația (2) și relația $u = R \cdot i + e$, se realizează următoarele echivalențe:

$$\begin{cases} u \Leftrightarrow u_C(t_{k+1}), \\ R \Leftrightarrow R_C = \dfrac{\Delta t}{2C}, \\ i \Leftrightarrow i_C(t_{k+1}), \\ e \Leftrightarrow e_C = u_C(t_k) + i_C(t_k) \cdot \dfrac{\Delta t}{2C}. \end{cases} \tag{3}$$

Relațiile (3) conduc la modelul discretizat Euler implicit din fig. 1 pentru orice condensator liniar:

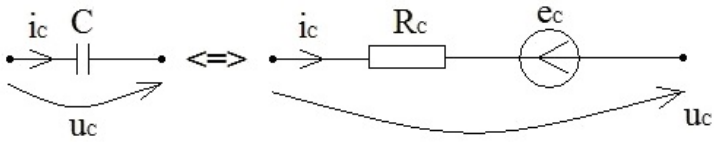

Fig. 1: Modelul discretizat Euler implicit pentru condensatorul liniar

În cazul în care circuitul conține câteva diode cu două porțiuni liniare, atunci o metodă foarte eficientă poate fi metoda Katzenelson. Această metodă se aplică pe circuitele companion. Procedura constă în încercarea celor două caracteristici ale diodei la rezolvarea circuitelor liniare. Modelul Ebers-Moll pentru un tranzistor este echivalent cu două diode și două surse comandate liniar la frecvențe mici de lucru.

3 Metoda balanţei armonice

Metoda balanţei armonice [2] compusă cu metoda celor mai mici pătrate se realizează prin descompunerea circuitului analizat în două subcircuite: un subcircuit liniar și un subcircuit alcătuit numai din elemente neliniare. Elementele de circuit considerate neliniare sunt următoarele:

- rezistoarele neliniare controlate în tensiune și în curent,
- sursele independente de tensiune și de curent.

Dacă circuitul a ajuns la regimul permanent nesinusoidal, atunci se descompun în serie Fourier tensiunile la bornele rezistoarelor cu caracteristici neliniare [3]:

$$\begin{aligned} x_i(t) &= x_{i,0} + \sum_{k=1}^{M} \left(x_{i,2k-1} \cos \omega'_k t + x_{i,2k} \sin \omega'_k t \right) = \\ &= \mathrm{Re}\left\{ x_{i,0} + \sum_{k=1}^{M} \left(x_{i,2k-1} - j x_{i,2k} \right) \exp\left(j \omega'_k t \right) \right\} \text{[2]} \end{aligned} \tag{4}$$

Analiza circuitului liniar în curent alternativ se va realiza prin înlocuirea tuturor rezistoarelor neliniare controlate în tensiune si curent prin surse ideale independente de curent şi, respectiv, tensiune. După efectuarea acestor înlocuiri se va studia circuitul pe fiecare armonică k prin analiza hibridă în complex. Analiza subcircuitului neliniar se realizează cu metoda celor mai mici pătrate, prin conectarea unor surse ideale independente de tensiune și curent la bornele tuturor rezistoarelor care au caracteristici neliniare și sunt controlate în tensiune, respectiv, în curent. Soluţiile ecuaţiei se află cu algoritmul Newton-Raphson.

4 Exemplu

In fig. 1 este prezentată schema demodulatorului MA, iar in fig. 2 este prezentata caracteristica liniarizata pe portiuni $u-i$ a diodei D.

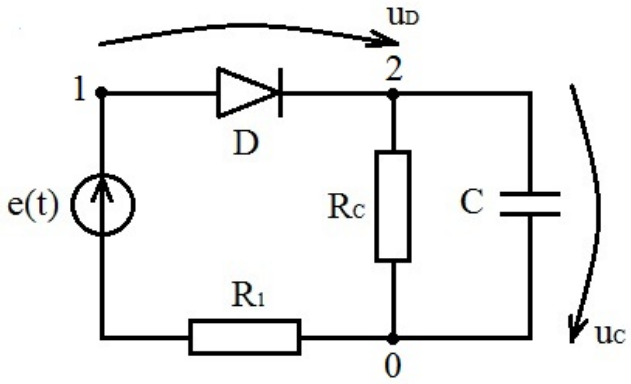

Fig. 2: Schema demodulatorului MA

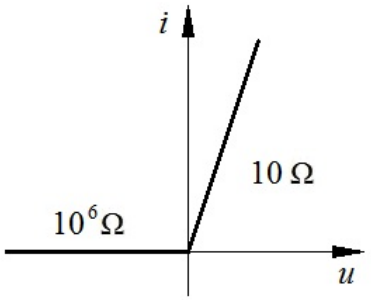

Fig. 3: Caracteristica $u-i$ a diodei D

Circuitul este caracterizat de următorii parametrii: $R_1=1\,\Omega$, $e(t)=10\sin(2\pi f_1 t)\sin(2\pi f_2 t)$ V, unde $f_1=1kHz$ și $f_2=10MHz$, $R_C=1000\,\Omega$, $C=1\mu F$.

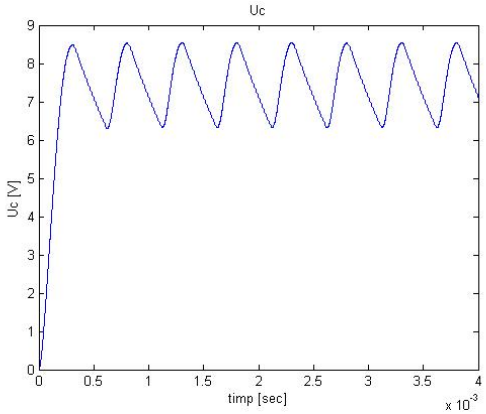

Fig. 4: Tensiunea la bornele condensatorului prin metoda Katzenelson pentru primele 4 perioade

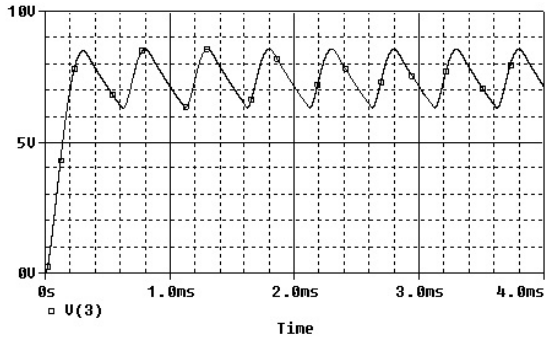

Fig. 5: Tensiunea la bornele condensatorului cu PSpice pentru 4 perioade

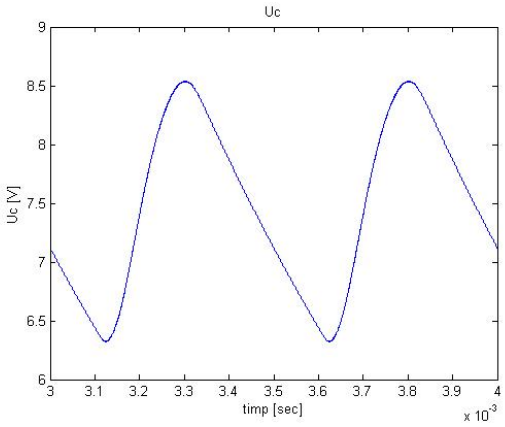

Fig. 6: Tensiunea la bornele condensatorului prin metoda Katzenelson pentru o perioadă

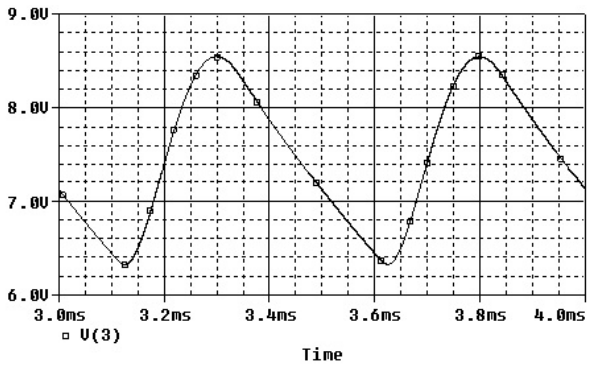

Fig. 7: Tensiunea la bornele condensatorului cu PSpice pentru o perioadă

5 Concluzii

- Metoda Newton-Raphson folosită în metoda balanței armonice nu este întotdeauna convergentă. Pentru a asigura convergenţa, funcţia trebuie să fie continuă și derivabilă.
- În cazul în care frecvențele la care lucrează circuitul sunt mult diferite, atunci analiza în domeniul timp este laborioasă. Acest lucru se întâmplă deoarece pasul de timp trebuie ales astfel încât să fie diviziune a celei mai mici perioade.
- Simulatorul PSpice utilizează metoda forței brute. Din această cauză rezultatele sunt precise dacă se analizează circuite compuse numai din elemente liniare sau cu neliniarități slabe.
- Rezultatele obţinute cu metoda Katzenelson implementată în MatLab sunt apropiate cu cele obținute folosind programul Pspice, atât pentru o perioadă, cat și pentru primele 4 perioade analizate pentru demodulatorul MA.

Referinţe

[1] *T. R. Kuphaldt*, „Introducere în circuite electrice şi electronice”, 10.07.2010, pag. 262, 291, http://www.scribd.com/doc/37088762/Vol1-Curent-Continuu-v2, [Online - valabil la data de 29.11.2012];

[2] *L. O. Chua*, *A. Ushida*, „Algorithms for computing almost periodic steady-state response of nonlinear systems to multiple input frequencies”, IEEE Trans. on Circuits and Systems, Vol CAS-28, No. 10, Oct. 1981, pag. 953-971;

[3] *Mihai Iordache, Lucian Mandache*, „Analiza asistată de calculator a circuitelor analogice neliniare”, Ed. Politehnica Press, Bucureşti, 2004, pag. 74-75;

[4] *M. Preda*, *P. Cristea*, „Bazele electrotehnicii”, vol. 2, Ed. Didactică și Pedagogică, București, 1980, pag. 318-319;

A Numerical Study of the Heat Transfer Management Provided by a Thermoelectric Sink-and-Fan System

Jean B. DUMITRU[1], Alexandru M. MOREGA[1,2], Mihaela MOREGA[1]

[1]*University POLITEHNICA of Bucharest, Romania*
[2]*"Gh. Mihoc – C. Iacob" Institute of Statistical and Applied Mathematics, Romanian Academy*
dumitrujeanbogdan@yahoo.com, alexandru.morega@upb.ro, mihaela.morega@upb.ro

Abstract. This paper presents a mathematical model and its finite element (FEM) implementation for the thermoelectric processes that occur in a Peltier sink-and-fan device aimed at enhancing the heat exhausted by power electronics. The heat transfer management for several key parameters (the heat released by the electronic module, the ambient temperature, the convection heat transfer coefficient) is analyzed to find optimal working conditions.

1. Introduction

An important issue in the design of modern electronic systems is the heat transfer management. The heat produce by "hot" electronic devices can lead to their thermal failure, lifespan reduction of the final electronic system, or it can significantly reduce the overall performance of the device. To keep the temperature within safe working limits heat transfer methods are required. One such solution is the "Peltier" thermoelectric cooler (TEC) that can "pump" the heat exhausted by the power electronic unit.

A contemporary TEC is a solid-state device that uses the electrical current instead of the refrigerant used by the refrigerators to carry the heat released by thermal sensitive devices to the environment [1-4]. To ensure best yet economic cooling, optimal control techniques are required. Heat transfer can be controlled either by adjusting the electrical current through the TEC or by controlling the heat transfer removal rate at the hot end of the Peltier cell [5].

This paper is concerned with the numerical study of the heat transfer management provided by a TEC unit with respect to several key parameters: the heat released by the electronic module, the ambient temperature, the convection heat transfer coefficient, with the aim of finding optimal working conditions for the electronic modules.

2. The TEC used for Thermal Control

A TEC is essentially a Carnot device, and it provides for several important advantages: solid state construction, chip integrating possibility, silent operation, compact dimensions, lightweight, higher reliability, accurate temperature stability (better than +/- 0.1 °C), localized cooling, short response times to temperature change, reduced power consumption, cooling under the ambient temperature, *etc*. [1-4].

A single-stage TEC module is composed of thermoelectric cells made of *n* and *p*-type semiconductor columns, which are sandwiched and fixed by soldering between two ceramic plates (the hot and cold ends). The couples are connected electrically in series and thermally in parallel. Multistage TEC units are also available. They "split" the hot end – cold end temperature interval in several stages, providing for higher heat pumping efficiencies.

When a voltage is applied at the electric ports of the TEC a DC current flows through the unit, which (by Peltier effect) conveys the heat released by the device connected (thermally) to its cold end to the other (hot) end that is usually provided with a heat sink–and–fan device (figure 1) [5]. In this situation, in addition to the Joule-Lenz (electro-thermal) effect that is related to the electrical current flow through the device, Seebeck effect is a menace also

because it acts into reducing the efficiency of the heat removal by a counter electromotive force, opposite to the voltage applied to the unit.

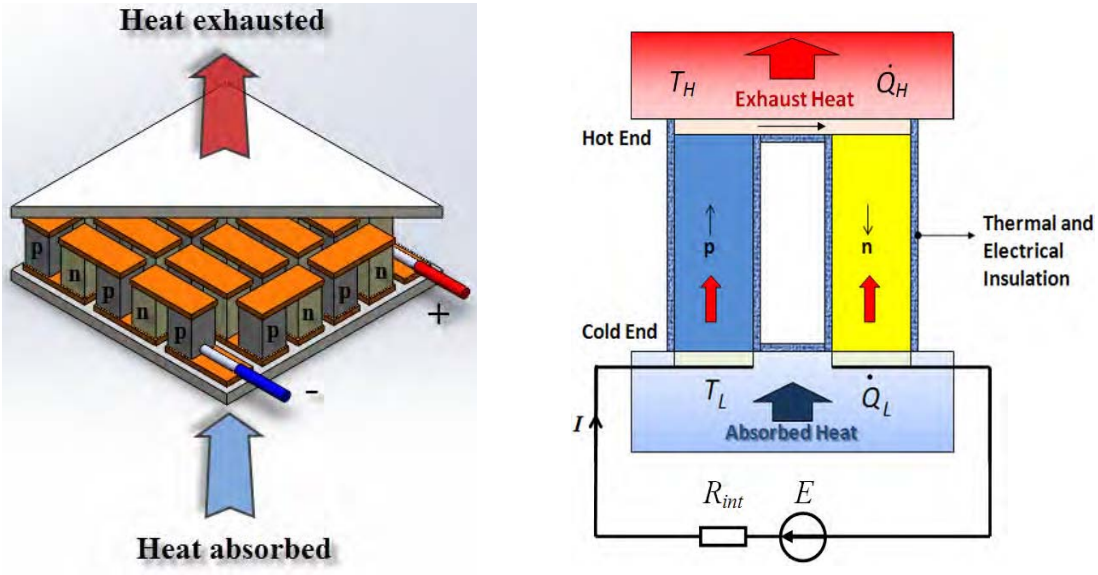

Figure 1: CAD representation of a TEC module and the working principle.

Therefore an optimal control of heat transfer should consider the complex interactions that occur in a TEC and mathematical modeling and numerical simulation may be needed in the design phase of the unit.

3. The Mathematical and Numerical Model

The mathematical models that describes the heat and current flow thorough the TEC under steady state working conditions is [5], [8]

$$\nabla \cdot \mathbf{J} = 0,\ \nabla \cdot \mathbf{q} = 0, \tag{1}$$

where $\mathbf{J}$ [A/m^2] is the electrical current density and $\mathbf{q}$ [W/m^2] is heat flux density, defined by

$$\mathbf{J} = \underbrace{-\sigma \nabla V}_{\text{Ohm}} - \underbrace{\sigma \varepsilon \nabla T}_{\text{Seebeck}}, \tag{2}$$

$$\mathbf{q} = \underbrace{V\,\mathbf{J}}_{\text{Joule}} - \underbrace{k\,\nabla T}_{\text{Fourier}} + \underbrace{\varepsilon T\,\mathbf{J}}_{\text{Peltier}}. \tag{3}$$

Here V [V] is the electrical potential, T [K] is temperature, ε [V·K^{-1}] is Seebeck coefficient, σ [S/m] is the electrical conductivity, and k [W·K^{-1}m^{-1}] is the thermal conductivity. All physical properties of the thermoelectric elements are temperature dependent [5], [10].

The mathematical model (1)-(3) was solved numerically by implementing a general form coefficient form PDE mathematical model [5], [8], [11]

$$-\nabla \cdot \left(c \nabla u + \alpha u - \gamma\right) = 0, \qquad \text{in } \partial\Omega \tag{4}$$

$$\begin{cases} \mathbf{n} \cdot \left(c \nabla u + \alpha u - \gamma\right) + qu = g - h^T \mu, & \text{on } \partial\Omega \\ hu = r, & \text{on } \partial\Omega \end{cases} \tag{5}$$

where Ω denotes the computational domain, $\partial\Omega$ is the boundary, u is the dependent variable (T for the heat transfer problem and V for the electrical problem), $\mathbf{n}$ is the outward normal, μ is a

Lagrange multiplier, *c*, α, γ, *q*, *h*, *r*, and *g* are defined to model the two PDEs (1).

The boundary conditions (BCs) that close the problem are set as following: *for the heat transfer problem*, either heat flux or temperature at the cold end (the heat source), convection heat transfer on the heat sink surface, and thermal insulation for all other boundaries; *for the electric field problem*, either normal current density or ground (zero voltage) at the terminals and electrical insulation for other all sides.

4. Numerical Results and Discussions

A series of parametric studies were conducted on an elemental cell fitted with a heat sink – fan unit to study the sensitivity of the heat pumping efficiency.

Figure 2 presents the computational domain for the elemental TEC and the temperature distribution for 1 A pumping current, and h = 100 W/m^{2}K convection heat transfer coefficient.

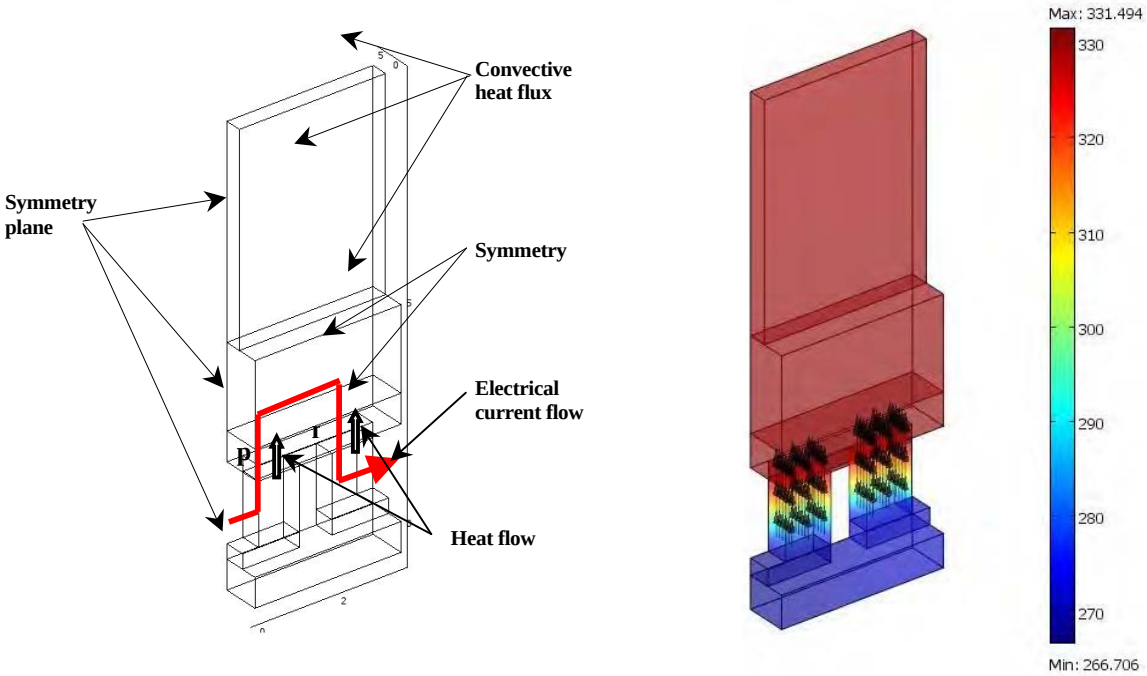

Figure 2: The elemental TEC. Temperature field (color map, in kelvins) and heat flux (arrows).

It is assumed that the heat flow between adjacent elemental cells is negligible small therefore the heat transfer problem can be studied at the cell level. Symmetry BCs (with respect to the coolant flow) are used to further reduce by half the computational domain.

Figure 3 presents the average temperature at the cold end versus electrical current for h = 20…180 W/m^{2}K. The total power per elemental cell is 0.078 W and the ambient temperature is set at 293 K.

Apparently, a heat transfer coefficient less than 20 W/m^{2}K, which means in fact natural convection, does not provide enough cooling to keep the heat source (the electronic unit) at a safe temperature.

On the other hand, increasing h beyond 100 W/m^{2}K may not be an option since it provides for an insignificant reduction in the average temperature, for a certain electrical current. We found that an optimal control interval for the convective heat transfer coefficient is then 20…100 W/m^{2}K.

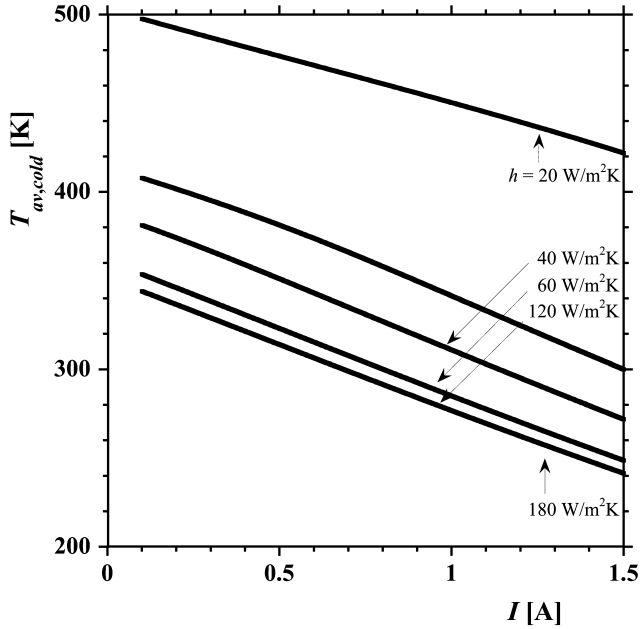

Figure 3: Average temperature at the cold end, $T_{av,cold}$, versus the electrical current for different convection cooling conditions.

Figure 4 shows the average temperature at the cold end of the TEC as function of the convection heat transfer coefficient, for different values of the electrical current. The total heat power per elemental TEC is 0.078 W and ambient temperature is set to 293 K. Apparently, a linear control may be conveniently implemented to manage the heat exhaust.

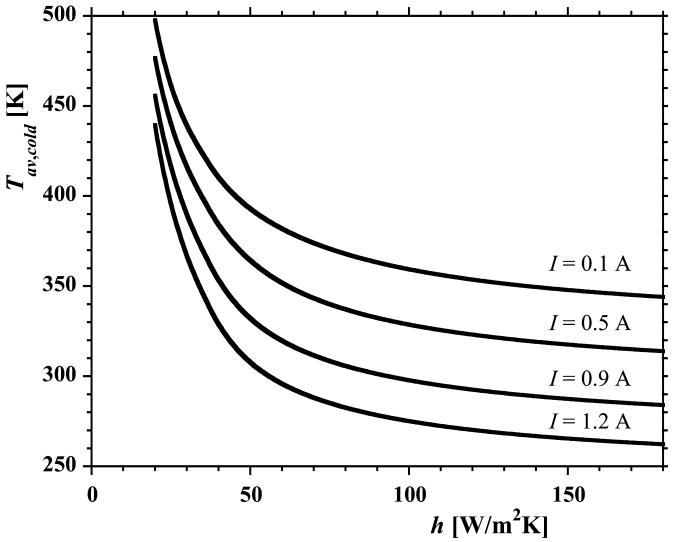

Figure 4: The average temperature at the cold end, $T_{av,cold}$, for a TEC with 127 elements.

A third parametric study, summarized in Figure 5, was conducted to outline the influence of the heat source power, Q [W], upon the temperature at the cold end of the TEC for different values of the electrical current. The convection heat transfer coefficient is 100 W/m^{2}K, and the ambient temperature is assumed 293 K.

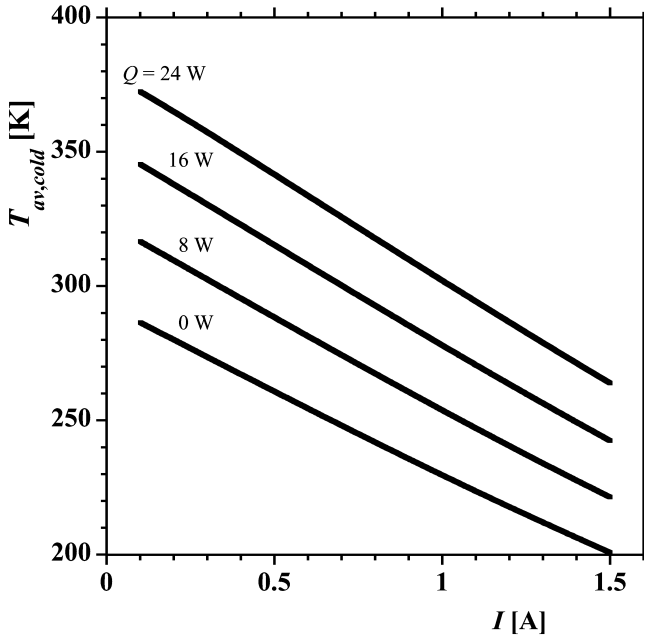

Figure 5: Average temperature at the cold end versus electrical current. The heat influx at the cold end is a parameter.

Finally, the coefficient of performance (COP) of the TEC for different hot end – cold end temperature differences was studied. Figure 6 shows the COP as a function of the electrical current. It may be noticed that the TEC reaches a unique COP(*I*) asymptotic behavior for electrical currents exceeding 1 A.

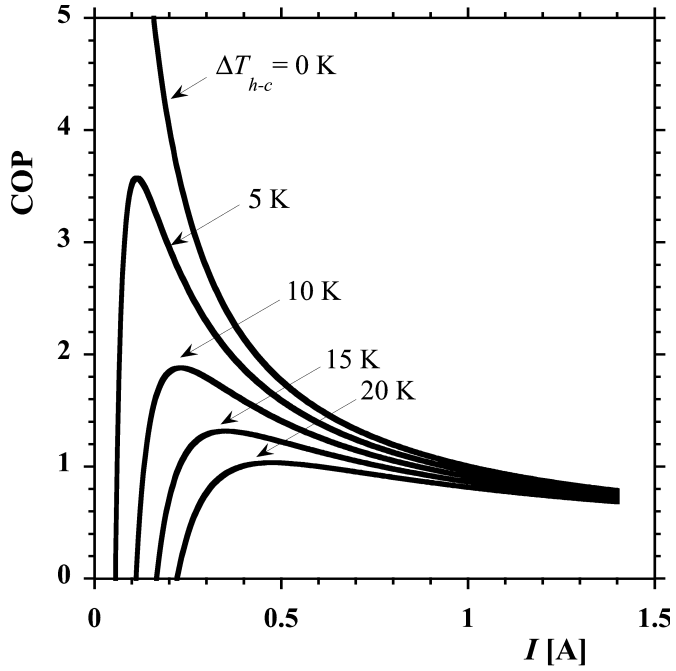

Figure 6: The COP of the TEC. The hot-cold ends temperature difference, ΔT_{h-c}, is a parameter.

These numerical simulation results are consistent with the available datasheet for the TEC device, prompting that such an analysis may evidence optimal working conditions for the TEC and can stand as base point for development an optimal control technique.

5. Conclusions

Modern power electronics require efficient means to exhaust the heat produced by operating at ever increasing heat transfer rates, to provide for safe thermal operating conditions. To this end, solid-state semiconductor devices may be added to the sink-and-fan systems providing for precise, controllable thermal management. This paper presents a mathematical model and numerical simulations for the thermoelectric processes that occur in a TEC under steady state working conditions, with the aim to analyze the heat transfer management provided by a TEC provided with a sink-and-fan system.

The sensitivity of the heat pumping efficiency was evaluated for different control parameters: the electrical current and the convective heat transfer of the sink-and-fan system (*e.g.*, by adjusting the mass flow rate of the coolant – air – through the fan speed).

The COP shows off an extremum (maximum) that is sensitive to the cold to hot end temperature drop, and a unique asymptotic behavior for electrical currents exceeding 1 A. These results are consistent with the available datasheet for the TEC device.

The hot end temperature *vs*. the electrical current characteristic is linear while the hot end temperature *vs. h* characteristic is nonlinear.

For a certain electrical current, the increase of the convective heat transfer coefficient *h* above 100 W/m^2K results in an insignificant reduction of the average hot and temperature.

It may be conjectured that the study may evidence the optimal working conditions for the TEC and can stand as base point for development an optimal control technique.

Acknowledgments – The work was conducted in the Laboratory for Multiphysics Modeling at UPB. The first author acknowledges the support offered by the Sectorial Operational Program Human Resources Development 2007-2013 of the Romanian Ministry of Labour, Family and Social Protection through the Financial Agreement POSDRU/107/1.5/S/76903.

References

[1] G. Jeffrey Snyder, M. Soto, R. Alley, D. Koester, B. Conner, *Hot Spot Cooling using Embedded Thermoelectric Coolers*, Extreme Thermal Solutions, Research Triangle Park, NC 27709, The 22nd IEEE SEMI-THERM Symposium, 2006.

[2] I. Sauciuc, et al., *Thermal devices integrated with thermoelectric modules with applications to CPU cooling*, Proc. InterPACK 2005, 73243, 2005.

[3] K. Fukutani, and A. Shakouri, *Optimization of bulk thermoelectric modules for chip cooling applications*, Proc. InterPACK 2005, 73410, 2005.

[4] J. Bierschenk, and D. Johnson, *Extendingthe limits of air cooling with thermoelectrically enhanced heat sinks*, The 9th Intersociety Conference on Thermal and Thermomechanical Phenomena in Electronic Systems (IEEE Cat. No.04CH37543), **1** (2004) pp. 679-684.

[5] J.B. Dumitru, A.M. Morega, D.G. Chamorro, M. Morega, *Numerical Simulation of Thermoelectric Heat Transfer Management*, The 11th International Conference on Applied and Theoretical Electricity-University of Craiova, 2012.

[6] Thermal Solutions, http://thermal.ferrotec.com/thermal-home/

[7] C.J.M. Lasance, R.E. Simons, *Advances in high-performance cooling for electronics*, Electronics Cooling, Nov. 1, 2005.

[8] A.M. Morega, M. Morega, *A FEM model for thermoelectric and thermomagnetic effects*, Rev. Roumaine Sci. Techn. Electrotech. et Energ., **48**, 2-3 (2003) pp. 187-197.

[9] A. Bejan, *Heat Transfer*, New York: Wiley, 1993.

[10] M. Jaegle, *Multiphysics simulation of thermoelectric systems – modeling of Peltier-cooling and thermoelectric generation*, Proc. of the COMSOL Conference, 2008 Hannover.

[11] Comsol A.B., v.3.5a (2010), v.4.2a (2012), Sweden.

Estimation of Van der Pol Oscillator Parameters Based on Transfer Functions

Mihai IORDACHE[1], Lucia DUMITRIU[1], Lucian MANDACHE[2] and Dragos NICULAE[1]

[1] Politehnica University of Bucharest, Romania, e-mail iordache@elth.pub.ro
[2] University of Craiova

***Abstract*— The paper presents a new method for the parameter estimation of the Van der Pol models used in the study of the voltage-controlled oscillators. The procedure is based on the network function generation in symbolic form. Using the measured parameters as reference and the symbolic transfer function computed before, the model parameters are obtained by an iterative identification algorithm based on Output Error Method. To this end two objective functions are defined. They can be minimized using one of the *fminimax* or *fminunc* procedures from the Matlab toolbox. Both algorithms are based on iterative computation starting from certain initial values. They are efficient for less than four parameters to be estimated, and are suitable for linear circuits, as well as for small-signal nonlinear circuits in the operating points. A third method for the identification of the model parameters is also proposed. It is based on solving of a system of nonlinear algebraic equations with real or complex coefficients. The proposed estimation techniques are tested for validation on an illustrative example.**

I. Introduction

The methods used for parameter determination are very different as concept and are suitable for the application of interest.

Many approaches have been developed for model identification based on available data. Most of these approaches formulate the estimation problem as a nonlinear minimization problem of least squares and estimate all the unknown parameters simultaneously. The task is very difficult and can be solved either by traditional numerical techniques (Newton type methods) or by computational intelligent techniques (genetic algorithms). To be applied, the numerical techniques require good knowledge of the analytical models used, and even very efficient, they are not considered to be very robust, providing either suboptimal solutions or no solution at all, depending on the stiffness of the problem and on the initialization of the iterative process. Computational intelligent techniques require less information on the mathematical model and are more robust.

Recently a new interest in Output Error techniques can be noted. These methods are based on iterative minimization of the output error quadratic functional by a Non Linear Programming (NLP) algorithm, [1 – 9]. They require much more computation effort and even they do not converge always to a unique optimum, they are attractive because the simulation of the output model is based only on the knowledge of the input and also can be used for parameters estimation both for linear and nonlinear systems, [12 – 15].

In this paper we present a new method to estimate the analog circuit parameters based on a transfer function of the circuit expressed in symbolic form. Starting from the equivalent scheme of the oscillating circuit in sinusoidal behavior, the transfer function with respect to all the circuit parameters is generated. The approach is based on an appropriate frequency space representation of the network function, using the complex or Laplace modified nodal equations (MNE) and on the Matlab procedures *fminimax* or *fminunc* which minimize some objective functions.

II. Methods for Circuit Parameter Estimation using the Transfer Function

Consider a linear circuit which contains only lumped circuit elements and independent sources. The circuit is described in time domain by a set of ordinary differential linear equations which can be transformed either by using the Laplace or Fourier transform in algebraic linear equations in frequency domain. Because we need information about the magnitude and the phase of the output variable, the transfer function in complex form $\underline{H}(j\omega)$ is useful [10, 11].

It will be generated from the equivalent scheme in sinusoidal behavior and it will be expressed as a function of frequency $\underline{H}(f)$.

1. *The first method for parameter estimation.* Using the transfer function in which the p circuit parameters to be estimated (x_1, x_2, ..., x_p) are kept as variables, while the other parameters are substituted by their nominal values, the following objective functions are built for n_f frequency samples (usually $n_f > p$):

$$f_k = \left(\left|\underline{H}(f_k)\right| - \left|\underline{H}(f_k, x_1, x_2, ..., x_p)\right|\right)^2, k = \overline{1, n_f} \qquad (1)$$

The objective functions (1) are minimized using the *fminimax* routine from the Matlab toolbox [6, 8, 15].

This routine finds the minimum of a problem specified by:

$$\min_{\boldsymbol{x}} \max_{[\boldsymbol{F}_i]} \{\boldsymbol{F}_i(\boldsymbol{x})\} \text{ such that } \begin{cases} \boldsymbol{c}(\boldsymbol{x}) \le \boldsymbol{0} \\ \boldsymbol{c}_{eq}(\boldsymbol{x}) = \boldsymbol{0} \\ \boldsymbol{A} \cdot \boldsymbol{x} \le \boldsymbol{b} \\ \boldsymbol{A}_{eq} \cdot \boldsymbol{x} \le \boldsymbol{b}_{eq} \\ \boldsymbol{lb} \le \boldsymbol{x} \le \boldsymbol{ub} \end{cases} \qquad (2)$$

where: $\boldsymbol{x}$, $\boldsymbol{b}$, $\boldsymbol{beq}$, $\boldsymbol{lb}$, and $\boldsymbol{ub}$ are vectors, $\boldsymbol{A}$ and $\boldsymbol{A}_{eq}$ are matrices, $\boldsymbol{c}(\boldsymbol{x})$, $\boldsymbol{c}_{eq}(\boldsymbol{x})$, and $\boldsymbol{F}(\boldsymbol{x})$ are linear or nonlinear functions that return vectors.

Fminimax minimizes the worst-case value of a set of multivariable functions, starting from an initial estimate.

The syntax of this routine is:

$$[\boldsymbol{x}, \boldsymbol{f}_{\mathbf{val}}] = \text{fminimax}(@\text{myfun}, \boldsymbol{x}_0), \tag{3}$$

where $\boldsymbol{x}_0$ is the guess initial values of the unknown parameter vector, $\boldsymbol{f}val$ is the vector values of the function f at the n_f frequency samples. The solution is searched within the domain [$\boldsymbol{l}b$, $\boldsymbol{u}b$] specified by the user.

This is generally referred to as the *minimax* problem.

2. *The second method for parameter estimation.*

The other procedure from the Matlab toolbox, *Fminunc*, finds the minimum of a problem specified by

$$\min_{\boldsymbol{x}} f(\boldsymbol{x}), \tag{4}$$

where $\boldsymbol{x}$ is a vector and $f(\boldsymbol{x})$ is the objective function, a scalar function of several variables, having the expression

$$f = \sum_{k=1}^{n_f} \left(\left| \underline{H}(f_k) \right| - \left| \underline{H}(f_k, x_1, x_2, ..., x_p) \right| \right)^2 , \quad \text{with } n_f = 1 \text{ or } n_f \le 3 . \tag{5}$$

The *fminunc* routine attempts to find the minimum of the scalar function starting from an initial estimate, and has the following syntax [3 – 9, 12 - 15]:

$\boldsymbol{x}$ = *fminunc*(*fun*,$\boldsymbol{x}$0); $\boldsymbol{x}$ = *fminunc*(*fun*, $\boldsymbol{x}_0$, *options*);
$\boldsymbol{x}$ = *fminunc*(problem); [$\boldsymbol{x}$,$\boldsymbol{f}$val] = *fminunc*(...);
[$\boldsymbol{x}$,fval,exitflag] = *fminunc*(...);
[$\boldsymbol{x}$,fval,exitflag,output] = *fminunc*(...);
[*x*, *fval, exitflag, output,grad*] =** *fminunc*(...) ;
[$\boldsymbol{x}$,fval,exitflag,output,grad,hessian] = *fminunc*(...). (6)

This is generally referred to as *unconstrained nonlinear optimization*.

The parameter estimation methods based on objective functions (1) and (5) are called - *output error methods.*

3. *The third method for parameter estimation.*

Usually $\underline{H}(f)$ is a rational function of frequency. The polynomial coefficients of the nominator and of the denominator are complex products of the system parameters. Taking that into account, the parameter estimation can be done by solving a system of p nonlinear algebraic equations (in p frequency samples) with real or complex coefficients as follows:

$$\left| \underline{H}(f_k) \right| - \left| \underline{H}(f_k, x_1, x_2, ..., x_p) \right| = 0, \; k = 1,2,..,p \tag{7}$$

for real coefficients and

$$\underline{H}(f_k) - \underline{H}(f_k, x_1, x_2, ..., x_p) = 0, \quad k = 1,2,..., p \tag{8}$$

for the complex ones.

The number of the parameters which can be estimated with the equations (7) and (8) (in general ≤ 3) depends on the efficiency of the routine used for solving. Because, in general, the nonlinear algebraic equation systems have multiple solutions, the designer has to choose the solution corresponding to the real system.

III. Example

Consider the oscillating circuit with two single ended Van der Pol oscillators coupled through a two-port passive network, as it is shown in Figure 1. The two voltage-controlled nonlinear resistors represent the active part of the two oscillators.

The nonlinear characteristics of the two voltage-controlled nonlinear resistors are expressed as follows:

$$\begin{aligned} i_{nel1} &= -a v_1 + b v_1^3 \\ i_{nel2} &= -a v_2 + a b v_2^3, \end{aligned} \tag{9}$$

where a is the negative conductance necessary to start the oscillation and b a parameter used to model the saturation phenomenon.

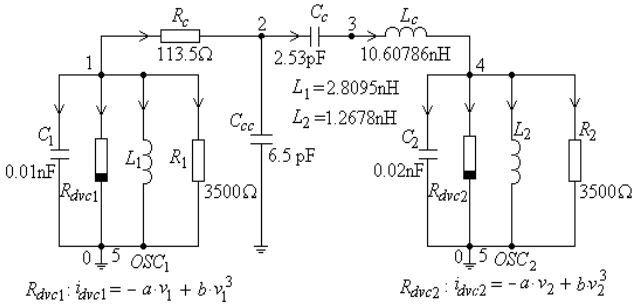

Fig. 1. Two oscillators coupled through a two-port passive network.

With $v(t) = A\cos(\omega_0 t)$, from the above characteristics we get the expressions of the currents through the two nonlinear resistors as:

$$i(t) = \left(-a + \frac{3}{4} b A^2 \right) A cos(\omega_0 t) + b \frac{A^3}{4} cos(3\omega_0 t). \tag{10}$$

Assuming a sinusoidal oscillation of the currents (neglecting the third harmonics), it results that in sinusoidal behavior we can model the two nonlinear resistors by two linear resistors having the conductances

$$G_{01} = -a + \frac{3b}{4} A_1^2, \;\; G_{02} = -a + \frac{3b}{4} A_2^2, \tag{11}$$

where A_1 and A_2 are the magnitudes of voltages v_1 and v_2.

Performing SPICE simulation in transient behavior we get the magnitude values A_1 = 3.1891 V, A_2 = 3.69 V, and the synchronization frequency f_s = 908.247 MHz, for the initial conditions $v_1(0)$ = 2.0 V and $v_2(0)$ = 1.0 V. Thus, in sinusoidal behavior the two voltage-controlled nonlinear resistors can be substituted by two linear resistors having negative slopes. In this case the circuit in Fig. 1 can be analyzed by the complex representation method [5, 11, 14].

We can use as transfer function the driving point impedance $\underline{Z}_{ii} = \underline{Z}_{1\,0\,1\,0}$ expressed in full symbolic form as a function of the frequency and of all the circuit parameters.

The magnitude-frequency characteristic of this transfer function is represented in Fig. 2.

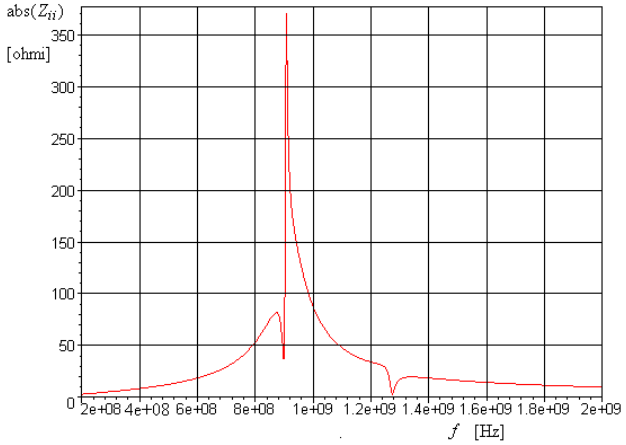

Fig. 2. Magnitude – frequency characteristic of driving point impedance.

We want to estimate the parameters a and b of the Van der Pol model which have the nominal values:

$$a = 0.0085 \text{ S}; \quad b = 0.00071 \text{ S/V}^2.$$

To this end we use the following procedures:

1. Using $\underline{Z}_{ii}$ we generate the objective function (1) by the routine *myfunab*1_*Zii* which has the following command line:

$$[\boldsymbol{x}, \boldsymbol{f}_{\mathbf{val}}] = fminimax(@myfunab1_Zii, \boldsymbol{x}_0), \qquad (12)$$

Considering the initial guess vector:

$$\boldsymbol{x}_0 = [0.0085*0.0933; 0.00071*0.0933],$$

we get the following solution:

$$x = \begin{bmatrix} 0.00849805 \\ 0.000712 \end{bmatrix}$$

The relative errors are:

eps_a = -0.0235 [%]; eps_b = 0.282 [%].

2. Identification of a and b using the expression (5) and the *myfunab*2_*Zii* routine whose command lines are:

```
option = optimset('fminunc');
option = optimset(option, 'GradObj', 'off', 'HessUpdate',…
'steepdesc', 'LargeScale', 'off', 'Display', 'iter');
[len_opt, D,flag, output] =...
fminunc({@myfunab2_Zii},SL,option),
```

Considering the following variation limits for these parameters:

$$a \in [0.008, 0.0009] \text{ and } b \in [0.0007, 0.0008],$$

we get the following solution:

$$x = \begin{bmatrix} 0.009 \\ 0.0007 \end{bmatrix}$$

The relative errors are:

eps_a = 5.88 [%]; eps_b = - 1.408 [%].

3. Solving the nonlinear algebraic equation with real coefficients (7) we obtain:

$$Solution_ab_sim := [a = 0.0085021682, b = 0.00071027854]$$

$$Solution_ab_exp := [a = 0.0085089086, b = 0.0007119205]$$

$$esp_a := 0.079278601 \quad esp_b := 0.12861292$$

If the equation system with complex coefficients (8) is solved, the results are:

$$Solution_ab_sim := [a = 0.008504 + 0.4228\,10^{-6}\,I, b = 0.0007105 + 0.4816\,10^{-7}\,I]$$

$$Solution_ab_exp := [a = 0.008707 + 0.0000975I, b = 0.000737 + 0.0000126I]$$

$$eps_a := 2.3935313 \quad eps_b := 3.7449261$$

For the estimation of the parameters C_2, L_2 (which have the nominal values 0.02 nF and 1.2678 nH) we use the equation systems (7) and (8) and we get:

$$C2L2_sim := [C2 = 0.1999\,10^{-10}, L2 = 0.1268\,10^{-8}]$$

$$C2L2_exp := [C2 = 0.19998\,10^{-10}, L2 = 0.126789\,10^{-8}]$$

$$eps_C2 := 0.04002 \quad eps_L2 := -0.015773$$

respectively

$$C_{2_sim} = 0.1999 \cdot 10^{-10} - 0.242 \cdot 10^{-15}\, j;$$

$$C_{2_exp} = 0.1999 \cdot 10^{-10} - 0.277 \cdot 10^{-14}\, j;$$

$$L_{2_sim} = 01268 \cdot 10^{-9} - 0.2065 \cdot 10^{-13}\, j;$$

$$L_{2_exp} = 0.1268110^{-8} - 0.1631 \cdot 10^{-12}\, j.$$

$$exp_C2 := -0.0221 \quad exp_L2 := 0.02124$$

If four parameters are to be estimated, let they be a, b, A_1 *and* A_2, using the *myfunabA1A2_Zii* function we get the following solution:

$$\boldsymbol{x}_{_optim} = [\mathbf{0.008325, 0.000748, 3.39, 3.72}]^t$$

We considered the following limits of variation:

$$a_0 \in [0.00764, 0.008595], \; b_0 \in [0.0006545, 0.000748],$$
$$A_{1_0} \in [2.825, 3.39] \text{ and } A_{2_0} \in [3.1, 3.72].$$

With the above nominal values of the parameters, the relative errors are:

eps_a = 5.88 [%]; eps_b = - 1.408 [%].
eps_a = -2.0588 [%]; eps_b = 5.352 [%];
eps_A1 = 6.3 [%]; eps_A2 = 0.813 [%].

Remarks

1. In the case of the two Matlab routines, the accuracy of the parameter estimated values deeply depends on the guess initial values;

2. For the parameters in respect to which the transfer function has small sensitivities, the variation limits must be very closed to the nominal values;

3. If the number of the parameters which have to be estimated is greater than four, we must introduce some restrictions in the *fminimax* routine to get the procedure convergence;

4. When the number of estimated parameters is less or equal to 2, the formulas (7) and (8) are very efficient. Over three estimated parameters is very difficult to solve the nonlinear equation system.

IV. CONCLUSIONS

The paper presents a new method to estimate the parameters of the Van der Pol models used in oscillating circuits. The approach is based on using a transfer function of the circuit. Even the oscillating circuit is a nonlinear one, we proof that in sinusoidal behavior it can be modelled by a linear equivalent scheme. Starting from this scheme we can generate any transfer function in full symbolic form. It captures the parameters to be estimated.

Three estimation methods were developed either by minimizing some objective functions built with the generated transfer function, or by solving a system of nonlinear algebraic equations with real or complex coefficients, obtained also by using the transfer function.

When the number of the estimated parameters is greater than two, minimization procedures using the routines from Matlab (*fminimax* or *fminunc*) are the most efficient.

All equations corresponding to the above estimation techniques are nonlinear. The convergence of the computational process deeply depends on the considered frequency domain.

REFERENCES

[1] E. Walter and L. Pronzato, "Identification of parametric models from experimental data", Communication and Control Engineering Series, Editions Springer, 1997.

[2] H. Unbehauen, G.P. Rao, "A review of identification in continuous-time systems", Annual Reviews in Control 22, pp. 145-171, 1998.

[3] D. W. Marquardt, "An Algorithm for least-squares estimation of non-linear parameters", Soc. Indust. Appl. Math, VOL. 11, NO. 2, pp. 431-441, 1963.

[4] Iulia Dumitrescu, Smail Bachir, David Cordeau, Jean – Marie Paillot, Mihai Iordache, "Modeling an Characterization of Oscillator Circuits by Van der Pol Model Using Parameter Estimation", Journal of Circuits, Systems, and Computers (JCSC), ISSN; 0218 – 1266, Volume 21, No. 5 (August 2012), pp. 1587 – 1605.

[5] Iulia Dumitrscu, "Contribution to the Analysis and Identification of Analog Autonomous Circuits", PHD Thesis, Politehnica University of Bucharest, Bucharest, 2012.

[6] Won Young Yang, Wenwu Cao, Tae-Sang Chung, John Morris, "Applied Numerical Methods using MATLAB", John Wiley & Sons, Inc., Publishing.

[7] H. Unbehauen, G.P. Rao, "Identification of Continuous-Time Systems", IEE Proc. Control Theory App., Vol. 153, No. 2, March 2006, pp. 185-220..

[8] L. L. Sharfe, T. R. Behreus, "A First Course in Electrical and Computer Engineering with MATLAB Programs and Experiments", Addison-Wesley Publishing Company, Reading, Massachusetts, 1990.

[9] L. Ljung, "System Identification – Theory for the User", Prentice-Hall, Upper Saddle River, N.J., 2nd edition, 1999.

[10] M. Iordache, Lucia Dumitriu, I. Matei, "SYMNAP program – SYmbolic Modified Nodal Analysis Program", User Guide, *Department Electrical Library*, Politehnica University of Bucharest, 2002.

[11] M. Iordache, Lucia Dumitriu, I. Matei, "SYTFGP – SYmbolic Transfer Function Generation Program", User Guide, *Department Electrical Library*, Politehnica University of Bucharest, 2000.

[12] AQ. Buonomo, A. Lo Schiavo,"The Effect of Parameter Mismaches on the Output Waveform of an LC-VCO", Inter. Journal of Circuit Theory Applications, Vol. 38, No. 5, June 2010, pp. 487/501.

[13] Grace, A.C.W., "Computer-Aided Control System Design Using Optimization Techniques", Ph.D. Thesis, University of Wales, Bangor, Gwynedd, UK, 1989.

[14] S. Bachir, C. Duvanaud, "New Identification Procedure for Continuous-Time Radio Frequency Power Amplifier Model", Journal of Circuits, Systems, and Computers (JCSC), ISSN; 0218 – 1266, Volume 19, No. 06, 2010, pp. 1259 – 1274.

[15] Powell, M.J.D., "A Fast Algorithm for Nonlinear Constrained Optimization Calculations," Numerical Analysis, ed. G.A. Watson, Lecture Notes in Mathematics, Vol. 630, Springer Verlag, 1978.

Package Capacitors' Impact on System Supply Impedance

Alin-Constantin FLOREA
eSilicon Corporation, Dinu Vintila 11, Bucharest, Romania; aflorea@esilicon.com

Abstract. In this paper I will present the impact on the system supply impedance of the capacitors placed on the package. Two extreme case studies will be presented and we will draw conclusion on the improvement when using on-package capacitors and also when does it make sense to use them.

1 Introduction

The following experiments were performed to determine the impact of the capacitors mounted on the package (on the DIE side and/or on the BGA side of the substrate) on the power supply impedance seen at the bumps and when it would make sense to add capacitors on the package. Please note that the PCB capacitors were included in all experiments.

We chose 2 cases for this:

- **a.** Flip-chip package (12 layers) where you have a lot of room on the TOP package layer to place capacitors since there is no routing on that layer and also BGA side capacitors, due to large package size. Also this package uses many layers for VDD/VSS and many vias placed very close to each other, resulting in a very low inductance path from the capacitors to the DIE bumps
- **b.** Wirebond package (4 layers) where the space to place capacitors is limited due to routing. In this type of package the vias are drilled and large so the number of vias you can have is smaller and the distance between them is larger, leading to a higher inductive path. Also to note here is that we have only 2 layers available to route VDD and VSS from capacitor to the DIE

2 Flip-Chip case

For this experiment we included the entire system with all active and passive elements: PCB and PKG models extracted from the design databases, cap models from the vendors in SPICE format and one current source at the bumps modelling the power consumption at the DIE level, along with the estimated on-DIE decap.

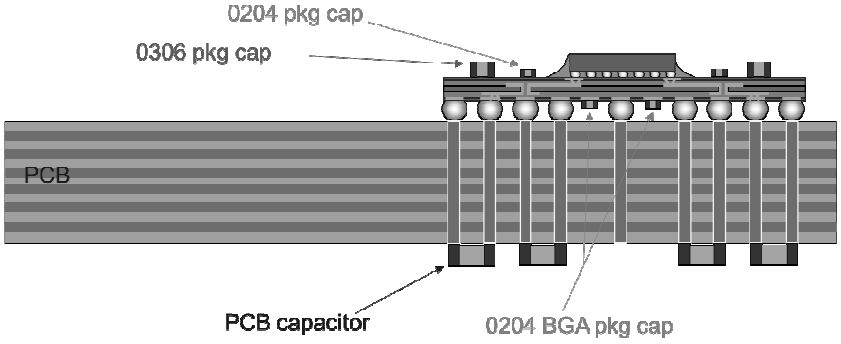

Figure 1: Flip-Chip experiments setup

For this case only TOP side and BGA side on-package caps were included/removed during the following experiments.

In Figure 2 we observe TOP side vs. BGA side on-package capacitors effect.
The TOP side on-package capacitors include 0204 caps that are closer to the die (2.5mm away) and 0306 caps that are further away from the die (5.5mm)

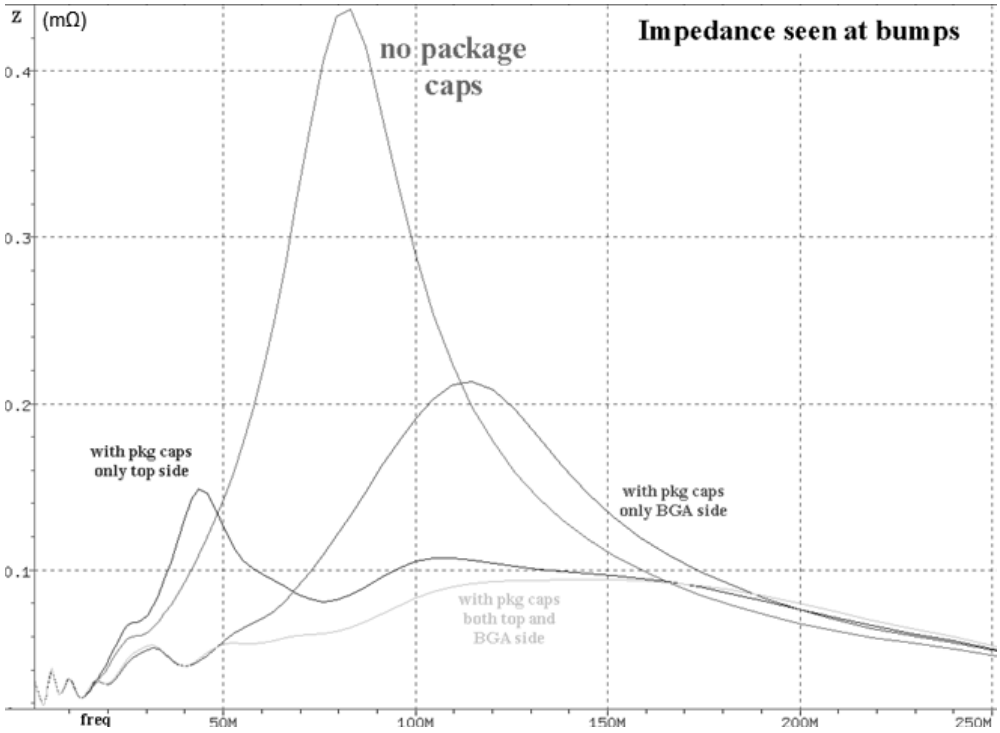

Figure 2: TOP side vs. BGA side on-package capacitors effect

We notice that the TOP side caps have influence in the range of 60-150MHz while the BGA side caps have impact on the 20-80MHz range.

In the next experiment we removed the BGA side capacitors and varied only the TOP side capacitors.

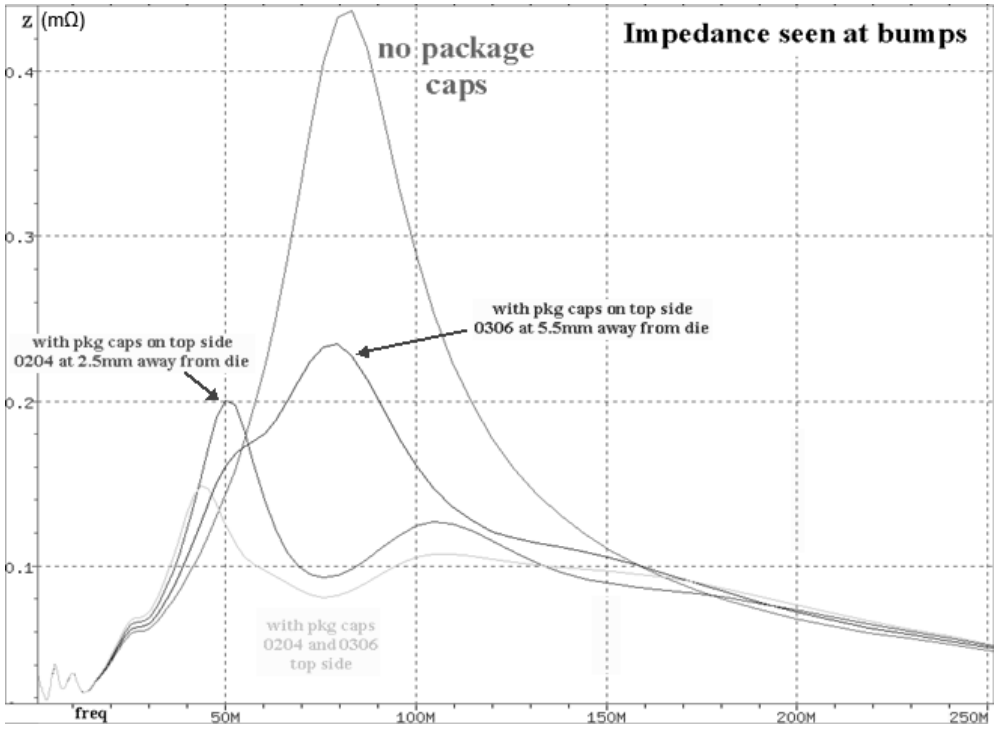

Figure 3: TOP side on-package capacitors effect for flip-chip package

The 0204 caps that are closer to the DIE have a smaller loop inductance to the DIE and they impact especially the 60-100 MHz range, while the 0306, that are further away, they impact the entire 60-150 MHz range but with smaller effect.

The last experiment performed for the Flip-Chip case is to observe the on-DIE capacitors effect.

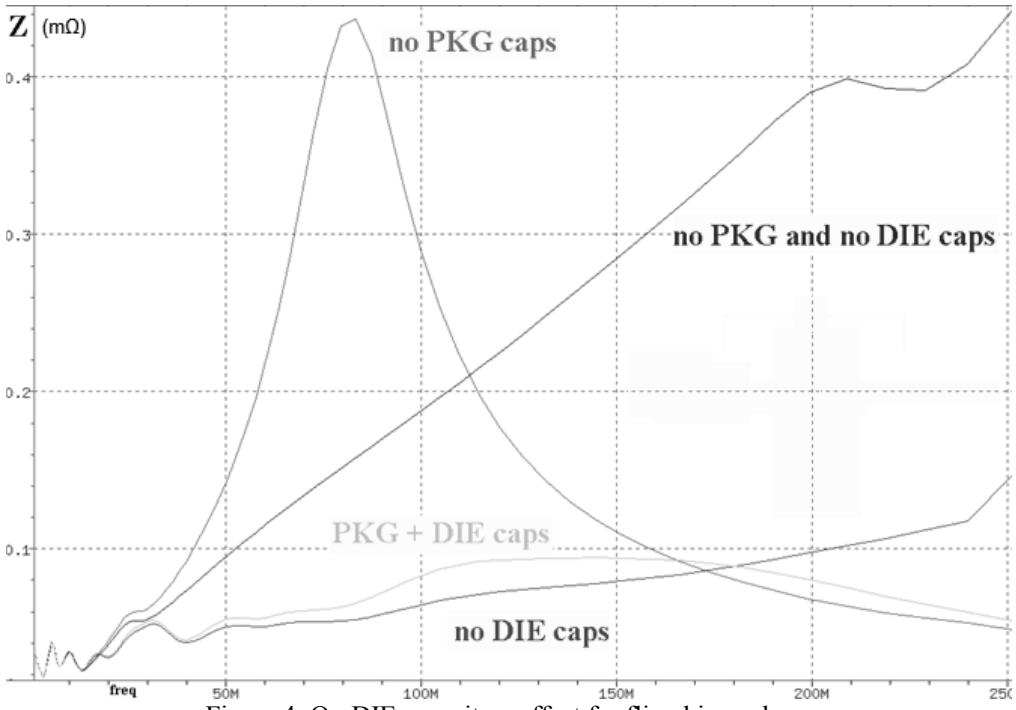

Figure 4: On-DIE capacitors effect for flip-chip package

The on-die caps have impact starting 150MHz. Up to this frequency the on-pkg caps have the main impact on the system supply impedance.

3 Wirebond case

For this experiment we included the entire system with all active and passive elements: PCB and PKG models extracted from the design databases, cap models from the vendors in SPICE format and one current source at the bumps modeling the power consumption at the DIE level, along with the estimated on-DIE decap.

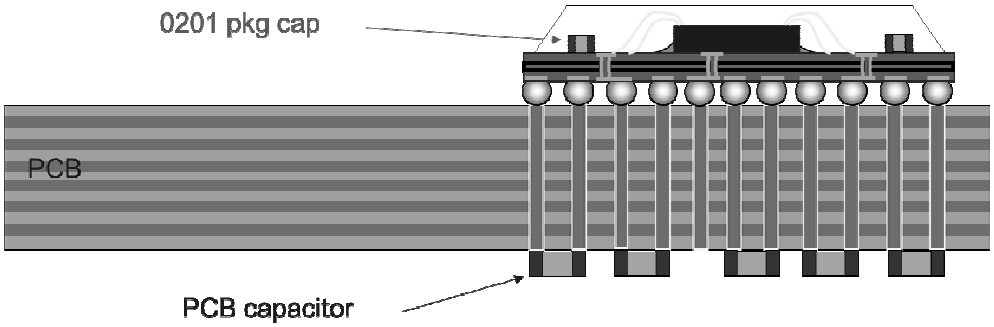

Figure 5: Wirebond experiment setup

TOP side on-package capacitors include 0201 caps that are about 5mm away from the DIE (due to top side routing and bondfinger placement)

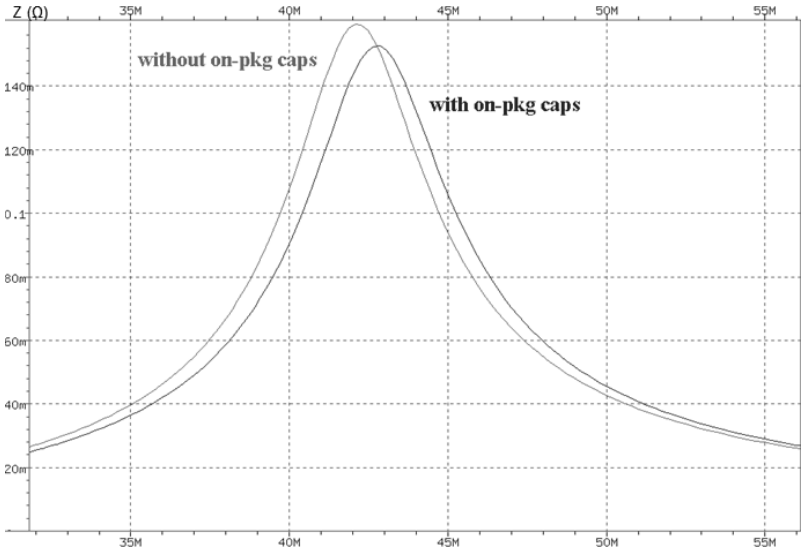

Figure 6: TOP side on-package capacitors effect for wirebond package

We notice only small improvement due to the TOP side on-package capacitors. We used 11 capacitors in this experiment, but the inductive path from cap to the die is making these capacitors inefficient.

4 Conclusion

- From the Flip-Chip package experiments we notice that the on-package decoupling is effective in the 20MHz-150MHz range, while the on-die decoupling starts to have effect after 150 MHz. If the power consumption is too great and/or the operating frequency of the core is within this gap frequency range of 20 – 150MHz, then we will have to consider adding on package capacitors:
    - TOP side capacitors have impact in the 60-150 MHz range
    - BGA side capacitors have impact in the 20-80 MHz range
    - On the TOP package layer, it is better to have the caps as close as possible to the DIE. The limiting factor can be underfill bleeding or TOP layer signal routing if any.
    - For frequencies higher than 150MHz only the on-die decoupling has effect! Adding or increasing the on-package decoupling is not the solution if there are issues above this frequency.

- For Wirebond packages, the capacitors on the package have very little impact on the system supply impedance, so it would make more sense to switch to a flip-chip package in case power consumption is too high.

"Behind scene" for one of the keys to portability: the battery

Viorel C-tin PETRE
University Politehnica, 313 Spl. Independentei, Bucharest, Romania, viorel.petre@upb.ro

Abstract. Dealing with battery problems and aspects is still an open subject for engineers. A lot of ways to control the process of using batteries exist all over. For better results, users need to know more about different types of batteries. An important fact is underlined in the paper: in the case of "smart batteries" or for system controlled ones, a lot of information and data are available for the user but they stay hidden inside the system.

1. Introduction

Everyone may easily notice the fast development of electronics in this time. Mp3 players, mobile phones, photo cameras, tablets, laptops, even hybrid or electric cars and so on, with all sort of capabilities are coming out on the market almost every month. All of this, have however at least one thing in common: the (rechargeable) battery. In most cases, it can be one of the following: lithium ion (Li-ion), lithium ion polymer (Li-ion polymer), nickel metal hydride (NiMH), nickel cadmium (NiCd) or lead–acid.

The first thing a user becomes aware about the battery, is how "good" is it (comparing with the manufacturer statement), which minds how much autonomy it offers over time, with all the user requirements from the device.

The second one, is the accuracy of the power meter (indicator).

2. Some examples

The market is filled with all sorts of devices for controlling the charging and discharging processes and for displaying information for the user, from simple to sophisticated circuits and from cheap to expensive ones. Production costs are very important and they have a big impact over quality.

Moreover, it appears that device manufacturers using incorporated batteries recommend different ways of maintenance.

Let's see an example of a portable player with AAA type rechargeable battery. So, power monitoring circuit and charging circuit are separated. Figure 1 shows the first important thing: the displayed information about battery status with **only 3 steps** of indication.

Fig. 1 Battery status of a portable player

The second thing to notice is the tricky way of indication: even if the battery is fully charged, the 3rd step will last a short time comparing with steps 2 and 1. This behavior indicates a poor development of the power monitoring circuit.

Let's take a short look to a charger for NiMH and NiCd batteries [1]. Two important aspects are stated in the instruction guide: "*l) longer life for rechargeable batteries because of the **gentle charging** process; ll) after 12h, changeover from standard to **trickle charge**, signaled by the LED. By leaving the batteries in the plugged-in charger, you will have freshly charged batteries at any time, because of the trickle charge mode*".

There is also a table indicating charging times for the different battery sizes (Table 1). So, we're dealing with a charging process, manually adapted to the battery's capacity.

Table 1 Example of charging times

Temps de charge recommandé · Recommended charging times								
Size · Dimensione	AAA	AAA	AAA	AA	AA	AA	AA	9V
Tension Nominale Rated Voltage				1.2V				9V
Capacité Capacity	700 mAh	750 mAh	800 mAh	1400 mAh	1700 mAh	1900 mAh	2100 mAh	150 mAh
Courant de charge Charging current	110 mA	110 mA	110 mA	260 mA	260 mA	260 mA	260 mA	20 mA
Temps de charge (h.) Charging time (hrs.)	9,5	10,2	10,9	8,1	9,8	11	12	11,3

The user has also to take care of the data from the battery. For example: NiMH 850 - charge 16 hours at 85 mA (**10 %** of capacity !) or NiMH 900 - charge 7 hours at 180 mA (**20 %** of capacity !).

For another example of a portable player with incorporated rechargeable battery, one can find **an only indication** about the battery: "*Excessive charging or discharging may shorten the battery life*".

Let's see the case of a mobile phone. First thing to notice, at a group of such devices, is shutting down when the battery still has a certain amount of power. A known fact about mobiles' batteries is that they are Li-ion or Li-ion polymer type. Here it is what indications we can find: "*l) do not leave a fully charged battery connected to a charger, since **overcharging** may shorten its lifetime; ll) if left unused, a fully charged battery will lose its charge over time; lll) leaving the battery in hot or cold places will reduce the capacity and lifetime of the battery*".

When coming to the case of a laptop, things are different. We can get data about the remaining capacity expressed in hours and in percentage (Figure 2).

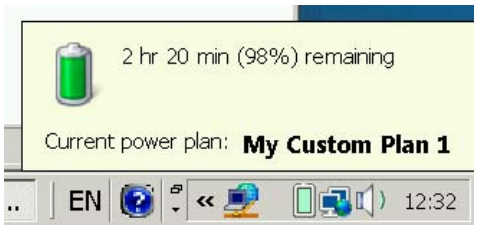

Fig. 2 Battery status of a laptop computer

Moreover, the user can set thresholds of alarming and actions related to them (Figure 3).

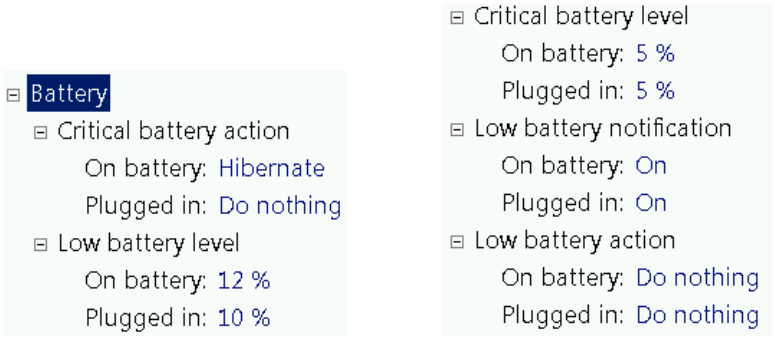

Fig. 3 Thresholds of alarming and actions for a laptop computer

Interesting information is written down for the user, related to Li-ion batteries: "*To ensure that the battery pack maintains its maximum capacity, operate the computer on battery power* ***at least once a month*** *until the battery pack is* ***fully discharged****. If the computer is continuously operated on AC power for an extended period, more than a month, the battery may fail to retain a charge. It may not function efficiently over the expected life of the battery and the battery indicator may not indicate a low-battery condition. The life of the battery pack is generally about 500 recharges*" [2].

Finally, the operating system of a laptop computer may have additional information and recommendations for the users. Here it is an example: "*Battery hardware and sensor circuitry. Li-ion batteries gradually lose their capacity to store energy as they age, whether or not you charge them. Over time, this change in storage capacity significantly affects the accuracy of the battery meter. If you frequently drain and then recharge a Li-ion battery, it can quickly lose its ability to hold a charge. The practice of completely draining and then fully charging a battery is advice that applied to NiCd batteries and, to a lesser extent, NiMH batteries.* ***Li-ion batteries last longer if you charge them often, a little at a time,*** *to maintain a* ***minimum charge of about 40 percent capacity****. Other factors that influence the accuracy of the battery meter are the circuitry that measures battery temperature and power consumption, and the equations that the circuitry uses to estimate the remaining charge and time. Newer, "smart" batteries are equipped with circuitry that calculates these measurements and reports the information to the battery meter.* " [3].

And here it is another way of dealing and using batteries: "*Battery Calibration. The fuel gauge has the inherent drawback that it needs periodic calibration, also known as capacity* ***re-learning****. This is unfortunate, but* ***is required*** *to correct the tracking error that develops between the chemical and digital battery over many charge and discharge cycles*" [4]. More information is suplied at the mentioned reference.

One can observe that there are different recommendations concerning the use of the batteries so the user must analyse and act the way he thinks is better.

3. A short look inside a "smart battery"

When speaking about rechargeable batteries we have "3 players on the scene": the battery, the charger and the (power) monitoring circuit. A charger can not operate without any control. If the monitoring circuit is inside the battery and is communicating with the charger or is controlling it in a smart and sophisticated manner, then we have a smart battery.

A very used system is the SBS (Smart Battery System) which uses the SMBus (System Management Bus) communication between the monitoring circuit and the charger [5]. Let's take, as an example, a gas gauge integrated circuit with SMBus interface, used to maintain an accurate record of available battery charge for NiCd, NiMH, and Li-Ion chemistries [6]. As seen

in Table 2, a set of about **50 data** (20 points for flags and alarms and the rest about electrical and technical data) are available inside the system ! Depending on the manufacturer, a very limited number of data are transmitted and displayed to the user (generally the Relative state of charge, the Runtime to empty and the 2 corresponding alarms). The rest of the data stay hidden inside the system but can provide useful and valuable information about the battery.

Table 2 Battery data used in SBS

Initial data	Measurements	Flags	Alarms
Design capacity	Voltage	Initialized	Remaining capacity
Design voltage	Current	Valid charge	Remaining time
Voltage offset	Average current	Valid discharge	Over-charge
Voltage gain	Temperature	Fully charged	Over-temperature
End of discharge voltage 1	Cycle count	Fully discharged	Terminate charge
End of discharge voltage final	Battery mode	Over-voltage	Terminate discharge
Charging current	Relative state of charge	Over-current	$\Delta T/\Delta t$
Fast charging current	Absolute state of charge	Low temperature fault	
Maintenance charge current	Full charge capacity	Stop EDV*	
Current measurement gain	Remaining capacity	First EDV	
Current integration gain	Runtime to empty	Final EDV	
Maximum charge temperature	Average time to empty		
Temperature offset	Battery status		
Self-discharge rate	Max error	* End of discharge voltage	
Charge compensation			
Hold-off timer			
Device chemistry			
Manufacturer name			
Manufacture date			
Serial number			
Device name			

4. Conclusion

The users have to instruct themselves about the proper use of the device's battery (corresponding to a certain type) in order to ensure a long life for it. That should not be limited to the manufacturer indications.

The price has a big impact over quality of the power controlling and monitoring circuits.

For smart batteries, an extended useful knowledge and data about the battery is available (but hidden) inside the system.

References

[1] www.varta-consumer.com (Chargers)
[2] http://eu.computers.toshiba-europe.com
[3] www.microsoft.com (Windows Vista)
[4] http://batteryuniversity.com
[5] http://sbs-forum.org/specs
[6] www.ti.com (BQ2092)

Digital mixer with current steering DAC

Cătălin BRÎNZEI, Florin CONSTANTINESCU, Iulian URSAC
"Politehnica"University Bucharest, Spl. Independenţei 313, 060042,Romania

Abstract. A new approach of a fully differential transmitter for a multi-standard communication system is proposed in this paper. The main components consist of a digital multiplier combined with a DAC (digital-to-analog converter). This architecture has some important advantages given by the digital blocks such as the low power consumption, speedy operation, robustness and portability over a wide range of technologies.

1 Introduction

A frequency mixer combined with a DAC (digital-to-analog converter) is proposed and it is the main component of an almost all digital transmitter chain. The operands or signals in binary format which need to be multiplied are computed on the DSP level (base band) and are sent to a Wallace tree digital multiplier [1]. The output of the digital frequency mixer is an eight bit word and represents the multiplication of the input signals. The digital-to-analog converter uses as input the output of the digital multiplier and generates an analog voltage corresponding to the digital word. The main up-conversion at high frequency is performed by using a quadrature modulation employing two mixers. These two I and Q mixers are driven by a LO (Local Oscillator) signal and are embedded in the output of the current steering DAC and also share the same biasing current minimizing in this way the power consumption.

2 Block diagram and principle of operation

The most important advantages of this architecture are the low power consumption and low SFDR (Spurious Free Dynamic Range) which is around 67dB. The proposed mixer achieves a high spectral purity by using a minimal analog circuitry in the output represented by an optimized DAC. Because of this hybrid implementation, this circuit can be easily implemented in a digital CMOS technology enabling a low voltage and low power architecture.

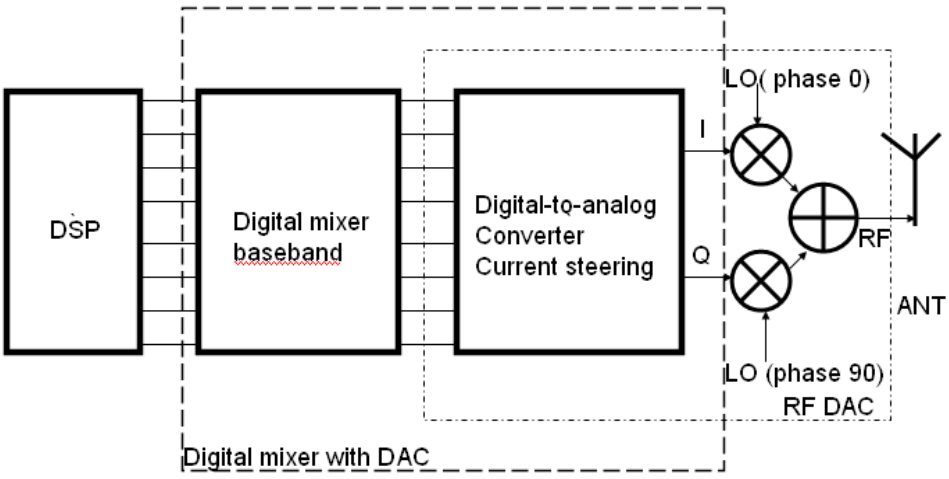

Figure 1: Transmitter chain using a digital mixer and DAC, block diagram.

The performance of the entire chain is limited by the performance of the analog part so the DAC will play an important role for this architecture. The chosen DAC topology is a segmented one and it is actually a hybrid between the binary weighted topology and the thermometric encoded topology. The most significant (MSB) five bits are thermometric coded since the variation of the

current is significant and the other least significant three bits (LSB) are binary weighted coded since the variation of the current is smaller.

This architecture is preferred since it exhibits a good linearity looking to the static parameters, even if we encounter large process variations on wafer. The second advantage is the low area consumed on the die lowering the production cost. The optimum segmentation number showing a good linearity has been proved to be between four and seven [2]. We chose a five plus three segmented architecture (five thermometric coded bits and three binary weighted bits) so the converter has eight bits. Basically a current steering DAC is based on an array of matched current sources and the input digital word is divided in five MSB which control thirty-one unary weighted current sources using a binary to thermometer decoder and three LSB bits which control the binary weighted current sources.

The current cells are properly biased using simple current mirrors and it is expected to use a supply which has a low voltage drop. These kinds of supply blocks are usually present on mobile communication platforms and because of this the biasing schematic is relaxed for our digital mixer with DAC. The current cell consists in a simple open drain differential pair which is biased using a cascoded current source. The utilization of the cascodes is mandatory since the DAC‘s output impedance depends on the output impedance of the current source and this should be as high as possible to minimize the errors in the output.

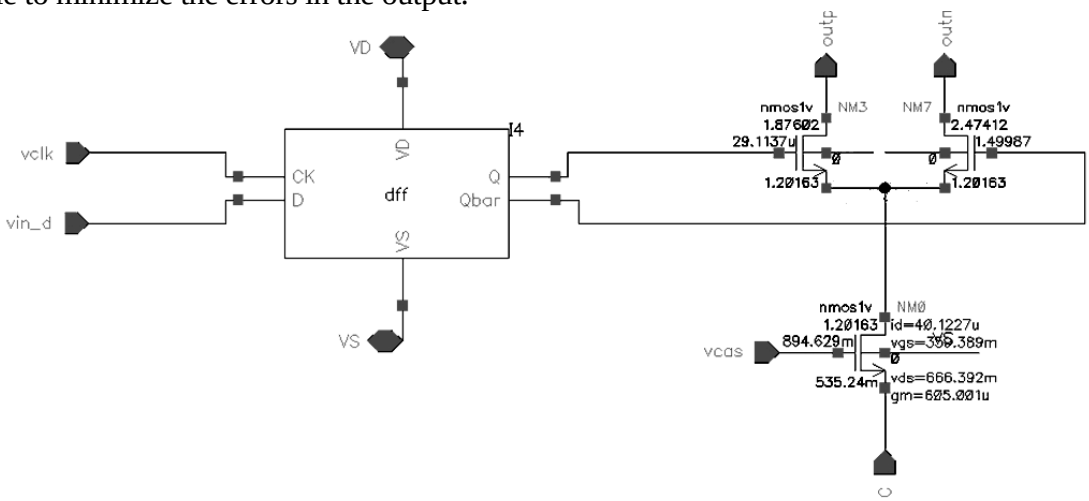

Figure 2: DAC current cell

The basic current cell consists of a cascoded current mirror (transistor NM0) which is connected to the resistive output load using MOS switches (transistors NM3 and NM7). The transistor NM0 is stacked over another current source transistor which is placed on biasing block of the proposed DAC. The C input of the current cell represents a current input and that connection is routed from the current cell up to the biasing block location. Since the principle of the biasing current transfer is implemented, the effects of parasitics extracted from the layout of each cell is minimized and the design becomes more robust. For example the output impedance of the current source which is high from the biasing block will be in series with the parasitic resistance of the wire which is quite low and it gives an overall impedance where the output impedance of the current source is the dominant factor. For synchronization purposes a flip-flop is used which drives the MOS switches [4]. Since the thermometric coded unary current sources occupy a significant area on chip it is possible that, due to different lengths for routing, the commutation timing of the switches varies randomly and because of this a clocked latch (differential flip-flop –dff) is implemented near the switches. The commutation decision is made on the positive edge of the clock (CK) signal which represents actually the DAC update frequency. The current reference generated on the biasing side is chosen to be 20uA and is doubled by the M0 transistor (Fig. 3) and

used as biasing for DAC's current cells. The 40uA current is the value of a unary current cell controled by the MSB side of the DAC which uses a thermometric decoder.

3 Power consumption and W/L sizes of the current sources and switches

For the architectures using steering MOS current sources the power consumption is given mainly by the analog part and hence by the sum of all thirty one unit current sources. The analytical expression of the power consumption is given below:

$$Ptotal = (2^n - 1) * I * VD25 \quad (1)$$

The index n represents the total number of bits which is eight in this case. I shows the unit current source value of 40uA for the unary MSB and 5uA for the binary weighted LSB. VD25 is the voltage supply of the analog part.

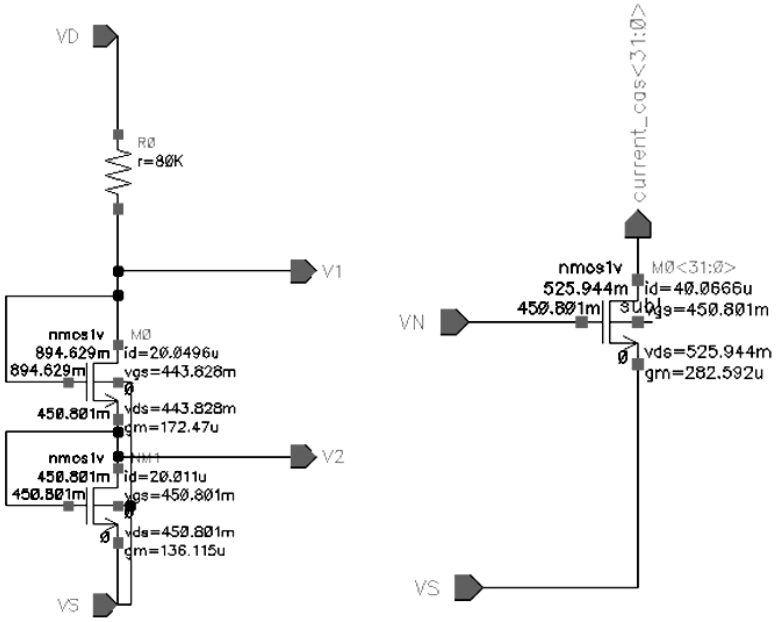

Figure 3: Biasing block

The maximum power consumption is determined by:

$$Ptotal = 255 * 5uA * 2.5 = 1275uA * 2.5V = 3.18mW \quad (2)$$

Considering the process parameter given by the technology being $K = \mu_n * Cox = 320uA/V^2$ results that the form factor W/L of the current source is approximatively around four. For a channel length of L=450nm results a W of 2um. Using the transistor equation in saturation, the analytical sizing method is given below:

$$I = \frac{\mu * Cox}{2} * \frac{W}{L} * (V_{GS} - V_{TH})^2; V_{GS} = 0.5; V_{TH} = 200mV$$
$$K = \mu * Cox = 320uA/V^2; I = 40uA; \frac{W}{L} = \frac{2 * I}{K * (V_{GS} - V_{TH})^2} = \sim 4 \quad (3)$$

The drain-source resistance of the switch is calculated for the transistor in triode region:

$$\frac{\partial I}{\partial V_{DS}} = Rout = \frac{1}{\frac{1}{2}\mu Cox \frac{W}{L}(V_{GS} - V_{TH})} \quad (4)$$

Due to speed requirements a minimum value for L (120nm) should be considered but W cannot be too high since this will increase the parasitic capacitance and errors due to the charge injection in the output will increase [3]. It has been appreciated that 2um is a good choice for the width of the MOS switch. The output current needs to charge and discharge the load capacitor from the output of the DAC, which is relatively big considering that all the basic current cells are summed in the output and the parasitic capacitor is significant. The estimated total capacitor value in the output node is 2.5pF and the needed current to charge and discharge it is determined by:

$$I = C * \frac{\Delta V}{\Delta T}, I = 1.275mA, C = 2.5pF, \Delta V = 1.3V$$
$$\Delta T = \frac{\Delta V * C}{I} = 2.54nS -> Freq_{MAX} = 393MHz \quad (5)$$

It can be determined that the maximum operation speed is 393MHz when the load resistance is 500Ω. The operation speed can be increased by the future implementation of the concept of RF DAC which means that an additional up conversion mixer, which employs the same biasing current as the main DAC, is placed in the output.

4 Simulation results

DAC transfer function

All possible digital codes to the input of the DAC have been successively applied and the analog voltage has been determined at the output.

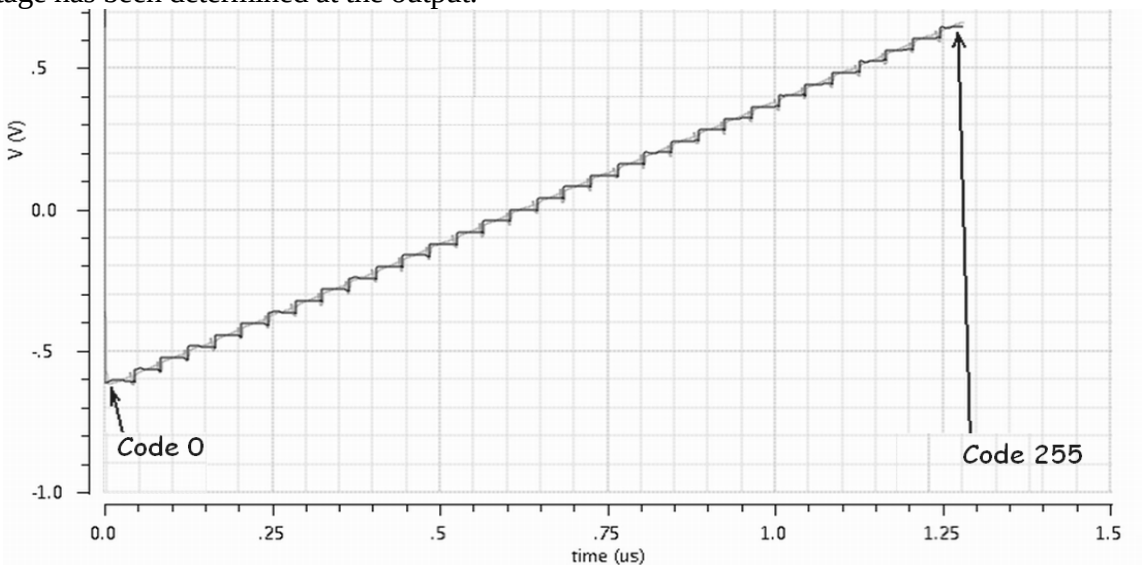

Figure 4: DAC Output with and without binary weighted bits active

Static performance parameters INL and DNL

The most important static error parameters for a DAC are the INL („Integral Non Linearity") and DNL („Differential Non Linearity") and have been computed based on the simulations results obtained with SPECTRE.

A Spurious Free Dynamic Range of 67dB has been obtained while using a maximum current consumption Imax of 1.275mA. The maximum power consumption Pmax is 3.18mW and the DNL and INL are 0.41 LSB and 0.48 LSB respectively.

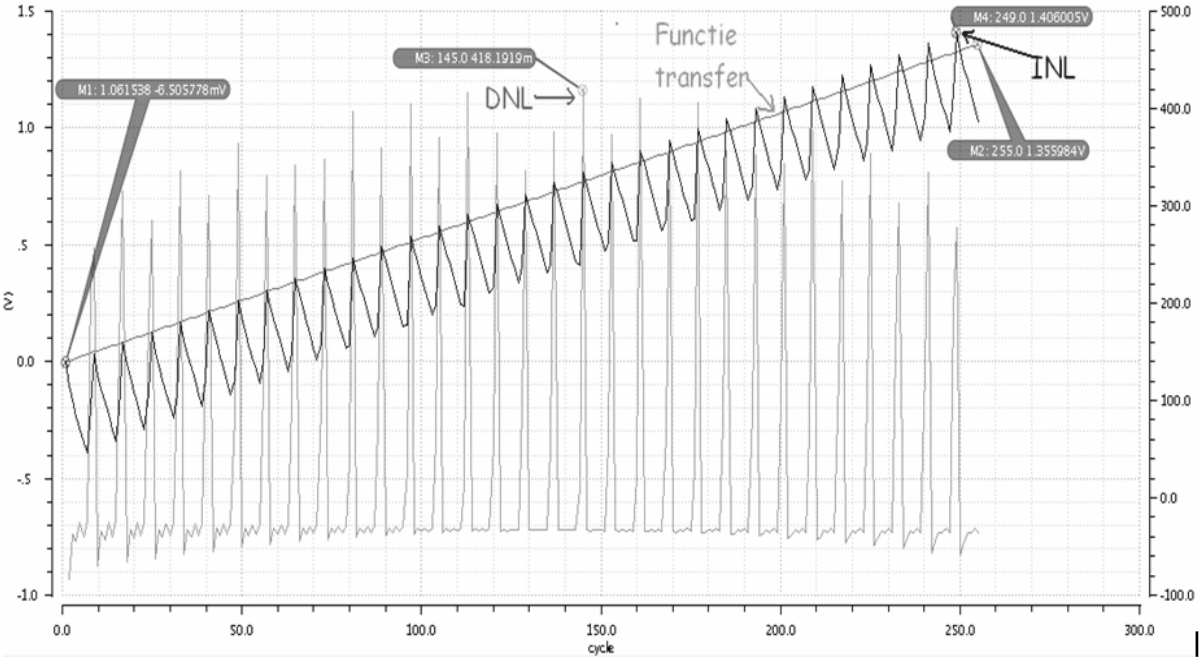

Figure 5: INL, DNL and transfer function for a segmented DAC

Digital multiplier

The schematic of the digital multiplier implemented with CMOS gates is given below and represents a detail of the digital mixer block shown in Figure 1.

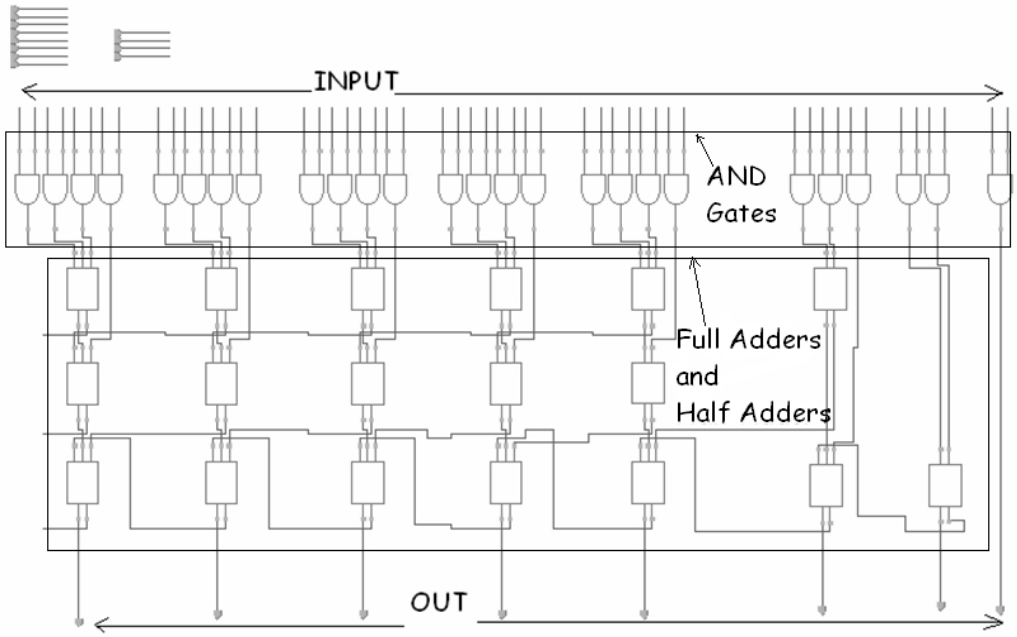

Figure 6: Digital multiplier

Output spectrum for the digital mixer

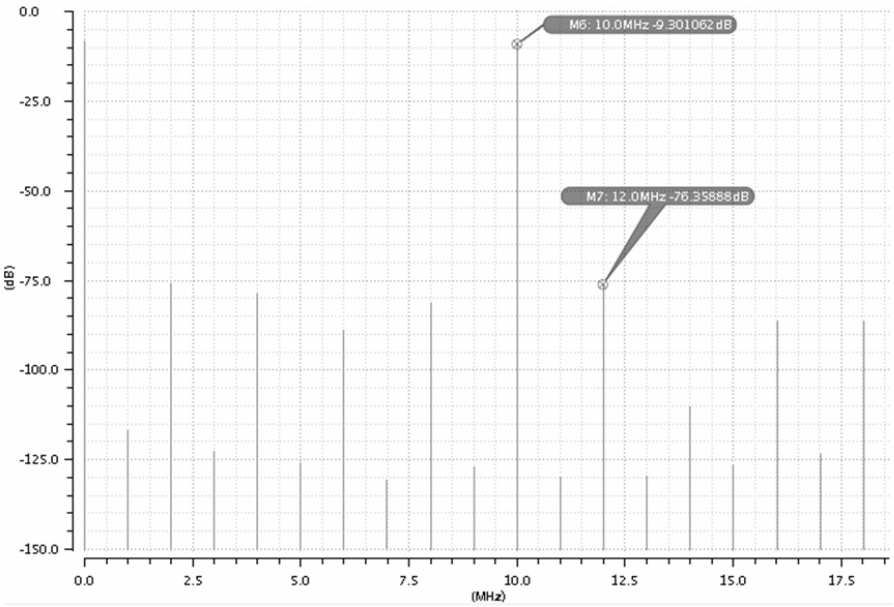

Figure 7:Output spectrum

5 Conclusions

▪ The working frequency for the proposed implementation is estimated (up to 400MHz) as much higher than that reported in [5]. The output bandwidth may increase to cover more standards like GSM, Bluetooth if a RF DAC is implemented in the output.

▪ The shown architecture has some common aspects with some low speed architectures described in literature but those were not used for the transmission chain at high frequency. An important contribution consists by using of some special techniques in design to overcome the effect of the parasitics from layout.

▪ The SFDR parameter which is 67 dB shows a good spectral purity for the proposed architecture and if we compare to [5] where an SFDR of 52dB is reported we can conclude that this solution is suitable for GSM and blootooth applications.

▪ Static parameters INL=0.48LSB and DNL=0.41LSB are showing good performances.

▪ The performances shown above including the low power consumption due to the use of the digital circuitry are very attractive and we can predict that the analog mixing will be replaced soon by the digital one in all consumer electronic devices.

References

[1] N. Rahman, R. Yun, *8x8 Booth-Encoded Wallace Tree Multiplier*, Tufts University, Dept.of Electrical and Computer Engineering, 2011.

[2] Hugo Hernandez, Wilhelmus Van Noije, Elkim Roa, *Design strategy of current source in current steering*, Integrable Systems Laboratory – Polytechnic School of San Paulo University, 2011.

[3] Jacob Wikcner, *Studies on CMOS digital-to-analog converters*, Linköping Studies in Science and Technology, 2001.

[4] Sam Blackman, *A Low Power, 8-bit, 200 MHz Digital-to-Analog Converter*, College of Engineering University of California, Berkeley, 1999.

[5] P. Sotiriadis, W. Ling, *Almost All-Digital Sinewave-Product Generation for Frequency Synthesis Applications*, Frequency Control Symposium, Joint with the 22nd European Frequency and Time forum. IEEE International, 2009.

THD Analysis in multi-level converters

Eng. Cristina Chiorean, PhD Candidate, Eng. T. Vaida, PhD Candidate,
Prof. Eng. H. Bălan, PhD
Technical University of Cluj Napoca, 28, Memorandumului Street, Cluj Napoca, Romania

Abstract. The issue of developing offshore sustainable energy has brought on the need of implementing better solutions for the transport and grid insertion of the produced energy. This paper presents a comparative analysis of the performance of different multi-level converters topologies. Using the CTS California Instruments System, several multi-level converting topologies were simulated, along with the influence of the level number on the total harmonic distortion.

1. Introduction

The development of converter topologies has been influenced by the development of "off-shore" renewable energy sources and the issue of the transportation and injection of the energy thus produced. A simplified scheme would be: rectifier – DC transport – DC conversition – voltage injection into the grid.

The total harmonic distortion THD will be reduced by increasing the number of levels. It is clear that an exit pressure with a small total harmonic distortion is desirable, but the increase in the number of levels requires more components, which also means that the control method will be more complicated. This calls for a compromise between price, weight, complexity and a very good voltage output with a small total harmonic distortion.

Previous works on the subject matter were more focused on the THD and the switching pattern of the multilevel inverters. Past papers were more focuse on the issue of utilizing different patterns in order to achieve a better output voltage and current with lower THD. The importance of the switching angles cannot be stressed enough, because it can affect the THD of both output current and voltage.

2. Multi-level converters

In general, the batteries used in most applications are in DC mode and the motor that drives the wheels is usually in AC mode, thus it is necessary to convert from DC to AC, using a power converter. To achieve this, the easiest topology is one comprised of a two-level converter made of four switches. This topology uses anti-parallel diodes in each switch.

There are also other topologies available to us, one of them being a power electronic system that synthesizes a sinusoidal voltage output from several DC sources called a multilevel converter. Fuel cells, solar cells, ultra capacitors, etc all can act as viable DC sources for the converter. The purpose behind the design of the multilevel converter is to obtain a a better sinusoidal voltage and current output by using switches in series. Therefore, by using switches in a series configuration, the importance of the switching angles becomes apparent, because the voltage and current output must have a low harmonic distortion[4].

The multilevel converters can be: diode clamped multilevel converters, flying capacitor multilevel converters, cascaded H-bridge multilevel converters.

2.1. Diode Clamped multilevel converter

The concept behind this type of multilevel converter is the use of diodes to limit the power devices voltage stress. The voltage over each capacitor and each switch is Vdc. An n level converter needs (n-1) voltage sources, 2(n-1) switching devices and (n-1) (n-2) diodes.
In a 5-level diode clamped multilevel converter: n=5. Therefore:Number of switches=2(n-1)=8; Number of diodes= (n-1) (n-2) =12;Number of capacitors= (n-1) =4.
A 5-level diode clamped multilevel converter is shown in Fig. 1. To achieve a specific output voltage, e.g. Vdc/2, switches S1 to S4 should conduct at the same time. For each voltage level, four switches must conduct. The output voltage has a maximum value equal to half the value of the DC source. This is one the main disadvantages of the diode clamped multilevel converter. To solve this, we can use a voltage source twice as bigger or we can cascade two diode clamped multilevel converters. In order to attain the lowest THD of the output voltage, it is necessary to calculate the switching angles accordingly. This is accomplised by using the harmonic elimination method. This method allows the elimination of the lower dominant harmonics by choosing calculated switching angles.

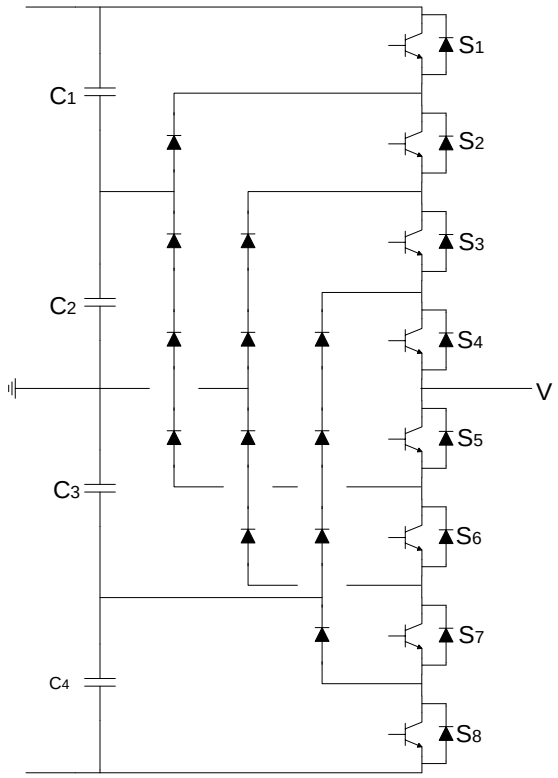

Figure 1. One phase of the 5-level multilevel converter

3. Harmonic elimination methods

Regarding the switching pattern, this paper uses for all multilevel converters the harmonic elimination method. This method is based on the elimination of the lower dominant harmonics when calculating the switching angles. The paper focuses on 5-level converters, in which case the 5th harmonic will be eliminated. In other cases, such as the 9-level converter, the 5th, 7th, 11th harmonics will be eliminated. To achieve this, we need to determine the frequency spectra of the output waveform through the Fourier analysis [5].

3.1. Calculation examples

The Fourier series of a 5-level unity DC source is shown in (1):

$$f(t) = f_{\theta_1}(t) + f_{\theta_2}(t) = \frac{2V_{dc}}{\pi}\sum_{n=1}^{\infty}[\cos(\mathrm{h}\theta_1) + \cos(\mathrm{h}\theta_2)] = \frac{2V_{dc}}{\pi}\sum_{h=1}^{\infty}\left[\sum_{i=1}^{2}(\cos(\mathrm{h}\theta_i)\frac{\sin(h\omega t)}{h})\right] \quad (1)$$

Where:

V_{dc} - Voltage of each voltage source that is unity

θ_i – The switching angles

h – The harmonic orders

From (1) four equations will be resulted for eliminating the harmonics 5th.

$$V_{dc} = V_1 + V_2$$

$$\frac{2V_{dc}}{\pi}(\cos\theta_1 + \cos\theta_2) = h_1 \quad (2)$$

$$\frac{2V_{dc}}{\pi}(\cos 5\theta_1 + \cos 5\theta_2) = h_5 \quad (3)$$

Equations (2) and (3) refer to the harmonics that should be eliminated, so (3) should be equal to zero. The DC sources are constant, so:

$$V_{dc} = 2V_1 \quad (4)$$

$$M = \frac{h_1}{2V} \quad (5)$$

The modulation index is 1 since the voltage that is used in these calculations is in per unit. From (2) to (5) the nonlinear equations will be calculated.

$$\cos\theta_1 + \cos\theta_2 = \frac{\pi}{2} \quad (6)$$

$$\cos(5\theta_1) + \cos(5\theta_2) = 0 \quad (7)$$

The equations are solved using the Newton-Raphson method, which calls for the creation of the following matrixes:

1. Switching angles matrixes

$$\theta = \begin{bmatrix}\theta_1 \\ \theta_2\end{bmatrix}$$

2. The nonlinear system matrix

$$F = \begin{bmatrix}\cos\theta_1 + \cos\theta_2 + \cos\theta_3 + \cos\theta_4 \\ \cos 5\theta_1 + \cos 5\theta_2 + \cos 5\theta_3 + \cos 5\theta_4\end{bmatrix}$$

$$dF = \begin{bmatrix}-\sin\theta_1 & -\sin\theta_2 \\ -5\sin 5\theta_1 & -5\sin 5\theta_2\end{bmatrix}$$

3. The answer matrixes

$$t = \begin{bmatrix}\frac{\pi}{2} \\ 0\end{bmatrix}$$

$$d'F = \frac{T - F}{dF}$$

For each iteration loop

$$\theta_{nouă} = \theta_{veche} + d'F$$

Applying MATLAB iterations, the switching angles for a 5-level and 9-level multilevel converter are calculated.

Θ_1=16.3286^0 θ_2=52.3286^0

4. Simulations and experimental results

An important part of the California Instruments CTS System is the power analyzer in compliance with the IEC standards, which provides detailed information regarding the voltage and the current. Measurements of both harmonics and interharmonics are made in real-time with no measurement gaps to fully conform to the latest revision of the IEC 61000-4-7 test standard [10].

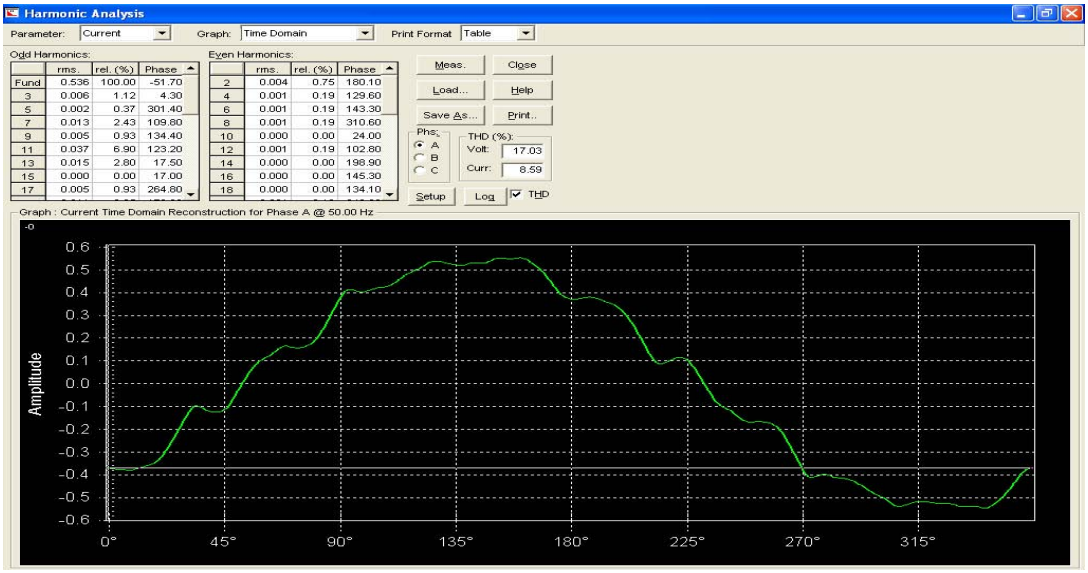

Figure 2. The current for a 12-level converter

For a better comparison between converters, we used the CTS system to simulate the output values of multilevel converters with 12 levels and 24 levels, respectively. The scope of the simulations was to compare THD values in regard to the number of levels per converter. The THD current value decreases from 8.59% to 4.67% and the THD voltage value decreases from 17.03% to 11.89%. It is noticeable the decrease in THD value, but we must also point out that it involves an increase in costs and weight.

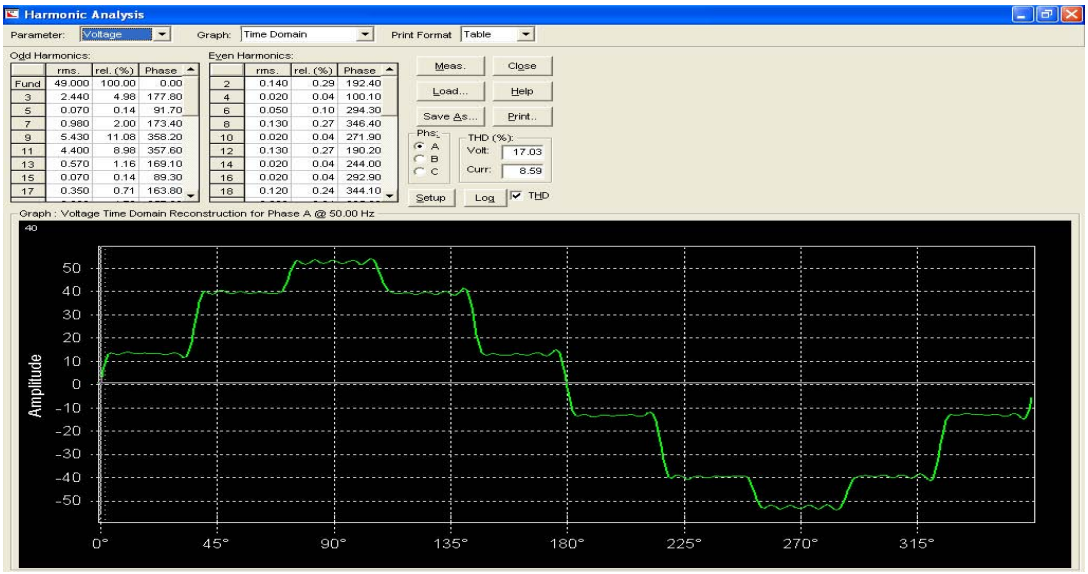

Figure 3. The voltage for a 12-level converter

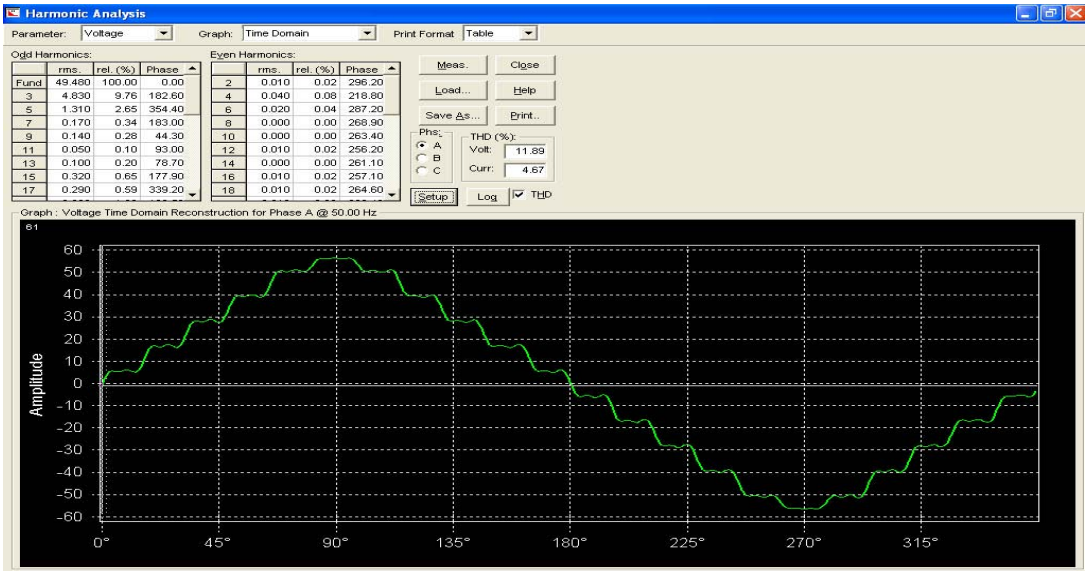

Figure 4. The voltage for a 24-level converter

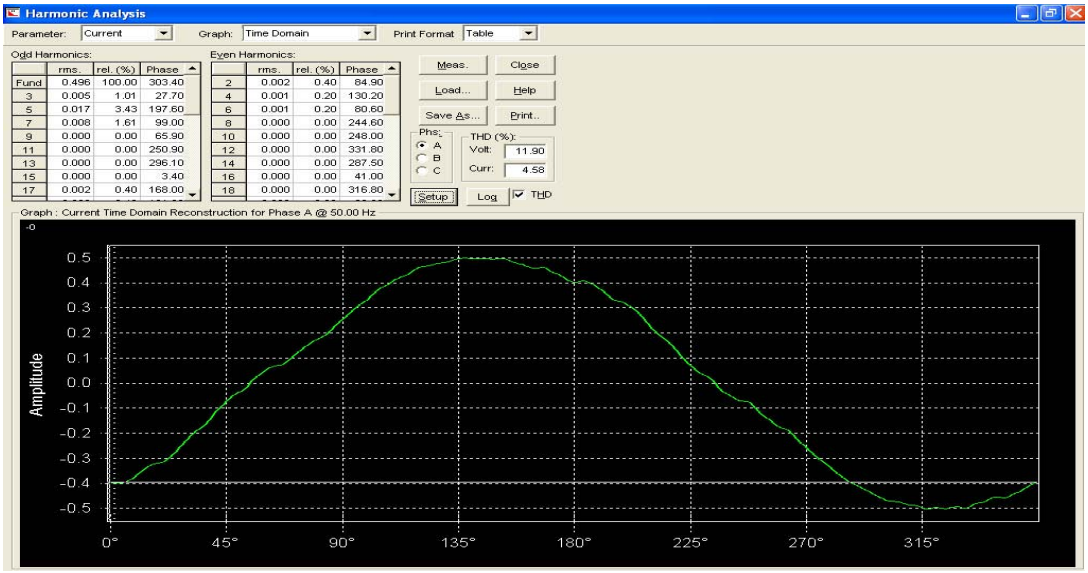

Figure 5. The current for a 24-level converter

5. Conclusions

Choosing the topology for a converter must take into account the intended usage of said converter. Each topology has certain advantages and disadvantages. By increasing the number of levels, the THD value will decrease, whereas costs and weight will increase. Furthermore, because the switching angles are not identical, each switch has a separate control circuit.

The two-level converter has the lowest cost and weight compared to other converter topologies. Moreover, this converter has a very high THD value, approximately 40% when the commutation occurs on the fundamental harmonic. When calculating the final cost and weight, the cost and weight of the filter must be taken into account, because it is not efficient to have a output voltage with a 40% THD value. Thus, the cost and weight of the 5-level converter seem to be preferable to the 9-level converter. By increasing the number of levels, the cost and weight of the converter will increase. The advantage of the 9-level converter compared to the 5-level converter is given by the lower THD value.

The THD values for 5-level converters and 9-level converters are 15% and 7%, respectively. However, a filter is necessary, thus a configuration comprised of a 5-level converter and a filter is more adequate.

Acknowledgements
This paper was supported by the project "Improvement of the doctoral studies quality in engineering science for development of the knowledge based society – QDOC" contract no. POSDRU/107/1.5/S/78534, project co-funded by the European Social Fund through the Sectorial Operational Program Human Resources 2007-2013.

References

[1] Leon M. Tolbert, Fang Zheng Peng, Tim Cunnyngham, John N. Chiasson, *Charge balance control schemes for cascade multilevel converter in hybrid electric vehicles,* IEEE transactions on industrial electronics, Vol.49, 2002

[2] John N. Chiasson, Leon M. Tolbert, Keith J. McKenzie, Zhong Du, *Control of a multilevel inverter using resultant theory*, IEEE transaction on control systems technology, Vol.11, 2003

[3] Fang Z. Peng, *A Generalized Multilevel Inverter Topology with Self Voltage Balancing*, IEEE transaction on Industry applications, Vol. 37, 2001

[4] L.M. Tolbert, F.Z. Peng, D.J. Adams, J.W. Mckeever, Multilevel inverters for large automotive electric drives, 1997, Darborn, Michigan

[5] Mohammadreza Derakhshanfar, *Analysis of different topologies of multilevel inverters,* Department of Energy and Environment Division of Electric Power Engineering, Chalmers University of Technology, Göteborg, Sweden, 2010

[6] Leon M. Tolbert, Fang Z. Peng, *Multilevel Converters as a Utility Interface for Renewable Energy Systems*, Power engineering society summer meeting, 2000, IEEE

[7] Leon M. Tolbert, John Chiasson, Keith McKenzie, Zhong Du, *Elimination of harmonics in a multilevel converter with non equal DC sources,* IEEE transaction on Industry applications, Vol.41, 2005

[8] D. Grahame Holmes, Thomas A.Lipo, *Pulse width modulation for power converters*, 2003 by Wiley interscience Inc.

[9] Busquets-Monge, S., Rocabert, J., Rodriguez, P., Alepuz, S., Bordonau, J., *Multilevel diode-clamped converter for photovoltaic generators with independent voltage control of each solar array*. IEEE Transactions on Industrial Applications 55 (7), 2713–2723, 2008

[10] Jianlin Li,Ying Zhu,Hongyan Xu,et al, *CPS-SPWM flying capacitor three-level back-to-back converter applicative direct-drive wind power generator system*, SUPERGEN'09, International Conference on Sustainable Power Generation and Supply, 2009, pp.1-6.

[11] Compliance Test System - User Manual CTS 3.0, California Instruments

ALGORITMI DE OPTIMIZARE EVOLUTIVI UTILIZAȚI ÎN PROIECTAREA DISPOZITIVELOR DE ÎNCĂLZIRE PRIN INDUCȚIE

Mihaela NOVAC[1], Ecaterina VLADU[1], Ovidiu NOVAC[1], Adriana GRAVA[1]
[1]*Universitatea din Oradea, Facultatea de Inginerie Electrică şi Tehnologia Informaţiei,*
Str Universităţii Nr.1, Oradea, Romania, mnovac@uoradea.ro

Abstract. În lucrare se prezintă optimizarea parametrilor geometrici ai unui inductor, folosind patru algoritmi de optimizare evolutivi: AG (Algoritm Genetic), SA (Călire Simulată), DE (Evoluţie Diferenţială) şi AG multiobiectiv, iar în final se analizează şi se compară rezultatele. Algoritmii abordaţi se pot folosi în proiectarea dispozitivelor de încălzire inductivă, ei conducând la rezultate comparabile în raport cu obiectivele şi variabilele de proiectare considerate.
Cuvinte cheie*: Optimizare, AG (Algoritm Genetic), SA (Simulated Annealing – Călire Simulată), DE (Evoluţie Diferenţială) şi AG multiobiectiv.*

1 Introducere

O metodă de proiectare (în sens de optimizare) a unui dispozitiv electromagnetic necesită analiza mai multor configuraţii posibile. Mersul metodei de optimizare este influenţat de informaţiile rezultate dintr-o astfel de analiză. Din acest motiv, un aspect care trebuie rezolvat în vederea optimizării unui dispozitiv de încălzire prin inducţie îl constituie alegerea metodei de analiză a dispozitivului. Ca metode de optimizare pot fi folosite metode directe de căutare sau metode stochastice cum ar fi algoritmii genetici, călirea simulată şi evoluţia diferenţială.

Tehnicile de optimizarea sunt abordate în [3], [4], unde se face o prezentare pe larg a utilizării algoritmilor genetici în inginerie. Algoritmii genetici fac parte din categoria algoritmilor evolutivi, ei au fost introduşi de Holland,[5], fiind aplicaţi în multe probleme practice [1], [8] şi [9].

Călirea simulată (Simulated Annealing (SA)) a fost utilizată pentru prima oară în 1988 de Cornwell, la optimizarea unor reţele de antene. Este un algoritm care emulează procesul de călire industrială care conduce la mărirea performanţelor obţinute, fiind în esenţă folosit tot pentru optimizarea unui singur obiectiv [4].

Evoluţia diferenţială (differential evolution) este un algoritm evolutiv, propus în 1996 de Storn şi Price, folosit şi de către alţi cercetători la soluţionarea problemelor tehnice [2], [6], [7].

Cele mai multe probleme din lumea reală implică însă optimizări simultane a unui număr de două sau mai multe obiective. Pentru rezolvarea acestora s-au dezvoltat algoritmii multiobiectiv sau multicriteriu, care identifică o mulţime de soluţii numite soluţii Pareto optime, după numele economistului Vilfredo Pareto care a pus bazele optimizării multiobiectiv.

2 Optimizarea parametrilor dispozitivelor electromagnetice de încălzire prin inducţie

Scopul principal al dispozitivelor de încălzire inductivă este acela de a furniza temperatura necesară în piesă pentru următoarele stadii ale procesului tehnologic. Un astfel de dispozitiv trebuie să corespundă cu diferite criterii de performanţă, precum: distribuţia uniformă a temperaturii, timpul de încălzire cât mai redus, randament electric cât mai mare, ş.a.

Procesele de încălzire prin inducţie sunt caracterizate de un număr mare de variabile şi de restricţii tehnologice şi fizice, precum şi prin dificultatea formulării funcţiilor obiectiv. Din aceste motive, optimizarea acestor procese este o sarcină dificilă.

Algoritmii AG, SA şi DE folosesc în etapa de evaluare o mărime scalară care se obţine printr-o combinaţie liniară ale celor două obiective folosind coeficienţi de ponderare, în timp ce AG multiobiectiv are la bază conceptul Pareto optim.

În această lucrare se realizează modelarea numerică a procesului de încălzire prin inducţie electromagnetică a unei piese de secţiune cilindrică din oţel magnetic având diametrul de d_{piesa}=80mm şi lungimea piesei de L_{piesa}=200mm, diametrul inductorului de d_{ind}=90mm şi lungimea inductorului de L_{ind}=220mm. Parametri de proiectare sunt frecvenţa *f* a tensiunii de alimentare, lunginea inductorului L_{ind} şi întrefierul *h* dintre piesă şi inductor. Pentru analiza numerică s-a folosit metoda elementului finit (FEM), presupunând că permeabilitatea magnetică este constantă. Modulul numeric FEM analizează câmpul electromagnetic cuplat cu cel termic, având ca şi variabile de intrare *f*, L_{ind} şi *h*, efectuează modelarea şi evaluează soluţiile posibile returnând ca şi variabile de ieşire randamentul (rand) şi diferenţa de temperatură în piesă la sfârşitul încălzirii (ecart). Aceste valori sunt folosite de un AG simplu, un algoritm SA, un algoritm DE şi un AG multiobiectiv, aşa cum se observă în figura 1.

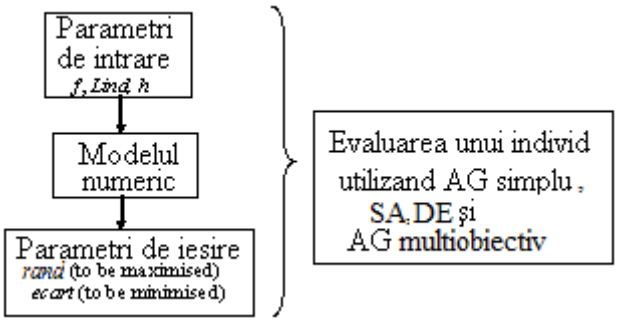

Fig 1: Modelarea numerică a dispozitivelor de încălzire prin inducţie

Piesa din oţel este încălzită de la temperatura iniţială θ_i=20°C până la valoarea medie a temperaturii piesei cilindrice la sfârşitul încălzirii θ_f=1300°C.

Domeniul de căutare al variabilei în toate cazurile este frecvenţa: f ∈ [250 3000] Hz, lungimea inductorului: L_{ind} ∈ [0.100 0.145] m, întrefierul: h ∈ [0.001 0.015] m şi densitatea de curent J_i=22 A/mm^2.

2.1. *Optimizarea parametrilor inductorului folosind AG simplu*

Deoarece AG simpli realizează implicit o maximizare a unei valori scalare se urmăreşte obţinerea unui randament maxim şi un ecart de temperatură minim, funcţia Fitness, care este o mărime scalară, se obţine folosind metoda coeficienţilor de ponderare, [4]. Metoda coeficienţilor de ponderare a fost prima metodă aplicată pentru generarea unor soluţii Pareto optime.

$$Fitness=w_1Ob_1+(1-w_1)Ob_2 \quad (1)$$

unde Ob_1 şi Ob_2 se maximizează.

Deoarece uzual randamentul ia valori în intervalul 0.1...0.9 [%], iar ecartul între 80....1000[°C], este necesară o transformare a obiectivelor de aşa manieră încât ele să ia valori în interval comparabile, astfel încât fiecare obiectiv să contribuie pe cât posibil în aceeaşi măsură la valoarea Fitness.

S-a considerat la început o funcţie obiectiv care îşi propune eliminarea influenţei domeniului de variaţie al celor două obiective astfel:

$$F_{obj} = w_1 \cdot \frac{(ecart - ecart_{min})}{(ecart_{max} - ecart_{min})} + (1 - w_1) \cdot \frac{(rand_{max} - rand)}{(rand_{max} - rand_{min})} \quad (2)$$

Deoarece AG simplu face implicit o maximizare a funcţiei Fitness, s-a ales o transformare a problemei de minimizare într-o problemă de maximizare printr-o divizare a lui F_{obj} de forma:

$$Fitness = \frac{1}{F_{obj}} \quad (3)$$

În scopul găsirii soluţiilor celor mai performante, problema s-a reluat pentru diferite valori ale lui w_1=0...1. Operatorii genetici de încrucişare şi de mutaţie au fost: încrucişare aritmetică cu probabilitate Pi=0.6 şi mutaţie simplă cu probabilitate de Pm=0.1.

Etapa de evaluare a indivizilor s-a realizat printr-o modelare numerică, folosind metoda elementelor finite, implementată cu toolboxul PDE din mediul Matlab. Am aplicat AG simpli, cu 25 indivizi şi 15 generaţii, considerând pe rând w_1=0; 0.1; ... 0.9; 1.

Rezultatele obţinute sunt prezentate în tabelul 1 unde avem: în coloana 1 valoarea coeficientului de ponderare, coloanele 2,3,4 parametri de intrare: frecvenţa -f, lungimea inductorului -L_{ind} şi întrefierul -h, iar în coloanele 5 şi 6 parametri de ieşire: diferenţa de temperatură -ecart şi randamentul -rand.

Tabel 1. Soluţiile obţinute cu AG

w1	f [Hz]	Lind [m]	h [m]	ecart [°C]	rand [%]
0.0	2447	0.1353	0.0125	150.1	69.52
0.1	1120	0.1460	0.0010	204.9	69.21
0.2	**1422**	**0.1242**	**0.0102**	**109**	**63.79**
0.3	2464	0.1279	0.0088	225.7	60.89
0.4	2846	0.1052	0.0109	182.8	59.27
0.5	2207	0.1097	0.0096	244.9	56.72
0.6	2154	0.1476	0.0114	199.7	53.05
0.7	256	0.1492	0.0148	157.9	50.65
0.8	2191	0.1373	0.0134	133.3	48.8
0.9	903	0.1002	0.0134	201.0	45.97
1.0	2383	0.1159	0.0010	184.2	38.83

O soluţie este cu atât mai bună cu cât randamentul este mai mare şi ecartul este mai mic.

Avantajul acestei metode este obţinerea unui număr mare de soluţii care permit proiectarea optimă a inductorului, dezavantajul fiind numărul însemnat de rulări necesare, ceea ce implică un timp mare de proiectare.

2.2. Optimizarea parametrilor inductorului folosind algoritmul de călire simulată (SA)

Algoritmul SA a fost utilizat într-o manieră similară cu AG. Metoda de codare folosită, precum şi combinarea obiectivelor folosind metoda coeficienţilor de ponderare sunt aceleaşi cu cele folosite în cazul AG, singura diferenţă fiind faptul că algoritmul SA realizează implicit o minimizare. SA caută un minim global al unei funcţii într-un spaţiu mai mare de căutate. Este un proces iterativ în care la fiecare pas soluţia curentă este înlocuită cu o soluţie aleatoare din vecinătate aleasă cu o probabilitate care depinde de un parametru numit temperatură globală T. S-au efectuat multiple rulări pentru diferite valori ale parametrului: w_1 = [0; 0.1; ...; 0.9; 1].

Rezultatele obţinute sunt prezentate în tabelul 2.

Tabel 2. Soluţiile obţinute cu SA.

w_1	f [Hz]	L_{ind} [m]	h [m]	ecart [°C]	rand [%]
0.0	**821**	**0.128**	**0.0132**	**227.29**	**61.43**
0.1	805	0.1414	0.0112	226.1	61.38
0.2	983	0.1437	0.0015	217.2	60.79
0.3	1231	0.1158	0.0011	194.5	60.32
0.4	781	0.1368	0.0118	227.4	61.19
0.5	1531	0.1206	0.0137	170.5	58.47
0.6	1168	0.1210	0.0143	200.6	60.26
0.7	1705	0.1337	0.0015	159.	57.67
0.8	2778	0.1289	0.0053	120.5	51.37
0.9	2781	0.1061	0.0071	120.6	51.36
1.0	2981	0.1241	0.0115	116.3	49.68

Examinând rezultatele obţinute, se observă că algoritmul SA funcţionează bine în rezolvarea problemelor de proiectare optimală, având acelaşi dezavantaj ca şi AG.

2.3. Optimizarea parametrilor inductorului folosind algoritmul de evoluţie diferenţială (DE)

Algoritmul DE este un algoritm de optimizare stochastic bazat pe populaţii. Ideea de bază a DE este o schemă pentru generarea unui proces de perturbare a unui individ din populaţia curentă cu diferenţele scalate a unor indivizi distincţi selectaţi aleatoriu, adăugând practic diferenţa ponderată dintre doi indivizi la un al treilea individ. Algoritmul DE a fost implementat în Matlab, folosind aceleaşi variabile de proiectare şi aceleaşi obiective ca şi algoritmii AG şi SA.

Am aplicat DE utilizând funcţia obiectiv dată de relaţia (2), pentru o populaţie de 40 indivizi şi algoritmul a evoluat 40 de generaţii, cu un factor de ponderare F = 0.8 şi cu o constantă încrucisare CR = 0.9, iar F_{obj} este minimizată. În scopul de a găsi mulţimea Pareto optimă, am efectuat multiple rulări pentru diferite valori ale coeficientului de ponderare: w=0; 0,1; ... 0,9; 1. Rezultatele obţinute sunt prezentate în tabelul 3.

Tabel 3. Soluţiile obţinute cu DE

w	f[Hz]	Lind [m]	h [m]	ecart [°C]	rand [%]
0	929	0.154	0.007	172.15	66.91
0.1	1000	0.120	0.005	150.66	66.88
0.2	637	0.142	0.003	118.61	66.76
0.3	1062	0.127	0.004	119.27	66.21
0.4	**1062**	**0.127**	**0.006**	**113.73**	**66.07**
0.5	1062	0.127	0.01	117.08	64.01
0.6	2637	0.144	0.003	313.36	62.36
0.7	1562	0.107	0.006	180.17	61.00
0.8	546	0.118	0.014	202.32	59.23
0.9	2550	0.132	0.009	225.00	58.91
1.0	2962	0.122	0.013	109.84	50.36

Examinând rezultatele obţinute, se observă că algoritmul DE funcţionează bine în rezolvarea problemelor de proiectare optimă. Un avantaj al metodei este faptul că rezultatele se obţin într-un timp mult mai scurt comparativ cu celelalte metode.

2.4.Optimizarea parametrilor inductorului folosind AG multiobiectiv

Algoritmul genetic multiobiectiv are avantajul căutării celor mai bune soluţii care îndeplinesc cât mai bine ambele obiective, fiind un algoritm bazat pe relaţia de dominanţă care există între indivizi. Un individ al AG este reprezentat ca un vector de numere reale. S-a folosit selecţia turneu, încrucişare uniformă cu probabilitatea egală cu Pi= 0.6, mutaţie simplă cu probabilitatea egală cu Pm=0.1. În tabelul 4 sunt date rezultatele rulării programului.

Tabel 4. Soluţiile obţinute cu AG multiobiectiv

f[Hz]	L_{ind}[m]	h[m]	Ecart [°C]	rand [%]
277	**0.127**	**0.0135**	**177.25**	**86.70**
311	0.105	0.0129	185.82	81.07
413	0.115	0.0142	195.86	71.55
1694	0.112	0.0149	118.25	59.32
409	0.110	0.0125	225.22	56.17
1093	0.116	0.0147	164.52	53.66
807	0.135	0.01487	204.27	52.23
2870	0.120	0.0138	108.13	48.06
1220	0.134	0.0145	167.96	46.38
2186	0.134	0.0142	119.36	44.82
885	0.137	0.0138	217.40	42.62

Avantajul algoritmilor de optimizare multiobiectiv constă în capacitatea lor de a folosi mai multe obiective simultan, ceea ce conduce la reducerea semnificativă a duratei optimizării.

3 Analiza rezultatelor

În continuare sunt prezentate cele mai bune rezultatele obţinute cu cei patru algoritmi de optimizare AG simpli, SA, DE şi AG multiobiectiv pentru randament *rand,* în tabelul 5 *şi* rezultatele obţinute cu cei patru algoritmi de optimizare pentru diferenţa de temperatură *ecart* în tabelul 6.

Tabel 5. Rezultatele obţinute cu AG simpli, SA, DE şi AG multiobiectiv –*rand*

	rand [%]	**L_i [m]**	**h [m]**	**f [Hz]**	**ecart [°C]**
AG simpli	**69**	0.135	0.0125	2447	150
SA	**61**	0.128	0.0132	821	227
DE	**67**	0.154	0.007	929	172
AG multiobiectiv	**87**	0.127	0.0135	277	177

Comparând datele din tabelul 5 care conţin rezultatele cele mai bune din punctul de vedere al randamentului, obţinute cu cei patru algoritmi de optimizare, se observă că cele mai bune rezultate s-au obţinut cu AG multiobiectiv.

Tabel 6. Rezultatele obţinute cu AG simpli, SA, DE şi AG multiobiectiv -*ecart*

	ecart [°C]	**L_i [m]**	**h [m]**	**f [Hz]**	**rand [%]**
AG simpli	**109**	0.124	0.010	1422	64
SA	**116**	0.124	0.0115	2981	49
DE	**109**	0.122	0.013	2962	50
AG multiobiectiv	**108**	0.119	0.014	2870	48

Comparând datele din tabelul 6 care conţin rezultatele cele mai bune din punctul de vedere al diferenţei de temperatură, obţinute cu cei patru algoritmi de optimizare, se observă că cele mai bune rezultate s-au obţinut cu AG multiobiectiv.

În ceea ce priveşte metodele de optimizare, tehnicile evolutive, algoritmii genetici, precum şi algoritmi genetici multiobiectiv sunt utilizate din ce în ce mai mult datorită capacităţii lor de a rezolva probleme dificile de proiectare.

4 Concluzii

Principalul obiectiv al acestei lucrări este elaborarea modelului numeric pentru procesul de încălzire a unui dispozitiv de încălzire inductivă şi găsirea unor soluţii de optimizare a procesului de încălzire.

Analizând rezultatele optimizărilor cu AG simpli, SA, DE şi AG multiobiectiv se poate trage concluzia că algoritmii abordaţi se pot folosi în proiectarea optimală a dispozitivelor de încălzire inductivă, ei conducând la rezultate comparabile în raport cu obiectivele şi variabilele de proiectare considerate. Dezavantajul celor patru metode utilizate, dar mai ales al AG simpli constă în faptul că problemele de proiectare electromagnetică sunt foarte solicitante în ceea ce priveşte resursele de calcul, necesitând rezolvarea unei probleme electromagnetice complexe la fiecare evaluare. În condiţiile creşterii performanţelor tehnicii de calcul, acest dezavantaj tinde să scadă.

Cercetările se pot continua prin utilizarea altor metode de proiectare optimală, cum ar fi optimizarea Particle Swarm, alte tehnici de optimizare multiobiectiv, sau proiectare experimentală (DOE), urmate de compararea rezultatelor obţinute.

ACKNOWLEDGMENTS

This work was cofinanced from the European Social Fund through Sectoral Operational Programme Human Resources Development 2007-2013, project number POSDRU/89/1.5/S/56287 „*Postdoctoral research programs at the forefront of excellence in Information Society technologies and developing products and innovative processes*", partner University of Oradea.

Referinţe

[1]D. E. Goldberg. *Genetic Algorithms In Search, Optimization, And Machine Learning*, Addison-Wesley, New York, 1989.

[2]E. Zitzler, M.Laumanns and S.Bleuler. A Tutorial on Evolutionary Multiobjective Optimization, Technical report, http://www.cs.tufts.edu/comp/150GA/ handouts/zitzler04.pdf

[3]E. Vladu. Genetic algorithms. An overview, *Proceedings of the EMES 99 International Conference*, Oradea, (1999).

[4]E Vladu. *Contribuţii la utilizarea algoritmilor genetici în inginerie,* Teza de doctorat, Universitatea Politehnica Timişoara, 2003.

[5]J. H Holland. *Adaptation In Natural And Artificial Systems*, Univ. Michigan Press, Ann Arbor, 1975.

[6] K. Fleetwood. *An introduction to Differential evolution*, http://www.maths.uq.edu.au/ MASCOS/ Multi-Agent04/Fleetwood.pdf

[7]R. Storn and K. Price. Differential evolution - a simple and efficient heuristic for global optimization over continuous space, *Journal of Global Optimization*, **11** (1997) 341-359 www.icsi.berkeley.edu/~storn/

[8]Camelia Petrescu, Lavinia Ferariu and Radu Olaru. Optimization of ferrofluid actuator using evolutionary algorithms and finite element method, *Revue Roumaine des Sciences Techniques– Électrotechnique et Électroenergetique*, Bucureşti, **54**, **1**, (2009) 77-86.

[9]H.-P. Schwefel. *Kybernetische. Evolution Als Strategie Der Experimentelen Forschung In Der Stromungstechnik*, Master's Thesis, Hermann Föttinger Institute For Hydrodynamics, Technical University Of Berlin, 1965.

PROIECTAREA OPTIMALĂ A UNUI DISPOZITIV DE ÎNCĂLZIRE PRIN INDUCŢIE

Teodor LEUCA[1], Ecaterina VLADU[1], Mihaela NOVAC[1], Ştefan NAGHI[1]
[1]*Universitatea din Oradea, Facultatea de Inginerie Electrică şi Tehnologia Informaţiei, Str Universităţii Nr.1., Oradea, Romania, tleuca@uoradea.ro*

Bogdan-Ciprian STANCIU[2]
[2]*SC UAMT Oradea,România*

Abstract. În lucrare se prezintă unele aspecte privind proiectarea optimală a unui dispozitiv de încălzire prin inducţie. Analiza numerică a câmpului electromagnetic şi termic cuplate s-a realizat prin metoda elementului finit (FEM), dezvoltând un program propriu folosind toolbox-ul PDE din Matlab. S-a abordat în continuare algoritmi de optimizare: algoritm genetic multiobiectiv (MOGA) şi modelarea surogat.
Cuvinte cheie: cuplajul dintre câmpul electromagnetic şi termic, analiza numerică prin FEM, algoritm de optimizare multiobiectiv, algoritmi genetici.

1 Introducere

Proiectarea optimală a dispozitivelor electromagnetice se bazează pe analiza numerică a câmpului electromagnetic cuplat cu cel termic, metoda elementului finit (FEM) fiind des utilizată. Aceasta se cuplează cu un algoritm de optimizare. Se utilizează softuri comerciale/module ale lor sau se dezvoltă programe proprii. În lucrarea de faţă s-a dezvoltat un asemenea program numit modulul FEM. Un studiu privind utilizarea FEM în electromagnetism este prezentat în [1], iar [2] şi [3] conţin referinţe bibliografice cu privire la modelarea procesului de inducţie electromagnetică.

În ceea ce priveşte metodele de optimizare, tehnicile evolutive precum algoritmii genetici şi algoritmi genetici multiobiectiv sunt utilizate din ce în ce mai mult datorită capacităţii lor de a rezolva probleme dificile de proiectare. Unele rezultate recente privind aplicarea acestor algoritmi în proiectarea dispozitivelor electromagnetice sunt prezentate în [4], [5], [6] şi [11]. Dezavantajul folosirii algoritmilor evolutivi (EA) în problemele care implică modelarea numerică de înaltă fidelitate constă în timpul mare de calcul necesar. În ciuda perfecţionării continue a tehnicii de calcul, complexitatea programelor utilizând FEM conduce la o durată de evaluare cuprinsă între câteva minute până la câteva ore. O posibilă alternativă la evaluarea folosind un model de calcul FEM constă în utilizarea unor metamodele ori modele surogat, care conduc la un timp de calcul mult mai mic.

Metamodelarea se referă la construirea unui model pe baza unui număr finit de date obţinute pe baza modelului de calcul şi evaluarea erorilor de estimare. Folosind modelul surogat, se obţin aproximări ale mărimilor de ieşire ale modelului pentru diferite date de intrare. Aceste aproximări se bazează pe informaţii limitate şi au la bază ipotezele simplificatoare, aşa cum se prezintă în [7], [8], [9]. Una dintre principalele ipoteze simplificatoare presupune că funcţia care descrie modelul este continuă şi netedă. Pe astfel de ipoteze se bazează metode precum funcţii radiale de bază, regresie cu suport vectorial, interpolare Kriging şi altele. Ipoteze suplimentare legate de forma funcţiei pot fi folosite suplimentar, de exemplu prin aplicarea regresiei polinomiale. Modelarea surogat este prezentată în [7] şi [10], iar [7], [12] se referă la fundamentele teoretice ale interpolării de tip Kriging.

2 Modulul FEM

Problema considerată se referă la procesul de încălzire prin inducţie a unei piese cilindrice. Dispozitivul are o simetrie cilindrică, astfel încât problema se reduce la o problemă 2D-în planul 0RZ, iar modelul numeric este considerat în coordonate cilindrice cu axele 0R şi 0Z (Figura 1). Modelarea numerică va folosi un sfert din sistemul fizic.

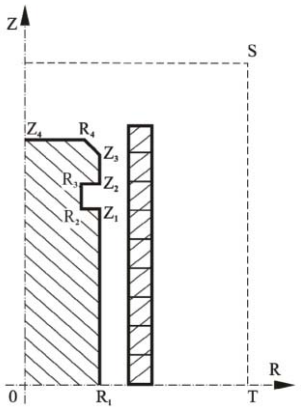

Fig 1: Problema 2D considerată

Piesă cilindrică de încălzit este din oţel, având diametrul de 0.080 m şi lungimea de 0.20 m. Diametrul intern al inductorului este *dint* = 0.110 m, iar diametrul său exterior este Dext = 0.130 m. Piesa este încălzită de la temperatura iniţială de 20 ° C până la temperatura finală de 1200 ° C. Variabilele de proiectare sunt: f-frecvenţa, Li - lungimea inductorului şi h - întrefierul dintre piesă şi inductor.

Modelul matematic al câmpului electromagnetic este descris de relaţia (1), iar câmpul termic de relaţia (2):

$$\mathrm{rot}\left[(1/\mu)\mathrm{rot}\mathbf{A}\right] + j\omega\mathbf{A}/\rho = \mathbf{J}_z \tag{1}$$

$$\gamma C\frac{\partial T}{\partial t} + \mathrm{div}\left(\lambda\,\mathrm{grad}\,T\right) = p \tag{2}$$

unde: **A** este potenţialul magnetic vector, $\mathbf{J}_Z$ este densitatea de curent, μ este permeabilitatea magnetică, $\omega = 2\pi f$ este pulsaţia, f este frecvenţa, T este temperatura, ρ este rezistivitatea, λ este conductivitatea termică, γC este capacitatea calorică specifică, iar p este densitatea de putere produsă prin efect Joule, dată de relaţia (3):

$$p = \frac{\omega^2|A|^2}{\rho} \tag{3}$$

În relaţia (1), al doilea termen este densitatea curentului indus, care are valoarea nenulă numai în piesa de lucru.

Modelul numeric este descris în coordonate cilindrice având pe 0Z axa verticală şi 0R axa orizontală. Frontiera pentru câmpul magnetic este formată de axa 0Z, care este paralelă cu liniile de câmp magnetic şi axa 0R, normală pe liniile de câmp magnetic.

Pentru câmpul termic, domeniul de analiză este piesa de lucru. Pe limitele $0R_1$ şi $0Z_4$, fluxul termic are valoarea nulă. În schimb, pe frontierele R_1Z_1, Z_1R_2, R_2R_3, R_3Z_2, Z_2Z_3, Z_3R_4 şi R_4Z_4 se produc pierderi prin convecţie, îndeplinind condiţiile de frontieră date de relaţia (4):

$$-\lambda\frac{\partial T}{\partial n} = \alpha\left(T - T_0\right) \tag{4}$$

unde: T_0 este temperatura mediului, iar α este coeficientul de transfer termic prin convecţie.

Modulul FEM a fost implementat software într-o manieră iterativă folosind toolboxul PDE din Matlab, considerând două subprobleme: o subproblemă de tip electromagnetic şi una de tip termic. Distribuţia câmpului electromagnetic se determină în condiţiile unor proprietăţi de material dependente de temperatură, iar curenţii turbionari produc pierderi Joule care conduc la creşterea temperaturii. Proprietăţile de material sunt actualizate, iar câmpul electromagnetic este determinat din nou.

3 Algoritmul genetic multiobiectiv (MOGA)

Găsirea parametrilor optimi pentru proiectarea dispozitivului de încălzire prin inducţie prezentat în secţiunea 2 presupune optimizarea în raport cu două obiective opuse, astfel încât se pune problema de a găsi cele mai bune soluţii care satisfac cât mai bine posibil ambele obiective. Există diferite tehnici utilizate în probleme de optimizare multiobiectiv. Multe publicaţii recente au arătat superioritatea tehnicilor de optimizare evolutive faţă de metodele clasice [13]. Acestea includ algoritmul genetic multiobiectiv (MOGA), bazat pe dominanţa Pareto. Acesta foloseşte o procedură de sortare bazată pe nedominanţă, aşa cum se prezintă în [14]. În această lucrare s-a utilizat algoritmul evolutiv multiobiectiv MOGA implementat în Matlab. [15]

Domeniul de căutare pentru variabile este prezentat mai jos:

$f \in$ [500 3000] Hz - frecvenţa

$L_i /2 \in$[0.08 0.145] m - lungime inductor (5)

$h \in$[0.005 0.015] m - întrefier

Cele două obiective sunt:

- *dT* care caracterizează uniformitatea distribuţiei temperaturii în piesă şi care trebuie minimizată;

- *Eff* care caracterizează randamentul electric care trebuie maximizat.

MOGA s-a utilizat cu o populaţie de P = 50 indivizi, care a evoluat timp de 50 de generaţii, încrucişarea aritmetică cu probabilitatea P_C = 0,80 şi mutaţia uniformă cu probabilitatea Pm = 0,1.

Rezultatele obţinute sunt prezentate în tabelul 1.

Tabel 1. Rezultatele obţinute folosind MOGA

f	$L_i/2$	h	dT	eff
759,8223	0,139499	0,006538	49,405	0,772
1285,157	0,120575	0,006736	34,649	0,771
1359,223	0,120285	0,007054	30,179	0,765
1282,915	0,119325	0,006819	53,290	0,773

Rezolvarea problemei de proiectare folosind MOGA a presupus un timp de calcul mare. Dezavantajul metodei constă în faptul că problemele de proiectare a dispozitivelor electromagnetice sunt foarte mari consumatoare de resurse de calcul, iar optimizarea presupune pentru fiecare evaluare rezolvarea problemei electromagnetice complexe cuplate cu problema termică. Din acest motiv, există un interes major în investigarea posibilităţilor de folosire a unor tehnici care să minimizeze timpul de calcul. Paragraful următor introduce unele tehnici de modelare surogat, evidenţiind modelele bazate pe interpolarea de tip Kriging, care ar putea fi folosite în acest scop.

4 Modelare surogat

În acest capitol este utilizată interpolarea de tip Kriging, care se bazează pe modele statistice. Kriging [8] presupune că datele caracterizează un proces stocastic staţionar (unele variante ale metodei presupun, de asemenea, o distribuţie normală a datelor). Există mai multe tipuri de interpolare Kriging, cu grade diferite de complexitate, cum ar fi interpolare Kriging normală, simplă şi universală.

Pentru a construi un model surogat al dispozitivului de încălzire prin inducţie prezentat, s-a folosit toolboxul DACE (Design and Analysis of Computer Experiments). DACE este un toolbox Matlab specializat pe interpolare de tip Kriging [16]. Folosind datele obţinute din experimente, toolboxul construieşte un model de tip Kriging universal, care poate fi folosit ca model de surogat al modelului de calcul. Toolboxul returnează şi eroarea de estimare pentru fiecare intrare, ceea ce permite evaluarea calităţii modelului generat. Funcţia de modelare DACE are ca argumente datele disponibile (obţinute prin experimente), o funcţie polinomială de gradul k ce modelează bias-ul datelor (modelul de regresie) şi funcţia de corelare a modelului, returnând modelul Kriging în forma unei structuri de date complexe [17].

Se abordează aceeaşi problemă de proiectare a inductorului prezentat în secţiunea 2, cu cele două obiective menţionate: *Eff* randament electric care se maximizează şi diferenţa de temperatură în piesă la sfârşitul procesului de încălzire *dT*, care se minimizează. Pentru a mări precizia modelului surogat pe baza datelor iniţiale disponibile, fără a creşte în mod semnificativ timpul de calcul, se foloseşte optimizarea modelului surogat. Iniţial se obţine un model surogat folosind datele disponibile obţinute pe baza unor evaluări costisitoare în timp folosind modelul de calcul, iar următoarele evaluări se obţin pe baza modelului surogat.

Procesul constă în următorii paşi:

Pasul 1. Selectarea variabilelor de optimizare, ţinând cont de importanţa lor, pe baza unor experimente preliminare;

Pasul 2. Alegerea valorilor de intrare ale variabilelor în modelul de calcul, pe baza unei strategii predefinite;

Pasul 3. Alegerea tipului de model surogat;

Pasul 4. Construirea modelului surogat folosind rezultatele evaluate pe baza modelului de calcul (informaţiile disponibile);

Pasul 5. Optimizarea folosind modelul surogat, cu scopul de a găsi noi puncte de interes şi evaluarea lor folosind modelul de calcul;

Pasul 6. Ajustarea modelului surogat, luând în considerare noile informaţii disponibile;

Pasul 7. Revenirea la pasul 4 până la îndeplinirea unui criteriu de oprire.

Criteriul de oprire poate fi un anumit număr de iteraţii sau o eroare de predicţie admisibilă.

Modelul surogat iniţial a fost construit prin utilizarea a 36 rezultate obţinute prin evaluarea modelului de calcul, cele 36 rezultate împreună fiind denumite în continuare *mulţime de calcul*. După fiecare etapă de optimizare, cele mai bune rezultate s-au adăugat la mulţimea de calcul, rezultând un model surogat îmbunătăţit.

Tabelul 2 prezintă rezultatele adăugate la mulţimea de calcul după primul pas de optimizare.

Tabel 2. Rezultatele adăugate la mulţimea de calcul după primul pas de optimizare.

f	L_{ind}	h	dT	Eff
1859	0,136	0,0050	257,39	0,803
1800	0,127	0,0053	189,39	0,793
1859	0,145	0,0050	299,26	0,803
1400	0,131	0,0055	165,71	0,786
1799	0,128	0,0075	168,94	0,784

În această manieră s-au parcurs 5 etape de optimizare. Cele mai bune rezultate obţinute sunt prezentate în Tabelul 3.

Tabel 3. Cele mai bune rezultate obţinute prin modelare surogat

f	L_{ind}	h	dT	Eff
1384,03	0,119	0,0070	35,26	0,768
1375,14	0,117	0,0069	57,15	0,765
1385,09	0,117	0,0068	56,87	0,766

Prin compararea rezultatelor prezentate în tabelul 3 cu rezultatele din tabelul 1, se poate observa faptul că optimizarea bazată pe modelarea surogat conduce la rezultate uşor mai slabe decât cele obţinute prin MOGA cu modelul de calcul, având însă avantajul că numărul de evaluări costisitoare este scăzut, reducându-se astfel semnificativ durata procesului de proiectare optimală a dispozitivului electromagnetic.

Aproximarea finală a randamentului prin optimizarea folosind interpolarea de tip Kriging pentru diferite valori ale frecvenţei şi întrefierului, menţinând valoarea constantă pentru L_{ind}=0.12 este prezentată în figura 2, iar aproximarea finală a temperaturii dT în aceleaşi condiţii în figura 3.

În ceea ce priveşte acurateţea, algoritmul prezentat are performanţe rezonabile. De asemenea, costurile de ansamblu pentru dezvoltarea metamodelului nu sunt mari. Deoarece, creşterea complexităţii problemei nu poate conduce la costuri suplimentare considerabil mai mari, metoda prezentată va determina o reducere însemnată a timpului necesar proiectării optimale în cazul unor probleme complexe din tehnică.

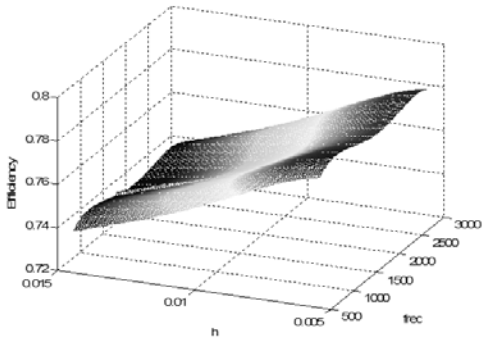

Fig 2: Aproximarea finală a randamentului prin optimizare folosind interpolarea de tip Kriging

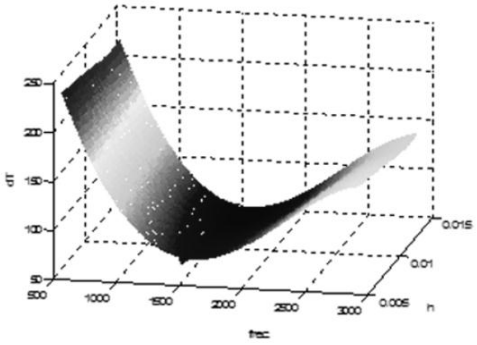

Fig 3: Aproximarea finală a diferenţei de temperatură în piesă prin optimizare folosind interpolarea de tip Kriging

5 Concluzii

Lucrarea de față prezintă modelarea prin metoda elementului finit (FEM), a problemei cuplate de câmp electromagnetic și termic cu referire la un dispozitiv de încălzire prin inducţie.

Dezvoltarea software s-a bazat pe toolbox-ul PDE din mediul de programare Matlab.

S-a utilizat un algoritm evolutiv multiobiectiv şi s-au folosit tehnici de modelare surogat combinate cu MOGA, în vederea optimizării dispozitivului de încălzire prin inducţie.

La optimizarea evolutivă modelul surogat oferă o aproximare a modelului de calcul, iar rezultatele obţinute sunt satisfăcătoare ca precizie, obținându-se astfel un timp de calcul redus.

Această lucrare poate fi dezvoltată utilizând alţi algoritmi de optimizare și alte tehnici de modelare surogat.

Referinţe

[1] C.W. Trowbridge, J.K. Sykulski. Some Key Developments in Computational Electromagnetics and their Attribution, *IEEE Transactions on Magnetics*, vol. 42, Issue **4** (2006) 503 – 508.

[2] J.D. Lavers. State of the art of numerical modeling for induction processes, *International Symposium on Heating by Electromagnetic Sources*, Padova, Italia, (2007) 13 – 24.

[3] Ajay Kumar, Sanjay Marwaha, Anupama Marwaha and N.S. Kalsi. Magnetic field analysis of induction motor for optimal cooling duct design, *Simulation Modelling Practice and Theory*, vol. **18**, Issue **2** (2010) 157–164.

[4] F. Zaoui and C. Marchand. Using genetic algorithm for the optimization of electromagnetic devices, *COMPEL - International Journal for Computation and Mathematics in Electrical and Electronic Engineering*, vol. **17**, Issue **1-3** (2007) 181 – 185.

[5] Camelia Petrescu, Lavinia Ferariu and Radu Olaru, Optimization of ferrofluid actuator using evolutionary algorithms and finite element method, *Revue Roumaine des Sciences Techniques– Électrotechnique et Électroenergetique*, **54**, **1**, Bucureşti, (2009) 77-86.

[6] L.S. Coelho and P. Alotto. Multiobjective electromagnetic optimization based on a nondominated sorting genetic approach with a chaotic crossover operator, *IEEE Transactions on Magnetics*, vol. **44**, Issue **6**, (2008) 1078 – 1081.

[7] H.B. Nielsen. *Surrogate modelling by Kriging*, (2003) http://www.imm.dtu.dk/~hbn.

[8] J. P.C. Kleijnen. Kriging metamodeling in simulation: A review, *European Journal of Operational Research* **192** (2009) 707–716.

[9] G.G. Wang and S. Shan. Review of Metamodeling Techniques in Support of Engineering Design Optimization, ASME Transactions, *Journal of Mechanical design*, vol. **129** Issue **4** (2006) 370 – 376.

[10] Y. Jin. A comprehensive survey of fittness approximation in evolutionary computation, *Soft Computing*, vol. **9**, Issue **1** (2005) 3 – 12.

[11] Alexandru Mihail Morega, Mihaela Morega and Marius A. Panait. Structural optimization of a thermoelectric generator by numerical simulation, *Revue Roumaine des Sciences Techniques– Électrotechnique et Électroenergetique,* Bucureşti, **55**, **1** (2010) 3-12.

[12] M.L. Stein. *Interpolation of Spatial Data: Some Theory for Kriging*, Springer, New York, 1999.

[13] M. Ashabani and Y.A.-R.I. Mohamed. Multiobjective shape optimization of segmented pole permanent-magnet synchronous machines with improved torque characteristics, *IEEE Transactions on Magnetics*, vol. **47**, Issue **4** (2011) 795 – 804.

[14]M. Martinez, J.M. Herrero, J. Sanchis, X. Blasco and Sergio-Garcia Nieto. Applied Pareto multi-objective optimization by stochastic solvers, *Engineering Applications of Artificial Intelligence*, vol. **22**, Issue **3** (2009) 455 – 465.

[15] J.M. Herrero. ev-MOGA Multiobjective Evolutionary Algorithm, Grupo de Control Predictivo y Optimizacion Heuristica, *Universitat Politecnica de Valencia* (SPAIN). http://www.mathworks.com/matlabcentral/fileexchange/31080-ev-moga-multiobjective-evolutionary-algorithm.

[16] http://www2.imm.dtu.dk/~hbn/dace/ (2012).

[17] H.B. Nielsen and K. Frisenfeldt Thuesen. Kriging and Radial Basis Functions, *SIAM Conference on Optimization* (2005). www2.imm.dtu.dk/~hbn/dace/SIOP.pdf;

IDENTIFICAREA PARAMETRILOR CIRCUITELOR REZONANTE UTILIZATE ÎN TRANSFERUL WIRELESS AL PUTERII ELECTROMAGNETICE

Daniel DAN[1,2], Dragoş NICULAE[1], Mihai IORDACHE[1]
1. Universitatea "Politehnica" din Bucureşti, Spl. Independenţei 313, 060042, Bucureşti;
2. ICPE-CA, Splaiul Unirii, Nr. 313, Sector 3, 030138, Bucureşti
dan@lmn.pub.ro

Abstract. Scopul lucrării îl reprezintă expunerea unei noi metode de identificare a parametrilor circuitelor rezonante reale utilizate în transferul fără fir al puterii electromagnetice. Prin folosirea parametrilor şi a funcţiei de transfer, determinată în regim sinusoidal se poate deduce modelul parametric de interes. În această lucrare sunt prezentate atât funcţia obiectiv cât şi metodele de optimizare. În final, se prezintă testarea tehnicii de estimare.

1 Introducere

Există mulţi algoritmi de optimizare, clasificaţi îndeosebi în algoritmi determinişti şi stocastici. Cei determinişti dau acelaşi rezultat când sunt rulaţi cu acelaşi set de parametrii şi care încep de la acelaşi punct, pe când cei stocastici au câteva caracteristici euristice implementate. Acest lucru face ca simulările efectuate cu aceiaşi parametrii şi care au acelaşi punct de start, să dea rezultate diferite. Algoritmii determinişti [1] au avantajul că folosesc un număr relativ mic de evaluări ale funcţiei obiectiv, dar nu pot să găsească optimul global al problemei, fiind ghidaţi către punctul de minim local. Invers, cei stocastici au o mare probabilitate să nu fie atraşi în minimul local, dar au nevoie de o mulţime de puncte pentru evaluare în timpul unei rulări. În lucrare sunt utilizaţi numai algoritmii determinişti.
Am testat convergenţa a 2 metode de optimizare deterministe: metoda gradientului şi quasi-Newton pentru ca în final să alegem pe cea mai rapid convergentă.

2 Estimarea parametrilor circuitului utilizând funcţia de transfer

Se consideră circuitul liniar din figura 1 căruia i se asociază sistemul liniar de ecuaţii diferenţiale aferent analizei în domeniul timp.

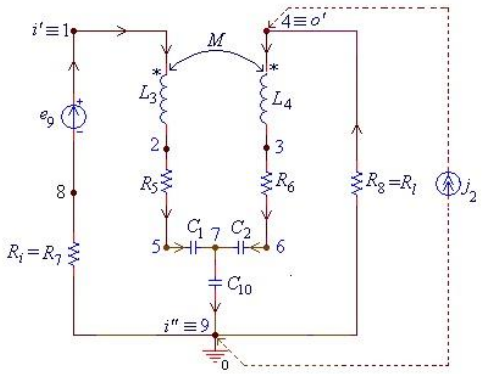

Fig. 1

Pentru determinarea parametrilor, acest sistem a fost transformat într-un sistem algebric liniar, în domeniul frecvenţei. Pentru aceasta se pot utiliza fie transformata Laplace, fie transformata Fourier. În acest caz, obţinem funcţia de transfer în domeniul complex, de forma $\underline{H}(j\omega)$. Astfel putem obţine informaţii atât despre fază cât şi despre amplitudinea variabilelor (semnalelor) de ieşire.
Procedura de estimare începe cu generarea în formă simbolică a funcţiei de transfer, ca funcţie de frecvenţă, $\underline{H}(f)$. Păstrăm parametrii funcţiei pe care dorim să-i estimăm $x_1, x_2, ..., x_p$, în timp ce restul parametrilor sunt înlocuiţi cu valorile nominale. Pentru n_f frecvenţe avem funcţiile obiectiv de forma:

$$f_k = \left(\left| \underline{H}(f_k) \right| - \left| \underline{H}(f_k, x_1, x_2, ..., x_p) \right| \right)^2, k = \overline{1, n_f} \quad (1)$$

Funcţiile obiectiv (1) se pot minimiza utilizând metodele deterministe de ordinul întâi (metode de tip gradient) – metoda gradientului, metode Quasi-Newton.
În Matlab funcţia *fminunc* [2], ce face parte din Optimization Toolbox, implementează în acelaşi timp metoda gradientului (Large Scale) precum şi două metode Quasi-Newton (Medium Scale), metoda Broyden-Fletcher-Goldfarb-Shanno (opţiunea HessUpdate fixată pe BFGS) şi metoda Davidson-Davidson-Fletcher Powel (opţiunea HessUpdate fixată pe DFP). Metodele menţionate vor fi prezentate în continuare, utilizând un caz particular.

3 Metode deterministe de ordin întâi

Fie funcţionala $f : R^p \to R$, de clasă C^2, care în cazul nostru este de forma:

$$f_1 = \left(\left| H(f_1) \right| - \left| H(f_1, x_1, x_2, ..., x_p) \right| \right)^2, \quad (2)$$

cu $f_1 = ct.$. Se cere să se calculeze minimul funcţiei f, respectiv punctul $\bar{x}^*$ a.î. $f(\bar{x}^*) \le f(\bar{x}), \forall \bar{x} \in \mathbb{R}^p$. Pentru determinarea minimului se pot utiliza metodele deterministe prezentate în continuare.

Metoda Quasi-Newton
Fie relaţia [3]:

$$\bar{x}_{k+1} = \bar{x}_k + \alpha_k \bar{S}_k \bar{g}_k \quad (3)$$

unde $\bar{S}_k$ este o matrice simetrică de dimensiuni $n \times n$ cu $n = 2$. Dacă $\bar{\alpha}_k \bar{S}_k$ este inversa matricei Hessian a lui f, atunci avem

$$\bar{x}_{k+1} = \bar{x}_k - \bar{H}^{-1} \bar{g}_k, \quad (4)$$

aceasta este corespunzătoare relaţiei Newton, unde $\bar{x}_k$ este soluţia la pasul k, $\bar{H}_k = \bar{H}(x_k)$ este matricea Hessian evaluată la x_k, iar $\bar{g}_k = \bar{g}(\bar{x}_k)$ este gradientul funcţiei f evaluată în $\bar{x}_k$.
Dacă $\bar{S}_k = \bar{I}$, atunci relaţia anterioară (1.7) devine

$$\bar{x}_{k+1} = \bar{x}_k + \alpha_k \bar{v}_k \quad (5)$$

cea corespunzătoare metodei gradientului (sau metoda celei mai rapide coborâri), unde:

$$\bar{v}_k = -\bar{g}_k = -\bar{g}(\bar{x}_k) = -\nabla f(\bar{x}_k), \quad (6)$$

şi $\bar{v}_k$ reprezintă direcţia de deplasare la iteraţia k, iar α_k este un coeficient care descrie amploarea deplasării în direcţia $\bar{v}_k$.

În continuare sunt prezentate două metode de aproximare a matricei Hessian.

Metoda Davidon-Fletcher-Powell (DFP)

$$\bar{H}_{k+1} = \bar{H}_k + \frac{\bar{q}_k \bar{q}_k^T}{\bar{q}_k^T \bar{p}_k} - \frac{\bar{p}_k \bar{H}_k \left(\bar{p}_k \bar{H}_k\right)^T}{\bar{p}_k^T \bar{H}_k \bar{p}_k}, \tag{7}$$

unde

$$\bar{p}_k = \bar{x}_{k+1} - \bar{x}_k, \quad \bar{q}_k = \nabla f\left(\bar{x}_{k+1}\right) - \nabla f\left(\bar{x}_k\right) \tag{8}$$

Pentru matricea H_0 se poate utiliza orice matrice simetrică, de exemplu se poate alege matricea unitate I.

Metoda Broyden-Fletcher-Goldfarb-Shanno (BFGS) [4]

$$\bar{S}_{k+1} = \bar{S}_k + \frac{\bar{p}_k \bar{p}_k^T}{\bar{q}_k^T \bar{p}_k} - \frac{\bar{S}_k \bar{q}_k \bar{q}_k^T \bar{S}_k^T}{\bar{q}_k^T \bar{S}_k \bar{q}_k}, \tag{9}$$

unde

$$\bar{S}_k = \bar{H}_k^{-1}, \quad \bar{p}_k = \bar{x}_{k+1} - \bar{x}_k, \quad \bar{q}_k = \nabla f\left(\bar{x}_{k+1}\right) - \nabla f\left(\bar{x}_k\right) \tag{10}$$

Pentru matricea H_0 se poate utiliza orice matrice simetrică, de exemplu se poate alege matricea unitate I.

4 Exemplul

Fie funcţionala $f : R^2 \to R$, de clasă C^2, de forma:

$$f = \left(\left|H\left(f_1\right)\right| - \left|H\left(f_1, x_1, x_2\right)\right|\right)^2 = \left(\left|H\left(f_1\right)\right| - \left|H\left(f_1, \bar{x}\right)\right|\right)^2, \tag{11}$$

cu $f_1 = ct.$, iar $L_1 = x_1, \quad L_2 = x_2$ corespunzătoare circuitului rezonator din fig 1. Se cere să se calculeze minimul funcţiei f, respectiv punctul $\bar{x}^*$ a.î. $f\left(\bar{x}^*\right) \le f\left(\bar{x}\right), \forall \bar{x} \in R^2$. Aici $\bar{x} = \left[x_1, x_2\right]$.

Tabel 1

$L_1\,[\mathrm{H}]$	$L_2\,[\mathrm{H}]$	$C_1\,[\mathrm{F}]$	$C_2\,[\mathrm{F}]$	$C_{10}\,[\mathrm{F}]$
$1.6748 \cdot 10^{-5}$	$1.6735 \cdot 10^{-5}$	$13.8915 \cdot 10^{-12}$	$13.8915 \cdot 10^{-12}$	$27.51354 \cdot 10^{-12}$
$R_1\,[\Omega]$	$R_2\,[\Omega]$	$R_i\,[\Omega]$	$R_s\,[\Omega]$	$M\,[\mathrm{H}]$
1.3520	1.3524	5.0	5.0	$1.4899 \cdot 10^{-6}$

Dacă considerăm valorile nominale din tabelul 1 şi păstrăm frecvenţa ca variabilă, atunci găsim expresia:

$$f \approx \frac{117591.16 \cdot f_1^2 \cdot \left(-0.25 \cdot 10^{22} + 0.41 \cdot 10^{22} f_1^2\right)^2}{0.31 \cdot 10^{65} - 0.82 \cdot 10^{51} f_1^2 + 0.80 \cdot 10^{37} f_1^4 - 0.34 \cdot 10^{23} f_1^6 + 0.53 \cdot 10^{8} f_1^8} \tag{12}$$

Egalând cu zero expresia (12) s-au determinat soluţiile ecuaţiei, dintre acestea au fost păstrate numai soluţiile pozitive şi reale.

Tabel. 2

$f_1\,[\mathrm{Hz}]$	$f_2\,[\mathrm{Hz}]$	$f_3\,[\mathrm{Hz}]$	$f_4\,[\mathrm{Hz}]$	$f_5\,[\mathrm{Hz}]$

$0.10938850\cdot10^{8}$	$0.24870731\cdot10^{8}$	$0.12634499\cdot10^{8}$	$0.37946886\cdot10^{8}$	$0.14184006\cdot10^{8}$
$P_1[\mathrm{W}]$	$P_2[\mathrm{W}]$	$P_3[\mathrm{W}]$	$P_4[\mathrm{W}]$	$P_5[\mathrm{W}]$
305.92870	$0.31790027\cdot10^{-18}$	0.44289964	0.000013219983	304.60900

Reprezentarea grafică se poate vedea în fig. 2. Dintre cele două maxime găsite se va considera numai P_1.

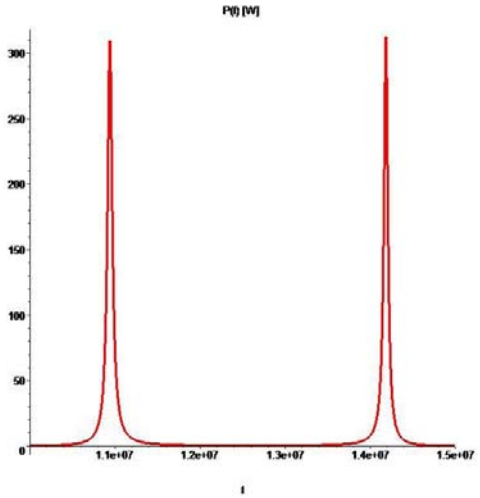

Fig. 2 – Puterea funcţie de frecvenţă

Considerăm acum ca variabile ale funcţiei $f = P$ pe L_1 şi L_2 pentru frecvenţa aleasă f_1, ceilalţi parametrii având valorile nominale din tabelul 3.

Tabelul 3

$L_1[\mathrm{H}]$	$L_2[\mathrm{H}]$	$C_1[\mathrm{F}]$	$C_2[\mathrm{F}]$	$C_{10}[\mathrm{F}]$
x_1	x_2	$13.8915\cdot10^{-12}$	$13.8915\cdot10^{-12}$	$27.51354\cdot10^{-12}$
$R_1[\Omega]$	$R_2[\Omega]$	$R_i[\Omega]$	$R_s[\Omega]$	$M[\mathrm{H}]$
1.3520	1.3524	5.0	5.0	$1.4899\cdot10^{-6}$

În urma calculelor a rezultat funcţia $f(x_1,x_2)=f(L_1,L_2)$. Datorită expresiei prea lungi a funcţiei rezultate, forma acestei funcţii nu a mai fost prezentată în lucrarea de faţă. În continuare ne propunem să găsim valorile optime $L_1 = x_1$ şi $L_2 = x_2$ pentru care funcţionala $f(x_1,x_2)=P(L_1,L_2)$ să fie minimă (minimul funcţionalei reprezentând maximul puterii). Acest lucru se poate realiza, de exemplu, cu ajutorul funcţiei Matlab *fminunc,* care utilizează metodele prezentate anterior.

Pornind de la o schemă de start de 500 de puncte aleatoare, prin optimizare rezultă forma punctelor optimizate care poate fi observată în figura 3. Pentru toate metodele de optimizare rezultă aceeaşi formă a graficului.

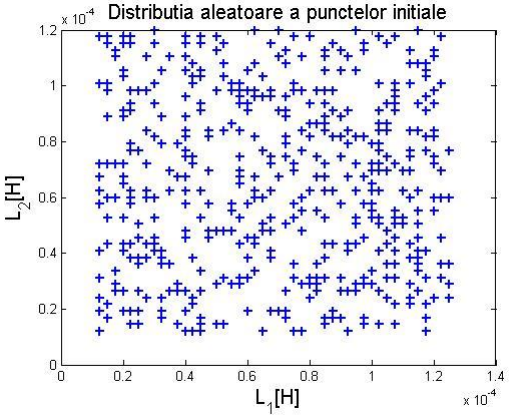

Fig. 3 – Distribuţia aleatoare a punctelor iniţiale

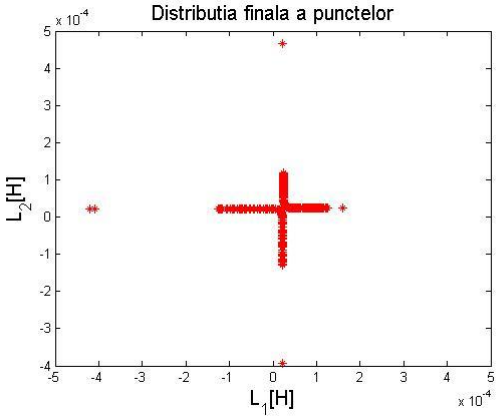

Fig. 4 – Distribuţia finală a punctelor

În tabelul se pot observa câteva rezultate ale parametrilor de optimizat $L_1 = x_1$ şi $L_2 = x_2$ dar şi a funcţiei obiectiv precum şi timpul de rulare.

Metoda			$f = P[\mathrm{W}]$	$L_1 = x_1[\mathrm{H}]$	$L_2 = x_2[\mathrm{H}]$	$t[s]$
Gradienţilor	Large Scale		311.442	$2.9274 \cdot 10^{-5}$	$2.9055 \cdot 10^{-5}$	14
Quasi-Newton	Medium Scale	BFGS	310.976	$1.6745 \cdot 10^{-5}$	$1.6737 \cdot 10^{-5}$	13
		DFP	309.0732	$1.7119 \cdot 10^{-5}$	$1.6329 \cdot 10^{-5}$	11
Valoarea nominală			305.93	$1.6748 \cdot 10^{-5}$	$1.6735 \cdot 10^{-5}$	------

5 Concluzii

- Metodele de optimizare quasi-Newton pot fi utilizate cu succes pentru determinarea minimului (respectiv maximului) unei funcţionale în diferite domenii tehnice, în lucrarea de faţă fiind folosite pentru determinarea parametrilor unui dispozitiv (circuite electrice rezonante), utilizat în transferul fără fir a energiei electrice, în condiţiile unei puteri maxime transmise.
- Metoda Gradientului este o metodă slabă pentru problema considerată, din punct de vedere al determinării parametrilor optimali.
- Cele două implementări ale procedurii Matlab pentru aproximarea matricei Hessian, metoda Broyden-Fletcher-Goldfarb-Shanno (BFGS) şi respectiv metoda Davidson-Davidson-Fletcher

Powel (DFP) conduc la rezultate aproximativ asemănătoare în ceea ce priveşte timpul de calcul şi parametrii obţinuţi.

Referinţe

[1] G. Ciuprina, D. Ioan, I. Munteanu, M. Rebican, R. Popa. *Optimizarea numerică a dispozitivelor electromagnetice*, Printech, Bucureşti, 2002.
[2] Fminunc function, Matlab – http://www.mathworks.com/help/optim/ug/fminunc.html
[3] Quasi-Newton method – wikipedia - http://en.wikipedia.org/wiki/Quasi-Newton_method
[4] BFGS method – http://en.wikipedia.org/wiki/BFGS_method

ENERGY EFFICIENCY ELEMENTS IN HOMES ELECTRIC HEATING

Nicolae VASILE
Universitatea VALAHIA din Târgovişte, B-dul. Carol I 2, 130024, Târgovişte; nvasile54@gmail.com
ICPE SA Bucureşti 3, Spl. Unirii 313, 030138, Bucureşti; nvasile@icpe.ro

Alexandru-Gabriel GURGU
Universitatea VALAHIA din Târgovişte, B-dul. Carol I 2, 130024, Târgovişte; gurgu_gabriel@yahoo.com

Abstract. In this geopolitical and economic crisis, when we reconfiguring a new balance between holders of primary resources and technology we have a more current problem, the increasingly ideea the use of electricity to heat homes that is very clear. Although, due to the successive conversions, the price of electric energy is higher than the various forms of primary energy, it can get a cheaper heating service through various technical and economic methods taken by the beneficiaries of this services and / or energy suppliers. This paper presents several such methods and also practical results of the monitoring of demonstration projects in recent winters, in the specific climate in Bucharest.

1 Introduction

The evolution of international energy mix targets the research to the renewable, especially wind and solar. The sources based on nuclear energy and energy obtained from waterfalls continues to grow. All these four forms of energy that attract investors specially lately come to increase the supply of electricity on the market in competition with traditional oil and gas supply. Bidders of oil and gas have different problems to exploit reserves that are in decline, of existence of military or political conflicts in the main production areas and with the excessive environmental pollution stages of production, transport and use. Electricity bidders have problems caused by the technical impossibilities. This form of energy must be consumed at the same time in that is produced. There are consumers that ensure constant consumption during the working day but there are problems with consumption in the night and weekend periods. Applications that can be used to balance day and night uses are electric cars that use energy to charge the batteries in the night time and electric heating of homes, which also involve consumption mainly nocturnal. For these reasons electricity suppliers are eager to offer different tariffs for day and night, making an interesting choice of a service based on electrical heating.

2 Technical constructive foundations

Classical forms of heating, the district heating based on water and its circulation through pipes placed in the wall or outside wall (Fig. 1), lead an energy loss greater than the loss by the Joule effect in the current-carrying electrical conductors.

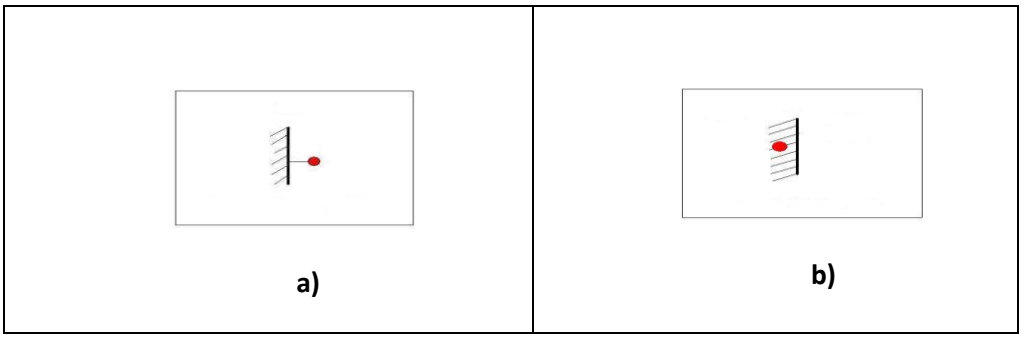

Fig 1: The placement of hot water pipes. a) outside wall, b) inside wall

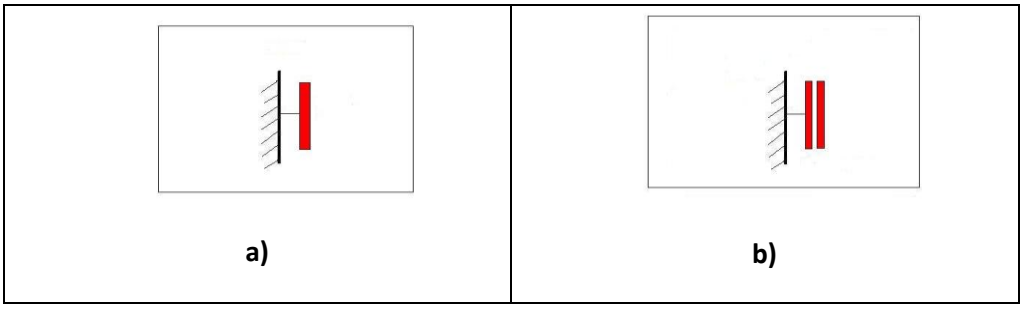

Fig 2: The placement of the heat sources.
a) radiator placed near the wall;
b) convector placed near the wall.

When we talk about radiators or convector we do not have an indifference about the placement within the room since according to their position, a quantity of heat a larger or smaller, will transfer to the walls, which do not contribute to the thermal comfort of the room. The interest in terms of energy efficiency is that the entire amount of heat shall warms the bodies inside the living room, directly, for radiators, or indirectly through air movement, for convectors. In the case of the convectors or radiators based on hot water, we have the only way to place them near walls, due to inconveniences of rigid connection pipes through which the water circulation. (Fig 2). It is improper to use of flexible hoses, because, in such situations, we have a risk of failure or breacking. It is observed (Fig. 3) that an important part of the thermal spectrum falls near the wall which means a significant loss of heat.

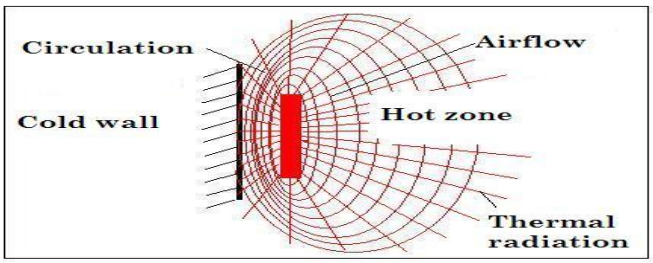

a)

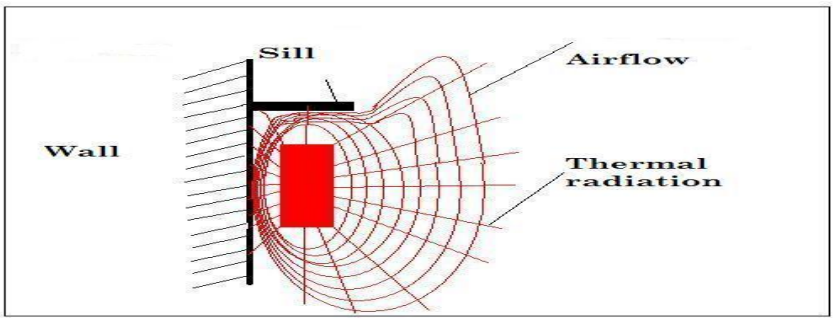

Fig 3: The radiator's heat spectrum when it is placed near the wall: a) without sill, b) with sill

If convectors are placed near the wall (Fig. 4a), we have a heat loss that is lesser than the case of radiator (Fig. 3a), because the additional circulation that brings heat from the wall and bring it into the useful space. In the case when there is a ledge above the heated body, for radiators (Fig. 3b) and respectively for converter (Fig. 4b), then the share of heat loss is even greater due to the negative effect brought by the windowsill, which unnecessarily increases the thermal spectrum. In case of the heated bodies freely in the rooms, (Fig 5) the case of convectors is more advantageous because the air fall brought by the forced circulation provided by the two sides of the convector. This option is provided only for practical electric convectors for theirs flexibility of their connections.

3 Theoretical and experimental results

The numerical analysis of thermal spectra and structures set and also from the experimental results measured over several winters is found in the following comparative data:

- Placing hot water pipes inside walls introduce a heat loss of about 23%, placing them outside a loss of about 7% and the power cord lose only about 0.2% of the energy transported;

- The place of heaters near the wall leads to a heat loss of about 27% for radiators, is about 18% for convectors;

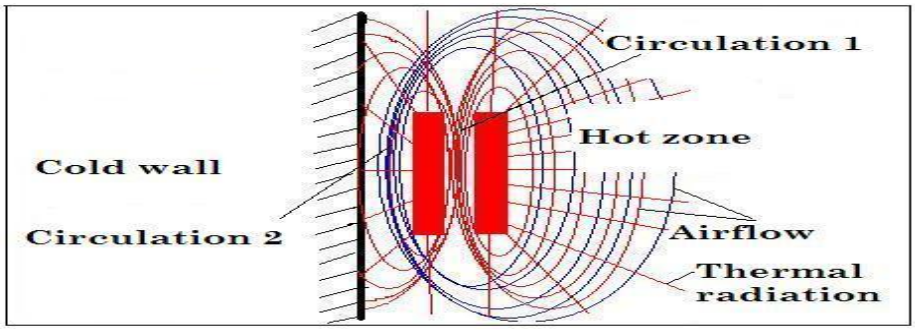

a)

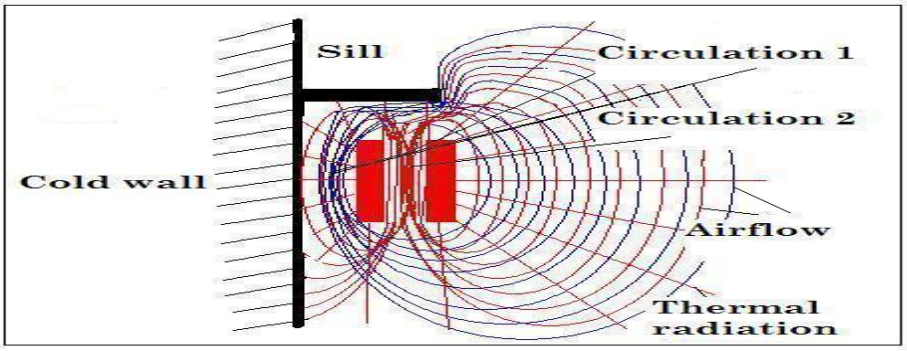

b)

Fig 4: The thermal spectrum when we place convectors near the wall : a) without sill, b) with sill

Existence of sills above the radiator introduces a further loss of about 14% to about 9% for radiators and convectors. Since these losses are multiplied successively, resulting an increased heat loss for bodies with water as heating agent placed near walls with 78%, for the radiators and pipes embedded in the walls, with sill, and with 65% for convectors in same conditions. If pipes are placed on the outside, the values are around 54% and 44%. If there is no sill, these values are reduced by 14% to 9% for convertors .Since the gas price is currently only of 74% less than the price of electricity tariff differential night, there is a gross approximation of the costs of heating values for the two forms of heating. For electric version an additional advantage is the flexibility of setting that provides programming of the heating intervals only when it is necessary. Existence of usual intakes program is equivalent to a further saving of about 10% which makes it more attractive this option.

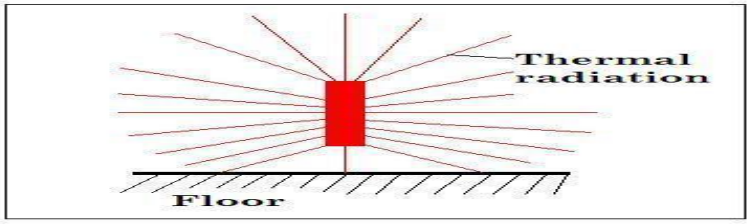

a)

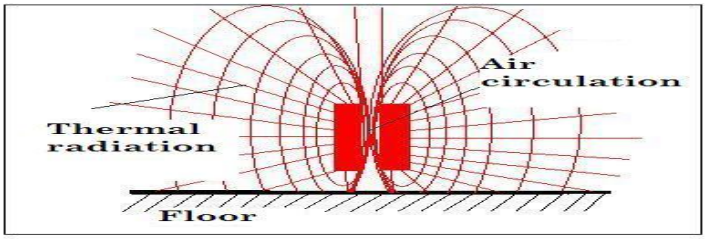

b)

Fig 5: Thermal spectrum cases: a) radiator placed on the wall; b) converter placed on the wall

The experimental results obtained in the conditions given in Table 1, are presented in Table 2.

Table 1 The conditions under which the experimental data were obtained.

Table 1 The conditions under which the experimental data were obtained.

Heating modes: Configuration 1: Winter 2006-2007 - Air Conditioning: October, November, March, April. - Electric panel heater for home: December, January, February. - Rate undifferentiated day and night. Configuration 2: Winter 2007-2008 - Air Conditioning: October, November, March, April. - Electric panel heater for home: December, January, February. Day-night-differentiated tariffs. Configuration 3: Winter 2008 to 2009 - Ceramic heaters: October, November, March, April. - Electric panel heater for home: December, January, February. - Rate differentiate day and night. Configuration 4: Winter 2009 to 2010 - Ceramic heaters all winter. - Rate differentiate day and night. Configuration 5: Winter 2010 to 2011 - Ceramic heaters all winter. - Rate differentiate day and night. - Thermally insulated attic	Technical data for house Ground floor: Living room with kitchen included - 30 sqm; Shower - 4mp. Floor: Bedroom 1 - 22 m; Bedroom 2 - 12 m; Bathroom - 9 m; Halls - 7 m. Attic: - 50 sqm. Scale: - 24 sqm. Technical Basement: - 16 sqm. Total: -174 sqm. The building is insulated on the outside 3cm thick extruded polystyrene.

4. Conclusions

The theoretical evaluations and the experimental results show that electrical heating is an option that should be taken into seriously consideration in the current economic and ecological context. Future developments are expected to emphasize the arguments in favor of this type of heating.

Acknowledgments

The paper was supported within:

- POSDRU Project 16 122, 2009-2011, entitled " "Încurajarea antreprenoriatului pentru inițierea de afaceri în domeniul Inginerie Electrică";

- POSDRU Project 77 497, PREDEX, 2010-2013, entitled "Pregătire doctorală de excelență pentru societatea cunoaşterii"

References

[1] N. Vasile, F. M. Stan. *Piața produselor şi tehnologiilor electrice,* Editura Bibliotheca, Târgovişte, 2012

[2] N. Vasile, F.Tudorache, S. Făsui, M. Guteş. *Energia-Probleme actuale, Raport de veghe Tehnologică,* Editura Electra, Bucureşti, 2007

[3] A. G. Gurgu, N. Vasile. "*Energy Efficiency in Heating our Homes and the Future of the Electric Heaters",* Electronica, Electrotehnica Automantica (EEA), ISSN 1582-5175, Nr. 3/ 2011;

[4] W. Patterson. *Electricitatea o industrie în schimbare,* Editura AGIR şi Editura Academiei Române, Bucureşti, 2000.

[5] D. Enescu , E.O. Vîrjoghe , O. Nedelcu. *Numerical simulation of thermal field distribution in the cross section of a cylindrical*. The scientific Bulletin of the Electrical Engineering Faculty, Targoviste, 2011

[6] R. Siegel, J. Hotwell. *Thermal radiation heat trensfer*. National Aeronautics and Space Administration, Washington, 1971.

[8] M. Modest. *Radiative heat trensfer*. U.S.A. Academic Press, San Diego, California, 2003

[9] H. J. Lienhard IV, H. J. Lienhard V. *A heat transfer textbook*, Philogiston Press, Cambrige U.S.A, 2002

[10] G, Palani, K.Y. Kim. *Joule heating and viscous dissipation effects on MHD flow plast a semi-infinite inclined plate with variable surface temperature,*Journal of Engineering Thermophysics, 2011

[11] T. Sameshima, Y. Kaneko, N.Andoh. *Rapid joule heating of metal films used to crystallize silicon films,* Applied Physics A Materials Science & Processing, 2002

Dual Loop PLL for a Radio Frequency Transceiver

Iulian URSAC, Catalin Adrian BRINZEI
"Politehnica" University, Spl. Independenţei 313, 060042, Bucharest, Romania;
ursac.iulian@gmail.com

Abstract. In this paper, a high frequency dual PLL for a radio frequency transceiver is proposed. This new PLL architecture, which relaxes the trade off design constrains, consists in two PLL loops that drive the same VCO. The first loop has a high current charge pump that drives the high gain VCO side and is aimed to improve the settling time performance. The second loop has a low current charge pump that drives the low gain VCO side in order to obtain a good phase noise performance. The simulations results show that this architecture has better performances than a single loop PLL.

1 Introduction

The wireless market has been rapidly increasing in last decade, and there has been worldwide development of new architectures that came to meet the new needs. In this way, new radio systems and circuit techniques design are being developed.
In this paper we present an improved phase looked loop (PLL) architecture, having low noise and fast settling time. The new topology is a dual loop PLL with modified voltage controlled oscillator (VCO), simultaneous low gain and high gain controls being incorporated in only one VCO. The Simulink simulation schematics are presented in Figure 1 for a classical PLL and in Figure 2 for a double loop PLL.

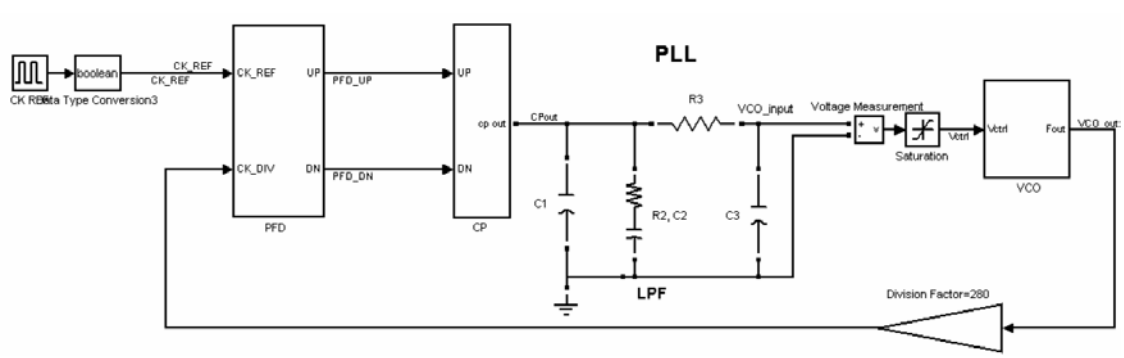

Figure 1: Classical PLL architecture

In Figure 1 is presented a classical PLL topology with phase frequency detector (PFD), 2mA charge pump (CP), third order low pass filter (LPF), 1GHz/V voltage controlled oscillator (VCO). The VCO output frequency is 6GHz.
The proposed dual loop PLL is presented in Figure 2. In literature we can find various dual loop PLL architectures [1], [2], [3], [4], [5], [6], [7], [8], [9]. This new topology was designed in order to improve the trade-off between acquisition behavior and locked behavior of a classical PLL.
The proposed dual loop PLL is presented in Figure 2 and contains two loops that control a dual gain VCO (VCO2g). Loop1 with phase frequency detector (PFD1), 2mA charge pump (CP1), second order low pass filter (LPF1) controls the Vctrl_Height_Gain input of VCO2g. Loop1 is similar as parameters with PLL in Figure 1. Loop2 with phase frequency detector

(PFD2), 40uA charge pump (CP2), second order low pass filter (LPF2) controls the Vctrl_Low_Gain input of VCO2g.

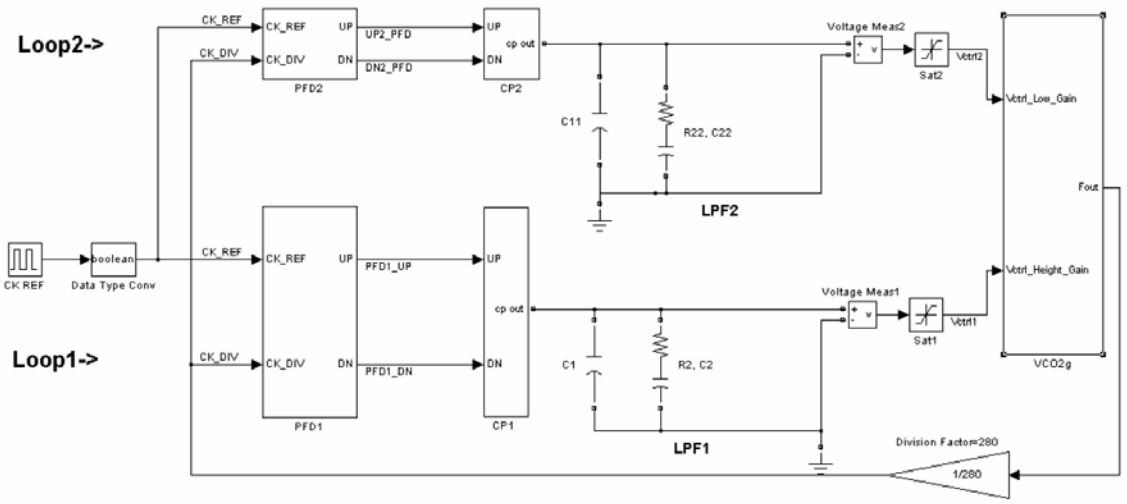

Figure 2: Dual loop PLL architecture

2 Comparison between classical PLL and dual loop PLLs

The first loop is used for large phase acquisition needed to decrease the settling time by increasing the first loop filter bandwidth. In this case the PLL will reach faster the permanent working domain. The first loop controls VCO2g frequency with a gain of 1GHz/V, having the dominant influence in VCO2g output frequency and is working just for phase error difference larger than DZ1.

The second loop has the same architecture as first loop, but with the appropriate block design parameters. This second loop is used for fine frequency adjustments in order to increase the noise system performance. The second loop of PLL controls VCO frequency with a gain of 10MHz/V influencing VCO output frequency and is working permanently.

In Figure 3 the transfer characteristics for PFD (a), PFD1 (b) and PFD2 (c) are presented. According to Figure 3 (a), the classical PLL PFD transfer characteristic, has a small dead zone DZ that produces a system noise. The DZ is obtained activating in the same time both CP inputs. Ideally the CP output current is zero in this case. But in practice, there is a mismatch between UP and DOWN charge pump currents, which can cause undesirable effects as reference spurs.

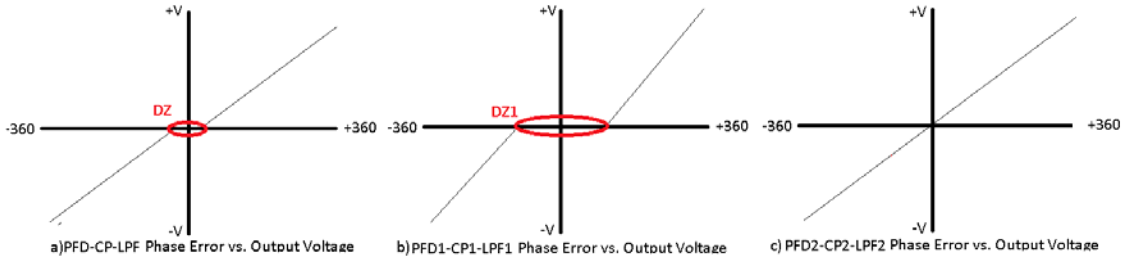

Figure 3: Transfer characteristics for PFD-CP-LPF (a), PFD1-CP1-LPF1 (b) and PFD2-CP2-LPF2 (c)

In PFD1 characteristic (Figure 3 (b)) we observe that the dead zone DZ1 is larger then DZ. PFD1 is specially designed that, during its staying in DZ1 region CP1 can not be controlled by PFD1. In this way, we avoid introducing noise in circuit due to charge

pump currents mismatch. The dual loop PLL functionality during its staying in DZ1 is maintained with PFD2 transfer characteristic (Figure 3 (c)), where the dead zone is neglected. Using of dual phase detectors as [9] has the advantage of using Loop1 just when we need frequency or large phase acquisition. At the small phase error values, only the second loop with a 40uA charge pump current is working. Because of the small CP2 current, the UP and DN currents mismatch is neglected.

The proposed 6GHz dual loop PLL architecture combines two distinct PLLs that have different contributions in the VCO2g output frequency. Loop1 controls the VCO frequency with a gain Kvco1=1GHz/V and Loop2, controls the same VCO frequency with a gain Kvco2=10MHz/V. The two gains Kvco1 and Kvco2 are obtained using two pairs of NMOS variable capacitors similar to those reported in [7].

The output frequency of the VCO is Fout=Vctrl1*Kvco1+Vctrl2*Kvc02.

Loop2 is designed with a charge pump current CP2=2%*CP1. LPF2 is designed with components scaled upon the current of CP2. The dual loop PLL use LPF1 second order filter that comes with next advantages with respect to the filter in the classical architecture:

-Less thermal noise by eliminating R3;

-Minimizes the impact of the VCO input capacitance having the largest capacitor C1 next to the VCO input.

Advantages of Dual Loop PLL

- Dual loop PFD1 and PFD2 does not use the simultaneous ON signals for CP to eliminate dead zone as PFD in Fig. 1 does. Loop2 minimizes the dead zone effect. Because of the low current CP2, the input CP2 capacitance is small. In this way the slew rate of PFD2 output signals will be neglected.
- Phase error pulses having width below DZ1 are processed by PFD2. For the tracking behaviour of the dual loop PLL is given only by Loop2. This fact leads to very small or negligible noise contributors:
  - we have no dead zone for PFD2, in this way the charge pump currents mismatch will not introduce noise in the system;
  - the small CP2 current value means small dimensions transistors producing small noise;
- The output signal of Loop2, Vctrl2 has a small noise. Loop2 contributions are multiplied with Kvco2=10MHz/v, the smaller gain of VCO2g. In this way in the VCO2g frequency output will have a smaller phase noise.
- Separation of the VCO gain in Low Gain and Height Gain has the advantages:
  - Large phase acquisition using Kvco1 high gain
  - Making of fine frequency adjustments using Kvco2 low gain

Advantages of Single Loop PLL

- Silicon area is with about 15% smaller than dual loop PLL
- Easier to design because of smaller degree of complexity

3 Simulations results

a. PLL Single and PLL Dual Loop time domain analysis

The classical PLL (Figure 4(a)) and Dual Loop PLL (Figure 4(b)) systems are simulated in close loop. We measure the settling time at the moment where the VCO2g voltage control Vctrl2 is set constant. The settling time of the classical PLL is with 0.4us faster than that of PLL dual loop. Single Loop PLL Settling time: = 9.2us. . Dual Loop PLL Settling time: = 9.6us

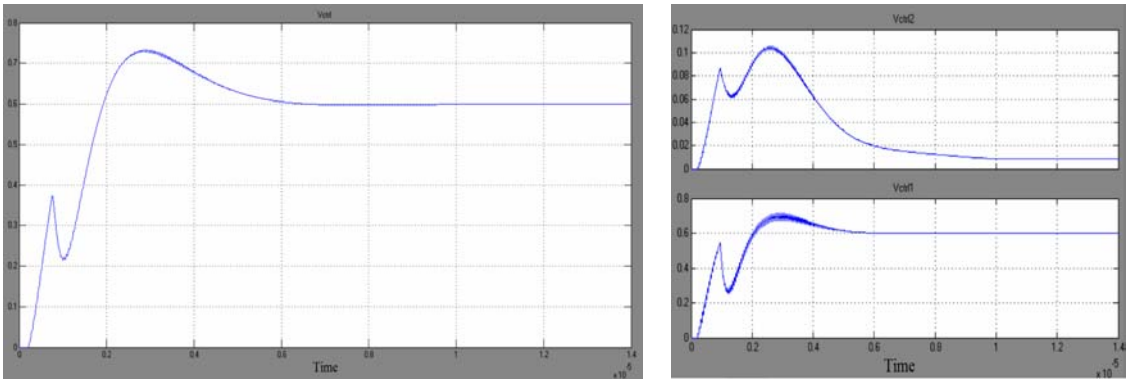

a b

Figure 4: PLL Single Loop (a) and Dual Loop (b) time domain analysis.

b. Classical PLL and Dual Loop PLL Stability

From the stability point of view, the Classical PLL (Figure 5(a)) has a 1.367degree phase margin more then dual loop PLL (Figure 5(b)). Single Loop PLL Phase Margin: PM = 57.793degree. Dual Loop PLL Phase Margin: PM = 56.426degree.

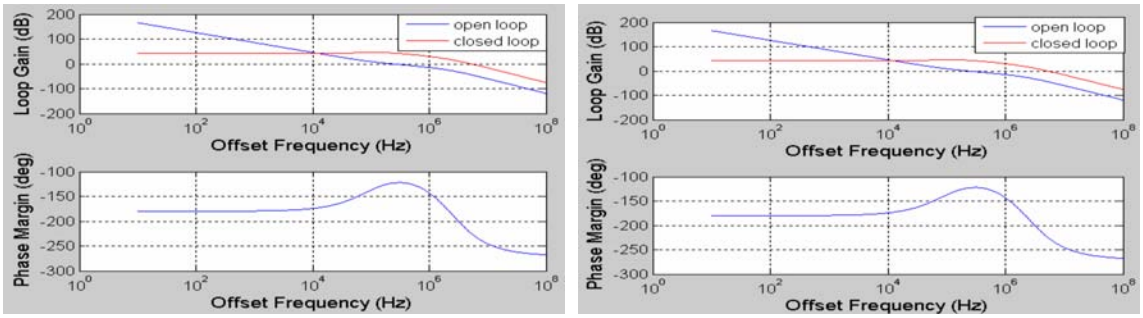

a b

Figure 5: PLL (a) and Dual Loop PLL (b) Stability.

c. Classical PLL and Dual Loop PLL Noise Analysis

The noise simulations take in to account the 90nm technology parameters, the 1/f noise parameters and an approximation of a sigma delta divider noise.

Loop1 is the principal noise contributor of the dual loop PLL. Loop1 introduces significant noise in the system just during the frequency or large phase acquisition. Usually Loop1 doesn't work so the noise performance is given mainly by Loop2.

The sources of Loop1 noise:

- –High current of CP1 determine the UP and DN currents mismatch to be considerable. Because of the CP1 big current the switch MOS transistors need to have large physical values. For the big transistors the charge pump leakage current became a noise contributor. In the locked state, CP1 is off, this means that the output current need to be 0mA (in practice this current is in the nA range).
- –Large value elements for LPF1 elements determine large thermal noise because of resistors noise (4*K*T*R)
- –VCO2g using the Kvco1 high gain, multiplies the noise signal, also.

The dual loop PLL (Figure 6(b)), presents 2.65dB better integer noise performance, than classical PLL (Figure 6(a)). This better noise performance is because of advantage of using the second loop for fine frequency tuning.

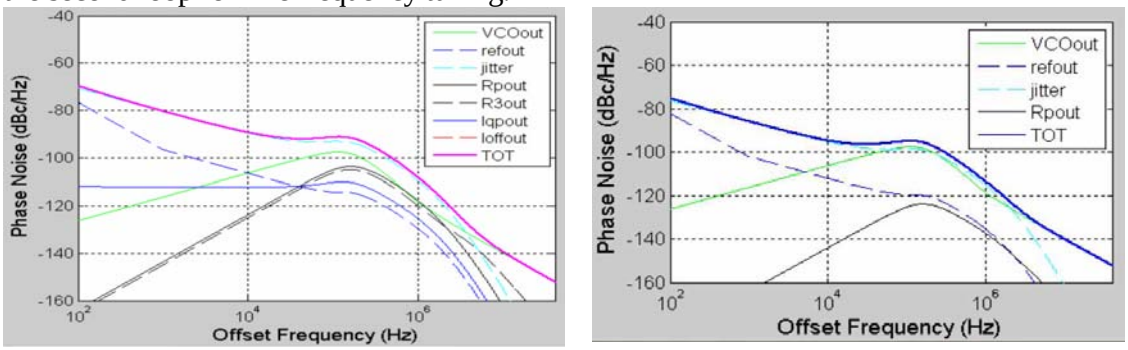

a b

Figure 6: Classical PLL and PLL dual loop output phase noise simulation.

4 Conclusion

- The proposed dual loop PLL in comparison with others dual loop PLLs [1], [2], [3], [4], [5], [6], [7], [8], [9], presents the advantage that without any other external control, Loop1, the main noise contributor of the system, is set off during the PLL phase tracking. In this way during the phase tracking operation, the dual loop PLL works just with Loop2.
- Dual loop PLL avoid use simultaneous ON signals for CP1 control by introducing of second loop.
- Dual loop PLL avoids use of the third order LPF, which confers less stability and is sensitive at VCO variable capacitance.
- The proposed VCO2g with two variable capacitor, make a gross adjustment of frequency from Kvco1, and a fine tuning using the small variable capacitor corresponding with Kvco2
- With dual loop PLL the constrains of the trade off between fast settling time and low phase noise are minimised:
    - To have fast PLL settling time is used the Loop1, with high CP1 current and the Kvco1 high gain. The main purpose of the Loop1 is for large phase acquisition.
    - To have low phase noise is used the Loop2, with low CP2 current and the Kvco2 low gain. Loop2 has the purpose to make the VCO2g frequency fine tuning. The second PLL loop, minimise the effect of charge pump currents mismatch

References

[1] Congyin Shi, Chuan Wang, Le Ye, Huailin Liao, *99dBc/Hz@10kHz 1MHz-Step Dual-Loop Integer-N PLL with Anti-mislocking Frequency Calibration for Global Navigation Satellite System Receiver*, Circuits and Systems (ISCAS), 2011 IEEE International Symposium, pp 1876-1879

[2] Yi-Cheng Chang and Edwin W. Greeneich, *Monolithic phase-locked loop circuits with coarse-steering acquisition aid*, Circuits and Systems, 1999. 42nd Midwest Symposium on Volume: 1, pp 283-286

[3] T. Nakamura , Y.Watanabe , E.Itaya , Y.Daido , T.Takano, *An 800 mhz low power consumption frequency synthesizer using intermittent operation of a modified pll circuit with dual loops*, Microwave Conference, 1987. 17th European, pp 309-314.
[4] Frank Herzel, Srdjan Glisic, Sabbir A. Osmany, J. Christoph Scheytt, Klaus Schmalz, Wolfgang Winkler, Michael Engels, *A Fully Integrated 48-GHz Low-Noise PLL with a Constant Loop Bandwidth*, Silicon Monolithic Integrated Circuits in RF Systems, 2008. SiRF 2008. IEEE Topical Meeting, pp 82-85.
[5] Ying Shen, Luc Villeneuve, Nacer Hassaine, *Dual Loop Push-Push Synthesizer for High Modulation Digital Radios at 38GHz*, Microwave Conference, 2007. APMC 2007. Asia-Pacific, pp 1-4.
[6] Frank Herzel, Sabbir A. Osmany, Klaus Schmalz, Wolfgang Winkler1, J. Christoph Scheytt, Thomas Podrebersek, Rüdiger Follmann, and Heinz-Volker Heyer, *An Integrated 18 GHz Fractional-N PLL in SiGe BiCMOS Technology for Satellite Communications*, 2009 IEEE Radio Frequency Integrated Circuits Symposium, pp 329-332.
[7] Xiaolei Gai, Sebastien Chartier, Andreas Trasser, and Hermann Schumacher, *A 35 GHz Dual-loop PLL with Low Phase Noise and Fast Lock for Millimeter Wave Applications*, Microwave Symposium Digest (MTT), 2011 IEEE MTT-S International, pp 1-4.
[8] Bodhisatwa Sadhu, Mark A. Ferriss, Jean-Olivier Plouchart†, Arun S. Natarajan, Alexander V. Rylyakov,Alberto Valdes-Garcia, Benjamin D. Parker, Scott Reynolds, Aydin Babakhani, Soner Yaldiz, Larry Pileggi, Ramesh Harjani, Jose Tierno and Daniel Friedman, *A 21.8−27.5GHz PLL in 32nm SOI Using Gm Linearization to Achieve −130dBc/Hz Phase Noise at 10MHz Offset from a 22GHz Carrier*, 2012 IEEE Radio Frequency Integrated Circuits Symposium, pp 75-78.
[9] Kurt M. Ware, Hae-Seung Lee, Charles G. Sodini, *A 200-MHz CMOS Phase-Locked Loop with Dual Phase Detectors*, IEEEJournal of Solid-State Circuits, Vol. 24, No. 6, December 1989, pp 1560-1568
[10] Keliu Shu, Edgar Sánchez-Sinencio, *CMOS PLL Synthesizers: Analysis and Design*, Springer Science 2005.

Frequency Mixer Based on a Resistor String Digital-to-Analog Converter

Cătălin BRÎNZEI, Iulian URSAC
"Politehnica"University Bucharest, Spl. Independenţei 313, 060042,Romania

Abstract. In this paper a frequency mixer which is the main block of a transmitter is proposed and is based on a fully digital multiplier circuit combined with a digital-to-analog converter with a resistor string topology. This architecture has some important advantages given by the use of digital blocks and these advantages are the low power consumption, robustness and portability to other technologies. The converter has a topology which uses resistors and the mismatches between the resistors should be taken into account since the performance is limited by this parameter.

1 Introduction

A digital frequency mixer combined with a DAC (digital-to-analog converter) which uses a string of resistors is proposed and the most important advantage is the low power consumption and low SFDR (Spurious Free Dynamic Range) which is around 64dB. The proposed mixer achieves a high spectral purity by using a minimal analog circuitry in the output and this is an optimized DAC.

2 Principle of operation

The proposed mixer architecture multiplies two signals which are provided in binary format by the base band processor built on the chip. The result which is still in binary format is converted to an analog voltage signal using a resistor string digital-to-analog converter. The output of the digital frequency mixer is a 6 bit word and represents the multiplication of the input signals .The digital-to-analog converter uses as input the output of the digital multiplier and generates an analog voltage according with the resulted six bit code. Because of this hybrid implementation the circuit can be easily implemented in a digital CMOS technology enabling a low voltage and low power architecture but it should be mentioned that the technology should support high precision resistors with low variation over process corners.

The implementation of an almost completely digital mixer has the advantage of the excluding from the signal path of the input filter on the base band section. This is a major advantage since often these filters are hard to implement on silicon and occupy a lot of area. The proposed mixer partially eliminates the filtering problem and takes the advantages of using of the digital circuits such as ease of low voltage design and also design portability over other technologies. The block diagram of the proposed architecture is given below:

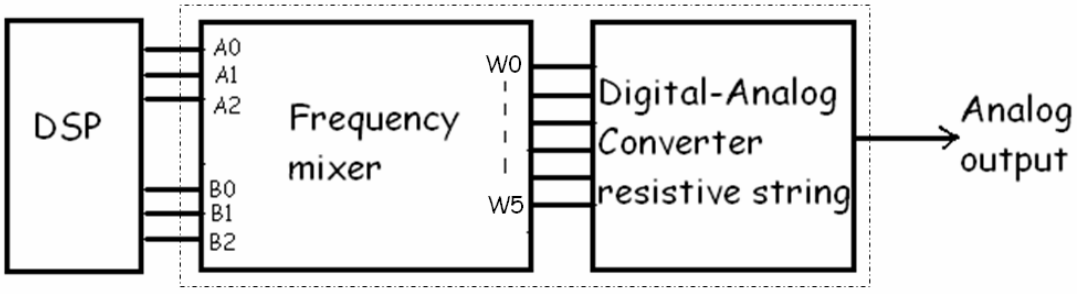

Figure 1: Block diagram

A digital mixer is proposed to be used for the base band section of radio frequency front end transmitters covering different communication standards and the main components consists from a digital multiplier followed by a six bit linear DAC which is used to convert the multiplication result from a binary format into an analog voltage. The multiplication is performed in the digital domain but the performance is limited by the analog part so we will focus to optimize the converter.

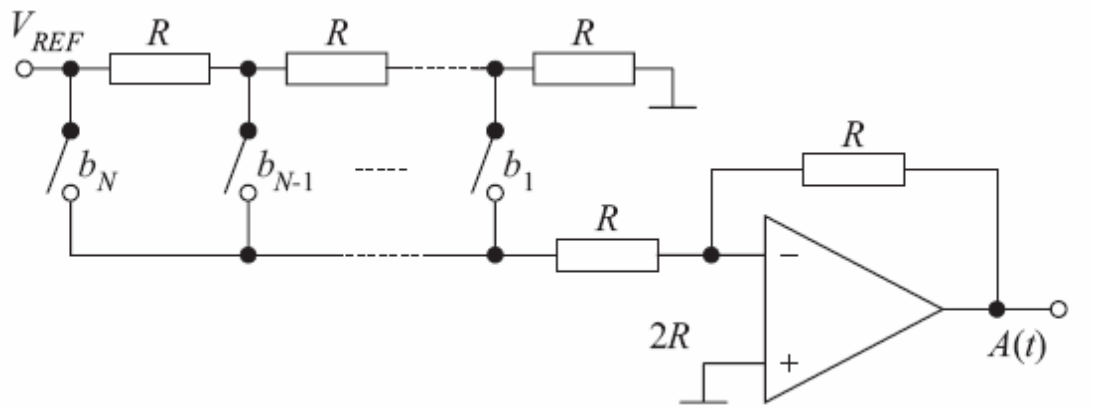

Figure 2: Resistor string digital-to- analog converter [2]

The performance of the system is limited by the analog portion and the main contributor is the mismatch between the resistors. These effects can be minimized by using proper resistor values and also by using enough area for these devices on silicon. Higher area of these resistors results in better matching values so a better overall performance of the entire system is expected.

The functionality is described by the following equation [2]:

$$V_m = \frac{m \cdot R}{R_{TOT}} \cdot V_{REF} = \frac{m}{2^N - 1} \cdot V_{REF} \qquad (1)$$

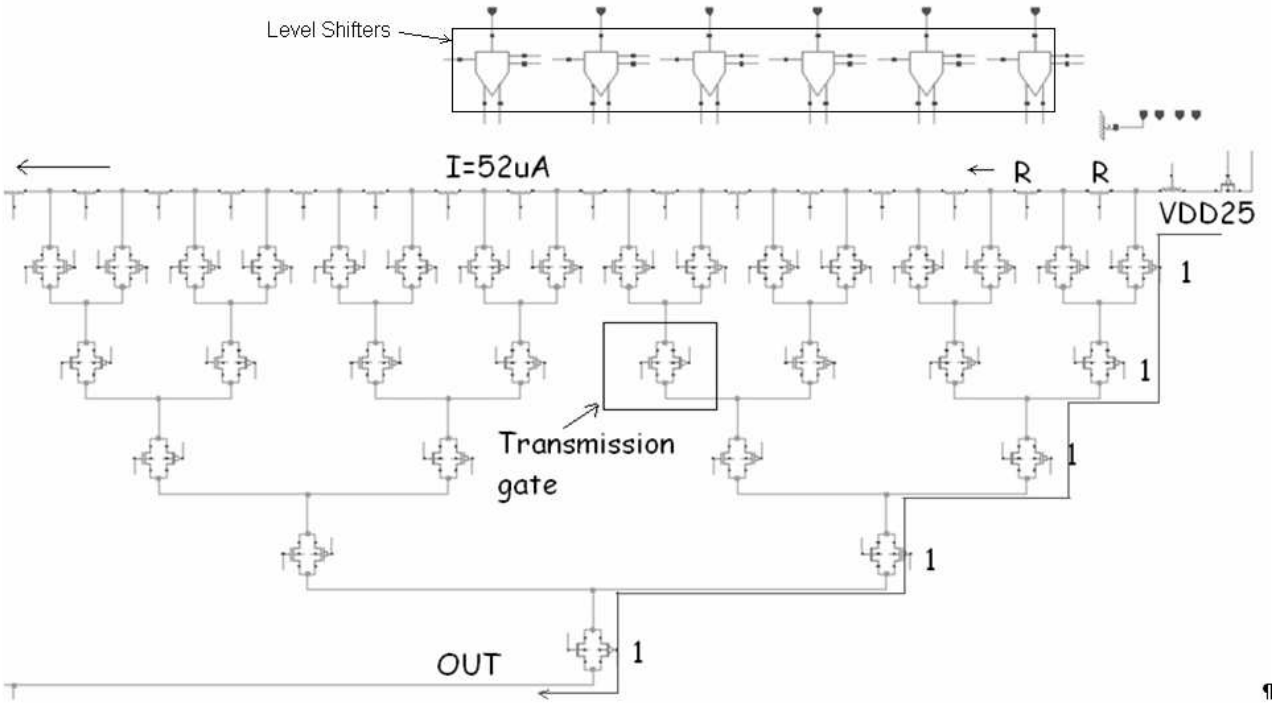

Figure 3: Schematic of the resistor string DAC

In equation (1) the variables have the following meaning:

- m is the number of the resistors used to divide the reference voltage, sixty four in total
- N is the total number of the bits of the converter which is six
- R is the value of a single resistor and R_{TOT} is the sum of all resistances in the string
- V_{REF} is a reference voltage of 2.1V generated using a 2.5V regulated voltage supply.

This DAC topology uses transmission gates built with MOS transistors and these connects the analog output to one tap in the string depending on the digital input code applied at the input of the level shifters. The continuous line in Figure 3 shows a signal path of the highest voltage converted and how the divided voltage is connected to the output. The MOS transmission gates were built using minimum values for the width and length of the PMOS and NMOS transistors to minimize the charge injection in the output. A current injection takes place due to this effect and unwanted voltage spikes which lead to errors and low performance might be seen in the output [2]. The maximum power dissipation will determine the current flowing through the resistor string. Considering that the maximum power is 130uW results $\mathrm{Im}\,ax$ from the following equation:

$$\mathrm{Im}\,ax = \frac{130*10^{-6}W}{2.5V} = 52\mu A$$
$$R = \frac{1}{32}\frac{2.5V}{52e^{-6}} = 1.502K\Omega \qquad (2)$$

Since the resulted resistor value is relatively high and occupies a significantly area, then an additional voltage divider is used enabling smaller values for the resistors down to $500\,\Omega$. These are much easier to be implemented on silicon occupying less area but having the drawback of the increased mismatches between resistor values. There is a trade-off between the silicon area or the cost and DAC linearity in the output which depends by the matching between resistors.

3 Simulation results

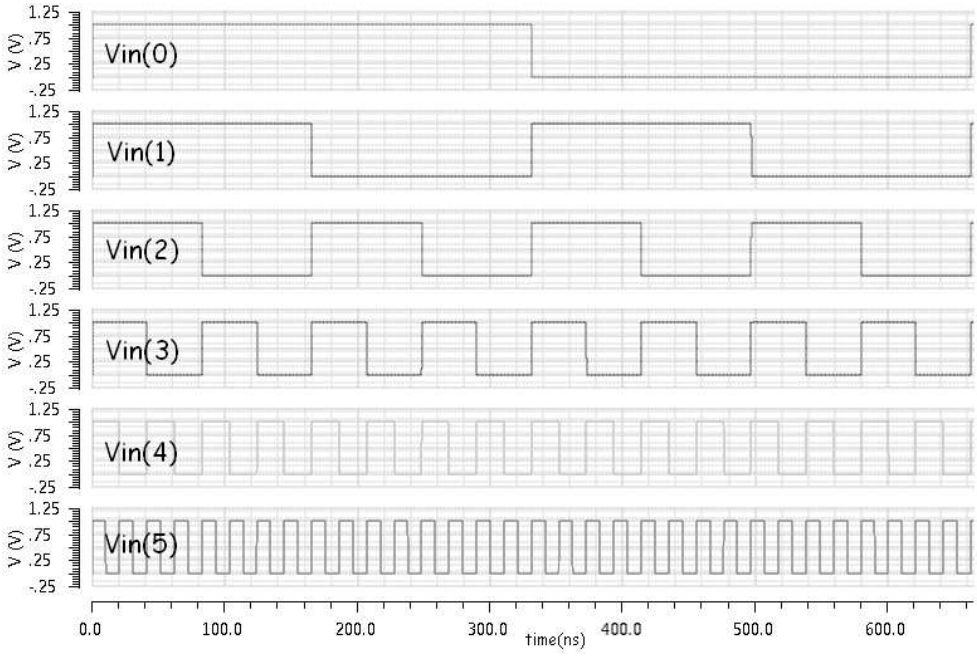

Figure 4: Control signals, input digital code generation

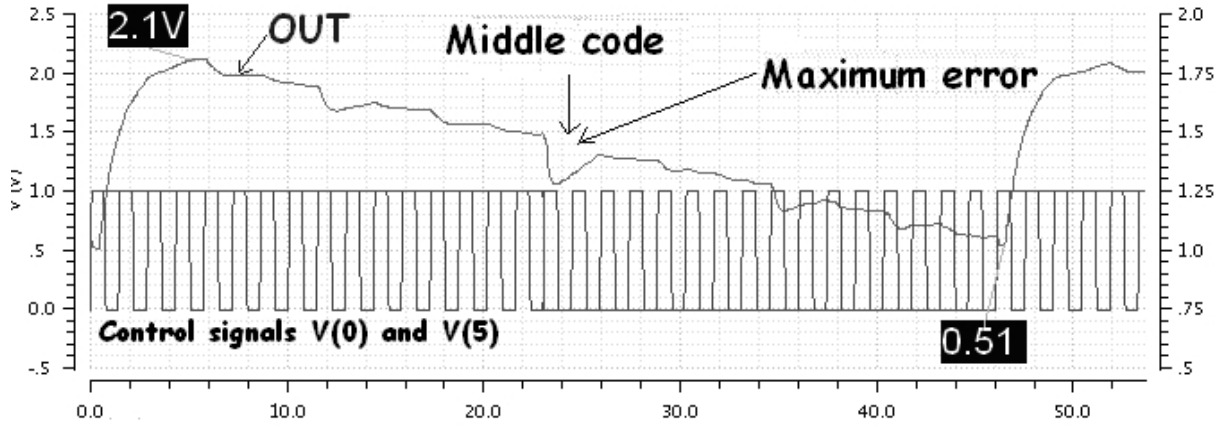

Figure 5: Output voltage of DAC using a "digital ramp" in input

All sixty four input codes were applied in the input creating a digital ramp meaning that all the codes are successively applied from 0 up to 63. The output voltage is varying almost linearly from 0.51V up to 2.1V. The maximum error is found near the middle code as expected where the glitch energy in the output is significant, leading to an unwanted voltage drop.

Static performance parameters INL and DNL

The most important static error parameters for a DAC are the INL („Integral Non Linearity") and DNL („Differential Non Linearity") and were computed based on the simulations results from Spectre.

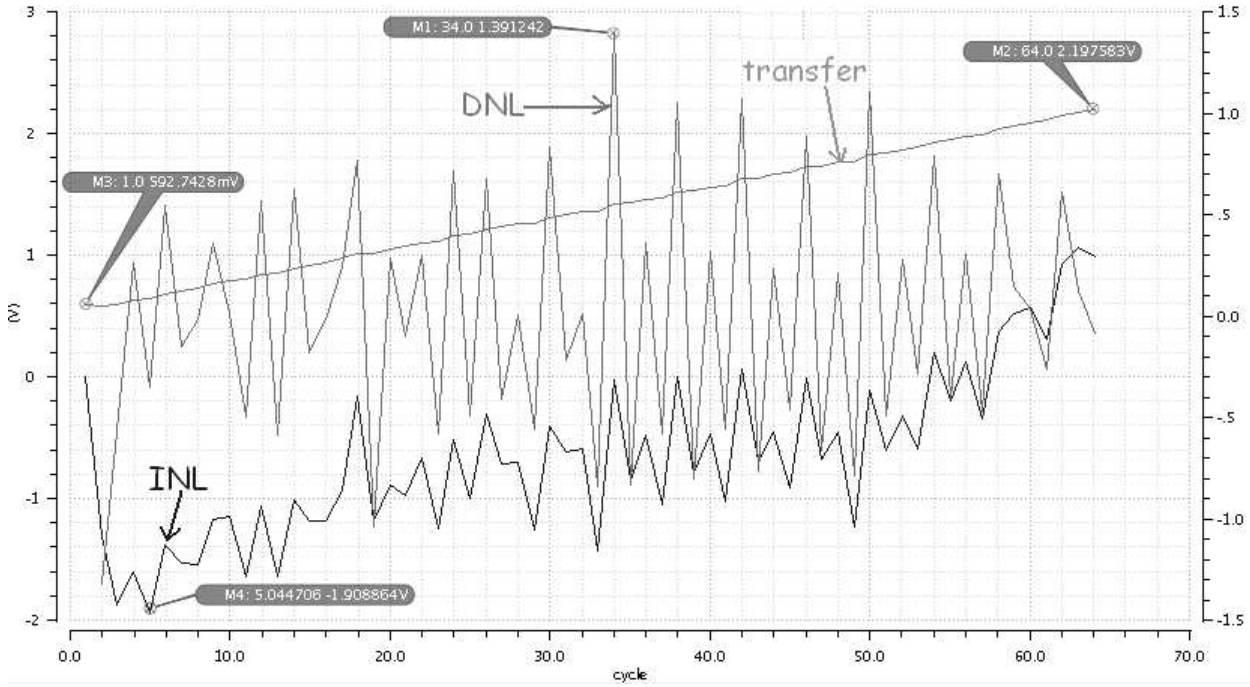

Figure 6: INL, DNL and transfer function for a resistor string DAC

It was obtained a Spurious Free Dynamic Range (SFDR) of 64dB while using a maximum current consumption Imax of 52uA only for the resistive network. The DNL and INL computed using the transient simulation results were 1.39 LSB and 1.9LSB respectively.

Procedure to get INL and DNL in Cadence using SPECTRE simulations results

The script given below uses the transient simulation results and computes the static performance parameters INL and DNL. The commands are written in CIW window on Cadence platform just after the simulation is complete. This script might be reutilized for characterization of any DAC type but the user should adjust the number of cycles (in this case is 64 since the converter has a digital input on six bits), the full scale range and the simulation time to match the time needed for DAC to experiment a full "digital ramp" in input or all possible analog voltage values in the output. The functional equations used in this script were described in [4].

```
avg_step=1.62/64
Sampled=value(v("/com" ?result "tran") 2.0n ?period 5n ?xName "cycle" )
plot(Sampled)
DNL= (deriv(Sampled)-avg_step)/avg_step
plot(DNL)
ymax=value(Sampled 64)
ymin=value(Sampled 1 )
temp=ymax-ymin
m=temp/64
c=ymin-m
x=xval(value(v("/com" ?result "tran") 2.0n ?period 5n ?xName "cycle" ))
mx=m*x
mxc=mx+c
Sampledmxc=Sampled - mxc
avg_step=1.62/64
INL=Sampledmxc/avg_step
INL=(Sampled-((m*x)+c))/avg_step
plot(INL)
```

Digital multiplier

The schematic of the digital multiplier implemented with full (FA) and half adders (HA) is given below and represents a detail of the frequency mixer block showed in Figure 1. The schematic below was used together with a six bit resistor string DAC considering the first two MSB bits to be zero.

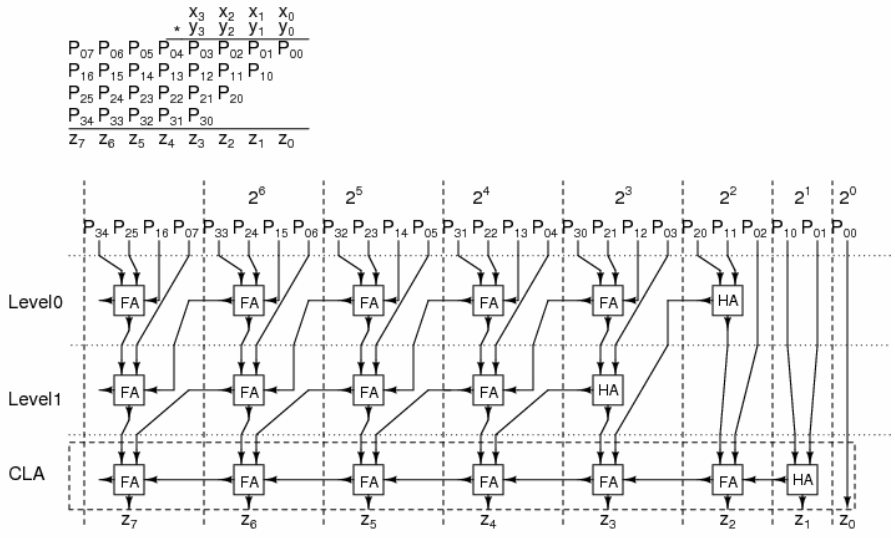

Figure 7: Wallace tree digital multiplier [3]

Output spectrum for the digital mixer

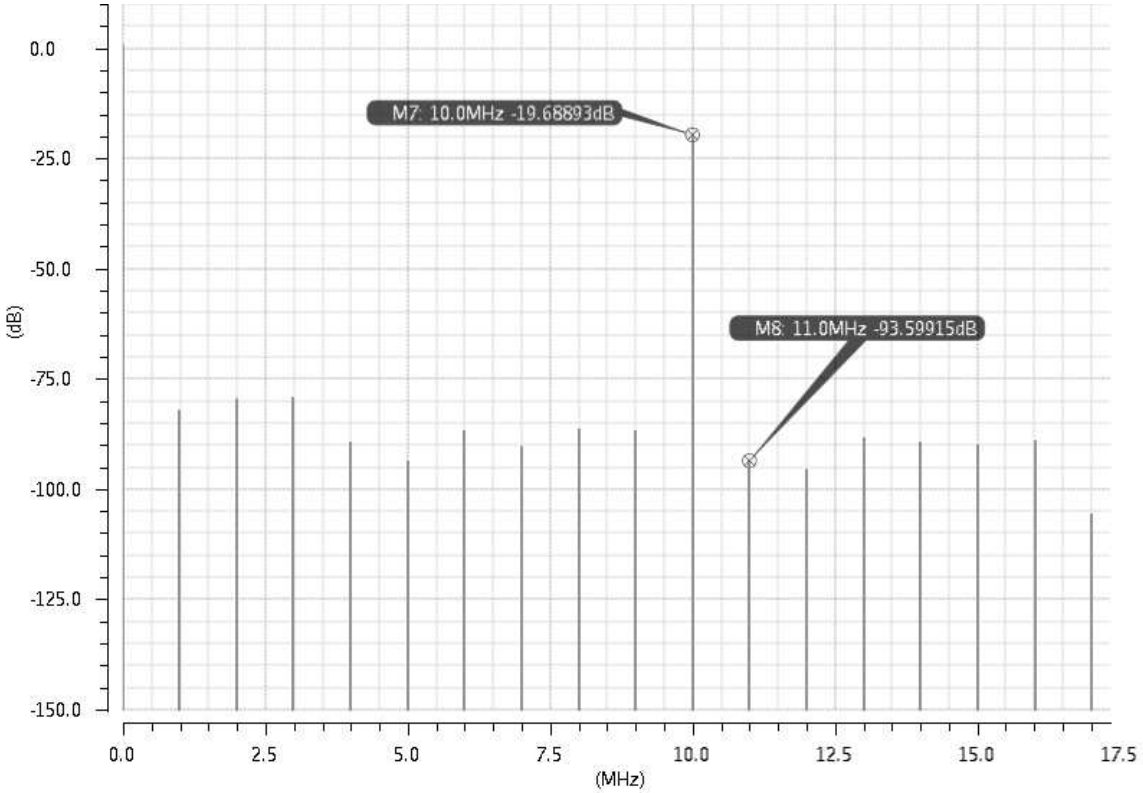

Figure 8: Output spectrum of the digital mixer

4 Conclusion

- The working frequency is significantly higher than 327 KHz which was reported in [1] and it was compared with a 10MHz analog signal at the output of the DAC.
- The SFDR parameter is around 64dB and shows a very good spectral purity which is much better than it was reported in [1] where the SFDR was 52dB.
- A major disadvantage comparing with [1] is that we still need to add a filter in the output of the DAC because the image component still needs to be minimized.
- The static parameters for linearity INL (1.9LSB) and DNL (1.39LSB) are in acceptable margins but much worse if we compare with a DAC segmented architecture.
- The combination between a pure digital multiplier and a digital-to-analog converter is very attractive to be implemented on chip due to higher performances compared with the case when an analog mixer is used in the transmitter chain.

References

[1] P. Sotiriadis, W.Ling, *Almost All-Digital Sinewave-Product Generation for Frequency Synthesis Applications*, Frequency Control Symposium, Joint with the 22nd European Frequency and Time forum. IEEE, 2009.

[2] J. Wikcner, *Studies on CMOS digital-to-analog converters*, Linköping Studies in Science and Technology, 2001.

[3] N. Rahman, R. Yun, *8x8 Booth-Encoded Wallace Tree Multiplier*, Tufts University, Dept.of Electrical and Computer Engineering, 2007.

[4] M. Omar, *DNL and INL calculations in Spectre*, Silicon Vision, June 2009.

Characterisation of circulant networks using eigenvalues, singular values and condition number

Dan MICU,
Technical University. Baritiu 26, Cluj-Napoca, Romania; d_o_micu@yahoo.com
Gilbert DE MEY
University of Ghent, Sint Pietersnieuwstraat 41, Ghent, Belgium

Abstract. In this paper the definition of a circulant network will be presented. The system matrix of such network are circulant matrices, which allow an analytical evaluation of all the eigenvalues and all the singular values. Resonance frequencies can then be calculated exactly as will be demonstrated on active circulant networks.

1 Introduction

A circulant network is defined as a series connection of identical basic cells connected in a closed loop. It is known that a closed loop can give rise to resonance or instability especially if active elements are involved. A will be shown furtheron, the system matrix of such networks turns out to be a circulant matrix, the reason the name circulant networks has been chosen. The major property is that all the eigenvalues of a circulant matrix can be calculated analytically. This offers the unique possibility to evaluate condition numbers of the system matrix exactly, so that eventual ill conditioning or resonances can be evaluated exactly.

2 Basic analysis

Let us consider the circulant network shown in Fig.1. The unit cell is composed of an impedance $\underline{Z}$ and an admittance $\underline{Y}$. The current sources $\underline{I}_i$ can be diferent. A circulant network implies that the chain of Fig.1 must form a closed loop or the node n + 1 = node 1.

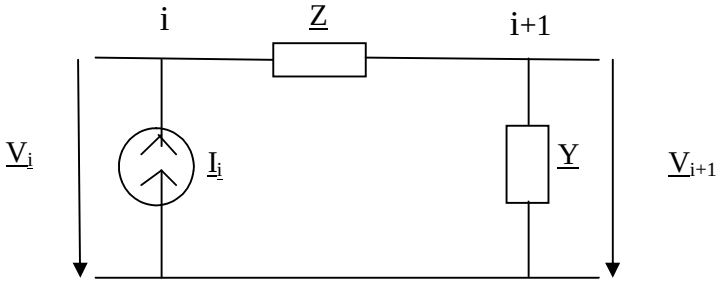

Fig.1 The unit cell of circulant network

The voltage $\underline{V}_i$ at node i satisfies the nodal equation:

$$\frac{\underline{V}_i - \underline{V}_{i-1}}{\underline{Z}} - \frac{\underline{V}_i - \underline{V}_{i+1}}{\underline{Z}} + \underline{Y}\underline{V}_i = \underline{I}_i \qquad (1)$$

for i=1,2,...n. If i=1 then $\underline{V}_{i-1}$ has to be replaced by $\underline{V}_n$ and if i=n then $\underline{V}_{i+1}$ has to be replaced by $\underline{V}_1$ in (1).

(1) can be slightly rewritten as:

$$(2+\underline{Z}\,\underline{Y})\underline{V}_i - \underline{V}_{i-1} - \underline{V}_{i+1} = \underline{Z}\underline{I}_i \qquad (2)$$

Or in matrix form:

$$[A][V]=[Z][I] \tag{3}$$

The system matrix [A] is then:

$$\begin{bmatrix} 2+\underline{Z}\underline{Y} & -1 & & & & & & -1 \\ -1 & 2+\underline{Z}\underline{Y} & -1 & & & & & \\ & -1 & 2+\underline{Z}\underline{Y} & -1 & & & & \\ & & -1 & 2+\underline{Z}\underline{Y} & \dots & \dots & & \\ & & & -1 & \dots & \dots & & \\ & & & & \dots & \dots & & \\ & & & & & -1 & 2+\underline{Z}\underline{Y} & -1 \\ -1 & & & & & & -1 & 2+\underline{Z}\underline{Y} \end{bmatrix} \tag{4}$$

[A] is obviously a circulant n x n matrix, the eigenvalues of which can be calculated analytically.

3 Eigenvalues analysis

The eigenvalues of a circulant matrix [A] can be evaluated as follows:

$$\lambda_0 = \sum_{k=1}^{n} A_{1,k} = \underline{Z}\underline{Y} \tag{5}$$

$$\lambda_m = \sum_{k=0}^{n-1} A_{1,k+1} \exp\left(2\pi j \frac{mk}{n}\right) = \underline{Z}\underline{Y} + 4sin^2\frac{\pi m}{n} \tag{6}$$

where m=1,2,…(n-1).

If $\underline{Z}\,\underline{Y}$ is real and positive and n even the maximum eigenvalue occurs for m=n/2 or $\lambda_{n/2}= \underline{Z}\,\underline{Y}+4$ The condition number is then (for circulant matrix):

$$\kappa=|\lambda_{n/2}|/|\lambda_0|=|\underline{Z}\,\underline{Y}+4|/|\underline{Z}\,\underline{Y}| \tag{7}$$

or the largest eigenvalue (in absolute value) divided by the smallest one.

Generally the condition number is defined with the so called singular values σ_i. These are defined by[1]:

$$\sigma_i = \sqrt{\mu_i} \tag{8}$$

where μ_i are the eigenvalues of the matrix $[A]^H[A]$, $[A]^H$ being the Hermitean (the transpose conjugate) of the system matrix [A].

If $\sigma_0 \le \sigma_1 \le \sigma_2 \le \dots \le \sigma_{n-1}$ the condition number κ is then defined by:

$$\kappa = \frac{\sigma_{n-1}}{\sigma_0} \tag{9}$$

A condition number close to unity guarantees the system matrix is well conditioned. High values of κ indicates ill conditioning which can be either due to numerical problems but also due to the fact the electric network is not stable (oscillator e.g.). An important difference between eigenvalues and singular values is that the latter ones are always real and positive numbers.

$[A]^H[A]$ is a circulant matrix too and all the elements are real numbers. The eigenvalues μ_i of $[A]^H[A]$ are found similarly by using (5) or (6):

$$\mu_0 = \sum_{k=1}^{n} A^H A_{1,k} = \underline{Z}\,\underline{Y}\,\underline{Z}^*\,\underline{Y}^* \tag{10}$$

$$\mu_m = \sum_{k=0}^{n-1} A^H A_{1,k+1} \exp(2\pi j \frac{mk}{n}) = \underline{Z}\,\underline{Y}\,\underline{Z}^*\,\underline{Y}^* + 4\,(\underline{Z}\,\underline{Y} + \underline{Z}^*\,\underline{Y}^*)\sin^2\frac{\pi m}{n} + 16\sin^4\frac{\pi m}{n} =$$

$$= (\underline{Z}\,\underline{Y} + 4\sin^2\frac{\pi m}{n})(\underline{Z}^*\,\underline{Y}^* + \sin^2\frac{\pi m}{n}) \tag{11}$$

It can be easily verified that

$$\mu_m = |\lambda_m|^2 \tag{12}$$

We note $\underline{Z}$ =r+jx, $\underline{Y}$ =g+jy so

$$\underline{Z}\,\underline{Y} = rg - xy + j\,(ry + gx) = a + j\,b \tag{13}$$

Let

$$\mu_{max} = \mu_p = (a + 4\sin^2\frac{p\pi}{n})^2 + b^2$$

$$\mu_{min} = \mu_q = (a + 4\sin^2\frac{q\pi}{n})^2 + b^2$$

The condition number is

$$\kappa = \sqrt{\frac{\mu_p}{\mu_q}} \tag{14}$$

If a>0 the condition number indicates a well conditioned system matrix. In this case $p=[n/2]$ and q=0 (the (7) formula is found once again for even n and b=0.

The ill-conditioned system is obtained only for b=0 and $a \in [-4,0]$ so $\underline{Z}$ =jωL and $\underline{Y}$ =jωC, p=0 and $a+4\sin^2\frac{\pi q}{n}=0$ or the resonance condition is

$$\omega^2 LC = 4\sin^2\frac{\pi q}{n} \tag{15}$$

For example if n=3 the condition is

$$\omega^2 LC = 3 \tag{16}$$

After the triangle-star transformation in the circulant circuit of Fig.1, the circuit is presented in Fig.2, where $\underline{E}_i = \frac{1}{j\omega C}\underline{I}_i$.

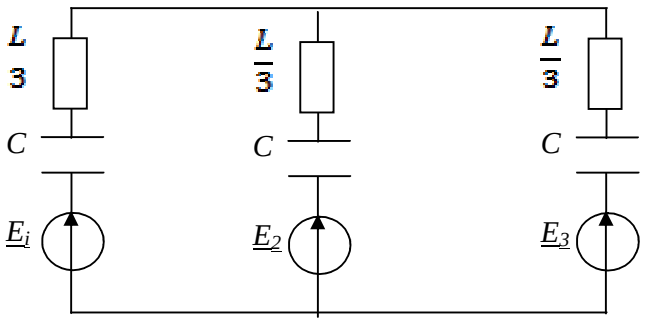

Fig.2 Resonance in circulant network with 3 cells

With (16) we have serie resonance in Fig.2 and if the sources are different the network is in great difficulty.

For q=0 one gets then a resonance at "DC" which means physically that all the capacitors in the lumped LC are being charged to the same constant but arbitrary voltage. The singular values are now:

$$\sigma_0 = \omega^2 LC$$

$$\sigma_m = |\omega^2 LC\text{-}4\ sin^2 \frac{\pi m}{n}| \qquad (17)$$

Regarding the resonance frequecies, the classical eigenvalue analysis (15) provides us the same values as the singular values (17).

5 Conclusion

It has been proved in this paper that the system matrix of a so called circulant network turns out to be a circulant matrix. These matrices have the major advantage that all the eigenvalues can be calculated analytically. It becomes then possible to analyse phenomena like resonance exactly, without any disturbance due to ill conditioned matrices. It was also observed that the results obtained from the eigenvalues or from the singular values are all in perfect agreement. This is a consequence of the fact that the singular values is equal to the absolute values of the eigenvalues for the circulant matrix,

References

[1] D. Micu, L. Chira "*Elemente de teoria circuitelor electrice*" Editura Dacia, Cluj-Napoca, 2010.
[2] G. De Mey "*Potential calculations in Hall plates* " Advances in Electronics and Electron Physics, 1983, vol.61, pp.1-61.
[3] R .A. Horn, C. R. Johnson, *Analiza matriciala* , (trad. I. Beltita, D. Beltita, R. Gologan) Ed. Theta, Bucuresti, 2001.

Aplicație MathCAD şi simulare MATLAB-Simulink pentru circuite electrice trifazate cu sarcini dezechilibrate particulare

Adrian PANĂ, Alexandru BĂLOI, Florin MOLNAR-MATEI
Universitatea "Politehnica" din Timişoara,
Piața Victoriei nr. 2, 300006, Timişoara; adrian.pana@et.upt.ro

Abstract. Lucrarea prezintă un studiu teoretic însoțit de o aplicație MathCAD şi apoi de o simulare MATLAB-Simulink, privind regimul de funcționare a unui circuit de curent alternativ trifazat, în cazuri particulare ale dezechilibrului sarcinii. Există structuri particulare ale receptorului nesimetric care determină fie ca tensiunile simple la bornele receptorului să fie nesimetrice în timp ce curenții pe fazele acestuia sunt echilibrați, fie ca tensiunile simple la bornele receptorului să fie simetrice, în timp ce curenții sunt dezechilibrați. Una dintre aceste structuri particulare îşi găseşte aplicare practică la simetrizarea sarcinii prin compensare reactivă transversală dezechilibrată

1 Introducere

Dezechilibrele din rețelele electrice trifazate funcționând în regim sinusoidal se datorează în principal receptoarelor dezechilibrate. Consumatorul complex, care are în componența sa receptoare de toate tipurile, inclusiv monofazate, nu poate fi perfect echilibrat.

Aprecierile calitative şi cantitative asupra cazurilor particulare de dezechilibre discutate în lucrarea de față, sunt valabile într-o rețea fără conductor neutru. Pentru dezvoltarea teoretică a problemei se consideră o rețea electrică redusă la structura sa minimală, sursă-receptor. Indiferent dacă cele două elemente au conexiunea Y sau Δ, concluziile sunt aceleaşi. Pentru considerațiile teoretice este mai util însă a se utiliza conexiunile Y la ambele elemente (fig. 1).

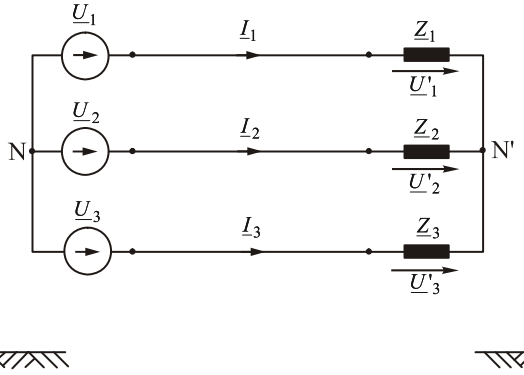

Fig. 1 Rețea redusă la configurația sursă-receptor, în conexiune stea-stea fără conductor neutru.

În această rețea se consideră că sursa generează un set simetric de tensiuni înlănțuite de succesiune pozitivă. Se notează cu N neutrul sursei, având $\underline{U}_N$ valoarea complexă a potențialului său în raport cu o referință arbitrar aleasă şi cu N' neutrul receptorului, având $\underline{U}_{N'}$ valoarea complexă a potențialului său, în raport cu aceeaşi referință. Absența conductorului neutru face ca $\underline{U}_N - \underline{U}_{N'} \neq 0$, această diferență fiind denumită de obicei "tensiune de dezechilibru". Calculul acesteia, a celorlalte tensiuni (înlănțuite, simple) şi a circulației de curenți într-o astfel de rețea se poate face în mai multe moduri, folosind teoremele cunoscute ale lui Millman, Thévenin, Kennelly. Se poate folosi de asemenea metoda componentelor de secvență +, - şi 0, metodă aplicată şi în expunerea de față.

Într-o astfel de rețea există câteva structuri particulare ale receptorului nesimetric care determină situații paradoxale, în care fie tensiunile simple la bornele receptorului sunt

nesimetrice în timp ce curenții pe fazele acestuia sunt echilibrați, fie tensiunile simple sunt simetrice, în timp ce curenții sunt dezechilibrați.

Cazurile particulare şi condiția aferentă impusă valorilor elementelor schemei echivalente a receptorului, $\underline{Z}_1$, $\underline{Z}_2$, $\underline{Z}_3$, sunt după cum urmează [1]:

Cazul 1. Curenții absorbiți de consumator formează un set echilibrat (de secvență pozitivă), dar tensiunile simple la bornele receptorului sunt nesimetrice.

Dacă valorile impedanțelor $\underline{Z}_1$, $\underline{Z}_2$, $\underline{Z}_3$ îndeplinesc condiția:

$$\underline{Z}_1 + a \cdot \underline{Z}_2 + a^2 \cdot \underline{Z}_3 = 0 \qquad (1)$$

se obține echilibrul curenților ($\underline{I}^+ \neq 0$, $\underline{I}^- = 0$, $\underline{I}^0 = 0$) şi simetria tensiunilor înlănțuite, dar nesimetria tensiunilor simple la bornele receptorului ($\underline{U}'^+ \neq 0$, $\underline{U}'^- = 0$, $\underline{U}'^0 \neq 0$).

Cazul 2. Curenții absorbiți de consumator formează un set echilibrat (de secvență negativă), dar tensiunile simple la bornele receptorului sunt nesimetrice.

Dacă valorile impedanțele $\underline{Z}_1$, $\underline{Z}_2$, $\underline{Z}_3$ îndeplinesc condiția::

$$\underline{Z}_1 + \underline{Z}_2 + \underline{Z}_3 = 0 \qquad (2)$$

se produce echilibrul curenților ($\underline{I}^+ = 0$, $\underline{I}^- \neq 0$, $\underline{I}^0 = 0$) şi simetria tensiunilor înlănțuite, dar nesimetria tensiunilor simple la bornele receptorului ($\underline{U}'^+ \neq 0$, $\underline{U}'^- = 0$, $\underline{U}'^0 \neq 0$).

Dacă receptorul are conexiunea Δ, aplicând relațiile de transformare Y/Δ cunoscute, condiția (2) se înlocuieşte cu o condiție impusă valorilor admitanțelor echivalente de pe laturile schemei în conexiune Δ a receptorului, $\underline{Y}_{12}, \underline{Y}_{23}, Y_{31}$:

$$\underline{Y}_{12} + \underline{Y}_{23} + \underline{Y}_{31} = 0 \qquad (3)$$

3. Tensiunile simple la bornele receptorului formează un set trifazat simetric de fazori (de succesiune pozitivă) dar curenții pe fazele rețelei sunt dezechilibrați.

Dacă valorile admitanțelor echivalente al receptorului îndeplinesc condiția:

$$\underline{Y}_1 + a^2 \cdot \underline{Y}_2 + a \cdot \underline{Y}_3 = 0 \qquad (4)$$

tensiunile înlănțuite şi cele simple la bornele receptorului trifazat sunt simetrice, de succesiune pozitivă ($\underline{U}'^+ \neq 0$, $\underline{U}'^- = 0$, $\underline{U}'^0 = 0$), dar curenții pe fazele rețelei sunt dezechilibrați ($\underline{I}^+ \neq 0$, $\underline{I}^- \neq 0$, $\underline{I}^0 = 0$). În relația (4), $\underline{Y}_1 = 1/\underline{Z}_1$, $\underline{Y}_2 = 1/\underline{Z}_2$, $\underline{Y}_3 = 1/\underline{Z}_3$.

2 Receptor trifazat dezechilibrat în conexiune Δ

Dintre cele trei cazuri particulare expuse mai sus, cazul al doilea îşi găseşte ca aplicație practică operația de echilibrare a sarcinilor trifazate prin compensare reactivă transversală dezechilibrată. Un receptor trifazat format numai din reactanțe (inductive şi capacitive), poate fi în aşa fel dimensionat încât să absoarbă un set de curenți de succesiune negativă, egal şi de semn contrar celui corespunzător sarcinii echivalente dezechilibrate. Pentru ca echilibrarea sarcinii să se facă atât ca putere activă cât şi ca putere reactivă, compensatorul trebuie să aibă conexiunea Δ [3].

În acest paragraf se prezintă proprietățile unui receptor în conexiune Δ, dezechilibrat, utilizând expresiile analitice ale curenților determinați de un astfel de receptor, în componente de fază respectiv în componente de secvență. Pentru deducerea acestor expresii, se vor utiliza notațiile din figura 2, ale căror semnificații sunt evidente.

Se va folosi aceeaşi ipoteză: tensiunile de alimentare, de linie şi ale fazelor față de referință (pământ) alcătuiesc un set trifazat echilibrat, poziționat în planul complex, conform convenției uzuale, cu tensiunea fazei 1 având originea, direcția şi sensul axei reale (fig. 3). Astfel, relațiile între tensiunile simple şi cele înlănțuite sunt date de relațiile (5).

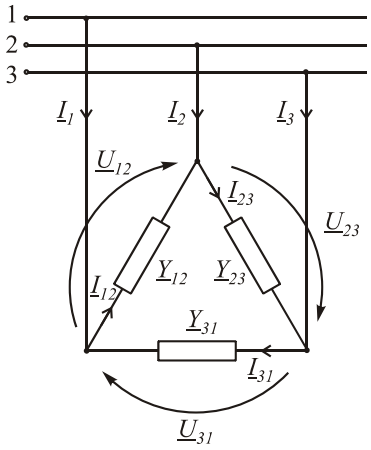

Fig. 2 Receptor trifazat în conexiunea Δ.

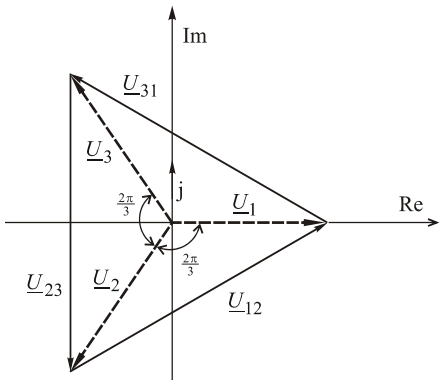

Fig. 3 Convenția de raportare a fazorilor.

$$\begin{aligned}\underline{U}_{12} &= U_1 - U_2 = U_f\left(1-a^2\right) = -j\cdot a\cdot U_l\\ \underline{U}_{23} &= U_2 - U_3 = U_f\left(a^2-a\right) = -j\cdot U_l\\ \underline{U}_{31} &= U_3 - U_1 = U_f\left(1-a\right) = -j\cdot a^2\cdot U_l\end{aligned} \tag{5}$$

Curenții pe laturile triunghiului au expresiile:

$$\begin{aligned}\underline{I}_{12} &= \underline{U}_{12}\underline{Y}_{12} = \underline{U}_{12}\left(G_{12} - jB_{12}\right) = -j\cdot a\cdot U_l\left(G_{12} - j\ B_{12}\right)\\ \underline{I}_{23} &= \underline{U}_{23}\underline{Y}_{23} = \underline{U}_{23}\left(G_{23} - jB_{23}\right) = -j\cdot U_l\left(G_{23} - j\ B_{23}\right)\\ \underline{I}_{31} &= \underline{U}_{31}\underline{Y}_{31} = \underline{U}_{31}\left(G_{31} - jB_{31}\right) = -j\cdot a^2\cdot U_l\left(G_{31} - j\ B_{31}\right)\end{aligned} \tag{6}$$

astfel că curenții pe fazele rețelei de alimentare a receptorului sunt:

$$\begin{aligned}\underline{I}_1 &= \underline{I}_{12} - \underline{I}_{31} = \frac{U_l}{2}\left\{\sqrt{3}\left(G_{12}+G_{31}\right) + B_{12} - B_{31} + j\left[G_{12} - G_{31} - \sqrt{3}\left(B_{31}-B_{12}\right)\right]\right\}\\ \underline{I}_2 &= \underline{I}_{23} - \underline{I}_{12} = \frac{U_l}{2}\left[-\sqrt{3}G_{12} - 2B_{23} - B_{12} + j\left(-2G_{23} - G_{12} + \sqrt{3}B_{12}\right)\right]\\ \underline{I}_3 &= \underline{I}_{31} - \underline{I}_{23} = \frac{U_l}{2}\left[-\sqrt{3}G_{31} + B_{31} + 2B_{23} + j\left(G_{31} + 2G_{23} + \sqrt{3}B_{31}\right)\right]\end{aligned} \tag{7}$$

Dacă receptorul în schema Δ conține numai elemente active și raportând fiecare curent de fază la tensiunea simplă corespunzătoare, cu scopul identificării componentelor active și reactive (notație *), curenții pe fazele rețelei de alimentare a receptorului au expresiile:

$$\begin{aligned}\underline{I}_1^* &= \underline{I}_1 = U_l\left[\frac{\sqrt{3}}{2}\left(G_{31}+G_{12}\right) + j\,\frac{1}{2}\left(G_{12}-G_{31}\right)\right]\\ \underline{I}_2^* &= a\cdot\underline{I}_2 = U_l\left[\frac{\sqrt{3}}{2}\left(G_{12}+G_{23}\right) + j\,\frac{1}{2}\left(G_{23}-G_{12}\right)\right]\\ \underline{I}_3^* &= a^2\cdot\underline{I}_3 = U_l\left[\frac{\sqrt{3}}{2}\left(G_{23}+G_{31}\right) + j\,\frac{1}{2}\left(G_{31}-G_{23}\right)\right]\end{aligned} \tag{8}$$

Din relațiile (8) se poate constata că deși conține numai elemente active, receptorul dezechilibrat în conexiune Δ debitează, respectiv absoarbe pe faze și putere reactivă, în funcție de sensul și mărimea dezechilibrului, fără a fi însă afectat bilanțul puterilor reactive pe ansamblul celor trei faze ($\sum Q_i = 0$).

Dacă receptorul în conexiune Δ conține numai elemente reactive (cazul compensatoarelor de putere reactivă), curenții, raportați fiecare la tensiunea simplă corespunzătoare, devin:

$$\begin{aligned}
\underline{I}_1^* &= \underline{I}_1 = U_l\left[\frac{1}{2}(B_{12}-B_{31}) - j\frac{\sqrt{3}}{2}(B_{31}+B_{12})\right] \\
\underline{I}_2^* &= a\cdot\underline{I}_2 = U_l\left[\frac{1}{2}(B_{23}-B_{12}) - j\frac{\sqrt{3}}{2}(B_{12}+B_{23})\right] \\
\underline{I}_3^* &= a^2\cdot\underline{I}_3 = U_l\left[\frac{1}{2}(B_{31}-B_{23}) - j\frac{\sqrt{3}}{2}(B_{23}+B_{31})\right]
\end{aligned} \tag{9}$$

Din relațiile (9) se poate constata că deşi conține numai elemente reactive, receptorul dezechilibrat în conexiune Δ, debitează respectiv absoarbe pe faze şi putere activă, în funcție de sensul şi mărimea dezechilibrului, fără să fie însă afectat bilanțul puterilor active pe ansamblul celor trei faze ($\sum P_l = 0$).

Receptorul dezechilibrat în conexiune Δ ce conține numai elemente reactive de circuit este cel care poate fi folosit cu funcția de compensator de echilibrare. Componentele simetrice ale curenților pe fazele acestuia, se obțin imediat [2]:

$$\begin{aligned}
\underline{I}^+ &= \frac{1}{3}(\underline{I}_1 + a\underline{I}_2 + a^2\underline{I}_3) = -j\frac{U_l}{\sqrt{3}}(B_{12}+B_{23}+B_{31}) \\
\underline{I}^- &= \frac{1}{3}(\underline{I}_1 + a^2\underline{I}_2 + a\underline{I}_3) = \frac{U_l}{2}(B_{12}-B_{31}) + j\frac{U_l}{2\sqrt{3}}(-B_{12}+2B_{23}-B_{31}) \\
\underline{I}^0 &= \frac{1}{3}(\underline{I}_1 + \underline{I}_2 + \underline{I}_3) = 0
\end{aligned} \tag{10}$$

Dacă acum se consideră că valorile celor trei susceptanțe echivalente îndeplinesc condiția (3) scrisă sub forma:

$$B_{12} + B_{23} + B_{31} = 0, \tag{11}$$

receptorul intervine numai asupra circulației de curenți de secvența negativă, confirmându-se astfel concluzia demonstrată mai sus:

$$\begin{aligned}
&\underline{I}^+ = 0, \quad \underline{I}^0 = 0 \\
&\underline{I}^- = \frac{U_l}{2}(B_{12}-B_{31}) + j\frac{\sqrt{3}U_l}{2}B_{23}
\end{aligned} \tag{37}$$

3 Aplicație MathCAD şi simulare MATLAB-Simulink

Aplicația numerică se referă la două receptoare trifazate nesimetrice, având structuri particulare ce îndeplinesc condițiile precizate mai sus, alimentate mai întâi individual şi apoi simultan, de la o sursă ce furnizează un set simetric de tensiuni înlănțuite. Pentru circuitul analizat se prezintă rezultatele unei aplicați MathCAD, constând în calculul tensiunilor şi curenților atât în componente de fază cât şi în componente simetrice şi apoi calculul puterilor active şi reactive pe faze.

Primul receptor este unul rezistiv plus reactiv inductiv pe fiecare fază, nesimetric, cu o schemă în conexiune stea (valorile parametrilor echivalenți îndeplinind condiția (4)). Cel de-al doilea receptor are o schemă în conexiune delta (valorile parametrilor echivalenți îndeplinesc condiția (11)), iar elementele sale, au fost dimensionate astfel încât acest receptor să absoarbă din circuit un set de curenți de succesiune inversă, egal şi de sens contrar setului de curenți corespunzător componentei de succesiune inversă din curenții de pe fazele receptorului în conexiune stea, prezentat anterior [3]. Rezultatele calculului sunt prezentate în tabelul 1.

Tabelul 1. Rezultatele aplicației MathCAD

Receptor Y	Receptor Δ	Receptor Y+Δ
Tensiunile de alimentare		
$\underline{U}_1 = 235\ V$, $\underline{U}_2 = 235 \cdot e^{-j\cdot\frac{2\cdot\pi}{3}}\ V$, $\underline{U}_3 = 235 \cdot e^{j\cdot\frac{2\cdot\pi}{3}}\ V$ $\underline{U}_{12} = 407{,}032 \cdot e^{j\frac{\pi}{6}}$, $\underline{U}_{23} = 407{,}032 \cdot e^{-j\frac{\pi}{2}}$, $\underline{U}_{31} = 407{,}032 \cdot e^{j\frac{5\pi}{6}}$		
Parametrii echivalenți		
$\underline{Y}_1 = (0{,}1 - j0{,}08)\ S$ $\underline{Y}_2 = (0{,}067538 - j0{,}079246)\ S$ $\underline{Y}_3 = (0{,}084422 - j0{,}05151)\ S$ $\underline{Y}_1 + a^2 \cdot \underline{Y}_2 + a \cdot \underline{Y}_3 = 0$	$\underline{Y}_{12} = j0{,}01249\ S$ $\underline{Y}_{23} = -j0{,}006499\ S$ $\underline{Y}_{31} = -j0{,}005996\ S$ $\underline{Y}_{12} + \underline{Y}_{23} + \underline{Y}_{31} = 0$	$\underline{Y}_1, \cdot\underline{Y}_2, \cdot\underline{Y}_3$ - conexiune Y $\underline{Y}_{12}, .\underline{Y}_{23}, \underline{Y}_{31}$ - conexiune Δ
Curenții în componente de fază şi componente de secvență		
$\underline{I}_1 = 30{,}095 \cdot e^{-j0{,}675}\ A$ $\underline{I}_2 = 24{,}468 \cdot e^{-j2{,}959}\ A$ $\underline{I}_3 = 23{,}24 \cdot e^{-j1{,}547}\ A$	$\underline{I}_1 = 4{,}405 \cdot e^{j2{,}595}\ A$ $\underline{I}_2 = 4{,}405 \cdot e^{-j1{,}595}\ A$ $\underline{I}_3 = 4{,}405 \cdot e^{j0{,}5}\ A$	$\underline{I}_1 = 25{,}731 \cdot e^{-j0{,}697}\ A$ $\underline{I}_2 = 25{,}731 \cdot e^{-j2{,}791}\ A$ $\underline{I}_3 = 25{,}731 \cdot e^{j1{,}398}\ A$
$\underline{I}^0 = 0$ $\underline{I}^+ = 25{,}731 \cdot e^{-j0{,}697}\ A$ $\underline{I}^- = 4{,}405 \cdot e^{-j0{,}547}\ A$	$\underline{I}^0 = 0$ $\underline{I}^+ = 0$ $\underline{I}^- = 4{,}405 \cdot e^{j2{,}595}\ A$	$\underline{I}^0 = 0$ $\underline{I}^+ = 25{,}731 \cdot e^{-j0{,}697}\ A$ $\underline{I}^- = 0$
Puterile pe faze şi pe ansamblul trifazat		
$\underline{S}_1 = (5522{,}5 + j4418)VA$ $\underline{S}_2 = (3729{,}77 + j4376{,}34)VA$ $\underline{S}_3 = (4662{,}21 + j2844{,}62)VA$ $\sum_{i=1}^{3} \underline{S}_i = (13914{,}48 + j11638{,}96)VA$	$\underline{S}_1 = (-884{,}34 - j538{,}34)VA$ $\underline{S}_2 = (908{,}39 - j496{,}68)VA$ $\underline{S}_3 = (-24{,}05 + j1035{,}03)VA$ $\sum_{i=1}^{3} \underline{S}_i = (0 + j0)VA$	$\underline{S}_1 = (4638{,}16 + j3879{,}66)VA$ $\underline{S}_2 = (4638{,}16 + j3879{,}66)VA$ $\underline{S}_3 = (4638{,}16 + j3879{,}66)VA$ $\sum_{i=1}^{3} \underline{S}_i = (13914{,}48 + j11638{,}96)VA$

Analizând rezultatele calculului, se observă că deşi receptorul nesimetric de conexiune Y este alimentat cu un set trifazat simetric de tensiuni (de secvență pozitivă), acesta determină şi circulația unei componente de secvență negativă a curenților (parametrii echivalenți ai receptorului respectă condiția (4)).

În ceea ce priveşte receptorul nesimetric de conexiune Δ, acesta determină doar circulația unei componente de succesiune inversă, care rezultă egală şi de sens opus celei determinate de receptorul în conexiune Y, pe care o compensează la alimentarea simultană. Se observă de asemenea că deşi conține numai elemente reactive de circuit, receptorul în conexiune Δ intervine şi asupra circulației de putere activă: debitează putere activă pe fazele 1 şi 3, absorbind putere activă pe faza 2. Pe ansamblul celor trei faze nu este influențat însă bilanțul puterilor active. O constatare similară se referă la intervenția asupra circulației puterii reactive: receptorul absoarbe putere reactivă pe faza 3, debitează putere reactivă pe celelalte două faze, fără a influența însă bilanțul puterilor reactive pe ansamblul celor trei faze.

Se poate înțelege acum mecanismul energetic al echilibrării obținute prin compensare nesimetrică: compensatorul în conexiune Δ efectuează o redistribuire a puterilor active şi reactive între fazele rețelei, echilibrându-le [3].

Alimentarea simultană a celor două receptoare determină absorbția dinspre sursă a unui set trifazat echilibrat de curenți, de succesiune pozitivă. Receptorul în conexiune Δ este de fapt un compensator nesimetric de putere reactivă, ce determină simetrizarea sarcinii, atât a celei active cât şi a celei reactive.

Rezultatele aplicației numerice sunt confirmate prin modelare MATLAB-Simulink şi sunt prezentate în figura 4. Folosind obiecte specializate pentru elementele de circuit respectiv pentru instrumentele de măsură, se obțin practic aceleaşi rezultate, atât pentru componentele de fază cât şi pentru cele simetrice.

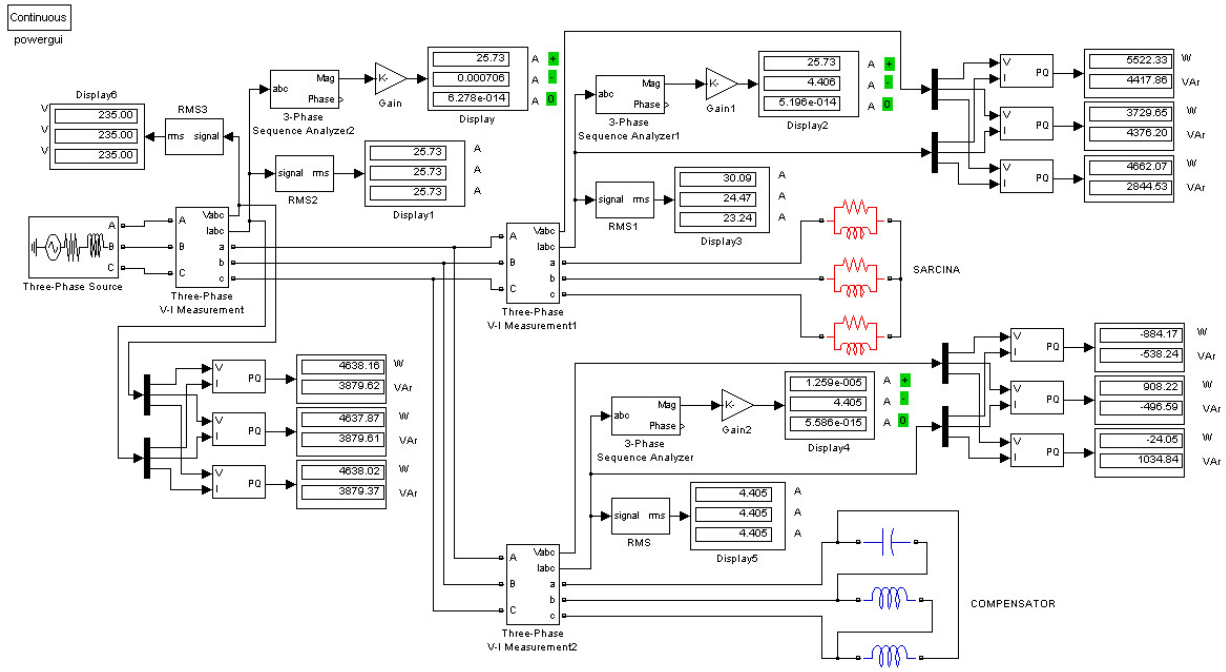

Fig. 4 Modelul MATLAB-Simulink şi rezultatele regimului permanent normal funcționare a rețelei trifazate alimentând simultan receptoarele de conexiune Y respectiv Δ.

4 Concluzii

- Există structuri particulare ale receptorului trifazat nesimetric care determină fie ca tensiunile simple la bornele receptorului să fie nesimetrice în timp ce curenții pe fazele acestuia sunt echilibrați, fie ca tensiunile simple la bornele receptorului să fie simetrice, în timp ce curenții sunt dezechilibrați.
- Dacă un receptor trifazat de conexiune Δ are numai elemente echivalente reactive de circuit (reactanțe (susceptanțe) inductive şi capacitive) a căror sumă algebrică este nulă, deşi este alimentat cu un set simetric de tensiuni de succesiune pozitivă, pe fazele rețelei se formează un set simetric de curenți, de succesiune negativă. Dimensionarea acestui receptor se poate face astfel încât acest set de curenți să fie egal cu setul trifazat corespunzător componentelor de secvență negativă din curenții unei sarcini trifazate dezechilibrate oarecare. Receptorul În conexiune Δ îndeplinește astfel funcția de compensator de echilibrare.
- Simularea cu MATLAB-Simulink confirmă corectitudinea calculului şi uşurează analiza rezultatelor şi înțelegerea mecanismului energetic al echilibrării sarcinii.
- Lucrarea oferă un instrument teoretic util în analiza regimurilor nesimetrice de funcționare a circuitelor electrice trifazate.

Referințe

[1] M. Bornand, *Electrotechnique.Réseau triphasé. Machines à courant alternatif*, VUIBERT, 1984.
[2] C. Şora, *Bazele electrotehnicii*, Editura didactică şi pedagogică, Bucureşti, 1982.
[3] A. Buta, A. Pană, *Simetrizarea sarcinii rețelelor electrice de distribuție*, Editura Orizonturi Universitare, Timişoara, 2000.

Low power, temperature and process compensated CMOS ring oscillator

Mihai Eugen MARIN, Răzvan Cristian MARIN
Universitatea "Politehnica" Bucureşti. Splaiul Independenţei 313 Bucharest, Romania;
mihai.marin@ieee.org

Abstract. The modern communication technologies require the use of CMOS monolithic oscillators because of their small manufacturing costs and high integration capabilities. The disadvantages of CMOS ring oscillators can be compensated through the use of a VCO architecture. The control voltage of this VCO should compensate for the frequency drift due to process and temperature.

1 Introduction

Although the more common quartz crystal oscillators is still preferred because of the stability with variations in supply voltage, temperature and process recent advances in the compensation techniques transform the integrated CMOS ring oscillator into a suitable replacement. Without any compensation scheme the central frequency drift of the CMOS oscillator can be up to 100% when the temperature is varied. The process corners also influence the central frequency of an oscillator. Process corners are determined by variations in oxide thickness, threshold voltage and deviations of the physical dimensions of the transistor (dW and dL). In this paper an on-chip ring oscillator is considered. The compensation can be done through the use of a simple microcontroller that has a DAC an ADC and a temperature sensor. The digital part of the voltage generation is simulated in the Cadence environment using a Verilog model for the control voltage generator. This voltage generator accounts not only for the Fast n-channel, Fast p-channel (FF) and Slow n-channel, Slow p-channel (SS) corners but also for the Fast n-channel, Slow p-channel (FS) and Slow n-channel, Fast p-channel (SF)

2 The Ring Oscillator

The ring oscillator considered has 4 differential delay cells; the first 3 cells are in a inverting connexion and the fourth is connected as a buffer. Using this connexion scheme (Fig1) 4 signals with 0°, 90°, 180°, 270° phase shift are generated.

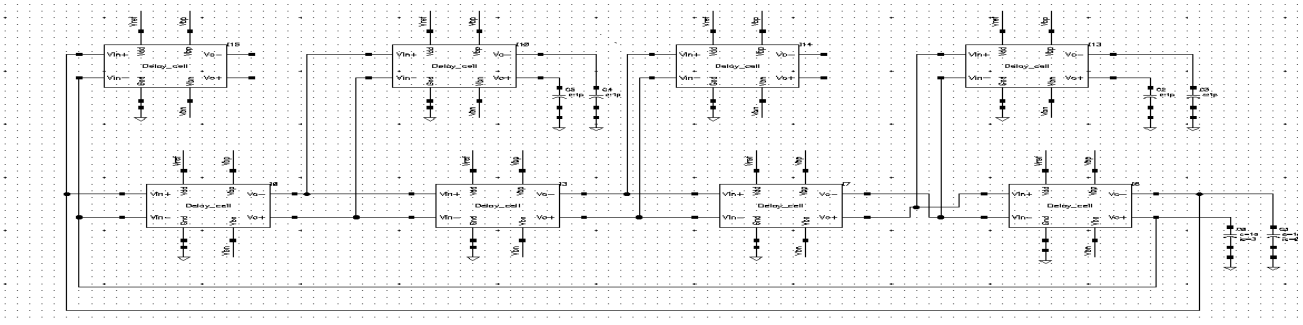

Figure 1: Oscillator core.

The differential delay cell is based on the delay cell proposed by Maneatis [1] and [2], (Fig. 2). The biasing of the circuit is done using a half buffer replica boosted dynamic bias (Fig 3) in order to reduce the supply noise [3]. Two half buffer circuits are used in order to isolate the control voltage input from the gate of the PMOS transistors in the oscillator.

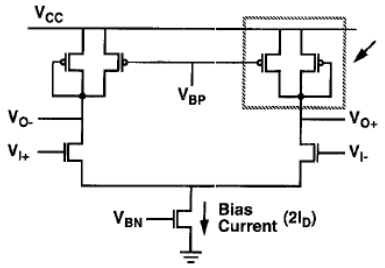

Figure 2: Delay cell [1].

Between the bias points of the PMOS and NMOS a bypass capacitor is introduced in order to prevent oscillations.

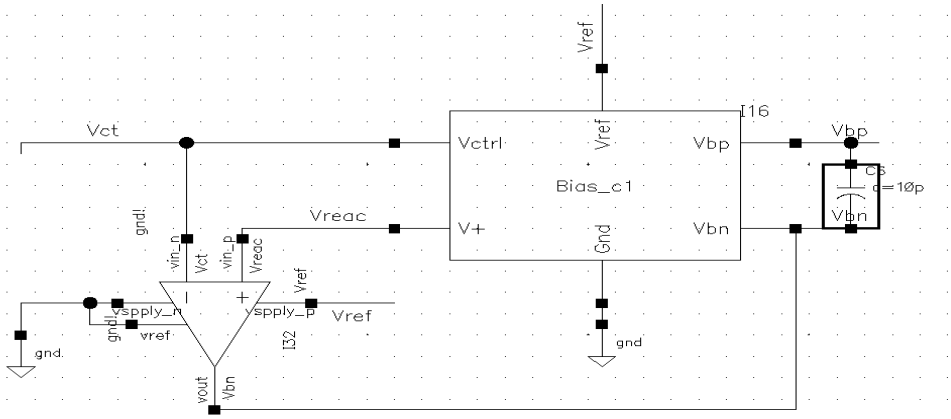

Figure 3: Bias circuit.

The output frequency of the ring oscillator is approximately represented in (1)

$$F = \frac{I_d}{2NC_oV_{SW}} = \frac{k_p\frac{W_p}{L_p}(V_{ref} - V_{Tp} - V_{ctrl})^2}{2NC_o(V_{ref-}V_{ctrl})} \tag{1}$$

3 Compensation of the ring oscillator

We want to see what happens when a temperature variation occurs. From the Bsim3.3V model [4] the threshold voltage has a linear variation with the temperature

$$V_{Tp} = V_{Tp0} + kt\left(\frac{T}{T_0} - 1\right) \tag{2}$$

where kt has a negative value.

The electron mobility also varies with the temperature

$$\mu(T) = \mu_0\left(\frac{T}{T_0}\right)^n \tag{3}$$

Considering C_{OX} temperature variation the same as for the output capacitance, then:

$$F = \frac{\mu_{p0} T_0^{\,n}\, C_{OX} \frac{W_p}{L_p} \left(V_{ref} - V_{Tp0} - V_{ctrl} + kt - kt\frac{T}{T_0}\right)^2}{2NC_O\left(V_{ref} - V_{ctrl}\right)T^n} \tag{4}$$

In Fig 4 the schematic of the corner detector is presented. The output voltage of this detector varies with temperature and process. An NMOS threshold detector architecture is preferred to the PMOS architecture presented in [5] and [6] because the generated values are unique.

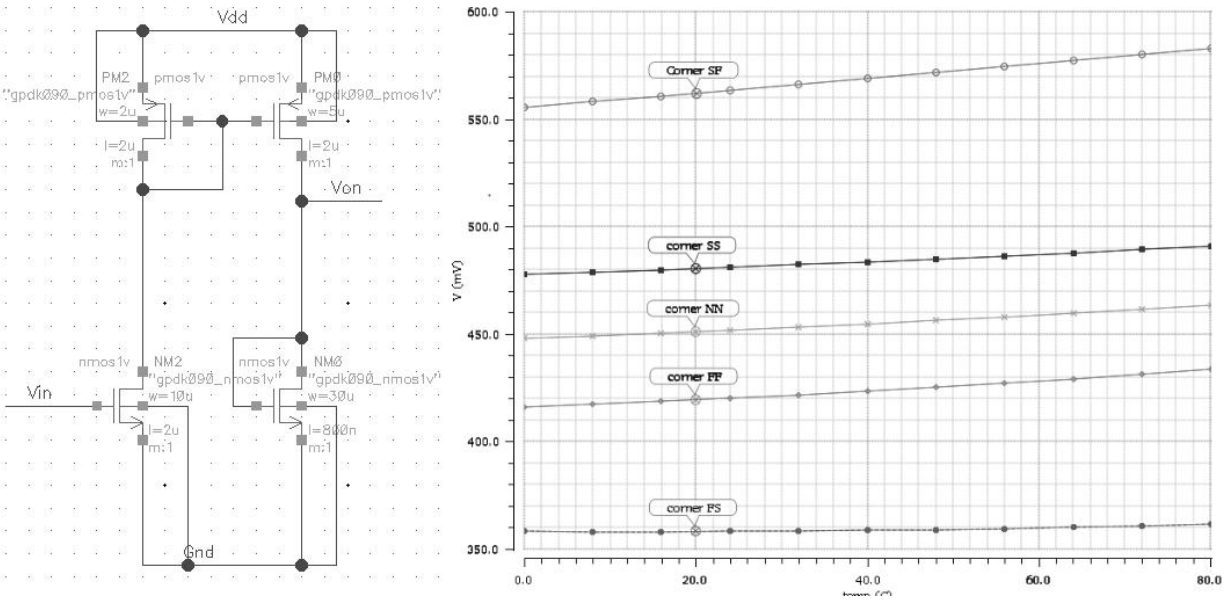

Figure 4: Process corner detector and output voltage.

Using this detector the corner is detected and the appropriate slope for the voltage can be generated.

4 Results

The oscillator was designed using the 90nm GPDK in Cadence. The supply voltage was set at 2.2V and the central frequency of the oscillator is 1GHz, Fig 5. The circuit draws a current of about 10mA so the power consumption without the control circuit of the circuit is about 22mW which qualifies the circuit as low power. In order to compensate the frequency across temperature and process the control voltage must take values between 0.7V and 1.5V. Using a resolution of 10mV a compensation of ± 3% is obtained over corners and a temperature variation of 0°-80°. This can be obtained using a 8-Bit DAC.

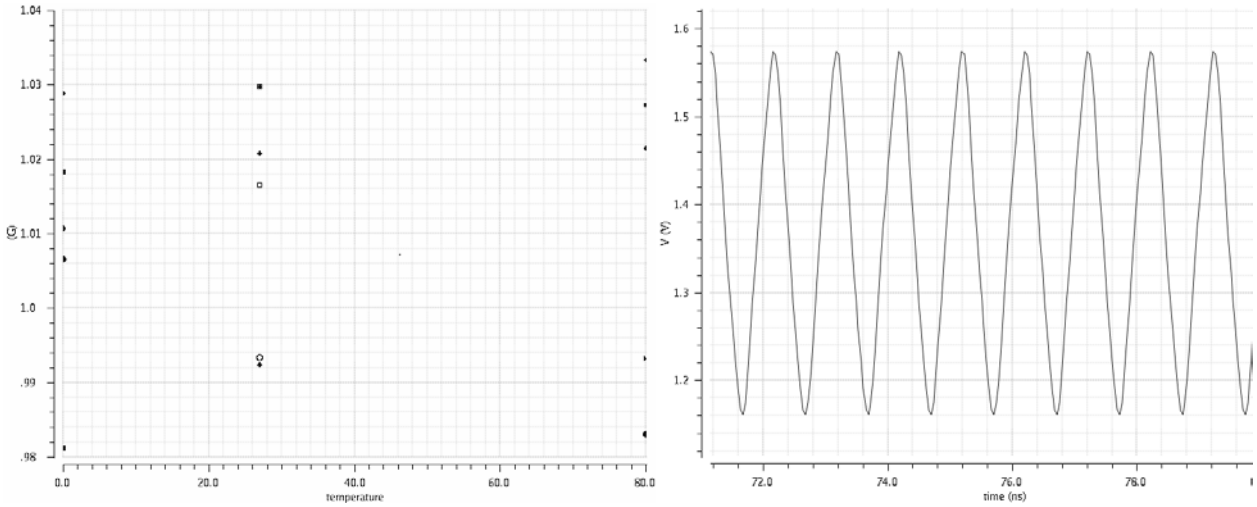

Figure 5: Oscillator frequency vs. temperature and output voltage at 25°C.

5 Conclusions

- In this paper a digital technique for the compensation of a ring oscillator is proposed
- A Verilog model is used in order to simulate the digital part of the circuit
- The proposed solution does not require calibration because the circuit generates the correct control voltage based on the output voltage of the threshold detector and the temperature reading.
- A variation of ± 3% is obtained over the temperature range of 0°-80° and the 4 corners.

References

[1] J.G Maneatis. Low-jitter process-independent DLL and PLL based on self-biased techniques, *IEEE Journal of Solid-State Circuits*, vol.31, no.11, pp.1723-1732, Nov 1996.

[2] J.G. Maneatis, M.A. Horowitz. Precise delay generation using coupled oscillators *IEEE Journal of Solid-State Circuits*, vol.28, no.12, pp.1273-1282, Dec 1993.

[3] J. Carnes, I.Vytyaz, P.K. Hanumolu, K. Mayaram, Un-Ku Moon. Design and Analysis of Noise Tolerant Ring Oscillators Using Maneatis Delay Cells, *14th IEEE International Conference on Electronics, Circuits and Systems, ICECS 2007*, vol., no., pp.494-497, 11-14 Dec. 2007.

[4] W. Liu, X. Jin, X. Xi, J. Chen, M.-C. Jeng, Z. Liu, Y. Cheng, K. Cn, M. Chan, K. Hui, J. Huang, R. Tu, P. K. Ko, C. Hu, Manual BSIM3v3.3 MOSFET Model Users, Department of Electrical Engineering and Computer Sciences University of California, Berkeley, CA 94720, 2005.

[5] J. Tang; F. Tang; , Temperature and process independent ring-oscillator using compact compensation technic, *2010 International Conference on Anti-Counterfeiting Security and Identification in Communication (ASID*) , vol., no., pp.49-52, 18-20 July 2010.

[6] K. Sundaresan, P. E. Allen, Process and temperature compensation in a 7-MHz CMOS clock oscillator, IEEE JSSC, Vol. 41, NO. 2, pp. 433-442, Feb. 2006.

NON-SYMMETRY POWER IN THREE-PHASE SYSTEMS

Liliana Marilena MATICA
University of Oradea, Universitatii str., no.1, 410087, Oradea; lmatica@uoradea.ro

Abstract. For three-phase electrical systems, in non-symmetrical situation, an analyze method consists on equivalent apparent power components computation. Such a component is the non-symmetry power, it may characterize the non-symmetrical situations (it has significant value in those situations). For draw this equivalent apparent power component, the paper describe a graphical model (this model represents the mathematical relationships for non-symmetry power). A new indicator, the non-symmetry factor is explicated (non-symmetry power versus equivalent apparent power); it is similar with power factor (reactive power versus apparent power). Also, the computation procedure is described for the non-symmetrical and periodic non-sinusoidal situations.

1 Introduction

Starting with 1929 year, the apparent power components problem was changed, essentially, by prof. C.Budeanu definition of deformant power. Scientific theories were developed [5] for define others apparent power components, for example non-fundamental power. Regarding non-symmetry power, considering its name and computing formula, it is an apparent power component. Mostly, it is useful for non-symmetrical situations analyze, in distribution electrical networks. The consumers which are not symmetrical are the cause [4] of non-symmetrical situations, in three-phase systems. The supply efficiency of electrical energy is affected. The explications and computations of those effects are important for the electrical energy supplier, who must justify the technological consumption increase. The non-symmetry power value (an apparent power component) is in proportion with non-symmetrical situation, and it may be useful for those situations analyze.

2 About non-symmetry power

In non-symmetrical situation, three-phase systems analyze [3] is realized considering (theorem Fortesque) sequence components for current and voltage (the positive sequence component indexed by „+", the negative sequence component indexed by „-" and the zero sequence component indexed by „0"), according to the following relationships:

$$I_e = \sqrt{\frac{I_R^2 + I_S^2 + I_T^2}{3}} = \sqrt{I_+^2 + I_-^2 + I_0^2} \tag{1}$$

$$U_e = \sqrt{\frac{U_R^2 + U_S^2 + U_T^2}{3}} = \sqrt{U_+^2 + U_-^2 + U_0^2} \tag{2}$$

; index R, S and T codify the three phases in three-phase system.
In non-symmetrical situation, apparent power is computed with relationship:

$$S_e = 3 \cdot U_e \cdot I_e = \sqrt{U_+^2 + U_-^2 + U_0^2} \cdot \sqrt{I_+^2 + I_-^2 + I_0^2} \tag{3}$$

Considering two apparent power components: active power of positive sequence P_+ and reactive power of positive sequence Q_+ (determinate conforming standard formula), it results the third component [1], namely non-symmetry power, noted N:

$$S_e^{\ 2} = P_+^2 + Q_+^2 + N^2 = S_+^2 + N^2 \tag{4}$$

, where S_+ is apparent power of positive sequence. The phase shift (between voltage and current of positive sequence) is noted with φ_+. The previous relationship may be expressed as:

$$S_e^{\ 2} = P_+^2 + Q_+^2 + N^2 = U_+^2 \cdot I_+^2 \cdot \cos^2 \varphi_+ + U_+^2 \cdot I_+^2 \cdot \sin^2 \varphi_+ + N^2 \tag{5}$$

So, it results a formula for compute the non-symmetry power:

$$N = \sqrt{S_e^2 - S_+^2} = \sqrt{(3 \cdot U_e \cdot I_e)^2 - U_+^2 \cdot I_+^2} \tag{6}$$

Considering only sequence components, it results next formula for compute the non-symmetry power:

$$N = \sqrt{S_e^2 - S_+^2} = \sqrt{(U_+^2 + U_-^2 + U_o^2) \cdot (I_+^2 + I_-^2 + I_o^2) - U_+^2 \cdot I_+^2} \tag{7}$$

The non-symmetry may be characterized [3] by several coefficients (of reverse non-symmetry, of anti-symmetry, total coefficient of non-symmetry) or ratios (of non-symmetry, differential of symmetry). This paper describe a new ones: ratio of minim non-symmetry r_{min}, that consider the minimum value (of the three ones), reported to arithmetic average of three phases values and ratio of maxim non-symmetry r_{max}, that consider the maxim value, reported to same arithmetic average (for electrical current and voltage).

Considering voltage reverse coefficient of non-symmetry, K_{ns}^-, current reverse coefficient of non-symmetry, k_{ns}^- and voltage zero coefficient of non-symmetry, K_{ns}^0, current zero coefficient of non-symmetry, k_{ns}^0, the formula for compute the non-symmetry power is:

$$N = \sqrt{S_e^2 - S_+^2} = \sqrt{U_+^2 \cdot I_+^2} \cdot \sqrt{(1 + K_{ns}^{-\ 2} + K_{ns}^{0\ 2}) \cdot (1 + k_{ns}^{-\ 2} + k_{ns}^{0\ 2}) - 1} \tag{8}$$

, be cause:

$$N = \sqrt{(U_+^2 + K_{ns}^{-\ 2} \cdot U_+^2 + K_{ns}^{0\ 2} \cdot U_+^2) \cdot (I_+^2 + k_{ns}^{-\ 2} \cdot I_+^2 + k_{ns}^{-\ 2} \cdot I_+^2) - U_+^2 \cdot I_+^2} \tag{9}$$

Clearly, rel.8 justify the affirmation that non-symmetry power has significant value only in non-symmetrical situations, its value depends on negative and zero sequence components values, so non-symmetric power may be assumed as an indicator of non-symmetry.

The graphical model, for describe the non-symmetry power, considers axles system Oxyz, the non-symmetrical power is drawn as a vector, perpendicular on Oxy plane, see fig.1 (it results the relationships for apparent power components, in accordance with Pitagora theorem). In the Oxy plane, it is drawn the standard graphical model and the apparent power has two components: active and reactive power (all about positive sequence components).

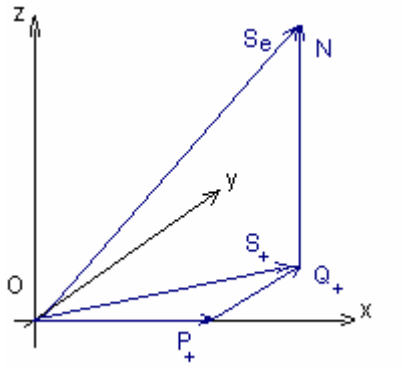

Fig.1. Graphical model about non-symmetry power.

The negative and zero sequence components determine the supplementary technological consumption of active power, comparing to symmetrical situations when positive sequence component exist, only:

$$\Delta P = \Delta P_{+} + \Delta P_{-} + \Delta P_{0} \tag{10}$$

3 Apparent power components in sinusoidal non-symmetrical and periodical non-sinusoidal situations

In periodical non-sinusoidal situations, the analyze starts from fundamental component evaluation, indexed with "1", and harmonic components, indexed with "i", (for voltage and current). Those components determine the fundamental component of apparent power, S_1 , and non-fundamental component of apparent power, S_{NF} , according to next relationship (U_H is the geometrical media of harmonic components for voltage and I_H for current):

$$S^2 = U^2 \cdot I^2 = (U_1^2 + \sum_{i \neq 1} U_i^2) \cdot (I_1^2 + \sum_{i \neq 1} I_i^2) = (U_1^2 + U_H^2) \cdot (I_1^2 + I_H^2) = S_1^2 + S_{NF}^2 \tag{11}$$

In a three-phase system, analyze is developed, starting with the components of equivalent apparent power, S_e:

$$S_e^{\ 2} = S_{e1}^2 + S_{eH}^2 = 3 \cdot U_e^2 \cdot I_e^2 = 3 \cdot (U_{e1}^2 + \sum_{i \neq 1} U_{e,i}^2) \cdot (I_{e1}^2 + \sum_{i \neq 1} I_{e,i}^2) \tag{12}$$

In previous relationship (rel.12), index "e1" codify fundamental component and S_{e1} is fundamental component of equivalent apparent power; index "eH" codify non-fundamental component of equivalent apparent power and S_{eH} is non-fundamental (harmonic) component of equivalent apparent power; index "e,i" codify "i" harmonic equivalent component for voltage or current.

In sinusoidal non-symmetrical and periodical non-sinusoidal situations, fundamental equivalent apparent power contains sequence components (positive, negative and zero). According to rel.5, this fundamental equivalent apparent power contains the non-symmetry power, N. The other component is equivalent apparent power of positive sequence, S_{1+} and it has two components: active power of positive sequence, P_{1+}, and reactive power of positive sequence, Q_{1+}, (according to analyze method of symmetrical and sinusoidal situations). It results next relationship:

$$S_e^{\ 2} = S_{e1}^2 + S_{eH}^2 = S_{1+}^2 + N^2 + S_{eH}^2 = P_{1+}^2 + Q_{1+}^2 + N^2 + S_{eH}^2 \tag{13}$$

, be cause:

$$S_{e1}^2 = S_{1+}^2 + N^2 = P_{1+}^2 + Q_{1+}^2 + N^2 \quad (14)$$

Similar with the power factor (in symmetrical and sinusoidal situations), we defined the ***non-symmetry factor***, k_{pN}, according with next relationship:

$$k_{pN} = \frac{S_{1+}}{S_{e1}} = \frac{\sqrt{S_{e1}^2 - N^2}}{S_{e1}} = \sqrt{1 - \frac{N^2}{S_{e1}^2}} \quad (15)$$

A formula of non-symmetry factor, considering the positive sequence components (fundamental ones), is:

$$k_{pN} = \frac{\sqrt{P_{1+}^2 + Q_{1+}^2}}{S_{e1}} \quad (16)$$

The "1" value of non-symmetry factor is characteristic of symmetry, about a three-phase system.

4 Some experimental results

An experiment did compute non-symmetry factor values, [3] in several knots of a three-phase system. Those knots were: first knot, electrical transformer; second knot, non-symmetrical consumer, supplied with an electrical line type ACYAbY, 3x95 + 70 of 150m length; third knot, non-linear consumer, placed after 75 m (after the symmetrical consumer, the same type of electrical line). The values of non-symmetry factor were computed with PSpice software.

Table 1. Non-symmetry factor values

No.Crt.	Knot	Value of non-symmetry factor	Percentage of non-symmetry power value from fundamental apparent power value
1.	Electrical transformer	0,864	13,6 %
2.	Non-symmetrical consumer	0,653	34,7 %
3.	Non-linear consumer	0,999	0,1 %

It can be observed the significant value (maximum) of non-symmetry power, in the knot (second) of non-symmetrical consumer.

The value of non-symmetry factor characterizes the non-symmetrical situations, considering negative and zero sequence components. Usually, the limitations, about non-symmetrical

situations, analyze the negative sequence component, only. For distribution electrical networks and medium voltage electrical networks, the limit of inverse coefficient is 2%. For high voltage electrical networks, the limit is 1% [2

5 Conclusions

In three-phase systems, *non-symmetry power* is a component of fundamental equivalent apparent power (rel.13). The non-symmetry power value may be an indicator of non-symmetrical situations; if the three-phase system is non-symmetrical, non-symmetry power has a significant value. The non-symmetry power value and some computation relationships may be explicated with a graphical model, (fig.1).

In non-symmetrical and periodical non-sinusoidal situation, *non-symmetry factor* estimates the proportion of apparent power of positive sequence value (or non-symmetry power value) versus fundamental equivalent apparent power value, (rel.15). Non-symmetry factor is similar with power factor (active power or reactive power versus apparent power values).

Considerations The author thanks for study coordination, about this subject, received from prof.dr.doc.ing. Sora Constantin.

References

[1] I. S., Antoniu, *Chestiuni speciale de electrotehnică,* Editura Academiei, 1956.
[2] Institutul de Cercetari si Modernizari Energetice – ICEMENERG S.A., *Normative de incercari si masuratori speciale in domeniul energetic,* Editura ICEMENERG, ISBN (10) 973-87476-8-6; ISBN (13) 978-973-87476-8-5, 2006.
[3] L.M., Matica, *Contribuţii privind analiza sistemelor trifazate în regimuri sinusoidal nesimetric şi periodic nesinusoidal,* Teză de doctorat, Timişoara, 2001.
[4] A., Tugulea, *Consideraţii privind efectele energetice în regimuri armonice nesimetrice ale sistemelor trifazate,* Revista Energetica, nr.3, pg.121, 1986.
[5] IEEE Working Group on Nonsinusoidal Situation, *Practical definition for Power in Systems with Nonsinusoidal Wafeforms ans Unbalanced Loads: A Discussion,* IEEE Transaction on Power Delivery, Vol.11, No.1, January 1996.

The influence of elementary cell properties on losses for soft composite materials

Adelina Rodica BORDIANU
University "Politehnica" of Bucharest, Spl. Independenţei 313, 060042, Bucharest; adelina.bordianu@upb.ro

Abstract. Soft magnetic composite materials are used in various applications. In order to correctly predict the losses it is important to take into consideration the material structure and its properties. A 2D structure and the homogenization technique are used to model the material and to show what the influences are on the eddy currents losses brought by the properties of the elementary cell.

1. Introduction

Composite materials are used in multiple applications: electrical interconnections, sensors, electrodes used for the fuel cells, electrical machines, electromagnetic shielding, microwave or medicine domain [1] ÷ [5] etc. A composite material can be defined as a combination of different materials designed to provide advanced features. At the microscopic level, the constituent materials maintain their separate identity in the composite, but at the mascroscopic scale the material has different properties [6], [7]. For this reason is important to analyse the composite material both at microscopic and macroscopic scales.

Eddy current losses are important for the devices that work in time-varying magnetic fields and high frequencies and because of this reason is very important to study their influence and to make some estimations of their values.

The granular structure of soft magnetic composite materials is important for frequency applications, especially for electrical machines applications, because these materials are able to reduce the eddy current losses [7].

Composite materials have a complex structure and, because of this reason, in order to easily characterise a material from the modelling point of view, some simplifying assumptions are frequently used. One of these assumptions implies the use of material symmetry and periodicity. In both cases the real material is composed from multiple representative volume elements (RVE) that are multiplied in space [8]. Other common assumption is to approximate the real material with an equivalent homogeneous material that is able to describe correctly all the real material properties.

The objective of this paper is to try to evidence how the elementary cell (the smalest RVE) properties, for a soft magnetic composite material, influence the eddy currents losses. The analysis starts from real composite materials and in order to compute the electromagnetic problem the author used the homogenization technique. The homogeneous material has the same properties in each point and for this reason the macroscopic rules can be applied with success [9]. The advantage of using the homogenization is that the time needed to obtain the desire solutions is reduced and more complex problems can be solved.

2. Numerical models and results

A two dimensional model, obtained by the repetition of an elementary cell (one grain surrounded by a insulating matrix) is used to represent the material and to investigate the influence of the cell parameters on the losses. The field problem is formulated in terms of an electric vector and magnetic scalar potentials and it is solved using the finite element method.

The first step in the analysis is to find the elementary cell that can model the best both the microscopic and macroscopic structure of the real material. In reality the material grains have irregular shape, contacts might appear between neighboring cells, the grains can have different dimensions etc. Also the 3D material must be correctly transposed into the 2D model.

Four different influences on losses were analyzed: the effect of the inclusion shape, material conductivity and permeability, inclusions concentration and contacts. In figure 1 the schemes of the elementary cells are presented. The shape of the elementary cell is a square, and the grains are circles or rectangles. The average dimension of a cell is 100 μm. By the repetition of the elementary cells different structures are obtained: 22x22 cells, 39x39 cells, 44X44 cells.

The analysis is split in multiple cases. In the first analyzed case a uniform magnetic flux density of 0.5 T is imposed along the direction normal to the sample cross-section and the frequency range is between 50 Hz and 10 kHz. The grain relative permeability is 7000 and its conductivity is 10MS/m. The matrix relative permeability is 1 and its conductivity is 10μS/m. The grain represents 50% from the elementary cell volume. The question is if the values for the losses are the same if the shape of the grain differs, but the concentration is the same. A spherical and a rectangular shape grains were considered. From the computed data and figure 2 it was observed that the shape influences the loss values. For small frequencies the values are similar, but with the increase of the frequency the differences become bigger. The relative error between the values is approximate 10% for the highest frequency.

The structure of a real soft magnetic composite material is formed by both inclusions and matrix (insulating surrounding layer). This means that when the analysis is performed using a 2D model is important to choose the correct permeability of the sample in order to obtain the same results as in the real case. In figure 3 are presented the results for the second case: the comparison between the results obtained for two different number of cells (S1= 44x44 cells and S2= 66x66 cells) for which two different relative permeabilities were considered: $\mu_r = 7000$ and $\mu_r = 450$. It was observed that with the increase of the number of cells (a bigger sample) and the frequency, the differences between the losses become bigger. One can conclude that the permeability values influence the losses and that is important to carefully choose its value.

The third and fourth cases analyze the influence of the sample conductivity (figure 4) and inclusions concentrations (figure 5) on losses. As expected in both cases with the grow of the conductivity and concentration, the losses grow also. In figure 6 it can be observed the losses in each elementary cell for two different concentrations.

The final case analyses the influence of grain density. In practice during the high stress compaction method that is used for obtaining the materials, contacts might appear between neighboring cells. The presence of contacts influences the values of the current losses.

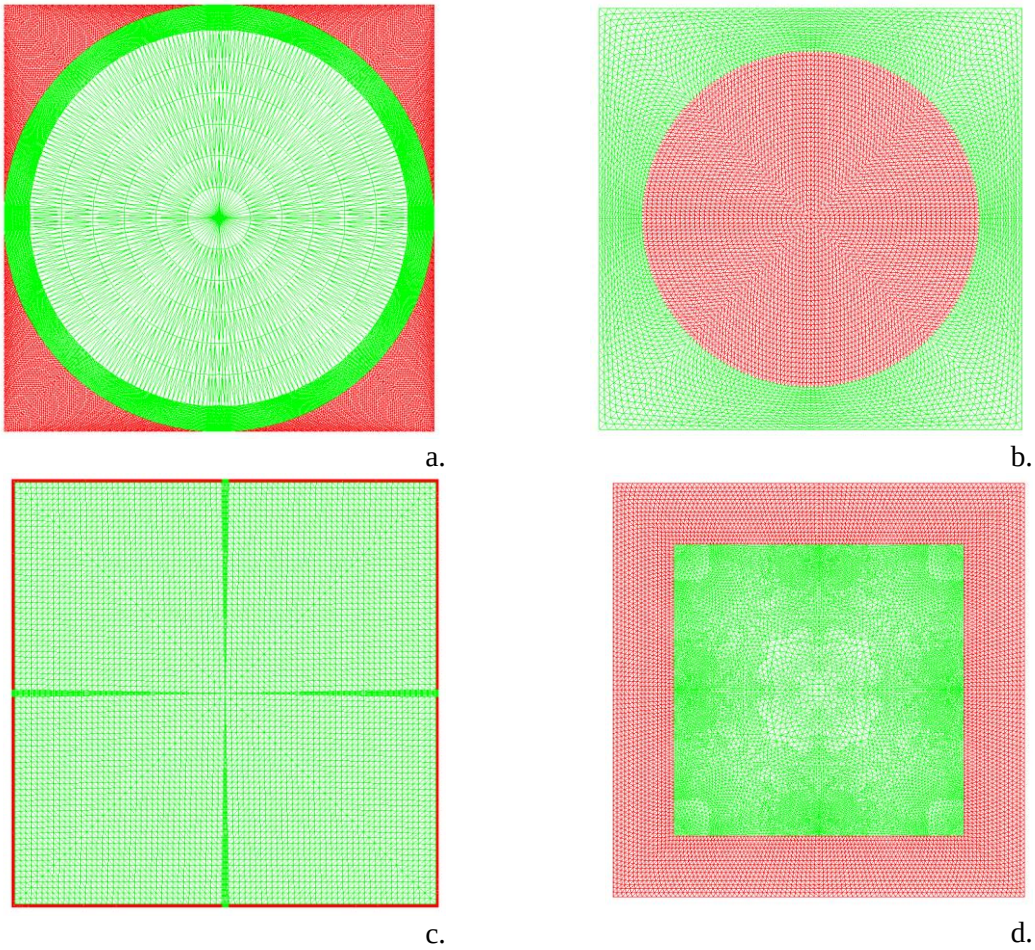

Fig. 1. Scheme of the different elementary cells

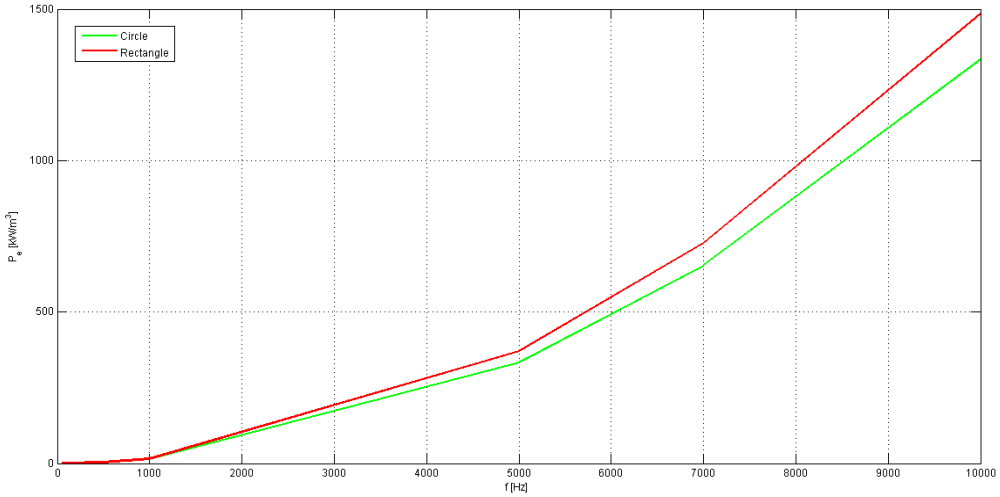

Fig. 2. Eddy current losses variation versus frequency for different inclusion shape

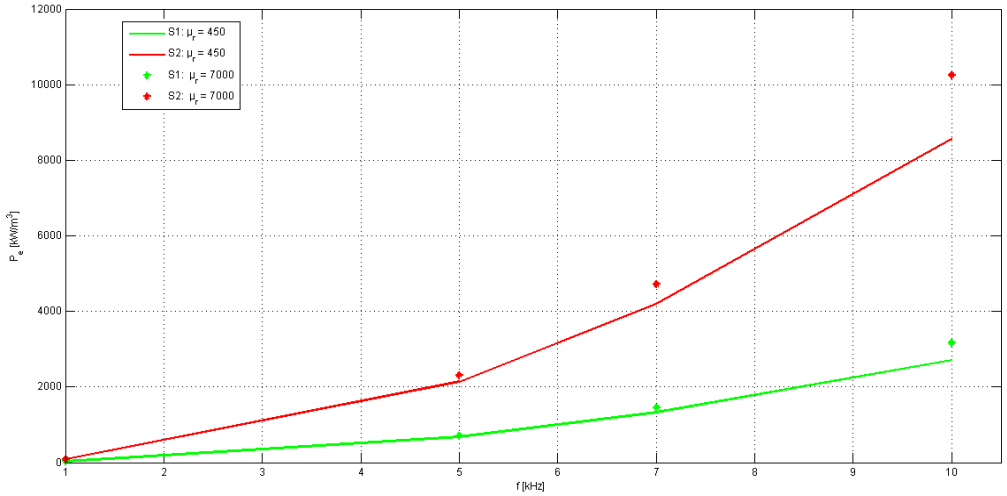

Fig. 3. Comparison between the losses obtained for two samples with different permeabilities

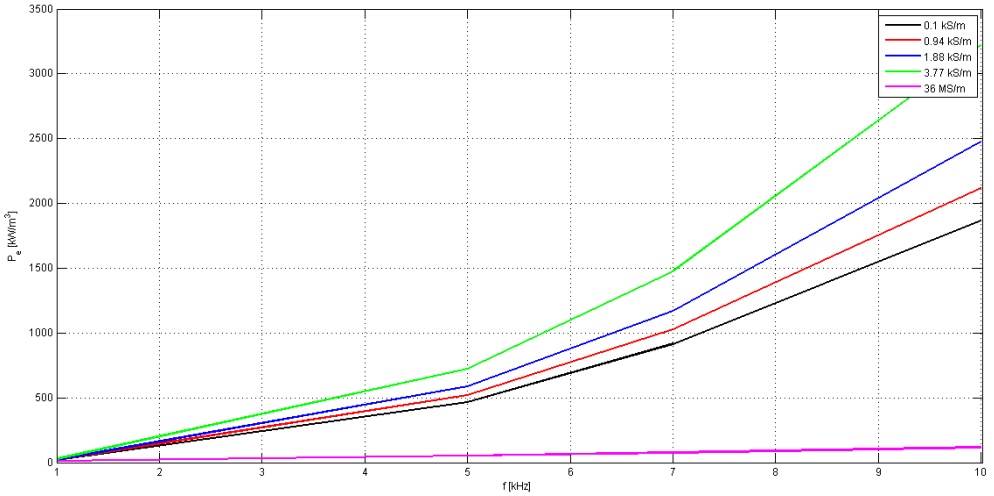

Fig. 4. Eddy current losses variation versus frequency for different contact conductivities

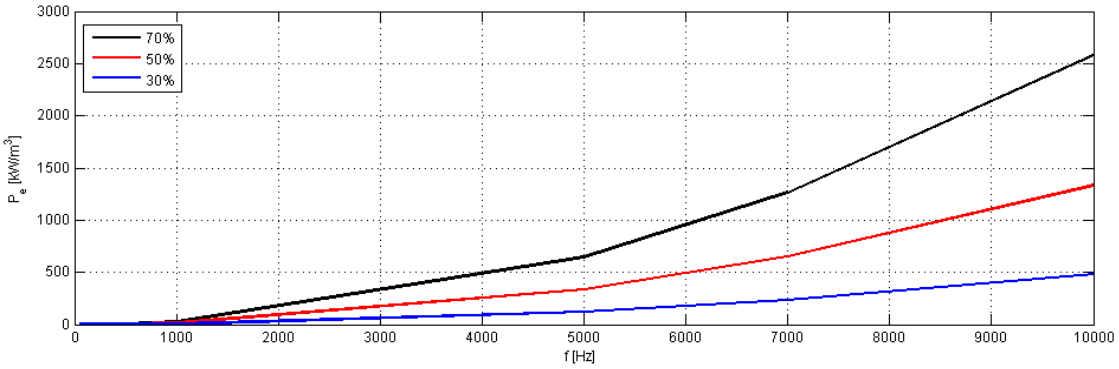

Fig. 5. Eddy current losses variation versus frequency for particle concentrations

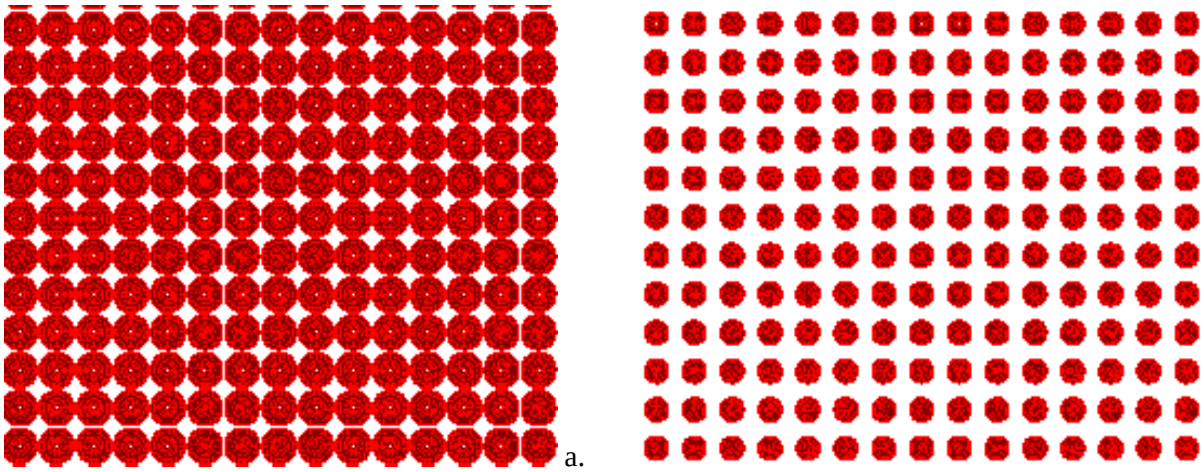

a. b.

Fig. 6. Eddy currents losses for each cell for a. 70%, b. 50% inclusions concentration

In figure 6 the eddy currents were only at the grain level because there was no contact between the cells. The presence of contact implies the one must take into considerations the macroscopic eddy current. The dimensions of this contacts influence the losses (figure 7) - a higher contact means a higher macroscopic current and higher losses.

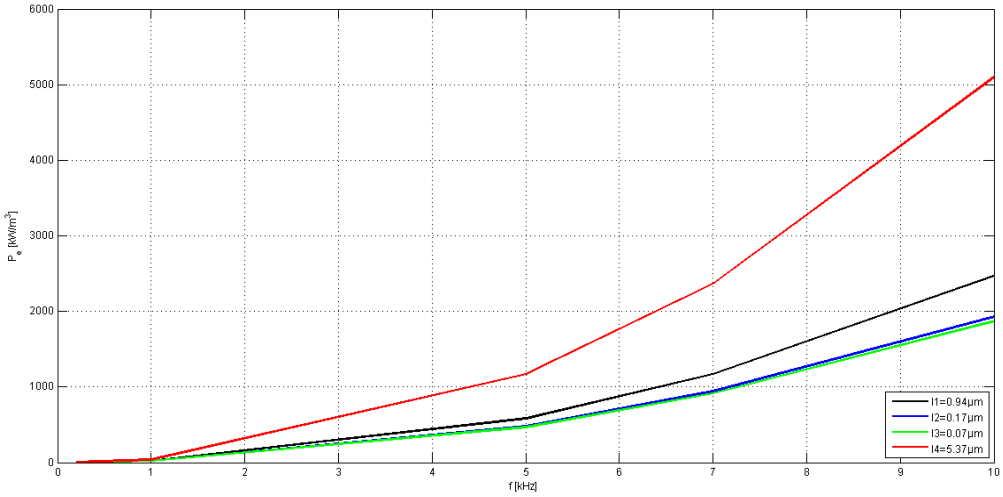

Fig. 7. Eddy current losses variation versus frequency for contact lengths

It is easy to observe that the elementary cells properties have big influences on the eddy current losses, so it is very important to define correctly the cell properties, especially if the analysis is made starting from real materials.

4. Conclusions

The paper presents the effects that the elementary cell properties have on eddy losses. The frequency has a high impact on the final results. It was observed that increasing the concentration for the inclusions leads to eddy current loss modifications. Also if one keeps the inclusions concentration constant, but changes their shape differences between the values of losses result from the analysis. The value of permeability as well as conductivity significantly change the values of losses. The presence of contacts between two neighbouring cells

complicates the analisys because one must take into account the eddy currents at the macroscopic level, besides the eddy currents that appear at the microscopic level

Using a 2D model to simulate a 3D real composite material implies a careful choice for the elementary cell and its parameters.

References

[1] C.M. Kanamadi et al., "*Dielectric and magnetic properties of (x) $CoFe_2O_4$ + (1−x) $Ba_{0.8}Sr_{0.2}TiO_3$ magnetoelectric composites*", Materials Chemistry and Physics, VOL. 116, 2009, pp. 6–10
[2] Byong-Taek Lee, Swapan Kumar Sarkar, Ho-Yeon Song, "*Microstructure and material properties of double-network type fibrous (Al_2O_3–m-ZrO_2)/t-ZrO_2 composites*", Journal of the European Ceramic Society, vol. 28, nr. 1, 2008, pp. 229–233
[3] Xiaokai Zhang, "*Novel magnetic composites for high frequency applications*", teză, University Of Delaware, 2009
[4] http://www.uni-kiel.de/aktuell/pm/2012/2012-121-biomagnetische-sensoren-e.shtml
[5] Guo-Dong Li, "*Contemporary magnetic materials and magnetism: research and applications*", Electromagnetic Materials, Proceedings of Symposium F, pp. 77-85, ICMAT 2003
[6] F.L. Matthews, R.D. Rawlings, "*Composite materials: Engineering and Science*", Woodhead Publishing Limited, England, 1999.
[7] J. R. Vinson, R. L. Sierakowski, "*The Behavior of Structures Composed of Composite Materials*", Kluwer Academic Publishers, 2004
[8] S. G. Mogilevskaya, S. L. Crouch, H. K. Stolarski, A. Benusiglio, "*Equivalent inhomogeneity method for evaluating the effective elastic properties of unidirectional multi-phase composites with surface/interface effects*", International Journal of Solids and Structures, vol. 47, 2010, pp. 407-418
[9] A. Bordianu, L. Petrescu, V. Ionita, "*Numerical testing of homogenization formulas efficiency for magnetic composite materials*", MURPHYS 2012, Suceava, Romania

Experimental Results versus FEM Based Analysis of a Squirrel Cage Induction Motor

Sorin VLĂSCEANU, Alecsandru SIMION,
Nicolae_Daniel IRIMIA, Adrian MUNTEANU, Ovidiu DABIJA
Faculty of Electrical Engineering "Gheorghe Asachi" Technical University of Iaşi
Bd. Mangeron nr.51-533, RO-700050, Iaşi, Romania
soryn_85@yahoo.com;

Abstract. This paper focuses a comparative study on the operating characteristics of a three phase induction motor in squirrel cage classical construction. Operating characteristics of the machine were obtained by performing experimental tests on a special stand from the electrical machines laboratory. These were then compared with the characteristics obtained by simulation using computer software FLUX 2D algorithm based on FEM (Finite Element Method). After studying the obtained results, some comparative conclusions were drawn.

1 Introduction

The generalization of the three phase system for transmission and distribution of the electricity during the last period, leaded to the construction of induction machines capable of operating in direct correlation with this type of system [1]. Squirrel-cage induction motors are some of the electric motors used due to the advantages they possessed. The technological advantages are: simplicity of construction, robustness, relatively high technical performance, operational stability etc. and the economic nature requiring low costs both for the construction process and also maintenance. A special attention should be paid to the design and validation results by simulation, which requires field calculation programs. Using simulation programs that operate with finite element method to achieve field calculations, represents a solution in determining the operating characteristics of the electric motors, successfully applied in this case to compare results obtained from measured parameters of the induction machines with those obtained in the simulation [2]. Therefore this paper aims to analyze an existing three-phase induction motor in electric machines laboratory. The motor initially is studied on the bench testing and drawn the operating characteristics. After measurements, the motor is simulated in a field analysis program where the results were compared with measured on the test stand.

2 Geometry Description

Figure 1: The view of the studied induction motor on the laboratory stand.

The motor studied is produced by german company “Quick ROTAN" Type NDK 880/12 and it was designed for laboratory tests being provided with an electromagnetic brake. To reduce any additional torque that could affect operating characteristics, this system was removed. In figure 1 is shown an image with the motor on the laboratory stand where the measurements took place. Figure 2 shows the induction machine's geometry that was realised in simulation software.

Further are presented the nominal motor data and main constructive parameters:

Table 1
Main parameters of the induction motor

Constuctive elements	**Value**
Number of stator slots	24
The length of the machine	70 mm
Outer diameter stator	136 mm
Inner diameter stator	70 mm
Stator yoke height	16,5 mm
Stator slot height	16,5mm
Stator tooth width	4 mm
Number of pole pairs (p)	1
Number of rotor slots	18
Outer diameter rotor	69,4 mm
Rotor yoke height	9,17 mm
Rotor slot height	14 mm
Rotor tooth width	5 mm
Shorting ring rotor thickness	14 mm
Height shorting ring rotor	15 mm
Shaft diameter	22 mm

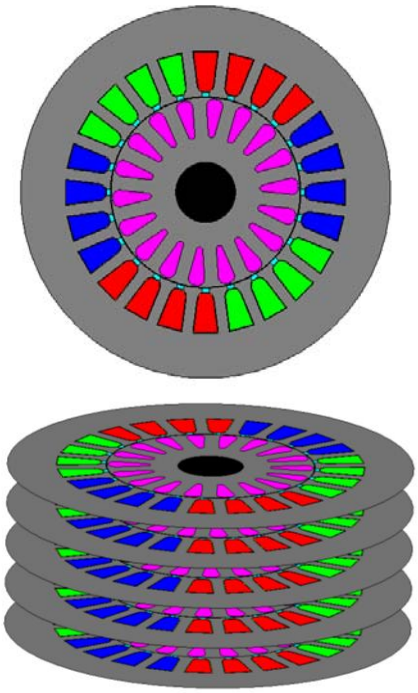

Figure 2: The transversal section of the induction motor.

The three phase motor parameters are: m = 3, 2p = 2, P_N = 0.55 kW, U_N = 380 V, being in star connection, I_N = 1.6 A, f = 50/60 Hz, n = 2850/3460 rpm. Machine’s stator core is made of steel laminations with a thickness of 0.5 mm, being provided with a lake isolation between them. The stator phase is curly type winding, arranged in a single layer, with the number of slots per pole and phase: y_1=4. The four coils that make up a stator phase are disposed in series. Each motor phase resistance has the value of R_f = 9.8 Ω, being measured at nominal operating temperature of the motor. Each slot of the stator core is crossed by 100 conductors of round wire with a diameter of 0.75 mm resulting a current density:

$$J_1 = \frac{I_N}{S_{Cu} \cdot a_1} = \frac{2.76}{0.4418 \cdot 1} = 6.24 \ \ A/mm^2 \qquad (1)$$

where I_N is nominal current for a stator phase, S_{Cu}- sectional area of conductor and a_1- number of parallel current paths.

Rotor core is made also from steel laminations. The rotor has 18 oval slots and the teeth have parallel walls. The main dimensions are given in the table above. Rotor bars are made from cast aluminum and are skewed towards generating with an angle of 20^0 which corresponds to the angle between two rotor slots. Tilt rotor slots lead to the removal of odd harmonics and electromagnetic torque increase.

3 Comparative results

Experimental tests of the three phase induction motor were performed on a Lucas Nulle stand (produced in Germany). Plotting operating characteristics were achieved by monitoring electrical quantities, tracked and analyzed both through analogical measuring instruments and virtual instrumentation performed by using an acquisition board (DAQ) with multiple input channels, such as NI-6062, at a sampling frequency of 500 kHz, produced by National Instruments. Also, using the LabVIEW software package, the acquisition and data processing diagrams were drawn.
Keeping rigorously the geometrical and electrical parameters, a simulation analysis was performed in skewed flow calculation package software produced by CEDRAT. Due to the tilt of the rotor bars, the motor geometry is divided lengthwise into 5 slices and the calculations are different for each slice independently. Figure 3 shows a detail of the meshed domain, flux lines distribution and flux density color maps.

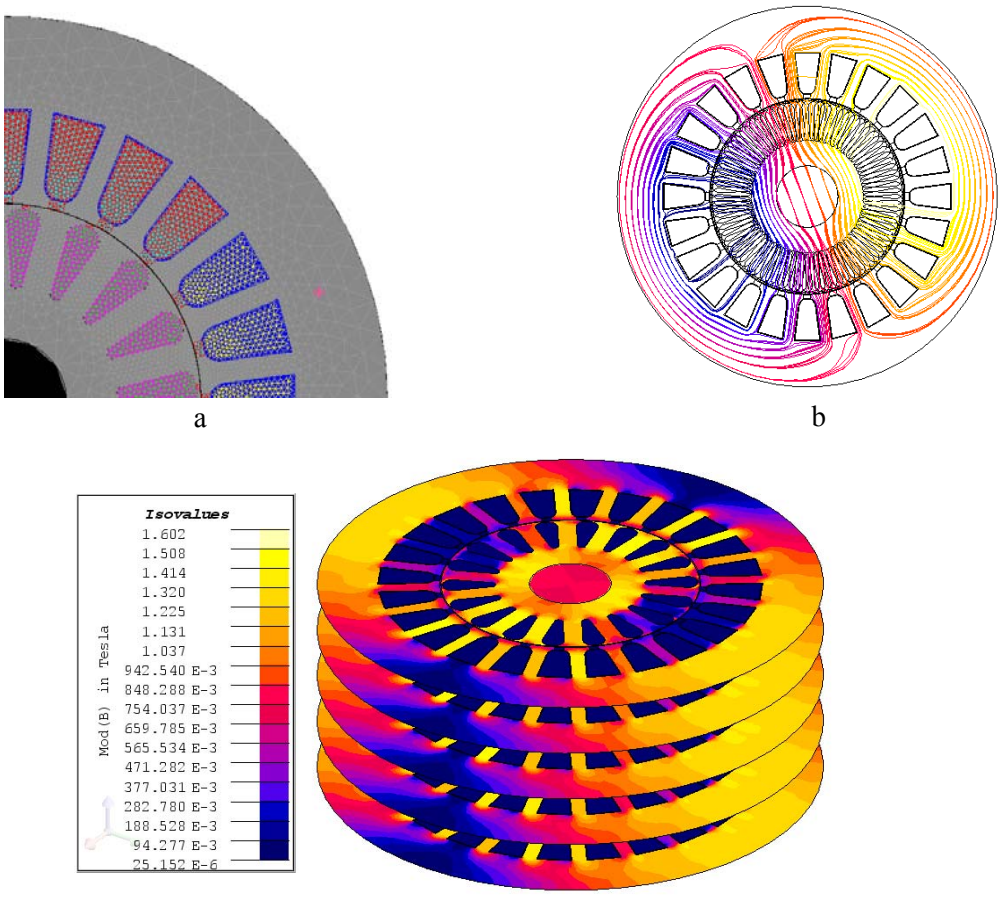

Figure 3: a) Mesh domain, b) Flux lines distribution and c) Flux density color maps.

The simulation software provides the magnetic induction values in different structural elements of the machine by which it can be determined the saturation degree of the magnetic circuit. From the spectral map of induction and its color scale attached thereto, it is found that the mean magnetic loading are within allowable limits of: 1.4 ÷ 1.6 T. From the experimental and simulated mechanical and respectively stator phase current characteristics, it can be observed that for the same values of the electromagnetic torque developed by the motor, the supply currents are lower in the simulation compared to those measured. This is because in the simulations were

not introduced any losses which usually occurs in a real type motor (ventilation losses, viscous friction, mechanical losses etc). The measured torque for the low speed values (at the beginning of the start-up process) it's not accurate represented because of the limited measuring possibilities of the working stand.

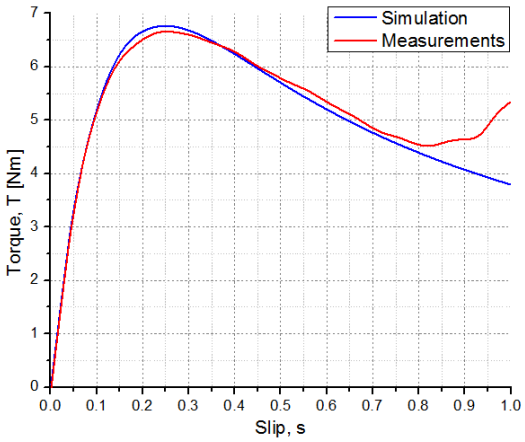

Figure 4: Torque-slip characteristics

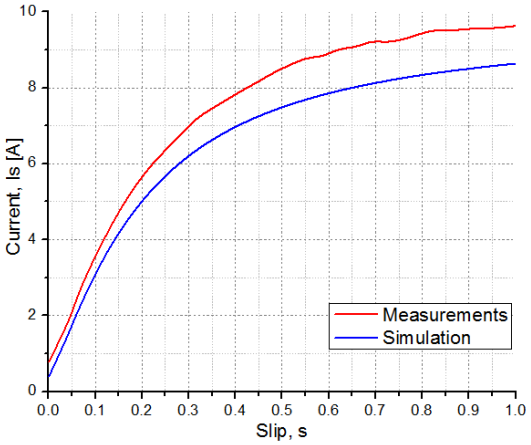

Figure 5: Stator current versus slip characteristics

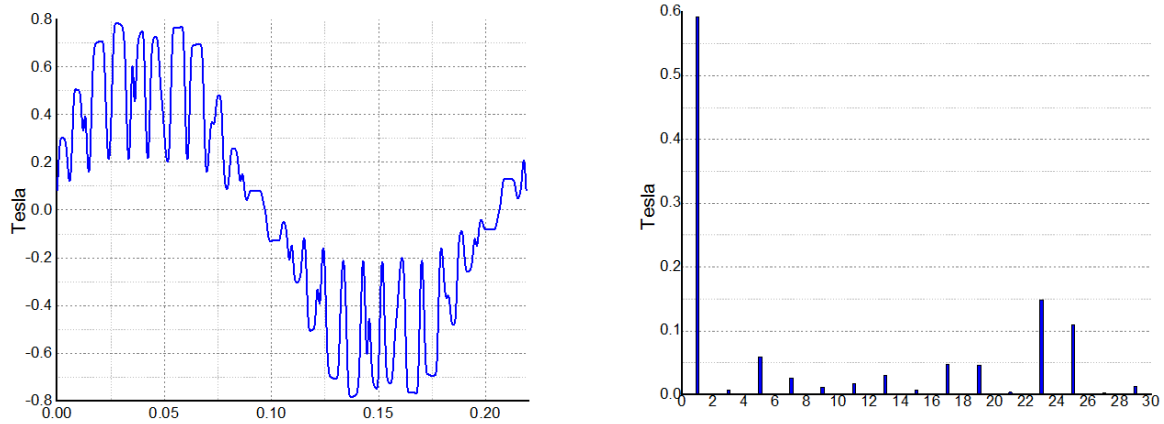

Figure 6: Air-gap flux density and content in high order harmonics.

Figure 6 shows the air-gap magnetic flux density for two poles of the motor and the high order harmonics content. The fundamental value is about 0.6 T. The presence of the stator and rotor teeth causes some oscillations in the waveform of the air gap flux.

It can be observed that the nominal air gap induction waveform is approaching a sine wave, due to the high number of slots forming a pair of poles.

Of a particular importance in assessing the start-up performance is the knowledge of the high order harmonics (3, 5 and 7). In case of the three-phase winding, the third harmonic, which usually draws attention, is generally suppressed by the star winding connection. In this context, the spatial harmonic of rank 5 (which is about 6 % of the fundamental) of the induction waveform will create a rotating field which speed is proportional to its rank and in the same moving sense as the rotor, while the 3 and 7 harmonics in reverse.

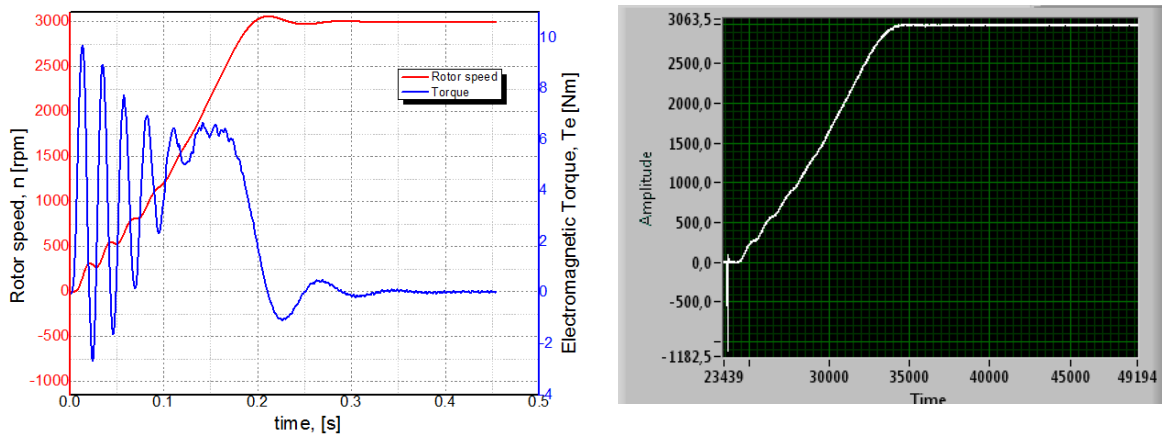

Figure 7: Variation of the torque and speed from start-up to the nominal speed.

By analyzing the speed characteristic from the figure 7, it can be seen that the motor has a start-up time (until it reaches the nominal speed) of approximately 0.2 seconds. In the first moments of the startup process, the electromagnetic torque oscillates around 4 Nm and then stabilizes at about 0.2 Nm. In the no-load regime, the value of the I_0 current absorbed by the motor is desired to be known. This current has an active component I_{0a}, which is much smaller than the reactive component I_{0r}, the motor having in this case a lower power factor value. If the active component is being neglected, the current absorbed by the motor is equal to the reactive component (which is actually magnetizing current) for the no-load regime [3].

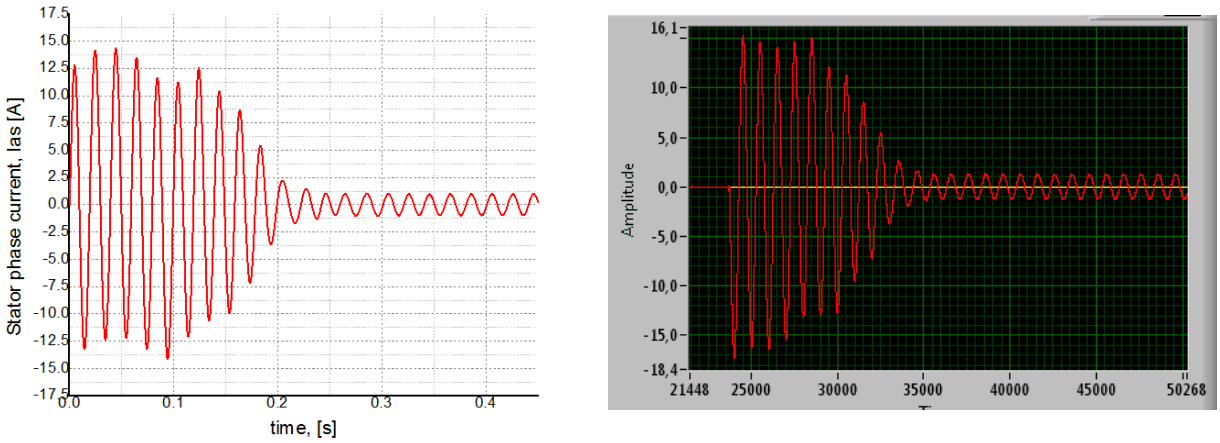

Figure 8: Current waveforms through the stator phases, from the start-up to the nominal speed.

At startup, the stator phase currents amplitudes are about 10 times higher than the nominal value. When the rotor is stabilized at the rated speed for the no-load regime, stator currents obtained both from laboratory measurements and also from simulations, reaches a peak value of about 1.3 A, which justifies the correctness of the computer simulation program. The next figure shows the induced voltages on the rotor bar and the waveform of the current from the start-up of the motor, to the nominal speed value.

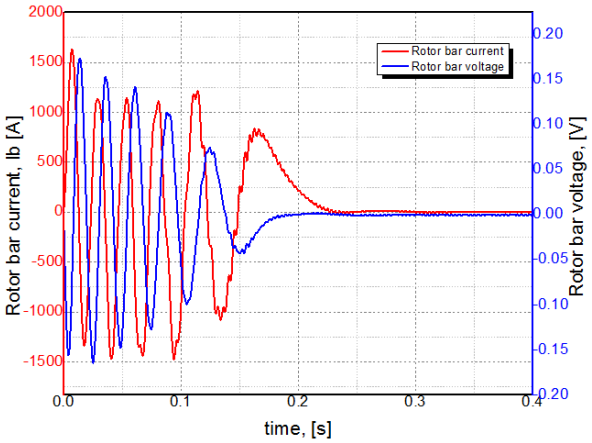

Figure 9: Rotor bar current and the induced voltage from start-up to the nominal speed.

4 Conclusion

• Using simulation programs that operate with finite element method to achieve field calculations, represents a convenient solution in determining the operating characteristics of electric motors, successfully applied in this case to compare the results obtained from measurements with those from the simulation.
• The analysis by simulation confirm the data obtained on the experimental model, thus validating the accuracy of the results. In addition, the accuracy of the results obtained by the simulation program is influenced by the accuracy with which various components were calculated and defined, in order to design the study model.
• The improvement of the electric motors performances can be done with quite high accuracy by successive simulations, leading to significantly reducing of the production costs.

Acknowledgments This paper was realised with the support of POSDRU CUANTUMDOC "DOCTORAL STUDIES FOR EUROPEAN PERFORMANCES IN RESEARCH AND INOVATION" ID79407 project funded by the European Social Found and Romanian Government.

References

[1] Simion Al., *Electrical Machines (in Roumain),* third volume*, Induction Machine,* PIM publisher, Iasi, Romania, 2012, ISBN 973-8050-26-X;
[2] Weili, L. Xie Ying, Shen Jiafeng, Luo Yingli, *Finite-Element Analysis of Field Distribution and Characteristic Performance of Squirrel-Cage Induction Motor With Broken Bars, Magnetics,* IEEE Transactions on Harbin Univ. of Sci. & Technol., pp: 1537 – 1540, April, 2007;
[3] Simion Al, Livadaru L, Munteanu A*, "Induction Motors - Modelling and Control, Chapter 1- Mathematical Model of the Three-Phase Induction Machine for the Study of Steady-State and Transient Duty Under Balanced and Unbalanced States"*, publisher InTech, pp: 3-44, November 14, 2012, ISBN 978-953-51-0843-6;
[4] Grantham C., McKinnon D. J., "*Rapid Parameter Determination for Induction Motor Analysis and Control",* IEEE Transactions on Industry Applications, Vol. 39, No. 4, pp: 1014-1020, july/august 2003;
[5] Balamurugan, S., Arumugam, R., Paramasivam, S., Malaiappan, M, "*Transient analysis of induction motor using finite element analysis",* Industrial Electronics Society Dept. of Electr. & Electron. Eng., IECON 2004. 30th Annual Conference of IEEE. Anna Univ., Madras, India, 2004;
[6] Kometani, H., Sakabe, S. ; Kameari, A., *" 3-D analysis of induction motor with skewed slots using regular coupling mesh"*, Magnetics, IEEE Transactions on Adv. Technol. R&D Center, Mitsubishi Electr. Corp., Hyogo, pp: 1769 – 1773, Jul 2000.

EVALUAREA CARACTERISTICILOR MAGNETICE ALE PIESELOR FEROMAGNETICE

Marilena STĂNCULESCU, Paul ANDREI, Mihai MARICARU, Marian VASILESCU, Ioan Florea HĂNŢILĂ
Universitatea "Politehnica" din Bucureşti, Spl. Independenţei 313, 060042, Bucureşti; marilena.stanculescu@upb.ro

Abstract. Evaluarea proprietăţilor magnetice ale pieselor feromagnetice nu permite prelevarea unor eşantioane potrivite aparaturii specializate pentru determinarea cu acurateţe a acestor proprietăţi. Totuşi, aceste proprietăţi modifică distribuţia câmpului electromagnetic şi se poate pune problema inversă a determinării caracteristicii *B-H* prin măsuratori ale câmpului magnetic din jurul piesei. Este esenţial ca procedura propusă să fie suficient de senzitivă pentru ca rezultatele să fie credibile. Lucrarea propune un dispozitiv de evaluare a caracteristicii *B-H*, admiţând distribuţia neuniformă a câmpului magnetic în interiorul pieselor feromagnetice şi liniaritatea mediului feromagnetic.

1 Introducere

Proprietăţile materialelor utilizate în realizarea unor piese sunt cunoscute din măsurătorile făcute pe eşantioane, utilizând instalaţii specializate. Ca urmare, dacă dorim să determinăm câmpul electromagnetic din piesă, utilizăm caracteristicile de material oferite de fabricanţi sau de bazele de date. Uneori, este posibil ca tipul de material utilizat la construcţia piesei să nu fie cunoscut. Alteori, chiar dacă este cunoscut, condiţiile de funcţionare ale piesei pot modifica caracteristicile materialului (încălziri, deformări, şocuri, etc.). Este posibil ca performanţele caracteristicii *B-H* a piesei să se modifice şi una din cauze poate fi modificarea permeabilităţii magnetice. Imposibilitatea prelevării unor eşantioane potrivite aparaturii de măsurare specializate, justifică interesul specialiştilor pentru elaborarea unor tehnici de măsurare a caracteristicii *B-H* aplicabile direct componentei feromagnetice a piesei [1].

Această lucrare face o scurtă analiză a posibilităţii de măsurare a permeabilităţii în regim de curenţi turbionari şi în câmp magnetic constant.

2 Analiza în curenţi turbionari

O tehnică simplă ar fi măsurarea mărimilor câmpului electromagnetic cvasistaţionar şi compararea măsurătorilor cu rezultatele obţinute prin calcul, testând diferite valori ale permeabilităţii magnetice. In Fig.1 este prezentată o schema 2D în care o bobină perfect conductoare cu dimensiunile 5 x 3 mm se află la o distanţă de 1 mm de piesa feromagnetică (fier) de conductivitate 10 MS/m, a cărei permeabilitate magnetică dorim să o măsurăm. Bobina are un flux magnetic Φ =2 Wb şi, pentru frecvenţele f= 50 Hz şi 1 kHz, se obţin valorile $\underline{I}$ ale curenţilor din bobină (vezi Tabelul 1). A fost utilizat programul FEMM. Admitanţele complexe lineice corespunzătoare se obţin cu relaţia:

$$\underline{Y} = \frac{\underline{I}}{j2\pi f\Phi} \tag{1}$$

În Fig. 2 este prezentată aceeaşi structură, la care s-a adăugat un jug din ferită (domeniul materialului fiind simbolizat cu “fe0”) de conductanţă nulă şi permeabilitate magnetică relativă 8000. Rezultatele calculelor sunt prezentate tot in Tabelul 1.

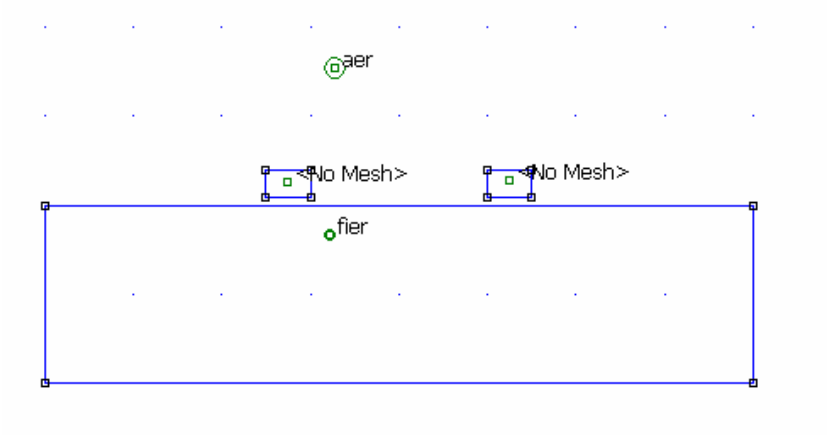

Fig.1. Bobina in vecinatatea unui corp feromagnetic conductor

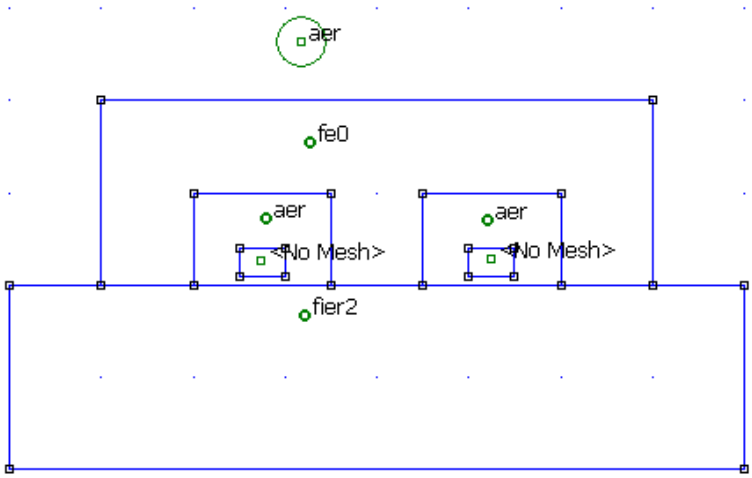

Fig.2. Bobina cu jug din ferita, in vecinatatea unui corp feromagnetic conductor

Tabelul 1 Admitante ale unei bobine aflate in vecinatatea piesei

	f(Hz)	μ_r	Re($\underline{I}$)	Im($\underline{I}$)	Re($\underline{Y}$)	Im($\underline{Y}$)	Y
fara jug	50	1000	1.41E+06	1.72E+04	2.74E+01	-2.25E+03	2.25E+03
	50	4000	1.41E+06	1.18E+04	1.88E+01	-2.24E+03	2.24E+03
	1000	1000	1.43E+06	2.00E+05	1.59E+01	-1.14E+02	1.15E+02
	1000	4000	1.42E+06	2.00E+05	1.59E+01	-1.13E+02	1.14E+02
cu jug	50	1000	1.58E+04	1.91E+04	3.04E+01	-2.51E+01	3.95E+01
	50	4000	6.34E+03	1.35E+04	2.15E+01	-1.01E+01	2.37E+01
	1000	1000	3.90E+04	2.40E+05	1.91E+01	-3.11E+00	1.94E+01
	1000	4000	2.00E+04	2.40E+05	1.91E+01	-1.59E+00	1.92E+01

Analizând rezultatele din Tabelul 1, se observă că cea mai bună senzitivitate se obţine atunci când adăugăm jugul din ferită şi frecvenţa este joasă. Creşterea permitivităţii conduce

la scăderea adâncimii de pătrundere a câmpului electromagnetic şi, în cazul frecvenţelor mici, această scădere este mai importanta.

3 Analiza în câmp magnetic constant

In cazul câmpului magnetic constant, se pot face măsurători ale inducţiei magnetice, folosind sonde Hall, care pot fi foarte sensibile. Unii autori [2] recomandă senzori speciali („fluxset"), care au miez dintr-un material feromagnetic cu o permeabilitate foarte mare în prima parte a caracteristicii, saturându-se apoi foarte puternic. În jurul miezului se află o bobină alimentată la tensiune sinusoidală. Existenţa de-a lungul miezului a unui câmp magnetic constant saturează miezul şi modifică impedanţa bobinei.

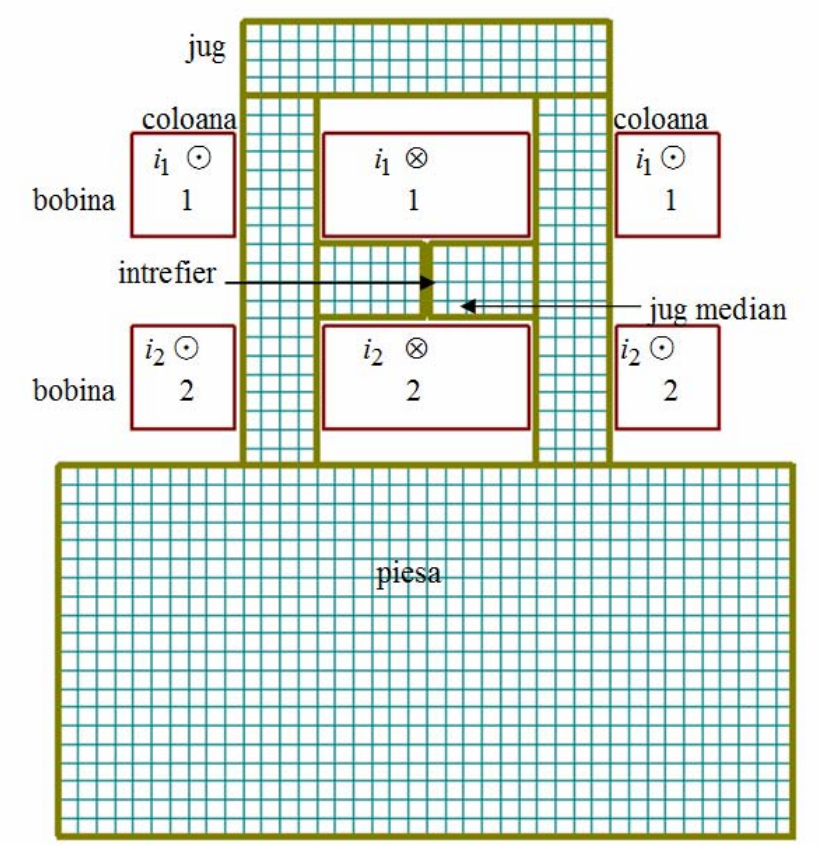

Fig.3. Dispozitiv da masurare in camp magnetic constant

Dispozitivul pe care-l propunem în continuare (Fig. 3) presupune măsurarea inducţiei magnetice într-un întrefier foarte mic, de dimensiune δ, şi se recomandă utilizarea unei sondei cu efect Hall de mare precizie. Un circuit magnetic in forma de H, este acoperit de un jug şi are un jug median, prevăzut cu un întrefier în care se poate introduce sonda Hall. Permeabilitatea magnetică relativă a materialului jugului este μ_{rj}. Circuitul magnetic se pune pe piesa a cărei permeabilitate dorim să o măsurăm. Bobinele 1 şi 2 sunt formate din doi galeţi ce înfăşoară coloanele circuitului magnetic şi sunt parcurse în aceleaşi sensuri de curenţii i_1 şi i_2. Fixând valoarea curentului i_2, se reglează valoarea curentului i_1 până când inducţia magnetică măsurată în întrefierul jugului median este nulă. În acest fel, se poate utiliza cea mai mică scală a gaussmetrului.

Pentru o valoare fixată a lui i_2, se calculează inducţiile B' si B'' corespunzătoare curenţilor $i_1^{'} = 0$ si $i_1^{''} \neq 0$ (am ales $i_1^{''} = 2i_2$). Deoarece considerăm mediul liniar, avem

$$B = bi_2 - ai_1 \ , \tag{2}$$

de unde $bi_2 = B'$ şi $a = \frac{B'-B''}{i_1^{''}}$. Inducţia magnetică calculată în întrefier este nulă dacă

$$i_1 = \frac{B'}{B'-B''} i_1^{''} \quad . \tag{3}$$

Se determină i_1 din relaţia (3) pentru diferite valori ale permeabilităţii piesei. Atunci când valoarea i_1 a curentului calculat este egală cu cea măsurată, rezultă permeabilitatea magnetică a piesei. În calcule au fost alese următoarele valori numerice: μ_{rj} = 4000, lăţimea jugului şi a coloanelor de 20mm, înălţimea coloanei (deci şi a ferestrei) de 100 mm, lăţimea ferestrei de 60 mm, dimensiunile galeţilor 28 x 28 mm, situaţi la 2 mm distanţă de coloane şi de jugul median, întrefierul δ = 2 mm şi curentul i_2 = 100 A (pentru simplitate am considerat că galeţii au o singură spiră, deci curenţii i_1 şi i_2 corespund solenaţiilor galeţilor). Calculele au fost făcute cu un program bazat pe funcţia Green, elaborat în cadrul Departamentului de Electrotehnică din Universitatea Politehnica din Bucureşti [3].

În Fig. 4 este trasat graficul permeabilităţii magnetice a piesei în funcţie de curentul i_1 pentru care se obţine inducţia magnetică nulă în întrefier.

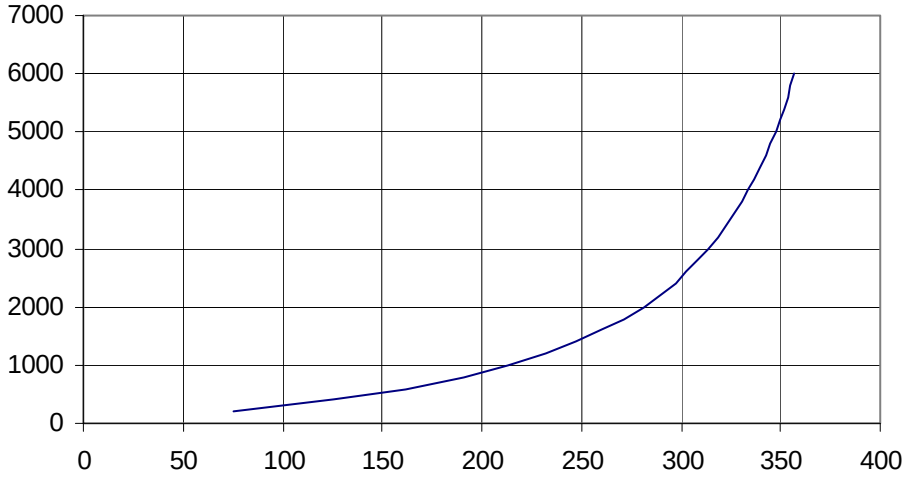

Fig.4. Dependenta permeabilitatii magnetice realtive a piesei in functie de curentul i_1

Prin comparaţie cu măsurarea în curenţi turbionari, permeabilităţilor magnetice de 1000 şi 4000, le corespund valorile curenţilor i_1 de 213, respectiv 334. Modificarea permeabilităţii relative a jugului la valoarea de 8000, nu a condus la o schimbare sesizabilă a graficului din Fig. 4. Ipoteza mediului liniar este valabilă pe porţiunile nesaturate ale caracteristicii *B-H*. Dacă este necesar, se poate modifica valoarea curentului i_2 în scopul reducerii valorilor inducţiei magnetice din domeniile feromagnetice.

4 Concluzii

În cazul utilizării măsurătorilor în câmp electromagnetic cvasistaţionar, este bine să folosim un jug din ferită şi o bobină ce poate fi alimentată la diferite frecvenţe. În altă lucrare se va analiza şi varianta alimentării bobinei cu o tensiune periodica nesinusoidală, cu un spectru de armonice suficient de bogat. Nu cunoaştem o demonstraţie a bijecţiei $\mu_r \to \underline{Y}$ sau $\mu_r \to Y$ pentru o configuraţie dată şi o frecvenţă dată a tensiunii de alimentare a bobinei, dar putem intui că, pentru un anumit interval de frecvenţe, ultima dependenţă este scăzătoare, având în vedere micşorarea adâncimii de pătrundere. Extinderea la medii neliniare a determinării caracteristicii *B-H* în câmp magnetic cvasistaţionar este o problemă foarte dificilă.

În câmp magnetic constant, dispozitivul propus conduce la senzitivităţi destul de bune. Trebuie sa menţionăm însă faptul că, în calcul, a fost neglijat întrefierul dintre coloane şi piesa studiată. În viitoarele cercetări, vom impune un mic întrefier (de exemplu de 0.2 mm) pe care-l adăugăm şi între coloane şi jugul superior, în dorinţa de a realiza un fel de simetrie a circuitului magnetic. Este o modificare de natura micşorării permeabilităţii magnetice a coloanelor. Programul care utilizează funcţia Green permite introducerea cu uşurinţă a unui întrefier de orice dimensiune. Extinderea metodei la determinarea caracteristicilor neliniare este posibilă şi va fi studiată într-o viitoare lucrare, folosind tot programul bazat pe funcţia Green.

În prezenta lucrare a fost adoptat modelul simplu 2D, scopul acestei comunicări fiind validarea unor proceduri „in situ" de determinare a permeabilităţii magnetice. Odata ce valabilitatea procedurii este confirmată, se poate trece la elaborarea programelor 3D necesare măsurărilor reale.

Aprecieri – Activitatea de cercetare prezentată în această lucrare a fost desfăşurată cu finanţarea din programul POSDRU, prin contractul de finanţare POSDRU/89/1.5/S/62557.

Referinţe

[1] R. Albanese, A. Bosavit, R. Fresa, D. Ioan, G. Rubinacci, A. Tamburino, F. Villone, "Identification of the B-H curve from external measurements using complementary formulation", *Physica B,* vol. 275, pp. 228-232, 2000.

[2] D. Ioan, F. Hantila, M. Rebican, C. Constantin, "FLUXSET sensor analysis based on nonlinear manetic wire model of the core", *Studies in Applied Electromagnetics and Machanics* , vol. 14, pp.160-169, 1998.

[3] F. Hantila, C. Mihai, C. Ifrim, and T. Leuca, "A New Procedure for Reconstruct the Aged Regions of the Ferromagnetic Bodies", *COMPEL* , vol. 24, no. 2, pp. 620-627, 2005.

ÎNCĂLZIREA CARCASELOR PRIN CURENŢI TURBIONARI

Valeriu ŞTEFAN-MINCULETE, Mihai MARICARU, Marius Aurel COSTEA, Ioan Florea HĂNŢILĂ
Universitatea "Politehnica" din Bucureşti, Spl. Independenţei 313, 060042, Bucureşti; mihai.maricaru@upb.ro

Stelian MARINESCU
ICPE S.A., Spl. Unirii 313, Bucharest, 030138, Bucureşti

Rezumat. Pentru analiza încălzirii carcaselor din materiale conductoare neferomagnetice prin curenţi turbionari se poate adopta un model foarte simplu de calcul al câmpului electromagnetic, în care o soluţia analitică poate fi obţinută. Deoarece excitaţia poate conţine un spectru bogat de armonice, o procedură deosebit de eficientă de determinare a pierderilor prin conducţie şi a evoluţiei încălzirii carcasei este dată de descompunerea problemei în serie de funcţii proprii spaţiale. Soluţia obţinută prin calcul este verificată prin măsurători experimentale.

1 Introducere

Utilizarea curenţilor turbionari la conversia energiei câmpului electromagnetic în căldură este frecvent aplicată în procesele de electrotermie din ingineria electrică, având câteva mari avantaje: piesele pot fi încălzite volumic, adâncimea de pătrundere şi valoarea pierderilor prin curenţi turbionari pot fi uşor controlate prin frecvenţa şi valoarea curentului sau tensiunii de excitaţie, timpii de încălzire pot fi determinaţi cu suficient de bună precizie, tehnologia este nepoluantă, etc. Un exemplu concret, aflat în atenţia specialiştilor din cadrul Centrului 3 Servomotoare al ICPE S.A., este încălzirea carcaselor de aluminiu, care. prin dilatare, se montează peste carcasele din tole feromagnetice ale servomotoarelor fără perii.
Problemele de curenţi turbionari în regim sinusoidal se rezolvă în complex, prin soluţionarea unei ecuaţii Helmholtz cu necunoscută complexă. În regimul periodic, se descompune soluţia în serie Fourier, fiecare componentă fiind obţinută prin utilizarea imaginilor în complex. Metodele numerice utilizate pentru soluţionarea ecuaţiei curenţilor turbionari sunt cele diferenţiale, integrale şi hibride. Cea mai populara şi, totodată cea mai utilizată metodă numerică diferenţială este metoda elementului finit (FEM), în care soluţia se aproximează cu o combinaţie liniară de funcţii de formă şi se proiectează ecuaţia diferenţială pe un set de funcţii "test". Pentru definirea funcţiilor de "formă" şi a celor de "test", se utilizează o reţea de discretizare spaţială căreia i se asociază elementele nodale sau, în structurile 3D, elemente de muchie [1]-[3]. Metoda se remarcă prin flexibilitate, permiţând calculul câmpului electromagnetic în aproape orice configuraţie geometrică, cu medii neomogene şi, uneori, neliniare. Are dezavantajul că domeniul de calcul este mărginit şi că introduce surse de suprafaţă parazite pe interfeţele dintre subdomeniile reţelei de discretizare (chiar şi în aer). Dar cel mai important dezavantaj specific calculului problemelor de curenţi turbionari constă în faptul că pentru a obţine o acurateţe corespunzătoare a soluţiei, reţeaua de discretizare spaţială trebuie să fie puternic neuniformă, mult îndesită în vecinătatea suprafeţelor corpurilor conductoare, dată fiind adâncimea de pătrundere a câmpului electromagnetic. Această neuniformitate este cu atât mai mare, cu cât frecvenţa este mai mare. În cazul regimului periodic, nu mai avem controlul adâncimii de pătrundere şi nu putem adapta fineţea reţelei de discretizare.

Metoda hibrida FEM – elemente de frontieră, aplică FEM în corpurile conductoare, condiţia de frontieră rezultând prin metoda elementelor de frontieră (BEM), care tratează soluţia în aer. Metoda nu introduce surse parazite şi poate fi aplicată în spaţii nemărginite. Matricea sistemului are dimensiuni mai mici dar se "umple" în comparaţie cu FEM şi îşi pierde simetria. Se păstrează dezavantajul adaptării reţelei de discretizare la adâncimea de pătrundere.

Ecuaţia integrală a densităţii de curent (ECIE) este deosebit de eficientă, având ca necunoscută curentul indus în mediile conductoare, care intra direct în calculul pierderilor. Pentru discretizarea spaţială se folosesc elementele de suprafaţă (în structuri 2D), sau elemente de muchie (în structuri 3D [3]). ECIE poate fi extinsă şi la medii neliniare, folosind metoda de punct fix a polarizatiei [4], [5]. Din păcate, şi ECIE suferă de dezavantajul major al adaptării reţelei de discretizare spaţială la adâncimea de pătrundere.

Metodele analitice sunt singurele care conduc la o soluţie de mare acurateţe a problemei de curenţi turbionari, indiferent de frecvenţa mărimilor câmpului electromagnetic. Metodele analitice nu pot fi aplicate la medii neliniare şi au marele dezavantaj că geometria domeniului de calcul trebuie sa fie foarte simplă, permiţând soluţionarea analitică a problemei Sturm-Liouville [6], [7]. Trebuie subliniat faptul că, în afara coordonatelor carteziene, funcţiile proprii sunt funcţii speciale, care îngreunează mult obţinerea rezultatelor numerice. Cărţile de matematici aplicate au acordat multă atenţie studierii acestor funcţii, au propus aproximaţii pentru comportarea asimptotica a acestor funcţii speciale, precum şi formule de aproximare a valorilor proprii (vezi, de exemplu [8], [9]). Din păcate efortul de calcul al acestor funcţii speciale nu justifică întotdeauna adoptarea metodelor analitice.

Şi în cazul metodelor analitice, efortul de calcul creşte atunci când regimul este periodic, fiind necesară descompunerea soluţiei în serie Fourier şi soluţionarea pe armonice. Pentru soluţionarea regimului periodic, M. Vasiliu a propus descompunerea soluţiei în serie de funcţii proprii spaţiale [10]-[14]. Din păcate procedura nu a putut fi finalizată cu rezultate numerice decât pentru configuraţii deosebit de simple, unde au putut să fie determinate valorile proprii. În [15] este propusă o metodă deosebit de eficientă de calcul al valorilor proprii, bazată pe principiul contracţiei şi metoda propusă de M. Vasiliu, care poate fi aplicată şi la carcasele conductoare. În această lucrare se foloseşte metoda descompunerii soluţiei în funcţii proprii spaţiale pentru a determina pierderile prin curenţi turbionari şi timpul de încălzire al carcaselor.

2 Câmpului electromagnetic în carcasele conductoare

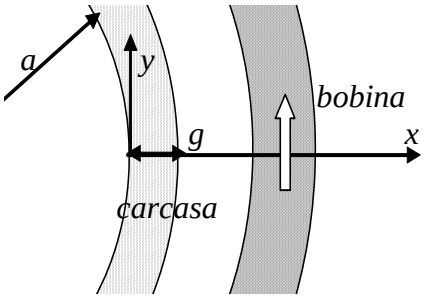

Fig.1. Domeniul de calcul

O bobina cu *N* spire, parcursă de curentul sinusoidal *i* (Fig.1.1), înconjoară concentric carcasa ce urmează să fie încălzită prin curenţi tubionari. Grosimea carcasei este *g*, diametrul interior *a*, conductivitatea σ şi permeabilitatea magnetică μ, constante în toată carcasa. Diametrul exterior al carcasei este $b = a + g$, iar lungimea ei este *l*. Admiţând că grosimea *g* este mult mai mică decât diametrul interior *a*, putem adopta coordonatele carteziene. Intensitatea câmpului magnetic $\boldsymbol{H}$ este orientată axial, pe direcţia axei *oz*, $\boldsymbol{H} = \boldsymbol{k}H_z = \boldsymbol{k}H(x,t)$ iar potenţialul vector $\boldsymbol{A}$, intensitatea câmpului electric $\boldsymbol{E}$ şi densitatea de curent $\boldsymbol{J}$ sunt orientate pe direcţia coordonatei *y*, de exemplu, $\boldsymbol{E} = \boldsymbol{j}E_y = \boldsymbol{j}E(x,t)$. Ecuaţiile câmpului electromagnetic sunt:

$$\frac{\partial E}{\partial x} = -\mu \frac{\partial H}{\partial t} \quad (1) \qquad -\frac{\partial H}{\partial x} = \sigma E \quad (2)$$

Potenţialul magnetic vector verifică relaţiile

$$\frac{\partial A}{\partial x} = \mu H \quad (3) \qquad E = -\frac{\partial A}{\partial t} \quad (4)$$

În zonele lipsite de densitate de curent, intensitatea câmpului magnetic este constantă (2), şi de aici rezultă că între carcasa şi bobină $H = \frac{\mu N}{l} i$ şi din (3) avem condiţia de frontieră pentru potenţialul vector la $x=g$: $\left.\frac{\partial A}{\partial x}\right|_{x=g} = \frac{\mu N}{l} i$. Integrând potenţialul magnetic vector pe faţa interioară a carcasei, rezultă $2\pi a A\big|_{x=0} = \pi a^2 \mu_0 H\big|_{x=0}$ şi, ţinând cont de (3), avem condiţia de frontieră pentru potenţialul magnetic vector pe faţa interioară a carcasei: $A_{x=0} = \frac{a}{2}\frac{1}{\mu_r}\left(\frac{\partial A}{\partial x}\right)_{x=0}$. Înlocuind (4) în (2) şi ţinând cont de (3) rezultă ecuaţia diferenţială a potenţialului magnetic vector

$$\frac{\partial^2 A}{\partial x^2} = \mu\sigma \frac{\partial A}{\partial t} \quad (5)$$

3 Funcţiile şi valorile proprii

Se poate arăta uşor [15] că operatorul $-\frac{d^2(\bullet)}{dx^2}$ este pozitiv definit şi simetric pe spaţiul vectorial $L^2(0, g)$, al funcţiilor cu condiţii de frontieră nule. Rezultă că există funcţiile proprii Φ_k şi valorile proprii λ_k^2 care verifică ecuaţia

$$-\frac{d^2\Phi_k}{dx^2} = \lambda_k^2 \Phi_k \quad (6)$$

Se deduce expresia funcţiilor proprii normate

$$\Phi_k = \frac{\sin \lambda_k x + \alpha_k \cos \lambda_k x}{Z_k} \quad (7)$$

unde $Z_k = \sqrt{\frac{g}{2}\left(1 + \alpha_k^2 + \frac{a}{2g\mu_r}\right)}$ şi $\alpha_k = \frac{a\lambda_k}{2\mu_r}$.

Ecuatia valorilor proprii este

$$\operatorname{ctg} \lambda_k g = \frac{a\lambda_k}{2\mu_r} \quad (8)$$

Ecuaţia (8) are câte o soluţie pentru argumentul $\lambda_k g$ aparţinând fiecărui interval $\left((k-1)\pi, (k-1)\pi + \frac{\pi}{2}\right)$, $k \in N^*$. Notăm $z_k = \lambda_k g - \frac{\pi}{2} - (k-1)\pi$, şi

$$\lambda_k = \frac{1}{g}\left(\frac{\pi}{2} + (k-1)\pi + z_k\right) \quad (9)$$

Ecuaţia (8) devine

$$\operatorname{tg} z_k = -\frac{\frac{\pi}{2}+(k-1)\pi+z_k}{g}\frac{a}{2\mu_r} \tag{10}$$

şi are câte o soluţie $z_k \in (-\frac{\pi}{2},0)$ pentru fiecare $k \in N^*$. Putem aplica acum funcţia *arctg* în relaţia (10) obţinând ecuaţia

$$f_k(z_k) = z_k + arctg\frac{\frac{\pi}{2}+(k-1)\pi+z_k}{g}\frac{a}{2\mu_r} = 0 \tag{11}$$

Funcţia f_k este lipschitziană şi uniform crescătoare, deoarece $\frac{df_k}{dz} \in (1,2r_k+1)$, unde

$$r_k = \frac{ag\mu_r}{(2g\mu_r)^2+(a(k-1)\pi)^2} \tag{12}$$

Putem folosi metoda Picard-Banach pentru rezolvarea ecuaţiei (11), căutând punctul fix al contracţiei $g_k(z) = z - \gamma_k f_k(z)$, unde $\gamma_k = \frac{1}{1+r_k}$. Pentru fiecare număr natural *k*, funcţia $g_k(z)$ are un punct fix z_k, şi din (9), obţinem valorile proprii λ_k. Dacă oprim iteraţiile din şirul Picard-Banach la iteraţia *n*, eroarea faţă de soluţia exactă z_k^* poate fi evaluata cu relaţia $\left|z_k^{(n)} - z_k^*\right| < \frac{\theta_k}{1-\theta_k}\left|z_k^{(n)} - z_k^{(n-1)}\right|$, unde $\theta_k = \frac{r_k}{1+r_k}$ este factorul de contracţie al lui g_k. Pentru *k*>3 sunt suficiente cel mult 4 iteraţii pentru a obţine o eroare aproape nulă ($<10^{-20}$). Pentru valori mai mari ale argumentului (la *k*>3), valorile proprii se apropie de forma asimptotică $\lambda_k \cong \frac{(k-1)\pi}{g}$, cu care se poate iniţializa şirul Picard-Banach.

3 Potenţialul magnetic vector descompus în serie de funcţii proprii spaţiale

Scriem

$$A(x,t) = A_f(x,t) + \sum_k C_k(t)\Phi_k(x) \tag{13}$$

unde A_f este o componenta care preia condiţiile de frontieră. O formă simplă pentru A_f poate fi: $A_f(x,t) = q(t)\left(x+\frac{a}{2\mu_r}\right)$ cu $q(t) = \frac{\mu N}{l}i(t)$. Înlocuim (13) în (5), ţinând cont de (6) şi de ortogonalitatea funcţiilor proprii, rezultă ecuaţia diferenţială a coeficienţilor C_k

$$\beta_k C_k(t) + \frac{C_k(t)}{dt} = -\frac{dq}{dt}\int_0^g\left(x+\frac{a}{2\mu_r}\right)\Phi_k dx = -W_k\frac{dq}{dt} \tag{14}$$

unde $\beta_k = \frac{\lambda_k^2}{\mu\sigma}$ si $W_k = \int_0^g\left(x+\frac{a}{2\mu_r}\right)\Phi_k dx = \frac{\left[\left(\frac{a}{2\mu_r}\right)^2+\frac{1}{\lambda_k^2}\right]\sin\lambda_k g}{Z_k}$. Ecuaţia (14) are soluţia

$$C_k(t) = C_k(0)e^{-\beta_k t} - W_k \int_0^t \frac{dq}{d\tau} e^{-\beta_k (t-\tau)} d\tau \tag{15}$$

Dacă dorim să obţinem soluţia periodică a ecuaţiei (15), atunci punem în relaţia (15) condiţia de periodicitate $C_k(T) = C_k(0)$, şi, ţinând cont că $q(T) = q(0)$, avem

$$C_k(0) = W_k \left(\frac{1}{e^{-\beta_k T} - 1} \int_0^T \frac{dq}{d\tau} e^{-\beta_k (T-\tau)} d\tau \right). \tag{16}$$

După câteva calcule [15] se obţine

$$A(x,t) = \frac{\mu N i(t)}{l} \left(x + \frac{a}{2\mu_r} \right)$$

$$- \frac{\mu N}{l} \sum_k W_k \left(U_k e^{-\beta_k t} \int_0^T \frac{di}{d\tau} e^{-\beta_k (T-\tau)} d\tau + \int_0^t \frac{di}{d\tau} e^{-\beta_k (t-\tau)} d\tau \right) \Phi_k(x) \tag{17}$$

unde $U_k = \frac{1}{1 - e^{-\beta_k T}}$.

3 Puterea transmisa carcasei

Media pe o perioadă a fluxului vectorului Poynting pe suprafaţa exterioară a carcasei, orientat spre interior este $P = -\frac{2\pi bl}{T} \int_0^T E\big|_{x=g} H\big|_{x=g} dt$. Deoarece $H = \frac{\mu N}{l} i$ şi ţinând cont de (4), rezultă $P = \frac{2\pi bN}{T} \int_0^T \frac{dA(g)}{dt} i(t) dt$. Integrând prin părţi şi ţinând cont de periodicitatea curentului şi a potenţialului magnetic vector, avem

$$P = -\frac{2\pi bN}{T} \int_0^T A(g) \frac{di}{dt} dt \tag{18}$$

Dacă admitem variaţia liniară pe porţiuni a curentului de excitaţie, atunci, după câteva calcule efectuate în (17), rezultă

$$P = -\frac{2\pi bN}{T} \sum_{m=1}^{M} (i_{m+1} - i_m) \sum_k C_k \left((m - 1/2)\Delta t \right) \Phi_k(g) \tag{19}$$

4 Exemplu

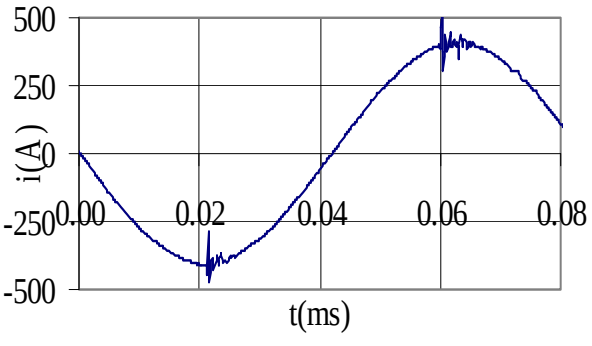

Fig.2. Curba curentului de excitaţie

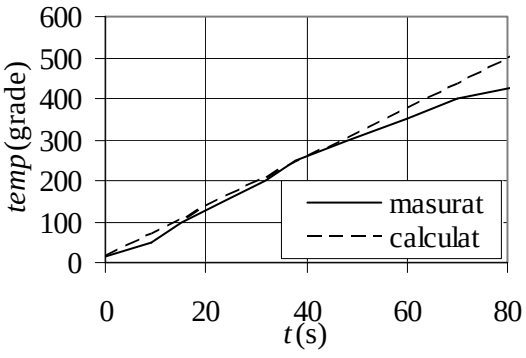

Fig.3. Evoluţia temperaturii carcasei

Aplicaţia numerică a fost făcută pentru o carcasa de aluminiu cu parametrii a= 0.0565 m, g= 0.004 m, l= 0.1 m, ρ = $2.6\cdot10^{-8}\Omega$m, $\mu_r = 1$. Bobina de excitaţie are 14 spire şi este alimentată de un curent cu frecvenţa de 12 kHz (vezi Fig. 2). Puterea activă absorbită de carcasă este $P = 2146.34\,\mathrm{W}$. Volumul carcasei este $V = 2\pi(a + g/2)gl = 1.47\times10^{-4}\,\mathrm{m}^3$. Admiţând că densitatea de masă a aluminiului este $\tau = 2700\,\mathrm{Kg/m}^3$, deci masa carcasei este $m = 0.397\,\mathrm{Kg}$, iar căldura specifică este $c = 900\,\mathrm{J/Kg/}^0\mathrm{K}$, rezultă că temperatura carcasei evoluează conform relaţiei $\Delta\theta = \frac{P}{cm}t = 6.006\,t$. În Fig. 3 este prezentată evoluţia în timp a temperaturii carcasei, calculată în ipoteza procesului adiabatic şi evoulţia temperaturii măsurată cu ajutorul unei termocamere în infraroşu.

5 Concluzii

Lucrarea prezintă o metodă analitică de determinare a soluţiei problemei de curenţi turbionari, a pierderilor şi a încălzirii carcaselor conductoare neferomagnetice. Avantajul metodei constă în faptul că acurateţea soluţiei nu depinde de forma şi frecvenţa curentului de excitaţie. O parte din mărimile ce intervin în expresia soluţiei depind doar de parametrii geometrici şi de material ai carcasei şi se pot utiliza pentru orice formă a curentului de excitaţie.

Bibliografie

[1] F. Hantila, G. Preda, M. Vasiliu, T. Leuca, E. Della Giacomo,"*Calculul numeric al curenţilor turbionari*", Editura ICPE, 2001, ISBN 973-8067-31-6.
[2] F. Hantila, E. Demeter, *"Rezolvarea numerică a problemelor de câmp electromagnetic"*, Ed. Ari Press, ICPE-ME, 1995.
[3] R. Albanese, G. Rubinacci, "Integral formulation for 3D Eddy-current computation using edge elements", *IEE Proc.*, 135, A, No. 7, sept. 1988.
[4] F. Hantila, G. Preda, M. Vasiliu "Polarization method for static dields", *IEEE Transaction on Magnetics*, vol.36, no.4, pp. 672-675, Jul. 2000.
[5] R. Albanese, F.I. Hantila, G. Rubinacci, "Integral formulation for nonlinear eddy current problem", *IGTE Symposium*, Graz, Austria, 1992.
[6] V.S. Vladimirev, *"Ecuaţiile fizicii matematice*", Ed. Ştiinţifică şi Enciclopedică, Bucureşti, 1980, (traducere din limba rusă).
[7] D. Ioan, *"Metode pentru calculul câmpului electromagnetic. Separarea variabilelor"*, Editura IPB, Bucureşti, 1988.
[8] I.Gh.Şabac, *"Matematici speciale"*, Ed. Didactică si Pedagogică, Bucureşti, 1965,
[9] A. Angot, "*Complemente de matematici pentru inginerii din electrotehnică şi telecomunicaţii"*, Ed. Tehnică, Bucureşti, 1966, (traducere din limba franceză).
[10] M. Vasiliu, "Nonsinusoidal two-dimensional eddy currents in a rectangular bar", *Rev. Roum. Sci. Techn.-Electrotechn. et Energ*., no.3, pp. 315-324, 1991.
[11] M.Vasiliu, "Eddy current core losses with trapezoidal magnetization", *Rev. Roum. Sci. Techn.-Electrotechn. et Energ*., no.1, pp. 33-45, 1992.
[12] M.Vasiliu, I.F.Hantila, "Eigenfunction expansion in a non-sinusoidal magnetic shielding problem", *Rev. Roum. Sci. Techn.-Electrotechn. et Energ*., no.2, pp. 199-206, 1993.
[13] M.Vasiliu, Al. Nicolae, I.F. Hantila, "Finite integral transform approach to non-sinusoidal eddy-current problems", *Rev. Roum. Sci. Techn.-Electrotechn. et Energ*., no.4, pp. 473-481, 1993.
[14] M.Vasiliu, "Eddy currents losses due to alternating magnet pulsesr", *Rev. Roum. Sci. Techn.-Electrotechn. et Energ*., no.1, p. 51, 1990.
[15] V. Stefan-Minculete, *„Contribuţii privind aplicarea conversiei electrotermice sau electromecanice în tehnică*", teza de doctorat, Universitatea Politehnica Bucureşti, decembrie 2012.

Study on the Magnetic Field Produced by Coils of Certain Shapes

Ioana-Gabriela SÎRBU, Lucian MANDACHE
University of Craiova, Electrical Engineering Faculty, Decebal Blv. 107, Craiova; osirbu@elth.ucv.ro

Mihai IORDACHE
University POLITEHNICA Bucharest, Electrical Engineering Faculty, Spl. Independenței 313, Romania

Abstract. This paper proposes to determine analytically or numerically the magnetic field produced by the coil windings. In this context the estimation of the magnetic field strength produced by one single turn of different shapes has an important role. One starts from the magnetic field strength produced by a circular single turn, then the principle of calculation was generalized for the elliptic single turns. This study is useful for the finite length coils' case.

1 Introduction

The role of a solenoid in an electromagnetic system is to create a magnetic field. Depending on its geometry and its position relative to the other components of the system one can obtain magnetic fields that have certain distributions or specific orientations. Therefore its behaviour and its exact role in the operation of such a system must be known with accuracy.

The fundamental element of a solenoid is the single turn coil. Its behaviour, when it is passed by an electrical current, was studied during the time by many theorists that proposed different solutions to solve this problem. One can mention here the possibility of treating this coil as a sufficient number of conducting segments connected each other those contribution is summing up [1], and the analysis based on a numerical modelling of the magnetic field produced around it [2]. These studies proceed specially from the analysis of some shapes often met in practice, the obtained results being presented in works as [3], [4], [5], [6], [7]. Whatever it was the method of solving this problem, analytically, numerically or experimentally, it remains a problem of actuality. In order to tackle it a good knowledge both of the electromagnetic field theory [8] and of the mathematic calculus instruments (analytic, geometric and numeric) is necessary.

In this overall idea this work proposes to offer an alternative possibility to evaluate the magnetic field produced by a single turn coil. Two different shapes of practical importance are analysed here: the circle and the ellipse. For each of these cases one follows to determine the magnetic field strength H in a point placed on a straight line that passes through the centre of the coil, perpendicular or not. The obtained mathematical formulae were solved analytically or using numerical techniques of calculation. The results were analysed comparatively, inclusively using specialized programs for the electromagnetic field modelling (QuickField), thus proving the correctness and the utility of the proposed formulae.

2 Analysis of the Circular Single Turn Coil

Our study begins with the case of the circular coil (fig.1), easier to be analysed due to its geometric symmetry. One specified firstly the procedure of calculation the magnetic field in the points placed on a straight line (axis) perpendicular on the coil plane. One passes that to a generalisation of the results, for points placed on a straight line inclined with a certain angle with respect to the coil plane that passes through the centre of the circle. Practically we are interested specially by the field oriented along this line, so that our study focuses on this component.

Case of a perpendicular axis

The determination of the magnetic field strength H in a point placed on the coil axis, perpendicular on its plane, is a problem already solved [5]. This magnetic quantity is determined starting from the Biot-Savart-Laplace's formula [8]:

$$H = \frac{I}{4\pi}\oint_{\Gamma}\frac{\mathrm{d}\bar{r}\times\bar{R}}{R^3}, \qquad (1)$$

where I represents the intensity of the electric current through the coil, and R is the distance from the point P to the elementary section of the coil $d\bar{r}$, oriented in the direction of the current (fig.1, (a)).

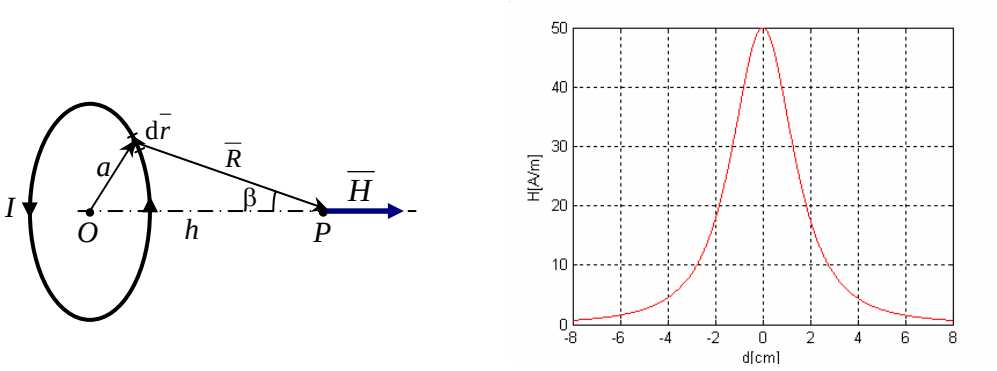

(a) (b)

Figure 1: Circular coil (a) and its magnetic field strength (b) in a point on its perpendicular axis.

Taking into account the symmetries and knowing that the components of the magnetic field on the direction perpendicular on the axis cancel each others, the magnetic field strength in the point P situated at a distance h from the centre of the coil of radius a is oriented following the direction of the axis and it is calculated with the analytic formula [5]

$$H = \frac{I\cdot a^2}{2\cdot\left(a^2+h^2\right)^{3/2}}. \qquad (2)$$

The variation curve of H as function of the position of the point P on the axis was represented in fig. 1, (b).

Case of an axis inclined with a given angle

In case of an axis inclined with an angle α with respect to the coil plane (fig. 2) the problem becomes more complex, because some of its symmetry is lost. Thus the magnetic field strength will not have only one component along this line, but also a component on a direction perpendicular on it. Because this second component is less important in the practical cases, its study will not be presented here.

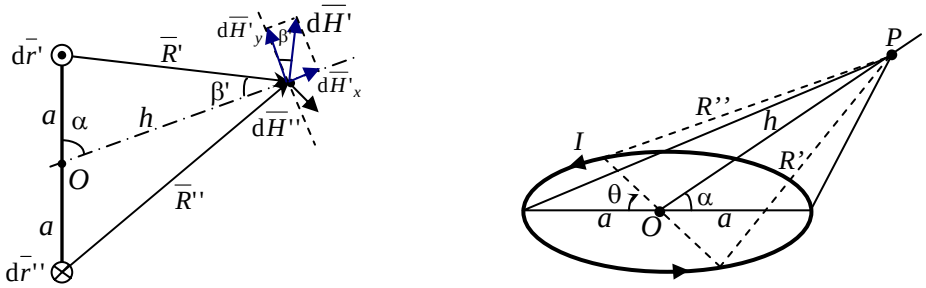

Figure 2: Explanatory figures for the determination of the magnetic field strength produced by a circular coil

The distance between the point P to two points diametrically opposite situated on the coil (fig. 2) is in this case different. By geometrical reasons the values of these two distances are calculated with the formulae:

$$R' = \sqrt{a^2 + h^2 + 2ah \cdot \cos\alpha \cdot \cos\theta}\,, \qquad R'' = \sqrt{a^2 + h^2 - 2ah \cdot \cos\alpha \cdot \cos\theta} \tag{3}$$

With the Biot-Savart-Laplace's formula, the magnetic field strength on the direction of the line, produced by two elementary sections diametrically opposite of the coil, $d\bar{r}'$ and $d\bar{r}''$, are calculated with the relations

$$\begin{aligned} dH_x' &= \frac{I \cdot a \cdot d\theta}{4\pi R'^2} \cdot \sqrt{1 - \left(\frac{h \cdot \cos\alpha \cdot \sin\theta}{R'}\right)^2} \cdot \sqrt{1 - \left(\frac{h + a \cdot \cos\alpha \cdot \cos\theta}{R'}\right)^2} \\ dH_x'' &= \frac{I \cdot a \cdot d\theta}{4\pi R''^2} \cdot \sqrt{1 - \left(\frac{h \cdot \cos\alpha \cdot \sin\theta}{R''}\right)^2} \cdot \sqrt{1 - \left(\frac{h - a \cdot \cos\alpha \cdot \cos\theta}{R''}\right)^2}, \end{aligned} \tag{4}$$

where θ is the angle measured in the centre of the coil (fig. 2).

The estimation of the global magnetic field in a point (tangential component) is made afterwards by summing up the contribution of the elementary pairs of sections, on a semicircle:

$$H_x = 2\int_0^{\pi/2} dH_x\,, \text{ where } dH_x = dH_x' + dH_x''. \tag{5}$$

Figures 3 and 4 represent the results obtained by analysing this situation. For verification, we made also the determination of the magnetic field distribution produced by a circular coil using the software package QuickField Professional (fig. 3). This permits to obtain the variation of H along any straight line, inclined or perpendicular on the coil.

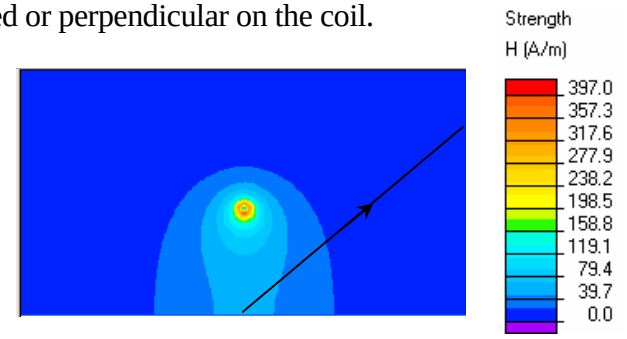

Figure 3: Magnetic field strength estimation along any inclined axis, using QuickField Professional.

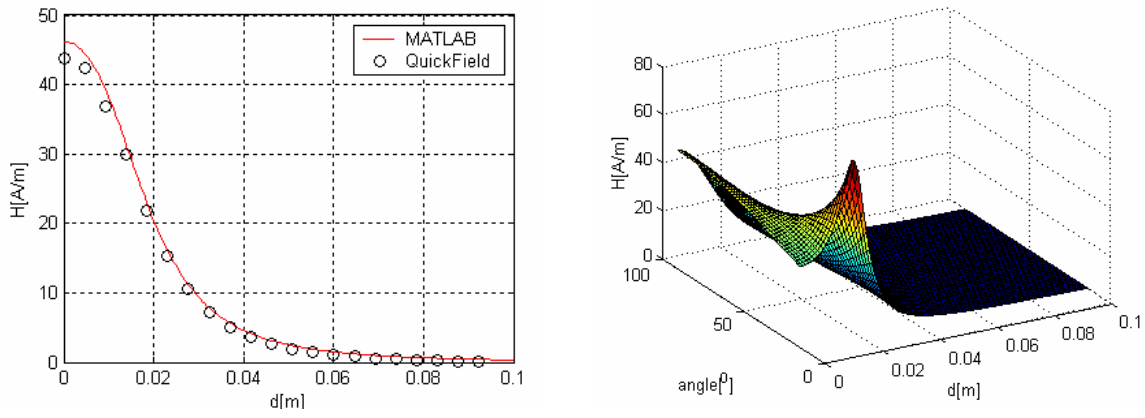

(a) (b)

Figure 4: Magnetic field strength along an inclined axis: comparative analysis for $\alpha = \pi/3$ (a); using formula implemented in MATLAB (b).

Figure 4 (a) presents the comparative analysis of the data obtained in QuickField Professional and using the relations (4)-(5) implemented in MATLAB. Due to the complexity of the integral formula it is very difficult to offer an exact solution of it. For this reason we applied a procedure of numerical integration using the composed formula of the trapeziums [9]. One can remark a good approach of the values obtained using these methods. Figure 4 (b) shows the variation curve of *H* along the straight line, for different angles of its inclination.

3 Analysis of the Elliptic Single Turn Coil

The ellipse can be shown as a more general case of the circle. Consequently the manner of solving the problem of determination of the magnetic field produced by an elliptic coil passed by a current will be similar to those presented previously, but adapted to the geometric particularities of it.

Case of a perpendicular axis

The dimension of the ellipse is characterized by the values of its semi-axis, *a* and *b*. A point *M* placed on it will be at a distance *x* of the ellipse centre (fig. 5). This distance can be calculated starting from the ellipse equation and the point coordinates:

$$\left.\begin{array}{l} x_M = x\cos\theta, \quad y_M = x\sin\theta \\ \dfrac{x_M^2}{a^2} + \dfrac{y_M^2}{b^2} - 1 = 0 \end{array}\right\} \Rightarrow x = \sqrt{\frac{b^2}{(b/a)^2 + \sin^2\theta \cdot \left(1 - (b/a)^2\right)}}. \tag{6}$$

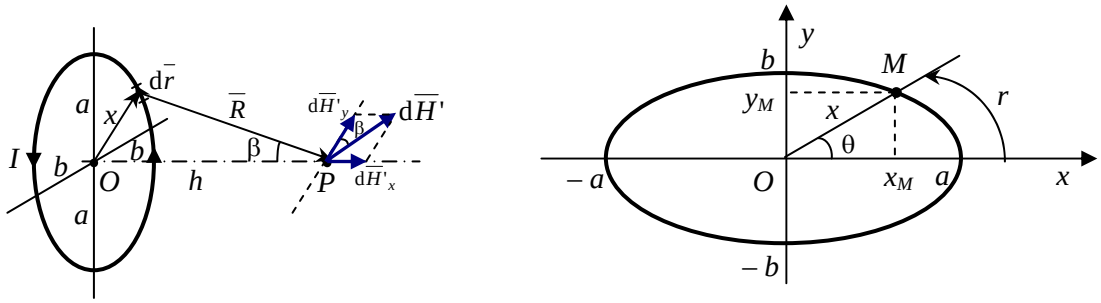

Figure 5: Explanatory figures for the determination of the magnetic field strength produced by an elliptic coil

In order to determine the magnetic field strength produced by the elliptic coil one starts from the Biot-Savart-Laplace's formula. The elementary section of the elliptic coil passed by the current *I* is estimated using the elliptic integral of second kind [10], [11]:

$$dr = a\sqrt{1 - \left(1 - \frac{b^2}{a^2}\right)\sin^2\theta} \cdot d\theta \tag{7}$$

Thus the magnetic field strength in any point on this line will be oriented along this axis and will be calculated with formula:

$$H = H_x = \frac{I}{4\pi}\int_0^{2\pi} \frac{xa\sqrt{1 - \left(1 - (b/a)^2\right)\sin^2\theta}}{\left(x^2 + h^2\right)^{3/2}} \cdot d\theta \tag{8}$$

Also in this case a numerical integration method will be used for the estimation of the values of *H* given by relation (8), creating a program in MATLAB. Some of the obtained results are depicted in fig. 6, for a circle ($a = b$) and for an ellipse. One observes that, for the circle case, the results are similar to those of fig. 1 (a).

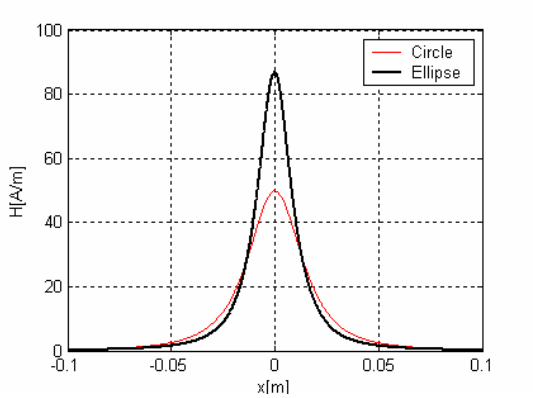

Figure 6: Results obtained using formula for the magnetic field of an elliptic coil (MATLAB)

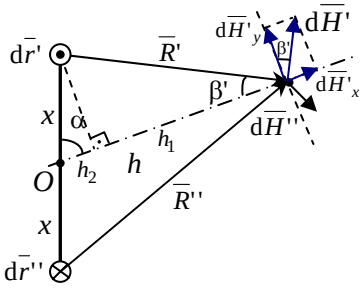

Figure 7: Explanatory figure in case of an inclined axis of the ellipse

Case of an axis inclined with a given angle

The approach of this case is based on the techniques presented in the previous cases. Following a similar principle of calculation that starts from Biot-Savart-Laplace's formula, and processing the results obtained for a circular coil and an axis inclined with an angle α [12], we obtained the following expressions that approximate the components of the field, along the axis and respectively perpendicular on it (fig.7):

$$H_x = \frac{I \cdot a \cdot \sin\alpha}{4\pi} \cdot F(\theta), \tag{9}$$

$$F(\theta) = \int_0^{\pi} x \sin\gamma \sqrt{1-\left(1-\left(\frac{b}{a}\right)^2\right)\sin^2\theta} \cdot \left(\frac{1}{\left(x^2+h^2+2xh\cos\alpha\right)^{3/2}} + \frac{1}{\left(x^2+h^2-2xh\cos\alpha\right)^{3/2}} \right) d\theta;$$

$$H_y = \frac{I \cdot a}{4\pi} \cdot G(\theta), \tag{10}$$

$$G(\theta) = \int_0^{\pi} \cos\gamma \sqrt{1-\left(1-\left(\frac{b}{a}\right)^2\right)\sin^2\theta} \left(\frac{|h - x\cos\alpha|}{\left(x^2+h^2-2xh\cos\alpha\right)^{3/2}} - \frac{|h + x\cos\alpha|}{\left(x^2+h^2+2xh\cos\alpha\right)^{3/2}} \right) d\theta,$$

where γ, the angle between the vectors $d\bar{r}$ and $\bar{R}$, was approximated with the relation

$$\gamma \cong \frac{\pi}{2} + \cos\alpha \cdot \left(\frac{2}{\pi}\alpha - 1\right) \cdot \theta\,. \tag{11}$$

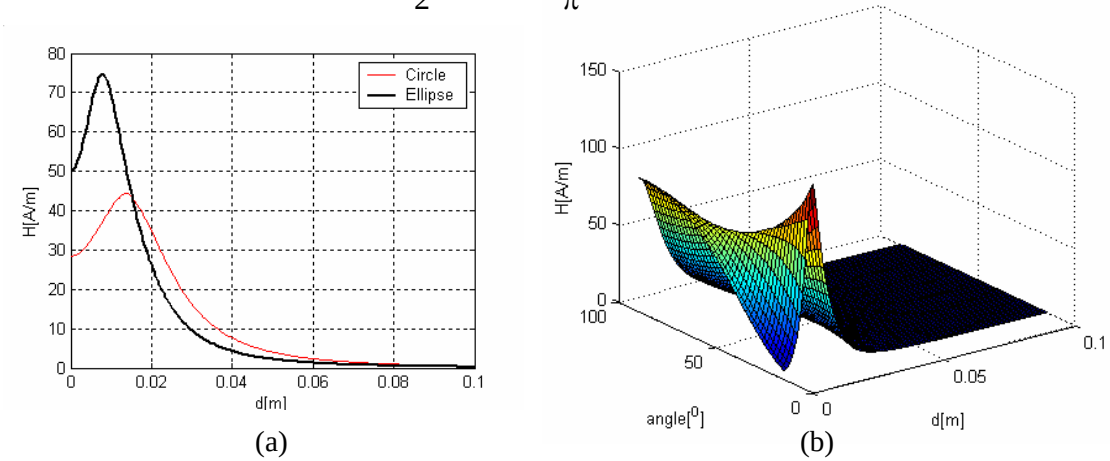

(a) (b)

Figure 8: Results obtained using the formula of the magnetic field strength of the elliptic coil, for $\alpha = \pi/4$ (a) and for different angles (b)

Figures 8 (a) and (b) presents some of the results obtained by implementation of the above relations in a MATLAB program. Figure 8 (a) depicts the variation curves of H_x (along the axis) with the distance to the ellipse centre, for a circle ($a = b$) and for an ellipse. The results obtained for the circle are similar to those obtained using the formulae (4)-(5) from the previous paragraph. Figure 8 (b) shows the variation of *H* along the axis, for different angles of inclination of the line.

4 Conclusion

From the analysis we made results that it is extremely difficult to obtain the exact formulae for the magnetic field strength, especially in case of an inclined straight line. The only solution in these cases is to use some numerical integration techniques that approximate the obtained integral formulae.

The study proposed and verified using alternative procedures could represent a more available solution in order to estimate the magnetic field, when we do not have a specialized program for the electromagnetic field modelling in 3D, rather expensive, necessary for geometric forms that do not have planar of axial symmetries.

This analysis could be extended afterwards to the coils with several turns or for other kind of shapes that include circular or elliptical sections.

This study is useful in the engineering practice, especially for the finite length coils' case, having the radius much bigger than their length or a reduced number of turns (as in case of the coils used in the wireless transfer of energy [13]).

References

[1] A. Garcia, J.A. Carrasco, J.F. Soto, F. Maganto and C. Moron. A Method for Calculating the Magnetic Field Produced by a Coil of Any Shape, *Sensors and Actuators*, **91** (2001) 230-232.

[2] G. Rousseaux, R. Kofman and O. Minazzoli. The Maxwell-Lodge Effect: Significance of Electromagnetic Potentials in the Classical Theory, *The European Physical Journal*, **D** (2008) 1-8

[3] R. A. Beth. Elliptical and Circular Current Sheets to Produce a Prescribed Internal Field, *IEEE Transactions on Nuclear Science*, (June 1967) 386-388

[4] S. Russenschuck. Coil-End Design and End-Spacer Manufacture, online: http://cdsweb.cern.ch/record/451091/files/p192.ps.gz?version=1 (1999) 192-199

[5] R. Răduleț. *Bazele electrotehnicii - Probleme*, vol. 1, Ed. Didactică şi Pedagogică, Bucureşti, 1970.

[6] P.L. Kalantarov and L.A. Teitlin. *Calculul inductanțelor*, Ed. Tehnică, Bucureşti, 1958.

[7] Claudia Păcurar, V. Țopa, Adina Răcăşan and C. Munteanu. Inductance Computation and Layout Optimization for Spiral Inductor, *Buletinul AGIR*, **3** (2012) 675-682.

[8] C.I. Mocanu. *Bazele electrotehnicii - Teoria câmpului electromagnetic*, Ed. Didactică şi Pedagogică, Bucureşti, 1991.

[9] Anca Tomescu, I.B.L. Tomescu and F.M.G. Tomescu. *Modelarea numerică a câmpului electromagnetic*, Editura Matrix Rom, Bucureşti, 2003.

[10] http://mathworld.wolfram.com/EllipticIntegraloftheSecondKind.html

[11] http://www.oocities.org/web_sketches/ellipse_notes/ellipse_arc_length/ellipse_arc_length.html

[12] http://www.nabla.hr/Z_IntermediateAlgebraEllipseAndLine_2.htm

[13] D. Niculae, Lucia Dumitriu, M. Iordache, A. Ilie and L. Mandache. Magnetic Resonant Couplings used in Wireless Power Transfer to Charge the Electric Vehicle Batteries, *Proceedings of the 4-th International Symposium on Electrical Engineering and Energy Converters*, Suceava, September 22-23, 2011,167-170.

The possibility to produce asynchronous motors with high energetically parameters

STOCHITOIU MARIA DANIELA, PASCULESCU DRAGOS
University of Petrosani, orban@upet.ro, pdragos_74@yahoo.com

GRUBER ALIN CRISTIAN
Grup scolar Aurel Vlaicu Lugoj

Abstract. The remarkable advantages of using electrical energy (high efficiency, lack of residues, the possibility to transport it easily, the possibility to divide it on any scale, to make accurate measurements, etc) have determined its penetration in new activity fields and at the same time it is used extensively in traditional domains.

1 Introduction

The alternative current electrical drives became a favorite opportunity in the industry drives field taping an annual increase rate about (10-12)% in dependence with only 3% for direct current drives in the last several years.

This increase was made by the new high efficiency requests and determined more complex operating cycles, high speed and easier maintenance.

As the operate element in alternative current drives, the main advantages of a.c. motors in dependence with d.c. motors are: a bigger overload factor; high reliable and robust, higher maximum speeds, a weaker report kW/kg, easily construction and maintenance but the main disadvantage is the reactive power consumption.

So, the electrical machine with high energetic results production is involved by existing concerns on the drives domain assuring large opportunity for requested commands of producers on intern and extern markets.

The problem is for asynchronous motors due to these are in operating in approximately 95% and determine the most important electrical active and reactive power consumption.

These motors can be made at the customer request, with high parameters and specifically protection degree for different states between IP23 to IP55 and satisfying the CEI 34-1 standard.

2 New techniques, based on new materials and modern technologies, in order to assimilate asynchronous motors with high energetic parameters

By adopting certain constructions and design methods, one can obtain motors with high energetic indexes. The energetic parameters of the asynchronous motor are defined by efficiency (η) and power factor (cosφ), which help calculating the loss of active power and the loss of reactive power.

For an asynchronous motor, the loss of active energy (p_a) is calculated by the following relation:

$$p_a = (1-\eta)\cdot\frac{P_N}{\eta} \quad \text{(kW)} \qquad (1)$$

where: η = nominal efficiency; P_N =nominal power

The loss of reactive energy (Q) is calculated by the following relation:

$$q = P_N \cdot tg\varphi \qquad \text{(kVAR)} \qquad (2)$$

Out of the losses generated in an asynchronous motor, the mechanical losses Pm are practically independent from the charging power, and only the losses from the wrappings and the ferromagnetic core remain variable according to the electrical and mechanical variations.

The losses from the wrappings are practically dependent only on the charge and the quantity of the materials.

Considering the American Standard API 541, which introduces the Lcc indicator (the cost of the life cycle), which is the basis used to evaluate the correlation price-performances of the electrical motors. This indicator is the sum of the purchase price and the costs generated by the loss of power/life cycle. The analytical expression for the calculation of the Lcc indicator is the following:

$$L_{cc} = C + C_e \cdot N \cdot P_N \cdot \left(\frac{100}{\eta} - 1 \right) \qquad (3)$$

Where: C= the price of the motor

Ce= cost of active energy

N= number of functioning hours

P_N = the nominal power of the motor (kW)

η = nominal efficiency (%)

The second term from Lcc's expression reflects the cost of active electrical power losses, which have a lower value if the efficiency is high.

The electro-caloric effect in the mass unit is p_{J2}, which for the whole resistance wrapping R, length L_{Cu}, with section S_{Cu} and current I becomes:

$$p_{Cu} = \frac{\rho \cdot L_{Cu}}{S_{Cu}} \cdot I^2 = R \cdot I^2 \qquad (4)$$

we can notice that for a given current , the only measure is to increase the section of the conductor, and so to decrease the density of electricity.

For the asynchronous motors with contact rings, this measure can be applied for both rotor and static armatures. The limit is given only by the possibility to place spires, limited by the exterior diameter of the machine.

In the case of asynchronous motors with a caged rotor, the measure can be applied only at the static wrapping. The rotor wrapping must satisfy other requests corresponding to the rotation moment necessary to accelerate and the starting current, as compared to the one with rings, so the degrees of freedom for this motor are lower.

Usually, the asynchronous motor with a caged rotor requires relatively big starting moments and low starting currents. This requires a certain shape of the rotoric notch, which must have a pronounced refutation of the current from the rotoric bar, in order to increase the apparent resistance.

In order to have a more pronounced refutation effect, we need a powerful magnetic field to disperse the notch, which generates an increased dispersion reactance, as a consequence of the reduced power factor.

In the design there is an optimal correlation between the apparent resistance increase factor of the caged bar and the value of the rotation moment at start-up, for a given section of the bar. If we achieve this and the rotation moment isn't the imposed one, the solution is to reduce the surface of the bar section surface, so to increase the density of the electrical current in the bar and implicitly the electrical resistance of the rotoric phase, with a negative impact on the efficiency.

The iron losses depend less on the load and in the standard method for the calculation of the efficiency they are considered constant, independent from the load. Still, they depend greatly on the material from which the core is made, and at a lesser extent on the shape (between iron, number of notches, opening of the notch), as well as on the applying of the closing solution of the open stator notches with magnetic wedges (the supplementary losses are reduced).

The importance of the plate quality from which the ferromagnetic iron is made results, without referring to a certain asynchronous motor.

It is known that there are several types of plate with different magnetic properties and losses, but the more the plate is magnetically and the loss figures smaller, the higher is the price. Our industry can purchase presently two types of indigenous plate: 2,3 W/kg, at 1T induction and a frequency of the sinusoidal variation in time of 50 Hz at the price of 2,7RON /kg and 1,4 W/kg at the price of 3,6 RON/kg, their magnetizing properties are similar.

So, considering the cost, it appears that the solution is to solve the problem at low costs, by purchasing the plate which has more losses, but cheaper. But the factory doesn't only execute motors for sales, but also to be used by the beneficiaries.

Presently the asynchronous motors are executed with medium magnetic solicitations for the entire machine, at around 1,5 T and 50 Hz. But for 1,5 T the losses per mass unit in both cases are:

Plate 2,3 W/kg- p_{Fe} = 5,18 W/kg and plate 1,3 W/kg- p_{Fe} =2,93 W/kg.

This means that for 1 kg of plate, the 1,3 W/kg plate has fewer losses the 2,3 W/kg one with formula. For a m_{Fe} mass of the core, on the T_D lifetime of the machine and the price for 1 kWh of N_E results a difference of the electromagnetic cost transformed into thermal energy:

$$\Delta C_U^{]} = \Delta p_{Fe} \cdot m_{Fe} \cdot T_D \cdot N_E \qquad (5)$$

Formula is in favorer of the machine made of the more expensive plate.

For 1 kg of plate the difference is 3,0 RON and the cost of the plate is 2,1RON ; that means that from the energy saving we can cover the cost of the plate and we can save 0,9 RON. Figuratively, if we buy a more expensive plate, the supplying factory not only asks for nothing In return, but it also gives us a prize of 30% from its cost.

The main losses, controllable, and so with reasonable opportunities to be reduced are those of iron and winding. Rotor losses are less free because the rotor must be sized with consideration of additional restrictions related to the mechanical characteristics (starting torque maximum torque) and nominal slip. Both types of losses are expressed as the mass of iron (or copper) and a specific mass loss (W / kg). The difference is that if the copper winding (copper electrical) this value is unique and expresses the square of the current density for iron (electrical board) is possible assortment of options .

In the case of the asynchronous motor with caged rotor, its efficiency diminishes because of the performances which are required at the motor`s starting up. The obtaining the big torques and small currents during the motor`s start up can be made only by reducing the efficiency because the pelicular effect implies a high rotor dispersion which determines a reducing for power factor. The increasement of electrical current density inside the rotor leads to more losses during the secondary wound which implies reducing the efficiency. Anyway, most of the situations don't require starting moments twice times the nominal moment. This is needed only in especial cases which require special construction machines with increased moment and weak efficiency.

The disadvantage of using axial ventilators is the fact that only allows a single direction for rotations either right or left. Also, to optimize the ventilation we can project a two directions ventilation circuit which is more efficient and assures a higher efficiency, as well as

a more uniform distribution of the temperature gradient along the active side of the electric motor. In order to increase the power factor we try the balanced charge magnetically the ferromagnetic circuit and establish magnetic solicitations at lower values than usual. Also, to improve the power factor is made an calculus by taking in considerations the minimum air gap which is possible by technological made and the use of magnetic wedges has as an effect besides reducing supplementary losses the increase of the power factor.

If are purchasing a technology of casting under pressure aluminum instead of copper in the rotor will get smaller rotor Joule losses in rotor. These are depending of sliding (Joule losses are proportional to the slip) and so in terms of yields no doubt that they will get those imposed with sufficient reserves in manufacturing series. It noted a significant decrease in the power factor, which makes reducing supply current efficiency be more moderate growth, the design of some reduction in air gap induction must be still more pronounced for keeping idle currents within reasonable limits. Starting couples are significantly larger than normal and necessary, the diminution of induction in the air gap will reduce the expected consequences with reference to the starting torque. In terms of temperature, cold engines are a natural consequence of reducing losses.

3. Conclusions

It clearly results from this the importance which the quality of plate has upon the economic indexes of an electric motor, fact which leads to the necessity of the plate factories to increase the quality of plate for the electromagnetic cores of electric motors as much as possible. An important increase of motor efficiency (for bigger speed more 1000rot/min) can be obtained by the substantial reduction of the losses generated by the ventilators and this can be done by replacing the radial ventilators with axial ventilators with a 30% function efficiency increasement.

References

[1] Constantin Ghita *Masini electrice* Editura Matrixrom , Bucuresti2005

[2] Dordea T., Campeanu A.: *Necesitatea maririi randamentului masinilor electrice* Conferinta Nationala a Energiei, CNE-2004, Neptun 13-17 06. 2004

[3]Sandru M. *Imbunatatirea actionarilor electrice la unele utilaje principale din Exploatarea miniera de cariere Jilt in vederea cresterii eficientei energetice*, teza de doctorat, Petrosani2012

New implementation of Preisach model

Octavian TABARA
University Politehnica of Bucharest 313, 6, Romania, tavi.tabara@gmail.com

Abstract. This article presents a new numerical implementation procedure for the classical Preisach model. Implementation has numerical improvements time needed for simulations are improved. Identification is done for a set of 3 different measurements and results have a good accuracy. A specific search algorithm for 2 variables is implemented and optimum parameters values are determined for an analytic Preisach type density function.

1 Introduction

Hysteresis is a phenomenon wide spread in technical domains and applications. It appears for example in economy, physics, mathematics, medicine. When it was discovered in the XVIII century it was defined as a delay that influences input and output values. Due to its complexity many definitions tried to explain intrinsic facts of it.

For example, Della Torre begins to explain the process in a mathematical way starting from physical description. The author highlights connection between hysteresis and speed of input/output values. If the value of input over output rises, then hysteresis effect is more obviously and it vanishes when the speed becomes 0 [1].

Visintin defines it as a phenomenon closely connected with memory effects [2]. In magnetism, Barkhausen jumps are determined by a displacement of domain. In magnetism, input is represented by magnetizing force and output is magnetization. Barkhausen jumps of magnetization, that initiate hysteresis, are determined by domain walls displacement. Due to complexity of phenomenon delay effects can't be determined only by time [3, 4]. Bertotti defines it as a complex phenomenon including delay between applied field and magnetization. Also thermal effects influence heat losses which are strongly related to hysteresis.

Many works contain details about numerical implementation of hysteresis models. For example Newton-Raphson method is studied and numerically implemented for materials with hysteresis. Although it is very old, classical Preisach model is still implemented due to its simplicity and speed passing its known limits [7, 8].

2 Classical Preisach model

Classical Preisach model considers the material composed from elemental dipoles, characterized by a rectangular cycle [9]. It was developed starting from an idea of Weiss and Freudenreich.

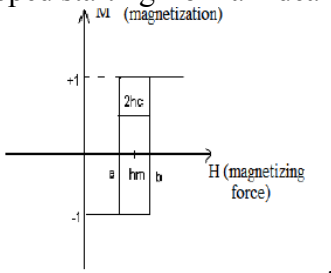

Figure 1: Preisach elemental particle

Magnetization is determined using the fallowing formula:

$$M = \iint_{S+} p(a,b)dadb - \iint_{S-} p(a,b)dadb \quad (1)$$

In above relationship p (a, b) represents probability density function which is defined as probability of an elemental particle to have a and b switching fields. Determination of probability density function is a difficult task that hasn't been solved in a very goof manner for now. Identification of Preisach function can be done analytically or numerically. Analytically identification can be done using Everett function [10], or Gauss-Gauss distribution).

In written code, Preisach density function, after calculations, is considered to have this form:

$$p(a,b) = \frac{128\ N}{128+16(A+B)+(A+B)^2} \quad (2)$$

Where the parameters A and B are given by:

$$A = (a-b-2)^2 \quad (3)$$

$$B = (a+b)^2 \quad (4)$$

In above relationships a and b represent the 2 switching values of classical Preisach model.
This way of determining density function can lead to strange errors because it does not have a real physical signification. This formulation it is still used for its simplicity and speed in determining density function for a certain category of materials.

3 New implementation method

Density function has a few unknown parameters which are correlated and must respect minimum error criterion. In developed code error is determined using least squares method. Optimum parameters are determined using a recursively search algorithm and obtained results are plotted. The novelty of this article represents state line memorization technique using a specially coded matrix. State line modifications are taken into account using a certain codification. Determined magnetization values are compared with measured ones and optimum Preisach function parameters are plotted. A recursive implementation method is used which less time is consuming. For determination of Preisach density function parameters, a search algorithm based on dividing by 2 search interval is used.

Parameters are transmitted to functions using classes. A new hypothesis is made to original model: on the edges of Preisach triangle particles have also a rotation movement. Special programing techniques are used to speed up execution of program.

Although analytical approximation amplifies the inherent errors of noise and unpredictable graphics can be obtained, due to its simplicity and speed of execution it is still implemented and used in program. Basic idea was to identify main functions characteristics for tested materials which can be used in other research processes. Another improvement concerning speed is done using parallelization programing. In case of a big number of measured data time consuming is a special characteristic that should be improved.

Search algorithm is based on the fallowing idea for each of the 2 parameters: first the total search interval is divided in equal sub-intervals and the algorithm searches for the best value witch has minimum error. After this there is a in depth search near that value for optimum value that suits well the input. The same thing is done for the second parameter, and after trying all the possible combinations with optimum values for first parameter, results are shown. This search

algorithm works for any form of Preisach density function. It is efficient for a small number of measured data.

4 Results and conclusions

Measurements were done using a Vibrating Sample Magnetometer Lake-Shore 7304. Samples were round in order to avoid demagnetization problems. Correction of measured data was done in order to characterize not only the tested probe but also the relationship between magnetic parameters. In order to determine magnetization a surface of 8 mm^3 was considered.

Results point out a comparison between initial magnetization curves for a transversal applied field at different angles and values. An homogenous magnetic medium (a diskette) was tested for comparison with non-homogenous magnetic medium (metro card).

Saturation values for a metro card with an applied field at 90 degrees are the fallowing: H_S=636500 A/m and M_S=29385 A/m. Number of measured points of initial magnetization curve is equal to 81 and comparison between measured and calculate values in the hypothesis that material starts from a demagnetized state are:

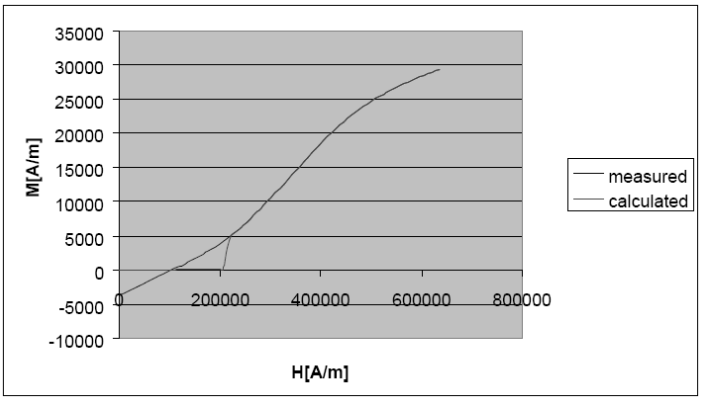

Figure 1: Comparison between measured and identified data for a metro card.

Optimum values of parameters are: *a*=-429,385 and *b*=421,6252. Minimum error obtained for these parameters is 6.2974e-13. Preisach plane represented for optimum values of parameters *a* and *b*

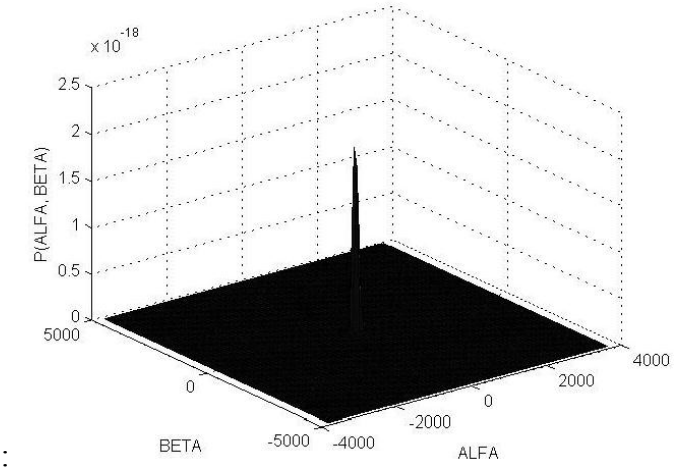

:

Figure 2: Preisach plane for a metro card with applied field at an angle of 90 degrees.

In case of a floppy disk (homogenous magnetic medium) with saturation values of field and magnetization, H_S=477488 A/m and M_S=883 A/m with 61 measured points good identification results were obtained. For an applied transversal field of approximately 480kA/m the fallowing identification was obtained:

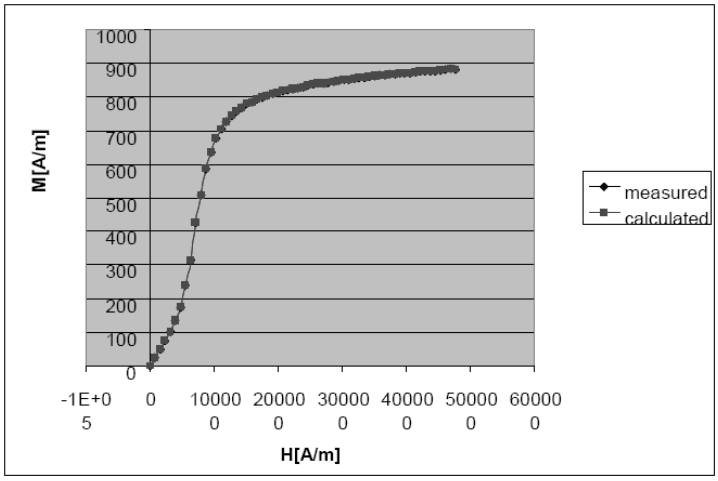

Figure 3: Comparison between measured and identified data for a floppy disk

Values of optimum parameters and minimum error obtained are *a*=623.976 and *b*=-5406.9. For these values the minimum error is equal to 2.8906 10^{-13}. Preisach plane obtained for these values is shown in figure 4:

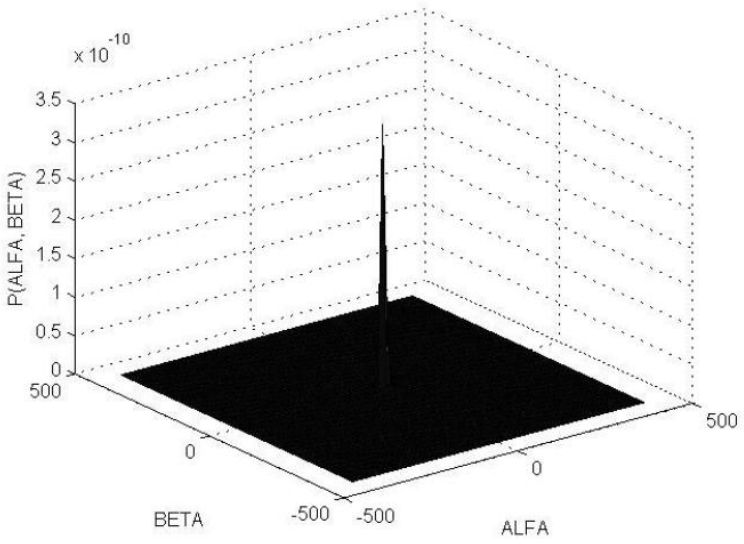

Figure 4: Preisach plane for a floppy disk.

Another test was done for a metro card with an applied field at 30 degrees that has the fallowing saturation parameters: H_S=636683 A/m and M_S=41330 A/m. Number of measured points for initial magnetization curve was N=81. Identification results are:

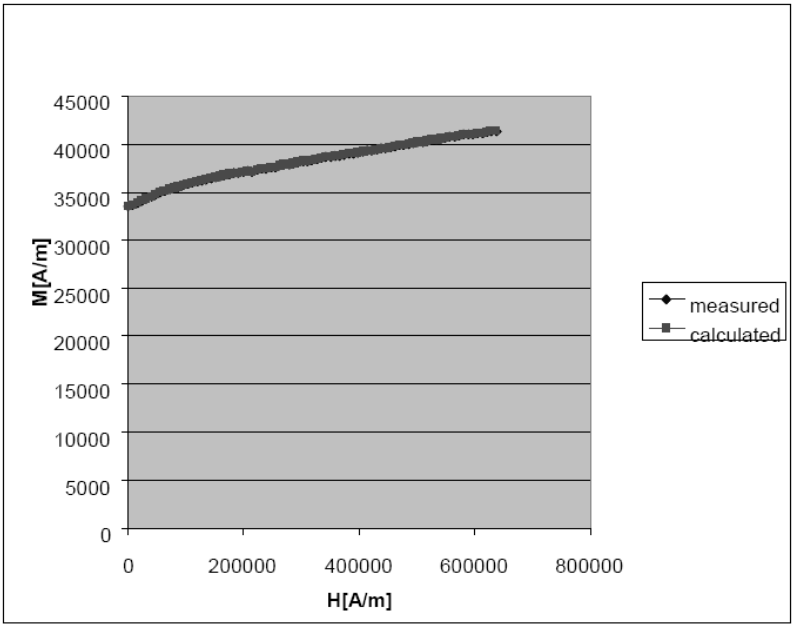

Figure 5: Preisach plane for a metro card.

Optimum values of parameters obtained are: a=4848 and b=3742.7. With these values minimum error is: $9.6470\ 10^{-13}$. For these optimum values the fallowing Preisach plane was obtained:

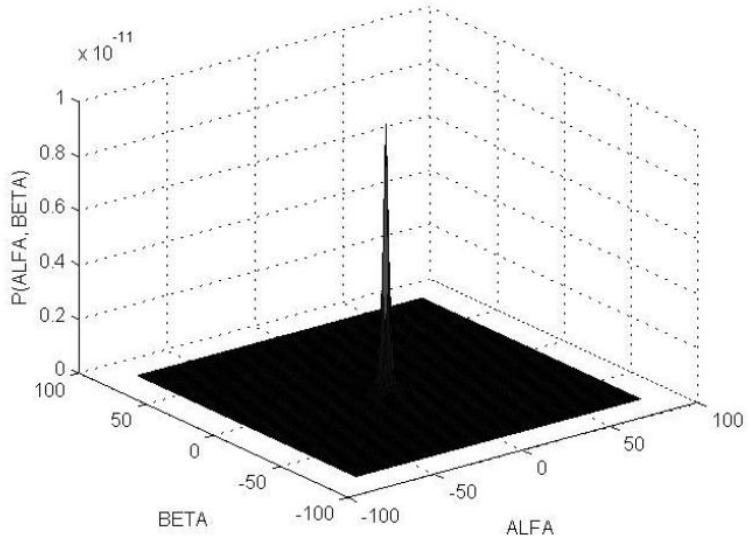

Figure 6: Preisach plane for an applied field at 30 degrees.

In conclusion a new implementation of Preisach model was done with advantages concerning speed. Results point out that model suits well homogenous magnetic mediums. A new way of memorizing state line in Preisach triangle was presented. Also a method of searching optimum parameters of a function with 2 unknowns is included in code. Numerical improvements concerning precision can be done for Preisach density functions with one

extremum value. Identification results are promising and a vectorization of model is a future task.

Acknowledgments - The work has been funded by the Sectorial Operational Programme Human Resources Development 2007-2013 of the Romanian Ministry of Labour, Family and Social Protection through the Financial Agreement POSDRU/107/1.5/S/76909.

.

References

[1] E. D. Torre. *Magnetic hysteresis* IEEE Press 1999.
[2] A. Visintin. *Differentials models of hysteresis*, Springer, Berlin, 1994.
[3] B. D. Culitty, C. D. Graham. *Introduction to magnetic materials*, Willey-IEEE Press, New-Jersey, 2009.
[4] G. Bertotti, I. D. Mayergoyz. *The science of hysteresis*, Academic Press, London, 2005.
[5] G. Bertotti. *Hysteresis in magnetism*, Academic Press, London, 1998.
[6] V. Ionita, L. Petrescu, A. Bordianu, O. Tabara. Optimal use of Preisach hysteresis model in Computer Aided Design, *to be published.*
[7] O. Tabara. Identification of numerical Preisach model by separating variables, *Proceedings of the 7th international Symposium Advanced Topics in Electrical Engineering*, Bucharest, (2011), 425-428.
[8] M. R. Zacherzadach, Mohsen Firouzi, Hassan, S. B. Shouraki. Hysteresis Nonlinearity Identification Using New Preisach Model-Based Artificial Neural Network Approach, *Journal of Applied Mathematics*, 2, Volume 2011, 2011.
[9] F. Preisach. Uber die magnetische, Nachwirkung, *Zeitschrift fur Physik*, 94, (1935), 277-302.
[10] T. Yamaguchi, F. Ueda, E. Yamamoto. Simulations of hysteresis characteristics of core materials using Everett function, *IEEE Translation Journal On Magn*., 4, 6, (1989), 353-357.
[11] O. Henze, W. M. Rucker. Identification procedures of Preisach model , IEEE Trans. on Magn., 36, 2, 2002, pp. 833-836.

PARAMETRII S ÎN APLICAŢII DE ÎNALTĂ FRECVENŢĂ

Gabriela CIUPRINA, Aurel Sorin LUP, Alina TOMESCU
Universitatea "Politehnica" din Bucureşti, Spl. Independenţei 313, 060042, Bucureşti;
gabriela.ciuprina@upb.ro, sorin@lmn.pub.ro, tomescu.alina@yahoo.com

Abstract. Parametrii S sunt mărimi complexe, dependente de frecvenţă, asociate unui sistem multiport. Există însă o multitudine de posibilităţi de introducere a lor, ceea ce face ca interpretarea lor fizică şi înţelegerea semnificaţiei lor să fie adesea greoaie. Această lucrare prezintă un studiu critic al modurilor de definire a parametrilor S, comentând semnificaţia lor pentru dispozitive pasive în care apare sau nu propagarea câmpului electromagnetic.

1 Introducere

Parametrii S (de împrăştiere, sau de repartiţie) sunt mărimi complexe, dependente de frecvenţă, asociate unui sistem multiport. Iniţial, au fost folosiţi în teoria liniilor electrice, pentru definirea lor fiind utilizate undele de tensiune incidente, reflectate sau transmise. Mai general, ei pot fi definiţi in sisteme cu microunde ce pot fi abordate în termeni de circuit. Există însă o multitudine de posibilităţi de introducere a lor [1,2,3] ceea ce face ca interpretarea lor fizică şi înţelegerea semnificaţiei lor să fie adesea greoaie.
Parametrii S nu au un corespondent în teoria circuitelor electrice, pentru că acestea nu conţin elemente de circuit în care să existe propagare ca în ghidurile de undă. Şi totuşi, în teoria circuitelor s-au extins raţionamente similare celor făcute pentru circuitele de microunde, introducându-se conceptul de "unde de putere", terminologie provenită din semnificaţia lor care are legatură cu dependenţa dintre puterea activă absorbită de o sarcină conectată la un port şi frecvenţa de lucru [4]. Există formule de conversie între parametrii S şi parametrii clasici ai teoriei circuitelor (impedanţa, admitanţa, etc), dar literatura trebuie privită cu atentie căci din cauza înţelegerii greşite a semnificaţiei, unele formule sunt inutile (de exemplu cele din [5], articol criticat de [6]). Înţelegerea parametrilor S este deosebit de importantă pentru aplicaţii de înaltă frecvenţă ce includ componente active şi pasive din circuitele integrate [7], inclusiv sisteme microelectromecanice (MEMS), precum şi sisteme de transfer "fără fir" (*wireless*) de putere [8].
Această lucrare prezinta un studiu critic al modurilor de definire a parametrilor S, comentând semnificaţia lor pentru două exemple. Primul exemplu este un sistem pasiv ce presupune propagare de unde electromagnetice (interconexiuni simple sau combinate cu microcomutatoare de RF), iar al doilea exemplu este un circuit tipic pentru transfer *wireless* de putere.

2 Prezentarea clasică: unde şi pseudo-unde

Abordarea în termeni de circuit a unui sistem de microunde poate fi făcută dacă se definesc terminelele unui astfel de sistem, precum şi tensiunea şi curentul acestor terminale. Aceste mărimi se pot defini în mod natural pentru sisteme cu microunde care funcţionează într-un mod transversal electromagnetic (TEM), pentru orice alt mod de propagare definirea fiind convenţională [3].
In Fig. 1 este reprezentat un sistem cu 2 porturi. În partea stângă sunt reprezentate sensurile de referinţă ale tensiunii şi curentului asociate terminalelor, parametrii de circuit ca matricea impedanţei **Z**, sau matricea admitanţei **Y** fiind asociaţi acestei reprezentări. În partea dreaptă sunt sugerate undele incidente şi undele reflectate asociate porturilor, parametrii S (matricea **S**) fiind asociaţi acestei reprezentări.

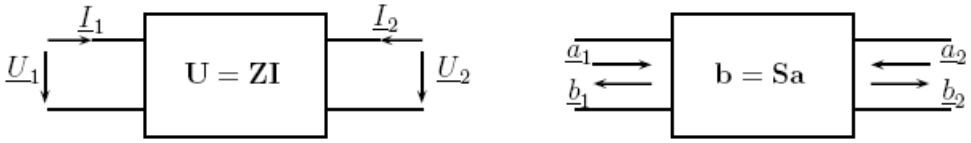

Fig.1. Mărimi asociate unui sistem diport: (stânga) tensiuni, curenţi, matrice de impedanţă **Z**; (dreapta) unde direct/incidente, inverse/reflectate, matricea parametrilor **S**

Pentru un sistem multiport cu microunde se defineşte o impedanţă caracteristică asociată modului de propagare corespunzător fiecărui port $\underline{Z}_{0k}$. În general, impedanţa caracteristică este reală [3], ea corespunzând unei situaţii de propagare fără distorsiuni. Tensiunea şi curentul unui port se exprimă ca fiind combinaţii liniare ale undelor directă (incidentă) notată cu indice + şi inversă (reflectată), notată cu indice − într-un mod similar ca în cazul liniei:

$$\underline{U}_k = \underline{U}_{k+} + \underline{U}_{k-} \qquad \underline{I}_k = \frac{1}{\underline{Z}_{0k}}\left(\underline{U}_{k+} + \underline{U}_{k-}\right) \qquad \text{k=1,2} \qquad (1)$$

Parametrii S fac legătura între undele transmise sau reflectate de tensiune (cele cu indicele −, care ies din sistem) şi undele incidente de tensiune (cele cu indicele +, care intră în sistem). De fapt nu se lucrează direct cu mărimile $\underline{U}_{k+}$ si $\boldsymbol{U}_{k-}$ ci cu valori asociate ale lor, notate cu $\underline{a}_k$ şi $\underline{b}_k$ şi definite astfel:

$$\underline{a}_k = \underline{U}_{k+}/\sqrt{\underline{Z}_{0k}} \qquad \underline{b}_k = \underline{U}_{k-}/\sqrt{\underline{Z}_{0k}} \qquad (2)$$

de unde

$$\underline{U}_k = \sqrt{\underline{Z}_{0k}}\left(\underline{a}_k + \underline{b}_k\right) \qquad \underline{I}_k = \left(\underline{a}_k - \underline{b}_k\right)/\sqrt{\underline{Z}_{0k}} \qquad (3)$$

Dacă impedanţele caracteristice sunt egale şi pur reale, atunci se poate vorbi de impedanţa caracteristică a multiportului, notată Z_0, iar puterea activă transferată sistemului prin terminalul k se exprima ca

$$P_k = a_k^2 - b_k^2 \qquad (4)$$

unde $a_k = |\underline{a}_k|$ si $b_k = |\underline{b}_k|$, deci puterea activă transmisă pe la borna k este diferenţa dintre puterea medie injectată prin unda incidentă şi puterea medie extrasă prin unda reflectată. Parametrii S (matricea de repartiţie/împrăştiere) sunt definiţi de relaţia dintre undele reflectate şi undele incidente pentru toate cele n terminale:

$$\mathbf{b} = \mathbf{Sa} \qquad (5)$$

unde **a** este vectorul coloană al mărimilor $\underline{a}_k$ care reprezintă unde normate incidente asociate celor n porturi, **b** este vectorul coloană al marimilor $\underline{b}_k$ care reprezintă unde normate reflectate, iar **S** este o matrice patrată de dimensiune n. Semnificaţia fiecărui parametru este imediată. S_{ii} reprezintă un coeficient de reflexie la terminalul i, fiind raportul dintre unda de tensiune reflectată la terminalul i şi unda incidentă la acelaşi terminal, când toate celelalte terminale sunt adaptate. S_{ij} reprezintă un coeficient de transmisie de la terminalul j la terminalul i, fiind raportul dintre unda de tensiune transmisă la terminalul i si unda incidentă la terminalul j când toate celelalte terminale sunt adaptate.

În [1] parametrii S sunt introduşi forţat. Se porneşte de la formulele (2) dar în care apare o aceeaşi mărime Z_0, numită impedanţă de referinţă, pentru toate porturile.

În [4] se face o prezentare asemănătoare, deşi formulele nu sunt chiar identice cu cele de mai sus. Tot aici se introduce şi o altă abordare, menită a realiza o punte cu definirea unor parametri S pentru circuitele de curent alternativ. În loc de o impedanţă caracteristică se foloseşte o impedanţă de referinţă Z_{ref} , cu restricţia ca partea ei reală să fie strict pozitivă şi se definesc pseudo-unde care nu mai au semnificaţie fizică, sunt numai artificii matematice, dar care au proprietăţi convenabile. Ele sunt echivalente cu undele din prezentarea clasică atunci când impedanţa de referinţă este egală cu impedanţa caracteristică a modului de propagare. Deşi pseudo-undele depind de impedanţa de referinţă, tensiunea şi curentul nu depind de valoarea

impedanţei de referinţă, deşi aceasta apare explicit în expresiile lor. Se definesc similar psedo-parametri S. Faptul ca pseudo-undele sunt aceleaşi cu undele normate definite în mod clasic dacă impedanţa de referinţă este egală cu impedanţa caracteristică, ar face acestă alegere una naturală. Ea nu este întotdeauna cea mai convenabilă. Dacă impedanţa caracteristică variază mult cu frecvenţa (aşa cum este cazul sistemelor cu pierderi), acesta reprezintă un inconvenient în interpretarea măsuratorilor (conform [4]).

3 Unde de putere

Parametrii S nu au un corespondent în teoria circuitelor electrice, pentru că acestea nu conţin elemente de circuit în care să existe propagare ca în ghidurile de undă. Este lipsit de sens să vorbeşti despre impedanţa caracteristică a unui circuit electric multiport. Şi totuşi, în teoria circuitelor s-au extins raţionamente similare celor făcute pentru circuitele de microunde. Se foloseşte o impedanţă de referinţă arbitrară. Se definesc prin analogie mărimi care sunt numite unde, însă corect ar fi să li se pună prefixul ”pseudo” [4]. O afirmaţie similară se face pentru parametrii S. Pseudo-undele si pseudo-parametrii S sunt mărimi compatibile cu ambele teorii. Pentru un port al unui circuit, se foloseşte un numar complex asociat portului, notat $\underline{\hat{Z}}_k$, iar pseudo-undele se definesc ca fiind (Youla, 1961, conf. [4])

$$\underline{a}_k = \frac{1}{2\sqrt{Re(\underline{\hat{Z}}_k)}}\left(\underline{U}_k + \underline{\hat{Z}}_k \underline{I}_k\right) \qquad \underline{b}_k = \frac{1}{2\sqrt{Re(\underline{\hat{Z}}_k)}}\left(\underline{U}_k - \underline{\hat{Z}}_k^{\,*} \underline{I}_k\right) \tag{6}$$

Impedanţa $\underline{\hat{Z}}_k$ este arbitrară, singura restricţie fiind ca ea să aibă partea reală strict pozitivă. Dacă este egală cu impedanţa de sarcină conectată la acel port, atunci $\underline{a}_k$ si $\underline{b}_k$ se numesc unde de putere. Cand $\underline{\hat{Z}}_k$ este pur reală, undele de putere se reduc la pseudounde cu $\underline{Z}_{ref} = \underline{\hat{Z}}$. Undele de putere satisfac relaţia (4) pentru orice $\underline{\hat{Z}}$. Pseudo-undele satisfac (4) doar dacă $\underline{Z}_{ref}$ este reală.

4 Conversii S-Z; Proprietăţi

În [1] se demonstrează uşor formulele de conversie de la **S** la **Z** şi de la **Z** la **S**, presupunând însă că toate porturile au asociate o aceeaşi impedanţă de referinţă Z_0:

$$\mathbf{S} = (\mathbf{Z} - Z_0\mathbf{I})(\mathbf{Z} + Z_0\mathbf{I})^{-1} \qquad \mathbf{Z} = (\mathbf{I} - \mathbf{S})^{-1}(\mathbf{I} + \mathbf{S})Z_0 \tag{7}$$

unde **I** este matricea unitate. Este interesant că în [5] se prezintă tabele de conversii între parametri pentru impedanţe complexe ale sursei şi sarcinii, iar din reacţia [6] rezultă că toate aceste formule bazate pe unde de putere sunt inutile.

Utilizarea matricei **S** poate fi folosită şi la circuitele active. In general, dispozitivele active au caracteristici neliniare, dar pentru semnale foarte mici, în vecinatatea unui punct static de funcţionare precizat, caracteristicile lor pot fi liniarizate [2]. In aceste condiţii, răspunsul la semnale mici ale dispozitivelor active poate fi descris prin matricea S care, în acest caz, depinde de punctul static de funcţionare. Se pot demonstra urmatoarele proprietăţi ale matricei S [2]:

• Dacă multiportul este reciproc, atunci matricea S este simetrică. Acest lucru se întâmplă pentru dispozitivele alcătuite din materiale liniare şi izotrope (cazul elementelor uzuale de circuit: rezistoare, bobine, condensatoare, bobine cuplate, interconexiuni).

• Dacă multiportul este pasiv, atunci modulele componentelor matricei **S** sunt subunitare.

• Dacă multiportul este pasiv şi fără pierderi (nedisipativ), atunci **S** este unitară, adică $\mathbf{S}^H\mathbf{S} = \mathbf{I}$. În acest caz, suma pătratelor modulelor parametrilor S pe orice linie sau coloană este egală cu unitatea, condiţie ce reflectă conservarea puterii în dispozitivul considerat; de asemenea, produsul scalar dintre orice linie a matricei S cu altă linie conjugată este zero, ceea ce evidenţiază existenţa anumitor relaţii între fazele parametrilor S.

• Pentru dispozitivele active, matricea **S** este nesimetrică, iar parametrii S pot avea modulul supraunitar.

5 Exemple

În acest paragraf sunt prezentate două exemple pentru care este utilă înţelegerea semnificaţiei parametrilor S. Rezultatele au fost obţinute folosind funcţii ale programului ROMWorkbench, dezvoltat iniţial de autori in [7].

Primul exemplu, a cărui schemă echivalentă este prezentată în Fig. 2 ilustrează folosirea unui microcomutator de radio-frecvenţă (RF) plasat transversal faţă de o interconexiune. Comutatorul este presupus a fi de tip capacitiv $Y_{switch} = j\omega C$, modificarea admitanţei sale echivalente făcându-se prin modificarea distanţei (capacităţii) dintre armăturile sale, o capacitate mică neperturbând trecerea semnalului de la poarta 1 la poarta 2, iar o capacitate mare blocând trecerea semnalului pe linie (Fig. 3)

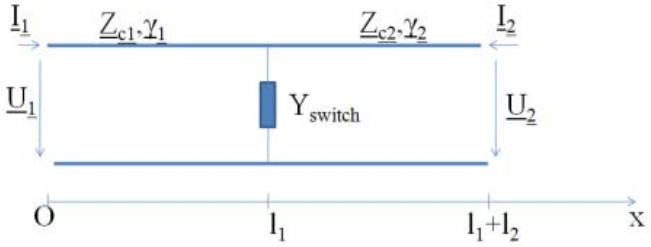

Fig. 2 Schema echivalentă a unui microcomutator capacitiv conectat transversal faţă de o interconexiune.

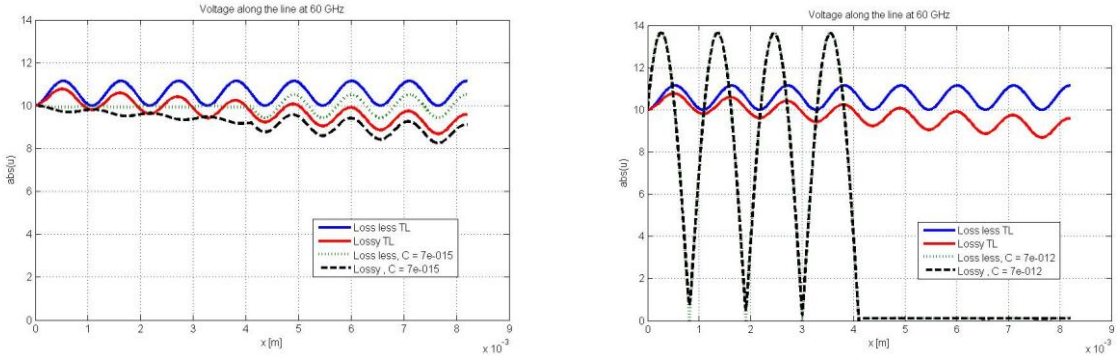

Fig. 3 Tensiunea pe linie în cazul în care semnalul trece (în stânga, capacitatea comutatorului este mare), respectiv în cazul în care semnalul este blocat (în dreapta, capacitate este mica).

Parametrul S_{11} în starea în care semnalul de RF trece reprezintă pierderi datorate reflexiei semnalului transmis, cauzate de neadaptarea sarcinii la linie (Fig. 4).

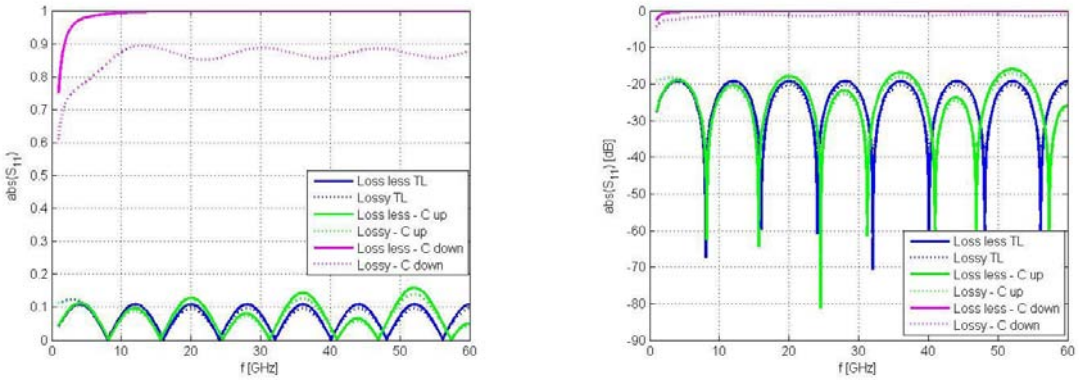

Fig. 4. Modulul parametrului S11 (stânga), respectiv valoarea lui in decibeli (dreapta) pentru cele două stări stabile: semnal trece ("C-up") şi semnal blocat ("C-down"). **Pierderi prin reflexie** = S_{11} în starea în care semnalul trece (curba verde).

Parametrul S_{21} în starea în care semnalul de RF trece sunt pierderi rezitive pe linie, inclusiv datorate efectul pelicular, iar în starea în care semnalul este blocat acelaşi parametru S_{21} reflectă izolarea între portul de intrare şi cel de ieşire (Fig. 5).

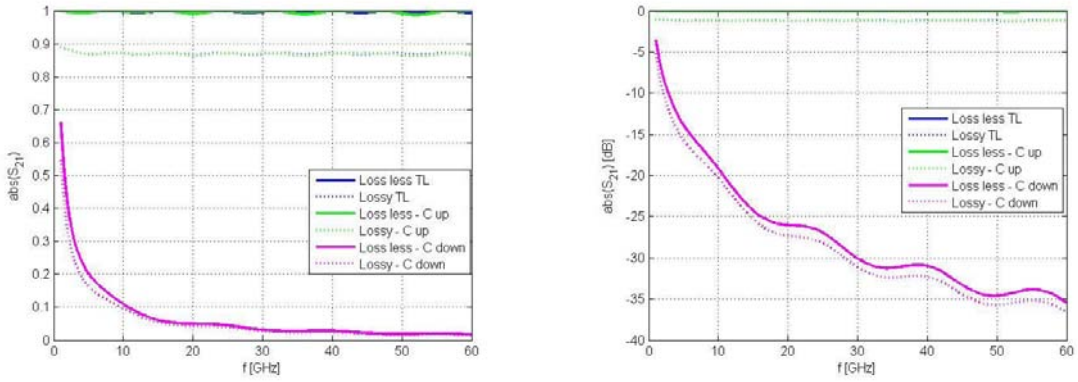

Fig. 5. Modulul parametrului S_{21} (stânga), respectiv valoarea lui in decibeli (dreapta) pentru cele două stări stabile: semnal trece ("C-up") şi semnal blocat ("C-down"). **Pierderi prin inserţie** = S_{21} în starea în care semnalul trece (curba verde). **Izolarea** = S_{21} în starea în care semnalul este blocat (curba mov)

Datorită ordinelor de mărime diferite, pierderile prin inserţie se reprezintă separat de izolare (Fig. 6 - în care ordinele de mărime obţinute sunt tipice pentru un microcomutator de tip capacitiv). În multe lucrări se omite a se mai pune semnul negativ la mărimile exprimate în decibeli, deşi acest lucru poate genera confuzii.

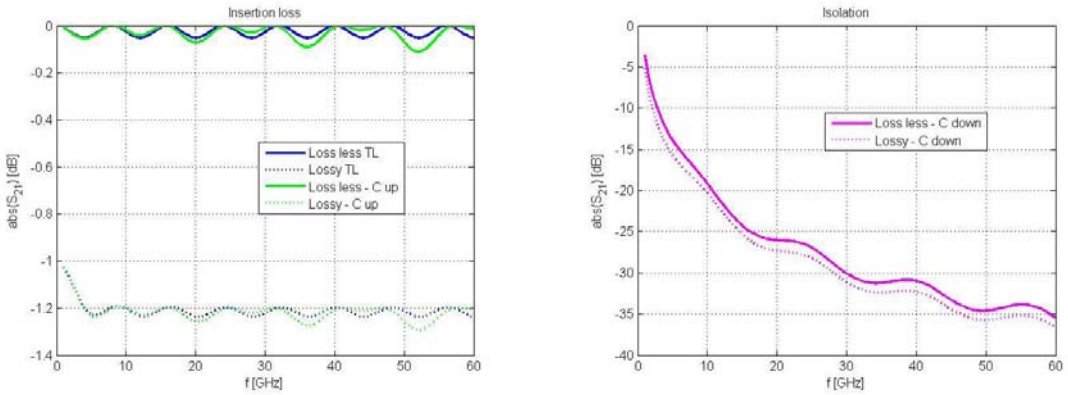

Fig.6. Exemplul tipic de raportare a rezultatelor măsurate/simulate pentru microcomutatoarele de radio-frecvenţă: pierderi prin inserţie (stânga), izolare (dreapta).

Pentru un microcomutator se doresc pierderi prin inserţie cât mai mici (în modul cât mai apropiate de 1, deci în dB cât mai aproape de 0 dB) şi izolare cât mai mare (în modul cât mai aproape de 0, deci în dB cât mai mare în valoare absolută). Un microcomutator ideal are pierderi prin inserţie de 0 dB izolare infinită (valori mici şi mari se referă la valorile în dB, luate cu semnul +).

Un al doilea exemplu este unul în care nu au loc fenomene de propagare. Schema de circuit echivalentă este prezentată în Fig. 7 şi reprezintă cel mai simplu model pentru ceea ce în limba engleză se numeşte cam pretenţios "wireless electricity". De fapt, principiul este acela al transferului maxim de putere, aplicat unui circuit de curent alternativ, în care există un sistem de bobine cuplate. Dacă se urmareşte dependenţa puterii active absorbite de sarcina R în funcţie de frecvenţa sursei care alimentează circuitul primar (curba albastră în Fig. 7) , atunci se observă că aceasta este în legatură cu modulul la pătrat al parametrului S_{21}, considerat a fi randamentul transferului de putere pentru un astfel de dispozitiv.

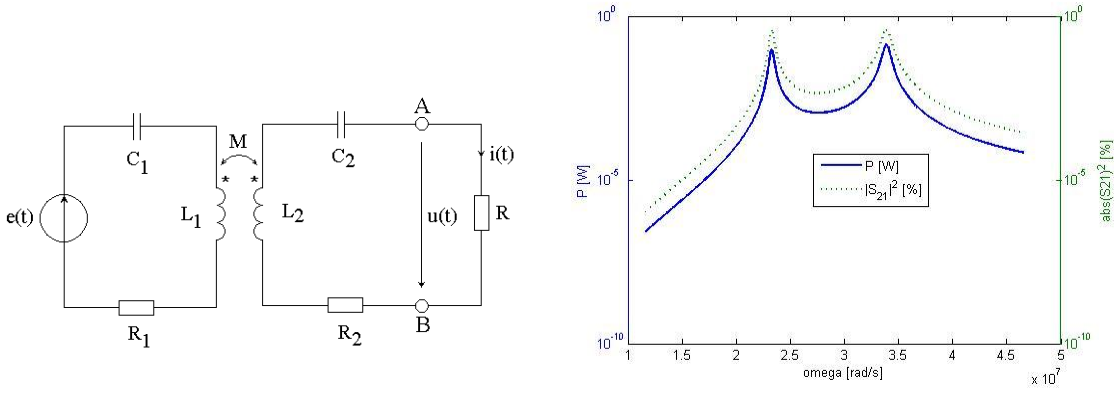

Fig.7 Model de circuit pentru "wireless electricity" (stânga). Puterea consumată de sarcina R (curba albastră) şi modulul la pătrat al parametrului S21 L = 15.1e-6 H; C = 1.2e-10 F; C1 = C2 = C; M = L/10; R = 1; E = 10; Rs = 0; L1 = L/2; L2 = L; R1 = R2 = 5 (dreapta)

6 Concluzii

Semnificaţia parametrilor S depinde de tipul de dispozitiv pentru care sunt calculaţi sau măsuraţi, dispozitiv în care pot exista fenomene de propagare a câmpului electromagnetic, sau nu. În cazul în care există fenomene de propagare, semnificaţia parametrilor S este legată de reflexia câmpului electromagnetic la un port sau de propagarea câmpului de la un port la altul. În cazul în care nu există propagare, atunci semnificaţia lor este legată de dependenţa puterii active absorbită de o sarcină în funcţie de frecvenţa de lucru, folosindu-se în mod forţat termenul de unde de putere. Parametrii S sunt importanţi pentru aplicaţiile de înaltă frecvenţă deoarece ei sunt cei care se pot măsura la astfel de frecvenţe, întrucât nu necesită îndeplinirea unor condiţii de gol sau de scurt-circuit ca în cazul măsurării impedanţelor sau admitanţelor, condiţii ce sunt dificil de îndeplinit la frecvenţe înalte.

Mulţumiri – Rezultatele prezentate în acest articol au fost obtinute cu sprijinul Ministerului Muncii, Familiei şi Protecţiei Sociale prin Programul Operaţional Sectorial Dezvoltarea Resurselor Umane 2007-2013, contract nr. POSDRU/89/1.5/S/62557 şi prin programul Parteneriate în domenii prioritare – PN-II-PT-PCCA-2011-3, derulat cu sprijinul ANCS, CNDI – UEFISCDI, proiect nr. 5/2012.

Referinţe

[1] S.J. Orfanidis. *Electromagnetic Waves and Antennas*, 2008. Disponibilă online la http://www.ece.rutgers.edu/orfanidi/ewa/.

[2] George Lojewski. *Dispozitive şi circuite de microunde*. Editura Tehnică, 2005.

[3] Anca Tomescu si F.M.G. Tomescu. *Sisteme cu microunde*. MatrixROM, 2001.

[4] R.B. Marks and D.F. Williams. A general waveguide circuit theory. *Journal of Research of the National Institute of Standards and Technology*, **97**(1992):533–562.

[5] Dean A. Frickey. Conversions between S, Z, Y, H, ABCD, and T parameters which are valid for complex source and load impedances. *IEEE Trans. on Microwave Theory and Techniques*, **42**(1994):205–211.

[6] Roger B. Marks and Dylan F. Williams. Comments on conversions between S, Z, Y, H, ABCD, and T parameters which are valid for complex source and load impedances. *IEEE Trans. on Microwave Theory and Techniques*, **43**(1995):914–915.

[7] D. Ioan and G. Ciuprina, Reduced Order Models of On-chip Passive Components and Interconnects, Workbench and Test Structures, Book chapter in the book *Model Order Reduction: Theory, Research Aspects and Applications* (W.H.A. Schilders, H.A. van der Vorst, J. Rommes, Eds.), in the book series Mathematics in Industry, Springer-Verlag, Heidelberg, **13 (**2008), 447-467.

[8] T. Imura, H. Okabe, Y. Hori, Basic Experimental Study on Helical Antennas of Wireless Power Transfer for Electric Vehicles by using Magnetic Resonant Couplings, *IEEE conf. on Vehicle Power and Propulsion Conference*, 2009, 936-940.

EROAREA DE METODĂ ÎN DETERMINAREA EXPERIMENTAL ANALITICĂ A CÂMPULUI UNUI ELECTROMANGET PENTRU ACCELERATOARELE DE PARTICULE

Daniel DAN[1] , Daniel IOAN[1,2] ,
1. Universitatea "Politehnica" din Bucureşti, Laboratorul de Metode Numerice, Spl. Independenţei 313, 060042, Bucureşti; lmn@lmn.pub.ro,
2. ICPE-CA, Splaiul Unirii, Nr. 313, Sector 3, 030138, Bucureşti

Abstract. Lucrarea prezintă măsurarea câmpului magnetic al unui electromagnet multipolar și o metodă analitică de calcul a câmpului din interiorul aperturii, pornind de la datele măsurate. Se analizează efectul pe care îl au erorile datelor măsurate, asupra câmpului calculat. Verificările s-au făcut pe un electromagnet octopolar, pentru care câmpul a fost determinat cu o metodă numerică.

1 Introducere

În lucrare este prezentat calculul câmpului din interiorul zonei active a unui electromagnet multipolar, pornind de la măsurătorile experimentale efectuate cu bobina rotitoare sau cu sonda Hall, pe frontiera domeniului de interes (apertura multipolului).

Obiectivul este de a analiza efectul pe care îl au erorile datelor măsurate, asupra preciziei câmpului determinat în apertură. Pentru aceasta se determină senzitivitatea soluţiei analitice faţă de datele ei. Este un aspect de maximă importanţă metrologică, necesar pentru a asigura consistenţa procedurii de control calitativ. În partea a doua a lucrării se analizează un electromagnet octopolar. Pentru acesta, câmpul din apertură a fost calculat cu o metoda elementului finit, iar rezultatele au fost comparate cu cele analitice.

2 Armonicele câmpului magnetic

Se consideră apertura electromagnetului, reprezentată de un domeniu 2D, circular cu frontiera sa:

$$G=\left\{(x,y)\in \mathrm{IR}^2 \,\middle|\, x^2+y^2<r_0^2\right\};\quad \partial G=C=\left\{(x,y)\in \mathrm{IR}^2 \,\middle|\, x^2+y^2=r_0^2\right\}. \tag{1}$$

Deoarece atât intensitatea câmpului magnetic, cât şi inducţia magnetică sunt în apertură câmpuri irotaţionale şi solenoidale, ele admit atât un potențialul magnetic vector cât și unul scalar, care satisfac în acest domeniu ecuaţia Laplace, care în coordonate carteziene și respectiv polare are forma [1], [2]:

$$\begin{cases}\Delta V_m=\dfrac{\partial^2 V_m}{\partial x^2}+\dfrac{\partial^2 V_m}{\partial y^2}=0 \text{ pe } (x,y)\in G\\ V_m\big|_C=f,\end{cases}\quad\Leftrightarrow\quad\begin{cases}r^2\dfrac{\partial^2 V_m}{\partial r^2}+r\dfrac{\partial V_m}{\partial r}+\dfrac{\partial^2 V_m}{\partial \theta^2}=0,\\ f(\theta)=\alpha_0+\displaystyle\sum_{n=1}^{\infty}\left(\alpha_n\cos(n\theta)+\beta_n\sin(n\theta)\right).\end{cases} \tag{2}$$

Am adăugat condiția de frontieră de tip Dirichlet pentru potențialul magnetic scalar, pe care le-am descompus în serie Fourier, care au coeficienţii:

$$\alpha_0=\frac{2}{\pi}\int_0^{2\pi} f(\varphi)d\varphi;\quad \alpha_n=\frac{1}{\pi}\int_0^{2\pi} f(\varphi)\cos(n\varphi)d\varphi;\quad \beta_n=\frac{1}{\pi}\int_0^{2\pi} f(\varphi)\sin(n\varphi)d\varphi. \tag{3}$$

Aceasta corespunde cunoaşterii componentei tangenţiale (azimutale) a câmpului magnetic de pe frontieră, câmp care se poate măsura cu o sondă Hall şi apoi descompune în serie Fourier.

Aplicând metoda separării variabilelor [2], rezultă expresia potenţialului din domeniu:

$$V_m(r,\theta) = \alpha_0 + \sum_{n=0}^{\infty} r^n \left(\alpha_n \cos\left(n\theta\right) + \beta_n \sin\left(n\theta\right)\right), \tag{4}$$

din care, prin derivare, considerând $\mathbf{B} = -\nabla V_m$, rezultă expresiile componentelor radială şi azimutală a inducţiei magnetice:

$$\begin{cases} B_r(r,\theta) = -\dfrac{\partial V_m}{\partial r} = \displaystyle\sum_{n=1}^{\infty}\left(\frac{r}{r_0}\right)^{n-1}\left(B_n \sin(n\theta) + A_n \cos(n\theta)\right), \\ B_\theta(r,\theta) = -\dfrac{1}{r}\dfrac{\partial V_m}{\partial \theta} = \displaystyle\sum_{n=1}^{\infty}\left(\frac{r}{r_0}\right)^{n-1}\left(B_n \cos(n\theta) - A_n \sin(n\theta)\right), \end{cases} \tag{5}$$

unde $A_n = -n\alpha_n$, $B_n = -n\beta_n$ şi $B = \left\|\vec{B}\right\| = \sqrt{B_r^2 + B_\theta^2}$.

3 Metoda bobinei armonice, pentru măsurarea câmpului magnetic

Pentru electromagneţii din acceleratoarele de particule [3], tehnica *bobinei armonice*, bazată pe folosirea unei bobine rotitoare este la ora actuală cea mai convenabilă, exactă şi răspândită tehnică de măsurare a câmpului produs de aceşti electromagneţi la periferia aperturii [4]. O reprezentare schematică a secţiunii transversale a unei astfel de bobine, în varianta radială este dată în fig. 1. Fluxul unei astfel de bobine, cu N spire şi de lungime L are expresia:

$$\varphi(t) = NL\int_{R_1}^{R_2} B_\theta(r,\theta)dr = \sum_{n=1}^{\infty} S_n^{rad}\left[B_n \cos(n\theta) - A_n \sin(n\theta)\right], \tag{6}$$

$$S_n^{rad} = \frac{2NLr_0}{n}\left[\left(\frac{R_2}{r_0}\right)^n - \left(\frac{R_1}{r_0}\right)^n\right], \tag{7}$$

unde R_1 şi R_2 sunt razele bobinei, iar $\theta = \omega t$ este poziţia unghiulară la momentul t, proporţională cu viteza sa unghiulară ω. Tensiunea electromotoare indusă în bobină este

$$u(t) = \sum_{n=1}^{\infty} n\omega S_n^{rad}\left[B_n \sin(n\theta) + A_n \cos(n\theta)\right]. \tag{8}$$

Prin descompunerea în serie Fourier a semnalului de tensiune, măsurat la bornele bobinei rotitoare se obţin coeficienţii Fourier ai câmpului, iar apoi folosind (5) se determină câmpul în orice punct din apertură.

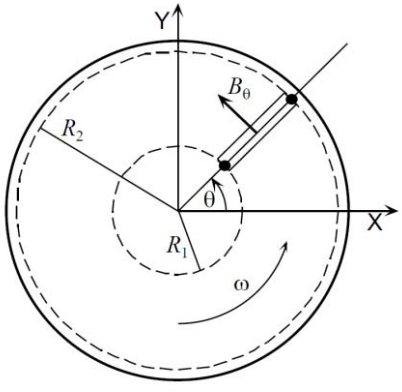

Fig. 1. Bobina rotitoare radială [4]

4 Analiza electromagnetului octopolar

Se consideră electromagnetul din fig. 2, la care zona de interes are un diametru de $d = 150\text{mm}$.

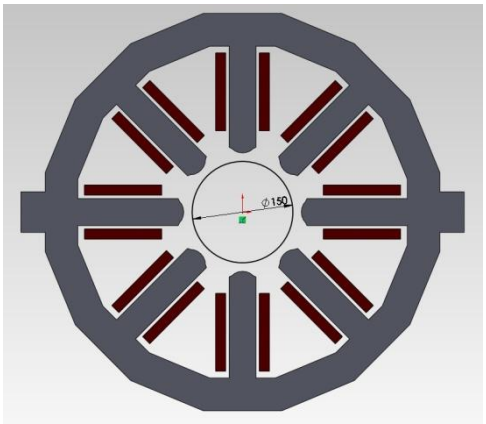

Fig. 2 Secțiune prin electromagnetul studiat

Acest electromagnet a fost modelat cu pachetul de element finit COMSOL [5], iar spectrul câmpului rezultat este reprezentat în fig. 3. Pentru discretizare, s-a folosit o rețea de 9.012 elemente finite triunghiulare de ordinul doi, care ulterior a fost rafinată la 144.192 triunghiuri.

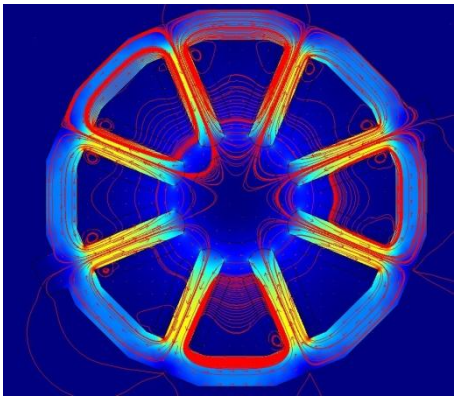

Fig. 3. Liniile de câmp magnetic rezultate prin modelare cu COMSOL

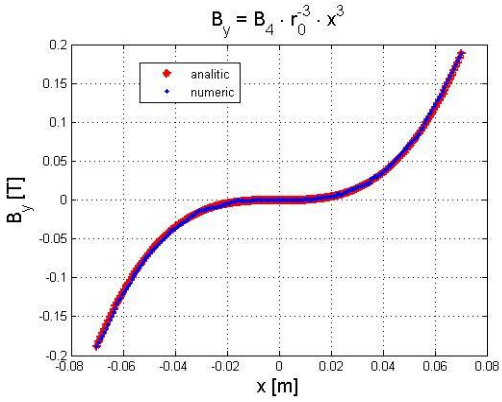

Fig. 4 Inducția magnetică în vecinătatea originii

În fig. 4 este reprezintă variația componentei B_y a inducției magnetice de-a lungul axei Ox, pe intervalul $-0,075 < x < 0,075$ m, de interes pentru particulele accelerate. Variația componentei verticale a inducției magnetice de-a lungul axei Ox $(\theta = 0)$ are descompunerea în serie de puteri:

$$B_y = B_0 + \frac{1}{1!}\frac{\partial B_y}{\partial x}x + \frac{1}{2!}\frac{\partial^2 B_y}{\partial x^2}x^2 + \frac{1}{3!}\frac{\partial^3 B_y}{\partial x^3}x^3 + \cdots \tag{9}$$

Restricția acestei funcții pentru $r = x > 0$ are conform cu (5) expresia

$$B_y = \sum_{n=1}^{\infty} B_n \left(\frac{r}{r_0}\right)^{n-1}. \tag{10}$$

Dacă electromagnetul nu are abateri geometrice și are simetrie octopolară, atunci, în baza relațiilor (3), rezultă că în această serie sunt nenuli doar termenii cu $n = 4k$, multiplu de 4.

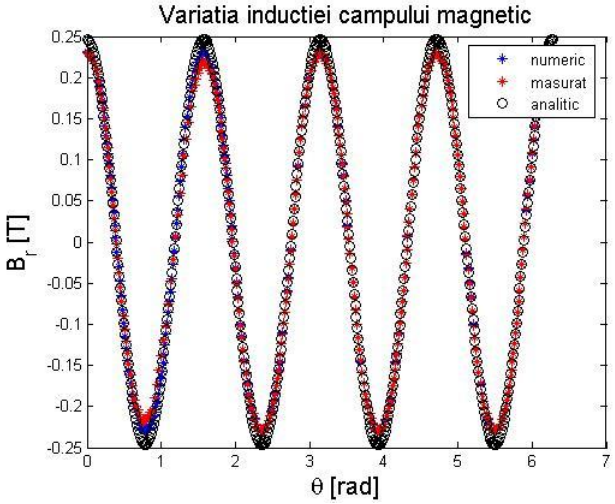

Fig. 5 – Variația componentei radiale a inducției magnetice

Prima armonică semnificativă este cea de ordinul 4, care generează câmpul cu componentele:

$$B'_r = r^4 B'_4 \sin(4\theta), \quad B'_\theta = r^4 B'_4 \cos(4\theta); \quad B'_r = B_4 / r_0^4, \tag{11}$$

numit câmpul *octopolar ideal*, corespunzător potențialului:

$$V'_m = B'_4 r^4 \sin 4\theta. \tag{12}$$

Utilizând valorile pentru componentele carteziene B_x și B_y ale inducției magnetice calculate cu COMSOL în l = 420 puncte echidistante (măsurătorile virtuale), de pe cercul ce delimitează zona de interes (fig. 2), s-a calculat variația pe acest cerc a componentei tangențiale a inducției magnetice. Folosind (3), mai exact transformata Fourier discretă [6], au fost determinați coeficienții Fourier ai acestei funcții, care au fost apoi folosiți pentru a determina, cu relația (5) vectorul inducția magnetică în cele 420 puncte de pe cercul de rază r = 0,075 m. Cu aceeași relație a fost determinată și valoarea componentei B_y, în m = 200 puncte echidistante din segmentul radial $0 \le x \le 0{,}075$m.

5 Analiza erorilor în cazul electromagnetului octopolar

Abateri care apar între soluția numerică şi cea analitică sunt determinate atât de erorile de calcul numeric ale metodei elementului finit, cât şi de erorile ce intervin în aproximarea analitică şi idealizarea câmpului din apertură. Pentru a evidenția ponderea fiecărei surse de erori, a fost recalculată soluţia numerică, folosind o rețea de discretizare rafinată (cu 72.193 noduri în loc de 4.531), care generează 288.577 grade de libertate, în loc de 18.073, cât au fost inițial. Soluția analitică a fost şi ea perfecţionată luând în considerare nu numai armonica fundamentală ci 128 armonici. Rezultatele numerice obținute sunt prezentate în Tabelul 1. Aici s-au folosit următoarele notaţii pentru abaterea dintre soluţia numerică şi cea analitică a componentei:

- radială, pe cercul de rază $r_1 = 0{,}075$ m: $\varepsilon_r = \max\left|B_r - B_r'\right| / \max\left|B_r\right| \%$;
- verticală a inducției, pe segmentul $0 \le x \le 0{,}075$m: $\varepsilon_0 = \max\left|B_y - B_y'\right| / \max\left|B_y\right| \%$.

Tabelul 1. Abaterile dintre soluția numerică și cea analitică

Caz	**MEF**	**Analitic**	ε_r [%]	ε_0 [%]
1	Minimal n_{DOF} = 18.073, *ord* = 2	Ideal (*B4*)	0.2050	0.1405
2	*Rafinat* n_{DOF} = 288.577, *ord* = 2	Ideal (*B4*)	0.1685	0.1193
3	Minimal n_{DOF} = 18.073, *ord* = *2*	Cu 128 armonici	0.2343	0.0589
4	*Rafinat* n_{DOF} = 288.577, *ord* = 2	Cu 128 armonici	0.1973	0.0505

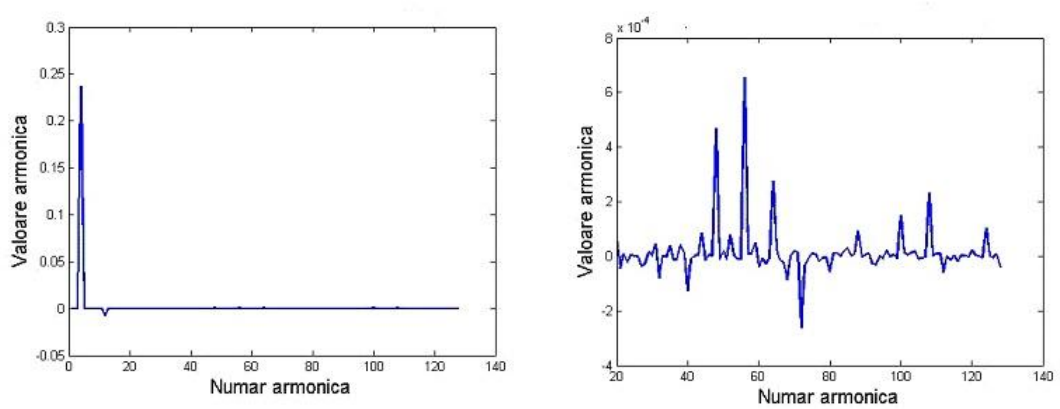

Fig. 6. Spectrul componentei tangențiale a inducției magnetice in cazul 3.

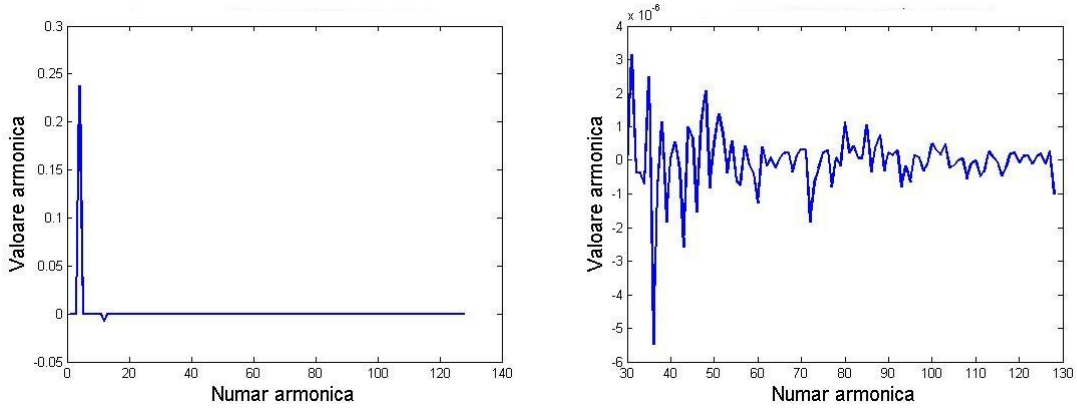

Fig. 6. Spectrul componentei tangențiale a inducției magnetice in cazul 4.

În fig. 6 este reprezentată variația valorii armonicelor componentei tangențiale a inducției magnetice, în funcție de ordinul lor, în cazul 3, (figura din stânga pentru armonicele 1-128, iar figura din dreapta pentru armonicele 30-128). În fig. 7 se reprezintă aceleași date, dar pentru cazul, numerotat în Tabelul 1 cu 4. Se constată că doar armonicile 4 și 12 au valori vizibile la scara folosită pentru graficele din stânga.

6 Analiza senzitivităţilor

Pentru a analiza felul în care erorile aparatului de măsură (sonda Hall sau voltmetrul ce măsoară tensiunea bobinei rotitoare) determină erorile asupra câmpului magnetic calculat în apertură, vom analiza senzitivitățile procedurii de calcul analitic al câmpului. Senzitivitatea relativă a unei mărimi de ieșire y în funcție de o mărime de intrare x se definește ca [7] $S_x^y = \frac{x}{y}\frac{\partial y}{\partial x}$. În consecinţă, $\frac{dy}{y} = \frac{\partial y}{\partial x}\frac{dx}{x} \Rightarrow \varepsilon_y = S_x^y \varepsilon_x$, deci abaterea relativă a mărimii de iesire y este eroarea relativă ε_x a mărimii de intrare x, amplificată de S_x^y ori. În cazul nostru, mărimea de ieşire este b_k, una din componentele inducţiei în punctul $k=1:l$ (max. 200), iar cea de intrare este valoarea funcției f, care descrie condiţia de frontieră, în punctul $j=1:m$ (max. 420), iar din (3) și (5), rezultă:

$$s_{kj} = \frac{\partial b_k}{\partial f_j} = \frac{\partial B_\theta(r_k,0)}{\partial f_j} = \sum_{n=1}^{\infty}\left(\frac{r_k}{r_0}\right)^{n-1}\frac{\partial B_n}{\partial f_j} = -\sum_{n=1}^{\infty} n\left(\frac{r_k}{r_0}\right)^{n-1}\frac{\partial \beta_n}{\partial f_j} = -\frac{1}{\pi}\sum_{n=1}^{\infty} n\left(\frac{r_k}{r_0}\right)^{n-1}\int_0^{2\pi}\frac{\partial f(\varphi)}{\partial f_j}\sin(n\varphi)d\varphi$$

$$-\frac{1}{\pi}\sum_{n=1}^{\infty} n\left(\frac{r_k}{r_0}\right)^{n-1}\int_{\varphi_j}^{\varphi_{j+1}}\sin(n\varphi)d\varphi \cong -\frac{1}{\pi}\sum_{n=1}^{\infty} n\left(\frac{r_k}{r_0}\right)^{n-1}\sin(n\varphi_j) \Rightarrow \left|S_{f_j}^{b_k}\right| = \left|\frac{f_j}{b_k}\frac{\partial b_k}{\partial f_j}\right| \le 1. \qquad (13)$$

7 Concluzii

Relația (7) evidențiază faptul că metoda bobinei rotitoare are sensibilitate maximă pentru $R_1 = 0$ şi $R_2 = r_0$. Din Tabelul 1, rezultă că inducția magnetică din apertură poate fi calculată cu precizie acceptabilă, considerând doar armonica *4*, cea mai importantă. Valorile câmpului, determinate cu metoda analitică au senzitivități relative subunitare, față de valorile măsurate pe frontieră, deci erorile inerente în măsurătoare nu sunt amplificate, prin calculul analitic.

Referinţe

[1] I. Gh. Șabac. *Matematici speciale 2*, Ed. Didactică și Pedagogică, București, 1965.

[2] G. Păltineanu și P. Matei. *Ecuații diferențiale și ecuații cu derivate parțiale cu aplicații*, București, 2007. http://civile.utcb.ro/cmat/cursrt/ecc.pdf.

[3] S. Russenschuck. *Field computation for accelerator magnets*, Wiley-VCH, 2010, www.amazon.com/Computation-Accelerator-Magnets-Stephan-Russenschuck/dp/3527407693/.

[4] Animesh Jain. Harmonic Coils - CERN Academic Training Program, *Brookhaven National Laboratory,* Upton, New York 11973-5000, USA. April 7-11, 2003.

[5] COMSOL Multiphysics - http://www.comsol.com/.

[6] Discrete Fourier Transform, http://en.wikipedia.org/wiki/Discrete_Fourier_transform

[7] M. Iordache, L. Dumitriu, D. Niculae, On the sensitivity of analog circuits. Analele Universitații din Craiova, 2008, **32**, 11-16, http://elth.ucv.ro/fisiere/anale/2008/1_2.pdf.

Transient and Steady State Analysis through Simulations of an Axial-Field Single-Pole Single-Phase Switched Reluctance Motor Prototype

Ovidiu DABIJA, Alecsandru SIMION, Leonard LIVADARU, Adrian MUNTEANU, Nicolae-Daniel IRIMIA

Technical University "Gheorghe Asachi" of Iasi, Faculty of Electrical Engineering, Bd. D. Mangeron 51-53, 700050, Romania; ovidiudabija@gmail.com

Abstract. This paper presents the dynamic regimes simulations of an axial-field single pole single-phase switched reluctance motor. These simulations are intended to reveal valuable information about the behaviour of the system and thus permitting the creation of a dedicated converter for the drive.

1 Introduction

Switched reluctance motors (SRMs) are a special category of motors that only recently received more attention from the scientific community. This happened once with the technological progress that took place in the field of the power electronics and microcontrollers. These allowed to many researchers to deal with the relative complicated problem of controlling the SRMs.

The electromagnetic torque is produced in a SRM on account of the fact that the rotor presents two axes of symmetry d and q, which have different reluctance. In this way, by properly supplying the winding of the stator, an overall variation of the coenergy occurs with the tendency to align the rotor in the position of minimum reluctance [1] [2].

The absence of an excitation winding and of permanent magnets has some advantages, such as reduced costs, simple mechanical construction and ruggedness. The main disadvantages come from the fact that the SRM requires a special converter in order to operate [3]. In most of the applications, it is necessary to use an accurate shaft position sensor. Sensorless control is also possible but this comes with the need of an even more sophisticated electronic control system.

The importance of simulation of the SRM along with its converter is not to be neglected in the stage of development of a successful product. The results offer important information about the behaviour of the drive and can reveal possibilities of improving its performances [3].

Because the characteristics of this motor are strongly nonlinear and they depend both on the excitation current i and on the angle θ, in order for this motor to be simulated it is necessary to obtain the characteristics $\Psi(i, \theta)$ and $T(i, \theta)$. These characteristics can be obtained either by FEM simulations or by direct measurements. Because the SRM treated in this paper was already built, direct measurements could be employed [3].

2 Description of the Motor

The geometry of the motor is presented in Figure 1. The stator was assembled from a stack of "U"-shaped laminations and has a concentric winding with 144 turns. The diameter of the copper wire is 1.19 mm, resulting in a fill factor of the coil of 0.15. The resistance of the winding is 0.6 Ohms. The rotor was built in the shape of a disc, half of it being made of ferromagnetic material and the other half of nonmagnetic material. An important parameter when it comes to describe the performances of any reluctance motor, particularly of a switched reluctance motor, it is the ratio between the values of the two extremes inductances L_d and L_q [1] [4]. In this case the ratio varies from $L_d/L_q=2.35$ for an excitation current i=1A to $L_d/L_q=1.43$ for i=20A.

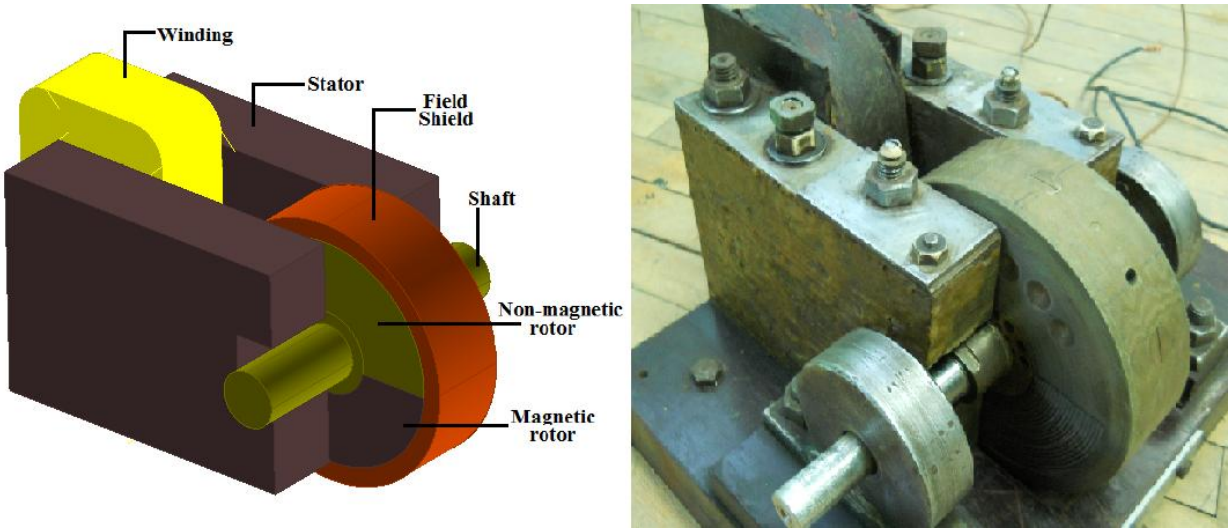

Figure 1: Geometry of the motor.

The bigger this ratio is the better the performances of the machine. This is due to the fact that the electromagnetic torque is produced by the variation of the coenergy, which in this case, assuming that the current is kept constant it is given only by the variation of the inductances [3] [4].

3 Determination of the Characteristics

In order to build a mathematical model for a SRM it is necessary to know its torque and flux characteristics. An easy method to obtain these when a physical model is already constructed is through direct measurements of the inductances [5]. The setup used for the measurement of the inductances is presented in Figure 2. The rotor is kept fixed in the position where the inductances are to be measured and the current is being varied from 0 to 20 Amperes, with equal steps of 1 Ampere. The voltage is measured by the help of the voltmeter. Knowing that the value of the phase resistance is R=0.6 Ohms and using the equations (1), (2) and (3) the inductances can be calculated. The procedure is repeated from unaligned to aligned position. In this case the inductance was measured in steps of 45 degrees.

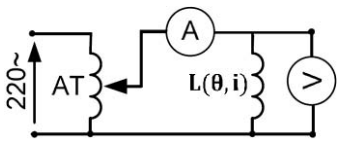

Figure 1: Setup used to measure the inductance.

$$Z = \frac{U}{I} \tag{1}$$

$$X = \sqrt{Z^2 - R^2} \tag{2}$$

$$L = \frac{X}{2\pi f} \tag{3}$$

In equations (1), (2) and (3), Z represents the impedance of the coil, U is the voltage measured by the voltmeter, I is the current running through the coil, X is its reactance, L is the impedance and fis the frequency of the supply voltage.

The result of the product between inductance and current is the magnetic flux and it is represented as a function of angular position and current in Figure 3 (a).
The instantaneous torque T can be calculated using equation (4) as a derivative of the coenergy W_c with respect to the relative displacement of the rotor θ [1] [2]. The results of these computations can be graphically observed in Figure 3 (b).

$$T = \frac{\partial W_c}{\partial \theta} \tag{4}$$

The magnetization curves displayed in Figure 3 (a) are extremely important because they offer important information about the performances of the machine. The area enclosed by the characteristic when the rotor moves for one conversion cycle (from unaligned to aligned position) represents the magnetic energy that is converted into mechanical energy. For this special case it can be observed that this area is not as big as it could be, mainly because the unaligned inductance, although it is linearly increasing it reaches a high value. As an improvement to this, special geometries could be developed so that the flux linkage to be increased in the aligned position and decreased in the unaligned one.
Another observation regarding the static torque curves can be made. It is easy to notice that towards the position of alignment and for higher values of the current the torque decreases. The explanation is that because the inductance tends to saturate for higher currents, its slope decreases. Assuming that the current is constant, the inductance is responsible for the variation of the coenergy, which in its turn is responsible for the torque production [2] [5]. A possibility to avoid this is to use materials with better ferromagnetic proprieties.
In addition to that, the magnetization and torque characteristics were used as look-up tables to build the mathematical model implemented in the Matlab/Simulink environment.

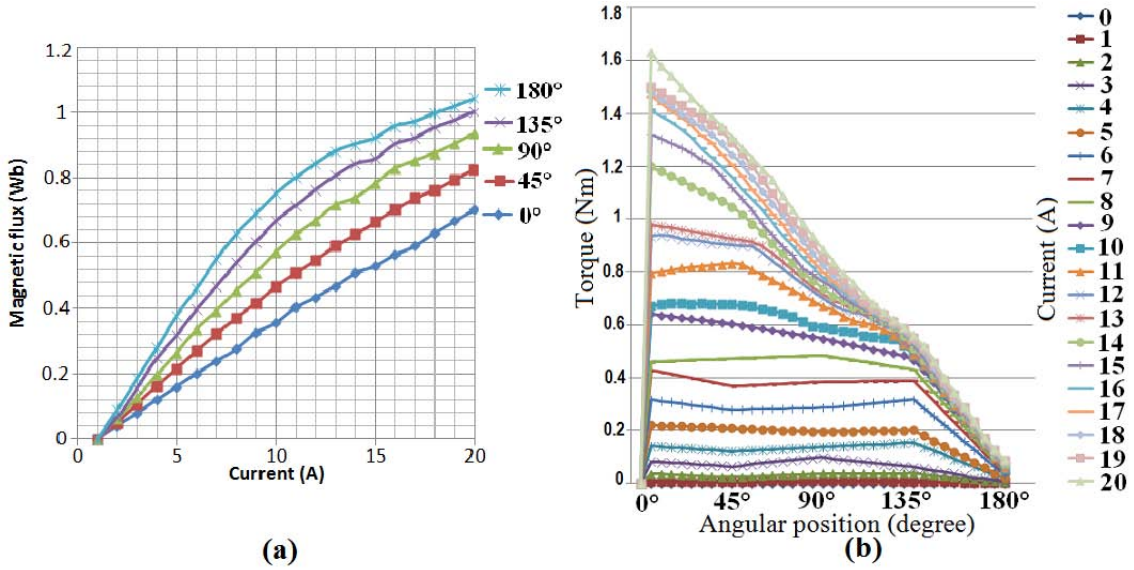

Figure 3: (a) Magnetic flux as a function of angular position and current (0°- unaligned, 180°- aligned), (b) Static torque curves as a function of angular position (0° to 180°) and current (0 to 20 Amperes).

4 Mathematical Model and Block Diagram

Two different systems are implemented in Simulink in order to model the behaviour of the SRM. One comprises the electromagnetic equations and the other the mechanical equations.
The voltage equation can be written as follows:

$$v = \frac{\partial \psi(i,\theta)}{\partial t} + Ri \tag{5}$$

where v is the supplied voltage, Ψ is the magnetic flux whose time variation represents the back EMF, R and i were already introduced as the resistance of the winding and the current that passes through it.

The mechanical system is characterized by the movement equation (6):

$$J\frac{d\omega}{dt} = T - T_L - B \tag{6}$$

where J represents the moment of inertia, ω- the angular speed, T- the developed torque, T_L- the load torque and B- the coefficient of viscosity.

The values for the produced torque and for the magnetic flux are approximated in the model by an interpolation-extrapolation technique from the static curves described earlier.

The SRM drive model implemented in Simulink is presented in Figure 4. Besides the two blocks for the electromagnetic system and for the mechanical system the model also makes use of an asymetric bridge type converter and a position sensor. The sensor has the role to provide a position feed-back to the look-up tables and to send command signals to the converter when the rotor is between the established conduction angles. The operation of the converter is simple. It receives command signals from the speed and current regulators and when the rotor is in the torque production area, that is for this specific case between 0 and 170 degrees, the source voltage is applied through the two transistors T1 and T2 to the winding. The rising slope of the current is determined by the time constant of the circuit. When the rotor is not between the two established conduction angles the transistors are turned-off and the energy stored in the magnetic field is permitted to flow back to the source through the diodes D1 and D2 [6] [7].

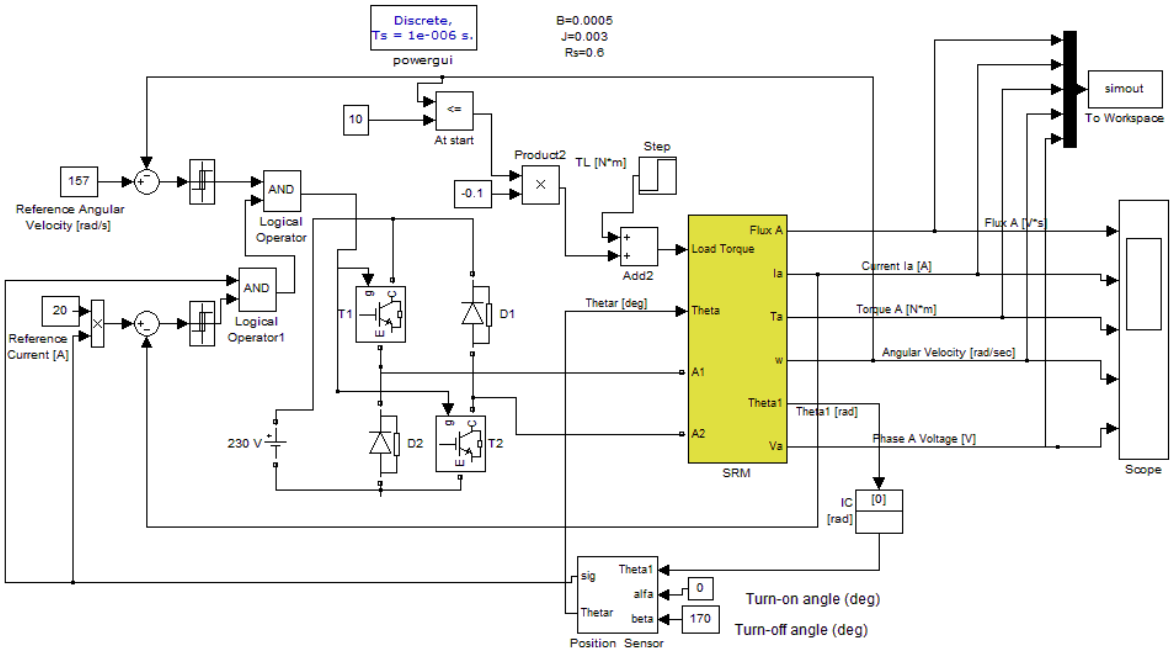

Figure 4: Block diagram of the SRM drive implemented in Simulink

5 Simulation Results

For both analyzed cases the coil resistance was set to R=0.6 (Ω), the momentum of inertia of the rotor to J=0.003 (Kg·m^2) and the coefficient of viscosity to B=0.0005 (N·m·s).

The observation is made that because the motor has a single-phase structure it is impossible to be started from any initial position. The solution implemented in these simulations was to apply a positive torque of 0.1 (Nm) until the rotor reaches the speed of 10 (rad/sec).

- *No-load start-up simulation –*

For this simulation the prescribed speed was 157 (rad/sec) and the reference current was set to 20 (A). The interest was in observing the transient of the motor during startup given the torque production capability and its momentum of inertia. The results shown in Figure 5 were obtained.

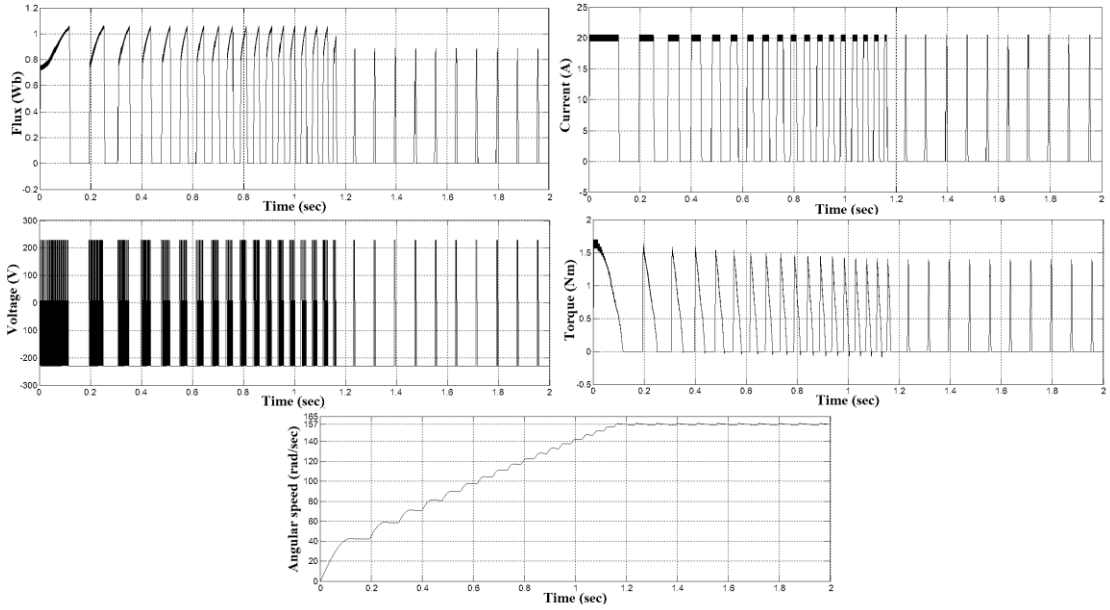

Figure 5: Waveforms for no-load condition

From the waveforms it is noticeable that the motor reaches the prescribed speed in approximately 1.2 seconds and after that it is maintained between the limits of (+0.5 and −0.5) with the help of a hysteresis block.

- *Under load simulation –*

The reference speed was set to 157 (rad/sec) and the reference current was set to 20(A). A load torque of 0.25 (Nm) was imposed after 1.2 (sec), the moment when the rotor reaches the prescribed speed.

The results presented in Figure 6 show that the torque produced by the motor and its momentum of inertia are enough to support the imposed torque and the resistive torque created by the coefficient of friction. The speed presents just a slight variation of approximately 4 (rad/sec) under its prescribed speed. This variation corresponds to the interval (170 − 360 degrees) where no torque is produced and the rotor rotates only as a consequence of its momentum of inertia. At the speed of 157 (rad/sec) the resistive torque created by the friction coefficient represents approximately 0.08 (Nm). It is worth mentioning that the momentum of inertia of the load was considered to be zero.

Another observation can be made regarding the high torque ripple. This is due to the fact that the geometry of the motor allows a torque production for only approximately half of a full rotation of the rotor. An improved variant would be a modular solution in which more such motors are placed on the same shaft offering an increased torque production area.

In addition, a high amount of this torque ripple is caused by the saturation of the inductance when the rotor approaches to the aligned position for high value of currents.

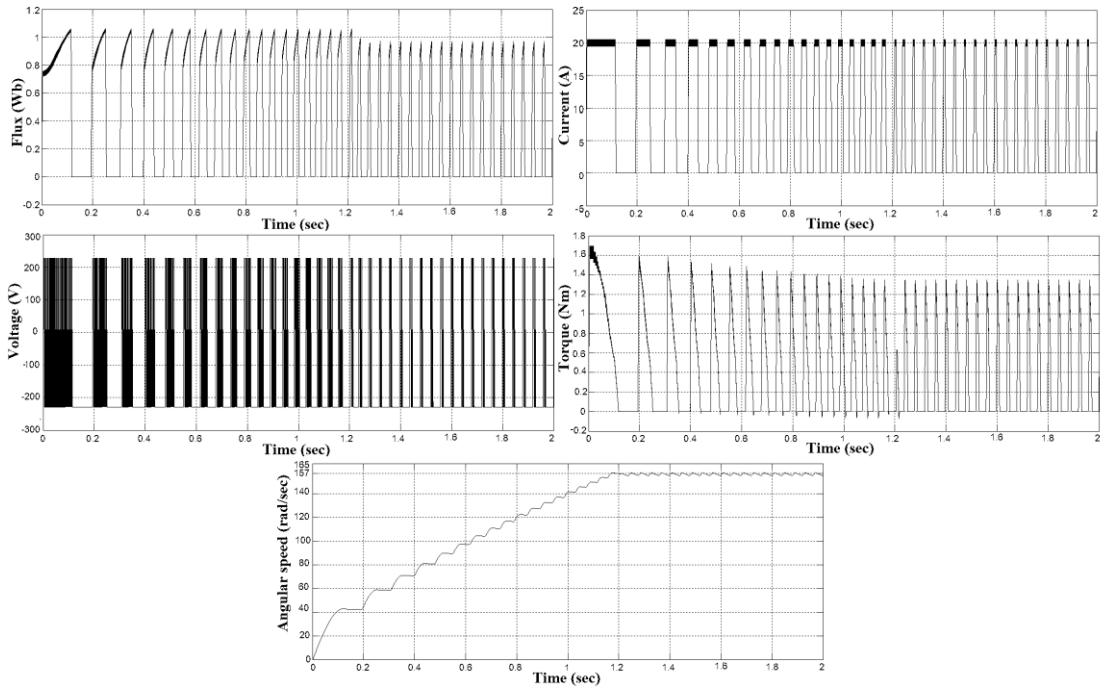

Figure 6: Waveforms for under load condition

6 Conclusions

This paper presented the transient and steady state analysis of an axial field single-phase single-pole switched reluctance motor prototype.

The magnetization characteristic for the motor was obtained by direct measurement and the torque characteristic was calculated as a derivative of the coenergy.

Although saturation of the inductance appears towards the position of alignment and that can cause a decrease of the torque it is advisable that the commutation to occur when the inductance is saturated so that the time constant of the circuit to permit a faster fall of the current to zero.

With adaptations of the geometry in order to obtain a greater ratio of the two extreme inductances this constructive variant can prove to be a good candidate for certain applications.

Acknowledgments - This paper was realized with the support of POSDRU CUANTUMDOC "DOCTORAL STUDIES FOR EUROPEAN PERFORMANCES IN RESEARCH AND INOVATION" ID79407 project funded by the European Social Found and Romanian Government.

References

[1] Al. Simion, *Special Electrical Machines for Automations (in Romanian),*Chisinau, Ed. Universitas, 1993.

[2] F. Soares and P.J. Costa Branco, "Simulation of a 6/4 Switched Reluctance Motor Based on Matlab/Simulink Environment," *IEEE Transactions on Aerospace and Electronic Systems,* vol. 37, no. 3, July 2001.

[3] T.J.E. Miller, "Optimal Design of Switched Reluctance Motors," *IEEE Transactions on Industrial Electronics,* vol. 49, no. 1, February 2002.

[4] I. A. Viorel et al., *Transverse Flux Machines – Their behaviour, design, control and applications,* Cluj-Napoca, Ed. Mediamira, 2003.

[5] R. Khrishnan, *Switched Reluctance Motor Drives – Modeling, Simulation, Analysis, Design and Applications,* Industrial Electronics Series, CRC Press, 2001.

[6] O. Dabija et al., *Modeling and Simulation of an axial field single-pole single-phase switched reluctance motor*, 13th International Conference on Optimization of Electrical and Electronic Equipment (OPTIM), 2012.

[7] I. Husain and S. A. Hossain, "Modeling, Simulation and Control of Switched Reluctance Motor Drives," *IEEE Transactions on Industrial Electronics,* vol. 52, no. 6, December 2005.

Aspects regarding the numerical analysis of the induction hardening process for spherical parts using a multilayer inductor

Mircea Nicolae ARION, Gabriel Remus CHEREGI, Vasile Darie SOPRONI and Carmen MOLNAR

University of Oradea, Faculty of Electrical Engineering and Information Technologies, Department of Electrical Engineering, 1-5University St 410087, Oradea, Romania; mnarion@gmail.com

Abstract. This paper deals with the numerical analysis of coupled electromagnetic and thermal field problem during the induction hardening process of spherical parts using a multilayer inductor. The numerical analysis is performed by using finite element method in order to determine the optimal design solution of the multi-layer induction coil. During analysis were considered different shapes of the inductor supposing different values for air gap between induction coils and layers. Results of the simulation will point out the influence of the electromagnetic field values on the thermal field distribution and also the required time for the process for each case analysed.

1 Introduction

Ones with the technological revolution from the last century, the new developed technologies with application in all industry allowed the development of new high quality materials. The induction hardening technologies are coming to answer to requests made by the auto motor subassembly manufacturers so as the provided parts to offer a high quality and reliability. This technologies allows the continuous control of the hardening process through penetration depth and the resulted product can provide a high hardness on the outside layer without alteration of the elasticity from the inside of the material [1].

Due to the complex geometry of the subassemblies was necessary to align the inductors shape to the geometric subassembly so as the electromagnetic induction hardened conversion rate to be increased. Research in the field point out that to increase the conversion efficiency of the inductor is necessary to try to adopt different innovative solutions [2], assumed solutions which assume the use of multilayer inductors used in order to increase the efficiency of induction heating process. In terms of inductor's section, we meet inductors with rectangular or circular section with a number of two- to n layers placed parallel or delayed between them [3].

Wishing to optimize the electromagnetic induction hardening process and also the phenomena which occurred during the induction heating process were developed numerical methods for eddy current problems, methods that are based on the use of different potential solutions.[4, 5, 6]. In this paper we study the optimization procedure of the inductor in order to be used as active tool for induction hardening process of a car towing ball. Due to the spherical geometrical shape of the subassembly which require the treatment, and in order to achieve high efficiency in the process is imposed the use of a multilayer inductor with a number of two layers with a number of one turn/layer in order to achieve the outer hardening of the assembly ball-hitch attachment.

Numerical analysis of eddy current problem under quasi-stationary electromagnetic field and thermal field that occur during the process [6], allow the increase of the efficiency ones with the reduction of the number of attempts. During numerical analysis were consider different constructive solutions so as the best solution can chosen and the final product to meet the requirements. Within the research process optimization is studied the shape of the multilayer

inductor used for the induction hardening of spherical subassemblies (Fig. 1). Due to the spherical geometrical shape of the subassembly treated, and the desire to achieve a high efficiency in the process, the used multilayer inductor will consists in a number of two turns which follow the outer surface of the hardened path for the rolling ball-hitch attachment assembly.

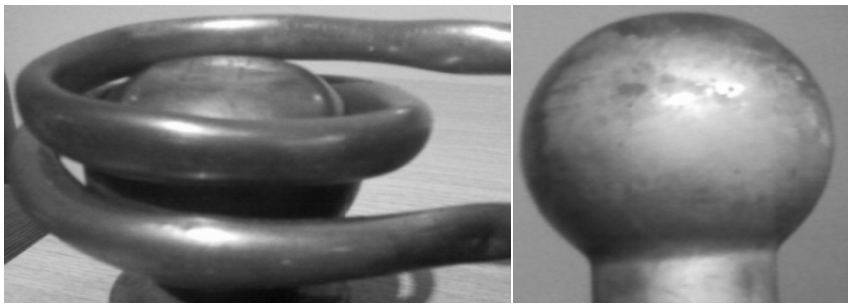

Fig 1. Sphere – inductor assembly

2 Field problem formulation

Due to the complexity of the electromagnetic field equation, majority of the field problem can be only solved by numerical methods, where the solutions represent an approximation of the real field. From this reason we consider the sinusoidal state, which is valid for non-linear media. The cvasiliniar approximation is considered, where magnetic permeability is corrected for each iteration with respect to magnetic induction. The computational domains are imposed for each analysed case in order to solve the electromagnetic field question. Maxwell's law describe the electromagnetic field, and its fundamental equations accrue [6]:

$$rot\,\nu rot\,\underline{\boldsymbol{A}} + \sigma(j\omega\underline{\boldsymbol{A}} + grad\,\underline{V}) = 0 \quad in\,\Omega_C \tag{1}$$

$$rot\,\nu rot\,\underline{\boldsymbol{A}} = \underline{\boldsymbol{J_0}} \quad in\ \Omega_0 \tag{2}$$

From equation (1) accrue:

$$div\,\sigma(j\omega\underline{\boldsymbol{A}} + grad\,\underline{V}) = 0 \tag{3}$$

The scalar electric potential $\underline{V}$ must be defined only for the conducting domains Ω_C, and on the edge of the conducting domain Ω_C the normal component to the surface of the current density needs to be zero:

$$\sigma(j\omega\underline{\boldsymbol{A}} + grad\,\underline{V})\boldsymbol{n} = 0 \quad on\,\partial\Omega_C \tag{4}$$

To insure the uniqueness for the ($\boldsymbol{A}$,V) formulae we have to impose an additional condition for the magnetic vector potential $\underline{\boldsymbol{A}}$ and this can be described by the Coulomb gauge:

$$div\,\underline{\boldsymbol{A}} = 0 \tag{5}$$

During analysis were considered the following boundary conditions:

$$\boldsymbol{n}\times\nu\,rot\,\underline{\boldsymbol{A}} = \boldsymbol{g} \qquad \text{on } S' \tag{6}$$

$$A_n = 0 \qquad \text{on } S' \tag{7}$$

$$\boldsymbol{A}_t = \boldsymbol{f} \qquad \text{on } S'' \tag{8}$$

3 Finite element method

The numerical solution is obtained by using the Galerkin technique. The equations (1), (2), (5) are projected on a set of functions $\boldsymbol{N}_k$, ϕ_k, V_k. For the $\boldsymbol{N}_k$ function is considered the null boundary condition and $rot\boldsymbol{N}_k$ are linear independents. The ϕ_k functions has constant values arbitrariness on S_i, i=1,2,...,n-1 and null values on S_n. The $\boldsymbol{N}_k$ and ϕ_k function are defined on Ω, and V_k on Ω_C.

$$\underline{\boldsymbol{A}} = \boldsymbol{N}_0(t) + \sum_{k=1}^{n_N} \alpha_k(t)\,\boldsymbol{N}_k + \sum_{k=1}^{n_\phi} \gamma_k(t)\,grad\,\phi_k\,, \tag{9}$$

$$\underline{V} = \sum_{k=1}^{n_v} \beta_k(t) V_k \tag{10}$$

where $\boldsymbol{N}_0$ carry out the boundary condition (8).

4 Thermal field formulation

In order to determine the solutions of the thermal field problem must be solved the thermal diffusion equation:

$$-\,\mathrm{div}\,\lambda \mathrm{grad} T + c\frac{\partial T}{\partial t} = p \tag{11}$$

where λ represents the thermal conductibility and p is the volume density of the power transformed from the electromagnetic form to heat and c is the volume thermal capacity. The associated boundary condition to equation (11) is:

$$-\lambda \frac{\partial T}{\partial n} = \alpha\left(T - T_e\right) \tag{12}$$

where α is the convective thermal coefficient and T_e the temperature outside of the conducting domain and the initial condition for the temperature is considerate: $T(0) = T_{in}$.

The Crank-Nicholson technique is used for the time discretization of equation (11), and the finite element method for space discretization..

5 Numerical application and results

In this study we consider a half finished spherical ferromagnetic part placed into an multilayer inductor set on the induction heating system. The problem presents axial symmetry, so as the numerical analysis is performed only for a quarter of the computational domain.

Wishing to achieve the improvement in conversion efficiency through the cross section of the inductor used in the electromagnetic induction hardening process of spherical subassemblies will consider two particular cases involving the use of a multilayer inductor with the same dimensions geometrical and electrical parameters with circular section first and rectangular section in the second case. Is assumed known the operating frequency of the installation as 10 [kHz] and the current density through inductor as 34 [A/mm2], with similar characteristic sizes of induction hardening equipment used for experimental measurements.

The spherical part studied consist in a tow ball presented in figure 1 made from stainless steel AISI-SAE-4145, with the following properties:

The resistivity ρ [Ωm] variation with the temperature $\rho(\theta)$ is described by the function:

ρ[Ωm] = 8,69779674E-13 $\cdot\theta^2$ + 4,78235404E-10 $\cdot\theta$ + 1,56565488E-07, for. $\theta \in [20, 780]$°C, and

ρ[Ωm] = - 2,01190476E-13 $\cdot\theta^2$ + 7,12976190E-10 $\cdot\theta$ + 6,54785714E-07,for. $\theta \in [780,1400]$°C

The ***B-H*** relationship variation with temperature is described by the following equation:

$$B(H, \theta) = \mu_0 H + (2/\pi)\cdot J_{s0} \cdot arctg\,[\pi(\mu_{r0} - 1)\,\mu_0 H/(2J_{s0})]\cdot\{1\text{-}exp[(\theta - \theta_c)/C]\}$$

In the first case of analysis the induction coil is realised from a number o two turns delayed between them (one turn /layer). First case of analysis presented in fig. 2 will assume that the induction coil cooled with water has circular cross section of 10 [mm]. The considerate distance between turns is 9 [mm] and 0.2 [mm] between layers. The lower turn will have the same coordinate over y axis as the side central edge of the ball with 4 [mm] air gap between induction coil and the ball.

Results of the simulation will point out the influence of the electromagnetic field up on the induction heating process. In this sense is presented the magnetic field action on the process and the thermal field distribution in the ball during the hardening process. These values are significant in order to determine the austenitic state of the material and depth of the hardened layer.

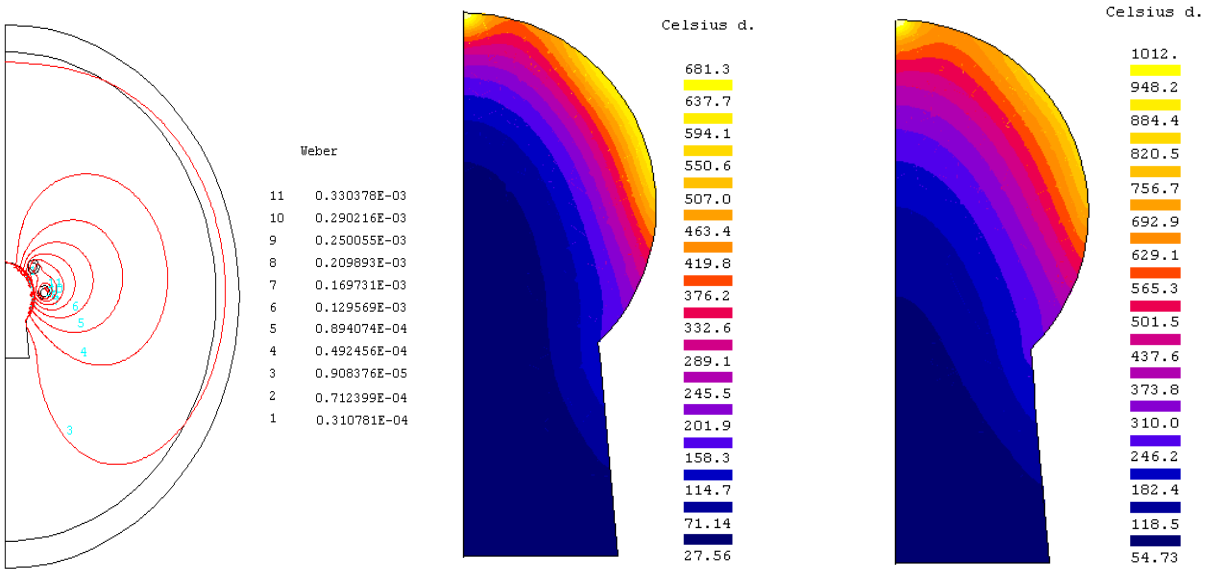

a. Magnetic field b. Thermal field map during the process t= 4.11 [s] c. Thermal field map at the end of the process t= 8 [s]

Fig 2. Field distribution in the first case of analysis for the circular cross section of the induction coil

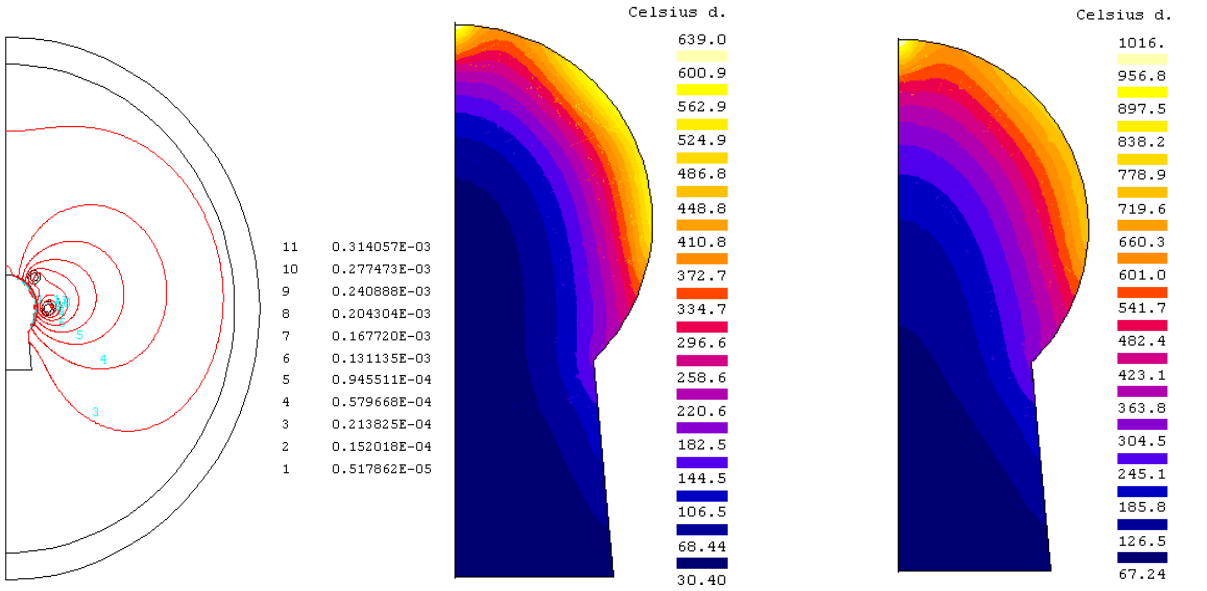

a. Magnetic field b. Thermal field map during the process t= 4.12 [s] c. Thermal field map at the end of the process t= 8.02 [s]

Fig.3 Field distribution in the second case of analysis for the circular cross section of the induction coil .

Analysing the obtained result presented in figure 2 can be observed the fact that the induction coil cannot provide a uniform distribution of the thermal field over the superior side of the ball. In order to obtain a uniform distribution of the thermal field over the superior side of the ball will be considerate a different position associated for each turn of the induction coil. From this reason the distance between turns will be increased to 13 [mm] and from layers to 2

[mm] in order to cover a higher side surface with better results in the thermal field distribution over the hardened surface.

In the second case analysed with it results presented in figure 3, can be observed a better distribution of the thermal field over the superior side of the ball, so as the whole running area between the tow ball and the coupling head will be hardened as is required by the technological process. The finished product presents a hardened layer at the surface, maintaining the elasticity of the material inside it so as the part won't be breakable. By knowing the fact that usually the induction coils with rectangular cross section can provide a better yield will assume the fact that we have a rectangular cross section multilayer induction coil in the analysis process. We will consider a rectangular cross section multilayer induction coil 10X10[mm] with its turns in the same position as the last case of analysis. The obtained results, presented in figure 4 will point out the field distribution during this process. Analysing the obtained numerical result can be observed a couple of high temperature points because of the geometry position of the induction coil compared to the spherical part. From this reason the air gap between the inductor and the part suffers considerable changes during hardening process with involvement in field distribution.

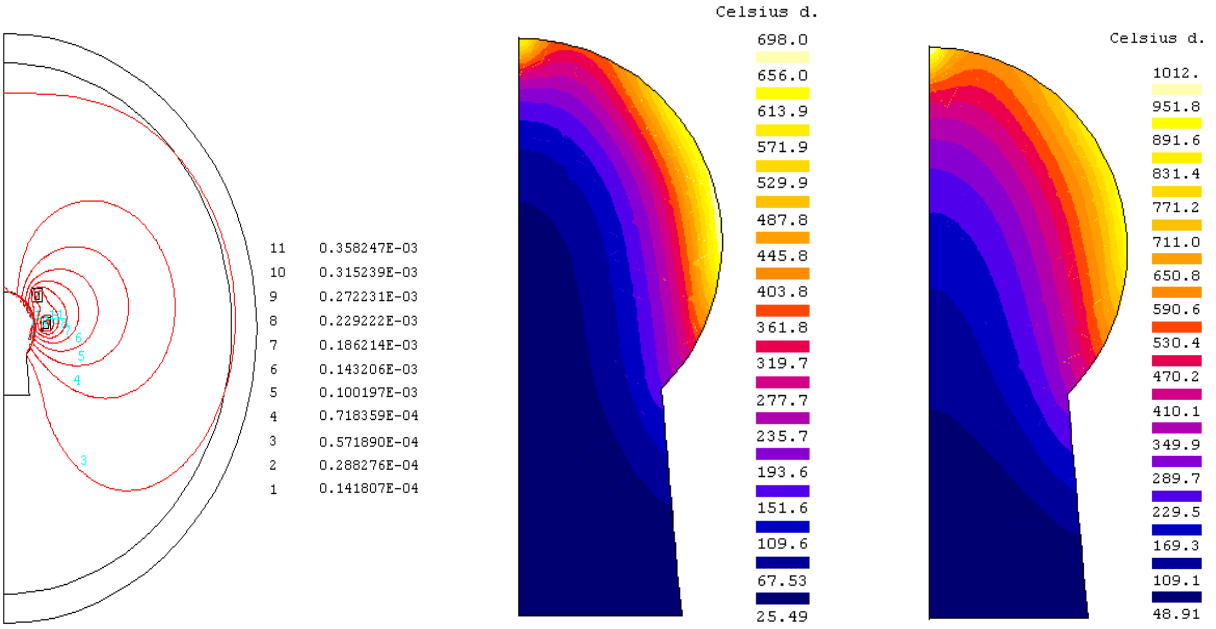

a. Magnetic field

b. Thermal field map during the process t= 3.52 [s]

c. Thermal field map at the end of the process t= 7.02 [s]

Fig. 4. Field distribution in the case of analysis with rectangular cross section of the induction coil .

6 Conclusion

Through numerical modelling, using numerical programs to solve the proposed application is obtained a full study of complex phenomena that occur during electromagnetic induction, study addressed to a specific problem of analysis for the heating processes through eddy currents, viewing the results and different possibilities for analysis of the model.

The precise knowledge of the electromagnetic field allows the analysis and the optimal design of the electro-thermal equipment. Usually this information is not available through analytic methods so as we have to apply mathematical methods in order to solve the complex electromagnetic field problem to determine the unknown values in the discrete representation.

In the paper is studied the geometrical influence of the induction coil up on the problems that appears during the practical applications from industry. During researches we intend to establish the optimal structural geometry of a multilayer inductor used for induction hardening treatment of spherical parts, taking into account the increase of the conversion efficiency. Was noticed the fact that the inductors cross section must be selected in accordance with the geometry of the processed part. Was evaluated the influence of the geometry of the induction coil over the field distribution. In order to point out the influence of the shape of induction coil up on the thermal field distribution were considered two different shapes for the cross section of the induction coil: circular and rectangular.

From this point o view, in the case of analysis for induction hardening process of spherical parts, in order to achieve a uniform distribution of the electromagnetic and thermal field over the upper side of the spherical part is recommended the use of circular cross section of the multilayer inductor. In this case, the induction coil and the half finished product presents a constant air gap between the induction coil and the spherical part through the parallelism of the edges of the induction coil and the spherical part.

The use of a multilayer inductor assure the increase of the electromagnetic energy conversion, and through the increas of the number of layers will result a more uniform flow distribution of the field in the processed product. The inductor can be realised in different shapes and through a construction artifice by increasing the number of layers will be achieved a decrease in the inductor resistance in the same time with significant increase in efficiency.

Acknowledgments - This work was co financed from the European Social Fund through Sectoral Operational Programme Human Resources Development 2007-2013, project number POSDRU/89/1.5/S /56287 „*Postdoctoral research programs at the forefront of excellence in Information Society technologies and developing products and innovative processes*", partner University of Oradea..

References

[1] Pavel Karban, Martina Donátová, *Continual induction hardening of steel bodies,* Mathematics and Computers in Simulation, Volume 80, Issue 8, April 2010, Pages 1771-1782.

[2] Ming-Shyan Huang, Yao-Lin Huang. *Effect of multi-layered induction coils on efficiency and uniformity of surface heating,* International Journal of Heat and Mass Transfer 53, M.-S. Huang, Y.-L. Huang (2010) 2414–2423,

[3] R. Bowtell and P. Robyr1, *Multilayer Gradient Coil Design,* Journal of Magnetic Resonance 131**,** 286–294 (1998) Article NO. MN981369

[4] F. Cajner, B. Smoljan, D. Landek, *Computer simulation of induction hardening,* Journal of Materials Processing Technology 157–158 (2004) 55–60,

[5] Matej Kranjc, Anze Zupanic , Damijan Miklavcic, Tomaz Jarm. *Numerical analysis and thermographic investigation of induction heating,* International Journal of Heat and Mass Transfer 53 (2010), 3585–3591

[6] F. Hantila et all - *The numeric computation of eddy currents*, Ed. ICPE, Bucharest, 2001 (in Romanian).

Modelarea câmpului electromagnetic cuplat cu cel termic într-un aplicator de microunde și utilizarea unui algoritm de optimizare

Simina (VICAȘ) COMAN , Teodor LEUCA, Ovidiu COMAN
Universitatea din Oradea, str.Universității, nr.1; simina_vicas@yahoo.com

Abstract. În lucrarea de față se prezintă aspecte legate de modelarea numerică a câmpului electromagnetic cuplat cu cel termic în instalațiile cu microunde utilizând softul Comsol Multiphysics și un algoritm de optimizare - full factorial utilizând softul Minitab. Obiectul cercetărilor l-a constituit procesarea semințelor pentru a obține în final un nivel optim de umiditate pentru o bună depozitare.

1 Introducere

Evoluția softurilor de modelare numerică din ultimii ani reprezintă un pas important in conceperea și realizarea unor instalații performante și oferirea unei imagini realiste a fenomenelor și proceselor de încălzire. Softul de modelare numerică Comsol Multiphysics oferă posibilitatea realizării simulării numerice a câmpului electromagnetic și termic în sistemele cu microunde utilizând metoda elementelor finite [1].

Dezvoltarea tehnologiilor, tendința de a obține instalații cât mai performante au dus la necesitatea proiectării experimentale a sistemelor. În domeniul ingineriei electrice proiectarea experimentală a devenit importantă prin utilitatea ei în proiectarea de echipamente industriale inteligente. Utilitatea aplicării algoritmilor genetici în rezolvarea problemelor inginerești a fost reliefată de către mulți cercetători în lucrările lor [2], [3], [4], [5].

Avantajul principal al uscării produselor granulare în câmp de microunde este încălzirea simultană și transferul de masă prin care are loc reducerea conținutului de umiditate a semințelor la un nivel optim pentru o bună păstrare, depozitare. Studii privind efectul puterii microundelor asupra produselor granulare, folosind diferiți parametrii de intrare au fost realizate de către S.O. Nelson, S.Trabelsi, M. Hemis, M. Sempe, R. Filgueira W.Lewis [6].

2 Model Matematic

În sistemele de încălzire, distribuția energiei electromagnetice în câmp de microunde are la bază ecuațiile lui Maxwell.

Modelul realizat rezolvă ecuațiile lui Maxwell pentru problema de câmp electromagnetic și ecuația de transfer termic pentru distribuția temperaturii.

Ecuația câmpului electric pentru port este:

$$\nabla \times (\mu_r^{-1} \nabla \times \mathbf{E}) - k^2 (\varepsilon_r - j\sigma/\omega\varepsilon_0)\mathbf{E} = 0 \qquad (1)$$

unde: - μ_r este permeabilitatea relativă [H/m];
- $\mathbf{E}$ reprezintă câmpul electric [V/m];
- ∇ reprezintă operatorul Laplacian;
- ε_r reprezintă permitivitatea relativă [F/m];
- ε_0 reprezintă permitivitatea vidului [F/m];
- σ reprezintă conductivitatea [S/m];
- k reprezintă conductivitatea termică [W/mK];
- ω reprezintă pulsația unghiulară (Hz);

Problema termică este rezolvată cu ecuația de transfer termic, descrisă de următoarea relație:

$$\rho C_p \frac{\partial T}{\partial t} + \nabla \cdot (-k\nabla T) = Q(\mathbf{E}) \quad (2)$$

unde: - C_p reprezintă căldura specifică [J/kgK];

- k reprezintă conductivitatea termică [W/mK];
- Q reprezintă densitatea de volum a puterii disipate/absorbite [W/m^3];
- ρ reprezintă densitatea [kg/m^3];
- T reprezintă temperatura [°C].

Parametrii electrici ce prezintă importanță la procesarea în câmp de microunde a materialelor dielectrice sunt constanta dielectrică $\varepsilon^{'}$ și factorul de pierderi dielectric $\varepsilon^{"}$, reprezentând partea reală și imaginară a permitivității relative complexe:

$$\varepsilon_r = \varepsilon^{'} - j\varepsilon^{"} \quad (3)$$

3 Modelarea câmpului electromagnetic și termic

Analiza câmpului electromagnetic și termic în regim de microunde s-a realizat utilizând softul de modelare numerică Comsol Multiphysics. Realizarea analizei numerice are drept scop determinarea temperaturii materialului dielectric, semințe de grâu în funcție de anumite date de intrare.

Rezultatele numerice obținute în procesul de uscare s-au realizat pentru semințe de grâu cu umiditate de 26%, fiind descrise de proprietățile dielectrice - =3.47 și =0.62. Având în vedere că dielectricul procesat este compus dintr-un amestec de semințe, aer și apă, s-au calculat pe baza mediei volumelor ocupate de fiecare in parte, proprietățile de material pentru un amestec de materiale.

În cadrul modelului s-au utilizat proprietățile de material ale aerului =0 si = =1. În geometria realizată, pereții ghidului de undă cât și ai cavității au fost considerați din aluminiu, interiorul celor două incinte (ghid de undă și cavitate) fiind definite drept aer. Simulările numerice s-au realizat pentru un timp de procesare de 10 minute (600 de secunde) având ca și valori ale puterii microundelor de 10 W și o frecvență a microundelor de 2.45GHz.

Folosind softul de modelare s-au considerat geometria ghidului de undă și a cavității instalației de laborator din cadrul Centrului de Cercetare și Inginerie Tehnologică în Conversia Energiei Electromagnetice, Facultatea de Inginerie Electrică și Tehnologia Informației. În studiul efectuat s-a presupus că sarcina nu se află în mișcare. Dimensiunile aplicatorului sunt x = 109.22 mm, y = 300mm și z = 54.6 mm. În interiorul aplicatorului a fost introdusă sarcina într-un recipient din teflon, transparent la microunde având dimensiunile lungime= 85 mm, lățime =60 mm și înălțime= 43mm. Poziția sarcinii absorbante în interiorul aplicatorului este x=20 mm, y=120 mm și z=20 mm (figura 1).

Detalierea geometriei realizate și distribuția câmpului electric printr-o secțiune transversală prin model este prezentată în Figura 1. Maximul intensității câmpului electric poate fi observat în Figura 1 în mijlocul dielectricului, atingând valoarea de 2378.1 V/m.

În figura 2 se prezintă meshul geometriei realizate, putându-se observa și dielectricul din interiorul aplicatorului.

În figura 3 se prezintă distribuția câmpului termic prin 25 de secțiuni realizate în planul zx în dielectric.

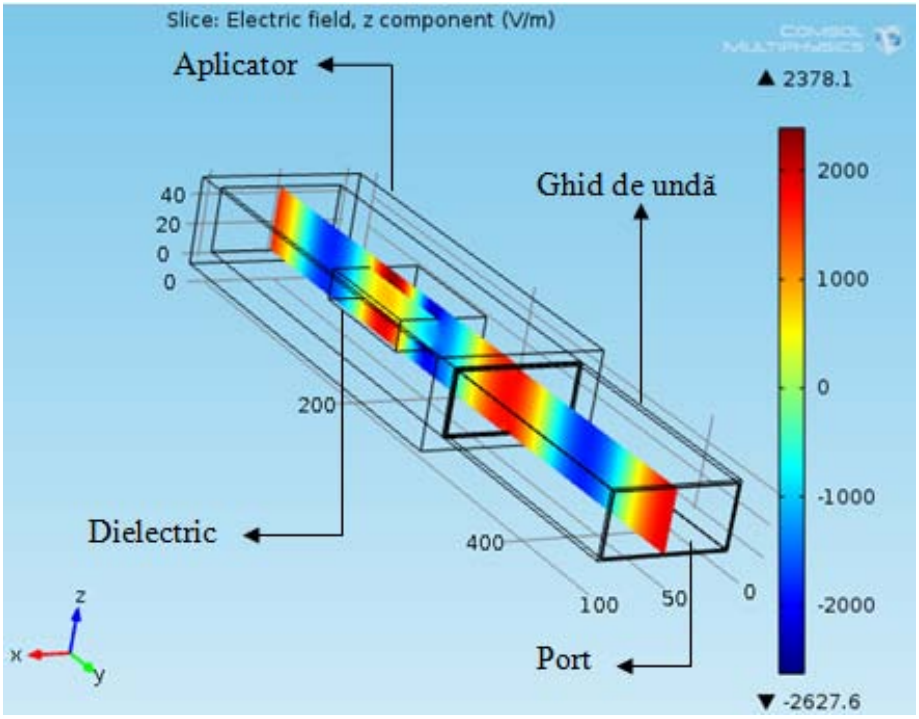

Figura 1. Distribuția câmpului electric în secțiune transversală prin aplicator, dielectric și ghid de undă

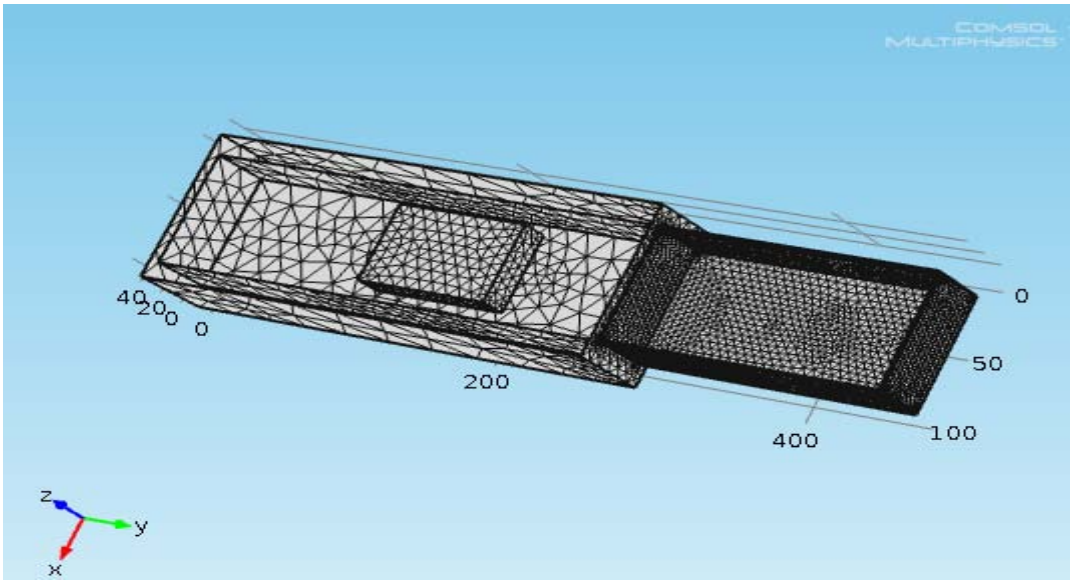

Figura 2. Meshul geometriei realizate

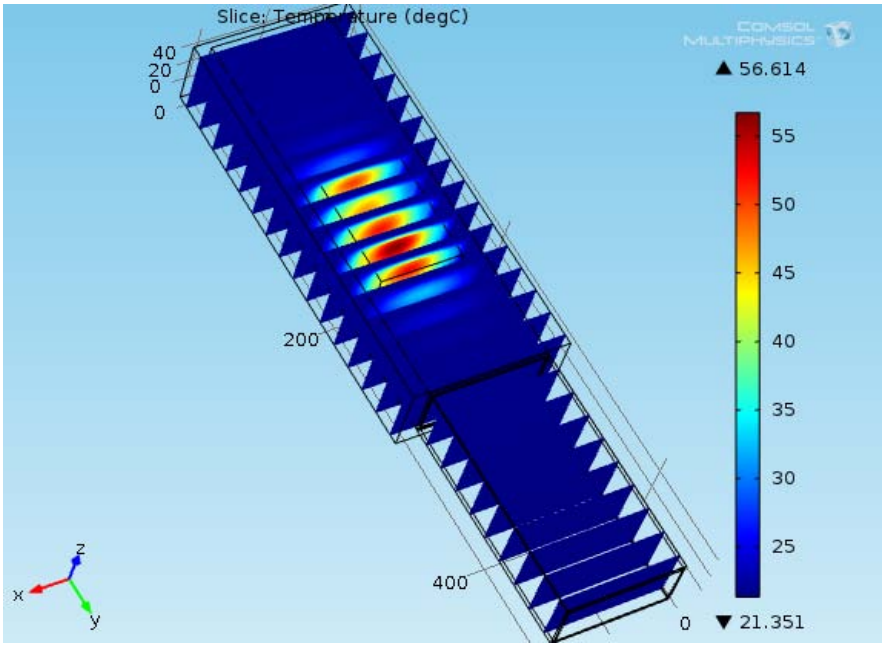

Figura 3. Distribuția câmpului termic prin sectiuni realizate în dielectric

4 Utilizarea algoritmului de optimizare - full factorial

Având in vedere faptul ca pentru anumite pozitii ale dielectricului in aplicator si valori ale puterii microundelor datele de iesire nu satisfac anumite cerinte impuse, ne propunem să găsim mărimile de intrare și poziția dielectricului pentru care atingem mărimi de ieșire impuse. Prin variabilele de intrare ne referim la pozitia dielectricului pe axa Oy, Oz si valoarea puterii microundelor, necesară pentru a usca dielectricul. Cerințele impuse pentru datele de ieșire sunt: temperatura calculată în dielectric nu trebuie să depășească valoarea de 70°C (peste această valoare calitatea semințelor este afectată), puterea totală absorbită și valoarea intensității câmpului electric să fie maxime. Constantele problemei sunt: timpul de procesare de 10 minute (600 de secunde), frecvența microundelor - 2.45GHz și poziția dielectricului pe axa Ox (20 [mm]). Pentru această optimizare, luând în calcul variabilele problemei și răspunsul așteptat am ales tipul de experiment - full factorial cu 2 nivele.

Întrucât avem un număr de 3 variabile de intrare, folosind datele generate de Minitab pentru realizarea optimizării, se vor realiza un număr de 23 rulări în softul Comsol Multiphysics. Pentru generarea tabelului în Minitab s-au ales pentru fiecare dintre cele trei variabile, valori de maxim și minim astfel: pentru pozitia pe axa Oz s-a ales minimul- 9 mm și maximul 13mm, pentru poziția pe axa Oy minimul ales a fost 20 mm și maximul de 200 mm, iar valorile de maxim și de minim pentru puterea microundelor au fost 5W, respectiv 10W. Datele obținute în urma simulărilor realizate în Comsol Multiphysics au fost atașate la tabelul realizat - Tabelul 1 (cu valori de minim și maxim).

Tabelul 1

Valorile obținute în Comsol Multiphysics

Nr.	Oz [mm]	Oy [mm]	P [W]	T[°C]	Putere Abs.[W]	E[V/m]
1	13	20	10	58.51	3.88	4090.1
2	9	20	5	52.84	2.64	3312.2
3	9	200	10	81.25	5.23	4710.3
4	9	200	5	53.31	2.66	3310
5	13	200	10	58.82	3.92	3613.2
6	13	20	5	40.25	1.92	2872.2
7	13	200	5	40.45	1.96	2554.9
8	9	20	10	80.95	5.19	4711.4

* T reprezinta temperatura calculata in dielectric [°C]
Putere Abs. reprezinta puterea totala absorbita [W]
E reprezinta maximul intensitatii campului electric [V/m]

Întrucât valorile obținute în urma rulărilor se maximizează, s-a propus o formulă de calcul pentru temperatură ca diferența dintre maximul impus și valoarea obținută prin modelare: $T_{limitare}$=70-T. Înlocuid valoarea temperaturii în Tabelul 1 se vor obține datele:

Tabelul 2

Conversia pentru temperatură

Nr.	Oz [mm]	Oy [mm]	P [W]	Tlimitare[°C]	Putere Abs.[W]	E[V/m]
1	13	20	10	11.49	3.88	4090.1
2	9	20	5	17.16	2.64	3312.2
3	9	200	10	-11.25	5.23	4710.3
4	9	200	5	16.69	2.66	3310
5	13	200	10	11.18	3.92	3613.2
6	13	20	5	29.75	1.92	2872.2
7	13	200	5	29.55	1.96	2554.9
8	9	20	10	-10.95	5.19	4711.4

Introducând Tabelul 2 în softul Minitab s-au prelucrat datele și s-a studiat gradul de interacțiune dintre factori și răspunsuri.
Pentru a realiza optimizarea în Minitab s-a folosit funcția factorial - Response Optimizer, obținându-se valorile:

Soluția Globală:
Oz = 0,689242
Oy = 0,676768
P = -0,252525

Astfel, pentru a afla valorile finale găsite de Minitab este necesară conversia în valorile definite de noi. În urma conversiei pentru poziția dielectricului pe axa Oz s-a obținut valoarea de 12.37 mm, pentru poziția dielectricului pe axa Oy s-a obținut valoarea 170.84 mm și pentru puterea microundelor valoarea de 6.87W.

Introducând aceste valori în softul Comsol și rulând s-au obținut următoarele valori de ieșire: temperatura maximă în dielectric - T=47.82°C, Puterea totală absorbită=2.76W și Maximul Intensității Câmpului E = 4074.3 V/m.

5 Concluzii

Analizând datele obținute în urma optimizării putem concluziona: temperatura calculată în dielectric, T=47.82°C, este potrivită pentru a usca semințele fără a afecta calitatea acestora; valoarea intensității câmpului electric, de 4074.3 V/m, este mare, iar puterea totală absorbită prezintă o valoarea bună, de 2.76W. Totuși pe viitor, ne propunem, să realizăm optimizări, folosind și alte tipuri de experimente oferite de softul Minitab, pentru a verifica soluția oferită de tipul de experiment full factorial cu 2 nivele. Cercetarea viitoare va urmări obținerea unei absorbții mai mari de putere în dielectric și o valoare a temperaturii calculate în dielectric mai ridicată, pentru o mai bună uscare, care să respecte condițiile de temperatură impuse.

Referinţe

1. Raj J.D., S. Birla, K. Pitchai, J. Subbiah, D. Jones - Modeling of Microwave Heating of a Rotating Object in Domestic Oven, *Excerpt from the Proceedings of the 2011 Comsol Conference*, Boston, 2011;
2. Younes M., M. Rahli, M. Abid, Kandouci Malika - Optimisation d'écoulement des puissances par algorithmes intelligents, *Revue Roumaine des Sciences Techniques– Électrotechnique et Électroenergetique*, 52, 1, pp. 3–12, Bucureşti, 2007;
3. Leuca T., Novac Mihaela - Optimization of eddy current heating process using genetic algoritms, *Revue Roumaine des Sciences Techniques– Électrotechnique et Électroenergetique*, 54, 4, pp.355-363, Bucureşti, 2009;
4. Petrescu Camelia, Ferariu Lavinia, R. Olaru - Optimization of ferrofluid actuator using evolutionary algorithms and finite element method, *Revue Roumaine des Sciences Techniques– Électrotechnique et Électroenergetique*, 54, 1, pp. 77-86, Bucureşti, 2009;
5. Morega A.M. , Morega Mihaela, M. A. Panait -Structural optimization of a thermoelectric generator by numerical simulation, *Revue Roumaine des Sciences Techniques– Électrotechnique et Électroenergetique*, 55, 1, pp.3-12, Bucureşti, 2010;
6. Hemis M., R. Choudhary, D. G. Watson - A coupled mathematical model for simultaneous microwave and convective drying of wheat seeds, *Biosystems Engineering*, *Elsevier*, 202-209, 2012;
7. Bandici Livia - Modelarea numerică a câmpului electromagnetic şi termic cuplat în instalaţiile de încălzire în câmp de microunde, *Editura Mediamira*, Cluj - Napoca, Romania, 2005;
8. Maghiar T., Şoproni D.– *Tehnica încălzirii cu microunde*, Editura Universităţii din Oradea, 2003;
9. Hănţilă F.I., T. Leuca, C. Ifrim - *Electrotehnică teoretică*, Editura Electra Bucureşti, 2002;
10. Mathews P.G. - *Design of experiments with Minitab*, ASQ Quality Press, 2004;

Procesarea unor semifabricate din lemn în câmp de radiofrecvență

Marcela Ioana LAZA (BULC), Dragoş SPOIALĂ, Gabriel CHEREGI
Universitatea din Oradea, Universității 1,410087, Oradea;România, ioana_marcela@yahoo.com

Abstract. În cadrul acestei lucrări sunt prezentate aspecte legate de încălzirea/uscarea unor semifabricate din lemn într-un aplicator de radiofrecvență, realizându-se modelarea câmpului electromagnetic cuplat cu cel termic pentru determinarea parametrilor procesului de încălzire/uscare în câmp de radiofrecvență.
Pentru evaluarea performanței procesului s-au urmărit valorile temperaturii în dielectric, timpul de încălzire/uscare si umiditatea.

1 Introducere

Datorită avantajelor oferite de utilizarea curenților de înaltă frecvență în procesele de încălzire/uscare precum şi a calității produselor rezultate, în cadrul lucrării se încearcă procesarea unor semifabricate din lemn de stejar în câmp de radiofrecvență.

Biryukov 1961, spune că primii care au sugerat şi implementat în industrie încălzirea lemnului cu ajutorul curenților de înaltă frecvență, au fost cercetatorii de origine rusă, care au observat că datorită caracteristicilor unice ale lemnului de a fi încălzit din interior spre exterior, pot obține rezultate foarte bune în uscarea, lipirea, împregnarea şi presarea acestuia. [1]

Având în vedere faptul că lemnul este în general un material dielectric eterogen, se poate spune că proprietățile sale dielectrice variază în funcție de parametrii de lucru.[2]

Proprietățile dielectrice sunt: constanta dielectrică relativă ($\varepsilon_r^{'}$), factorul de pierderi dielectrice relative ($\varepsilon_r^{''}$) şi tangenta unghiului de pierderi ($tg\delta$). Permitivitatea relativă complexă a materialelor dielectrice se exprimă [3]:

$$\varepsilon_r = \varepsilon_r^{'} - j\varepsilon_r^{''} \tag{1}$$

Tangenta unghiului de pierderi $tg\delta$ este definită ca raportul dintre factorul de pierderi dielectrice relative ($\varepsilon_r^{''}$) şi constanta dielectrică relativă ($\varepsilon_r^{'}$) [3]:

$$tg\delta = \frac{\varepsilon_r^{''}}{\varepsilon_r^{'}} \tag{2}$$

Conform A.C. Metaxas 1974 şi W.R. Tinga 1970, parametrii care afectează aceste proprietăți dielectrice sunt: umiditatea, densitatea, temperatura, frecvența, conductivitatea electrică, conductivitatea termică, căldura specifică şi adâncimea de pătrundere [4], [5].

2 Materiale şi metode

Ecuațiile lui Maxwell ce reglementează interacțiunea câmpului electromagnetic cu proprietățile dielectrice ale materialului sunt [6]-[10]:

$$rot\underline{\mathbf{H}} = \sigma\underline{\mathbf{E}} + \varepsilon\frac{\partial\underline{\mathbf{E}}}{\partial t} \tag{3}$$

$$rot\underline{\mathbf{E}} = -\mu\frac{\partial\underline{\mathbf{H}}}{\partial t} \tag{4}$$

unde, $\underline{\mathbf{E}}$ şi $\underline{\mathbf{H}}$ reprezintă intensitatea câmpului electric respectiv intensitatea câmpului magnetic, iar σ, ε şi μ reprezintă conductivitatea, permitivitatea şi permeabilitatea.

Pentru modelarea aplicatorului de radiofrecvență sunt folosite următoarele ecuații:

$$rot\underline{\mathbf{H}} = \sigma\underline{\mathbf{E}} + j\omega\varepsilon\underline{\mathbf{E}} \tag{5}$$

$$rot\underline{\mathbf{E}} = -j\omega\mu\underline{\mathbf{H}} \tag{6}$$

unde, ω este frecvența unghiulară, iar j este operatorul complex.

Relația de legătură între densitatea de curent $\underline{\mathbf{J}}$ şi proprietățile materialelor dielectrice este:

$$\underline{\mathbf{J}} = \left(\sigma + \varepsilon_0\varepsilon_r^{''}\omega\right)\underline{\mathbf{E}} + j\varepsilon_0\varepsilon_r^{'}\underline{\mathbf{E}} \tag{7}$$

Componenta pierderilor dielectrice importantă în procesul de încălzire/uscare în câmp de radiofrecvență precum şi factorul de putere disipată pe unitatea de volum P_v [W/m^3] pentru pierderile dielectrice se pot scrie după cum urmează:

$$\underline{\mathbf{J}} = \varepsilon_0\varepsilon_r^{''}\omega\underline{\mathbf{E}} \tag{8}$$

$$P_v = \varepsilon_0\varepsilon_r^{''}\omega\underline{\mathbf{E}}^2 \tag{9}$$

Încălzirea materialelor dielectrice este guvernată de ecuația lui Fourier:

$$\rho C_p\frac{\partial T}{\partial t} + grad\left(-kgradT\right) = P_v \tag{10}$$

unde, ρ este densitatea, C_p este căldura specifică, k este conductivitatea termică, iar T este temperatura.

Creşterea de temperatură în volum (ΔT), se poate calcula cu relația:

$$\Delta T = \frac{P_v t}{M_a C_p} \tag{3}$$

unde, M_a este masa materialului, iar t este timpul.

Din ecuația de mai sus putem spune că toată energia electrică este convertită în energie termică. Modelarea numerică a câmpului electromagnetic cuplat cu cel termic, oferă distribuția reală a potențialului electric, densitatea de putere precum şi temperatura în dielectric.

3 Modelarea numerică

Pentru optimizarea procesului de încălzire/uscare în câmp de radiofrecvență s-au realizat modelări numerice pe baza metodei hibride: metoda elemntului finit (FEM) şi metoda elementelor de frontieră (BEM), utilizând un program scris în limbaj fortran intitulat FEM-BEM-RF.for, produs al Centrului de Cercetare şi Inginerie Tehnologică în Conversia Energiei Electromagnetice de la Universitatea din Oradea, unde problema de modelare numerică a fost abordată şi de către alți doctoranzi şi cercetători, dezvoltându-se acest program cu următorul algoritm:

- se calculează matricele din modelarea BEM a câmpului exterior sarcinii;
- se calculează matricea de rigiditate ce reprezintă condiția de frontieră mixtă pentru problema de câmp electromagnetic din interiorul sarcinii;
-se construieşte matricea sistemului FEM cu condiții de frontieră BEM;
-se rezolvă sistemul algebric obținut;
-se determină pierderile în dielectric ;
-la următorul pas de timp se recalculează matricele de cuplaj;

-se reiau etapele de la pasul de timp precedent.

Programul FEM-BEM-RF.for a fost aplicat unui dielectric de formă dreptunghiulară, dispus într-un aplicator de tip "staggered-through field" cu 5 perechi de electrozi. Dielectricul reprezentat printr-un semifabricat din lemn de stejar cu proprietățile dielectrice $\varepsilon_r^{'} = 8.6$ şi $tg\delta = 0.1$.

Frecvența de lucru este 13,56 [MHz], iar tensiunile de alimentare au fost 1610 [V], 1690 [V] şi 1820 [V], fiind stabilită o limita de temperatură de 70 °C, urrmărindu-se echipotențialele câmpului electric dar şi timpul de încălzire/uscare până la limita de temperatură impusă.

În figurile de mai jos sunt prezentate echipotențialele câmpului electric şi izotermele pentru dielectricul staționar şi pentru dielectricul în mişcare. Se consideră că mişcarea porneşte din poziția în care jumătate din sarcină intră în spațiul dintre electrozi şi se termină când acea jumătate părăseşte spațiul dintre electrozi.

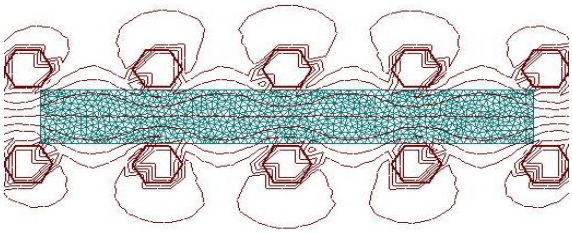

Figura 1. Echipotențialele câmpului electric când dielectricul este staționar

Figura 2. Valorile izotermelor când dielectricul este staționar la tensiunea anodica de 1820 [V]

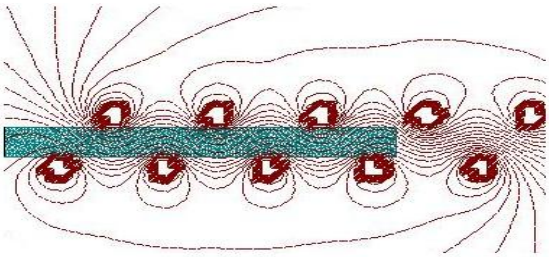

Figura 3. Echipotențialele câmpului electric la intrarea dielectricului în aplicator

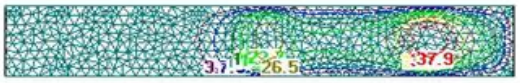

Figura 4. Valorile izotermelor la intrarea dielectricului în aplicator la tensiunea anodica de 1820 [V]

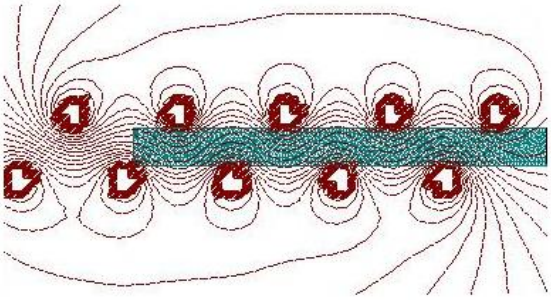

Figura 5. Echipotențialele câmpului electric la ieşirea dielectricului din aplicator

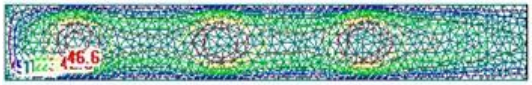

Figura 6. Valorile izotermelor la ieşirea dielectricului din aplicator la tensiunea anodica de 1820[V]

Programul de calcul FEM-BEM-RF.for, permite analiza numerică a procesului de încălrire/uscare a semifabricatului din lemn de stejar fiind prezentate în cele ce urmează curbele de variație ale temperaturii şi umidității în timp, la diferite tensiuni anodice.

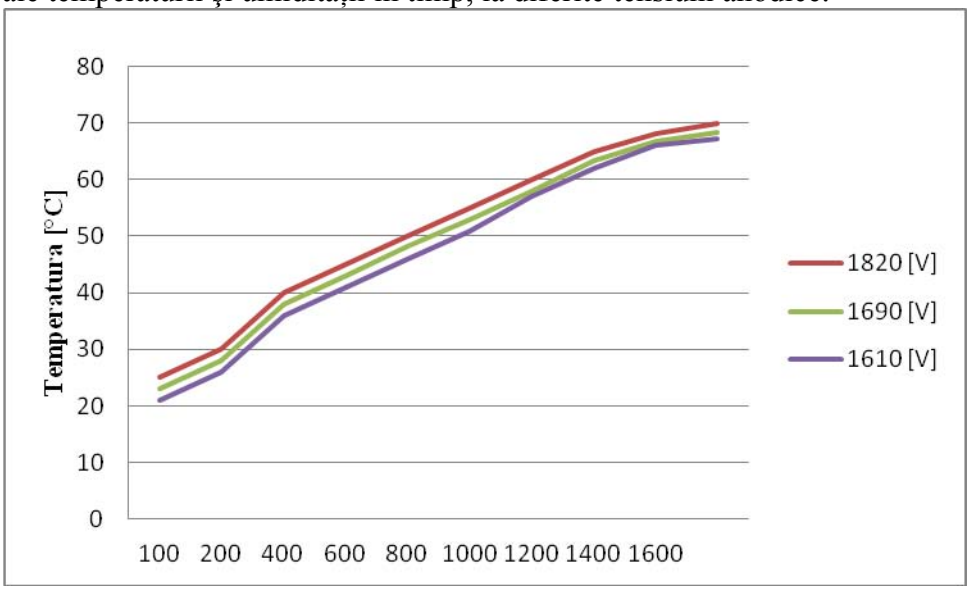

Figura 7. Variația temperaturii în raport cu timpul la diferite tensiuni pentru semifabricatul din lemn de stejar

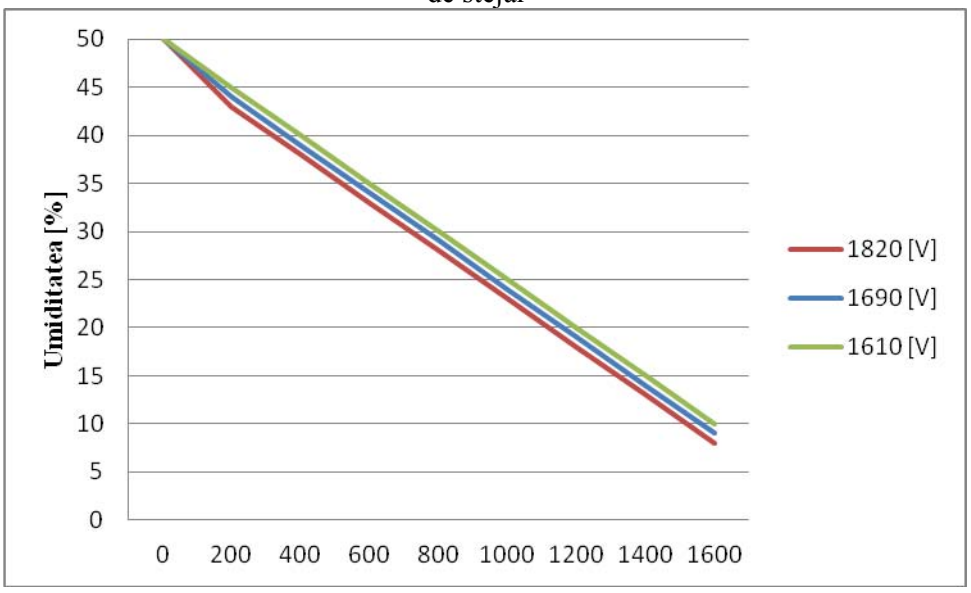

Figura 8. Variația umidității în raport cu timpul la diferite tensiuni pentru semifabricatul din lemn de stejar

4 Determinări experimentale

Determinările experimentale au fost realizate cu instalația de radiofrecvență a Centrului de Cercetare şi Inginerie Tehnologică în Conversia Energiei Electromagnetice de la Universitatea din Oradea, Figura 9, frecvența de lucru fiind de 13,56 MHz. La partea experimentala s-au folosit probe de semifabricat din lemn de stejar cu dimensiunile L=90[mm], l=10[mm] şi h=5[mm] cu o umiditate inițială de aproximativ 50%.

Determinarea umidității initiale si finale de-a lungul fiecarui proces experimental s-a facut prin măsurări periodice şi repetate, folosindu-se un umidometru de tip Testo 616, iar pentru măsurarea câmpului de temperatură s-a folosit o cameră termică Fluke 32i.

Figura 9. Instalația de laborator

Tabel 1. Temperatura şi umiditatea finală în urma determinărilor experimentale la diferite tensiuni

Tensiunea anodică U_A [V]	Timpul [s]	Temperatura [°C]	Umiditatea [%]
1610	1600	59,3	16
1690	1600	63	12
1820	1600	65,8	10

În figurile următoare sunt prezentate distribuțiile de temperatură în timpul procesului de încălzire/uscare pentru proba de stejar înainte de încălzire şi după încâlzire la diferite tensiuni anodice.

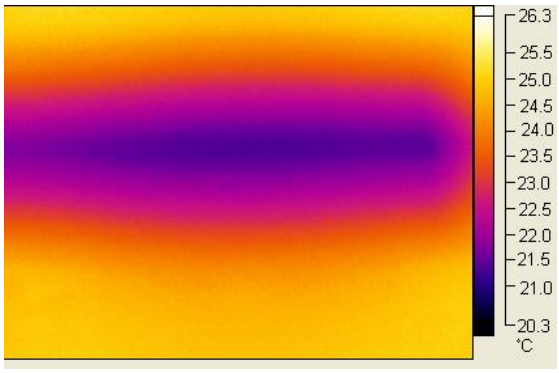

Figura 10. Distribuția temperaturii pentru proba de stejar înainte de încălzire

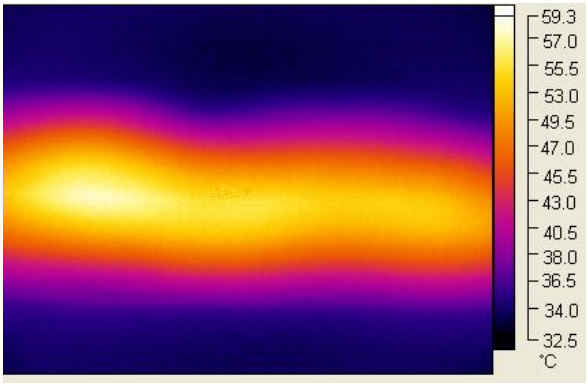

Figura 11. Distribuția temperaturii pentru proba de stejar la tensiunea de 1610 [V]

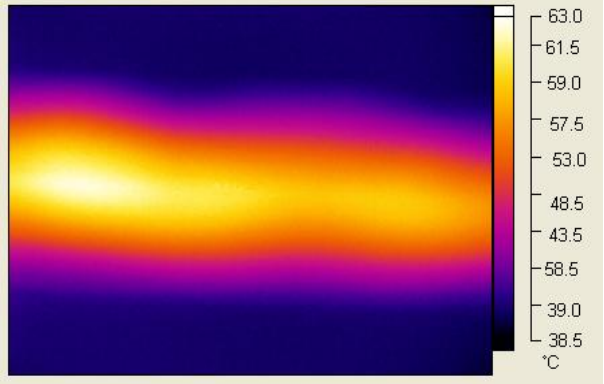

Figura 12. Distribuția temperaturii pentru proba de stejar la tensiunea de 1690 [V]

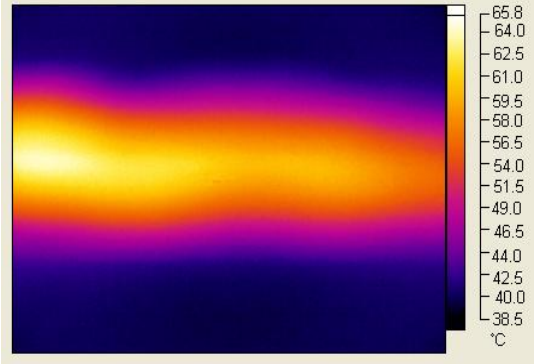

Figura 13. Distribuția temperaturii pentru proba de stejar la tensiunea de 1820 [V]

5 Concluzii

.

- Principalul avantaj al încălzirii în câmp de radiofrecvență constă în faptul că distribuția câmpului electromagnetic în interiorul sarcinii este mult apropiată de distribuția uniformă.
- Utilizarea metodei hibride FEM-BEM la anliza câmpului electric a permis utilizarea unei rețele de discretizare doar pentru semifabricatul din lemn de stejar, constantă în timpul deplasării şi valabilă atât pentru problema de câmp electric cât şi pentru cea de difuzie termică.

- Pe baza confruntarii cu modelarea numerică, unde prin limita de temperatură impusă de 70 °C s-a obținut un timp de încălzire/uscare de aproximativ 1600 de secunde, s-au constatat experimental similitudini în ceea ce priveşte timpul de expunere a probei de semifabricat din lemn de stejar la toate valorile tensiunii anodice.
- În timpul determinărilor experimentale, datorită limitei impusă de timp de 1600 s, nu s-a constat nici o degradare a probelor de semifabricate din lemn de stejar.
- În urma comparațiilor cu deteminările experimentale se constată validarea programului FEM-BEM-RF.for în 2D, utilizat în lucrare.

Aprecieri – This work was partially supported by the strategic grant POSDRU 107/1.5/S/77265 (2010) of the Ministry of Labor, Family and Social Protection, Romania, co-financed by the European Social Fund – Investing in people.

Referințe

[1] Biryukov, V. A., Dielectric heating and drying of wood, GLBI Goslesbumizdat, Moskva-Leningrad 1961
[2] Helmuth Resch, High-Frequency electric current for drying of wood – historical perspectives, Maderas, Ciencia y Tecnologia 8(2): 67-82, 2006
[3] Robert F. Schiffmann, Microwave and Dielectric Drying, Handbook of Industrial Drying, 2006
[4] A.C. Metaxas, Transactions of the International Microwave Power Institute, 2:19-47 (1974), Manassas, Virginia
[5] W.R. Tinga, Proceedings of the International Microwave Power Institute Short Course for Users of Microwave Power, Manassas, Virginia, 1970, pp. 19-29
[6] G. Tivari et.al., Analysis of radio frequency (RF) power distribution in dry food materials, Journal of Food Engineering 104, 548-556,2011
[7] V. Komarov et.al., Permittivity and Measurements, Encyclopedia of RF an Microwave Engineering, Edited by Kai Chang, John Wiley & Sons, Inc, 2005
[8] D. Stuerga, Microwave-Material Interactions and Dielectric Properties, Key Ingredients for Mastery of Chemical Microwave Processes, Microwave in Organic Synthesis, Second edition. Edited by A. Loupy, WILEY-VCH Verlag GmbH & Co., 2006
[9] Birla, S.L., Wang, S., & Tang, J., Computer Simulation of radio frequency heating of model fruit immersed in water. Journal of Food Engineering, 84(2),270-280.2008
[10]G. Brodie, Simultaneus heat and moisture diffusion during microwave heating of moist wood, Applied Engineering in Agriculture, Vol. 23(2): 179-187,2007.

Analiza comparativă privind utilizarea unor programe de specialitate pentru validarea proiectării unor transformatoare de mare putere

Dorinel CONSTANTIN
SC INAS SA, Str. N. Romanescu 37C, Craiova; office@inas.ro

Petre-Marian NICOLAE
Universitatea din Craiova, Bvd. Decebal 107, Craiova; http://elth.ucv.ro/

Abstract. În ultimii 20 de ani au apărut în industria constructoare de transformatoare, foarte multe programe capabile să facă validări de produse după un model geometric proiectat. Foarte multe dintre aceste programe oferă două tipuri de module: 2D şi 3D. Astfel se naşte întrebarea: ce variantă alegem? Acest articol tratează din punct de vedere al rezultatelor în urma rezolvării unui model de transformator proiectat, alegerea uneia dintre cele două variante şi validarea acestuia.

Introducere

Programul ANSYS oferă utilizatorilor pentru validarea transformatoarelor de putere module cu o mare acurateţe a rezultatelor, uşurinţa în utilizare, intuitive şi create pentru a determina cei mai importanţi parametrii: câmpul electromagnetic, densitatea de curent, pierderile totale în miez, temperatura, etc. Pentru calculul electromagnetic, ANSYS recomandă produsele Maxwell 2D şi Maxwell 3D, produse recent introduse şi în mediul de lucru Workbench, putându-se astfel realiza infinite aplicaţii prin co-simulare şi cuplare cu alte module. Inginerii implicaţi în munca de proiectare şi validare a transformatoarelor au posibilitatea fie de a crea modelul geometric direct mediul de lucru Maxwell, utilizând instrumentele de design ale acestuia, fie să importe geometria dintr-un alt soft de specialitate.

Transformatorul 325 MVA

Transformatorul la care se va face referire în acest articol este un transformator impregnat în ulei, cu o putere aparentă 325 MVA, trifazat cu 5 coloane. Miezul feromagnetic este construit din tole din oţel electrotehnic laminate la rece, cu cristale orientate, având 31 trepte, 5 trepte de izolaţie cu hârtie up-gradată, 2 spaţii de răcire pentru circulaţia uleiului şi încă una în centrul acestuia. De altfel, transformatorul are 3 înfăşurări: înfăşurarea de înaltă tensiune, înfăşurarea de joasă tensiune şi înfăşurarea de reglaj, cea din urmă fiind împărţită în două semibobine. Bobinele de înaltă tensiune au fiecare câte 690 de spire, bobinele de joasă tensiune au fiecare câte 55 spire, iar bobinele de reglaj au fiecare câte 10 galeţi şi 45 spire. Tipul de conexiune al transformatorului este YNd11. O altă particularitate a acestui transformator o constituie decupăturile miezului feromagnetic aflate la jugul superior şi inferior, cu rolul de a facilita transportul şi de asemenea reducerea de material.

Tabelul 1: Parametrii nominali ai transformatorului

		Înfăşurarea IT	Înfăşurarea JT
1.	Puterea aparentă	195 / 260 / 325 MVA	
2.	Sistemul de răcire	ONAN / ONAF / ONAF	
3.	Variaţia de tensiune	330 kV – 430 kV	17.5 kV +/- 10 %

Calculul electromagnetic s-a realizat pentru 3 tipuri de încărcări ale transformatorului:

a. încărcare minimă; $U_n = 330\,kV$;

b. încărcare 50 %; $U_n = 400\,kV$;

c. încărcare 100 %; $U_n = 430\,kV$.

Modul de realizare a modelelor geometrice

a. Geometria 2D – a fost creată folosind doar dreptunghiuri şi funcţiile de unire, substracţie şi intersecţie. De altfel, s-au ales ca şi materiale, cupru pentru bobine, aer pentru mediul înconjurător şi pentru miez s-a creat un nou material, în măsura în care aveam curbele esenţiale ale acestuia: dependenţa B-H şi dependenţa B-P (Fig. 2). Pentru a aproxima cât mai bine valorile principalelor mărimi, se va introduce o „adâncime" a modelului 2D în valoare de 153 cm.

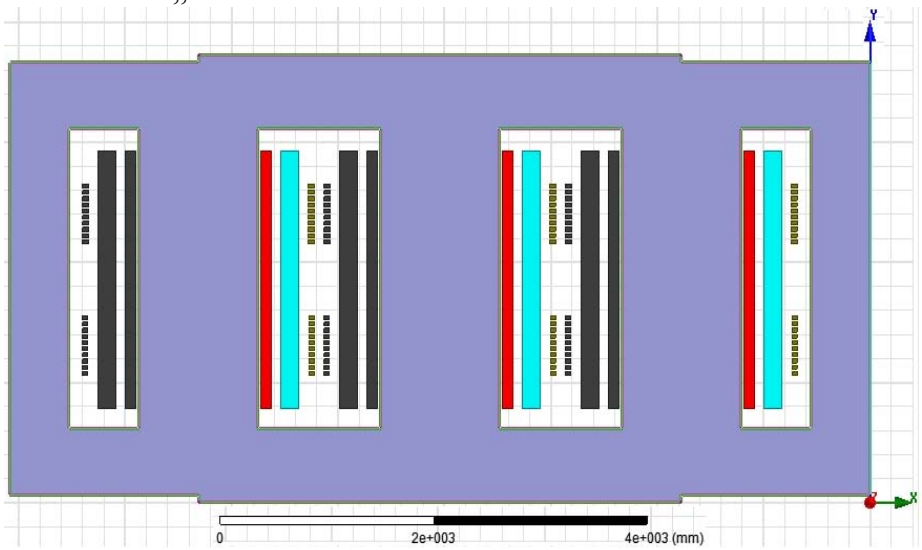

Fig 1: Geometria 2D a transformatorului 325 MVA

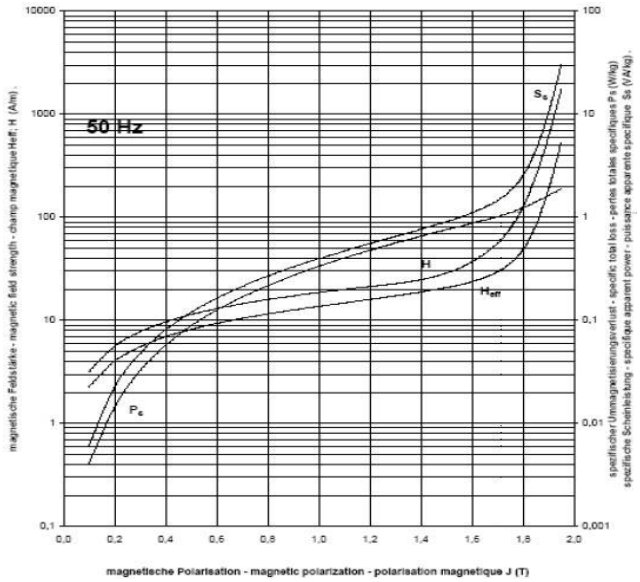

Fig 2: Curbele furnizate de producătorul miezului feromagnetic

b. Geometria 3D – a fost creată folosind doar paralelipipede dreptunghice, cilindri şi funcţiile de unire, substracţie şi intersecţie. Ca şi la geometria 2D, s-au ales ca şi materiale, cupru pentru

bobine, aer pentru mediul înconjurător, pentru miez s-a creat un nou material, la fel şi pentru izolaţie.

Tipul de problemă rezolvată a fost una de tip tranzitorie. Ca şi excitaţie s-a folosit o sursă sinusoidală de tensiune crescătoare în câteva cicluri, de altfel s-a introdus şi valoarea rezistenţelelor înfăşurărilor şi tensiunile maxime la pornire (Tabel 2).

Tabelul 2. Caracteristici tehnice ale transformatorului

	Valori rezistenţe		Surse de tensiune
	Înfăşurarea de Înaltă Tensiune	Înfăşurarea de Joasă Tensiune	IT şi JT
330 kV	0.4822 Ω	0.002306 Ω	1; 2; 3
400 kV	0.51 Ω	0.002306 Ω	1; 2; 3
430 kV	0.5504 Ω	0.002306 Ω	1; 2; 3

$$Vpeak\cdot\left[1-e^{(-50\cdot time)}\right]\cdot\cos\left(2\cdot\pi\cdot 50\cdot time+\left(2/3\cdot time\right)\right) \quad (1)$$

$$Vpeak\cdot\left[1-e^{(-50\cdot time)}\right]\cdot\cos\left(2\cdot\pi\cdot 50\cdot time+\left(2/3\cdot time\right)\right) \quad (2)$$

$$Vpeak\cdot\left[1-e^{(-50\cdot time)}\right]\cdot\cos\left(2\cdot\pi\cdot 50\cdot time+\left(4/3\cdot time\right)\right) \quad (3)$$

*Vpeak se modifică pentru înfăşurarea de înaltă teniune în funcţie de tensiunile fiecărui caz, 330, 400 şi 430 kV. Pentru înfăşurarea de joasă tensiune, tesiunea rămâne neschimbată pentru fiecare dintre cele 3 cazuri, adică 17.5 kV, întrucât tensiunea din secundarul transformatorului este constantă.

O altă caracteristică de intrare o constituie şi aranjarea în înfăşurări a bobinelor de înaltă tensiune, joasă tensiune şi reglaj, pentru fiecare dintre cele 3 analize. Trebuie menţionat faptul că reglajul se face pe înfăşurarea de înaltă tensiune, acesta intrând treptat în funcţiune. Primul caz este reprezentat de analiza transformatorului fără intervenţia înfăşurării de reglaj, al doilea caz îl constituie intrarea în funcţiune doar a 16 galeţi pe fiecare înfăşurare, iar cel de-al treilea caz îl reprezintă introducerea tuturor galeţilor înfăşurării de reglaj.

Rezultate ANSYS Maxwell 2D şi 3D

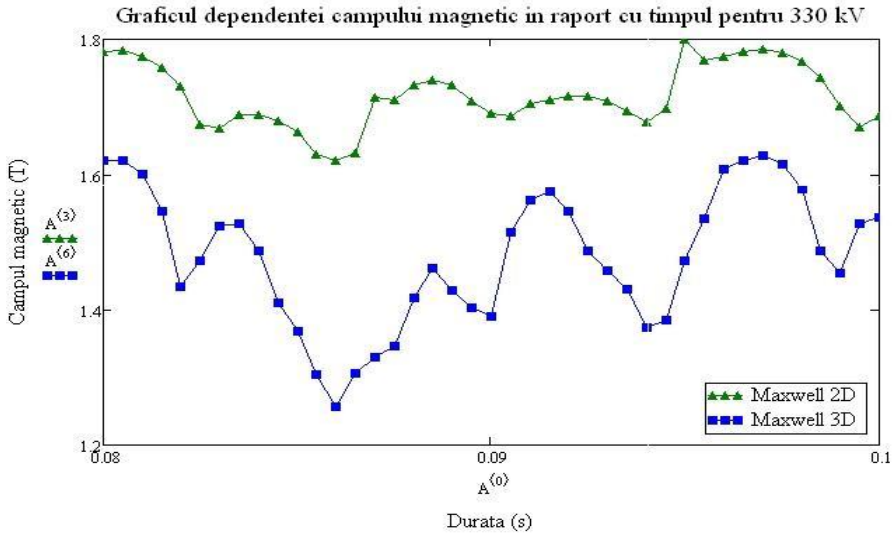

Fig 3: Distribuţia câmpului magnetic pentru tensiunea de 330 kV

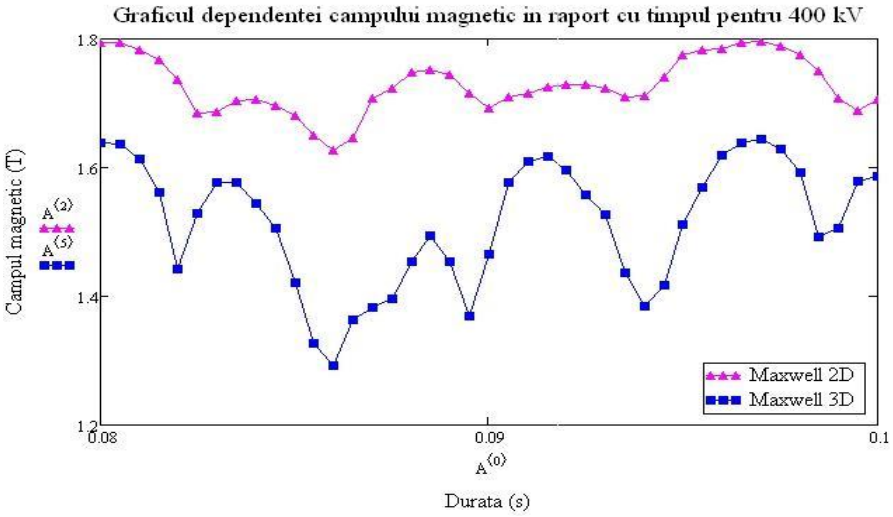

Fig 4: Distribuţia câmpului magnetic pentru tensiunea de 400 kV

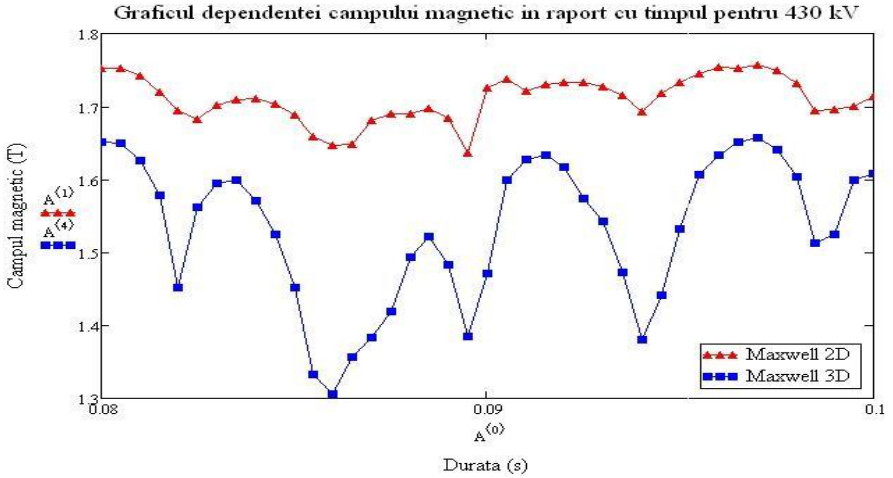

Fig 5: Distribuţia câmpului magnetic pentru tensiunea de 430 kV

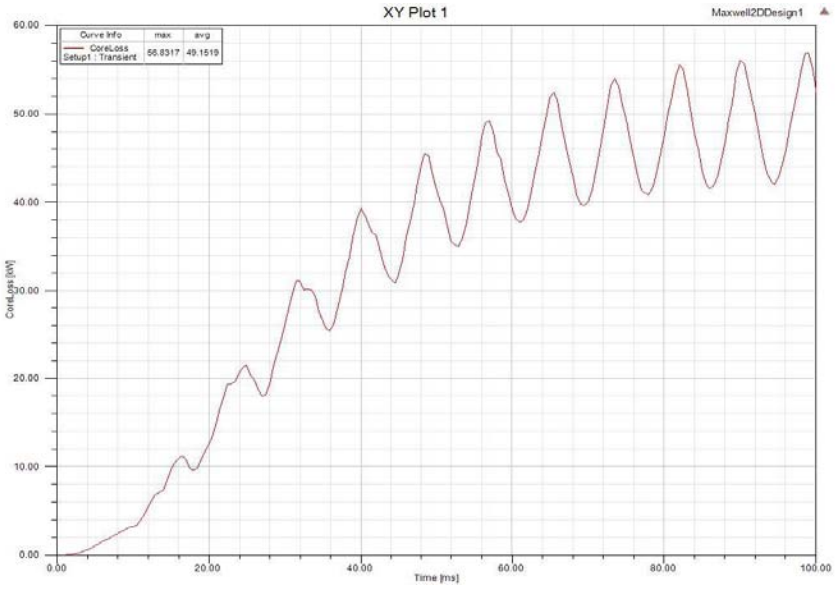

Fig 6: Nivelul de pierderi pentru tensiunea de 330 kV

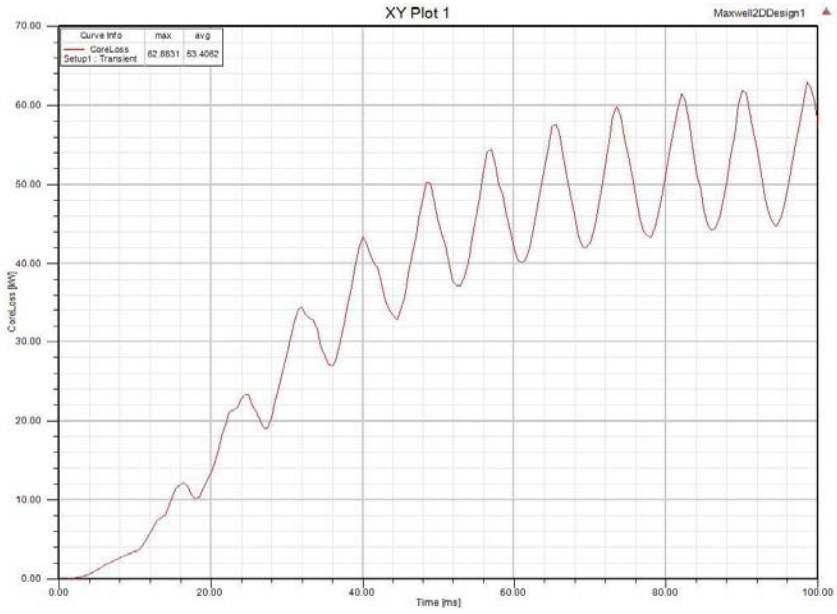

Fig 7: Nivelul de pierderi pentru tensiunea de 400 kV

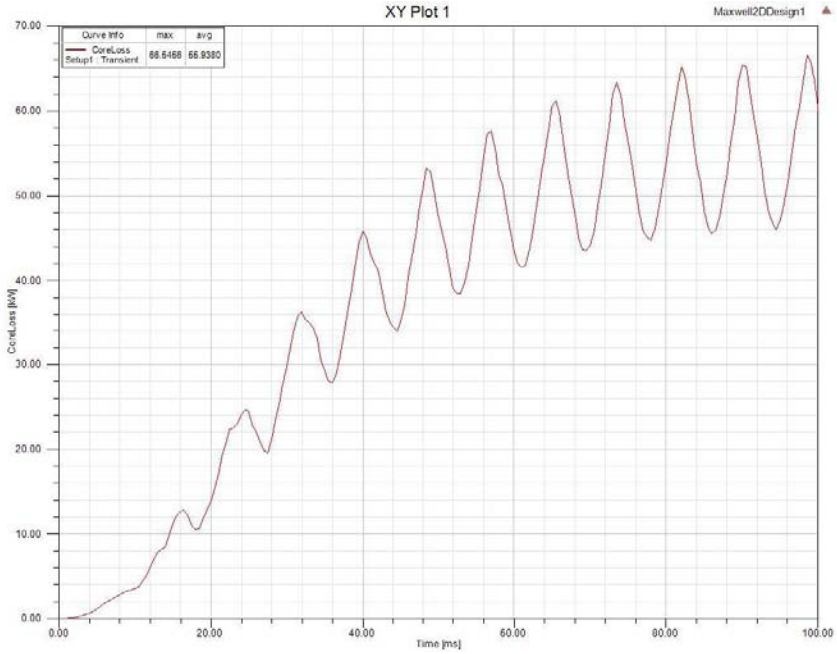

Fig 8: Nivelul de pierderi pentru tensiunea de 430 kV

Trebuie menţionat de altfel că analizele au fost făcute utilizând mediul de integrare al modulelor ANSYS Workbench 14.5, folosindu-se o unitate de procesare cu următoarele caracteristici:

- procesor: Intel Pentium 4, DualCore 3.2 GHz/procesor;
- memorie RAM: 4 GB;
- video: 256 MB; 1280 x 1024.

Concluzii

- Numărul de triunghiuri rezultate la crearea discretizării 2D este de 32 476 elemnte, în timp ce numărul de tetraedre pentru 3D este de 26 347 elemente, de aici rezultând o primă concluzie, aceea a numărului de ecuaţii semnificativ mai mare de rezolvat pentru modelul 3D.
- Timpul de soluţionare pentru analizele 2D este de 26 min., în timp ce pentru analizele 3D este de 393,44 min.
- Se constată de altfel că în cazul analizelor 2D, valoarea magnitudinii câmpului magnetic este de 1.7999T pentru 330 kV, în timp ce pentru cazul analizelor 3D, aceasta este mai mică, 1.6572 T (12.93%), pentru 430 kV.
- În urma calcului analitic al valorii magnitudinii câmpului magnetic la proiectarea transformatorului, a rezultat 1.67 T pentru 430 kV, valori apropiate de cele ale analizelor 3D (0.77%).
- Valorile maxime ale pierderilor sunt înregistrate pentru analizele 2D la tensiunea de 430 kV (66.5456 kW), valoare mai mică decât cea calculată în proiectare, 85 kW (21.71%).
- Se alege ANSYS Maxwell 3D ca fiind programul cu rezultate mai bune, urmând a se continua studiul termic, stabilitatea mecanică şi răcirea transformatorului cu alte module specializate în format 3D.
- În urma acestui studiu, se validează soluţia tehnică şi se propune spre proiectare transformatorul 325 MVA.

Aprecieri – Autorul mulţumeşte D-lui Director al SC INAS SA, Ing. Constantin CIOLOFAN pentru suportul acordat în realizarea acestui articol.

Referinţe

[1] www.ansys.com; User's guide Maxwell 3D, 650-700.
[2] E. Schmidt and S. Ojak. *3D MSC/EMAS simulation of a three phase transformer by means of anisotropic material properties*, Vienna, Austria.
[3] M. Jamali, M. Mirzaie and S. Asghar Gholamian, *Calculation and analysis of transformer Inrush current based on parameters of transformer and operating conditions*, 2011.
[4] R. Rahnavard, M. Valizadelu, A.A.B. Sharifian and S.H. Hosseini, *Analitical analysis of transformer inrush current and some new techniques for its redduction*.
[5] M. H.Amrollahi and S. Hassani, *Determination losses and estimate life of distribution transformers with three computational, measurement and simulation methods, despite harmonic loads.*
[6] Pavlos S. Georgilakis, *Spotlight on modern transformer,* Springer, 2009, 18-23, 33, 263-325.

Wireless Energy Transfer in a Medium-Range Charging Area

Corneliu URSACHI, Elena HELEREA
Transilvania University, 29 Eroilor Bd., Brasov, helerea@unitbv.ro

Abstract. The upward spiral of knowledge brings topical today, concerns and efforts of eminent scientists from times when there were no electricity transport networks. Wireless energy transfer, the subject that has captivated Nicola Tesla himself, is today a hot one again. Now, leading companies in mobile communications (Apple, Nokia), but not only, have patented or implemented solutions for wireless energy transfer in a medium-range charging area (10-100 cm). This article investigates ways and methods for strong coupling between a wireless power supply and peripheral devices, by near field magnetic resonance (NFMR) power transmission over non-negligible distances.

1. Introduction

Given the nature of this symposium, an theoretical one, our approach to wireless electromagnetic energy transfer phenomena (WET) will be a theoretical one, too. We will review the analytical methods used in actual research and their theoretical basis. Our approach will be one of a qualitative nature, we will analyze and describe the concepts and phenomena involved in wireless power transmission and we will analyze certain concepts (evanescent fields, strong coupling regime) which were presented in some articles, unclear, even nebulous. We will review the important experiments conducted by some researchers, related to the devices used and the obtained results whose value lies in transmission efficiency, the covered transmission distance, and a desirable less harmful effect to human beings. In order to further experimental approach to this topic, of the devices and methods described, taking into consideration the choices, by patents registered, they have already made important companies in the electronics and computers, we select the ones that seem most appropriate to achieve some new and original equipment.

2. Wireless Energy Transfer - theoretical and qualitative aspects

As a function of ratio between object dimensions, L_{OBJ}, and the distance between them, D, the wireless energy transfer can be achieved at:

- long range distances through directed radiation modes, in microwave domain ($D >> L_{OBJ}$);
- medium range distances through non radiative modes, in near field, by magnetic resonance energy transfer ($D =$ few$* L_{OBJ}$);
- very small distances through non radiative modes, magnetic induction ($D << L_{OBJ}$).

This article will address the phenomena and processes related to Wireless Energy Transfer in medium range distances, namely up to 2 m, and for "desk-top" type applications at distances up to 1 m. To achieve the wireless energy transfer to these distances, the transfer is based on Faraday's law of electromagnetic induction: in a source / emitter an alternating electrical current through a coil generates an electromagnetic field near the coil, which causes a voltage to be induced in the receiver's coil.

In most current research on efficient, medium-range wireless energy transfer, the non radiative near field magnetic resonance phenomenon is used. Objects with oscillating

parameters (geometry, materials they are made, resonance frequency) should be chosen in such a way that they operate in strong coupling regime.

Given the existence of an electromagnetic field in the vicinity of the energy transfer system, the requirement imposed to this technology to be a non-radiative one, should be evaluated, and, our approach is mainly a qualitative one, and less mathematically extended..

Let's analyze one by one the main concepts.

2.1. About resonance

At resonance, all parts of the system in question move / oscillate sinusoidally with the same frequency and the same phase. For example, a building, depending on size, structure, materials and links which it has with neighboring environment (boundary conditions) has one or more resonant frequencies. These resonant frequencies are also called natural frequencies or normal frequencies and correspond to so-called natural or normal modes of oscillation.

In electromagnetics, loads, voltages, currents, the intensity of the electric or magnetic field are oscillating sinusoidally at the same frequency and phase. When we refer to Wireless Energy Transfer, to achieve resonance conditions is absolutely necessary, but we will see later, not sufficient for efficient energy transfer.

At resonance, different objects oscillating with the same frequency, in certain circumstances, make possible efficient energy transfer in medium range distances. When we say "certain conditions" we mean that the resonance should occur in the near field, an area where radiation losses are small.

At magnetic resonance, the field is almost entirely magnetic in energy transfer area, common objects and human beings having permeability equal to that of free space, not having, by their presence, effects on energy transfer. By choosing equipment that performs the energy transfer, the main requirement is to maintain the field values in the regulated levels, to have no harmful effects on human’s health.

2.2. About near field

In American literature, the Americans possessing a remarkable sense of concrete [1], near field is classified as a storage field, a field that stores energy in source vicinity (storage fields), antithetical to fields that radiate (radiation fields) energy in free space. The following table makes a comparison between the two types of fields.

Table 1: Near field versus Far field Comparison

	Near (Reactive) Field	**Far (Radiated) Field**
Carrier of force	Virtual photon	Photon
Energy	It stores energy; It can transfer energy via inductive or capacitive coupling	It propagates (radiates) energy
Longevity	It extinguishes when source power is turned off	It propagates until absorbed
Interaction	Act of measuring field or receiving power from field causes changes in voltages/currents in source circuit	Act of measuring field or receiving power from field has no effect on source

Shape of field	Completely dependent on source circuit	Spherical waves. At very long distances, field takes shape of plane waves
Wave impedance	Depends on source circuit and medium	Depends solely on propagation medium ($Z = 120\pi = 377\ \Omega$ in free space)
Guiding	Energy can be transported and guided using a transmission line	Energy can be transported and guided using a wave guide

Near field disappears when the power source is interrupted, while the radiated fields propagate until it is absorbed. Near field has a local character, and it can not be detected, the radiated field, yes.

Near field can manifest as wave, but it may be static, it can be exclusively magnetic, exclusively electric only, or a combination of the two.

Radiated field must necessarily take the form of electromagnetic wave must have a magnetic component and an electric component, perpendicular to each other and to the direction of propagation. Radiated field has the ratio of ***E*** and ***H*** in free space, equal to the free space impedance of Z=377 Ω and it propagates with the speed of light c=3x10^8 m/s.

Near field energy density decreases faster than $1/r^2$, where r is the distance from the source. In contrast, the radiant field energy decreases exactly by $1/r^{2,}$ scattering involving radiation field on the surface of a sphere of radius r. Sphere surface is $4\pi r^2$, total energy of the field at any distance is the same, so that the field that radiates energy is called **far-field**.

For example, an electric current creates a magnetic field in a coil, a near field, in coil turns vicinity when the charge is accelerated and the magnetic field is restoring energy to source in the period in which the load is decelerated, this mutual transfer of energy in an ideal coil, being without losses.

Another important aspect to note is linked to the way a near versus a far field source reacts when another object absorbs energy from the field. For a source of radiated field, be it a TV broadcaster, once energy leaves the antenna, it propagates until it is absorbed by a TV-set or other objects. The fact that someone receives television signals has no effect on source, emissions power does not depend on how many people are receiving signal at a time.

In near field, if another object, in our case a receiver in resonance with the source, absorbs energy, it causes a reaction in source circuit , so the near field is called **reactive field**. The mere act of measuring field changes the characteristics of the field we are trying to measure.

2.3. Nebulous concepts

2.3.1. Strong coupling regime

If the system where resonant energy transfer occurs is well designed, energy is transferred efficiently; the losses by absorption and radiation in surrounding non resonance objects are small. Meaning of "strong coupling" lies in the fact that the energy transferred between objects in resonance is high (coupling is effective, hard) compared with energy loss produced during this process.

The term "strong coupling", under application of Coupled Mode Theory [2], becomes

nebulous, fragile, even contradictory. First of all, CMT is a theory applicable only to resonant weakly coupled objects. Then, CMT which understands the total electromagnetic field of a wireless energy transfer system as a superposition of modes due to each object, but the principle of superposition requires interaction between resonant objects must not be so strong as to significantly disrupt oscillation modes (eigenmodes) of individual objects.

2.3.2. Evanescent field

In [3] the notion of evanescent resonant coupling is defined as a coupling mechanism achieved by non-radiative near fields overlap of the two objects, the source / transmitter and the receiver device of the wirelessly energy transfer.

But what is this evanescent field about which researchers at MIT, the authors of articles [3] and [4], are speaking about. What is its physical significance?

An enlightening, good quality explanation is given in [5]. Solving Maxwell's equations for a homogeneous and isotropic medium, there are put in evidence the terms depending on $1/r$ at different orders of magnitude, where r is the distance from the source of the electromagnetic field. Power density, p_d, can be expressed as:

$$p_d = C_1/r^2 + C_2/r^3 + C_3/r^4 + ... \quad (1)$$

But the power contained in a sphere of radius r with the source as its center will be:

$$P = \text{Area} \times p_d = 4\pi r^2 \times (C_1/r^2 + C_2/r^3 + C_3/r^4 + ...) = 4\pi (C_1 + C_2/r + C_3/r^2 + ...) \quad (2)$$

Note that the first term is constant, regardless of the radius of the sphere, the same total power is flowing through it, and this relationship, mathematically show that some power leaves its source. This is the radiated power. At large distances, when the radius, r, is large, all other terms are negligible, allowing constant term to be dominant; we are in the far field region.

At small distances (in medium range distances of 1-2 m in our case, small for low frequencies, but still small even at 10 MHz, where the wavelength, λ, is 30 m, and we stand in near field zone $d = \lambda/2\pi \sim 6$ m, too), the variable terms, those in relationship (2) which depend on r will dominate, and the constant term becomes now, negligible. These terms can be attributed to inductive and electrostatic fields which become significant at small distances from the source, and together constitute the near-field power.

If we consider only two terms in equation (2), the first is a constant term, representing the radiated field strength, and, the second, consisting of the sum of the other terms are dependent of different orders of $1/r$ (which decreases exponentially with distance), and it will represent that nebulous "evanescent field".

This grouping of all these terms, which characterizes the non-radiative near field as "evanescent field" in the articles of MIT researchers, generates confusion, hide physical significance, especially through the use of the term "evanescent field" in the wave theory, and not related to electromagnetic phenomena. A more comprehensive physical, mathematical, and engineering, analysis with identical results was performed by F.Z. Shen in [6].

2.4. Theories applied

The applied theories are: Coupled Mode Theory (CMT) and Perturbation Theory (PT). Coupled Mode Theory (CMT) perceive reality of electromagnetic interaction between different objects as a superposition of the modes due to each object, as a linear, constant

parameters, system of equations:

$$da_m(t)/dt = -(i\omega_m - i\Gamma m)a_m(t) - \sum ik_{mn}a_n(t) + F_m(t) , \quad (3)$$

where:

m, n different resonant objects,
$a_m(t)$ variables are defined so that the energy contained in object m is $|am(t)|^2$
Example: an LC circuit, where $U=LI_0^2/2 = Q^2/2C$, $am(t)=(L/2)^{1/2}I_0$
ω_m the resonant frequency of m isolated object,
Γ_m intrinsic decay rate (absorption and radiated losses),
k_{mn} coupling coefficients,
$F_m(t)$ driving terms.

Assumptions:

a. the range of frequencies of interest is sufficiently narrow that the phenomenological parameters in Eq.(3) can be treated as constants;
b. coupled differential equations can be treated as linear;
c. the overall field profile can be described as a superposition of the modes due to each object.

The (c) condition usually implies that the interaction between the resonators must not be strong enough so as to significantly distort the individual eigenmodes. In that sense, the "strong" in "strong-coupling regime" is a relative term, even contradictory

3. Current experiments and results

Because a picture says more than a thousand words, we present below pictures of the devices used and the results joined in representative research projects **[2], [7], [8].** The figure 2 (a) shows a transmitter and receiver consisting of a primary coil of a few turns and a secondary coil of many turns and experiments results **[7]**. The figure 2 (b) shows a rectangular transmitter and receiver, working at 1.2 MHz, 3 MHz, 4.8 MHz, 8 MHz and experiment results **[8].**

Figure 1: Spectrum of field lines [7] and [3]

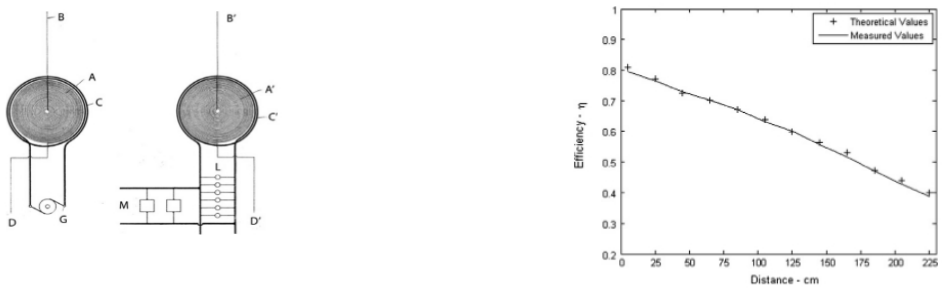

(a)

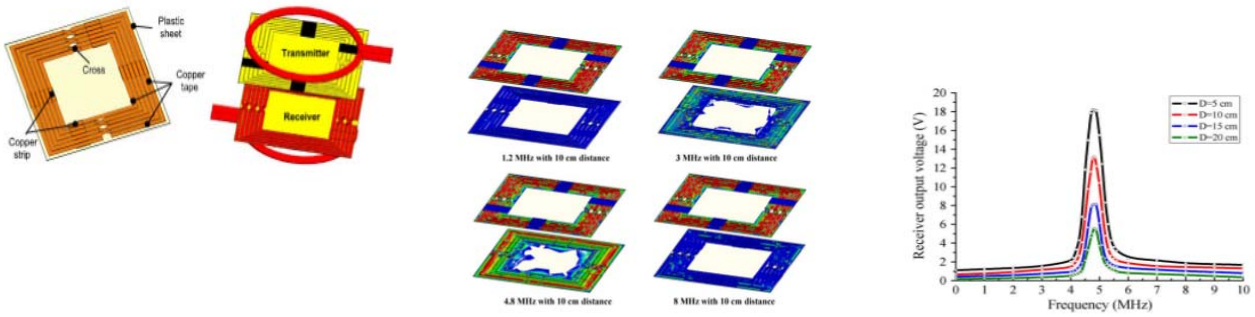

(b)

Figure 2: Devices and transfer efficiency [7] and [8]

4. Analysis of transfer efficiency. Directions to follow

The average efficiency is that of [3], to power a 60 W load, over a distance of 2 m, a 400 W power was necessary from the mains socket, with an efficiency of 15%. The explanation lies in the fact that energy transfer coil to coil around 45 % at this distance was reduced by the efficiency of Colpits oscillator.

Research shows that efficiency is higher at higher frequencies, but also higher frequencies can create fields higher than the permissible effect on the human's health.

Efficiency in terms of energy transfer and removing adverse health effects are therefore two conflicting requirements that research must satisfy.

References

1. R. Schmitt, *Understanding Electromagnetic Fields and Antenna Radiation Need No Math*' March 2000, www.ednmag.com.
2. H.A. Haus, W. Huang,"Coupled Mode Theory", *IEEE Proceedings*, vol-79, Page No-1505-1518.
3. A. Karalis, J.D. Joannopoulos, M. Soljacic, "Efficient Wireless Non-radiative Mid-range Energy Transfer", *Annals of Physics* 323, (2008) 34-48.
4. A. Kurs, A. Karalis, R. Moffatt, J. D. Joannopoulos, P. Fisher, M. Soljacic, "Wireless Power Transfer via Strongly Coupled Magnetic Resonances", *Science*, Volume 317, 6 July 2007. www.sciencemag.org
5. A. E. Umenei, "Understanding Low-frequency Non-radiative Power Transfer", *Fulton Innovation*, LLC, 2011.
6. F.Z. Shen, W.Z. Cui, W. Ma, J.T. Huangfu, L.X. Ran, "Circuit Analysis of Wireless Power Transfer by 'Coupled Magnetic Resonance",' *IET CCWMT* 2009, Pg 602.
7. C.A. Tucker, K. Warwick, W. Holderbaum, "A contribution to the wireless transmission of power", *Electrical Power and Energy Systems*, 47 (2013) 235–242.
8. W. Junhua, L. H. Siu, F. Weinong, T. K. Cheung, S. Mingui, "Finite-Element Analysis and Corresponding Experiments of Resonant Energy Transfer for Wireless Transmission Devices", *IEEE Transactions on Magnetics*, VOL. 47, NO. 5, MAY 2011
9. N. Tesla, *Apparatus for transmitting electrical energy*, US patent number 1,119,732, issued in December1914.
10. L.W. Epp, A.R. Khan, H.K. Smith, R.P. Smith, "A compact dual-polarized 8.51-GHz rectenna for high-voltage (50 V) actuator applications", *IEEE Trans. Microwave Theory Tech*., vol. 48, pp. 111-120, 2000.
11. [13] W.C. Brown, J.R. Mims and N.I. Heenan, "An Experimental Microwave-Powered Helicopter", *965 IEEE International Convention Record*, Vol. 13, Part 5, pp.225-235.
12. W. C. Brown, "*The History of Power Transmission by Radio Waves*", *IEEE Transactions on Microwave Theory and Techniques* (September 1984), Volume: 32, Issue: 9 On page(s): 1230-1242 + ISSN: 0018-9480). http://ieeexplore.ieee.org/xpl/freeabs_all.jsp?arnumber=1132833.

FEM Modeling of the Induction Motor with Rotor Faults

Anca CIOBANU, Elena HELEREA
Transilvania University of Brasov. 29, 500036 Brasov, Romania; anca.ciobanu@unitbv.ro

Abstract. This paper presents the results of the finite element (FE) modelling of a three-phase squirrel cage induction motor using Flux V11.1 package in order to diagnose the broken rotor bar fault type. For the simulation, three cases of rotors were proposed: healthy rotor, one broken rotor bar and two broken rotor bars. The analysed characteristic parameters are: stator currents, magnetic flux density and magnetic vector potential.

1 Introduction

The faults issue for the three-phase squirrel cage induction motor has been the subject of numerous studies. As the functions of the induction motors became more complex, new methods of fault monitoring and diagnosis have been designed and improved [1]-[3]. A stringent requirement in diagnosis is the early detection of faults within the shortest possible time to establish the most effective preventive maintenance, with direct implications on reducing material and financial losses.

A correct diagnosis of faults in the induction motor involves identifying the types of faults and their location, and a substantiation of a precise diagnosis method involves a detailed analysis of the effects of faults on the induction motors operating parameters. In this context, finite element method (FEM) can be successfully used, because it takes into account the non-linearity of the magnetic material being suitable for a detailed study of the induction motor behaviour with faults, and in this case of the broken rotor bar fault type.

Rotor faults are due to various stresses like environmental, mechanical, electrical, thermal, electromagnetic, as well as casting (blowholes or porosity, low quality of aluminium alloy, leakage between lamination) and manufacture procedure.

Rotor bar and end-ring faults yield asymmetrical operation of induction machines causing unbalanced currents, torque pulsation, increased losses, poor starting performance and higher thermal stress [2].

Rotor cage manufacturing influence the induction motors operating parameters. Efficiency, slip, rated current, winding temperature rise, starting torque are the most important operating parameters affected. Usually, the poor quality of the rotor cage it is observed at the final testing of the induction motor [4].

The objectives of this investigation are: the implementation of the finite element (FE) modelling for a three-phase squirrel cage induction motor, the analysis of the simulation results for motors with broken rotor bar faults, using FLUX V11.1 package, in order to establish a diagnosis method for this fault type. For the simulations was considered a three-phase induction motor with an output power of 0.37 kW, a synchronism speed of 1500 rpm, the voltage of 400 V and the frequency of 50 Hz. The simulations and the analyses were conducted for three cases: healthy rotor, rotor with one broken bar and rotor with two broken bars. The simulation accuracy was verified by the experimental measurements on the models of motors with this fault type.

2 FEM for the Induction Motor

For FEM modelling of the induction motor some assumptions are necessary in order to reduce the complexity of the model and therefore its computing time, as follows [5]:

- The induction motor is considered as a 2D entity;

- The air surrounding the motor and the rotor shaft will not be modelled;
- The coils will be modelled considering that the conductors are evenly distributed in the slots;
- The hysteresis will be neglected due to the isolated iron sheets that are building the core for the stator and rotor.
- For the FE calculations will be necessary a discretisation of the geometry into elements.

Specifications and rated parameters of the studied induction motor are given in Table 1.

Table 1. Specifications and parameters of the studied induction motor

Power[W]	370
Synchronism speed [rpm]	1500
Operating mode	S1 (continuous operating)
Rated voltage [V]	400
Frequency [Hz]	50
Protection rank	IP55
Insulation class	F
Iron length [mm]	85
Diameter of copper wire [mm]	0.4
Number of turns per slot	143
Number of current paths in parallel	1
Number of stator slots	24
Number of rotor bars	22
Efficiency [%]	63.57
Power factor	0.74
Starting torque/rated torque	2.2
Starting current/rated current	3.25
Slip [%]	15.33
Stator winding resistance at 20ºC [Ω]	24.9
Rated current [A]	1.13
No-load current [A]	0.9

FLUX 2D is a commercial software package that it is based on the finite element method. The results can be expressed in local quantities when the measures (e.g. magnetic field, magnetic flux) are available in each point of the calculation domain or in global quantities when the quantities (e.g. magnetic force, magnetic torque, the magnetic flux through a coil) derive from the integration of the local quantities over the entire calculation domain or only on a part of it.

The steps for the modelling and simulation of the induction motor with the software support are:

a. Defining of the parameters.
The parameters are defined by three attributes: name, comment and mathematical expression (size in millimeters). This function facilitates the resizing of the model.

b. Creating the coordinate system for the motor geometry.
All geometrical characteristics must be defined on a coordinate system. With a user-defined system, time can be saved by defining of small pieces of the geometry and then doubling and positioning of these parts to complete the model.

c. Creating inner and outer diameters of the motor to achieve the final geometry.

d. Controlling the mesh for points and lines that build the motor geometry.
The software uses the second order triangular elements characterized by six nodes, three in peaks and three in the sides of the triangle, and so as the number of nodes is greater the more accurate the results are.

Mesh can be done automatically by the software, but the results are not always satisfactory being necessary a refining of the mesh in the area of interest.
For the model in this paper, refining was done at the top and the bottom of the rotor bars, at the bottom of the stator slots and at the air gap.

e. Generating, checking and saving of the mesh.
The mesh analysis for the studied induction motor is shown in Table 2.

Table 2. Surface elements for the induction motor

Number of elements not evaluated	0 %
Number of excellent quality elements	99.44 %
Number of good quality elements	0.56 %
Number of average quality elements	0 %
Number of poor quality elements	0 %
Number of nodes	60453
Number of line elements	4145
Number of surface elements	30190
Mesh order	2-nd order

f. Defining of the induction motor materials.
The materials can be imported from the software database or they can be defined by the user depending on the B-H curve or on the resistivity. For the studied motor were used three types of materials, namely: Fe-Si iron sheet M700-65A, aluminium and steel. All materials were defined by the user, thus it is possible to create a database of their own. Fe-Si iron sheet was used as material for the stator and rotor core, aluminium was used as material for the rotor bars and steel for the rotor shaft.

g. Creating the external circuit of the induction motor.
The schema of the stator and rotor cage is shown in Figure 1.

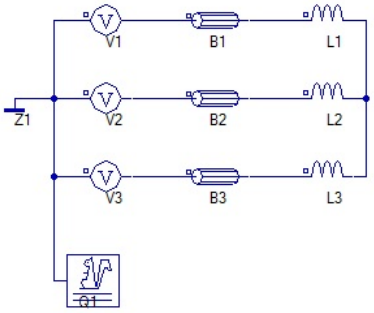

Figure 1: External electric circuit of the studied induction motor.

h. Calculation of the external electric circuit of the induction motor.
For the electric circuit calculation the following equations were used [6]:

- Calculation of the end-winding resistance R_{ew} [Ω]:

$$R_{ew} = \frac{8\varphi_{Cu} l_{ew} N_{tpp} N_{spp}}{N_c N_w \pi d_w^2}, \quad (1)$$

where φ_{Cu} is the resistivity of a wire, in Ωm; l_{ew} is the length of the end-winding, in m; N_{tpp} is the number of turns per slot per phase; N_{spp} is the number of slots per pole per phase; N_c is the number of coils in parallel per phase; N_w is the number of current paths in parallel; d_w is the diameter of a wire, in m.

- Calculation of the end-winding inductance L_{tb} [H]:

$$L_{tb} = \frac{\mu_0}{18p}\left(\frac{N_{ss}N_{tpp}}{N_c}\right)^2 P\,, \tag{2}$$

where p is the number of pole pairs; N_{ss} is the number of stator slots; μ_0 is the magnetic permeability of vacuum; P is a parameter which depends on the winding.

- Calculation of the end-ring resistance R_r [Ω] [7]:

$$R_r = \rho_{Al} \cdot \frac{\pi D_r}{Z_2 S_r}\,, \tag{3}$$

where ρ_{Al} is the resistivity of aluminium, in Ωm; D_r is the average diameter of the end-ring, in m; Z_2 is the number of rotor bars; S_r is the cross-section of the end-ring, in m^2.

- Calculation of the end-ring inductance L_r [H]:

$$L_r = \mu_0 l_r \lambda_r\,. \tag{4}$$

- The moment of inertia and the friction coefficient are required. Equation (5) shows the results integration of the finite element and the mechanical coupling [5]:

$$J\frac{d\Omega_r}{dt} = T_{em} - F\Omega_r - T_l\,, \tag{5}$$

where J is the moment of inertia, in kg m^2; Ω_r is the rotor speed, in 1/s; F is the friction coefficient, in Nms; T_{em} is the electromechanical torque, in Nm; T_l is the load torque, in Nm.

i. Definition of the solving problem.
In this case was chosen the Transient Magnetic module with a depth of domain of 85 mm. The simulation for the induction motor with broken rotor bar fault was made by considering that for a broken bar the resistivity is 10^5 higher than the resistivity of the healthy bars [8] and recalculating the end-rig resistance from the external electric circuit.

j. Define of the physical properties
The connection between the external electric circuit and geometry is made and the direction of current through the coils is defined.
It is also necessary that the fixed and moving parts of the motor to be defined. In this case, the stator is the fixed part, the rotor is the moving part having the speed and position equal with 0 rpm, respectively 0 degree at time t=0 and the moment of inertia, experimentally measured, J=0.0003 kg m^2. The air gap is defined as the compressible part.

k. Solving scenario and options
At this step it is established the accuracy with which the model is solved as well as the time step and the simulation time.

l. Results analysis.

3 Simulation Results obtained with FLUX V11.1

The results are presented in a comparative way between the healthy rotor and the faulty ones. The analyses are performed at t = 0.5 s.

Figure 2 shows the distribution of the field lines and the value of the magnetic vector potential in the case of the healthy rotor, one broken rotor bar, respectively, two broken rotor bars. It can be seen that the distribution is uniform for three motors, having two slots on pole.

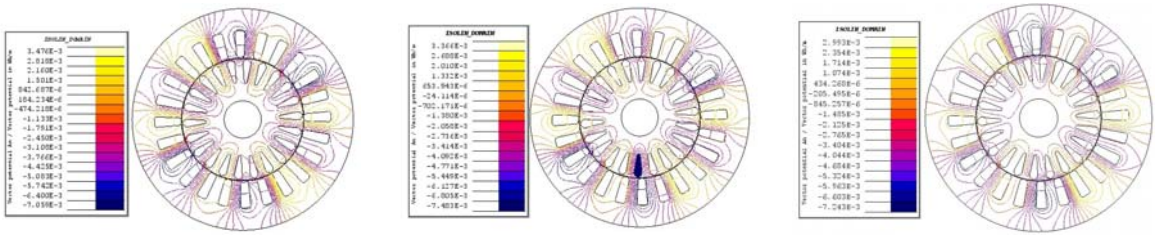

a) b) c)

Figure 2: Magnetic vector potential: a) healthy rotor; b) one broken rotor bar; c) two broken rotor bars.

In Figure 3 is shown the magnetic flux density for the three cases.

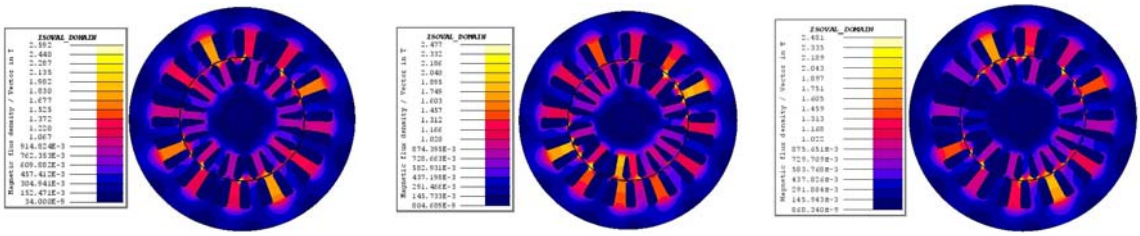

a) b) c)

Figure 3: Magnetic flux density: a) healthy rotor; b) one broken rotor bar; c) two broken rotor bars.

The magnetic flux density distribution is symmetric in the case of healthy induction motor and appears distorted when the broken bar fault type occurs.

In Figure 4 is shown the variation in time of the phase currents.

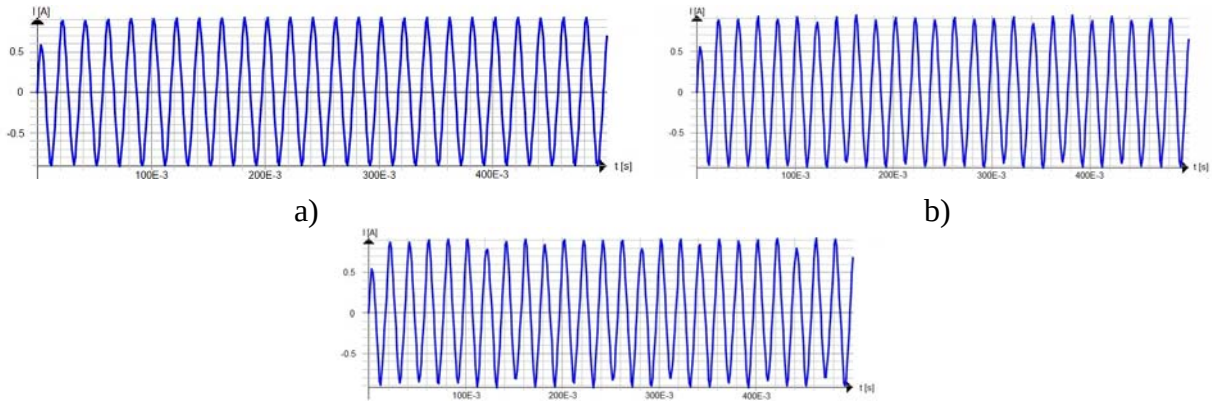

a) b)

c)

Figure 4: Variation of the phase currents: a) healthy rotor; b) one broken rotor bar; c) two broken rotor bars.

It can be seen that in the case of the healthy rotor the current amplitude is constant in time, and as the number of the broken rotor bars increases the phase current amplitude varies.

In Table 3 is presented a comparison between measurement and simulation for the effective values of the phase currents for the three cases of no-load motors.

The stator currents value of the healthy motor is very close to the stator current value of the faulty motor. At the rotor turning, every rotor bar successively meets the winding slots, so each bar will be influenced by the stator magnetic field and all the rotor bar currents become uniform around the rotor periphery.

Table 3. Effective values of the phase currents for the studied induction motors

No-load phase current [A]					
Healthy rotor		One broken rotor bar		Two broken rotor bars	
Measured	Simulated	Measured	Simulated	Measured	Simulated
0.9	0.97	0.9	0.95	0.89	0.93

When a bar is broken or partially broken, some of the initial current flowing through that bar will be redistributed to the adjacent bars leading to Joule losses increasing. The flux distribution around broken bar changes, this phenomenon causing the increased steel losses in the bar next affected [9].

In this paper the focus was on the stator current spectrum study in the case of the rotor with broken bars. Mechanical or magnetic asymmetries may lead, in their turn, on the distortion of the analysed parameters.

4 Conclusions

The finite element method was used to simulate the operation of the induction motor without and with broken rotor bar faults. The simulation allowed a first study on the influence of the broken rotor bars upon the stator current distribution, the magnetic flux density and magnetic vector potential. The results provided by the simulation are close to those determined experimentally for the no-load currents case. By using this model can be simulated and other induction motor faults.

Acknowledgments – This paper is supported by the Sectoral Operational Programme Human Resources Development (SOP HRD), ID76945 financed from the European Social Fund and by the Romanian Government.

References

[1]R. Fiser, S. Ferkolj, "Application of a Finite Element Method to Predict Damaged Induction Motor Performance", *IEEE Transactions on Magnetics*, vol. 37, no. 5, pp. 3635-3639, September 2001.

[2]X. Ying, "Characteristic Performance Analysis of Squirrel Cage Induction Motor With Broken Bars", *IEEE Transactions on Magnetics*, vol. 45, no. 2, pp. 759-766, February 2009.

[3]M. F., Cabanas, F., Pedrayes, M. G., Melero, C. H., Rojas García, J. M., Cano, G. A. Orcajo, J., González Norniella, "Unambiguous Detection of Broken Bars in Asynchronous Motors by Means of a Flux Measurement-Based Procedure", *IEEE Transactions on Instrumentation and Measurement*, vol. 60, no. 3, pp. 891-899, March 2011.

[4]A. Ciobanu, E. Helerea, I. Peter," An Experimental Comparative Analysis for Broken Rotor Bars Diagnosis", Applied and Theoretical Electricity (ICATE), 2012 International Conference on Applied and Theoretical Electricity, October 25-27, Craiova, Romania, pp.75-78, ISBN 978-1-4673-1809-9.

[5]J. Sprooten, *Finite Element And Electrical Circuit Modelling Of Faulty Induction Machines–Study Of Internal Effects And Fault Detection Techniques*. Thesis, 2007.

[6]Cedrat, "Flux-Induction motor with skewed rotor-technical paper", 2005.

[7]A. Nicolaide, *Electrical Machines - Theory – Design* (in Romanian), Ed. Scrisul Romanesc, Craiova, 1975.

[8] C. W. Steele, *Numerical Computation of Electric and Magnetic Fields*. New York: Chapman & Hall, (1997).

[9]X. Ying, „Investigation of Broken Rotor Bar Faults in Three-Phase Squirrel-Cage Induction Motors". *INTECH: Finite Element Analysis-From Biomedical Applications to Industrial Developments*, pp. 477-496, 2012.

Efficiency of 2D homogenization formulas for magnetic nanocomposite materials

Lucian PETRESCU, Adelina BORDIANU, Valentin IONITA
Faculty of Electrical Engineering, University Politehnica of Bucharest, 060042, Romania
lucian.petrescu@upb.ro

Abstract. Magnetic nanocomposite materials are used in a large area of applications. In many cases the solution of homogenizing these materials could make work easier. This paper studies the efficiency of two homogenization formulas (Maxwell-Garnett and Bruggeman) for different situations: varying the number of particles for the same volume ratio, varying the dispersion of inclusions in the material. The investigations were made for 5 different volume ratios (approximate 10%, 20%, 30%, 40% and 50%) and 4 different ratios for the magnetic permeability of the inclusions and of the domain. The discussions were referred to the response of the composite and homogenized materials through two curves on the exterior of the domain.

1 Introduction

Magnetic composite materials were used in various applications ranging from magnetic sensors and micro electrical machines to electromagnetic shielding and biomedical applications (such as magnetic drug delivery into the human body or enhancing the contrast image in magnetic resonance) [1] ÷ [3]. Some of the composite materials had very complex structure and thus sometimes the study of their properties is difficult. One solution for this problem is to make some simplifying assumptions. For example, we can consider that all the material inclusions have exactly the same form and geometric size and that they are perfectly embedded in the matrix. Other common assumption is the homogenization technique. The idea behind this technique is to replace the complex structure of the real material with a homogeneous one which is able to describe correctly all the material properties. Using the homogenization technique it was determined that the medium has the same properties in each point and the macroscopic rules and formulas can be applied with success. One of the immediate results of using homogenization is that the time needed to obtain the desired solutions is reduced [4].
Homogenization techniques are based on analytical formulas (such as Maxwell Garnett, Bruggeman, Clausius-Mossotti) or different computational methods (finite difference method, finite element method, boundary element method) [5] ÷ [7]. The aim of this paper is to analyze the numerical 2D results of the homogenization process, using two analytical formulas (Maxwell-Garnett and Bruggeman) for several situations involving different volume ratios between inclusions and matrix, different magnetic permeability ratios and, also, observing how the number and position on the inclusions into the material influences the homogenization process.
The initial Maxwell-Garnett formula was used for the dielectric permittivity of a material, but it was successfully applied to magnetic material as follows [8]:

$$\frac{\mu_o - \mu_m}{\mu_o + 2\mu_m} = f \cdot \frac{\mu_i - \mu_m}{\mu_i + 2\mu_m} \tag{1}$$

where the indexes are indicated as: homogenous (*o*), matrix (*m*), respectively the inclusions (*i*), μ is the magnetic permeability, and *f* is the ratio volume between the inclusions and the domain.
The Bruggeman formula (using the same notations) is a bit more elaborated, by taking into account the interaction between the particles in the composite material [8]:

$$(1-f)\cdot\frac{\mu_m-\mu_o}{\mu_m+2\mu_o}+f\cdot\frac{\mu_i-\mu_o}{\mu_i+2\mu_o}=0 \quad (2)$$

The following study was based on these formulas to calculate the homogenous magnetic permeability of the material.

2 Numerically Investigated Situations

The sample studied is a discus of 50 nm radius. The inclusions are discuses with different radiuses arranged symmetrically in the matrix. The investigation focused on the median relative errors (relation (3)) between the magnetic flux density obtained in the homogeneous and the inhomogeneous cases on two exterior curves (one of 52.5 nm radius, named C_1 and the other of 60 nm radius named C_2).

$$\varepsilon_r=\frac{\sum_{k=1}^{n}\left(B_{incl}^{(k)}-B_{\text{hom}}^{(k)}\right)}{n}, \quad (3)$$

where n is the number of points determined by the software (FEMM plots 300 points for each curve). The domain is placed in uniform magnetic flux density of about 22 *mT* from the bottom of the investigated domain for each case studied.

The study uses different variables to present the importance of each parameter in the numerical simulation. Different values for the matrix and inclusions permeability were used, following four ratios between them as follows:

Table 1. Situation simulated for magnetic permeability

Situation / μ	S_1	S_2	S_3	S_4
μ_m	10	5	100	5000
μ_i	1000	50	10	50
ratio (μ_m/ μ_i)	0.01	0.1	10	100

Another important aspect is the influence of the volume ration between the inclusions and the matrix and 5 concentrations are simulated: 10%, 20%, 30%, 40%, respectively 50%.

The last two aspects included in this study were the influences of the number of inclusions (there were simulations for 4 inclusions, named "*few - f*" and 10 inclusions – "*many – m*") and the placement of these inclusions in the matrix (simulations for the situation of "*center – c*" or "*peripheral – p*" dispersions of the inclusions in the matrix).

3 Results and discussion

For the first comparison, the magnetic flux density spectrum was presented (figure 1) in the cases of central, respectively peripheral dispersion of 4 inclusions. For these situations the relative errors were presented on the closest curve on the graph (C_1) using equation (3), for two concentrations of inclusions (20%, respectively 50%) using both formulas (Maxwell-Garnett - MG and Bruggeman - B). The ratio of the magnetic permeabilities for the horizontal axis corresponds to the values from table 1.

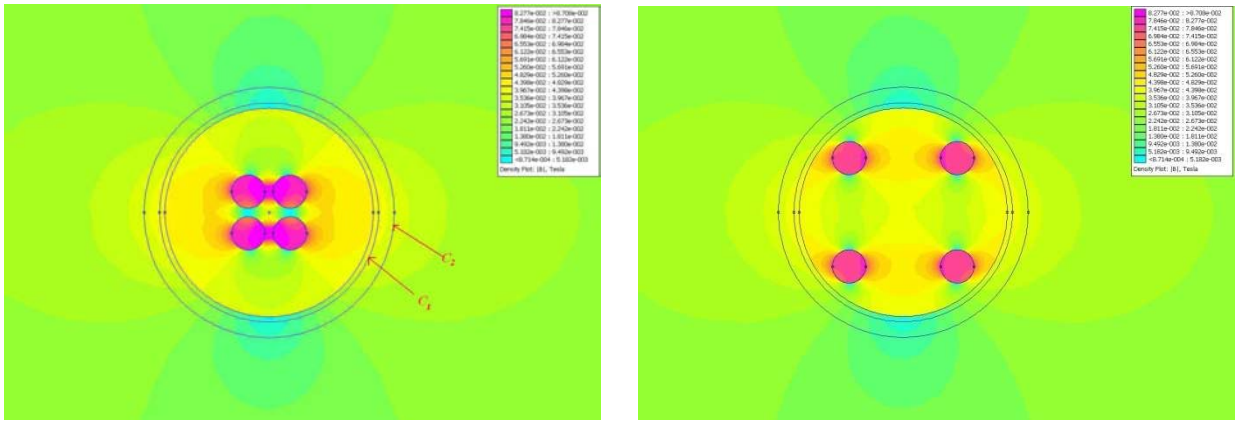

Fig.1. Magnetic flux density for central and peripheral dispersion of 4 inclusions

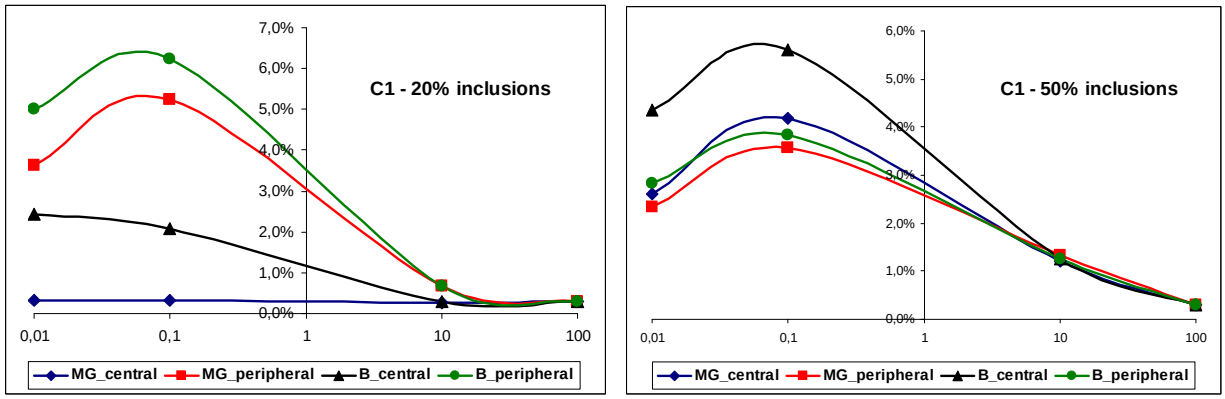

a) b)

Fig.2. Relative errors for considered situations on curve C_1 for a concentration of 20% (a), respectively 50% (b) of the inclusions in the matrix

In figure 3 and 4, are presented the same situations for central and peripheral dispersions of 10 inclusions into the matrix.

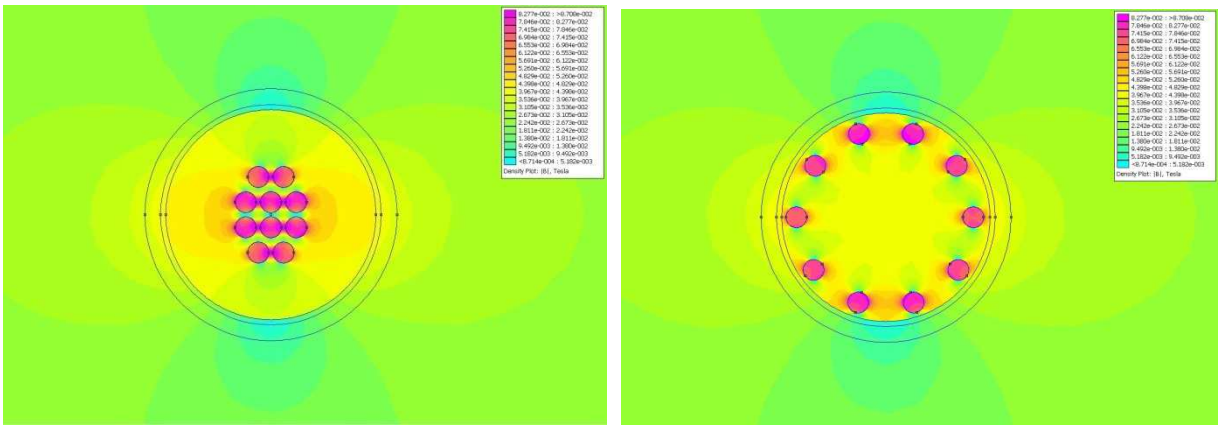

Fig.3. Magnetic flux density for central and peripheral dispersion of 10 inclusions

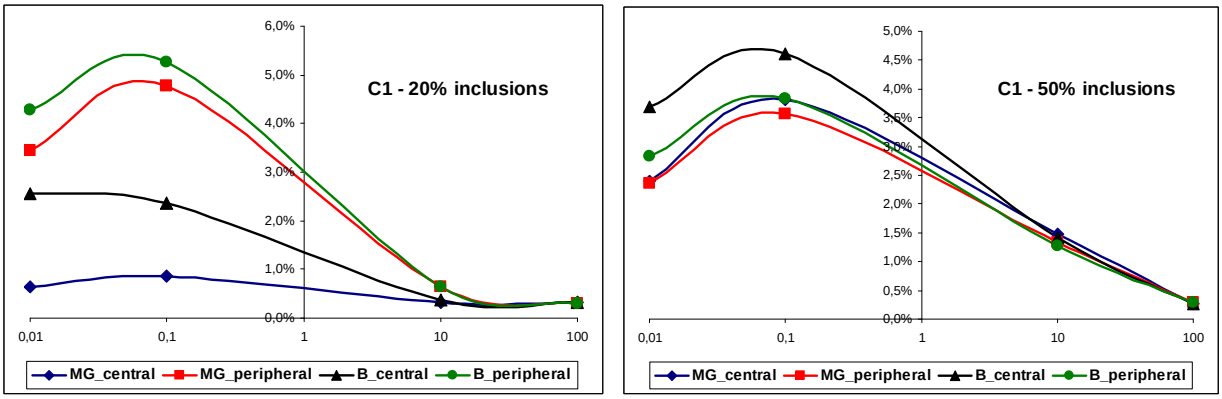

a) b)

Fig.4. Relative errors for considered situations on curve C_1 for a concentration of 20% (a), respectively 50% (b) of the inclusions in the matrix

To study the influence of the position of the inclusions into the matrix, in figure 5 and 6 are presented the relative errors using equation (3) for 4 and 10 central and peripheral inclusions.

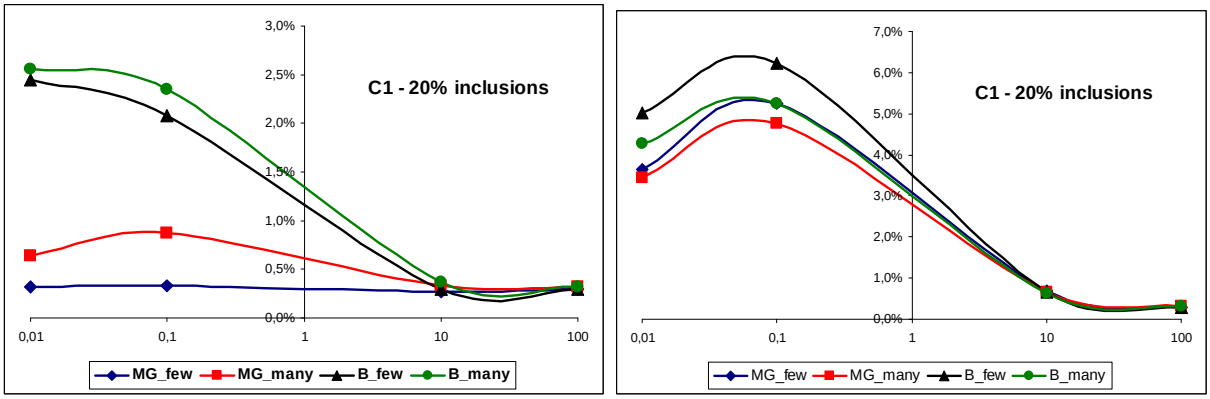

a) b)

Fig.5. Relative errors for considered situations on curve C_1 for central (4 and 10) (a) and , respectively peripheral (4 and 10) (b) inclusions (concentration 20%)

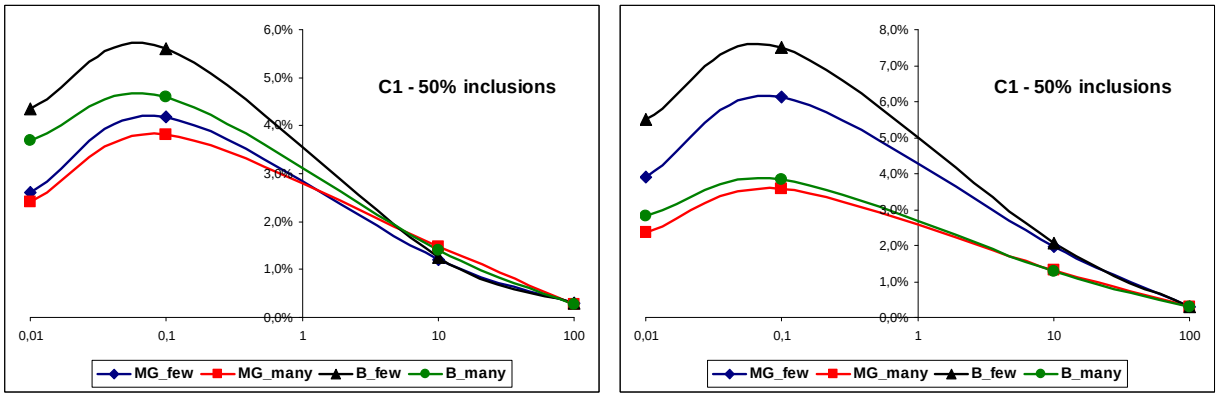

a) b)

Fig.6. Relative errors for considered situations on curve C_1 for central (4 and 10) (a) and , respectively peripheral (4 and 10) (b) inclusions (concentration 50%)

In the previous graphs concentrations of 50% were selected because this situation produces the highest relative errors, as it can be seen in the figure 7, for 4 and 10 central inclusions.

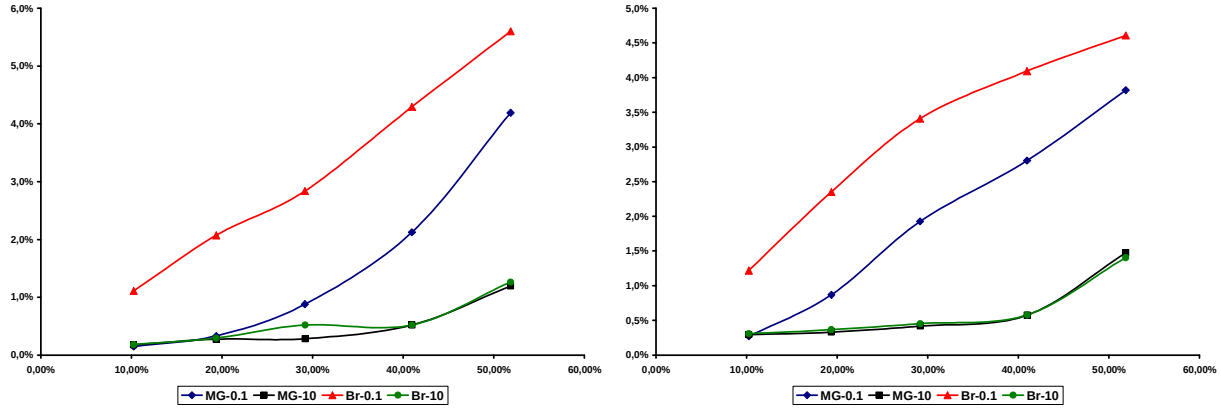

a) b)

Fig.7. Relative errors of considered situations on curve C_1 for 4 (central) (a), respectively 10 (central) (b) inclusions

In the last part of the study the objective was to emphasize the variation of the relative errors for all inclusion concentrations (10% to 50%), for the four situations presented in table 1, using Maxwell-Garnet formula only.

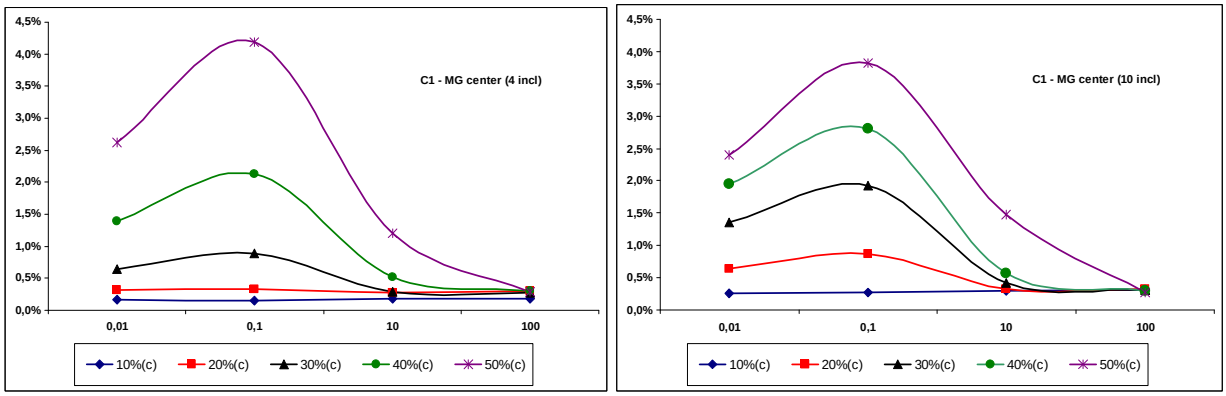

a) b)

Fig.8. Relative errors of considered situations on curve C_1 for 4 (central) (a), respectively 10 (central) (b) inclusions to all concentrations investigated (10% to 50%)

4 Conclusions

The aim of this study was to establish the influence of different parameters to the analytical homogenizations techniques involving Maxwell-Garnett and Bruggeman formulas. First of all, Maxwell-Garnett formula gave more accurate results than Bruggeman ones for most of the investigated situations. Although, in the cases of 10 inclusions it was observed that the relative errors for both formulas were close. This aspect can be regarded to the fact that Bruggeman formula is taking into account the interaction between the particles which is more intense for 10 inclusions. Also, for a ratio of 100 between the matrix permeability and the inclusions permeability the relative errors for both formulas are also very close independent of the other parameters taken into account in this study. On the other hand, the most disadvantageous situation is the one with ratio 0.1.

The influence of inclusion position into the matrix was showed in figure 2 for 4 inclusions and in figure 4 for 10 inclusions. For lower concentrations (such as 20%) it was obvious that, for both formulas, central dispersion is more accurate then the peripheral one. In the case of 50% particle concentration, the relative errors for central and peripheral dispersion become closer,

especially when Maxwell-Garnett formula is used. One can conclude in this case that the position of the inclusions into the matrix is important only in a dilute composite material.
Both formulas considered in this study do not explicit take into account the number of inclusions for the same inclusion concentrations in the material. The relative errors shown in figure 5 marked out that Maxwell-Garnett formula provides more accurate results for 4 then 10 inclusions, but for higher concentrations the relative errors were similar with the two previous cases.
All cases studied on the second curve C_2, gave smaller relative errors, as it was expected.
The study might be continued with investigation of 3D inclusions, with different shapes of the particles and even considering inclusions with different magnetic permeabilities.

References

[1] S.K. Sahoo, S. Parveen, J.J. Panda, *The present and future of nanotechnology in human health care*, Nanomedicine: Nanotechnology, Biology, and Medicine 3 (2007), 20 – 31.
[2] P. Pouponneau, J-C. Leroux, S. Martel, *Magnetic nanoparticles encapsulated into biodegradable microparticles steered with an upgraded magnetic resonance imaging system for tumor chemoembolization*, Biomaterials **30** (2009), pp. 6327–6332.
[3] L.L. Lao, R.V. Ramanujan, *Magnetic and hydrogel composite materials for hypertemia applications*, JMS: Materials in Medicine 15 (2004), 1061-1064.
[4] A. Bordianu, L. Petrescu, V. Ionita, *Numerical testing of homogenization formulas efficiency for magnetic composite materials*, MURPHYS 2012, Suceava, Romania
[5] Kévin Santugini-Repiquet, *Homogenization of the demagnetization field operator in periodically perforated domains*, J. Math. Anal. Appl. **334** (2007), 502–516.
[6] A. Lakhtakia, W. S. Weiglhofer, *Maxwell Garnett formalism for cubically nonlinear, gyrotropic, composite media*, INT. J. ELECTRONICS, 1998, Vol. 84, No. **3**, 285-294.
[7] H.T. Banks, V.A. Bokil, D. Cioranescu, N.L.Gibson, G. Grisco, B. Miara, *Homogenization of Periodically Varying Coefficients in Electromagnetic Materials*, Technical Report #2005-2, Statistical and Applied Mathematical Sciences Institute (2005)
[8] Ari Sihvola, *Electromagnetic mixing formulas and applications*, The Institution of Electrical Engineers, London, United Kingdom (1999)

ASPECTE PRIVIND TESTE DE EMISII ŞI IMUNITATE LA PERTURBAȚII ELECTROMAGNETICE ÎN CELULE GTEM

Petre-Marian NICOLAE, Dan-Gabriel STĂNESCU, Marian-Ştefan NICOLAE
Universitatea din Craiova, B-dul Decebal, nr. 107, 200440, Craiova, pnicolae@elth.ucv.ro

Abstract. Sunt prezentate aspecte teoretice privind teste de emisii şi imunitate la perturbații electromagnetice efectuate în celule GTEM. Este descrisă modalitatea pentru obținerea zonei de câmp uniform în cazul testelor de imunitate. Sunt prezentate principalele tipuri de echipamente utlizate în cadrul testelor de emisii şi imunitate în celula GTEM. Este exemplificată utilizarea celulei GTEM 250 pentru teste de imunitate la perturbații pentru un circuit electronic.

1 Introducere

Celula GTEM este o linie de transmisie care simulează transmiterea energiei electromagnetice în modul TEM (Transversal ElectroMagnetic) prin care se propagă unda electromagnetică plană în spațiul înconjurător. Ea poate fi utilizată atât pentru teste de susceptibilitate la radiații, cât şi pentru măsurarea de emisii conduse şi radiate ale echipamentelor electrice şi electronice de la domeniul curentului continuu până la frecvențe de 1 GHz – sau chiar mai mari [1]. Începând cu 1996 toate produsele electronice manufacturate în Uniunea Europeană şi care pătrund pe piața Uniunii Europene trebuie testate pentru a satisface conformitatea cu standardele în vigoare. În acest sens ele trebuie testate la: (a) susceptibilitate la perturbații conduse şi radiate datorate altor echipamente sau dispozitive (teste de "imunitate"); (b) emisii conduse şi radiate pe care le produc.

Celulele GTEM sunt utilizate ca o alternativă la testele de emisie şi imunitate în aer liber sau în camere semi-anechoice [2]. Configurații de câmp bine definite pot fi obținute în cadrul acestora. Celulele de testare GTEM pot fi de diferite dimensiuni (250...2000) mm, dimensiunea acestora depinzând de dimensiunea echipamentului testat (EUT).

Dezavantajul principal al testării în celule GTEM este legat de faptul că permite testarea numai a unui echipament de dimensiuni reduse – datorită dimensiunilor reduse ale zonei de testare.

2 Aspecte teoretice privind testele efectuate în celule GTEM

Celula GTEM este, în principiu, o linie coaxială conică, plecând de la un punct de alimentare coaxial, având dielectric aer şi impedanța caracteristică Z = 50 Ω.

2.1 Aspecte teoretice privind testele de emisii efectuate în celule GTEM

Testele de emisii ale obiectului de încercat în cele trei poziții se determină după cum urmează. Un sistem de axe (x,y,z) sunt atribuite celulei TEM. O alegere standard este de a alinia axa z în direcția de propagare, axa y paralel cu câmpul electric E (vertical) şi axa x paralel cu câmpul magnetic, H. Centrul obiectului de încercat este plasat la (x=0, y, z) cu x=0 în mijlocul septumului. Un sistem local de coordonate (x', y', z') este atribuit obiectului de încercat. Poziția *a* aliniază x' cu x, y' cu y, respectiv z' cu z, aşa cum este prezentat în Fig. 1. Poziția *b* este obținută printr-o permutare simplă a axelor obiectului de încercat: x' la y, y' la z, respectiv z' la x. Aceasta este echivalentă cu două rotații de 90º ale obiectului de încercat.

Poziția *c* este obținută de o permutare suplimentară: x' la z, y' la x, z' la y [3]. Puterea totală radiată P_0 datorată obiectului de încercat este dată de [4]:

$$P_0 = \frac{Z_0}{3\pi} \cdot \frac{k_0^2}{e_0^2 Z_C} \cdot S^2, \quad [\text{W}] \tag{1}$$

unde [5]:

$$S = \sqrt{V_{p1}^2 + V_{p2}^2 + V_{p3}^2} \qquad (\text{V}_\text{p} \text{ măsurat în [V]}) \tag{2}$$

(V_{p1}, V_{p2}, V_{p3} - reprezintă tensiunile măsurate pentru cele trei poziții ale obiectului de încercat);

$$Z_0 = \sqrt{\mu_0 / \varepsilon_0} = 120\pi [\Omega] = 377\ [\Omega] \tag{3}$$

Z_C - este impedanța caracteristică a ghidului de undă TEM (în general 50 Ω);

e_{0_y} - este factorul de câmp pe axa y.

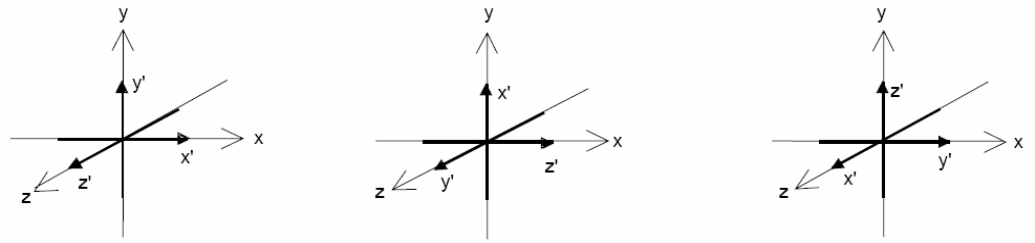

Poziția a Poziția b Poziția c

Fig. 1. Pozițiile în care poate fi plasat obiectul de încercat pentru măsurarea emisiilor acestuia

Algoritmul descris necesită măsurarea componentei pe axa y a câmpului electric. Există două metode posibile pentru definirea factorului de câmp e_{0_y} (metoda experimentală; metoda analitică).

Pentru testele de emisii pot interveni mai multe surse de eroare: programele software de prelucrare, terminația de 50 Ω (care nu este perfectă); cablurile de interconectare în punctele de racord; cordoanele prin care se transferă puterea la intrare şi la impedanța de 50 Ω [6].

2.2 Aspecte teoretice privind testele de imunitate efectuate în celule GTEM

Unitatea de comandă şi punctul de alimentare pentru obiectul de încercat sunt disponibile pentru diferite tipuri de celule GTEM. În funcție de cereri există posibilitatea de alimentare monofazată sau trifazată - utilizând filtre de rețea. Volumul de testare al unității GTEM este, prin urmare, protejat cât mai mult posibil de perturbări/interferențe electromagnetice

Calculul puterii necesare pentru testare este explicitat prin formula de mai jos. În esență, trebuie să luăm în considerare intensitatea câmpului electric, înălțimea peretelui despărțitor, o toleranță pentru vârfurile de tensiune cauzate de modulația în amplitudine, şi filtrarea. Puterea cerută pentru testele de imunitate este dată de relația [7]:

$$RE = [\,(E \cdot h)^2 \,/\, R\,] \cdot F \cdot \text{cota de modulare} \tag{4}$$

unde: *E* reprezintă intensitatea câmpului electric; *h* – înălțimea peretelui de separație; *F* – factor de filtrare. O toleranță (dată de producător între factorii din membrul drept al relației (4)) este folosită pentru a putea lua în considerare vârfurile de tensiune cauzate de modulația în amplitudine şi de filtrare.

Celula GTEM prezintă un grad ridicat de uniformitate a câmpului, în concordanță cu Standardul IEC/EN 61000-4-20, dacă sunt îndeplinite următoarele cerințe [8]:

• Mărimea echipamentului (EUT – „Equipment Under Test") care este testat nu trebuie să depăşească *h*/3.

• Cablurile de legătură sunt non-radiative.

• EUT – ul este testat de-a lungul celor trei direcţii.

3 Zona de câmp uniform pentru teste de imunitate la perturbaţii electromagnetice

Se foloseşte conceptul de „zonă uniformă" care este un plan vertical în direcţia de propagare a câmpului în care variaţiile de câmp sunt mici. Dimensiunile ghidului de undă TEM determină mărimea unei zone uniforme (plane). Dimensiunea maximă a unui obiect de încercat este strâns legată de dimensiunea „suprafeţei utile de testare". În principiu, zona uniformă poate fi localizată la orice distanţă de la portul de intrare (locaţia va depinde de geometria ghidului de undă). Zona uniformă este valabilă numai pentru acea distanţă de la intrarea în port la care s-au făcut măsurători pentru a se vedea uniformitatea câmpului. Zona uniformă este determinată în incintă fără EUT, folosind un semnal nemodulat (Fig. 2).

În funcţie de dimensiunea zonei, aceasta poate fi considerată uniformă dacă în punctele de măsură câmpul electric este considerat uniform [8]:

a)valorile componentei primare a câmpului electric în zona definită este cuprinsă între $^{0}_{6}$dB din componenta primară nominală a câmpului, în cel puţin 75% din punctele măsurate;

b) valorile componentelor câmpurilor electrice secundare sunt cu cel puţin 6 dB mai mici decât componenta primară - în cel puţin 75% din punctele măsurate.

Cele 75% din punctele de măsură de la a) nu trebuie să fie identice cu cele 75% din punctele de măsură de la b). La diferite frecvenţe, punctele de măsură trebuie să se încadreze în limitele toleranţei. Toleranţa a fost exprimată ca $^{0}_{6}$dB pentru a asigura că rezistenţa câmpului să nu coboare sub cea nominală. Toleranţa de 6 dB este considerată a fi valoarea maximă admisă pentru teste. O componentă a câmpului electric primar cu toleranţa cuprinsă între $^{0}_{6}$dB până la $^{0}_{10}$dB sau o componentă a câmpul electric secundar cu o valoare de (-2) dB din componenta câmpului primar este permisă cu condiţia ca actuala toleranţă şi frecvenţele de încercare să fie declarate în raportul de testare [8].

Calibrarea câmpului se bazează pe metoda „puterii constante de intrare" [8]. Pentru determinarea puterii necesare se mai poate proceda apelând la metoda câmpului electric constant [9], [10].

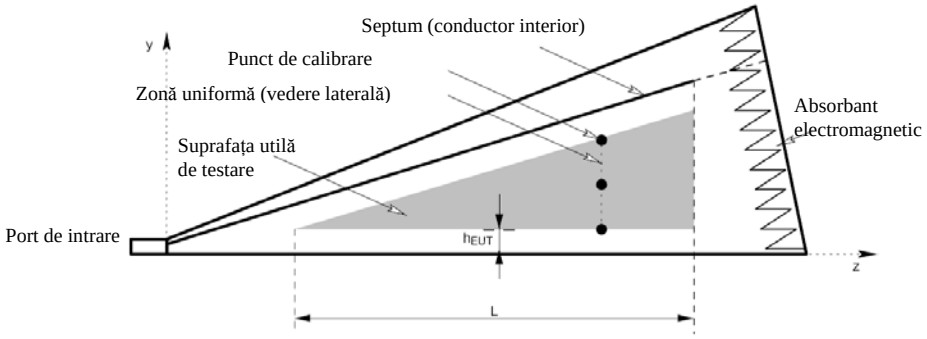

Fig. 2.Vedere laterală

4 Echipamente utilizate în cadrul testelor de emisie şi imunitate în celula GTEM

Celula GTEM 250 (Fig. 3), folosită pentru testele de emisii conduse şi radiate şi pentru imunitate la perturbaţii electromagnetice, se găseşte în dotarea laboratorului de Compatibilitate Electromagnetică din cadrul Facultăţii de Inginerie Electrică a Universităţii din Craiova.

Fig.3. Vedere asupra celulei GTEM 250

În cazul frecvenţelor înalte, pentru a se putea obţine o adaptare între impedanţa conductorului central şi a celui exterior, se utilizează grupuri de rezistenţe conectate în serie şi paralel, aşa cum este exemplificat în Fig. 4, precum şi un perete realizat cu elemente absorbante de formă piramidală (Fig. 5) - cu rol de reducere a eventualelor reflexii care pot să apară în celula GTEM [11].

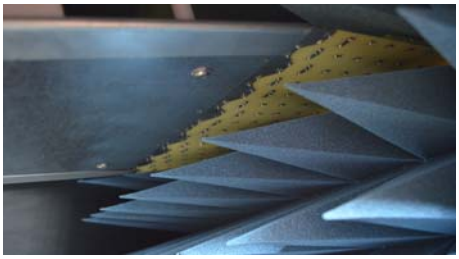

Fig.4. Vedere asupra plăcii pe care se află rezistenţele de adaptare

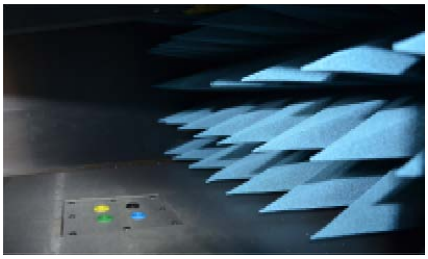

Fig.5. Peretele realizat cu materiale absorbante

Pentru testele menţionate mai sus se utilizează un calculator personal (PC), pe care sunt instalate programele software dedicate pentru testele de emisii (conduse şi radiate) şi pentru testele de imunitate. Rezultatele obtinute pot fi salvate sub forma grafică sau tabelară într-un fişier. Fişierul mai conţine informaţii privind setările făcute în cadrul testelor, configurarea echipamentelor, etc. Acestea, impreună cu celula GTEM din Fig. 3, permit realizarea testelor împreună cu echipamentele din schema de testare. Sistemul utilizat mai conţine un generator de semnal RF (1), un power meter (2) de tipul NSG 4070 – aşa cum se observă în Fig. 6. Generatorul de semnal poate fi utilizat în plaja 9 kHz - 1 GHz. Cele trei canale de măsură ale power meter-ului sunt utilizate pentru măsurători la frecvenţe în plaja 9 kHz - 1 GHz astfel: canalul 1: (-15 dBm ... +27 dBm); canalele 2,3: (-25 dBm ... +20 dBm).

Pe lângă acestea mai sunt incluse: un amplificator de putere (3), un cuplor bidirecţional (4), precum şi un analizor de spectru (5) (Fig. 6). Amplificatorul de putere este de tipul CBA 1G-018, putând genera câmpuri de testare cu valori de până la 10 V/m sau şi mai mari dacă se foloseşte

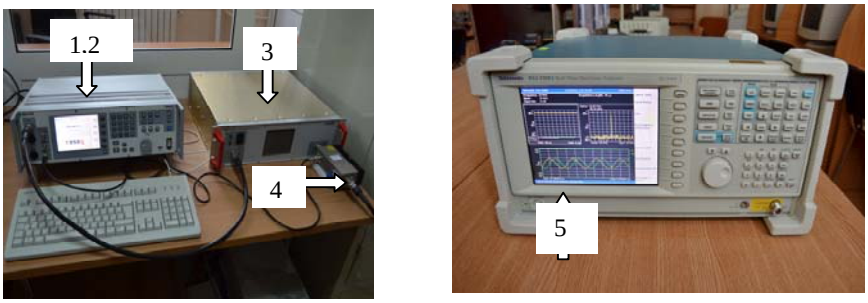

Fig.6. Vedere asupra principalelor echipamente folosite la testele de emisie şi imunitate

cu rețele de cuplare /decuplare (CDN). Valoarea puterii nominale de ieşire este de minimum 18 W (uzual 20 W). Cuplorul bidirecțional este utilizat pentru măsurători de înaltă acuratețe a puterii de intrare şi a puterii reflectate în cazul testelor de imunitate radiate sau a celor de tipul BCI (Bulk Current Injection), la frecvențe cuprinse între 10 kHz şi 1GHz [11].

5 Teste de imunitate în celula GTEM

Testele pentru imunitate la perturbații electromagnetice externe sunt realizate pentru a evalua comportarea unui echipament atunci când este supus acțiunii unui câmp electromagnetic incident. Testele trebuie să fie conforme cu standardele specifice. Fig. 8 descrie schema utilizată pentru testele de imunitate la câmp perturbator de 10 V/m, conținând echipamentele descrise la punctul anterior.

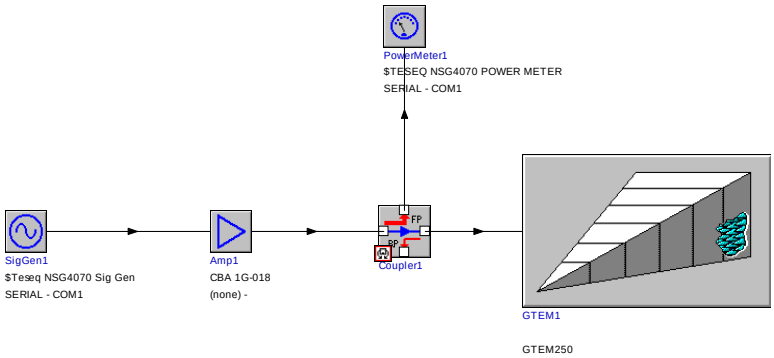

Fig. 7 Configurația echipamentelor folosite la testul de imunitate

Programul software pentru testele de imunitate include mai multe secvențe pentru testele standard la care este supus EUT. Dacă starea EUT se poate identifica numai prin imagine vizuală sau audio, utilizatorul poate verifica erorile de intrare din tastatură sau folosind mouse-ul [11].

Echipamentul ("EUT") testat în celula GTEM a fost o placă electronică cu microcontroler. În concordanță cu testele de imunitate standard, aceasta a fost testată la un câmp de 10 V/m. Aceste standarde prevăd îndeplinirea primului criteriu, şi anume cel pentru teste de radiofrecvență. Astfel, obiectul de încercat trebuie să continue să funcționeze la parametrii nominali în timpul testului şi după aceea. Nu trebuie să existe nicio schimbare a parametrilor în timpul testului şi după aceea.

Tabelul I conține principalele concluzii privind comportarea echipamentului la testele de imunitate pentru frecvențe diferite ale semnalului de intrare.

Tabelul I. Rezultatele testului de imunitate pentru o placă electronică cu microcontroler

Frecvența (MHz)	Generator de semnal (dBm)	Puterea utilizată (W)	Câmpul standard (V/m)	Câmpul estimat (V/m)	Comportarea EUT la diverse valori ale câmpului (dacă a cedat sau nu)
80.000000	-28.1	0.120	10.000	10.936	Nu
201.826295	-30.2	0.090	10.000	10.350	Nu
300.491852	-28.8	0.162	10.000	10.532	Nu
401.007541	-30.4	0.088	10.000	10.766	Nu
504.131851	-27.2	0.117	10.000	10.851	Nu
603.016041	-28.3	0.116	10.000	10.659	Nu
700.082903	-30.2	0.103	10.000	10.864	Nu
804.727244	-31.0	0.070	10.000	10.669	Nu
906.786801	-30.1	0.079	10.000	10.729	Nu
1000.000000	-29.7	0.083	10.000	10.252	Nu

6 Concluzii

- Realizarea testelor de imunitate prezentate în această lucrare cu celula GTEM 250 a presupus studierea unor standarde pentru testele de imunitate realizate cu această celulă. Aceste standarde impun o anumită mărime a obiectului de încercat şi plasarea acestuia într-o zonă a celulei, zonă în care câmpul electric trebuie să fie uniform în cel puțin 75% din punctele de măsură [8].
- Obiectul care a fost încercat în celula GTEM a fost o placă electronică cu microcontroler. Conform standardelor de imunitate, placa a fost testată la o valoare a câmpului de 10 V/m. Astfel obiectul de încercat trebuie să continue să funcționeze la parametrii nominali în timpul testului şi după aceea. Nu trebuie să existe nici o schimbare a parametrilor în timpul testului şi după aceea. În cazul prezentat aceste cerințe au fost îndeplinite pe perioada derulării testelor.
- Testele de emisie şi de imunitate realizate în celula GTEM necesită un studiu amănunțit asupra modului de propagare a câmpului electromagnetic, o cunoaştere a standardelor care trebuie respectate, a modului de funcționare a echipamentelor utilizate pentru realizarea acestor teste, precum şi a softurilor dedicate pentru emisie şi imunitate.
- Testele de imunitate realizate în celulele GTEM pot fi efecuate în bune condiții, nefiind necesară utlizarea unor antene sau conductoare care să influențeze acuratețea măsurătorilor.

Aprecieri – Autorii mulțumesc IEEE, Societatea EMC (SUA), pentru sprijinul acordat prin ***EMC Society University Grant***.

Referințe

[1] M. Montrose, E. Nakauchi, *Testing for EMC Compliance – Approaches and Techniques*, IEEE Press, 445 Hoes Lane, Piscataway, NJ 08854, 2009

[2] M. J., Thelberg, E. L., Bronaugh., J. D. M., Osburn, „GTEM to OATS emission correlation 1-5 GHz", *Procedings of IEEE International Symposium on Electromagnetic Compatibility*, 387-392, Chicago, IL, August 1994

[3] D. Steinbach, „A review on measurements techniques in OATS and GTEM cell", *Procedings of The International Conference on Electromagnetic Interference and Compatibility*, pp.211-218, 6-8 dec. 1999

[4] T.E. Harington, Total-radiated-power-based OATS-equivalent emissions testing in reverberation chambers and GTEM cells, *Procedings of IEEE International Symposium on Electromagnetic Compatibility*, pp. 23-28, 21-25 aug., 2000

[5] M. Heidemann, H. Garbe, Using TEM waveguides according to the new IEC 61000-4-20, *Procedings of IEEE International Symposium on Electromagnetic Compatibility*, pp. 457 – 460, vol.1, 11-16 may, 2003

[6] D. Weiss, „A User's Insight Into Radiated Emission Testing with GTEM Cells", *Procedings of IEEE International Symposium on Electromagnetic Compatibility*, pp.157-162, 1991, Chicago, US

[7] D., Bozec, L., McCormack, A. C., Marvin, A., Nothofer, M., Alexander, „A good practice guide for the use of GTEM cells in EMC measurements according to IEC 61000-4-20", *Procedings of IEEE International Symposium on Electromagnetic Compatibility*, Aug. 9-13, 2004, vol 2, pp. 660-665

[8] *** IEC 61000-4-20, Electromagnetic Compatibility (EMC) - Part 4: Testing and measurement techniques, Section 20: Emission and immunity testing in transverse electromagnetic (TEM) waveguides, International Electrothenical Commission, Geneva, Switzerland, 2003.

[9] C. Paul, *Introduction to Electromagnetic Compatibility*, 2d ed., Wiley-Interscience, published by John Wiley&Sons Inc., Hoboken, New Jersey, 2006

[10] H. Ott, *Electromagnetic Compatibility Engineering*, Wiley, published by John Wiley&Sons Inc., Hoboken, New Jersey, 2009

[11] http://www.teseq.com/com/en/products_solutions/emc_radio_frequency/gtem_tem_cells/GTEM_Test _cells_e.pdf

Analiza temperaturii şi umidităţii la dezhidratarea ciupercilor în câmp de microunde

Mircea PANTEA, Adriana GRAVA , Marcela LAZA (BULC)
Universitateadin Oradea, Universităţii 1, 410087 Oradea, Romania, *mpantea@uoradea.ro*

Abstract. Principalul obiectiv al acestei lucrări este de a determina temperatura optimă pentru conservarea ciupercilor Button Mushrooms, Arimillaria Mellea şi Pleurotus Ostreatus în camp de microunde.
S-a constatat că temperaturile ridicate din timpul procesării în camp de microunde pot deteriora ciupercile, fiind indicată utilizarea unei instalaţii de vacuum pentru menţinerea temperaturii cât mai scăzută.

1 Introducere

Această tehnologie a microundelor este tot mai des folosită şi în industria alimentară datorită avantajelor oferite de rapiditatea transferului de căldură faţă de procesele de uscare convenţionale. În acest scop cea mai des utilizată frecvenţă în Europa este de 2,45GHz, datorită costurilor de producţie reduse. [6].

Utilizarea microundelor la uscarea ciupercilor pe lângă avantajul oferit de uscarea rapidă mai are şi un aport benefic, neutralizând enzimele care se regăsesc în compoziţia acestora. [3].

Ciupercile sunt sensibile la temperaturi ridicate, motiv pentru care în procesul de uscare ar fi indicată şi folosirea unei instalaţii de vacuum pentru a menţine temperatura cât mai scăzută, caz în care acestea îşi păstrează aproape în totalitate proprietăţile şi culoarea. [4]

După cum a prezentat Delgado şi colaboratorii acestuia în 2002, calitatea ciupercilor poate fi determinată cu ajutorul izotermelor şi a umidităţii acestora. [2]

În timpul procesului de uscare ciupercile suferă modificări structurale care pot influenţa atât calitatea acestora cât şi aspectul fizic, motiv pentru care trebuie avută mare grijă la valorile de temperatură la care se lucrează, deoarece peste un anumit prag al temperaturii unele zone din masa dielectricului se deteriorează semnificativ.[7]

Astfel principalul obiectiv al acestui studiu este de a determina puterea şi temperatura de lucru optimă pentru a putea discuta de o conservare a speciilor de ciuperci mai sus menţionate.

2 Materiale şi metode

Agoricus bisporus **(**"button mushrooms"), Pleurotus Ostreatus şi Arimillaria mellea (Ghebe) au fost recoltate de pe Câmpia de Vest a ţării şi anume zona Miersig.

Pentru procesarea în camp de microunde s-au folosit atât ciuperci tăiate în felii cât şi întregi.

Din punct de vedere taxonomic, acestea fac parte din clasa Basidiomycetes, subclasa Holobasidiomycetes, ordinul Hymenomycetales, familia Agaricaceae, fiind formate din pâlărie şi picior, pălăria fiind formată din carpofor în partea aeriană şi hife miceliene dedesupt. [1].

Din prezentările făcute de T. Volk şi K. Ivor, USA este ce-a mai mare producătoare a acestei specii, estimând valoarea recoltei anuale la 800 milioane de dolari, iar ca şi conţinut de proteine acestea pot avea de 15 ori mai multe proteine decât grâul, având şi un conţinut important de vitamine D şi complexul B.

2.1. Echipamentul

Pentru a reduce timpul de uscare naturală de 2-3 zile la temperatură de minim 55^0C, se vor face experimente cu următoarele echipamente: un cuptor cu microunde cu putere reglabilă între 100 - 800W, balanță electronică cu precizie de 0,1g, umidometru FHT 60 şi termometre cu infra roşu 62 Fluke şi Fluke 87 TRUE RMS MULTIMETER.

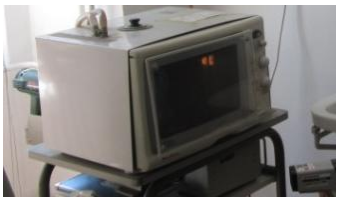

a)

b)

Fig 1. a) Inatalația şi b) echipamente şi eşantioane

Temperaturile au fost măsurate atât cu ajutorul unei sonde de fibră optică cât şi cu termometrul, şi datorită existenței unor diferențe de temperaturi între diferite zone ale eşantioanelor s-a luat media arimetică a temperaturilor de pe eşantioane pentru fiecare caz.

Având la dispoziție şi echipament de scanare Kessel & Shih, 1976 şi Speilberg, Evensen, Bratberg, si Skjerve, 1993 au înghețat probele în azot, după care tăiate în felii foarte subțiri au realizat o analiză structurală a ciupercilor în urma finalizării procesului de uscare. (Kessel & Shih, 1976 şi Speilberg, Evensen, Bratberg, si Skjerve, 1993).

Despre umiditate însă se poate spune că este de suprafață şi de interior, existând diferențe mari între acestea, umiditatea de suprafață ajungând la echilibru doar în momentul în care a fost încheiat procesul de uscare, în primele faze ale experimentelor variind foarte mult.

2.2. Date experimentale.

Pentru o soluție optimă de uscare cu ajutorul microundelor în scopul reducerii timpului de uscare naturală de 2 - 3 zile la o temperatură a aerului din mediul ambiant de minim 550C, [1] s-au folosit trei eşantioane de ciuperci de dimensiuni mici din specia:

Agoricus bisporus (ciuperci de câmp):

Tabelul 1

Greutatea inițială [g]	Puterea [W]	Timp [s]	Temperatura [^{0}C]	Greutatea la timpul t [g]	Umiditatea [% RH]	Cantitatea de apă eliminată [%]
9,1 / 9,9 / 11,4	100	60	31	8,7 / 9,5 / 11,0	60,2	3,5
8,7 / 9,5 / 11,0	100	120	58,8	8,1 / 9,2 / 10,3	96,5	8
8,1 / 9,2 / 10,3	100	180	57	6,9 / 8,6 / 9,5	94,1	16,6
6,9 / 8,6 / 9,5	100	240	69	5,2 / 7,5 / 8,0	93,2	29,82
5,2 / 7,5 / 8,0	100	300	59,2	3,9 / 5,6 / 6,6	88	42,1
3,9 / 5,6 / 6,6	100	360	61,2	2,7 / 4,2 / 4,8	72,7	57,89
2,7 / 4,2 / 4,8	100	420	71,2	1,7 / 2,7 / 2,9	50,4	74

În acest caz s-a putut observa o creştere bruscă a umidității de la suprafață, proporțională cu creşterea temperaturii până în momentul în care începe de fapt procesul de uscare (180s), moment în care ciupercile sunt acoperite de o peliculă de apă.

Se poate ajunge la un randament maxim în ceea ce priveşte eliminarea apei, de până la 75% la această putere, însă cu cât masa ciupercilor este mai mică, (9,1 – 2,7) fată de (11,4 – 4,8) cu atât şi randamentul la această putere este mai bun, aproximativ 80%.

În cazul în care aceeaşi categorie de eşantioane au fost uscate direct la timpul de 420s (vezi tabelul 2), randamentul depăşeşte puțin peste 25%.

Tabelul 2. Eşantioanae întregi.

Greutatea inițială [g]	Puterea de penetrare [W]	Timp [s]	Temperatura [^{0}C]	Masa la timpul t [g]	Umiditatea [% RH]	Cantitatea de apă eliminată [%]
11,9	100	420	18 / 72,2	8	44,8 / 99,7	13
12,9	300	60	64,8	11,3	91,7	12,4
11,3	300	120	73,2	6,8	91,2	47,28
6,8	300	180	75,8	1,8	54,8	86,04

Fig 2. Eşantioane uscate la 100W şi 300 W

Fig 3. Eşantioane corespunzătoare tabelului 3.

Dacă uscarea este făcută direct în timpul de 420 secunde, ciupercile sunt doar încălzite, şi ajung să fie învelite de o peliculă de apă, motiv pentru puterea de lucru este mărită la 300W, pentru o temperatură inițială de 19,6^{0}C şi umiditate de 49,4% RH. La puterea de 300W se observă o creştere a randamentului de uscare, ajungându-se la 56% pentru un interval de timp mult mai mic, la umiditatea de 54,8%, însă datorită apariției unor zone arse pe carpofor a fost oprit procesul.

Următorul tabel este corespunzător feliilor de ciuperci la puterea de 300W, pornind de la temperatura de 21,4^{0}C şi umiditatea de 49,2% RH.

Tabelul 3 . Eşantioane întregi

Greutatea inițială [g]	Puterea de penetrare [W]	Timp [s]	Temperatura [^{0}C]	Masa la timpul t [g]	Umiditatea [% RH]	Cantitatea de apă eliminată [%]
8	300	60	59,2	5,9	99,5	12,4
5,9	300	120	67,4	2,4	46,9	60,22%
2,4	300	180	75,8	1,2	40,7	47%

La eşantioanele cu picior şi pălărie, s-au observat apariția unor zone arse, pe când la eşantioanele fără picior aceste zone nu au apărut. Măsurând temperaturile şi umiditatea, la eşantioanele cu picior şi pălărie s-a constat o diferență de temperatură de 3-50C şi umiditate de 14,5% RH, fiind oprit procesul datorită acelor zone.

În încercarea de a usca direct eşantioanele felii la putere de 300W timp de 180 secunde, s-a constatat apariția arcului electric în zona în care lipsea piciorul ciupercii, mare parte din eşantioane fiind făcute scrum.

În continuare au fost folosite eşantioane de 5 ori mai mare decât anterior, dar s-a observat un randament mai scăzut acestea reținând mai multă apă

Tabelul 4

Greutatea inițială [g]	Puterea de penetrare [W]	Timp [s]	Temperatura [^{0}C]	Masa la timpul t [g]	Umiditatea [% RH]	Cantitatea de apă eliminată [%]
55,4	100	60	16,6	55,1	46,9	0,72
55,1	100	120	39,2	51,5	76	7,02
51,5	100	180	54,2	45,4	97,3	18,05
45,4	100	240	60,2	39,6	99,6	28,51
39,6	100	300	60	34,2	77,3	38,26
34,2	100	360	64,2	28,8	88,9	48,01
28,8	100	420	65,8	21,7	93,4	60,83
21,7	100	480	68,4	16,3	86,6	70,58

Tabelul 5 prezintă rezultatele experimentale obținute de la temperatura inițială de 19,6^{0}C şi umiditatea de 49,5% RH.

Tabelul 5.

Greutatea inițială [g]	Puterea de penetrare [W]	Timp [s]	Temperatura [^{0}C]	Masa la timpul t [g]	Umiditatea [% RH]	Cantitatea de apă eliminată [%]
28,2	300	60	55,8	26,4	88,6	6,38
26,4	300	120	72,8	19,3	92,7	31,56
19,3	300	180	81,2	9,4	70,8	66,66
9,4	300	240	96,4	2,4	41,2	91,49

Arimillaria mellea (Ghebe)

Fig.4. Eşantioane de ghebe

Fig.5. Determinarea umidității

Fig. 6 Corespunzător tab. 6

În cazul acestei specii de ciuperci s-a realizat un studiu experimental pe eşantioane mici şi mari pentru comparaţie, la care s-a crescut în prima fază doar timpul de expunere, iar apoi s-a crescut şi puterea microundelor

Tabelul 6

Masa [g]	Temperatura inițială [^{0}C]	Puterea [W]	Timp [s]	Umiditatea parțială[%RH]	Masa la timpul t [g]	Temperatura parțială [^{0}C]	Cantitatea de apă eliminată [%]
6,5 / 3,9 / 2,7	17,2	100	60	67,8	6,3 / 3,6 / 2,5	35,4	3,17
6,3 / 3,6 / 2,5	33,2	100	120	53,3	5,4 / 3 / 1,9	57,4	16,92
5,4 / 3 / 1,9	54,3	100	180	49,7	3,8 / 1,9 / 1,4	56,3	41,53
3,8 / 1,9 / 1,4	53	100	240	46,3	2,3 / 1 / 1	66,8	64,61

Temperaturile parțiale sunt mediile celor trei eşantioane, fiecare dintre ele având o altă temperatură, existând o diferență de 2-3 ^{0}C.

După cum se poate observa la această putere, uscarea este ce-a mai eficientă pentru cazul eşantioanelor medii, care ajung la un randament al uscării de până la 70%

Eşantioanele mari expuse la puterea de 100 W, pierd mai greu umiditatea conform tabelului următor, însă pentru o putere de 300W şi un timp de 300s s-a constatat un comportament destul de bun, ciuperca nefiind deteriorată (tabelul 7).

Tabelul 7

Masa [g]	Tempeeratura inițială [^{0}C]	Puterea [W]	Timp [s]	Umiditatea parțială[%RH]	Masa la timpul t [g]	Temperatura parțială [^{0}C]	Cantitatea de apă eliminată [%]
13,1 / 8,1 / 7	19,4	100	60	41,2 / 79,3	12,9 / 7,9 / 6,8	35,7	1,52
12,9 / 7,9 / 6,8	34,2	100	120	82,6	11,7 / 7,2 / 6,1	57,4	10,68
11,7 / 7,2 / 6,1	54,3	100	180	93,6	10,4 / 7,3 / 5,6	67,4	20,61
10,4 / 7,3 / 5,6	72,4	100	240	78,6	9,3 / 6,2 / 4,3	72,8	29,01
9,3 / 6,2 / 4,3	63,5	100	300	72,4	8,5 / 5,7 / 3,8	77.6	35,11
8,5 / 5,7 / 3,8	74,3	100	360	68,4	5,9 / 2,8 / 1,9	83,7	54,96
5,9 / 2,8 / 1,9	80,4	100	420	50,8	3,1 / 1,3 / 0,8	93,7	76,34
16,7	21,1	300	60	53,6	16,1	88,6	3,59
16,1	82,4	300	120	77,6	11,2	92,7	32,93
11,2	88,6	300	180	84,7	3,6	70,8	78,44
3,6	64,5	300	240	96,6	1,7	41,2	89,82
6,3	18,2	300	300	48,7 / 59,8	3,4	58,6 / 63,2	46,03

Pleurotus ostreatus

Aceasta este cunoscută ca fiind o ciupercă xilofagă, ce poate creşte atât pe trunchiurile sau cioturile putrede ale arborilor, regăsindu-se în păduri în general toamna, dar şi primăvara, fiind

capabilă să valorifice atât celuloza cât şi hemiceluloza din materialele folosite de către acestea ca şi substrat şi care unt bogate în lignin. [8]

Ca şi substrat se poate folosi divere materiale vegetale: rumeguş, vrejuri de fasole,... dar s-a observant că prin adaugarea de deşeuri vegetale de soia, productivitatea acestora va creşte.[9]

Fig. 7. Eşantioane de pleurotus

A la puterea de 300W
B la puterea de 300W direct
C - la puterea de 450W direct
D - la puterea de 800W direct

Fig.8. Pleurotus ucat

În primul experiment s-au utilizat eşantioane mai mici de Pleurotus Ostreatus la o putere de 100W fiind mărit timpul de uscare tot cu 60s.

Tabelul 8.

Masa [g]	Temperatura inițială [^{0}C]	Puterea [W]	Timp [s]	Umiditatea parțială[%RH]	Masa la timpul t [g]	Temperatura parțială [^{0}C]	Cantitatea de apă eliminată [%]
9,1 / 5,8 / 5	20,4	100	60	39,2 / 59,6	9 / 5,8 / 4,9	42,4	1,10
9 / 5,8 / 4,9	39,6	100	120	71,3	8,1 / 5,4 / 4,5	57,2	10,99
8,1 / 5,4 / 4,5	53,4	100	180	70,4	7,1 / 4,7 / 3,8	54,8	21,98
7,1 / 4,7 / 3,8	50,6	100	240	80,3	5,8 / 3,7 / 3,1	51,6	36,26
5,8 / 3,7 / 3,1	48,7	100	300	54,7	4,2 / 2,7 / 2,4	67,8	53,85
4,2 / 2,7 / 2,4	63,4	100	360	62,6	2,5 / 1,5 / 1,4	62,4	72,53
2,5 / 1,5 / 1,4	59,6	100	420	46,4	1,7 / 1 / 0,8	72	81,32
20,3	20,8	100	420	37,3	16,5	65,2	23,08
16,5	21	300	60	42,4 / 98,2	14,5	61,8	30,29
14,5	58,7	300	120	72,4	9,8	70,4	52,88
9,8	66,8	300	180	61,2	3,1	81,6	85,09
19,2	20,6	300	240	41,4 / 92,4	13,6	72,8	33,98
14,9	20,8	450	180	41,4 / 92,4	2,9	66,4	86,06
10	25,2	800	60	25,2 / 87,4	2,3	87,4	90,87

Cu cât eşantioanele sunt mai mici cu atât cantitatea de apă pierdută este mai mică, şi observând că puterea este mică s-a trecut mai repede la eşantioane mari şi puteri mai mari.

Față de uscarea la puterea de 100W, s-a evidențiat o creştere aproximativ constantă a temperaturii cu scăderea umidității, deci este mult mai eficientă, însă în cazul în care eşantioanele de Pleurotus Ostreatus au fost supuse procesului de uscare direct la aceeaşi putere dar pentru un timp mai mare s-a observat un comportament mai bun, fără zone arse, dar având o umiditate foarte mare, (figura 8.b).

La putere mai mare ciuperca s-a uscat complet, însă au apărut şi zone arse datorită timpului mare de expunere.

Mărind în continuare puterea, dar reducând timpul de expunere s-a observat o uscare mai bună decât în cazul de mai sus, şi deci recomandabil pentru acest soi de ciuperci ar fi o putere mare şi un timp scurt, față de celelalte două soiuri unde este recomandabilă utilizarea unei puteri mică, dar intervalul de timp mai mare.

Printr-un control bun asupra temperaturii se poate obține o uscare foarte bună şi eficientă, proces influențat de cantitatea de ciuperci introdusă în incintă, deoarece atât umiditatea cât şi temperatura diferă de la o poziție la alta, temperatura fiind mult mai mare în interiorul masei care se încălzeşte pe o perioadă de timp mai lungă față de extremități, uscarea fiin mai lentă.

În experimentele analizate puterea de intrare a fost cuprinsă în intervalul 100 - 800W, unde a fost posibil şi nu a existat limită de temperatură, obținându-se şi temperatură de 150 0C.

Dezavantajul acestei metode îl reprezintă uscarea neomogenă, datorită diferenței de temperatură existente între eşantioanele situate în diferite puncte ale incintei, deoarece acest parametru influențează structura internă a eşantioanelor şi implicit calitatea finală a acestora.internă şi calitatea finală a acestora fiind interesant de observat până unde se poate ajunge, obținând şi temperatură de 150 ^{0}C.

3 Concluzii:

Se poate afirma că pentru o uscare mai bună în cazul soiului de Pleurotus Ostreatus ar fi recomandabil o putere mare şi un timp scurt în procesul de uscare, față de celelalte două soiuri unde este recomandabilă utilizarea puterilor mici, iar intervalul de timp mai mare.

Locul din care se face citirea temperaturilor este esențială în reuşita procesului de uscare, deoarece acesta are o deosebită influență asupra structurii produsului uscat, precum şi a ratei de uscare.

Recomandabil pentru aceat gen de dehidratare ar fi utilizarea unor incinte prevăzute cu mai multe magnetroane în jurul acestora, dar fără ca acestea sa intre în rezonanță, iar în partea de sus să se amplaseze extractoare de umiditate care sa intre în funcție în momentul în care magnetroanele nu funcționează.

Aprecieri - This work was cofinanced from the European Social Fund through Sectoral Operational Programme Human Resources Development 2007-2013, project number POSDRU/89/1.5/S/56287 *„Postdoctoral research programs at the forefront of excellence in Information Society technologies and developing products and innovative processes", partner University of Oradea.*

Referințe

[1]. http://www.incasa.ro/Ciuperci_Agaricus_bisporus_3846_815_1.html

[2]. Delgado A.S, Sun D.W (2002) – *Desorption isotherms for cooked and cured beef and pork* Journal of Food Engineering 51(2), pp 163 – 171

[3]. Devace C, Rodriguez-Lopez J.N, Fernoll L.G, Catana J.M, et al (1999) – *Enzyme inactivation analysis for industrial blanching applications: comparasion of microwave, convențional, and combination heat treatmentson mushroom polyhenoloxidase activity*. Journal of Agricultural and Food Chemistry 47(11), pp 4506 – 4511

[4]. Drouzas A.E, Schubert H (1996) Microwave application in vacuum drying of fruits of Food Engineering 28(3), pp 203 – 209

[5]. Lombrana J.I, Rodriguez R, Ruiz U – *Micorwave–drying of sliced mushroom, Analysis of temperature control and pressure* Innovative Food Science and Emerging Technologies 11, 652 – 660.

[6]. Nijhuis H.H, Torriaga H.M, Mureşan S, Yuksel D, Leguijt C, at ol (1998) – *Approaches to improving the quality of dried fruit and vegetables,* Trends in Food Science and Technology 9 (1),13-20

[7]. Rodriguez R, Lombrana J.I, Kamel M, Elvira C. (2005). - *Kinetic and Quality study of mushroom drying under microwave and drying. Drying Technology*, 23(9–11), pp 2197−2213.

[8]. http://www.pleurotus.daky.ro/ciuperci_pleurotus.htm]

[9]. http://www.gradinamea.ro/Cultivarea_ciupercilor_Pleurotus_2706_543_1.html

Influența frecvențelor înalte asupra uscării perelor întregi şi feliate glasate cu pudră de zahăr

Mircea PANTEA, Adriana GRAVA, Marcela LAZA (BULC), Marius SILAGHI
Universitatea din Oradea, Universității 1, 410087 Oradea, Romania, mpantea@uoradea.ro

Abstract. În lucrarea de față s-a încercat determinarea temperaturilor şi a umidității optime în urma procesului de uscare cu microunde a perelor atât întregi cât şi felii, care au fost comparate cu diferența dintre masa inițială şi finală pentru a putea fi observat cel mai bun randament, realizându-se modelarea procesului de uscare cu programul comercial HFSS.

1 Introducere

Chiar dacă exitența microundelor a fost presupusă pentru prima dată printr-un model matematic de către Maxwell şi experimental de Hertz încă din secolul trecut, aplicarea acesteia în practică a continuat să întârzie. [1]

Primele experimente în acest domeniu al procesării fructelor în camp de microunde au apărut după anii 70 în S.U.A. şi Japonia, observând o reducere considerabilă a cantității de apă şi a volumului acestora, totodată oferind şi un mare avantaj anume eliminarea sistemelor de răcire şi conservare a fructelor, dintre care putem aminti: prune, caise, struguri, mere, pere, etc. [2]

Studiul s-a axat pe pere ce provin din România, fiind folosite atât pere întregi cât şi tăiate felii, în stare naturală dar şi glasate cu pudră de zahăr, în final fiind făcute simulări cu programul HFSS.

Cu ajutorul energiei radiante de înaltă frecvență timpul de uscare al perelor se reduce substanțial, față de o uscare convențională, în care nici după 8 zile de expunere la soare sau 2-3 zile în cuptoare încălzite cu lemn nu ajung la aceleaşi caracteristici foarte importante.

Pe perioada procesului de uscare perele suferă unele modificări atât din punct de vedere al densității cât şi a porozității acestora.

Scopul acestei lucrări este de a deretmina timpul şi puterea de uscare a perelor în funcție de dimensiunile acestora şi de soi în vederea conservării.

Conținutul de umiditate a fost analizat pe baza raportului dintre masa inițială şi masa la un moment dat pentru fiecare eşantion în parte cu ajutorul unei balanțe şi determinat cu ajutorul umidometrului FHT 60, iar temperaturile au fost determinate cu ajutorul instrumentului Fluke 62şi Fluke 87 TRUE RMS MULTIMETER.

S-a folosit un cuptor cu microunde cu putere reglabilă între 100 – 800W, care poate funcționa cu aer cald, aer cald combinat cu microunde şi doar microunde. Energia radiantă îşi schimbă direcția de propagare de miliarde de ori pe secundă, fiind tranmisă spre incintă cu ajutorul unui ghid de undă, incintă a cărui pereți constituie o ecranare şi creează astfel un sistem de rezonantă. [1]

2 Partea experimentală

Perele absorb energia microundelor transformându-se în căldură în primul rând datorită conducției ionice, dar şi a rotației dipolului, această încălzire depinzând atât de proprietățile dielectrice, fizice şi chimice, cât şi de caracteristicile sursei generatoare şi transparența ambalajului la penetrarea microundelor.

În momentul începerii procesului de uscare perele captează undele electromagnetice încălzindu-se în funcție de amplitudinea de pătrundere a câmpului electric influențată de distanța dintre locul pe unde intră undele în incintă şi eşantion, dar şi de lungimea de undă.

În primul experiment s-au utilizat eşantioane de pere tăiate sub formă de felii putând fi observat fenomenul prin care apa va înmuia particulele în raport cu granulele solide din mediului poros

Tabelul 1

Nr. exp.	Putere [W]	Timp [s]	Temperatura intermediară [^{0}C]	Umiditatea intermediară [%RH]	Greutatea la timpul t [g]	Cantitatea de apă eliminată [%]
1	100	60	42,2	52,6	9,2 / 11,1 / 12,5	1,09 / 1,8 / 0,79
2	100	120	55,5	88	8,7 / 10,7 / 12,2	6,45 / 5,31 / 3,17
3	100	180	60	99,7	7,8 / 9,9 / 11,5	16,13 / 12,39 / 8,73
4	100	240	75	86	6,7 / 8,8 / 9,9	29,96 / 22,12 / 21,43
5	100	300	77	80	5,1 / 7,6 / 8,8	45,16 / 32,74 / 30,16
6	100	360	85	85	4,1 / 6,3 / 7,4	55,91 / 44,25 / 41,27
7	100	420	96	39,4	3,0 / 4,9 / 4,9	67,74 / 56,64 / 61,11
8	100	540	42,2	38	11,8 / 9 / 8,8 10,1 / 7,1 / 6,6	14,41 / 21,11/ 25

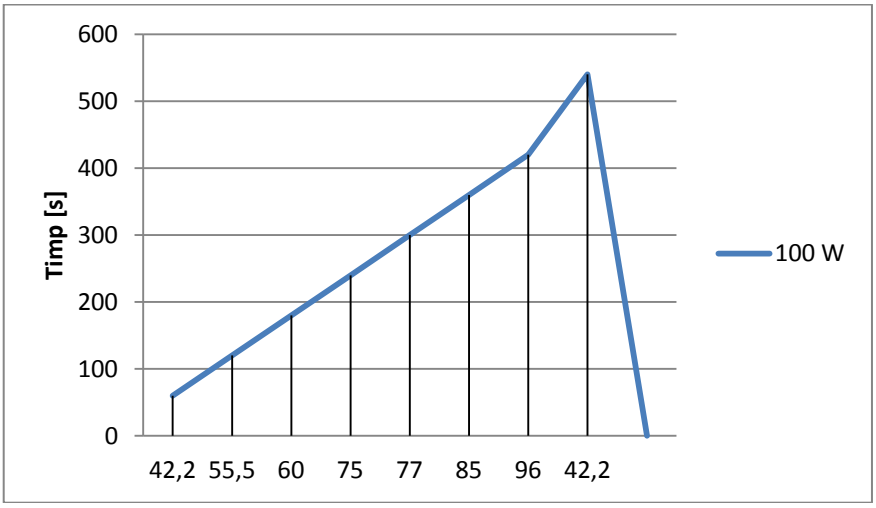

Figura 1. Variația temperaturii în raport cu timpul la puterea de 100W

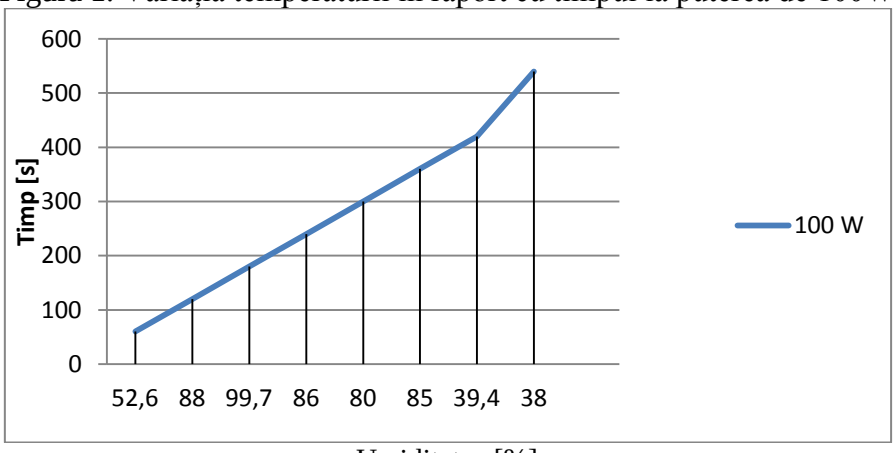

Figura 2. Variația umidității în raport cu timpul la puterea de 100 W

Valorile de temperatură diferă cu 3 – 4 ^{0}C între eşantioane şi umiditatea cu 12 – 14% RH, datorită poziţiei acestora în incintă, iar în tabel am trecut mediile acestora.

Se observă că la aceată putere feliile mai mari reţin mai multă apă, şi chiar dacă temperatura creşte, umiditatea acestora scade.

După timpul de 120 s s-a observat că feliile de pere erau învelite cu un strat de apă şi s-a continuat experimentul până s-a ajuns la temperatura de 96^{0}C. În continuare s-au folosit alte felii dar de această dată pentru un timp de 9 min (vezi rândul 8), mai mare decât timpul din rândul 7 al tabelului de mai sus.

Se observă că timpul de procesare la această putere este mare, motiv pentru care s-a crescut puterea de lucru la 300W continuând măsurătorile tot cu eşantioane ca în exemplul de mai sus, pornind de la temperatura acestora de 21,2^{0}C, umiditate de 44,95% RH şi greutatea de 20,3 grame.

Tabelul 2

Nr. exp.	Putere [W]	Timp [s]	Temperatura intermediară [^{0}C]	Umiditatea intermediară [%RH]	Greutatea la timpul t [g]	Cantitatea de apă eliminată [%]
1	300	60	58	95,1	19,9	1,97
2	300	120	74	54,3	14,8	27,09
3	300	180	87	47,2	8,5	63,05
4	300	240	101,6	50,1	6,1	69,95
5	300	300	91,6	44,9	26,7 / 10,2	61,80

Ultima linie îi corespunde unei uscări directe.

Din analiza tabelului s-a observat că în prima parte a experimentului creşte foarte mult umiditatea pentru primul interval de timp, după care valoarea acesteia scade pâna la temperatura de 101,6 ^{0}C.

Deşi uscarea directă la o putere de 300W este reuşită, produsul mai poate fi uscat, motiv pentru se creşte puterea.

Tabelul 3

Nr. exp.	Putere [W]	Timp [s]	Temperatura intermediară [^{0}C]	Umiditatea intermediară [%RH]	Greutatea la timpul t [g]		Cantitatea de apă eliminată [%]
					Iniţială	Finală	
1	450	240	88,2	54,6	21,8	8	63,30
2	800	60	82	60,3	27,9	17,5	44,44
3	800	180	136	arsă	18,3	5	72,68
4	800	60	95,2	98,7	84,6	73,7	12,88
5	800	180	104,2	97,8	86,5	57,8	33,18

Ultimele două linii sunt pentru pere întregi la o putere de 800W, pornind de la o temperatură iniţială de 15,4 ^{0}C.

Dacă se ţine cont de calitate şi aspect commercial, în cazul uscării feliilor de pere cu dimensiuni mai mici puterea optimă este de 450W într-un interval de timp de 200 - 240 secunde, iar dacă dimensiunile acestora sunt mari, puterea este de 800W pentru un interval de 90 – 120 secunde.

Putem spune aşadar că se pot usca perele la puterea de 800W dar în intervale de timp mici, în care acţionează microundele cu pauză pentru răcirea şi evaporarea excesului de apă de 1 minut.

S-au continuat experimentele cu eşantioane de pere glasate cu zahăr pudră pentru a fi observate avantajele şi dezavantajele utilizării zahărului asupra fructelor.

În primul caz s-au folosit eşantioane tăiate felii glasate cu zahăr, uscate direct la diferite puteri, pornind de la temperatura de 18,4 ^{0}C, umiditate de 39,7%RH şi greutate de 9,3 grame.

Tabelul 4

Nr. exp.	Putere [W]	Timp [s]	Temperatura intermediară [^{0}C]	Umiditatea intermediară [%RH]	Greutatea la timpul t [g]	Cantitatea de apă eliminată [%]
1	100	60	54,8	39,7	8,7	6,45
2	100	120	62,8	44	6,8	26,88
3	100	180	68,4	64,4	5,2	44,09
4	100	240	76,4	57,2	4,1	55,91
5	100	300	83,7	62,2	2,9	68,82

Tabelul 5

Nr. exp.	Putere [W]	Timp [s]	Temperatura intermediară [^{0}C]	Umiditatea intermediară [%RH]	Greutatea la timpul t [g]		Cantitatea de apă eliminată [%]
					Inițială	Finală	
1	100	300	71,6	98,2	9,3	5,6	39,78
2	300	240	98,4	81,4	8,6	3	67,47
3 x	450	120	93 75	45,2 54,6	10,8 13	4,7 5,1	56,48 / 60,76
4	450	180	151	ars	7,2	2,2	Ars 69,44
5	600	120	88,7	94,6	11,2	3,6	67,85
6 xx	600	60	44,8	43,8	100,2	98,4	1,80
7 xx	600	120	95	84,6	98,4	84,6	15,57
8	800	60	94	98,9	112	76,8	31,43

Unde:

- x au fost folosite eşantioane şi cu zahăr şi fără
- xx s-au făcut determinările la acelaşi eşantion de pere întregi în continuare.

Observația în acest caz este faptul că perele glasate cu zahăr se încălzesc mai repede deoarece acestea pierd mai multă umiditate.

a) b)

Fig.5. Eşantioane de pere: a) naturale, b) glasate cu zahăr

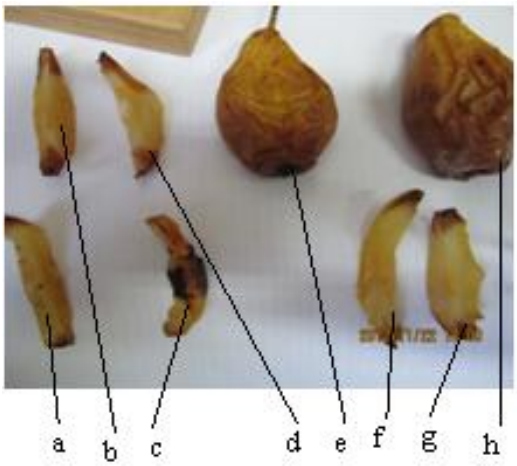

Fig. 6. Eşantioane de pere uscate la diferite puteri:
a) 300W direct cu zahăr, b) 100W treptat cu zahăr,
c) 450W treptat cu zahăr d) 100W direct fără zahăr,
e) 800W direct fără zahăr, f) 450 direct cu zahăr,
g) 450 W direct fără zahăr, h) 600W treptat cu zahăr.

3 Modelarea numerică

Prezentul studiu s-a axat şi pe analiza distribuției câmpului electromagnetic în cavitate. Astfel a fost simulat procesul de uscare a perelor într-un aplicator de microunde cu dimensiunile de x=310, y=290, z=190 cu HFSS (programul High Frequency Structure Simulator).

Proprietățile dielectrice ale perelor şi anume constanta dielectrică şi tangenta factorului de pierderi au valoarea ε'=66,5 şi tgδ=13,96 [4], [5].

Dimensiunile materialului dielectric au fost calculate astfel încât acesta să fie plasat în mijlocul cavității, fiind folosită o frecvență de lucru de 2.45 GHz.

În cele ce urmează sunt prezentate rezultatele obținute în urma simulărilor:

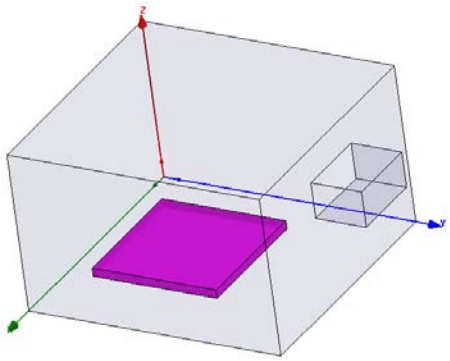

Figura 7. Geometria realizată în HFSS

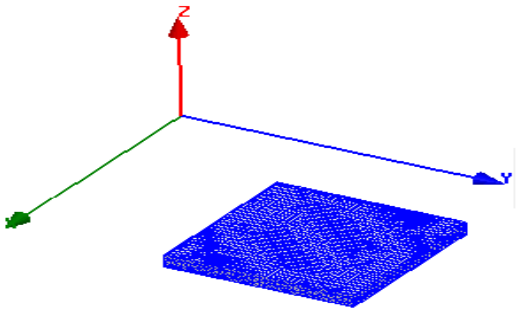

Figura 8. Meshul dielectricului

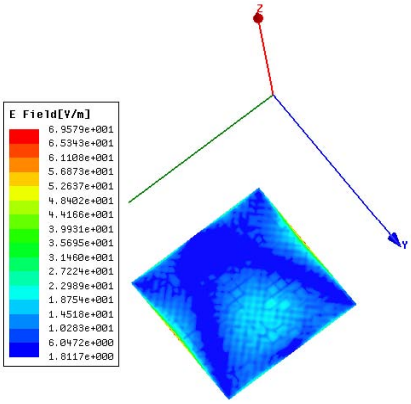

Figura 9. Distribuția câmpului electric pe suprafața dielectricului

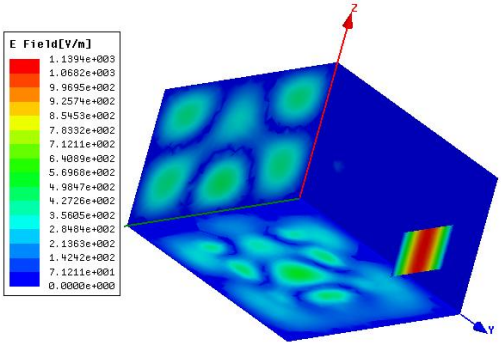

Figura 10. Distribuția câmpului electric pe fețele cavității şi în port

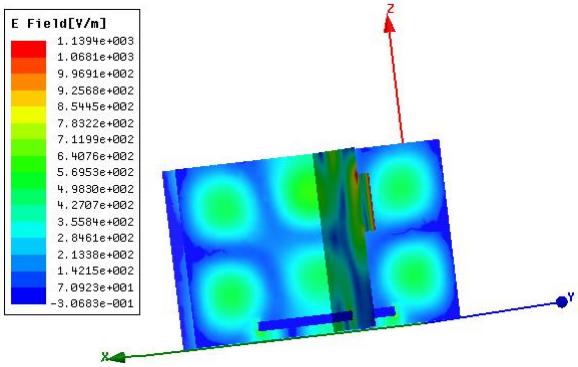

Figura 11. Distribuția câmpului electric prin secțiuni realizate în cavitate, dielectric şi port

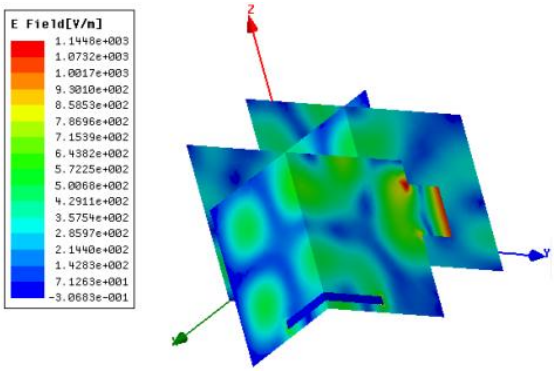

Figura 12. Distribuția câmpului electric prin secțiuni realizate în cavitate, dielectric şi port

4 Concluzii

Uscarea oferă posibilitatea de conservare a fructelor într-o stare stabilă şi sigură, având un termen de valabilitate extins comparativ cu fructele proaspete.

În urma rezultatelor experimentale se poate spune că într-un interval de timp relativ scurt probele de fruct supuse procesării au arătat o creştere a temperaturii foarte mare.

Modul de amplasare al dielectricului în interiorul aplicatorului de tip multimod pentru evitarea apariției fenomenului de supraîncălzire este determinat în urma rezultatelor obținute prin modelarea numerică a procesului de uscare cu ajutorul programului HFSS.

Aprecieri - This work was cofinanced from the European Social Fund through Sectoral Operational Programme Human Resources Development 2007-2013, project number POSDRU/89/1.5/S/56287 *„Postdoctoral research programs at the forefront of excellence in Information Society technologies and developing products and innovative processes", partner University of Oradea.*

Referințe

[1]. http://www.managusamv.ro/fisiere/file/DOC_CERCETARE/Proiect_PNII_nr_3168_2007/Baza_de dateInformatiitehnicedesprecultivareasipastrareaunorspeciipomicole_files/Pastrare_Metodesitehnicidepastrareaproduselorhorticole.pdf

[2]. INFLUENCE OF DRYING METHOD ON DENSITY AND POROSITY OF PEARS R. DE P. F. GUINE Department of Food Engineering, ESAV, Polytechnic Institute of Viseu, Quinta da Alagoa, Ranhados, www.icheme.org/fbp.

[3] Drouzas A.E, Schubert H (1996) Microwave application in vacuum drying of fruits of Food Engineering 28(3), pp 203 – 209

[4] A.A. Barba, G. Siani, M. D'Amore, G. Lamberti, Non-conventional heating of food: the crucial role of the dielectric properties in microwave assited processes, New Challenges in Food Preservation, 11-13 November 2009-Budapest, hungary

[5] O. Sipahioglu, S.A. Barringer, Dielectric Properties of Vegetables and Fruits as a function of Temperature,Ash, and Moisture Content, journal of Food Science-Vol.68, Nr.1, 2003

Dielectric properties and electromagnetic interference shielding behaviour of multi-walled carbon nanotubes MWCNT's/polymer composites

Ştefan URSACHE, Romeo Cristian CIOBANU, Vlad SCARLATACHE, Alina NEAMŢU
"Gheorghe Asachi" Technical University of Iasi, Bd. Dimitrie Mangeron, nr. 21- 23, Iasi, Romania

Abstract. The paper presents the electrical characteristics of a composite polymer matrix based on polypropylene (PP) with insertion of multi-walled carbon nanotubes (MWCNTs). The dielectric characteristics investigated are the real and the imaginary part of permittivity of the sample based on PP with 5% insertion of MWCNTs. The frequency range was 1 MHz to 3 GHz. The electromagnetic properties for shielding applications are taken into account under numerical tests. The proposed material shows some interesting electromagnetic interference (EMI) shielding properties and promises better performance using different amounts of MWCNT's.

1 Introduction

Electromagnetic shielding is frequently used to reduce emissions and to improve immunity of electronic equipment or in the area of protective panels for locative, working, medical spaces against high power EM emitters. Electromagnetic Interference (EMI) and Electromagnetic Compatibility (EMC) are becoming important issues in the design of novel high-speed transmission networks and producing safe and sure equipment, especially at base-sites, with fast growing market at more than 5-7 % per year.

Classical cellular solids used in shields/absorbers and Salisbury screen applications are either massive metallic or metal-multilayer structures. These material solutions do not offer enough degrees of freedom to the EM designer especially at GHz frequency domain, neither do they offer optimised configuration for the structural loading or thermal effects they have to bear. As we know, any enclosure shielding integrity is compromised by the presence of slots and shutter arrays for heat dissipation and for other purposes. If currents following on conducting surfaces of a shielding structure cross these slots or apertures, they become unintentional antennas. One of the ways to eliminate this problem is to use absorbing dielectric materials to design shielding structures. Composite dielectric materials that contain randomly distributed conductive inclusions, including carbon nanotubes, at small concentrations can be used for absorbing electromagnetic waves at RF and microwave frequencies [1]. However, requirements to reduce the weight and the cost of this protective structures demand substitution of metal by conducting polymers and composites. These composites may contain metal, carbon or other insertions [2, 3].

In this paper, there are illustrated the dielectric characteristics and electromagnetic behavior of a nanocomposite polymer matrix based on polypropylene (PP) with insertion of multi-walled carbon nanotubes (MWCNTs).

2 Materials

Polypropylene is part of polyolefin's thermoplastics with a wide spread of products that are made by injection. Is a semi-crystalline polymer that is used extensively due to its unique combination of properties, cost and easy to processing. Polypropylene can be processed by a variety of fabrication techniques like film/sheet extrusion, multifilament, non-woven, injection moulding, blow moulding and profile extrusion [4]. Nowadays we try to develop composite materials based on polypropylene

materials with different inserts, which could improve certain physical, mechanical or chemical properties. One of these materials may consist of a mixture of polypropylene with multi-walled carbon nanotubes, which would result in a material with better mechanical and physical properties that can be improved by increasing or decreasing percentage of multi-walled carbon nanotubes in polymer matrix [5]. A lot of studies were made on this kind of nanocomposite material in general for developing mechanical and electrical properties. The recent commoditization of multiwall carbon nanotubes (CNT) in particular, as substitute for conductive carbon black (CB) based composites has attracted immense interests from different sector of industries. Typically, CNT can achieve similar or greater electrical property at a fraction of CB loading level, therefore retaining the ease of processing. It appeals especially in applications requiring stringent cleanliness property where contamination is detrimental to materials performance e.g. high-end electronics. The key challenges to successful fabrication of CNT thermoplastic nanocomposites that combined outstanding electrical and mechanical properties rest in understanding of its processing behavior to obtain high degree of percolating morphology (i.e. inter-connective network structure of CNT in polymer matrix) [6].

Because of the very low conductivity of the insulating polymer, a model that has any conduction of charge would have conductivity not very different from the polymer; hence, nanotubes must carry all the charge for high conductivities to be achieved. If nanotubes are in contact, then transfer of charge from one nanotube to another will offer much higher resistance than charge traveling along nanotubes, even for the case of semiconducting tubes. High resistances occur because of the limited contact area between two tubes. This type of resistance, termed constriction resistance, has been shown to be limiting because increasing compression forces or decreasing the hardness of the filler leads to higher conductivities; that is, constriction resistance is the limiting resistance [7].
The percolation threshold of multi-walled carbon nanotubes in polypropylene matrix depend on the processing behavior to obtain nanocomposition of these two materials.

The MWCNTs used in this study, known under their commercial name as NC7000, are high conductivity MWCNTs, characterized by an average diameter of 9.5 nm, a mean length of 1.5 μm, a carbon purity of 90% and surface area of 250-300 m^2/g, products manufactured by Nanocyl S.A.

The PP/MWCNTs nanocomposites were prepared separately by melt compounding PP pellets with 5 % MWCNTs powders. Compounding was performed at 175 °C for 8 minutes, while the mould temperature was maintained at 50 °C. The samples were performed by direct melt compounding and have a diameter of 5 mm and a thickness of 2.9 mm. This sample was cut from material with a specialized perforating punch.

3 Dielectric analysis

In the analysing process of the characteristics of dielectric parameters was used Agilent E4991A impedance analyser, a dielectric cell BDS 2200 that were connected using the extension 002 of the broadband spectrometer Novocontrol, concept 80. Also for temperature control was used the system Quatro Cryosystem.

With Agilent E4991A impedance analyser can be measured both the magnetic and dielectric characteristics of the materials, but with different cell. In this paper we will focus on measuring the dielectric characteristics with the system presented in Figure 1.

Figure 1: The measurement system of the dielectric characteristics at high frequency

The Agilent E4991A impedance analyzer has the following characteristics/seetings for the measurements:

- The frequency band: 1 MHz ÷ 3 GHz;
- The rank of the impedance: 100 mΩ ÷ 100 kΩ;
- The accuracy: 0.3% of measured value (maximum);
- The rank impedance: 100 fF ÷ 100 nF;
- The rank of tan(Delta): 3m ÷ 3k;
- The accuracy of tan(Delta) 3m (max);
- The rank of θ: 0 ÷ 360 degrees;
- The accuracy: 0.2 degrees (maximum);
- The voltage rank DC: ± 40 V;
- The accuracy: 46 mV;
- Calibration: Open, closed, full, capacitor with low loss and capacitor 50 Ω.

The analyzer uses a dielectric cell BDS 2200 which has the following characteristics:

- The frequency band: 1 MHz ÷ 3 GHz;
- Electrodes of gold metal with 5 mm dimension that are differentiated by a border for superior electrode;
- Calibration: Open, Closed.

The measurements were performed in the frequency band: 1 MHz ÷ 3 GHz in 20 points with a logarithmic scale. The temperature range is the same as at low frequencies, 30 ÷ 120 °C, with an increment of 10 °C. Sample used for measurements in this frequency range have a thickness of 2.9 mm. The Graphical representation is made in 2D and 3D form for the clarity of the results.

The 2D and 3D representation of the real and imaginary permittivity for sample PP-MWCNT at high frequency depend on temperature variation are presented in Figure 2 and Figure 3. A slight relaxation can be observed at around frequencies of 500 MHz, due to ionic polarization mechanism, a mechanism that is specific to this frequency band, but that is not specific to these types of materials.

Regarding the imaginary permittivity, Figure 3, it is observed that decreases with increasing frequency and increased slightly with increasing temperature. Is not observed a peak value for the loss dielectric factor, and we can say that in this band don't have the resonance phenomena.

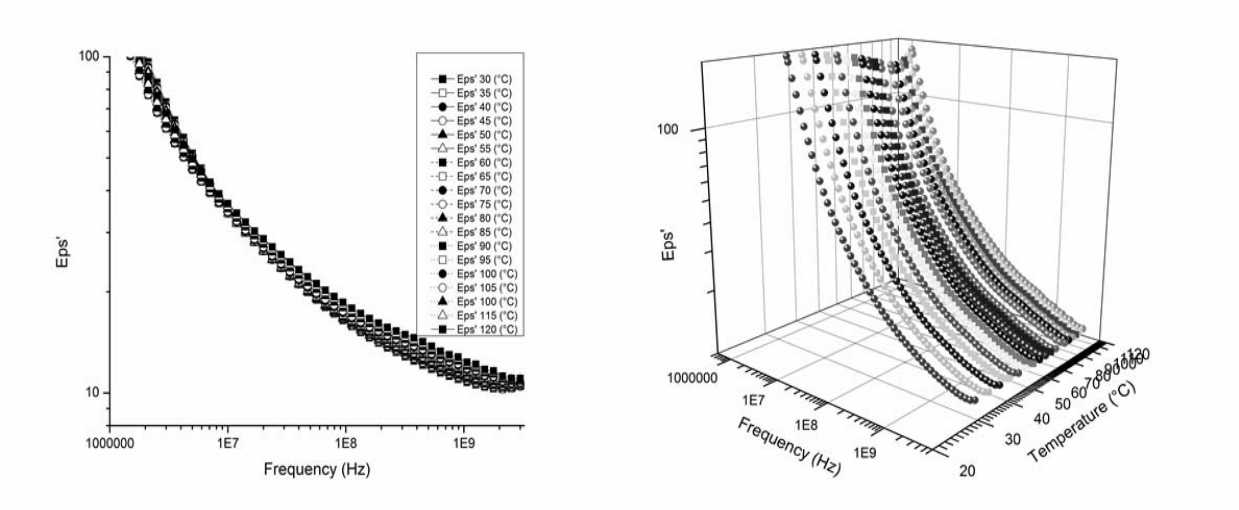

Figure 2: The 2D and 3D diagram of real permittivity for sample PP-MWCNT at HF in function of the temperature variation

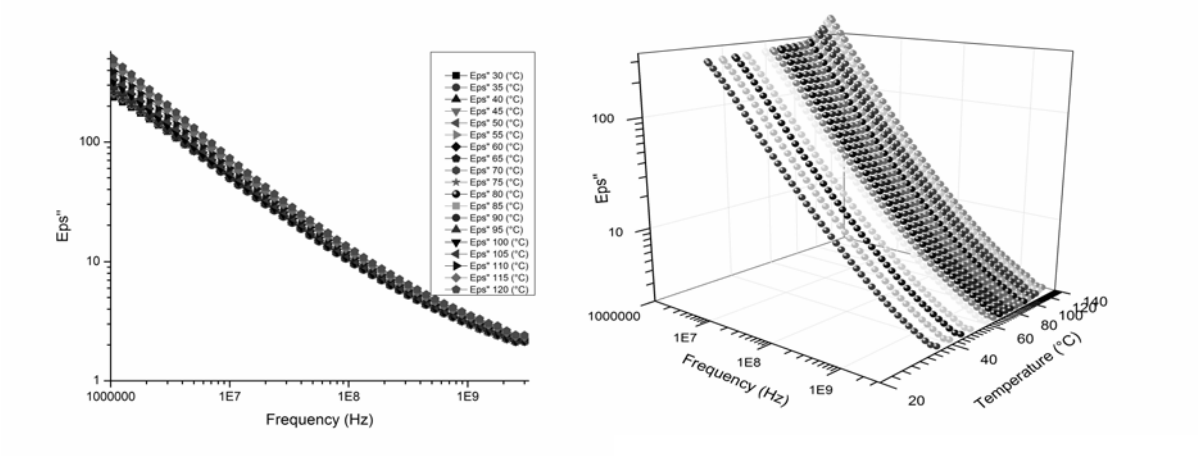

Figure 3: The 2D and 3D diagram of imaginary permittivity for sample PP-MWCNT at HF in function of the temperature variation

4 Electromagnetic shielding – numerical analysis

Electromagnetic solvers simulate the Maxwell's equations [11] and their variations on a computer depending on electromagnetic field and material properties. The results were obtained in transient solver, which can cover the entire broadband frequency behavior of the simulated device from only one calculation run (in contrast to the frequency stepping approach of many other simulators). This solver is very efficient for most kinds of high frequency applications such as connectors, transmission lines, filters, antennas and many more. This simulator is equipped with the new Multilevel Subgridding Scheme (MSS™) which helps to improve the meshing efficiency and thus can significantly speed up simulations especially for complex devices.

Electromagnetic simulation results show the S (scattering) parameters for the structure an represent reflected or transmitted power flow between two ports through a certain medium – Figure 4 left. In the shielding theory the typical macroscopic parameters that define the reflectance, transmittance and absorption are defined relative to the electromagnetic power and are related to the S parameters [10] as shown in equations (1-3):

$$R = |S_{11}|^2 \tag{1}$$

$$T = |S_{21}|^2 \tag{2}$$

$$A = 1 - R - T = 1 - |S_{11}|^2 - |S_{21}|^2 \tag{3}$$

The structure designed under numeric tests is a material sample with defining dimensions 45 mm x 20 mm x 4 mm and the materials properties, electric permittivity real and imaginary, were parametric varied with the values from dielectric measurements previously performed corresponding of different temperatures. The discretization was made in tetrahedral meshing for better accuracy – Figure 4 left.

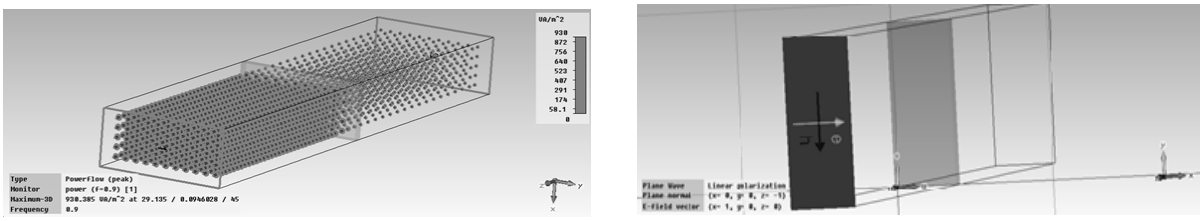

Figure 4: Power flow reduction by the composite shield (left) and boundary condition (right)

It was investigated the interaction between a plane wave and the considered sheet of conductive polymer with material's parameters obtained in the dielectric measurements, at normal incidence. The boundary conditions are set to electric wall (both walls on x directions) and magnetic wall (y direction walls) Figure 4 right. An input wave port is placed at some space from the structure; the second (exit) wave port is added only when losses inside the structure are taken into account.

The simulations of the electromagnetic behaviour for the structure was made using parametric sweep simulations tool of the CST software for different values of dielectric permittivity (ε) obtained previously with dielectric spectroscopy.

The frequency range for de solver was set in the range 0.1 to 3 Ghz because it cover the frequencies most used in the domestic mobile communications (GSM, UMTS, Wi-Fi, Bluetooth), the target application of the structure propose.

Typical results are those from Figure 5 that shows the S11 parameter, defining the electromagnetic reflective properties of the material.

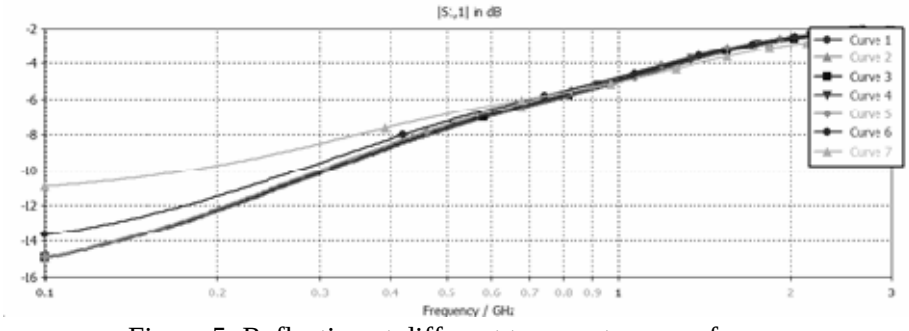

Figure 5: Reflection at different temperatures vs. frequency

5 Conclusion

This paper presents the dielectric characteristics of a polymer nanocomposite material with insertion of multilayer nanotubes carbon. These materials have a very interesting evolution of the

dielectric characteristics in frequency and temperature variation, due to the polarization mechanisms present. At frequencies in order of MHz appears the polarization of orientation that increase with increasing the temperature. Analysing the dielectric characteristics at high-frequency, observe that mechanism of polarization is present at all temperatures. The electrical permitivity of this material decreases with increasing the frequency. If at low frequency this material has an insulating character, with increasing the frequency it has a semiconductor character.

Electromagnetic predictions show that the EMC performances are influenced by the dielectric properties of the composite and indirectly by the nanocomposite components, which means that the growing or decrease the percent of MWCNT will expect better results. These parameters are also influenced by the temperature variation, so it is better to take into account that information in applications with this kind of materials or in future research.

Acknowledgments - This paper was supported by the project "Development and support of multidisciplinary postdoctoral programmes in major technical areas of national strategy of Research - Development - Innovation" 4D-POSTDOC, contract no. POSDRU/89/1.5/S/52603, project co-funded by the European Social Fund through Sectorial Operational Programme Human Resources Development 2007-2013.

This work was also supported by: PERFORM-ERA "Postdoctoral Performance for Integration in the European Research Area" (ID-57649), financed by the European Social Fund and the Romanian Government.

References

[1] H. Chang, Y-M. Yeh, K-D. Huang, Electromagnetic Shielding by Composite Films Prepared with Carbon Fiber, Ni Nanoparticles, and Multi-Walled Carbon Nanotubes in Polyurethane, *Materials Transactions*, **51**, 6, pp. 1145-1149, (2010)..

[2] I. Plesa, F. Ciuprina, P. V. Notingher, D. Panaitescu, Inorganic Nano-filler Effects on Resistivity and Absorption Currents in low density polyethylene Nanocomposites (Part I: Electric field problem), *Rev. Roum. Sci. Techn. – Électrotechn. et Énerg.*, **56**, 3, p. 277–284, (2011)..

[3] C. Morari, I. Balan, J. Pintea, E. Chitanu, and I. Iordache, Electrical conductivity and electromagnetic shielding effectiveness of silicone rubber filled with ferrite and graphite powders, *Progress In Electromagnetics Research M*, **21**, pp. 93-104, (2011).

[4] S. Lee, M. W. Kim, S. H. Kim, Rheological and electrical properties of polypropylene/MWCNT composites prepared with MWCNT masterbatch chips, *European Polymer Journal*, **44** (2008) 1620-1630.

[5] K. Prashantha, J. Soulestin, M.F. Lacrampe, P. Krawczak, G. Dupin, M. Claes, Masterbatch-based multi-walled carbon nanotube filled polypropylene nanocomposites: Assessment of rheological and mechanical properties, *Composites Science and Technology*, **69**, 11–12, pp. 1756-1763, (2009).

[6] C. Y. Lew., M. Claes, F. Luizi, The Influence of Processing Conditions on the Electrical Properties of Polypropylene Nanocomposites Incorporating Multiwall Carbon Nanotube, Nanocyl, 2009.

[7] A. E. Daugaard, Katja Jankova, J.M.R Marín, J. Bøgelund, S. Hvilsted, Poly(ethylene-co-butylene) functionalized multi walled carbon nanotubes applied in polypropylene nanocomposites, European Polymer Journal, 48, 4, pp. 743-750, (2012).

[8] F. Kremer, A. Schonhals, *Broadband Dielectric Spectroscopy*, Springer, 2003.

[9] M. Olariu, V. A. Scarlatache, A. Niagu, S. Ursache, R. C. Ciobanu, The Influence of Frequency and Temperature upon Dielectric Behavior of Polypropylene reinforced with Multi-walled Carbon Nanotubes (MWCNTs), Proceedings of the 13th International Conference on Optimization of Electrical and Electronic Equipment, Brasov 2012.

[10] R. F. Damian, R. Ciobanu, C. Schreiner, EMC tests and properties vs. microstructure for auxetic materials", 15th IMEKO TC4 Symposium on Novelties in Electrical Measurements and Instrumentation, Iasi, Romania, 2007.

Dielectric and Magnetic Measurements for Nanocomposite Materials

Vasilica Alina NEAMTU, Cristina BRATESCU, Ramona BURLACU, Stefan URSACHE
"Gheorghe Asachi" Technical University, Faculty of Electrical Engineering, Prof. dr. docent Dimitrie Mangeron Rd., Iaşi, zip: 700050, Iasi, Romania

Abstract. This paper refers to dielectric and electromagnetic properties measured for nanocomposites materials. We used HF2030 and PU (polyurethane) adhesive matrices, with different percents of nanofillers to study the behaviour of these properties at various temperatures (35°C- 105°C) and frequencies (10^{-1} Hz – 10^{7} Hz). The magnetic measurements were carried out using a Broadband Dielectric Spectrometer (Novocontrol GMBH) encompassing an Alpha frequency response analyzer.

1 Introduction

The properties of nanocomposites materials rely particularly on the matrix material [1]. In the present paper a new concept of adhesives with different percent of nanofillers was studied to obtain modified adhesives with enhanced properties with respect to the starting materials. Adhesives allow different materials to be permanently bonded in an energy-efficient manner and without the need for other auxiliary parts. The benefits of structural adhesives [2] are particularly evident when different materials need to be bonded to each other. This research reveals a new class of materials: modified adhesives with nanostructured bonding particles [3], highly reliable and able of providing a strong and effective combination of energy efficient processes that can be used in disassembly of components to the action of a specific trigger. This could provide the manufacturing industries with a new approach for immediate reuse and recycling of parts before the crushing - shredding processes. Such tailored receipts of adhesives applied with various concentrations of nanoparticles within the joints can significantly increase the functionality of the structure, when activated by use of electromagnetic field of certain frequency.

Electrical and electronic equipment recycling involves dismantling the equipment first. This means separating the different parts of it including the metal part, wires, chips, plastic and others. Sometimes this process is dangerous, especially in the developing countries where this step involves great risks for the workers. Using a modified adhesive [4], electromagnetically active, the risks are eliminated.

The innovative technology is based on designing functionally graded joints by incorporating in polymer matrices of specialized adhesives with electromagnetically active ingredients at nanoscale. The addition of the graded nanostructures within traditional adhesives enhances the mechanical and thermal properties of the joints, leading to stronger and faster assembly of components.

In particular the formulation of the innovative adhesives formulations [5] leads to an increased heating-up rate applying electromagnetic fields. The electromagnetic field of the electromagnetic wave magnetize and demagnetize each particle per every cycle, dissipating a quantity of heating equal to the magnetization/demagnetization work made on the particle [6]. The amount of the generated heat depends on nature, percentage and morphology of ferromagnetic particles and the dissipated heat is able to reach quickly the melting temperature of the thermoplastic polymeric matrix in order to activate the adhesive for a rapid assembling or disassembling process.

2 Analysis of dielectric properties

The samples we used for testing the dielectric properties were obtained by Vaber Industriale R&D *HF Matrix Tests*

1. Dielectric constant (ε')

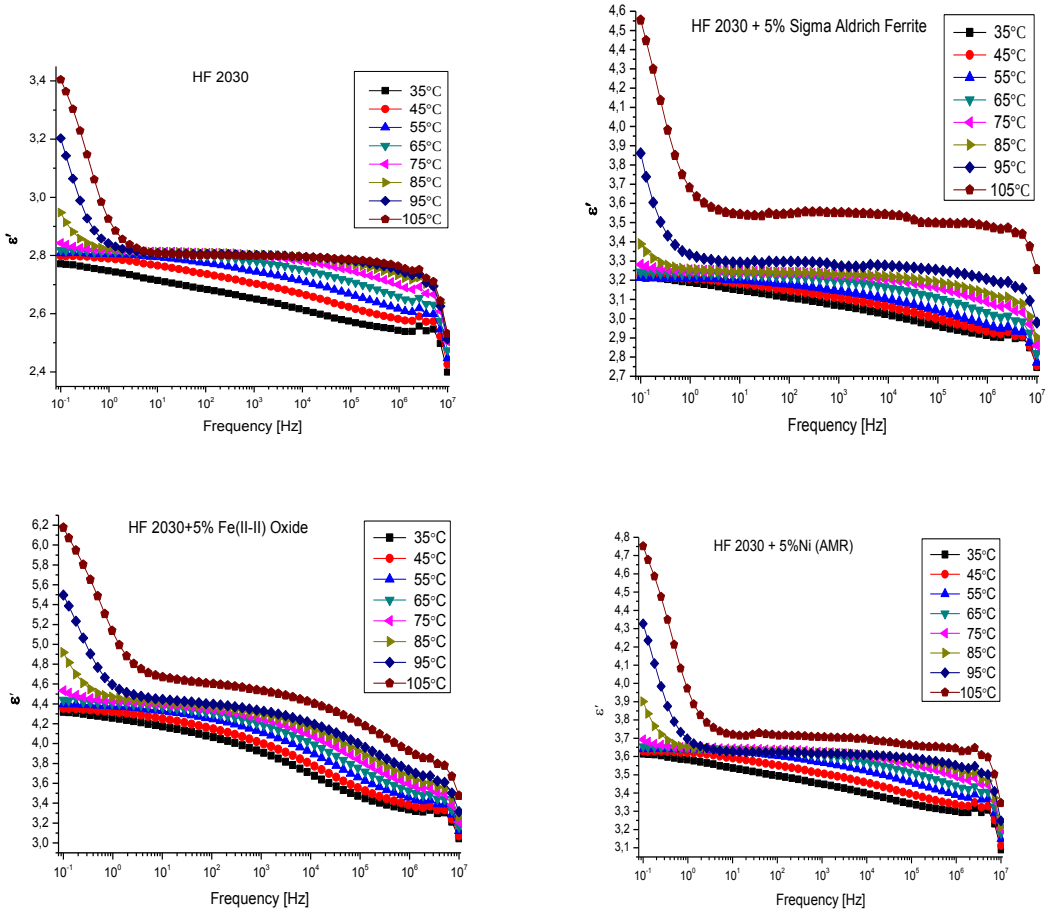

Figure 1. The frequency dependencies of dielectric constant, ε', corresponding to samples HF 2030, HF 2030 + 5% Sigma Aldrich Ferrite, HF 2030 + 5% Fe (II_III) Oxide, HF 2030 + 5% Ni (AMR), at different temperatures

In figure 1 is presented the frequency (10^{-1} Hz to 10^{7} Hz.) dependencies of dielectric constant, ε', at different temperatures, corresponding to different samples obtained by mixing the matrix HF2030 with different ellectromagnetically active nanoparticles.

When we increased the temperature (gradually, with a step of 5°C), the value of ε' increased too and is due to greater freedom of movement of the dipole molecular chains within the adhesive at high temperature. But the most interesting and unexpected feature was the remarkable stability of characteristic vs. frequency for entire domain of temperature, especially for temperatures higher than 80°C.

2. Loss tangent (tgδ)

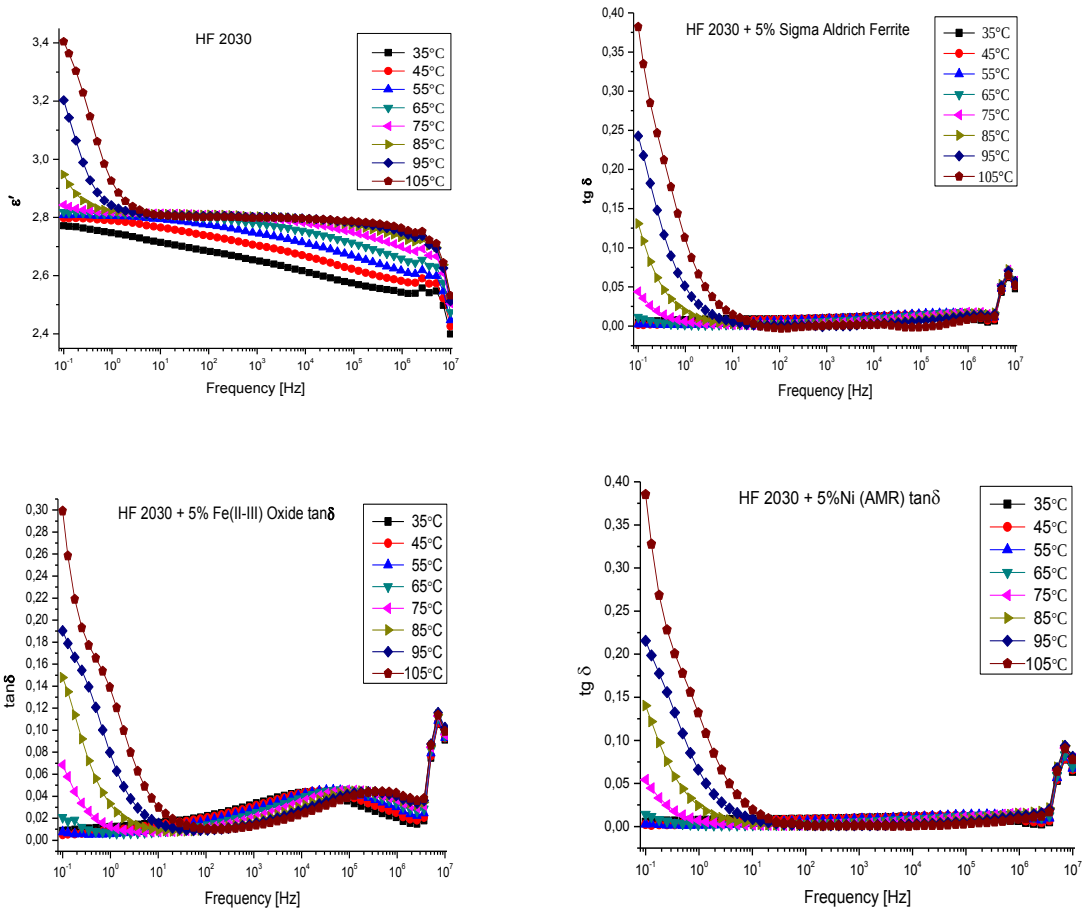

Figure 2. The frequency dependencies of loss tangent, tgδ, corresponding to samples, HF2030 matrix, HF 2030 + 5% Sigma Aldrich Ferrite, HF 2030 + 5% Fe (II_III) Oxide, HF 2030 + 5% Ni (AMR), at different temperatures

The characteristics of loss tangent vs. frequency showed a more than expected increase of relative and a remarkable stability of characteristic vs. frequency for entire domain of temperatures, especially for temperatures higher than 80°C.

Polyurethane (PU) Matrix Tests

1. Dielectric constant (ε')

A second sample matrix that we have used is the PU (polyurethane) matrix.
In figure 3 are shown the frequency dependencies of dielectric constant, at various temperatures (35°C - 105°C), in the domain of frequency 10^{-1} – 10^{7} Hz.

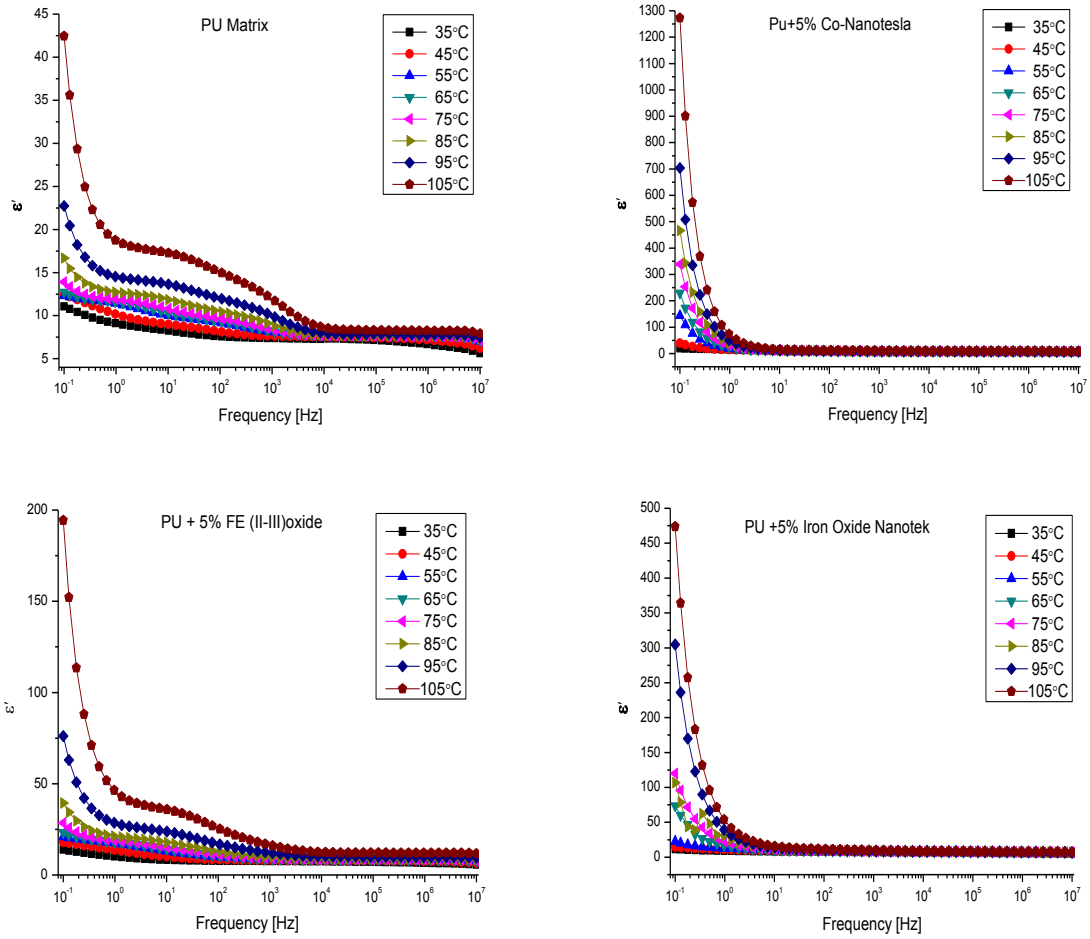

Figure 3. The frequency dependencies of dielectric constant corresponding to samples, PU matrix, PU + 5% Co Nanotesla, PU + 5% Fe (II_III) Oxide, PU + 5% Iron Oxide Nanotek, at different temperatures

In figure 3 it can be observed the same stability of characteristic vs. frequency for entire domain of temperature as for HF2030 matrix.

2. Loss tangent (tgδ)

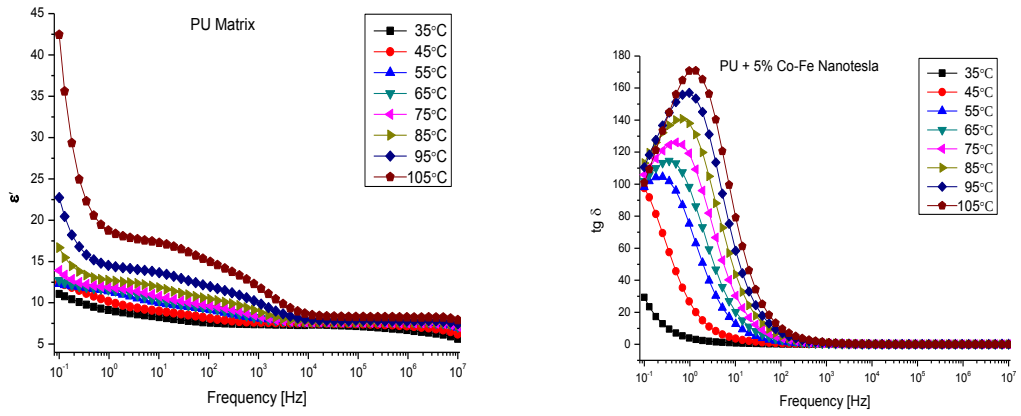

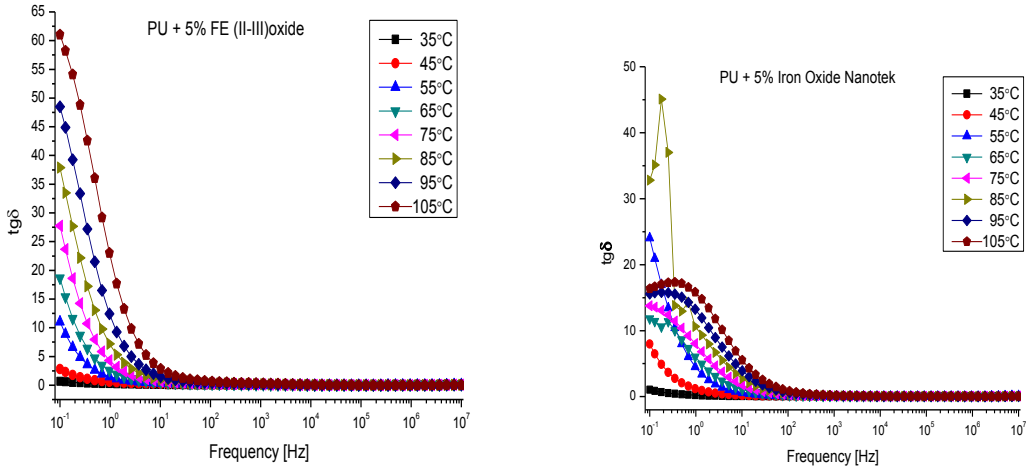

Figure 4. The frequency dependencies of loss tangent corresponding to samples, PU matrix, PU + 5% CoFeNanotesla, PU + 5% Fe (II_III) Oxide, PU + 5% Iron Oxide Nanotek, at different temperatures

Figure 4 shows the frequency dependencies of loss tangent corresponding to different samples, also obtained in Vaber Industriale Laboratories, by mixing the PU matrix with 5% of different nanoparticles. In each of the last 3 figures it may be noticed the stability of this dielectric characteristic (loss tangent) for the entire domain of temperature

3 Analysis of magnetic properties

The samples were placed on a large fixture and it is mounted at the RF extension line of the RF extension system which operates between 1MHz and 1GHz. The complex permeability $\mu^*(f) = \mu'(f) - i\mu''(f)$ has been determined in the frequency range from 1 MHz to 1GHz. The AC voltage applied to the capacitor was equal to 0.1 V. We used the same HF2030 matrix for these tests.

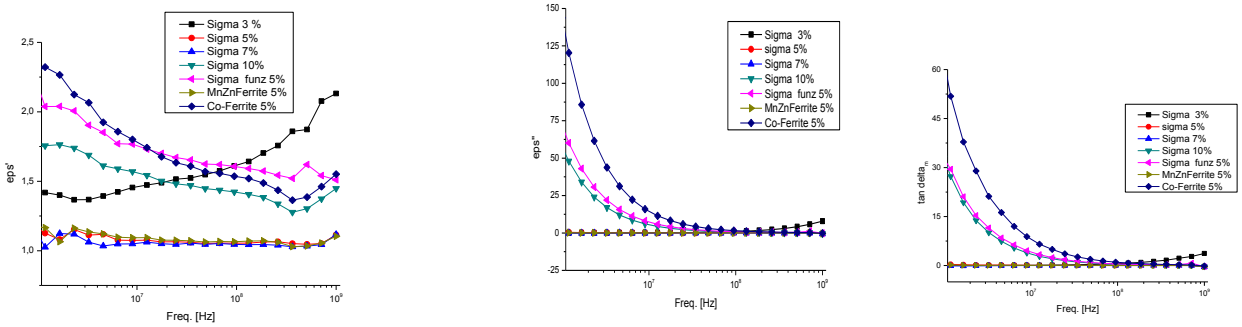

Figure 5. The frequency dependencies of dielectric constant, ε',dielectric loss, ε'', and loss tangent tgδ.

In figure 5 it can be observed a stability for the entire domain of frequency for loss factor and loss tangent.

4 Conclusion

There were studied the dielectric and magnetic properties for HF2030 and PU matrices with different percent of nanofillers. The results showed that dielectric constant increases with the

temperature, due to the greater mobility of the particles. The characteristics present a remarkable stability for the entire domain of frequency.
The main potential benefit of this adhesives is related to the immediate reuse and/or superior recycling of components of high value, offering important technological advantages in terms of cycle time, energy saving, simplification of productive lay-out, flexible design of the manufacturing processes etc., beyond the significant economic benefit.
The decrease in ε' with increase of frequency is due to the orientation polarization
The increase in ε' with increase of temperature is due to greater freedom of movement of dipole molecular chain of adhesive at high temperature.
5% addition of nanoparticles would be a reasonable solution for the proposed composites in association with electromagnetic field.

Acknowledgments - This paper was supported by the MANUNET ERANET MAGBOND 7-042/2011 project financed by UEFISCDI and the project PERFORM-ERA "Postdoctoral Performance for Integration in The European Research Area" (ID-57649), financed by European Social Fund and the Romanian Government.

References

[1] Michael F. Ashby, Paulo J. Ferreira, *Nanomaterials, Nanotechnologies and Design,* An introduction for engineers and architects, ISBN: 978-0-7606-8149-0.
[2] T.H. Dawdy, *Modified Structural Adhesives,1988.*
[3] Jackie Yi-Ru Ying, *Nanostructured Materials: Applications to Sensors, Electronics, and Passivation Coatings,* Academic Press, 14.12.2001 - 222 pages.
[4] Terrance H. Dawdy, *Epoxy Modified Structural Adhesives Having Improved Heating Resistance,* Patent No. 4467071, 21.Aug. 1984.
[5] Gary Thomas*, Development of Innovative Adhesives Using Renewable Raw Materials,* July 3, 2012.
[6] Ralph Skomski, G. C. Hadjipanayis, David J. Sellmyer, *Effective Demagnetizing Factors of Complicated Particle Mixtures,* IEEE Transactions On Magnetics, Vol. 43, No. 6, June 2007.

Considerations Concerning the Losses Separation in Amorphous Cobalt Based Ribbons

Veronica PALTANEA, Gheorghe PALTANEA, Horia GAVRILA
Politehnica University of Bucharest, Electrical Engineering Department, Romania;
gheorghe.paltanea@upb.ro

Abstract. We report an investigation on magnetic energy losses in near-zero-magnetostriction toroidal samples of $Co_{67}Fe_4B_{14.5}Si_{14.5}$ amorphous ribbons from DC to 5 MHz at a given magnetic flux density of 20 mT. The loss behaviour of this material was studied on field-annealed samples as-cast at 11 μm. Amorphous ribbons annealed under transverse field benefit by limited irreversible domain wall activity, which implies reduced hysteresis and excess losses in comparison with the values, measured on longitudinal annealed field samples.

1 Introduction

Application of amorphous soft magnets in electric-utility and industrial transformers is increasingly being adopted, helping to solve global warming and energy-saving problems. Co-based amorphous components are used in power electronics, telecommunication equipment, sensing devices, etc. All of these applications are justified due to faster flux reversal, lower magnetic loss and more versatile properties achievable in amorphous alloys through thermo magnetically treatments.

An amorphous alloy may be described as a random ensemble of structural units, each extending over a distance equal to few atomic spacings, that have definite symmetry properties and are therefore characterized by a local magneto-crystalline anisotropy of strength *K*, randomly oriented.

In 3d-based alloy, where *K* is of the order of 10^4 - 10^5 J/m^3, the anisotropy is not large enough to force the local alignment of the magnetization to the easy axis of the individual structural units. The negligible value of the average magneto-crystalline anisotropy is the key to the soft magnetic properties of the amorphous alloys. In fact, under these conditions, coercivity and permeability are due only to the residual anisotropies of magneto-elastic origin, or induced anisotropies created by suitable treatments.

The influence of stress anisotropies becomes negligible in the vanishing magneto-striction Co-rich alloys. These materials exhibit the lowest energy losses and the highest permeability at all frequencies. In addition, their properties can be tuned to specific needs by suitable thermal treatments under a saturating magnetic field. These treatments can induce a large-scale anisotropy, as a consequence of localized atomic rearrangements [1].

In this paper we present a theoretical study concerning the amorphous materials and an experimental characterization on $Co_{67}Fe_4B_{14.5}Si_{14.5}$ amorphous ribbon in the range of MHz.

2 Preparation of Amorphous Alloys

Amorphous alloys are obtained by rapid solidification method as thin laminations and ribbons. Today, the predominantly employed rapid solidification technique is Planar Flow Casting (PFC), by one can prepare ribbons of variable width (up to 100 - 200 mm) and thickness usually ranging between 10 and 40 μm. The PFC is a method where a molten metal stream is ejected onto a rotating metallic drum, and the results of this process are thin ductile ribbons. In a typical PFC setup, a quartz crucible, which holds the liquefied master alloy, is placed nearly in contact with the surface of a rotating metallic drum, which drags the composition at a velocity of 10 - 40 m/s. This

ensures a cooling rate of the order of 10^5 - 10^6 °C/s, sufficient to under cool the alloy through the glass transition temperature T_g, where it achieves the typical viscosity of a solid, retaining, at the same time, the disordered atomic arrangement typical for a liquid.

With a more complex method, the so-called in water quenching technique, amorphous wires with a diameter of 50 - 100 μm are prepared. In this case, the molten metal jet is plunged into rotating water.

The usual composition of magnetic amorphous alloys is $T_{70-80}M_{30-20}$, where T is a transition metal (Fe, Co) and M is a combination of metalloids (B, Si, P, C). The radius of the metalloid atoms is much smaller than that of the metals and their most important role is to provide the eutectic composition necessary to achieve the amorphous state.

Lack of crystalline order does not prevent the formation of ferromagnetic order. The existence of a large-scale magnetic moment is basically unaffected by disorder, although its strength is reduced by the presence of the metalloids.

3 Short Presentation of Co-based Alloys

The Co-based alloys are ideal materials as cores of inductive components used up to frequencies of the order of 1 MHz in digital telecommunications circuits, as found, for instance, in the switched-mode power supplies. Their low saturation polarization value J_S is not a disadvantage in these cases, where, in order to limit core heating, the working magnetic induction is always kept small and the working frequency can be very high (in the range of MHz) [2]. To better analyze the behaviour of these materials the authors characterized Co-based alloys at low peak induction values, from low to high frequencies, to prove that the applicability for these alloys is the range of high frequencies.

These alloys are characterized by vanishing magneto-striction and their magnetic properties can be largely modified by means of mild field annealing treatments. For instance samples of $Co_{71}Fe_4B_{15}Si_{10}$ amorphous ribbons [3], have been subjected to a series of field annealing treatments at temperatures of 200 – 250 °C, and uniaxial anisotropies, ranging between K_u = 100 J/m^3 (longitudinal, with square hysteresis loop) and K_u = -84 J/m^3 (transverse, with almost linear hysteresis loop) have been induced. It was observed that the influence of stress anisotropies becomes negligible in the vanishing magneto-striction Co-rich alloys. The properties can be modified to specific needs by suitable thermal treatments under a saturating magnetic field. These can induce a large-scale anisotropy K_u, as a consequence of localized atomic rearrangements having a definite directional order. Being the only form of anisotropy present in the material, K_u fully governs coercive field, permeability and loops shape [1].

For this study, the $Co_{67}Fe_4B_{14.5}Si_{14.5}$ amorphous samples have been prepared in the INRIM Torino laboratories. The samples have been longitudinally and transversally annealed under saturating magnetic field. More details are presented in paragraph IV.

4 Material properties of Co-based Amorphous Ribbons

Two near-zero-magnetostrictive alloys of composition $Co_{67}Fe_4B_{14.5}Si_{14.5}$ were prepared as toroidal samples with the specific mass ρ = 7730 kg/m^3, electrical conductivity σ = 0.709×10^{-6} S/m, Curie temperature T_c = 310 °C and geometrical properties as presented in Table I.

The samples were annealed, in vacuum conditions, under saturating magnetic field as follows: the first ribbon sample, SMP1, was treated in a transversal magnetic field at 250 °C for 45 minutes, the second sample, SMP2, in a longitudinal magnetic field at 250 °C for one hour.

The transverse field treatment resulted into a induced transverse macroscopic anisotropy $K_{u\perp} = (10-15)\,\mathrm{J/m^3}$.

Table 1. Geometrical properties of the samples.

Sample ID	Length L [m]	Toroidal section S [m2]	Thickness d [m]
SMP1	0.493	0.705×10^{-6}	11×10^{-6}
SMP2	0.504	0.613×10^{-6}	11×10^{-6}

Magnetic properties characterization was made from 5 Hz to 5 MHz at fixed peak polarization value J_p = 20 mT and sinusoidal flux by means of a built-on-purpose hysteresisgraph-wattmeter [4].

Acquisition of primary current, supplied through a DC-10 MHz NF-HSA4101 type power amplifier, and secondary voltage was made by a 500 MHz TDS 714L oscilloscope.

The whole system was driven by software in a VEE environment. In the MHz range, for the minimization of any effect of stray parameters, it was used very short leads and a few turn bifilar windings.

5 Energy Losses Separation

The total energy losses required for a magnetization cycle can be decomposed into the sum of hysteresis, classical and excess loss components. This separation allows to separately treat loss mechanisms occurring on different space-time scales once at a time, as if they were independent of each other.

The hysteresis losses are generated by fine-scale instabilities and can be analyzed by coercivity mechanisms.

In the case of classical losses W_{cl} generated by eddy currents, calculated supposing that the material is a homogenous medium, the sample geometry is important.

The direct consequence of the existence of magnetic domains and walls are the excess losses, which are very difficult to determine, because of the great variety of domain structures.

The energy loss separation was made using for the calculation of classical energy loss (W_{cl}), in the approximation of linear magnetization and arbitrary frequency [1], [5], [6], the following relation:

$$W_{\mathrm{cl}} = \frac{\pi}{2}\frac{\gamma J_p^2}{\mu(f)\rho}\frac{\mathrm{sh}\gamma - \sin\gamma}{\mathrm{ch}\gamma - \cos\gamma} \tag{1}$$

where: J_p - peak magnetic polarization, $\mu(f)$- magnetic permeability as a function of frequency, $\gamma = \sqrt{\pi\sigma\mu(f)d^2 f}$ - a dimensionless parameter, and f - measuring frequency.

Further, the sum of excess losses W_{exc} and hysteresis losses W_h is:

$$W_{\mathrm{diff}} = W_{\mathrm{exc}} + W_{\mathrm{h}} = W_{\mathrm{total}} - W_{\mathrm{cl}} \tag{2}$$

Making a graphical extrapolation of W_{diff} to zero, the W_h and the W_{exc}, were been successively determined.

Hysteresis energy loss and excess loss are quantities directly related to the path of micro eddy currents closely surrounding the moving domain walls. In (1) the dependence $B(H)$ is converted into measured permeability μ as a function of frequency. Reversible process associated with magnetization rotations and domain walls displacements are favored in the transverse anisotropy materials. Figure 1 show the specific energy losses and its components

versus frequency in two Co-based amorphous ribbon samples (SMP1, SMP2) with the same thickness.

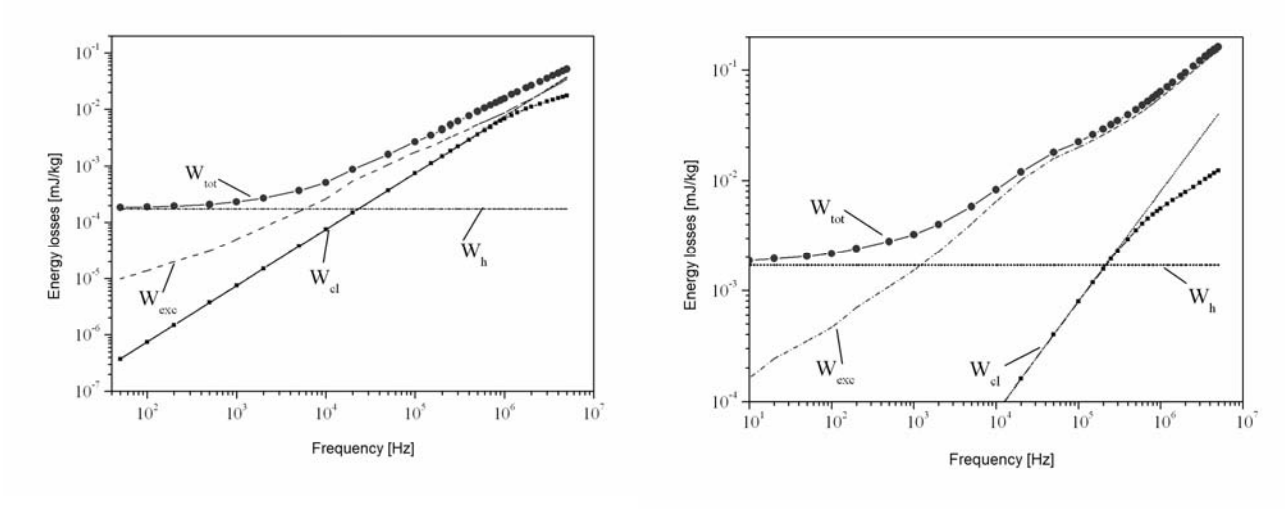

Figure 1: Specific energy losses and its components versus frequency in a Co-based amorphous ribbon. The measurements are made up to 5 MHz at a peak polarization J_p = 20 mT on a tape-wound ring sample annealed under transversal saturating field (SMP1 – left side) and annealed under longitudinal saturating field (SMP2 – right side).

The cobalt base amorphous materials can be subjected to some thermal treatments made under saturating magnetic field for the modification of magnetic properties according to the specification of the devices where the alloy is intended to be used. Because of the induced transversal anisotropy generated by the applied thermo-magnetically treatment, the principal driving mechanism it is the rotation of magnetization, which determines the decrease of the energy losses and some superior magnetic properties at high frequencies.

6 Conclusion

Amorphous ribbons $Co_{67}Fe_4B_{14.5}Si_{14.5}$ transversally and longitudinally annealed show an excellent soft magnetic behavior up to 5 MHz. This results from the combined role of the easy magnetization rotations and weak domain wall activity, in the case of transversally annealed sample, and important domain wall activity, in the case of the longitudinally annealed ribbons, and subsidiary intense eddy currents in the case of transversal induced anisotropy.

References

[1] F. Fiorillo, *Magnetic characterization of magnetic materials*, Elsevier Academic Press, 2004.
[2] G. Bertotti, *Hysteresis in magnetism*, Academic Press, San Diego, 1998.
[3] C. Appino, C. Beatrice, E. Ferrara, F. Fiorillo, The mechanism for loss minimization at medium and high frequencies in field annealed amorphous alloys, *J. Magn. Mater.*, **254**, 2003, pp. 213-215.
[4] G. Bertotti, F. Fiorillo, M. Pasquale, Measurement and Prediction of Dynamic Loop Shapes and Power Losses in Soft Magnetic Materials, *IEEE Trans. Magn*, **29**, no. 6, 1993, pp. 3496-3498.
[5] H. Gavrila, V. Ionita, et all., *Magnetism Tehnic si Aplicat*, Editura Academiei Romane, Bucuresti, 2000.
[6] E. Barbisio, F. Fiorillo, and C. Ragusa, Predicting loss in magnetic steels under arbitrary induction waveform and with minor hysteresis loops, *IEEE Trans. Magn*, **40**, no. 4, 2004, pp. 1810-1819.

Peştera – Generator eolian

Isoc Tudor
Universitatea Tehnică din Cluj-Napoca, tudor_isoc@yahoo.com

Abstract. Lucrarea de față propune exploatarea curentului de aer din peşteri cu ajutorul unui generator eolian care foloseşte un dispozitiv oscilant. Se va prezenta modul de proiectare al unui astfel de generator precum şi al sistemului de conversie al energiei mecanice în energie electrică. Aplicațiile acestui generator au fost concepute de autor prin prisma experienței sale speologice şi a nevoilor cercetătorilor din acest domeniu.

1 Introducere

Lucrarea de față propune exploatarea energiei eoliene dintr-o zonă neexploatată din acest punct de vedere până în prezent şi anume interiorul peşterilor, cu ajutorul unui generator eolian care foloseşte un dispozitiv oscilant precum şi o serie de aplicații pentru deservirea nevoilor acestei zone. Datorită particularităților constructive ale peşterilor se impun unele limitări în ceea ce priveşte modelele de generatoare eoliene care se pot instala în interiorul lor. Autorul propune un model constructiv de astfel de generator adaptat cerințelor din teren. Este prezentat principiul de funcționare al acestui generator (în ceea ce priveşte partea de conversie a energiei eoliene în energie mecanică), principiu care are la bază fenomenul de "flutter". In ceea ce priveşte partea de conversie, este utilizată inducția electromagnetică, generatorul având o parte fixă reprezentată din două bobine şi o parte mobilă reprezentată de doi magneți permanenți. Se va prezenta modul de proiectare al unui astfel de generator precum şi sistemul de conversie al energiei mecanice în energie electrică. Aplicațiile practice ale acestui generator în interiorul peşterii vor fi prezentate deasemenea. Ideea de consumatori de energie electrică în interiorul peşterilor a apărut din prisma cercetărilor care se efectuează în mediul subteran precum şi din nevoia de protecție a peşterilor care sunt arii naturale protejate. Aplicațiile acestui generator au fost concepute de autor prin prisma experienței sale speologice şi a nevoilor cercetătorilor din domeniul speologic.

2 Peştera – sursă constantă de curent de aer şi posibil consumator de energie electrică

In cazul unei generări care se bazează pe o singură resursă, trebuie încercat ca acea resursă să fie cât mai constantă şi exploatabilă. Vântul este relativ permanent sau suficient din punct de vedere al vitezei în România [1], pentru a se putea vorbi despre o constanță a resursei, în doar câteva cazuri, în condiții naturale şi anume în zonele înalte de munte pe toată întinderea lor, în zona Litoralului Mării Negre, Deltei Dunării şi a nordului Dobrogei, zonă cu viteze medii anuale de peste 6 m/s.

Noua zonă, pe care autorul o propune, care însă nu apare pe nici o hartă datorită specificității ei şi a faptului că nu prezintă interes din punct de vedere industrial este interiorul peşterilor.

Cauza principală a formării vântului este diferența de presiune atmosferică dintre două regiuni. Aerul cald fiind mai uşor se înalță şi produce astfel un minim de presiune, locul lui va fi preluat de masele de aer din zona rece (maxim de presiune atmosferică), până când se va egala diferența de presiune dintre cele două regiuni. Viteza vântului depinde direct proporțional de diferența de presiune dintre cele două zone geografice.

In cazul peşterilor sunt doi factori principali care duc la formarea curentului de aer. In primul rând este vorba despre temperatură. O foarte mare parte a anului, există o diferență considerabilă de temperatură între temperatura aerului din interiorul peşterii şi temperatura aerului din exteriorul peşterii. Temperatura din interiorul unei peşteri este relativ constantă pe durata unui an şi este aproximativ egală cu media temperaturilor anuale din acea zonă [2]. Al doilea factor care ajută la formarea curentului de aer este dat de modalitatea de formare a peşterilor. Apa dizolvă în timp calcarul, săpând cavități sub diverse forme. Faptul că peşterile sunt formate sub acțiunea apei face ca în marea lor majoritate să aibă o intrare superioară, unde apa şi-a început acțiunea şi una sau mai multe intrări inferioare, unde apa a ieşit în cele din urmă. Diferența de nivel dintre intrare şi ieşire constituie de asemenea un factor important în ceea ce priveşte curentul de aer existent în peşteri.

Datorită acestor doi factori autorul afirmă că în zona intrării peşterii sau în funcție de configurația cavităților în anumite zone se formează un curent puternic de aer. Acest curent este relativ constant si permanent.

Clasificarea peşterilor ca în Legea nr. 462/2001 modificată şi completată prin Legea nr. 345/2006 şi în OM nr. 604/2005 privind clasificarea peşterilor se face în funcție de mai mulți factori dintre care autorul aminteşte doar speciile de viețuitoare care se găsesc în peşteră (lilieci, chiroptere etc.), diversele vestigii arheologice precum şi formațiunile care se găsesc în peşteră. Toți aceşti factori fac ca vizitarea peşterilor să fie dorită de un mare număr de oameni, în scop turistic sau de cercetare.

Pentru a controla accesul în interiorul acestor zone de o mare însemnătate pentru patrimoniul național şi pentru a colecta date pentru cercetare, autorul propune realizarea unor sisteme de supraveghere a peşterilor, folosind energia eoliană.

Autorul are în considerare trei tipuri de supraveghere şi anume: turistică, de cercetare şi de protecție.

Supravegherea turistică presupune instalarea unor senzori care să contorizeze numărul de persoane care vizitează peştera şi eventual a unor surse de lumină pentru ghidarea în peşteră. De asemenea, deoarece peştera este parcursă de apă pe o mare porțiune este luată în calcul instalarea de senzori care să măsoare nivelul apei şi un sistem de avertizare când acesta creşte prea repede şi există pericolul de viitură.

Supravegherea de cercetare presupune instalarea de senzori pentru a măsura temperatura şi umiditatea în peşteră precum şi diverse aparate cu ajutorul cărora să se observe dinamica coloniilor de lilieci.

Supravegherea de protecție constă în instalarea la intrarea peşterii a unui sistem de supraveghere video care să poată transmite capturile în timp real, unui observator cu acces la internet.

3 Soluția de captare a energiei eoliene

Alegerea variantei potrivite de generator pentru mediul subteran a presupus stabilirea nevoilor specifice ale unui astfel de generator bazate pe specificul acestui mediu.

Spațiul relativ îngust din zonele din interiorul peşterilor unde curentul de aer este mai puternic face ca dimensiunile generatorului eolian să trebuiască să fie reduse. Pe lângă dimensiunile reduse ale generatorului şi datorită faptului că peşterile sunt situate în general în zone izolate sau foarte izolate este necesar ca generatorul să poată fi instalat relativ uşor iar eventualele intervenții să poată fi realizate de persoane fără o pregătire tehnică deosebită şi fără deplasarea unui număr mare de echipamente. Aşadar dispozitivul de captare eolian trebuie să

răspundă următoarelor cerințe: să fie de dimensiuni mici, să fie uşor de transportat, să fie uşor de montat, să fie conceput pe module.

Dintre modele de generatoare eoliene analizate de autor din prisma cerințelor amintite mai sus pentru găsirea celei mai potrivite variante pentru mediul subteran, modelul de genenerator Humdinger a răspuns cel mai bine acestor cerințe. Generatorul Humdinger [3]este un generator eolian a cărui funcționare mecanică se bazează pe exploatarea fenomenului numit „flutter” [1].

„Flutter” este o vibrație auto-alimentată si potențial distructiv mare, care apare când vibrațiile naturale ale unei structuri sunt antrenate de forțe aerodinamice, rezultând mişcări periodice rapide. „Flutter”-ul poate apărea in orice structură dacă fluxul de aer este destul de mare, în condițiile în care există o reacție pozitivă între vibrațiile naturale ale structurii şi forțele aerodinamice. Din aceste motive structurile supuse forţelor aerodinamice - aripi, poduri, coşuri de fum etc. – sunt proiectate în aşa fel încât să evite „flutter”-ul. In structuri complexe în care nu se cunosc nici aerodinamica nici proprietățile mecanice ale structuri, efectul „flutter” se poate evita doar prin testare. „Flutter” -ul ca şi un fenomen aerodinamic instabil controlat poate fi utilizat intenționat în scopuri pozitive, cum ar fi generatoarele eoliene.

Varianta propusă de autor preia unele caracteristici din brevetul de invenție [3] căruia îi aduce unele modificări în ceea ce priveşte concentrarea curentului de aer precum şi tensiunea cu care este întinsă membrana elastică aşa cum se vede în figura Fig. 1.

Soluția constructivă propusă conține următoarele componente:

In tubul de polivinil 8 membrana elastică 6 este fixată in capătul de jos cu şurubul 3 şi cu un tambur de cauciuc 7. In partea de sus a tubului 8 există un mecanism de întindere a membranei elastice 6 format din flanşa 9 şurubul de fixare 10 şi şurubul de tensionare 11. In vederea de sus a secțiunii transversale se pot vedea cele două bobine 2 si cei doi magneți permanenți 5. La vederea laterală se vede fanta prin care trece masa de aer pusă în mişcare de vânt. Membrana elastică 6 pusă în mişcare de vânt va mişca magneți permanenți 5 pe un plan vertical față de cel al bobinelor 2 şi induce astfel un curent. Această inducere este posibilă datorită şuruburilor de fixare a bobinelor 1 care acționează ca un întrefier.

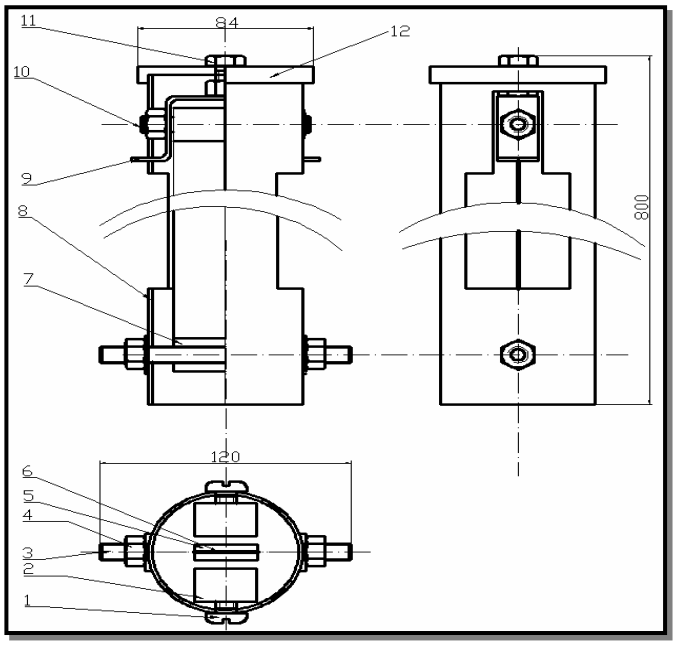

Fig. 1 Generator eolian cu membrana oscilantă. 1- şurub I M4, 2 - bobina, 3 – şurub II M10, 4 – piuliță, 5 - magnet permanent, 6 – membrană elastică, 7 – tambur, 8 – tub, 9 – flanşă (ramă de tragere), 10 – şurub III M10, 11 – şurub IV M10, 12 - capac

[1] Flutter – (lb. engleză). A flutura, a agita, a bate neregulat, a vibra, a undui.

Proiectarea generatorului eolian implică atât proiectarea captatorului eolian oscilant cât şi proiectarea unui generator electric oscilant, deoarece nu există în fabricația curentă generatoare electrice oscilante.

Calculul suprafeței de captare necesare:

S−a considerat că puterea maximă a generatorului trebuie să fie P=1W. Se va folosi formula de la puterea vântului unde C_p este coeficientul de putere:

$$P = C_p * \frac{\rho S v^3}{2} \quad (1)$$

Am folosit pentru simularea vântului, la prototipul construit, 2 ventilatoare care debitau un jet de aer cu o viteză măsurată de un anemometru de:

$$v = 5m/s \quad (2)$$

Din formula (1) am calculat suprafațade captare necesară a captatorului eolian:

$$S = \frac{2P}{C_p \rho v^3} = \frac{2*1}{0.5*1.3*5^3} = 0.025m^2 \quad (3)$$

Suprafața de captare a energiei eoliene în cazul generatorului poiectat este egală cu suprafața ferestrei din tubul de polietilenă şi anume:

$$S_f = L*l = 0.66*0.05 = 0.037m^2 \quad (4)$$

Calculul frecvenței coardei vibrante

Generatorul flutter prezentat in figura de mai sus are distanta L=0.75m intre punctele de suspensie ale coardei vibrante. Aceasta corespunde unei semi-lungimi de unda λ/2. Deci λ=1.5m. S-a cantarit banda elastica si are o masa unitara de m_l=0.004 kg/m. Cu aceste date se poate calcula viteza undelor prin banda:

$$c = \sqrt{\frac{F}{m_l}} = \sqrt{\frac{10}{0.004}} = 50m/s \quad (5)$$

unde F=10N este forța de tensionare a corzii vibrante.

Atunci frecvența de vibrație va fii:

$$f = \frac{c}{\lambda} = \frac{50}{1.5} = 33.3Hz. \quad (6)$$

Schema electrică echivalentă pentru generatorul eolian cu membrană elastică este prezentată in Fig. 2.

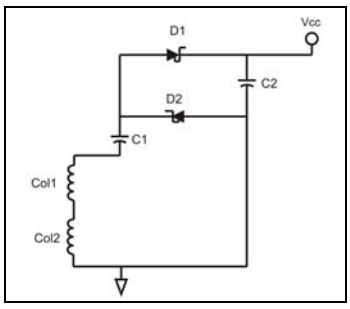

Fig. 2 Circuit electric echivalent. Col1, Col2 – bobine, D1, D2 – diode Schottky, C1,C2 - condensatoare

Circuitul este format din două bobine Col1 şi Col2 înseriate, două diode Schottky D1 şi D2 legate în paralel şi două condensatoare C1 şi C2. Bobinele vor fi fixate cu şuruburi M5 care vor fi folosite şi pe post de miez magnetic care va concentra liniile de câmp magnetic de la magneții permanenți fixați pe membrană elastică.

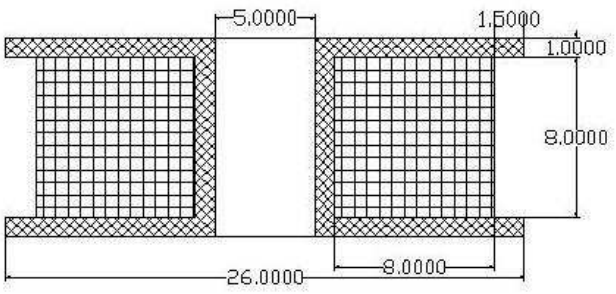

Fig. 3 Secțiune în bobină

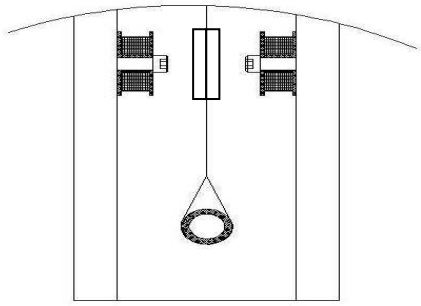

Fig. 4 Secțiune transversală a tubului pentru a se vedea poziționarea bobinelor

Bobinele vor fi fixate cu şuruburi M5 care vor fi folosite şi pe post de miez magnetic care va concentra liniile de câmp magnetic de la magneții permanenți fixați pe membrană elastică ca şi în Fig. 34.

Calculul teoretic al tensiunii de pe bobine:

Inducția magnetică maximă la suprafața miezului bobinei se estimează la

$$B_{\max} = 0,3T \tag{7}$$

pe baza unor măsurători cu Teslametru şi sonda Hall pentru magneții permanenți folosiți.

Fluxul magnetic maxim prin bobină va fi:

$$\phi_{\max} = B_{\max} * S \tag{8}$$

unde:

$$S = \frac{\pi * d^2}{4} = \frac{\pi * 4^2}{4} = 12.56mm^2 \tag{9}$$

Deci inducția magnetică maximă va fi:

$$\phi_{\max} = 3,768 * 10^{-6} Wb \tag{20}$$

Inducția magnetică minimă când magneții permanenți vibrează cu amplitudinea de $\pm 1mm$ va fi determinată pentru

$$B_{\min} = 0,1T \tag{11}$$

Fluxul magnetic va fi:

$$\phi_{\min} = B_{\min} * S = 0,1 * 12,56 * 10^{-6} = 1,256 * 10^{-6} Wb \tag{13}$$

Frecvența de oscilație a membranei la o viteză a vântului de 5m/s este de 33.3 Hz. Perioada vibrației este:

$$T = \frac{1}{f} = \frac{1}{33.3} = 30ms \tag{13}$$

In timpul unei perioade fluxul magnetic prin bobină variază între $\phi_{\max}$ şi $\phi_{\min}$, astfel se induce o tensiune între spire:

$$U_{sp} = \frac{\Delta\phi}{\Delta t} = \frac{\phi_{\max} - \phi_{\min}}{T} = \frac{(3,77 - 1,26) * 10^{-6}}{30 * 10^{-3}} = 0.083 * 10^{-3} V \tag{14}$$

Tensiunea pe o bobină cu $N = 4000$ spire şi conductor de diametru 0,12mm va fi:

$$U = N * U_{sp} = 4000 * 0,1 * 10^{-3} = 0,33V \tag{15}$$

Tensiunea pe două bobine înseriate va fi $U = 0,66V$. Dacă se va folosi schema de redresare-multiplicare a tensiunii ca în Fig.2 se va dubla tensiunea, adică se va obține o tensiune de $U = 1.32Vcc$, care va fi suficientă pentru aprinderea unui LED, care necesită circa 0,5V

pentru aprindere. Tensiunea de 1,32 Vcc este o valoare maximă, s-ar putea ca LED-ul să se aprindă doar intermitent.

Datorită faptului că puterea dezvoltată de aceste generatoare este mică precum şi datorită variației vitezei vântului pe durata unei zile un singur generator nu poate asigura necesarul de energie electrică pentru alimentarea diferiților consumtori. De aceea autorul a prevăzut o construcție modulară a acestor generatoare în aşa fel încât ele să poată fi utilizate în baterii de generatoare, pentru a putea face față cerințelor consumatorilor dar şi pentru putea fi instalate la fața locului cu uşurință. O schemă simplificată a unei secțiuni laterale dintr-o peşteră precum şi locurile posibile de poziționare ale bateriilor de generatoare sunt prezentate în Fig.

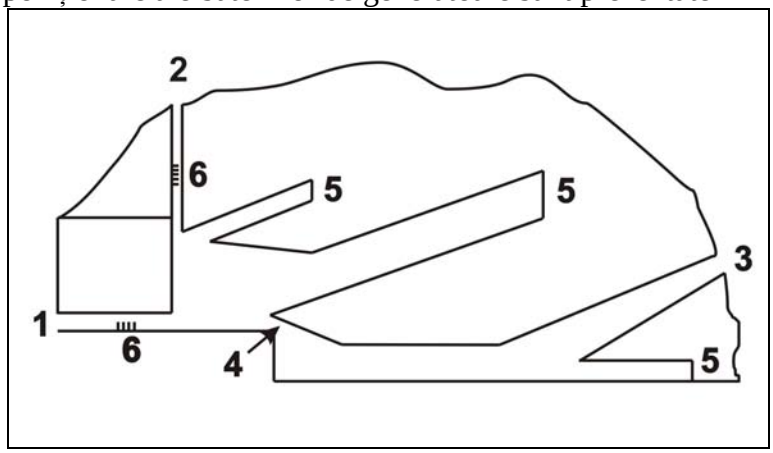

Fig. 5 Vedere laterală (simplificată) a unei peşteri cu 2 posibile poziționări ale bateriilor de generatoare. 1 – intrarea principală, 2 – puț care comunică cu exteriorul, 3 – galerie care comunică cu exteriorul neaccesibilă, 4 – strâmtoare, 5 – galerii înfundate, 6 – baterii de generatoare.

4 Concluzii

Peştera ca şi sursă de energie eoliană are două mari avantaje față de orice altă zonă din care se doreşte exploatarea acestei resurse. Curentul de aer care se formează în peşteră este constant iar valoarea vitezei acestui curent este relativ constantă.

Din punct de vedere al consumului de energie, în peşteră se pot instala o serie de consumatori care însă sunt strâns legați de cercetările care se efectuează în fiecare peşteră în parte precum şi de nevoile amenajărilor turistice din fiecare peşteră în parte.

Lucrarea de față este doar un prim pas spre dezvoltarea unor astfel de generatoare, care să răspundă tuturor nevoilor unor astfel de zone şi care mai târziu vor putea fi folosiți şi în alte zone asemănătoare, apropiate ca şi nevoi şi specificitate, dar care sunt situate chiar în interiorul aşezărilor umane.

Referințe

[1] ICEMENERG sa, ICPE sa – Studiu privind evaluarea potențialului energetic actual al surselor regenerabile de energie in România (solar, vânt, biomasă, microhidro, geotermie), identificarea celor mai bune locații pentru dezvoltarea investițiilor în producerea de energie electrică neconvențională, Bucureşti, 2006

[2] M.Bleahu, V.Decu, St.Negrea, C.Pleşa, I.Povară, I.Viehmann – Peşteri din România, Editura ştiințifică şi enciclopedică, Bucureşti 1976

[3] Fraine, Shawn M., US – Generator utilizing fluid-induced oscillations, US 7573143 B2, 2009

Optimization conditions of stator winding insulation of hydrogenerator

Mihaela RĂDUCA, Cornel HAȚIEGAN, Ana Maria BUDAI, Eugen RĂDUCA
"Eftimie Murgu" University of Resita, Piata Traian Vuia, nr. 1-4, 320085, Resita, Romania;
m.raduca@uem.ro, c.hatiegan@uem.ro, am.pittner@uem.ro, e.raduca@uem.ro

Nicolina POP
"Politehnica" University of Timisoara, Bv. Mihai Viteazu nr. 1, 300222, Timisoara, Romania;
nicolina.pop@et.upt.ro

Abstract. This paper aims to optimize the conditions of stator winding insulation using a monitoring system of that. This optimization requires the existence of two subsystems of the insulation monitoring stator conditions. The first subsystem is one of data acquisition and the second is one of stator temperature adjustment. The first subsystem is designed and implemented in LabVIEW graphic language and the second is designed with fuzzy controller and implemented in MATLAB\SIMULINK program. Depending on the values of the temperature purchased the second subsystem into action only when they exceed the nominal values.

1 Introduction

This paper aims to optimize the conditions of stator winding insulation using a monitoring system of that. This optimization requires the existence of two subsystems of the insulation monitoring stator conditions. The first subsystem is one of data acquisition and the second is one of stator temperature adjustment.

The first subsystem is designed and implemented in LabVIEW graphic language and the second is designed with fuzzy controller and implemented in MATLAB\SIMULINK program. Depending on the values of the temperature purchased the second subsystem into action only when they exceed the nominal values.

2 Monitoring system of insulation condition

Fault diagnosis can be made by various methods, the most important being [1,2]: the diagnosis methods based on analytical models; methods using fuzzy logic; methods based on neural network models; methods based on expert systems; methods based on vector analysis of electric machines; methods based on partial discharge analysis in insulations; methods based on magnetic flux monitoring in electric machine.

In the paper was designed a monitoring system of insulation state used to prevent hydro-generator damaging due to insulation destruction during operation. The proposed block diagram for this system is presented in Figure 1:

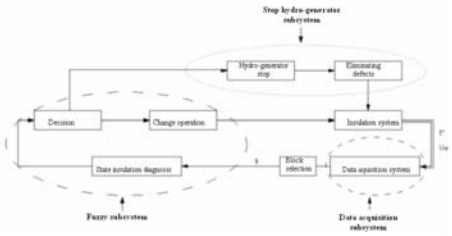

Figure 1. Monitoring system of state insulation.

For stator winding system monitoring, using data acquisition system, are collected and stored all stator coil temperature and voltage values. Through selection block is established, using a

suitable algorithm, the reaction temperature tr for fuzzy system. The reaction temperature represents the highest temperature of stator coils.

Through fuzzy system is decided if the coil temperature must be reduced, or, if this thing is not possible, the hydro-generator should be stopped. If it is decided that the coil stator temperature must be modified, the fuzzy controller of the fuzzy system provides to output the value size order for execution element, which is represented by a fan (turbocharger) [3,4].

2.1. Data acquisition subsystem

The block diagram of the whole production platform - data acquisition system is presented in Figure 2.

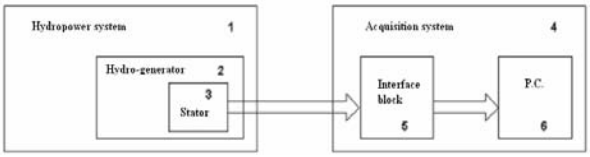

Figure 2 The block diagram of whole production platform – data acquisition system.

The whole production platform is represented by hydropower system 1 and hydro-generator 2 that represent a subsystem of the first one. The directly targeted monitoring component is the hydro-generator stator.

For some stator parameters the monitoring is possible (for example: the temperature in different points, the work voltage) [5], but others can not always be known (for example: insulation thickness in each coil) but only in times when the machine is in revision [6].

The data acquisition system 4, allows the continuous collection and storage of parameters that can be continuously and directly measured [7]. In Figure 3 is presented the designed program (M-AQ-DW1.VI), developed and tested for stator data acquisition. The program is a graphical one, realized in LabVIEW language and has two interdependent components (Figure 3.a – The front panel and Figure 3.b – The block diagram).

a) b)

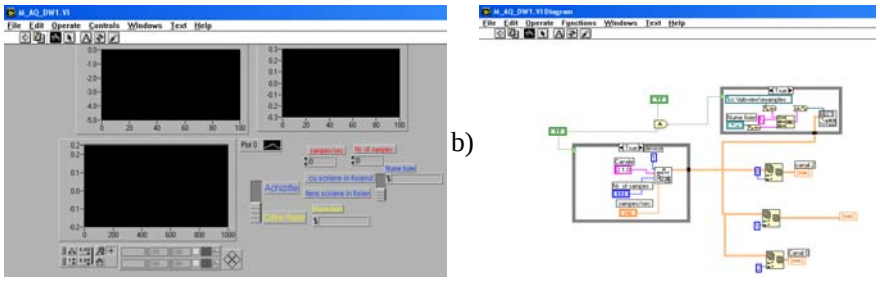

Figure 3 Data acquisition program of interest values
a) The frontal panel; b) The block diagram.

From block diagram can be observed that the program was designed for dates simultaneous analysis, in single precision, on three channels, noted channel 0, channel 1 and channel 2.

From frontal panel of DI Mult PI block (presented in Figure 3) the operator chosen the total number of samples acquired, and also the number of samples acquired per time unit. Precision and speed of sampling are primarily conditioned by used acquisition board. Was used a acquisition board type NI LabPC+. On frontal panel are observed that the values purchased can be viewed either on each device with plotters. In the same time, they can be stored or not in a file (using selection “acquisition with writing in file”, or “acquisition without writing in file”).

The acquisition dates can be read later any time from file in which they were memorized (“reading file”). Another problem that must be solved consisted in data transmission from file to

other peripheral of PC in which the acquisition was realized. For this purpose has been designed, developed and tested the program named D_EX_D2K.VI whose front panel is presented in Figure 4.a. The associated block diagram is presented in Figure 4.b.

Using this program the acquired dates in initial file can be transferred into another file by button "Signal generation from file". The transmission can be made to outside using the PC parallel portal, or to another PC file.

a) b)

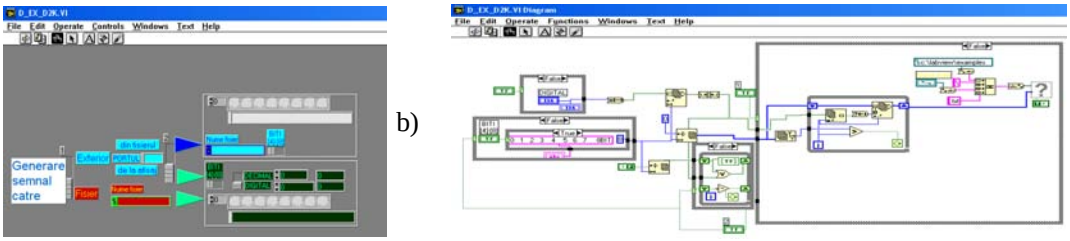

Figure 4 Dates transmission program between acquisition system and monitoring system
a) The frontal panel; b) The block diagram.

2.2. Fuzzy subsystem

The methods based on fuzzy logic [7] did not have algorithms clearly indicate. In that case, the result depends on specialist's experience. The fault diagnosis is made linking specialists experience with a data base. The used data based contains information collected during testing generators, their exploitation and at revision. As results, is obtained the decision which diagnoses the condition of generator insulation [8].

Based on Figure 1 can be chosen one of below decision: generating set of commands using decision subsystem for safe operation of the generator; hydro-generator off, in order to remedy defects found; taking in consideration that there were no major defects (unit off), can be estimate that the problems will be quickly remedied and without high costs.

The fuzzy system designed for diagnosis, evaluation and decision of hydro-generator insulation system is presented in Figure 5.

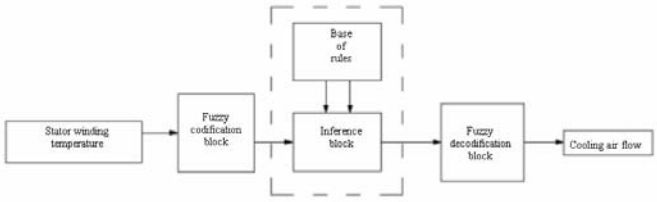

Figure 5
The fuzzy system.

It is found that, from process, the stator set temperatures are taking over and the controlled parameter will be the cooling airflow for stator winding. The cooling airflow will change stator temperature.

To control the airflow were designed and analyzed several options for control system through simulation specialized environment MATLAB/SIMULINK [9].

2.2.1 The fuzzy system for adjustment of airflow

It is aims to adjust the stator winding temperature by changing the airflow of a fan using a fuzzy controller. The controller has like input dates the prescribed temperature error and the derivative of this error. Inside the system, the controller was designed with two ascendants and a consequent, with triangular and trapezoidal class affiliation functions. The fuzzy brake codification block is centered type. The fun represents the execution element.

Implementation and simulation of airflow management system using fuzzy controller was made in MATLAB/SIMULINK. In Table 1 is presented the decision table for studied case.

Table 1

Airflow		Error (p)				
		p1	p2	p3	p4	p5
The derivative of error	dp1	c1	c1	c1	c2	c2
	dp2	c1	c2	c2	c2	c3
	dp3	c1	c2	c4	c4	c4
	dp4	c2	c2	c4	c4	c5
	dp5	c2	c3	c4	c5	c5

In the case studied the used linguistic terms are: for error: p1, p2, p3, p4, p5 and the attached affiliation functions are presented in Figure 6; for derivative of error: dp1, dp1, dp3, dp4, dp5 the attached affiliation functions are presented in Figure 7; for airflow: c1, c2, c3, c4, c5 and the attached affiliation functions are presented in Figure 8 and also in Figure 9 are presented the elements control surface that characterizing the quality of identified model depending on the temperature error and derivative of error.

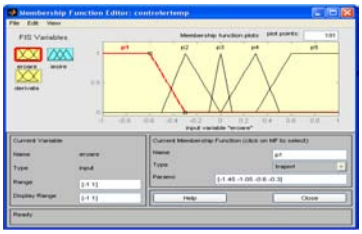

Figure 6 The affiliation functions for temperature error

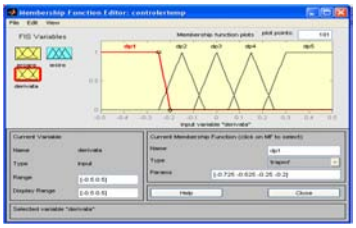

Figure 7 The affiliation functions for derivative of error

Figure 8 The affiliation function for output

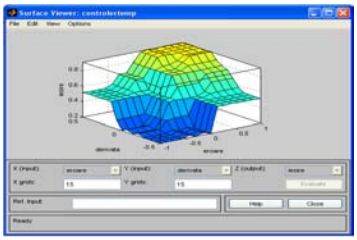

Figure 9 The elements control surface

The implemented fuzzy controller was introduced in the control system presented in Figure 10. Can be observed that, to the input controller are brought the temperature error (Discrete Filter) and the derivative temperature error (Discrete Filter 1).

The working temperature range for stator winding was considered being between 20ºC and 120ºC. To this range were associated a continuous linear domain having values from 0 to 1. The 0 value is associated with minimum temperature and the 1 value with maximum temperature.

The error of the output adder block occurs due to the difference between prescribed temperature (Step) and the measured one inside stator winding. To output of controller are obtained the value that command the execution element, modeled by an element of type PT1 (Transfer Fcn1), which is a group of turbochargers (the fan).

The process consists of stator winding in which are desired to maintain the prescribed temperature is modeled, also, like an element type PT1 (Transfer Fcn).

In Figure 10 it is believed that over the process acting a stage type perturbation (Step 1) and in Figure 11 is presented waveforms at points of interest. In real system the perturbation is represented by stator voltage variation. The grow of this, determine a rise of current through the winding and thus a stator winding temperature rise.

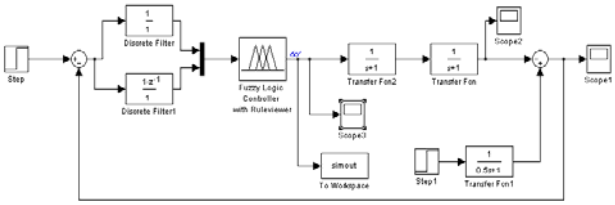

Figure 10 The Simulink model of control system with unit jet with perturbation

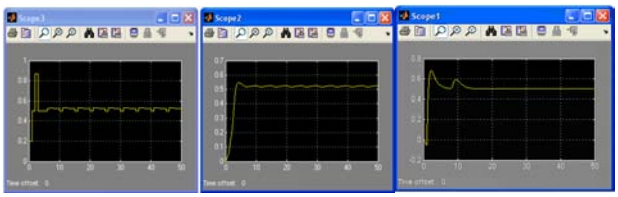

Figure 11 The signal wave forms for control system with unitary reaction with step perturbation

From Figure 11 can be observed that the output value have a small variation around equilibrium value. Also, it has been study the system behavior if the perturbation acts on both, the process and the fuzzy regulator (Figure 12 and Figure 13).

In this case the fuzzy regulator was designed with 3 ascending and a consistent, with triangular and trapezoidal class affiliation functions.

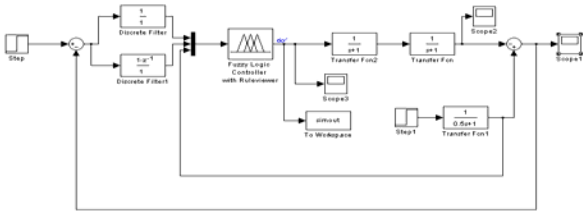

Figure 12 The Simulink model for control system with unitary reaction with perturbation on both, the process and the fuzzy regulator

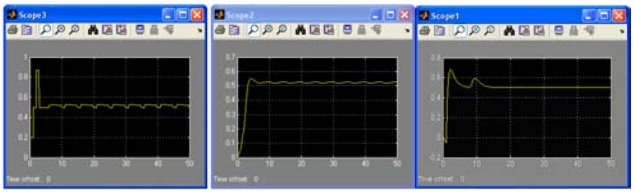

Figure 13 The signal wave forms for control system with unitary reaction with perturbation on both, the process and the fuzzy regulator

Making a comparative analysis of obtained wave forms it is found that the quality of regulation it is weaker then in case when the perturbation acts only to the process. This fact is revealed by answer evolution around equilibrium value with a slightly higher value (Figure 13). The system was designed like a supplementary protection system of generator. His necessity can be justified by decreasing of performances in time for insulation system due to aging and operating overloads. In the current mode of operation, if it is finds that insulation parameters are worsening, to prevent the occurrence of a catastrophic failure, this system will became operational.

The entering into operation of presented system can be occurring in the following directions: if through command set resulted from the decision process the current parameters of hydro-generators are modified in nominal deviation limits, can be consider that intervention of decision system is totally transparent; if through command set resulted from the decision process the current parameters of hydro-generators are modified outside of nominal deviation limits, the effect consists in worsening, in qualitative way, of generator performance; if through command set resulted from the decision process the hydro-generator is stopped means that a fault has been detected and the hydro-generator will be stand out of operation until the problems will be solved. In this way is avoiding the occurrence of a catastrophic failure caused by insulation condition.

3 Conclusion

The designed and realization of o monitoring system for detect the insulation condition making possible to prevent the hydro-generator failure due to destruction of insulation in operation time. Because this monitoring system is a complex one, the system is regarded as having in component two subsystems namely: data acquisition system and fuzzy system.

Data acquisition system allow the acquisition of the interest values from process and in the same time, through it's, was created a strong database about current status of hydro-generator insulation. Through presented fuzzy system is not achieved the operating of generators, he being designed like a additional system used for a good function of generator.

After the implementation in MATLAB/SIMULINK of control system, is found, based on the analysis of wave forms, that: for control system with step perturbation type it is found that the output value have a small variation around equilibrium value; the regulation quality it is weaker in case in which the perturbation acts on both, the process and the fuzzy regulator, than for case when the perturbation acts only over the process; the made fuzzy controller have higher quality than the classic one, providing a faster evolution of regulation value towards the stationary value, having damped oscillations with small amplitude.

References

[1] Gh. Liuba. *Metode moderne de determinare experimentală a parametrilor electrici ai maşinilor electrice de curent alternativ*, Ed. Eftimie Murgu, Reşiţa, 2003.

[2] M. Negrea, P. Jover and A. Arkkio. *A comparative investigation of electrical parameters for fault detection and condition monitoring in induction motors-stators winding current and electromagnetic flux*, Proceedings of XVII International Conference on Electrical Machines, Chania, Crete Island, Greece, September, 2006.

[3] A. Kheirmand, M. Leijon and S. M. Gubanski. *Advances in online monitoring and localization of partial discharges in large rotating machines*, IEEE Transactions on Energy Conversion, Volume 19 (1).

[4] M. Răduca. *Sisteme de măsurare şi instrumentaţie*, Ed. Eftimie Murgu, Reşiţa, 2010.

[5] M. Răduca, E. Răduca, C. Haţiegan and D.Ungureanu. *Fuzzy controller of liquid level in the tank*, Annals of the University of Craiova, Mathematics and Computer Science Series, Volume 37 (1), 2011.

[6] M. Răduca, E. Răduca and A. Uyetani. *Fuzzy controller for alarm at air flow systems for generators*, Analele Universităţii "Eftimie Murgu" Reşiţa, anul XV, nr.1, Ed. Eftimie Murgu, Resita, 2008.

[7] V. Duraisamy, N. Devarajan, D. Somasundareswari and S. N.Sivanandam. *Designing of fuzzy logic fault detector with hybrid membership function*, Proceedings on Power Conversion and Industrial Control, Palakkad, January 2003.

[8] R. Wawryk and J. Rafałowicz. *Heat transfer in microsphere insulation*, Journal of thermal analysis and Calorimetry, JAN/FEB 1988, Volume 34 (1).

[9] C. P. Chioncel. *Contribuţii privind controlul turaţiei la maşina asincronă*, Ed. Politehnica, Timişoara, 2008.

ANALIZA COMPORTAMENTULUI LA DESCĂRCARE PENTRU O BATERIE $LiFePO_4$ UTILIZATĂ LA UN ATV ELECTRIC

Emilian LEFTER, Bogdan-Adrian ENACHE, Ştefan OPREA
Universitatea din Piteşti, str. Târgu din Vale, nr. 1, 110040, Piteşti, Argeş

Abstract. Studiul comportamentului la descărcare, al unei baterii utilizate pe un automobil electric, este obligatoriu. În acest sens au fost elaborate o serie de teste pentru evaluarea performanţelor electrice ale bateriilor. În lucrare, mai întâi, se trec în revistă cele mai importante teste, precum şi aparatura necesară efectuării lor. În continuare se prezintă concepţia unui sistem programabil pentru descărcarea unei baterii. Sistemul poate efectua atât descărcarea la curent constant cât şi la un curent care se modifică în timp după un ciclu prestabilit. Sistemul este destinat testării bateriilor LiFePO4 care echipează un ATV electric Se prezintă rezultatele preliminare ale testelor efectuate.

1 Introducere

O dată cu dezvoltarea automobilelor electrice a apărut şi nevoia evaluării constante a caracteristicilor bateriilor care le echipează. Pentru aceasta o serie de teste au fost elaborate de către specialiştii Departamentului de Energie din SUA în colaborare cu specialiştii de la trei mari companii producătoare de autovehicule: GM, Ford şi Chrysler.

Aceste teste au fost elaborate pe două direcţii principale care apoi au fost materializate prin două manuale de încercare a bateriilor şi anume: USABC Test Procedures Manual şi PNGV Test Manual.

USABC Test Procedures Manual cuprinde testele necesare pentru evaluare bateriilor în conformitate cu cerinţele de termen mediu şi lung ale U.S. Advanced Battery Consortium. Aceste teste sunt organizate în două categorii:

- teste de bază: descărcarea la curent constant, determinarea vârfului de putere, descărcarea la putere constant, performanţa termică, descărcarea parţială
- teste pentru determinarea duratei de viaţă a unei baterii: îmbătrânirea accelerată, simularea situaţiilor reale, etc. [2]

PNGV Test Manual cuprinde testele necesare pentru evaluarea performanţelor bateriilor în conformitate cu cerinţele Partnership for a New Generation Vehicle. Dintre aceste teste amintim: caracterizarea impulsului de putere, performanţa termică, eficienţa energetică, durata de viaţă. [3]

Procedurile prezentate în aceste manuale se aplică pentru toate tipurile de baterii, ele neprecizând, în schimb, aparatura necesară efectuării lor. [1]

2 Aparate folosite pentru determinarea performanţelor bateriilor

În momentul de faţă aparatele folosite pentru determinarea caracteristicilor bateriilor respectă doar parţial cerinţele de testare prevăzute în cele două manuale de referinţă, practic ne existând un singur dispozitiv care să poată îndeplini toate cerinţele.

În funcţie de testele care le pot efectua aparatele existente se împart în două mari categorii: aparate pentru evaluarea parametrilor neelectrici: temperatura, vibraţii, etc. şi aparate pentru evaluarea parametrilor electrici: tensiune, curent, putere.

2.1 Aparate folosite pentru evaluarea caracteristicilor neelectrice

Pentru evaluarea caracteristicilor termice ale unei baterii de acumulatoare cel mai important aparat este calorimetrul (Battery Performaqce Calorimeter - BPC). Acest aparat este folosit pentru determinarea schimbărilor de temperatură ce apar în cadrul procesului de încărcare/descărcare.

Principul de funcţionare se bazează pe detecţia căldurii radiate în cadrul proceselor de încărcare/descărcare printr-un senzor (heat-flux senzor), care poate fi o suprafaţă THT(multipunct).

Domeniul de temperatură folosit este între -40 şi +200 °C, precizia este foarte bună de ±15mW, singura limitare fiind dată de dimensiunea cuvei. Variantele moderne au un sistem cu „thermal diode" care permite alimentarea bateriilor prin calorimetru fără a folosi conductoare electrice.

2.2 Aparate folosite pentru evaluarea caracteristicilor electrice

Aparatele folosite pentru evaluarea caracteristicilor electrice se împart la rândul lor în două categorii, echipamente folosite în determinarea caracteristicilor statice: descărcătoarele, analizatoarele şi echipamente folosite în determinarea caracteristicilor dinamice: sarcinile electronice, aparatele specializate, etc.

2.2.1 Descărcătoarele

Sunt echipamente folosite la descărcarea bateriilor la curent constant. De obicei sunt aparate portabile care deşi suporta curenţi de până la 100A şi tensiuni până la 400 V, domeniul de putere este foarte limitat la doar câteva sute de W, acest lucru restrângându-le funcţionare doar la celulele bateriilor.

Schema bloc a acestor aparate prezentată, în figură 1, cuprinde: un etaj de putere realizat cu tehnologie MOSFET sau IGBT şi un etaj de comandă care are dublu rol de a genera impulsurile de comandă şi de a înregistra caracteristicile electrice ale bateriilor. [5]

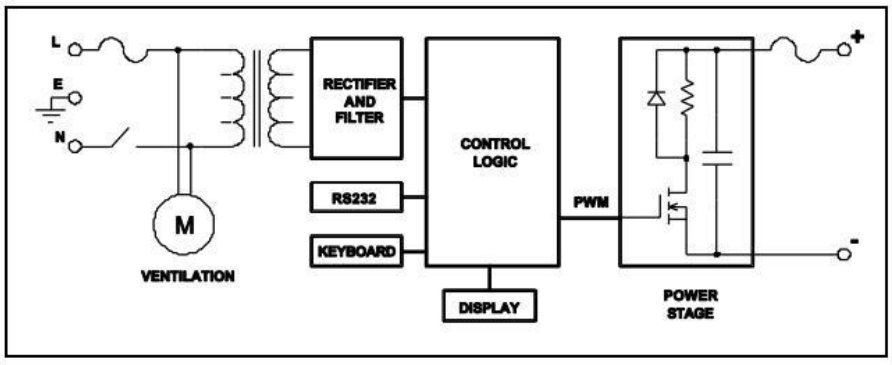

Fig 1: Schemă bloc descărcător

Aceste aparate sunt uşor de folosit, iar prin intermediul unei interfeţe USB sau RS-232 toate datele necesare pot şi preluate şi prelucrate pe calculator.

O variantă îmbunătăţită a descărcătoarelor o reprezintă descărcătoarele de mare putere care sunt format dintr-o serie de module de putere prevăzute cu răcire forţată cu aer şi care pot suporta putere mari de ordinul kW. Aceste aparate pot funcţiona până la două zile fără oprire.

2.2.2 Sarcinile electronice

Sunt aparate care permit atât evaluarea caracteristicilor statice cât şi dinamice ale bateriilor. Modurile de operare cuprind: descărcarea la curent constant, descărcarea la putere constantă, descărcarea la rezistenţă constantă. [4]

Aceste aparate pot funcţiona pe mai multe canale dintre care unul îndeplineşte rolul de master, iar restul de slave.

Operaţiile de regim dinamic sunt realizate cu ajutorul unui modulator care permite tranziţia între două nivele de descărcare.

Toate aceste dispozitive sunt interfaţate cu calculatorul şi permit înregistrarea parametrilor: tensiune, curent, putere, dar nu şi temperatura.

2.2.2 Dispozitive specializate pentru testarea bateriilor electrice

Aceste dispozitive sunt destinate testării modulelor de baterii şi acceptă tensiuni de ordinul miilor de volţi şi puteri de până la 400 kW. Au un design modular cu module de forţă de tip IGBT, răcire cu aer şi sunt capabile să lucreze autonom 24 de ore din 24, 7 zile din 7.

Sunt singurele dispozitive care pot fi folosite pentru evaluarea duratei de viaţă a bateriilor şi pot simula sarcini specifice EV şi HEV, care pe lângă cicluri de descărcare pot cuprinde şi cicluri de încărcare (recuperare de energie). [6]

Toate aceste dispozitive permit conexiunea cu calculatorul, unele dintre ele fiind echipate chiar cu calculatoare de proces şi pot efectua înregistrarea parametrilor electrici dar şi neelctrici.

3 Concept de dispozitiv pentru testarea bateriilor

În cele ce urmează prezentăm un dispozitiv de laborator, conceput în cadrul Centrului de Cercetare ELECTROMET al Universităţii din Piteşti, proiectat pentru a respecta cele mai importante cerinţe de testare din cadrul manualelor de referinţă USABC şi PNGV. Cu ajutorul acestui dispozitiv se pot efectua: descărcarea la curent constant, determinarea vârfului de putere, caracterizarea vârfului de putere, etc.

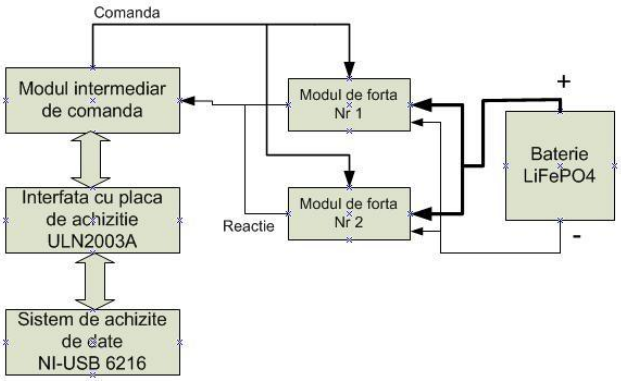

Fig 2: Schema bloc a dispozitivului conceput

Schema bloc cuprinde:

- O serie de module de putere grupate în paralel;
- Un modul intermediar de comandă;
- Un buffer pentru interfaţarea sistemului cu placa de achiziţii de date;
- O placă de achiziţie de date.

Modulul de putere are rolul de a stabili curentul de descărcare din circuit şi este realizat dintr-un Power MOSFET prevăzut cu radiator şi răcire activă pentru disiparea căldurii degajate.

Performanţe tranzistorului influenţează în mod decisiv performanţele întregului sistem. In cazul nostru avem un MOSFET IRFP 460A cu caracteristicile: VDSS = 500V, ID = 20A şi P = 280W la 25°C.

Modulul intermediar de comandă este format dintr-un comparat care are rolul de a urmări variaţia tensiunii de la bornele bateriei şi de a comanda deschiderea modulului de putere în aşa fel încât valoarea curentului în circuit să rămână constantă.

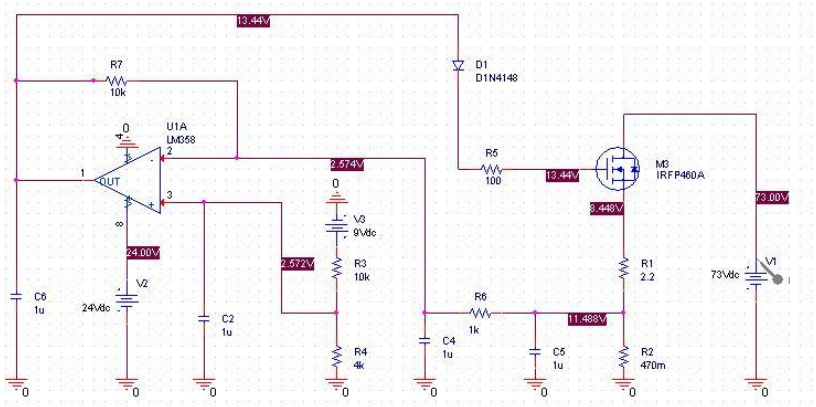

Fig 3: Modulul intermediar de comandă

Placa de achiziţii de date furnizează tensiunea de referinţă pentru comparator şi determină în acest fel valoarea curentului de descărcare din circuit. Generarea tensiunii de referinţă se realizează software în funcţie de tipul testului care trebuie efectuat.

Sistemul pentru testarea bateriilor cuprinde şi o parte software realizată în LabView şi care permite efectuarea, în momentul de fată, a două teste: descărcarea la curent constant cu I_{MAX} = 8 A şi descărcarea după un ciclu prestabilit.

Panoul frontal al aplicaţiei permite alegerea testului care se doreşte a fi efectuat precum şi configuraţia modulelor de putere folosite.

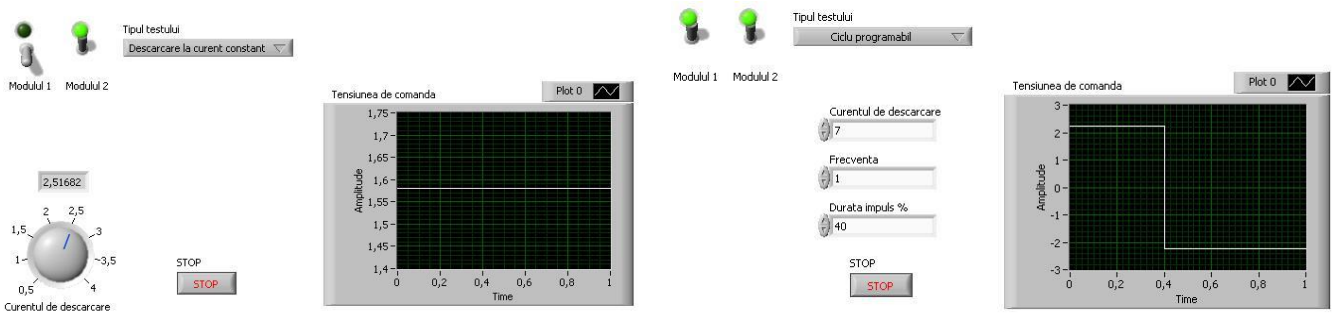

Fig 4: Panoul frontal al aplicaţiei

Tot de aici se pot stabili valoarea curentului de descărcare dar şi durata perioadelor de descărcare sau repaus.

În funcţie de datele stabilite din panoul frontal se activează o anumită ramură de comandă din cadrul diagramei bloc care va conduce la generarea unui anumit nivel de tensiune folosit ca referinţă de modulul intermediar de comandă.

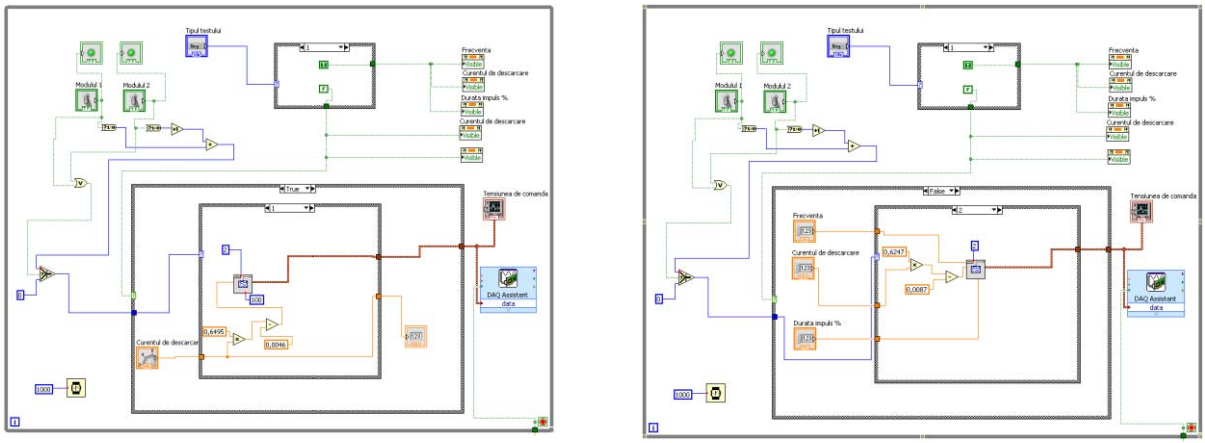

Fig. 5: Diagrama bloc a aplicaţiei

Pentru determinarea pragurilor de comandă s-au determinat valorile tensiunilor de referinţă pentru fiecare modul de comandă precum şi pentru cele două module împreună.

Valorile obţinute se găsesc în următoarele tabele:

Tabelul 1 Tensiunile de comanda pentru fiecare modul

$I_{descărcare}$ [A]	Tensiune referinţă modul 1[V]	Tensiune referinţă modul 2[V]
0,5	0,256	0,321
1,0	0,623	0,646
1,5	1,044	0,964
2,0	1,318	1,231
2,5	1,645	1,586
3,0	1,945	1,851
3,5	2,303	2,156
4,0	2,520	2,560

Tabelul 2 Tensiunile de comanda pentru cele două module

$I_{descărcare}$ [A]	Tensiune referinţă modul 1 + modulul 2[V]
1,0	0,288
2,0	0,634
3,0	1,004
4,0	1,274
5,0	1,615
6,0	1,898
7,0	2,229
8,0	2,540

În urma interpolării datelor s-au obţinut următoarele ecuaţii care exprimă dependenţa tensiunii de referinţă de valoarea curentului de descărcare.

În cazul funcţionării separate a modului 1 ecuaţia este:

$$V_{ref1} = 0.6495 \cdot I_1 - 0.0046 \quad (1)$$

Pentru modulul 2 avem ecuaţia de funcţionare:

$$V_{ref2} = 0.6247 \cdot I_2 + 0.0087 \quad (2)$$

În cazul funcţionării celor două module simultan avem:

$$V_{ref1+2} = 0.3186 \cdot I_{1+2} + 0.0021 \quad (3)$$

Aceste ecuaţii au fost implementate în cadrul programului LabView pentru a stabili tensiunea de referinţă a modulului intermediar de comandă.

4 Analiza capacităţii unei baterii $LiFePO_4$

Pentru determinarea efectivă a capacităţii unei baterii se foloseşte testul de descărcare la curent constant. Pentru realizarea acestui test sunt necesare trei cicluri de descărcare la următorii curenţi: C3/3, C2/2 şi C1/1. Capacitatea bateriei se consideră determinată în momentul în care avem trei cicluri de descărcare consecutive a căror valoare pentru C3/3 se încadrează într-o eroare de 2%.[2]

Bateria folosită este model 15P20S-18650 are capacitatea de 20Ah şi tensiunea nominală de 64V. Tensiunea pentru care bateria se consideră descărcată este de 50±0,1V, curentul standard de descărcare este 10A, curentul pentru o descărcare rapidă este de 20A iar curentul maxim suportat (pt. 30s) este 40A.[7]

Pentru bateria noastră LiFePO4 cu o capacitate C20 = 20Ah curenţii de descărcare sunt: C3/3 = 2,22A, C2/2 = 5A şi C1/1 = 20 A.

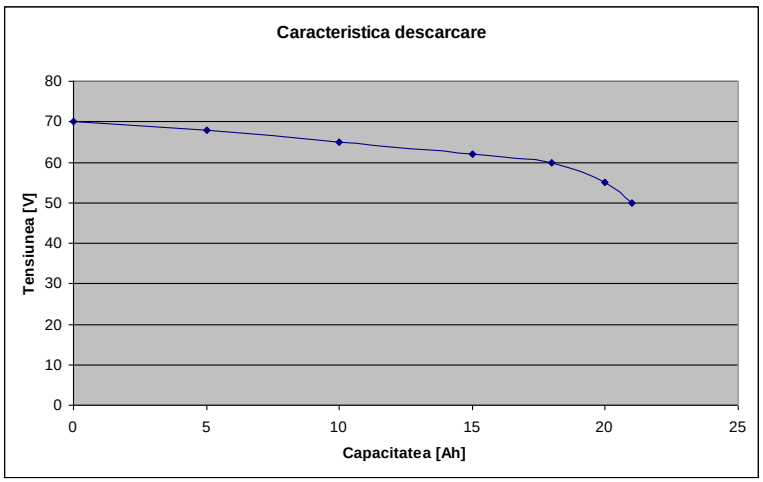

Fig. 6: Caracteristica la descărcare pentru o baterie $LiFePO_4$

Conform specificaţiilor producătorului, pentru tensiunea de descărcare de 50V, se constată o capacitate a bateriei este de 21Ah, superioară specificaţiilor. Acest lucru se poate justifica prin faptul că bateria este relativ nouă fiind supusă doar la câteva cicluri descărcare-încarcare.

5 Concluzii

Bateriile $LiFePO_4$ constituie noua generaţie de surse de alimentare pentru industria auto, datorită capacităţii ridicate, raportată la dimensiuni, precum şi a stabilităţii tensiunii de ieşire pe toată durata procesului de descărcare.

Pentru determinarea caracteristicilor bateriilor $LiFePO_4$ rămân valabile toate metodele de analiză prezentate, dar aparatura necesară va trebui adaptată la nivelul mare de putere implicat.

Referinţe

[1] Tien Duong. *USABC and PNGV test procedures*, Journal of Power Sources no. 89, (2000) 244-248.
[2] USABC *Electric Vehicle Battery Test Procedures Manual Revision 2, 1996.*
[3] PNGV *Battery Test Manual Revision 3, 2001.*
[4] http://www.bkprecision.com/products/dc-electronic-loads.html
[5] http://www.zivanusa.com/Discharger.htm
[6] http://www.digatron.com/en/hybrid-electric-vehicle-testing/bidirectional-battery-tester/
[7]*** *$LiFePO_4$ Rechargeable Battery Pack Product Specification.*

PV Charger System Using A Synchronous Buck Converter

Adriana FLORESCU
"Politehnica" University of Bucharest,Spl. Independenței 313 Bd., 060042, Bucharest, Romania, adriana.florescu@yahoo.com

Sergiu OPREA
MICROCHIP Technology, Bucharest, Romania, sergiu.oprea@microchip.com

Abstract. The paper describes the design, simulation and practical implementation of a PV system specifically designed for battery charging applications. A DC-DC synchronous Buck converter is digitally controlled by a dsPIC33F to extract the maximum power from the PV panel and feed it to the battery, according to the data received through the sensors. The system proves to be stable to rapid weather changing conditions due to the MPPT algorithm together with the two PI controllers.

1 Introduction

The energy demand increase continuously during last years, consolidating the position of the renewable sources like the photovoltaic panels and wind generators.Although still expensive compared with the conventional sources, the renewable energy offers certain long term advantages like the "eco friendly" property. The renewable energy becomes now a competitive alternative to the conventional sources as his price continuous to drop over the years.The solar energy is probable the best known for his fast growth during last decades. Some studies (a projection by the International Energy Agency) states that within fifty years most of the energy will be produced by the solar generators. The solar energy can be directly converted into electricity by meaning of the photovoltaic cells (PV). However, some technical challenges are associated with the PV panels that must be overcome in order to get the full advantage of this kind of energy generators. This paper will present the implementation of a solar battery charger that can be used to provide electricity to a fully autonomous system.

2 The PV Cell

A PV cell is basically a large photodiodethat will convert the incident solar energy to electricity based on the well known photovoltaic effect. The electrical equivalent model of a PV cell is depicted in Figure 1.

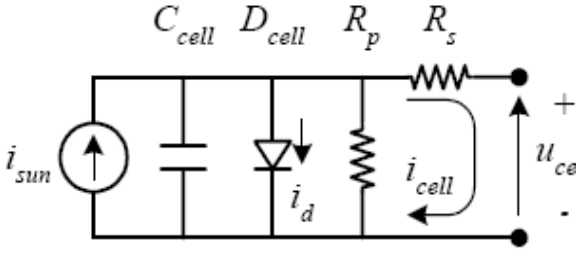

Fig 1: PV cell equivalent model [1]

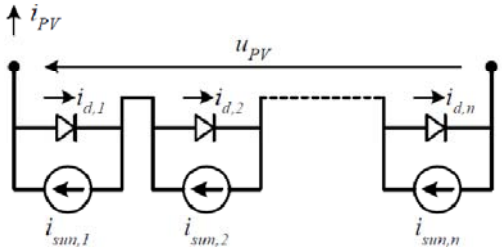

Fig 2: PV panel schematic[1]

A PV panel is made from n cells connected in series like in Figure 2. The cell must be identical in terms of the electrical characteristics. The current source in Figure 1, i_{sun}, is proportional to the amount of irradiation,and linear with respect to the PV cell temperature. The current is given by Equation 1:

$$i_{sun} = \left(i_{sun,STC} + k_{temp} * (T_{cell} - T_{cell,STC})\right) * \frac{P_{sun}}{P_{sun,STC}} \quad (1)$$

wherei_{sun} and $i_{sun,STC}$ is the short circuit current at the given working point and STC (standard test conditions),respectively. The constant k_{temp} is the temperature coefficient of i_{sun}. T_{cell} and $T_{cell,STC}$are the actual and STC cell temperatures, respectively. Finally P_{sun} and $P_{sun,STC}$ arethe irradiations at the present operating point and at STC, respectively [1]. The current through the diode is expressed by Equation 2,

$$i_d = i_S * \left(e^{\frac{q*u_d}{k*A*T_{cell}}} - 1\right) \quad (2)$$

wherei_S is the reverse saturation current, A is the diode idealization factor (usually defined between 1 and 5), and u_d is the voltage across the diode.

ThePV cell equivalent model contains some additional elements R_p andR_s. These circuit elements are associated with parasitic like the connection wires between cells. A more detailed description of these parasitic elements is found in [4]. The C_{cell} is the capacity associated with the PN junction of the diode. Finally, the current, voltage and power generated by a single PV cell are expressed by the Equations (3), (4) and(5).

$$i_{cell} = i_{sun} - i_d \quad (3)$$

$$u_d = u_{cell} + R_s * i_{cell} \quad (4)$$

$$P_{cell} = u_{cell} * i_{cell} \quad (5)$$

A family of curves that plot the i_{cell} and u_{cell} versus the irradiation is depicted in Figure 3 [1].

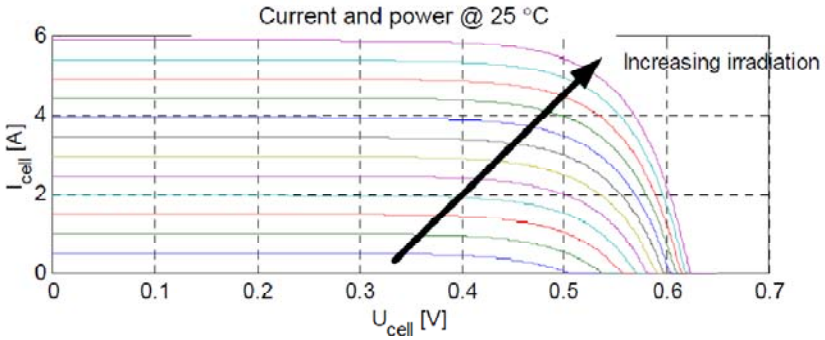

Fig 3: i_{cell} and u_{cell} vs. iradiation

The power delivered by the PV cell under different irradiation conditions is depicted in Figure 4 [1].

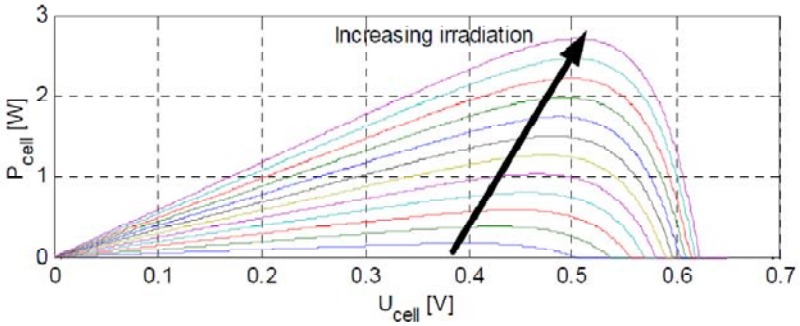

Fig 4: P_{cell} and u_{cell} vs. iradiation

The power delivered by the PV cell has a maximum at certain voltage and this maximum depends on the irradiation. In order to extract the maximum available power delivered by the PV panel in certain illumination conditions, a certain techniques must be implemented in the system that process the photovoltaic energy (ex. a battery charger or a grid connected inverter).

3 The Maximum Power Point Tracking (MPPT) algorithms

The main problem solved by the MPPT algorithms is to automatically find the panel operating voltage that allows maximum power output. In a larger system, connecting a single MPPT controller to multiple panels will yield good results but in the case of partial shading the combined power output graph will have multiple peaks and valleys (local maxima). This will confuse most MPPT algorithms and make them track incorrectly. Some techniques to solve problems related to partial shading have been proposed but they either need to use additional equipment (like extra monitoring cells, extra switches and current sensors for sweeping panel current) or complicated models based on the panel characteristics (panel array dependent). These techniques only make sense in large solar panel installations and are not the scope of this paper.

Ideally, each panel or small cluster of panels should have their own MPPT controller. This way the risk of partial shading is minimized, each panel is allowed to function at peak efficiency and the design problems related to converters handling more than 20-30 Amperes are eliminated.

A typical solar panel power graph in Figure 5 shows the open circuit voltage to the right of the maximum power point. The open circuit voltage (V_{OC}) is obviously the maximum voltage that the panel outputs, but no power is drawn at this voltage. The short circuit current of the panel (ISC) is another important parameter because it is the absolute maximum current you can get from the panel.

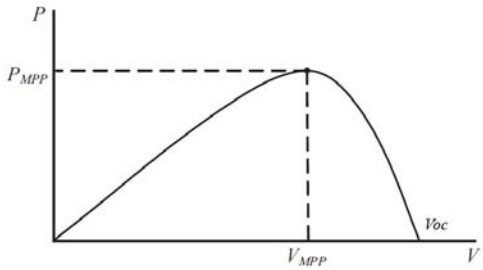

Fig 5: Solar Panel Power Graph

The literature on this subject generally agrees that the maximum amount of power that can be extracted from a panel depends on three important factors: irradiance, temperature and load.

Matching panel and load impedances with a DC-DC converter makes sense because for example if you have a 5V/2A load and a 20W panel that has the MPP at 17.5V/1.15A, connecting the load directly won't even work. Considering a simple resistive load, and the short circuit current of 1.25A, the panel will only be able to provide about 3V/1.2A or less than 4W out of 20W.

Temperature mainly changes the panel voltage operating point while irradiance mainly changes the panel operating current. The available power at certain moment will depends on the atmospheric conditions, the sun irradiance and the temperature. The MPPT algorithm will ensure that the maximum available power is extracted from the PV regarding the atmospheric conditions.

There are a few MPPT algorithms that can be easily implemented using an 8/16-bit microcontrollers. Most notables are the "Fractional Open Circuit Voltage", "Fractional Short Circuit Current", "Perturb and Observe" and "Incremental Conductance". The first algorithms have some drawbacks that make them "suboptimal" for the MPPT implementation. The "Perturb and Observe" algorithm will be described and implemented in this application.

4 Perturb and Observe (P&O) algorithm

This is one of the most discussed and used algorithms for MPPT. The algorithm involves introducing a perturbation in the panel operating voltage and observing the effects in the output power. The flow chart of this algorithm is depicted in Figure 6.

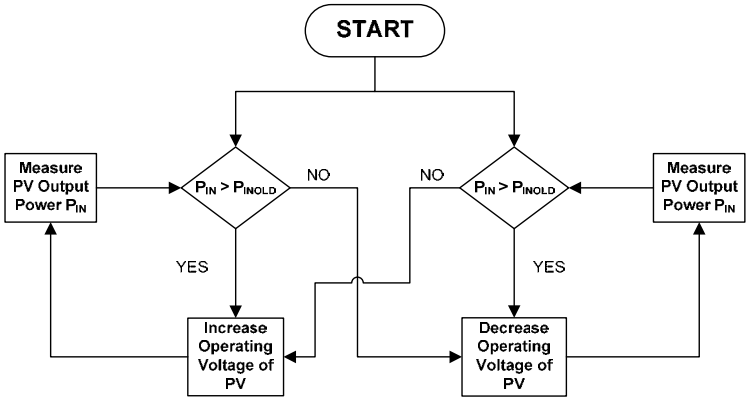

Fig6: Perturb and Observe Algorithm Flowchart

Looking at Figure 6 makes it easy to understand that decreasing voltage on the right side of the MPP increases power. Also increasing voltage on the left side of the MPP increases power. This is the main idea behind P&O algorithm. Modifying the panel voltage is done by modifying the converter duty cycle. The way this is done becomes important for some converter topologies.

Let's say that after performing an increase in panel operating voltage, the algorithm compares the current power reading with the previous one. If the power has increased it keeps the same direction (increase voltage), otherwise changes direction (decrease voltage). This process is repeated at each MPP tracking step until the MPP is reached.After reaching the MPP, the algorithm naturally oscillates around the correct value.The basic algorithm uses a fixed step to increase or decrease voltage. The size of the step determines the size of the deviation while oscillating about the MPP. Having a smaller step will help reduce the oscillation but it will slow down tracking, while having a bigger step will help reach MPP faster but will increase power loss when it oscillates.To be able to implement P&O MPPT, the application needs to measure the panel voltage and current. While implementations that use only one sensor exist, they take advantage of certain hardware specifics, so a general purpose implementation will still need two sensors.

5 MPPT Hardware Platform

The implementation is usually a kind of DC-DC converter with current and voltage sensors on the input side (solar panel). If battery charging is implemented on the same platform, then another set of current and voltage sensors is required on the output side.

For this application the synchronous Buck converter with digital control was chose. The block schematic is depicted in Figure 7. The entire MPPT and charging algorithm is fully digitally controlled by the microcontroller.Two PI controllers that run concurrently are used to regulate the output voltage and current in order to implement the charging sequence from Figure 8.

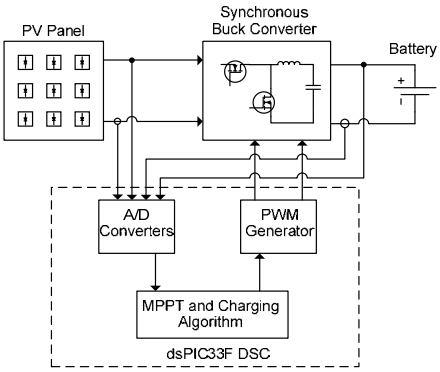

Fig 7: Block schematic of the hardware implementation

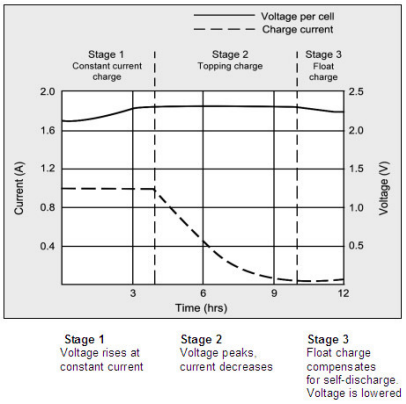

Fig 8: Charging sequence for sealed acid batteries

In order to implement the MPPT and charging algorithms, the input and output voltages and currents are monitor with sensors. The battery is a sealed acid, 12V nominal one. The typical charging algorithm for sealed acid batteries is presented in Figure 8. As we can see in this figure the constant current charge period lasts somewhere between 4-6 hours depending on the battery and charges it roughly 70% of the nominal capacity. The remaining 30% of required energy is filled with the slower voltage constant charge that lasts another 6-9 hours. The last stage of the battery charging (float charge) is essential for the well-being of the battery as it compensates for self discharge and keeps the battery at full charge. If this stage is not performed in time the battery will lose the ability to receive full charge and due to sulfation the performance will decrease.

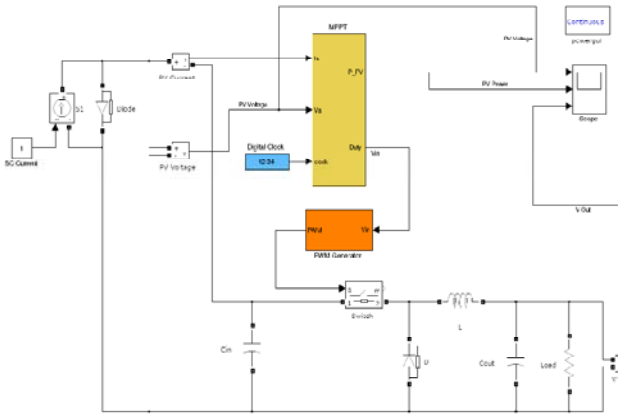

Fig 9: Simulink© model for the MPPT P&O algorithm and the associated waveforms

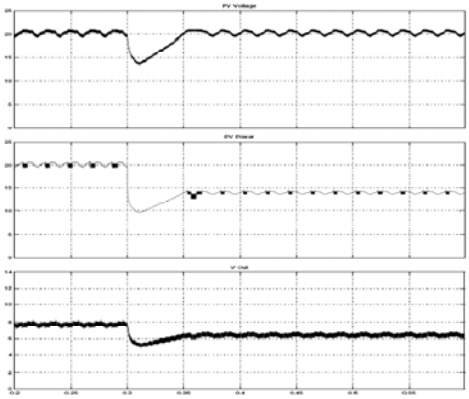

Fig 10: The associated waveforms

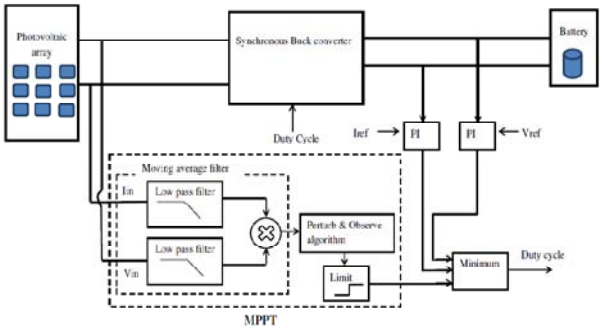

Fig 11: Hardware implementation for the MPPT P&O algorithm

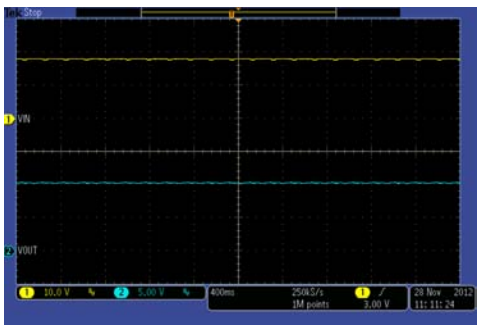

Fig 12: The associated waveforms

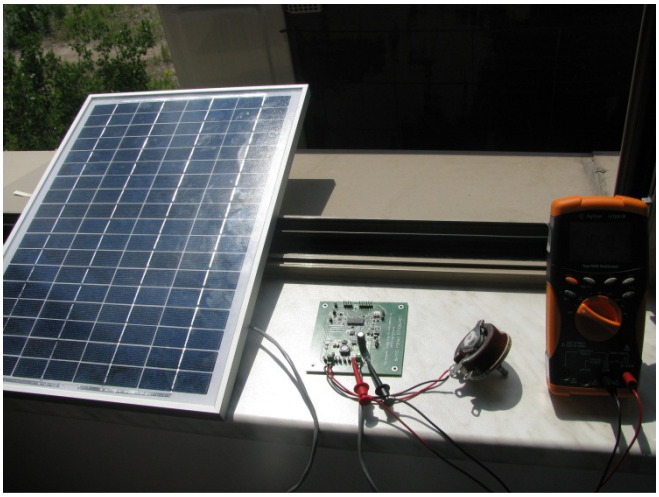

Fig.13: Prototype of the PV system

A Simulink© model was developed in order to validate the proposed MPPT algorithm. The diagram is depicted in Figure 9. The hardware was constructed around the dsPIC33FJ16GS502 digital signal controller (DSC) from Microchip. Block schematic of the practical PV charger and the associated waveforms for the input and output voltages are depicted in Figure 11 and Figure 12. The practical results of the prototype (fig.13) are well correlated with the simulation. The main disadvantage of P&O MPPT algorithm is the relativelly high ripple produced in the PV voltage. This ripple is asociated with some power losses but even in these conditions the algorithm can extract more than 95% of the PV available power. Some tuning of the final application is necesary to achieve the maximum performance. The low computational power requested by this algorithm make possible implementation on a low cost, 8 bit microcontrollers. The overall performance is good and make this algorithm the most popular when for implentation of the MPPT controllers.

6 Conclusions

A PV charger that implements the Perturb & Observe algorithm was developed in order to maximize the power transfer from the PV panel to the battery. The Simulink© model match well the behaviour find in the practical implementation.The simplicity recommends this algorithm to be used by low cost microcontrollers. However, the drawbacks of this algorithm can be overcome by more advanced algorithm like the “Incremental Conduction” that will require more computational power. Further work will concentrate on the more advance algorithms that will improve the performance of the MPPT controller.

References

[1] S. B. Kjaer,*Design and Control of an Inverter for PhotovoltaicApplications*, Ph.D. thesis, 2005.
[2] K. H.Hussein, I. Muta, T. Hoshino, M. Osakada, *Maximum photovoltaic powertracking: an algorithm for rapidly changing atmospheric conditions*, IEEE proc. ofgeneration, transmission and distribution, vol. 142, pp. 59-64, 1995.
[3] M. Rosu-Hamzescu, S. Oprea, *High-Power CC/CV Battery Charger Using an InverseSEPIC (Zeta) Topology, Microchip Inc., 2012*
[4] C. Bendel, A. Wagner, *Photovoltaic measurement relevant to the energy yield*,IEEE proc. of the 3rd world conference on photovoltaic energy conversion, vol. 3, pp. 2227-2230, 2003
[5] dsPIC33FJ16GSX02/X04, High-Performance,16-bit Digital Signal Controllers, Datasheet, Microchip Inc. 2009

Investigations on the use of multilevel converters in wind energy generation

Lucian PÂRVULESCU, Dan FLORICĂU
Faculty of Electrical Engineering

Abstract. This paper presents an analysis and simulation of a Wind Turbine Generator (WTG) driving a low speed Permanent Magnet Synchronous Generator (PMSG). The results of the tests are obtained by using the PSIM computer simulation program. The voltage source PWM inverter is used to interface the system with the electrical utility that is simulated in this paper as a resistive-inductive load.

1 Introduction

With the increase of energy demands, the need for a renewable energy source that will not harm the environment has also increased. Indications are made that the global energy demands will almost triple in the next decades. A cheap and versatile way to meet the future need is represented by the generation of electrical energy by using the power of the wind [1]. Utilities have the flexibility to accept a contribution of about 20% or more from wind energy systems [2]. For this reasons it is important to increase the performances given by the wind energy systems by modifying the design of the mechanical and electrical systems [3].

Such a solution is to use a permanent magnet synchronous generator (PMSG) that can operate at low speeds equivalent to those of the wind turbine instead of induction generators operating at high speeds. Different types of converters for synchronous generator output voltage control can be employed in order to get improved results on a local network or the national grid. Such systems have been developed for example by using conventional converters with two voltage levels and two NPC converters in rear to rear mounting [4]. Using multilevel converters the filtering element and the voltage requirements of the semiconductor devices are reduced while a high reliability is obtained.

In this paper an analysis is made by simulations using the specialized program PSIM of a Wind Turbine Generator (WTG) driving a low speed PMSG is presented. The system consists of a wind turbine, a permanent magnet generator, a special multilevel three phase rectifier and a multilevel voltage source inverter.

The rectifier is modeled in the Neutral Point Clamped (NPC) configuration and controlled using an indirect control strategy. The voltage source PWM inverter is used to interface the system with the electrical utility that is simulated in this paper as a resistive load. The inverter is the Five-Level Active-Neutral-Point-Clamped with Coupled-Inductors (5L-ANPC-CI) and is controlled using a PWM strategy.

2 The drive model

The mechanical scheme consisting of a wind turbine with a rated power output of 20 kW at the rated speed of 25 rpm, a gearbox with the ratio of 60/1 and a permanent magnet synchronous motor (PMSM) working as a generator is presented. The output of the PMSM represents the three-phase AC system feeding the NPC rectifier [Fig.1]. The two input terminals in the wind turbine model represent the wind speed and the angle of the propeller. Based on these values, the speed of the turbine and the output power are obtained. In this model the maximum output power is obtained for a wind speed of 25 rpm and a zero slope propeller.

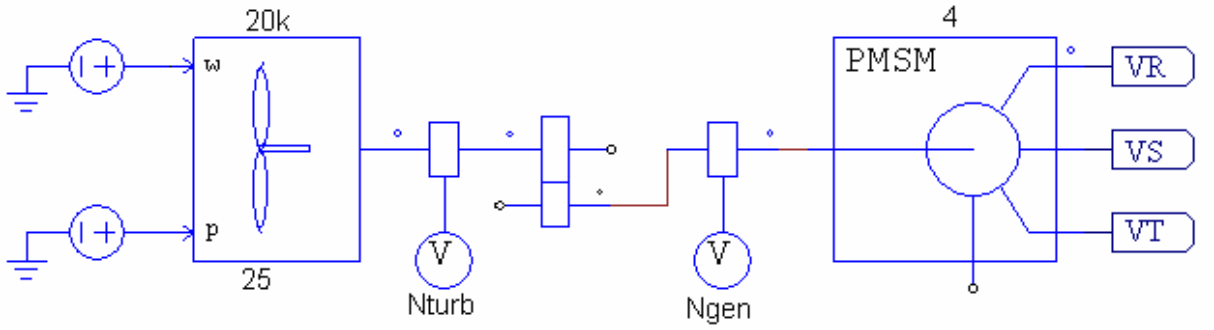

Figure 1: Mechanical scheme.

The synchronous generator was selected with four poles to achieve a synchronism speed of 1500 rpm equivalent to 60 times the speed of rotation of the wind turbine. The output of the synchronous generator is feeding the NPC rectifier [5] that produces the DC voltage for the 5L-ANPC-CI inverter [6]. The properties of this new converter compared with a similar high performances structure are described in [7]. The inverter is supplying a local network modeled by a resistive-inductive load (Fig.2). The three phase rectifier block has as an input parameter the reference voltage value Uref which has the value equal to the dc voltage supply of the inverter. The inverter block has as an input parameter the modulation index.

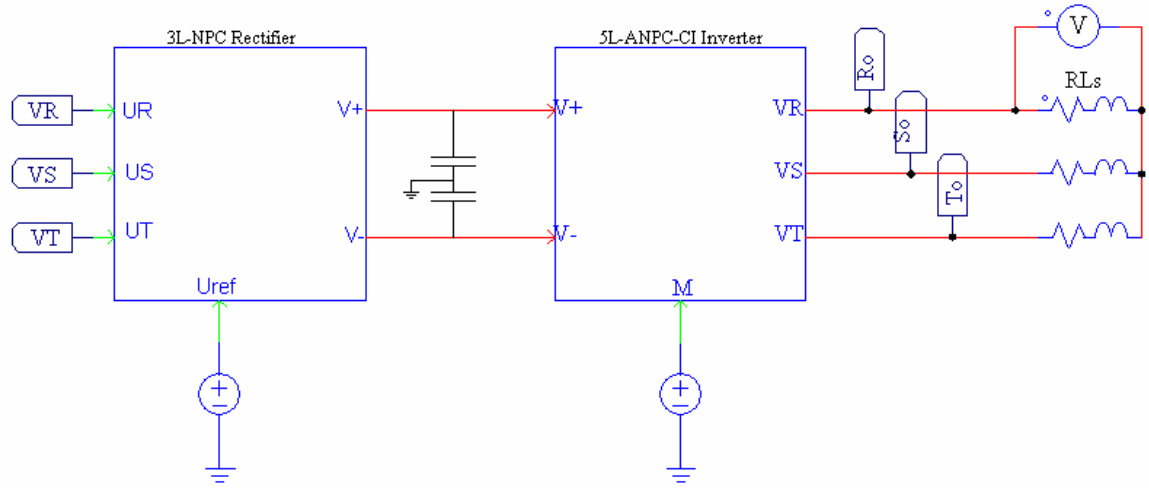

Figure 2: Electrical scheme.

The NPC rectifier control used is the indirect method with the compensation of the input voltage, while the inverter 5L-ANPC-CI is controlled with a sinusoidal PWM method. In Fig. 3 simulation results are presented considering the wind speed of 20 m / s, a 10 ° slope propeller, the reference voltage (Uref) of 700V and the modulation index (M) of 0.9. The dynamic regime of the wind turbine can be observed until the propeller reaches the maximum speed equal to the wind speed. At this moment the turbine uses about 80% of the rated power and the generator reaches the speed of 1200 rpm. The dynamic regime is also influenced by the time until the DC output of the rectifier reaches the prescribed value given by Uref which in this case is 700 V.

3 Simulation results

In Fig. 3 (a) and (d) the output phase and line voltages respectively are presented. These voltages have a low harmonic distortion factor due to the increased number of voltage levels.

Fig 3 (b) contains the input dc voltage of the inverter that stabilizes after the generator speed reaches 1200 rpm as shown in Fig. 3 (e). In Fig. 3 (c) the current absorbed by the inverter is described, which is continuous.

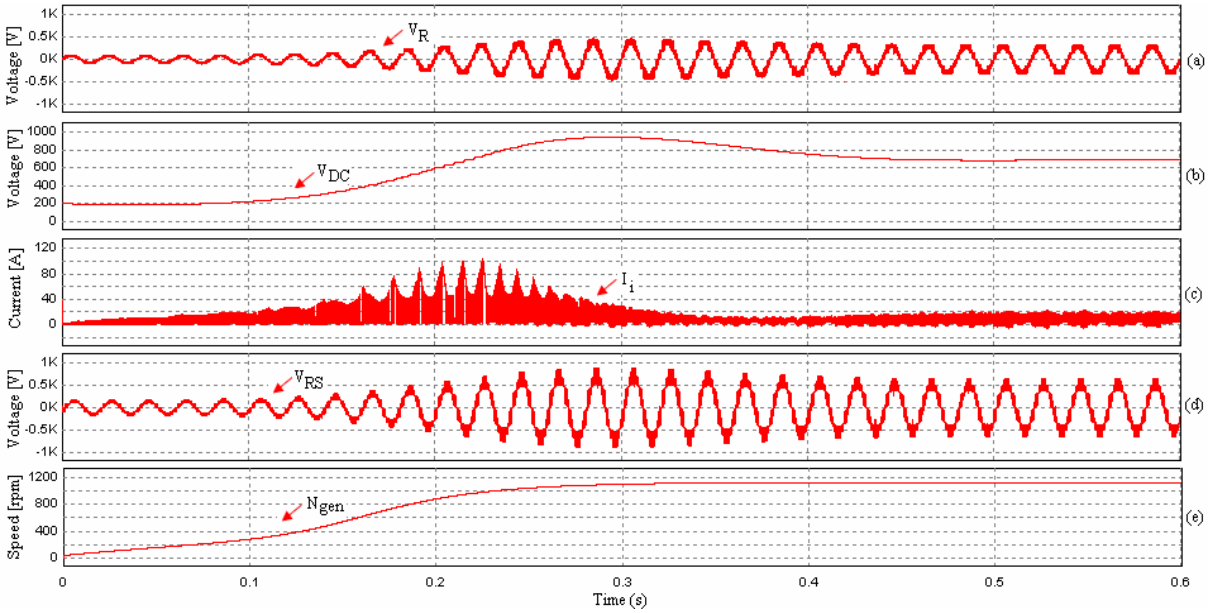

Figure 3: Simulation results at 80% of the rated power of the wind turbine: (a) phase output voltage V_R; (b) dc voltage V_{DC}; (c) rectifier output current I_i; (d) line output voltage V_{RS} ; (e) PMSG speed N_{gen}.

In Fig. 4 is presented a zoom of the previous figure after the DC voltage reached the reference voltage. The line voltage has nine levels for the five-level single arm inverter. In Fig. 4 (a) and (c) the output voltages and current on the local load are presented, while Fig. 4 (b) describes the current flow between the rectifier and the inverter. In Fig. 4 (d) the alternative voltage on phase A at the four poles generator output is presented. Through this indirect AC-DC-AC conversion the following advantages are obtained: voltage control, correction of the power factor and low harmonics content.

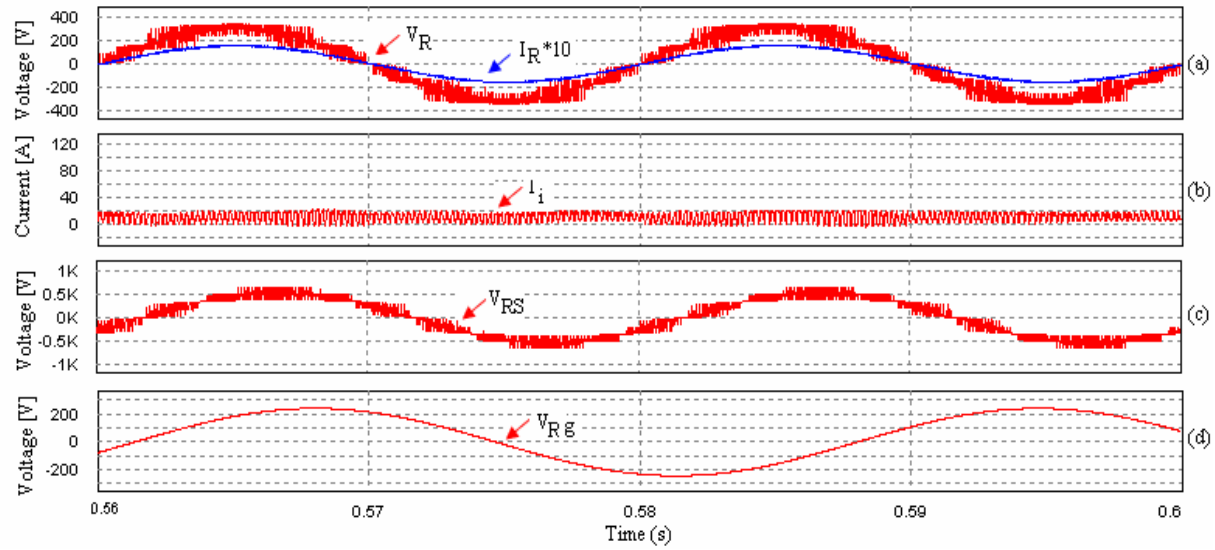

Figure 4: Simulation results for the stabilized regime: (a) phase output voltage V_R and the load current I_R; (b) rectifier output current I_i; (d) line output voltage V_{RS} ; (e) PMSG output voltage V_{Rg}.

In Fig. 5 the results of the simulations when the wind turbine operates at full power, at a wind speed of 25 m / s are described. The ANPC-CI inverter has a coupled inductor that increases the number of voltage levels and halves the current in half of the active devices.

The two currents through the inductor form the load current of the inverter and can be seen in Fig. 5 (a). Due to increase wind speed and hence of the wind turbine power the supply voltage of the rectifier can be increased which results in the production of more power in the local grid. In Fig. 5 (b) and (c) the line voltage with nine levels and the three phase sinusoidal currents system that results are described.

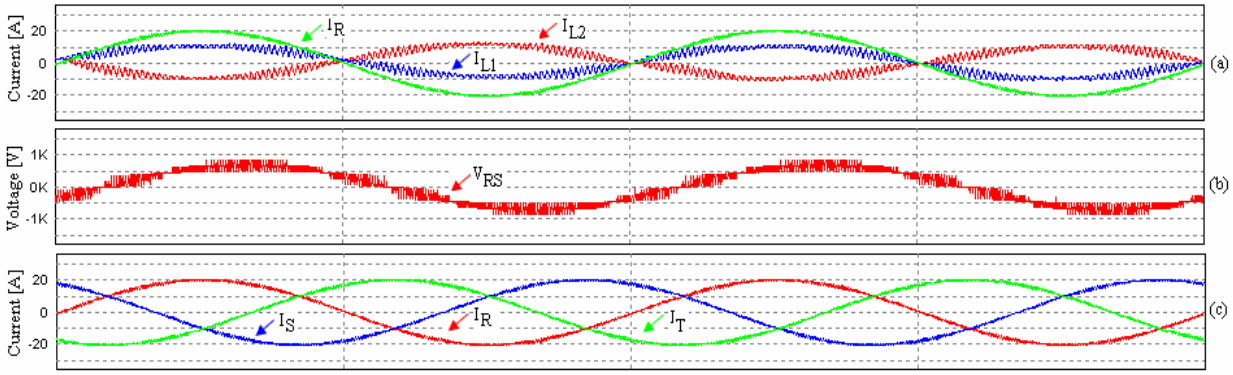

Figure 5: Simulation results at the rated power of the wind turbine:
(a) phase current I_R and through the coupled inductor I_{L1} and I_{L2}; (b) line output voltage V_{RS};
(c) three phase load current.

4 Conclusions

This paper presented a solution to increase the performances given by wind power generation using back-to-back multilevel structures. The simulations were performed using the PSIM software and described the advantages given by the special structures used. For the indirect conversion two special converters were used: the three-level NPC rectifier and the five-level ANPC-CI inverter. The output voltage harmonic content is low and therefore a small filter is required.

References

[1] Z.Chen, J.M.Guerrero, F.Blaabjerg, "A review of the state of the art of power electronics for wind turbines," IEEE Trans. Power Electron., vol. 24, no.8, pp.1859-1875, Aug.2009.

[2] G.D. Moor, H.J. Beukes, "Maximum Power Trackers for Wind Turbines", 35th Annual IEEE Power Electronics Specialists Conference, pp.2044-2049, 2004.

[3] A.M. Eltamaly, "Modeling of Wind Turbine Driving Permanent Magnet Generator with Maximum Power Tracking System", J. King Saud Univ, Vol. 19, Eng. Sci (2), pp. 223-237, Riyadh, 2007.

[4] S. Dieckerhoff, S. Bernet, D. Krug, "Power Loss-Oriented Evaluation of High Voltage IGBTs and Multilevel Converters în Transformerless Traction Applications", IEEE Trans on Power Electronics, vol. 20, No. 6, pp.1328-1336, 2005.

[5] L. Parvulescu, D. Floricau, M. Covrig, "Comparison between Three Level Rectifiers", U.P.B. Sci. Bull, Series C, vol.73, Iss.2, pp. 295-304, 2011.

[6] D. Floricau, E. Floricau, G. Gateau, "New Multilevel Converters With Coupled Inductors: Properties and Control", IEEE Transactions on Industrial Electronics, vol.58, no.12, pp.5344-5351, Dec. 2011.

[7] L. Parvulescu, D. Floricau, M. Covrig, "Comparison of Five Level Active Neutral Point Clamped Derived Converters", International Review of Electrical Engineering, IREE, vol.6, N.5, pp. 2100-2105, 2011.